Understanding the Role of Oxidation in Bonding of Aluminium Alloys

Guo Wu

St Cross College

Thesis submitted for the degree of

Doctor of Philosophy

Trinity Term 2014

ABSTRACT

Guo Wu D.Phil.
St Cross College Trinity Term 2014

Understanding the Role of Oxidation in Bonding of Aluminium Alloys

The main aim of this work is to study the bonding behaviour of Al alloys as a function of temperature, time and processing conditions from a perspective of oxidation so as to gain a comprehensive knowledge of the oxidation issues during processing and to design better bonding approaches for different alloy systems.

Two major parts of work have been carried out during the study: (a) the use of a stacking approach and a double pouring approach to potentially join two Al alloys and their effectiveness are assessed; and (b) a precise investigation of the oxidation mechanisms for Al-Cu and Al-Mg alloys using a combination of theoretical analysis and experimental characterization.

The project started with the use of a stacking approach to try to bond two stacked Al alloys. The stacked sample can be viewed as a bi-metal which has an oxide *bi-film* layer at the bond interface. It was found that the *bi-film* layer was a physical barrier preventing direct metallic bonding. How this *bi-film* layer evolves during the bonding process was then investigated.

The work then moved on to investigate the oxidation mechanisms of Al-Cu alloys and Al-Mg alloys in greater detail. The thermodynamics, kinetics of oxidation, chemistry and morphology of the oxide scale were particularly studied. Briefly speaking, in the case of the Al-Cu-O_2 system, the oxidation proceeds in the order of amorphous γ-Al_2O_3 - to - crystalline γ-Al_2O_3 - to - α-Al_2O_3; in the case of the Al-Mg-O_2 system, the oxidation proceeds as amorphous γ-Al_2O_3 to MgO to $MgAl_2O_4$ and the morphology of the oxide scale develops from a protective layer to a porously structured composite layer.

A double pouring approach was finally developed to bond Al and Al-5Cu but the method has still not been perfected due to the formation of *bi-film* defects along the bond interface. Induction melting, squeeze casting, and extrusion bonding were therefore studied as an attempt to reduce the harmful effect of *bi-film* defects. Although all of the approaches exhibit some limitations, they have potential for future development.

ACKNOWLEDGEMENTS

My deep and sincere thanks go to my supervisors Dr Keyna O'Reilly and Dr Marina Galano for their guidance and support throughout the project. They have not only provided me with endless encouragement and help, but also inspired me with their devotion in research and life. I learnt a lot from them.

I am thankful to members of the Department of Materials, in particular Gabriella Chapman for her patience and training in electron microscopes, Bob Lloyd for his help with the use of furnaces and his great humour, Laurie Walton for his help in the mechanical workshop, Trevor Knibbs for his support and assistance in facilities at Begbroke, Dr Alison Crossley and Dr Hugh Bishop for their guidance and assistance in XPS experiments, and Richard Turner for his help with my TGA experiments. I would also like to thank all other colleagues at Oxford. It has been a great pleasure to work with them. My thanks must go to, Nick, Stella, Iain, Kumar, Akash, Asad, Tahsina, and Jing for their encouragement, support and chats.

I thank Haibo, Sharon, Long, Qi, and Jun for their support and friendship. Meanwhile, I am very grateful to my ever-supportive teammates in the Oxford Chinese basketball team. They enriched my life here at Oxford. We worked hard, played hard and fought passionately for our dreams. We shared lots of great moments and memories. Basketball has become one thing that I couldn't live without. I must also thank my landlord Mrs Margaret Pinsent for her care and help during the time I stayed in her beautiful house in Park Town Oxford.

Finally, I would like to thank my parents and my fiancée Xia Jiang for their endless love, they have been giving me support and encouragement in every aspect of my life. They have influenced me in a way in which no one else could do.

Dedicated to my Mother

PREFACE

The work described in this thesis was carried out by the author in the Department of Materials, University of Oxford from October 2010 to June 2014, under the supervision of Dr. K. A. Q. O'Reilly and Dr. M. L. Galano. No part of this thesis has been previously submitted for a degree at this or any other university. The work of others has been freely drawn upon and is acknowledged accordingly in the text.

Some of the work described here has been presented in the following papers and presentations:

1. G. Wu, M. Galano and K. O'Reilly; "*Characterization of an Al/Al-5wt%Cu bond casted via a double-pouring approach*" Poster presentation - National Student Conference in Metallic Materials, Manchester, UK, 2012.

2. G. Wu, K. O'Reilly and M. Galano; "*Characterization of Casting Defects in Aluminium Alloys"*. Advanced Materials Research 430-432: 984-987, 2012.

3. G. Wu, M. Galano and K. O'Reilly; "*Interface Microstructure of a Double-poured Al/Al-5Cu Bimetallic Composite*". Poster presentation - The 19th International Conference on Composite Materials, Montreal, Canada, 2013.

TABLE OF CONTENTS

Chapter 1 Introduction

Chapter 2 Literature review

Chapter 3 Experimental details

Chapter 4 Processing studies: stacking approach

Chapter 5 Oxidation studies: the Al-Cu-O_2 system

Chapter 6 Oxidation studies: the Al-Mg-O_2 system

Chapter 7 Processing studies: double-pouring approach

Chapter 8 Conclusions and future development

Appendices

Figures and tables

CHAPTER 1

INTRODUCTION

1.1 Background

Aluminium and aluminium alloys have been ingeniously applied in various industry sectors, such as construction, energy, packaging, marine, aerospace and automotive [1]. Aluminium has a unique combination of attractive properties: aluminium is lightweight with a specific density of 2.70 g cm^{-3}, about a third that of steel (7.83 g cm^{-3}) [2], the continuous demand for lower energy consumption has made it an ideal candidate to substitute heavier metals in components [1, 2]; it has a thermal conductivity of 205.00 W m^{-1} K^{-1} which is around 3 times more than that of steel [1]; aluminium has excellent corrosion resistance, and can be easily cast and machined [1]; the strength of aluminium can be adapted to different applications by modifying the composition and microstructure of its alloys [3]; aluminium is 100% recyclable without loss of properties [4].

Some novel aluminium alloys and aluminium matrix composites have recently been drawing increasing attention due to their potential ability to cope with extreme conditions, such as elevated temperatures and high pressure. For example, Galano *et al*. [5-8] have developed some Al-based nanoquasicrystalline alloys which exhibit improved mechanical properties and thermal stability at high temperatures up to 450°C. A group of Al-Fe-Cr-based alloys containing a fourth alloying element (Ti, V, Nb or Ta) have been successfully produced either by melt-spinning [5, 7, 8] or by extrusion from gas-atomized powders [6, 7, 9, 10]. The alloys have a microstructure composed of ~100 nm quasi-spherical icosahedral quasicrystalline particles embedded in an α-Al matrix [7]. It has been shown that the quasicrystalline particles (consists of Al, Fe and Cr) usually decompose at approximately 300°C and the addition of the fourth alloying element results in an increase of the decomposition temperature and can stabilize the particles [5, 7, 9, 10]. As a result, the alloys exhibit improved mechanical properties at elevated temperatures compared with conventional Al

alloys [6]. For example, it was found that an $Al_{93}Fe_2Cr_2Ti_2$ nanoquasicrystalline alloy has a true ultimate tensile strength (UTS) around 420MPa at 350ºC, and the value is equivalent to more than 50% of the UTS measured at room temperature [6]. The materials have promising structural applications in the automotive industry. However, it may be difficult to scale up the alloys from laboratory to industrial applications via existing processing routes. Even if it were possible, the production cost can be very high. This disadvantage may potentially open up an idea to bond such materials to lower cost commercial aluminium alloys which can help reduce the manufacturing cost while the lightweight property of the component is still maintained. For example, the top surface of a piston head can be made from an Al-based nanoquasicrystalline alloy to withstand extreme conditions while the rest of the piston is made of a conventional Al alloy.

Of course, the bonding of aluminium alloys is not technologically straightforward. It is inferred from the literature that the main obstacle to bond aluminium alloys is the oxide layers formed at the bond interface: Al alloys can be readily oxidized to form protective oxide layers on surfaces, which prohibit metallic bonding at the interface and jeopardize the bond mechanically [11, 12]. The oxidation of aluminium alloys itself is a complex process. An in-depth study is required to determine the conditions under which different oxides may form and how they form. The developed know-how of the oxidation issue may in turn help predict the suitability of different bonding approaches for aluminium alloys and design appropriate bonding conditions.

The intention of the present work is to develop a systematic understanding of the role of oxidation in bonding of aluminium alloys under different bonding approaches, in particular casting related approaches. Two aluminium binary alloy systems, Al-Cu and Al-Mg, are used throughout the work. It is hoped that the knowledge gained through the oxidation studies could be further used to predict the oxidation behaviours of other systems and also to identify suitable bonding approaches for different alloys.

1.2 Outline of the thesis

The thesis contains two major parts of work: processing studies and oxidation studies. It starts with the description of a stacking approach which was used to bond aluminium alloys, and the analysis of the oxidation issue involved. Then the thesis moves on to discuss the oxidation mechanisms occurring in Al-Cu-O_2 and Al-Mg-O_2 systems, in terms of oxide formation thermodynamics, kinetics and oxide scale microstructures. The oxidation of aluminium alloys may be affected by a combination of factors, including oxidizing temperature, time, oxygen partial pressure, concentrations of alloying elements, etc. In the present work, how each factor influences the oxidation process is assessed both qualitatively and quantitatively. Finally, the thesis presents the study of some other bonding approaches and offers some suggestions on how to improve the processing parameters so as to obtain a reasonably good bond interface.

Specifically, in Chapter 2, the literature papers on the oxidation of Al alloys are reviewed and assessed. Chapter 2 also reviews the advantages and limitations of some existing bonding approaches for aluminium alloys. The experimental details are presented in Chapter 3. Chapter 4 deals with the characterization of the bonds produced using a stacking approach. Chapter 5 focuses on detailed oxidation studies of Al-Cu alloys. In parallel, Chapter 6 discusses the oxidation mechanism of Al-Mg alloys. A *double-pouring* approach is introduced in Chapter 7, together with a description of how the knowledge from previous oxidation studies can help tailor the processing conditions and make suggestions for improved bonding. The conclusions and suggestions for future development from the present work are given in Chapter 8.

1.3 References

[1] J. R. Davies, *Aluminium and aluminium alloys*: ASM international, 1993.

[2] W. Miller, L. Zhuang, J. Bottema, A. J. Wittebrood, P. De Smet, A. Haszler, and A. Vieregge, "Recent development in aluminium alloys for the automotive industry," *Materials Science and Engineering: A*, vol. 280, pp. 37-49, 2000.

[3] L. F. Mondolfo, *Aluminum alloys: Structure and properties* vol. 5: London Butterworths, 1976.

[4] J. S. Tenório and D. R. Espinosa, "Recycling of aluminum," *Handbook of Aluminum*, vol. 2, pp. 115-107, 2003.

[5] M. Galano, F. Audebert, B. Cantor, and I. Stone, "Structural characterisation and stability of new nanoquasicrystalline Al-based alloys," *Materials Science and Engineering: A*, vol. 375, pp. 1206-1211, 2004.

[6] M. Galano, F. Audebert, A. G. Escorial, I. C. Stone, and B. Cantor, "Nanoquasicrystalline Al-Fe-Cr-based alloys. Part II: Mechanical properties," *Acta Materialia*, vol. 57, pp. 5120-5130, 2009.

[7] M. Galano, F. Audebert, I. Stone, and B. Cantor, "Nanoquasicrystalline Al-Fe-Cr-based alloys. Part I: Phase transformations," *Acta Materialia*, vol. 57, pp. 5107-5119, 2009.

[8] M. Galano, F. Audebert, A. G. Escorial, I. C. Stone, and B. Cantor, "Nanoquasicrystalline Al-Fe-Cr-based alloys with high strength at elevated temperature," *Journal of Alloys and Compounds*, vol. 495, pp. 372-376, 2010.

[9] M. Galano, F. Audebert, I. Stone, and B. Cantor, "Effect of Nb on nanoquasicrystalline Al-based alloys," *Philosophical Magazine Letters*, vol. 88, pp. 269-278, 2008.

[10] F. Audebert, M. Galano, C. T. Rios, H. Kasama, M. Peres, C. Kiminami, W. Botta, and C. Bolfarini, "Nanoquasicrystalline Al-Fe-Cr-Nb alloys produced by powder metallurgy," *Journal of Alloys and Compounds*, vol. 577, pp. 650-657, 2013.

[11] A. A. Shirzadi, H. Assadi, and E. R. Wallach, "Interface evolution and bond strength when diffusion bonding materials with stable oxide films," *Surface and Interface Analysis*, vol. 31, pp. 609-618, 2001.

[12] N. F. Kazakov, *Diffusion bonding of materials*: Moscow Pergamon Press, 1985.

CHAPTER 2

LITERATURE REVIEW

2.1 Introduction

In metallurgy, oxidation usually refers to the chemical reaction process between the surface of a metal and the oxygen in the environment [1, 2]. The surface properties of a metal can be greatly affected by the oxide skin [3]. In the world of aluminium metallurgy, there are probably **four** main reasons why researchers are interested in oxidation: some researchers [4-7] are interested in aluminium anodising, which is an electrochemical technique used to form uniformly structured oxide layers on Al alloys in a controlled manner, so as to improve the corrosion resistance [8]; some researchers [9-11] study the oxidation of Al alloys in order to understand the potency of metal oxides as heterogeneous nucleation substrates for α-Al phase [10] and intermetallic phases [12, 13] during solidification; recently, Campbell [13-15] and Griffiths *et al*. [16-19] are increasingly interested in oxide *bi-film* [13] defects in Al castings and it has been shown that the mechanical properties of Al castings is somewhat related to the quantity of oxide *bi-film* defects [20-22]; and some researchers [23-28] are interested in the production of Al_2O_3/Al composites by directed melt oxidation of Al alloys. Different from the above mentioned reasons, in the present work, the oxidation studies are performed as an attempt to understand the effect of oxide formation on metallic bonding at the interface between two pieces of Al metals. This chapter consists of two parts: section 2.2 reviews the oxidation of Al alloys while section 2.3 reviews some of the existing approaches for bonding of aluminium alloys.

2.2 The oxidation issue

This section reviews the literature related to oxidation and highlights some key observations from literature sources and some questions which have not been fully addressed. Specifically, section 2.2.1 gives details of the fundamental science of oxidation thermodynamics and kinetics. Section

2.2.2 gives details of the literature related to oxidation of pure Al. Section 2.2.3 discusses the effects of different alloying elements on the oxidation behaviour of Al. The rest of the section reviews the recent developments of double oxide film defects, or *bi-film* defects [13], which is a technologically significant concept to help understand many casting related phenomena in the world of aluminium metallurgy.

2.2.1 Fundamentals of oxidation

2.2.1.1 Thermodynamics

A comprehensive understanding of the oxidation issue requires a determination of whether or not a component in the material reacts with oxygen and also the stability of the oxidation products [29]. The oxidation process is often complex as multiple components may be involved and react with oxygen to form different oxides [30]. Thermodynamic analysis is an important tool which enables us to ascertain: firstly, which products are possible under specific conditions; secondly, whether evaporation and condensation of a particular component will occur or not [31]; and thirdly, under which conditions the products are thermodynamically stable [29]. This section reviews some of the important thermodynamic concepts which are frequently mentioned in the literature.

The criterion used to determine whether an oxidation reaction can occur or not at a given temperature and pressure is the second law of thermodynamics [32, 33], usually in terms of Gibbs free energy [34]. The Gibbs free energy of a system or a species at a temperature T is given by

$$G = H - TS \tag{2.1}$$

Where H is the enthalpy and S is the entropy of the species [34]. Gibbs free energy of a species is an extensive variable, the value of which depends on the quantity of the species [34].

$$xM + yO_2 \rightarrow M_xO_{2y} \tag{2.2}$$

Taking the above metal-oxygen reaction as an example (x moles of metal M reacting with y moles

of oxygen to produce one mole of M_xO_{2y}), the amount of reduction in Gibbs free energy ΔG^o [29] (also quoted as *driving force* [35, 36]) of this reaction is calculated by

$$\Delta G^\circ = G_{M_xO_{2y}} - x \cdot G_M - y \cdot G_{O_2} \tag{2.3}$$

In many cases, the reactants are in solution and/or mixture with other species, so their values of chemical activity (the ability to participate in the reaction [31]) are reduced. This affects the free energy change (driving force) for the reaction. The driving force ΔG of the reaction is then expressed as in **Equation 2.4**,

$$\Delta G = \Delta G^\circ + RT\left(\frac{a_{M_xO_{2y}}}{a_M^x \cdot a_{O_2}^y}\right) \tag{2.4}$$

where a is the chemical activity [31, 37] of a species. The chemical activity is defined by

$$a_i = p_i / p_i^\circ \tag{2.5}$$

where p_i is either the vapour pressure of the species i over its condensed phase or its partial pressure in a gas phase and p_i^o is the same quantity corresponding to the standard state of i [31, 37]. According to the second law of thermodynamics [32, 33, 38]: if $\Delta G < 0$, the reaction may proceed spontaneously; if $\Delta G > 0$, the reaction may only proceed with extra external energy to compensate the increment of free energy; if $\Delta G = 0$, the reaction is at equilibrium [37], in this case, **Equation 2.4** becomes

$$\Delta G^\circ = -RT\left(\frac{a_{M_xO_{2y}}}{a_M^x \cdot a_{O_2}^y}\right) \tag{2.6}$$

Figure 2.1 shows the famous *Ellingham diagram* [39], which can be constructed based on **Equations 2.3** and **2.6**. The diagram compiles the standard Gibbs free energy of different oxides as a function of temperature and it can be used to compare the thermodynamic tendencies of different metal-oxygen reactions. In the extractive metallurgy industry, it is useful in predicting the conditions under which an ore may be reduced to its metal [40] and also predicting the stability of different oxides [39]. Similarly, in the present work, thermodynamics calculations are performed to understand the Al-Cu-O_2 and Al-Mg-O_2 systems. Details will be given in Chapters

5 and 6.

2.2.1.2 Kinetics

The oxide growth kinetics are usually graphically represented by a weight gain versus time curve [29]. Several common growth kinetic equations have been proposed: linear, parabolic, power law, logarithmic and inverse-logarithmic [41]. However, these behaviours are quite theoretical and a metal usually displays a more complex oxide growth behaviour in reality. The rate at which a metal oxidises depends on many factors, such as temperature, time, composition, pressure, surface area, crystal orientation, stability of the oxide film, etc [1, 30, 42]. The effects of these factors on the kinetics of oxidation of metals and alloys were first reviewed by Gulbransen [42].

(a) Continuous oxide scale

Most of the existing theories of oxide growth kinetics are based on the assumption that the oxide film is coherent, homogeneous and adherent to the metal substrate with a uniform thickness [42]. Cabrera and Mott [43] first proposed a theory to explain the experimentally observed logarithmic and inverse-logarithmic oxidation rates for some metals, including Al, Fe and Cu. As illustrated in **Figure 2.2**, the Cabrera-Mott theory states that a thin (usually less than 5nm) oxide film grows by the migration of metal cations under an electric field (usually 1 or 2 volts) across the film [43, 44]. Fehlner and Mott [45, 46] then modified the theory mathematically to account for the observed migration of oxygen anions during oxide growth. It was then suggested by Wagner [47, 48] that the Cabrera-Mott theory may not be applicable for thicker (usually more than 0.6 μm) oxide films or high temperature oxidation. Wagner proposed that oxide growth at high temperatures is controlled by the diffusion of ions and the growth rate is parabolic [48]. However, for the oxide growth kinetics between the region (in terms of oxide film thickness) of the Cabrera-Mott theory and Wagner's theory, there is currently no well-agreed model which can unify the two theories and interpret the oxidation behaviours of most metals. In this region, Jelski *et al*. [49]

reported a parabolic law for the oxidation of vanadium; Monceau *et al*. [50] also found a parabolic growth rate for the oxidation of nickel; however, the work by Xu *et al*. [51] has mathematically demonstrated that it should be a logarithmic law. It can be seen that the studies of the oxidation kinetics in this transition region are not in good agreement in the literature.

(b) Discontinuous oxide scale

Deviations from ideal behaviour have been found experimentally in the growth rates of some important metal oxides, such as Cr_2O_3 [52] and Al_2O_3 [41]. Several reasons have been proposed, including impurities, multi-layer growth and polymorphism of the oxides [30, 53]. As suggested by Atkinson [41], the oxidation rate is usually measured to be faster than the ideal behaviour and this is because the oxide film is not always coherent, adherent and uniform. During oxidation, the build-up of stress within the oxide scale may lead to the loss of protective properties. The stress may cause cracks and induce rupture [29, 30, 54, 55], and the oxide scale then becomes discontinuously structured, which complicates the overall oxidation kinetics [56]. Stress could arise from different sources. Firstly, the Pilling-Bedworth Ratio (PBR) [57] is a parameter equal to the ratio between the volume of the oxide and the volume of the metal and it is used to predict the types of stress generated at the metal/oxide interface: compressive stress is expected for systems with PBR>1 (such as ZnO, ZrO_2, Fe_2O_3, etc) while tensile stress is expected for systems with PBR<1 (such as MgO, CaO, etc). Secondly, for the oxidation of some polycrystalline metals, such as Ni [50, 58], the difference in oxide growth rates between neighbouring grains and grain boundaries may help build up stress [58, 59]. Interestingly, it has been shown that for the oxidation of some Fe-Cr alloys, the preferential formation of Cr_2O_3 layer on the surface may lead to the depletion of Cr in the bulk and this could trigger the ferrite-to-austenite transformation, bringing significant stress into the oxide scale [60, 61]. Meanwhile, it was also suggested that the oxide crystal structure transformation, such as tetragonal ZrO_2 to monoclinic ZrO_2 [62] and γ-Al_2O_3 to α-Al_2O_3 [63], may even lead to the mechanical breakdown of the oxide scale due to significant

volume contraction.

2.2.2 Oxidation of Al

In this section, the literature related to the oxidation of pure Al is reviewed. It is felt that the progress towards the development of oxidation mechanisms for solid and liquid Al is somewhat slow, probably due to the inconsistencies in results reported by different researchers. Some extrinsic factors, such as impurities in the oxide and oxidising environment, can differ significantly across the literature, which makes it unlikely that a collectively exhaustive model to reconcile the experimental results observed can be developed.

2.2.2.1 Low temperature oxidation

It has been shown that clean Al surfaces will be rapidly covered with a thin layer of amorphous aluminium oxide when exposed to an oxygen-containing environment at temperatures below 300ºC [64-67]. The growth mechanism of the amorphous oxide layer is still unknown. But it is suggested by Gronlund [68, 69] that the formation of the amorphous layer may contain three stages: oxygen atoms bombard onto the free surface and form bonds with Al atoms through both physisorption and chemisorption [70, 71]; individual oxide islands nucleate and grow laterally to cover the whole surface and form a continuous layer; the layer then grows to a certain thickness. The process is illustrated in **Figure 2.3**.

The thickness of the naturally formed amorphous aluminium oxide layer has been found to be limited. Hart [72] first reported that a limit of 3 nm thickness was reached after several days exposure to dry oxygen by studying the oxidation of an electrolytically polished Al single crystal. Hart also found an increased limit of up to 4 nm of the oxide layer formed in humid air and attributed the observation to the hydration of aluminium oxide which could potentially increase the mobility of Al^{3+} ions during oxide growth [72, 73]. Similarly, Olefjord and Nylund [74, 75]

reported a 1.5 nm thick oxide film after 5 h exposure to air and a growth of only 0.1 nm after a week. Jeurgen *et al*. [66] also found that the oxide layer grown on a bare Al substrate is still entirely amorphous with a thickness of 2 nm after 15 h of oxidation at a partial oxygen pressure of 1.33×10^{-4} Pa. Recently, Reichel *et al*. [76, 77] addressed the issue using a theoretical analysis based on thermodynamics. They suggested that the amorphous oxide film can be stable up to a critical thickness without crystallization, due to the interplay between **the sum** of the surface energy of the oxide and the interfacial energy between the oxide and Al (amorphous < crystalline), and **the bulk** Gibbs free energy of the oxide (amorphous > crystalline).

2.2.2.2 High temperature oxidation

It is inferred from the literature that the oxidation behaviour of Al at high temperatures (300-650ºC) differs from that at lower temperatures and the agreement on the preferential nucleation of crystalline oxides at the metal/oxide interface is quite strong, but the mechanisms proposed are still a little controversial.

Aylmore *et al*. [78] studied the oxidation of a high purity Al in dry oxygen in the temperature range 400-650ºC. Based on their observations, the authors proposed that the oxidation progress consists of three distinctive stages: the first stage is a fast, but gradually decreasing rate stage due to the thickening of the initially formed amorphous layer; it is then followed by a linear stage due to the nucleation of crystalline oxides at the metal/oxide interface with the crystalline oxides growing laterally until they impinge on each other; the final parabolic growth stage is controlled by the lattice diffusion of oxygen through a duplex layer consisting of an amorphous oxide layer and a crystalline oxide layer. The kinetic process is illustrated schematically in **Figure 2.4**.

The duplex layer model was further evidenced by Smeltzer [79] who additionally suggested that the crystalline layer has higher oxygen diffusion resistance than the amorphous layer and reported

an oxygen diffusion activation energy of 155.64 kJ mol^{-1} [79, 80], which is smaller than the value of 216 kJ mol^{-1} reported by Aylmore *et al*. [78], and this may indicate the existence of easy diffusion paths for oxygen within the duplex oxide scale. Similar results were reported by Dignam and Fawcett [81].

However, Beck *et al*. [82] reported a different result using nominally the same experimental conditions as described by Aylmore *et al*. [78]. They observed that the crystalline oxides grow under a complex law instead of a simple parabolic law. They also proposed that the crystalline oxides grow into the metal instead of growing laterally to form a duplex oxide layer. Doherty and Davis [83] then used TEM to characterize the oxide scale formed on single crystal Al at 500°C in air. They found that plate-like crystalline oxides grow at the metal/oxide interface and the crystalline oxides were identified to be face-centred cubic with a lattice parameter of 0.79 nm, i.e. γ-Al_2O_3. In addition, they also observed that the crystalline oxides grow into the metal with an epitaxial relationship (110) [110] γ-Al_2O_3 // (111) [110] Al. This observation is consistent with the model proposed by Beck *et al*. [82].

Eldridge *et al*. [84] later found that crystalline γ-Al_2O_3 oxides could both grow laterally, and inwardly into the metal, depending on crystal orientations of the metal substrate. Using an ^{18}O/SIMS technique (tracer marking), Eldridge *et al*. [84] also suggested that the growth of crystalline γ-Al_2O_3 oxides at temperatures above 500°C may be controlled by the inward diffusion of oxygen and proposed that there are some easy paths for inward diffusion of oxygen within the oxide scale. As shown in **Figure 2.5**, Shimizu *et al*. [85, 86] found that γ-Al_2O_3 crystals preferentially nucleated at ridge-like sites and suggested that the easy diffusion paths for oxygen proposed by Eldridge *et al*. [84] could be the microcracks generated at these ridges due to stress concentration.

2.2.2.3 Liquid state oxidation

It can be inferred from the literature that mechanism of oxidation in the liquid state may be significantly different from the solid state oxidation mechanisms discussed above. Unfortunately, there is currently no well-agreed theory. Oxidation of molten metals can be complex for several reasons: for example, there may be enhanced transport of metallic species to the surface [87], which could potentially change the oxidation thermodynamics; and the melt surface is also subject to a certain level of disturbance [88], which could potentially disrupt the scale morphology and affect the kinetics to an unknown extent.

Sleppy [89] first studied the oxidation of molten high purity Al in dry oxygen in the temperature range 660-850°C and only observed the presence of amorphous alumina and crystalline eta alumina (ε-Al_2O_3) [90]. The author also found that the oxidation kinetics were best described by a logarithmic law at temperatures below 750°C and by a parabolic law at temperatures above 750°C. It was suggested in that paper that parabolic growth is controlled by the outward diffusion of Al ions through the oxide film to the oxygen/oxide interface.

Impey *et al*. [63] later reported a study of the oxidation of molten commercially pure Al at 750°C in dry and humid atmospheres. The authors found that the oxidation in dry air initially proceeded quickly and then gradually decreased due to the formation of a protective crystalline γ-Al_2O_3 layer. The oxidation then accelerated again after 15 h due to the formation of a less protective α-Al_2O_3 structure at the expense of the γ-Al_2O_3 and the formation of α-Al_2O_3 is associated with a 24% reduction in oxide volume. Similar kinetic behaviour was observed recently by Hinton *et al*. [11]. Interestingly, first of all, different from the solid state oxidation mechanism discussed in section 2.2.2.2, Impey *et al*. [63, 91] proposed that the crystalline γ-Al_2O_3 oxides nucleate within the amorphous layer and the amorphous layer eventually transforms into a continuous crystalline layer; secondly, the authors suggested that the presence of humidity could stabilize the crystalline

layer and delay the γ-Al_2O_3 to α-Al_2O_3 transformation. It is implied from the work by Field *et al*. [92] that this may be sensible as the presence of hydroxyl ions could increase the strength of the oxide layer and thus reduce the tendency to crack. Kim [93] recently characterized the oxides formed on super purity Al at 950°C in air after 2 h oxidation time. The author found that the oxide mainly consisted of α-Al_2O_3 and proposed an oxidation mechanism for liquid state oxidation of Al similar to that described by Impey *et al*. [63].

Bergsmark *et al*. [94] further studied the oxidation of molten commercially pure Al in oxygen at different partial pressures in the temperature range 800-950°C. The authors only observed the presence of α-Al_2O_3 in the oxide scales formed above 850°C and found that the oxide scales were porous in nature with some entrapped Al metal.

Contrary to the mechanism proposed by Impey *et al*. [63], Bergsmark *et al*. [94] found the oxidation growth rate in a humid atmosphere was faster than the oxidation in dry air. The authors further suggested that the oxidation kinetics cannot be described by simple equations. On the other hand, Akagwu *et al*. [95] showed that the oxidation of molten Al may be described by a linear growth law at 950°C in air; similar results were given by Damoah *et al*. [96].

Overall, the liquid state oxidation of Al is far less studied than the solid state oxidation of Al. The oxidation of molten Al is undoubtedly an interesting topic. For example, the quality of cast products may be significantly affected by the oxide impurities in the melt [20, 21]; oxides may act as nucleation substrates during solidification and can potentially be used for grain refinement [9, 97]. Considering the objectives of the present work, there is also a strong scientific interest in determining the exact mechanism of liquid state oxidation of Al in order to fully understand the feasibility of using casting approaches to bond Al alloys.

2.2.3 Impact of alloying elements

It can be inferred from the literature that alloying elements may not only change the rate of oxidation (e.g. Mg [98], Cu [99-101], Fe [55, 102], Si [26, 103], Zn [104, 105], Ti [106, 107], etc) or oxide strength (e.g. Mg [91, 108, 109], Si [108], etc), but also incorporate their own oxides in the oxide scale (e.g. Mg [110], Cr [55, 111], etc). In sections 2.2.3.1 and 2.2.3.2, the effects of Cu and Mg are reviewed in detail.

2.2.3.1 Copper

Cu is the main alloying element of 2xxx series Al alloys [112]. The influence of Cu content on high temperature solid state oxidation of Al was first studied by Dignam [113] who found that an addition of 1.5wt% Cu to Al increased the thickening rate of the amorphous layer in the temperature range 250-450ºC. Later, Brock and Pryor [99, 100] studied the oxidation of some Al-Cu binary alloys in the temperature range 475-575 ºC in dry oxygen. As shown in **Figure 2.6**, the authors found the thickening rate of the amorphous layer obeys a parabolic law and increased as Cu content increased, which is consistent with the work by Dignam [113]. Interestingly, duplex films consisting of amorphous aluminium oxide and crystalline γ-Al_2O_3 were also observed in their work, consistent with the previously discussed (section 2.2.2.2) duplex layer model proposed by Aylmore *et al*. [78] for pure Al. In addition, Brock and Pryor [100] found that the crystalline γ-Al_2O_3 oxides formed on Al-Cu alloys have better dielectric properties than those formed on pure Al, probably due to the doping effect of Cu. However, the detailed mechanism was not specified.

The effect of Cu on liquid state oxidation of Al has also not been well addressed in the literature. The only work reported which may be relevant is a recent investigation carried out by Hinton *et al*. [11] who found the oxide growth rate of an molten Al-4wt%Cu alloy at 750ºC was slower than that of Al over a period of 7 h and only aluminium oxide was detected in the oxide scale.

2.2.3.2 Magnesium

Mg is the main alloying element of 5xxx series Al alloys [112]. Mg has a higher affinity for oxygen than Al [114]. As suggested by the literature, the formation of MgO [92, 115] or $MgAl_2O_4$ [116], or both [117, 118], are often observed in the oxide scales formed on Al-Mg alloys. Kinetically, the various oxide growth laws for long and short oxidation times reported by researchers [23, 98, 119-122] may imply that there is no generally agreed rate law and that the oxidation of Al-Mg alloys may be controlled by a mixture of mechanisms instead of a single mechanism.

In a study which set out to investigate the solid state oxidation kinetics of an Al-4.2Mg alloy under the environment of dry 20% O_2/Ar in the temperature range 520-575ºC, Field *et al*. [92] only observed crystalline MgO after 10 h oxidation. Conversely, under similar experimental conditions, Bahadur [116] found using X-ray diffraction, that $MgAl_2O_4$ was the only oxide formed on Al-4.5Mg after oxidation at 500ºC for 8 h. Shimizu *et al*. [65] later carried out a characterization of the oxide scale formed on an Al-0.5Mg alloy at 450-550ºC after 2 h in dry air. The authors observed fine MgO crystals together with randomly oriented $MgAl_2O_4$ nanoparticles, as well as the degradation of the initially formed amorphous aluminium oxide, implying a possible reduction mechanism whereby MgO or $MgAl_2O_4$ forms at the expense of amorphous aluminium oxide. As found by Ritchie *et al*. [117] in an earlier study on the solid state oxidation of an Al-1.2Mg alloy, $MgAl_2O_4$ can also form at the expense of MgO. However, the argument from a thermodynamics perspective made by Ritchie *et al*. [117] may be questionable, as they disregarded the effect of the activities of alloy components and did not take the specific experimental conditions into consideration when comparing the Gibbs free energy change between different oxidation reactions.

As for liquid state oxidation of Al-Mg alloys, the issue has not been properly addressed. Thiele [123] first observed the presence of swollen black oxide films formed on liquid Al-Mg alloys in

air (3-20% Mg) at 800ºC, the amount of which increased as Mg content increased. Cochran *et al*. [124] later identified $MgAl_2O_4$ to be the essential component of these oxide films while Belitskus [125] only identified crystalline MgO. Haginoya and Fukusako [118] found the oxides produced on Al-Mg (2-12%) at temperatures 650-900ºC in dry air consist of both MgO and $MgAl_2O_4$, as also observed in the work carried out by Impey *et al*. [63]. In addition, Haginoya and Fukusako also found an amorphous substance within the oxide scale and hypothesized that it is the amorphous layer formed during initial stages of oxidation. Belitskus [125] suggested that it may be a protective amorphous MgO layer and this view was also supported by Silvia [126]. Conversely, Impey *et al*. [63, 91] argued that the initially formed amorphous layer has the amorphous γ-Al_2O_3 structure, which may react with MgO to form $MgAl_2O_4$ in the later stages of oxidation.

Overall, it can be concluded that previous research findings into the oxidation mechanism of Al-Mg alloys have been somewhat inconsistent and the oxidation of Al-Mg alloys could be the result of multiple factors, including the Mg composition in the oxide scale, oxidizing temperature, time, oxygen partial pressure, etc. There are still some ambiguities and a lack of information within the literature on the MgO and $MgAl_2O_4$ growth mechanisms. There is a need for further studies and the present work has been undertaken to learn more about this topic.

2.2.4 Oxide *bi-film* defects in castings

2.2.4.1 Formation

Campbell [13, 15, 88] first proposed the concept of double oxide film defects, or oxide *bi-film* defects. As illustrated in **Figure 2.7**, aluminium and its alloys rapidly form an oxide layer on their top surface. Due to surface turbulence, the surface oxide film may fold on itself and the opposing dry oxide surfaces come into contact with entrapped gas from the local atmosphere. This type of folded oxide film defect is termed a double-oxide film defect or *bi-film* defect. **Figure 2.8** is a pair

of SE images showing the *butterfly-wing* like symmetric pattern of the split oxide *bi-film* halves observed in an Al-11Si-0.6Fe alloy [13].

Once the *bi-film* defect is entrained or submerged in the melt, it acts like a crack within the metal, deteriorating the mechanical properties [13, 88]. In an investigation into the relationship between *bi-film* defects and mechanical properties of Al alloy castings, Dispinar and Campbell [22] developed a new quantifiable index called the "*bi-film* index" to assess the quality of castings by measuring both the lengths and number of *bi-film* defects as observed in the microstructural section of a reduced pressure test (RPT) [127-129] sample. The authors suggested that the ductility of castings increases as the *bi-film* index decreases.

Besides, it is indicated that entrained oxide *bi-film* defects may also act as initiation sites for the formation of hydrogen pores and Fe-rich intermetallic phases [13], potentially further reducing the quality of castings. The harmful effects of *bi-film* defects on properties of Al alloy castings have gradually been recognized, and some researchers have started to investigate the possibility of designing new casting running systems to minimize the melt turbulence and to avoid *bi-film* defects [130-132].

2.2.4.2 Healing

It is usually the case that a certain amount of gas is trapped between the two halves of a *bi-film* pocket [88]. Nyahumwa *et al*. [133] suggested that the air inside a double oxide film defect might be gradually consumed by reaction with the surrounding melt and predicted that the formation of aluminium nitride (AlN) was likely once the oxygen was consumed. Later in an experimental study which set out to determine the history of the trapped air bubble in a liquid Al, Raiszadeh and Griffiths [19] observed that oxygen reacted to form Al_2O_3 first, and then nitrogen reacted to form AlN. Specifically, they found that an AlN layer (consists of islands of fine AlN) has formed

on top of an Al_2O_3 layer. This is in agreement with the hypothesis stated by Nyahumwa *et al*. [133]. The authors have also suggested that the reaction sequence (Al_2O_3 first, AlN second) may be due to the difference in free energy of formation between Al_2O_3 (-907.55 kJ mol^{-1} O_2) and AlN (-423.60 kJ mol^{-1} N_2) [19, 134]. Based on thermodynamics, it can be inferred that the AlN formation from air would occur presumably after all of the oxygen is consumed.

Interestingly, it was later noted in the work by El-sayed *et al*. [135] that the consumption rate of oxygen and nitrogen depends on the type of oxide forming the *bi-film* defects, with MgO showing the fastest rate, Al_2O_3 second, and $MgAl_2O_4$ the slowest. During the process of internal gas consumption, it is suggested by Raiszadeh and Griffiths [17, 19, 136] that the sides of the double oxide film defect may bond together to some degree, as also implied from the work by Nyahumwa *et al*. [133, 137].

Aryafar *et al*. [138] studied the healing of a large double oxide film defect by stacking two A356 Al alloy billets together in the liquid state and investigating the bonding after different isothermal holding times. They found that the degree of bonding increased as holding time increased and bonding particularly occurred after the oxygen and nitrogen within the *bi-film* layer had been consumed. Similarly, Bakhtiarani and Raiszadeh [139] studied the healing of a large double oxide film defect by stacking two commercial purity Al billets together under the same conditions used by Aryafar *et al*. [138]. They also found that a complete bond was only achieved when the oxygen and nitrogen between the two oxide layers were fully consumed. In addition, the authors proposed that the observed cracks in the oxide layers, which may have been due to the transformation of γ-Al_2O_3 to α-Al_2O_3, might also contribute to the bonding by allowing the liquid Al to come into contact with the entrapped oxygen and nitrogen, so facilitating the gas consumption.

Based on the work by Raiszadeh and Griffiths [19], Campbell [13] added that the application of

pressure to the casting metal prior to solidification could potentially accelerate the healing process. Unfortunately, little work has been reported on this topic. But as implied by the mechanism of hot isostatic pressing (HIPing) [140], it is expected that the applied pressure may help to disrupt the integrity of the oxide films and allow more contact area between the opposing oxide films and therefore diffusion bonding [141] may occur.

To conclude, the theory of entrained *bi-film* defects introduces a new way of thinking about some issues related to foundry practice and the mechanical properties of castings. As commented by Knott *et al*. [142], the effects of entrained *bi-film* defects on mechanical properties of castings may be limited for some other alloy systems. But in any case, the concept has been considered to be very reliable, based on the existing results in the literature so far.

2.3 Bonding of aluminium alloys

Components which are designed for high temperatures, stress, or corrosion resistant applications are mostly produced from one homogeneous Al alloy [143], the microstructure of which is usually tailored to cope with the extremes of working conditions. However, it may sometimes be the case that only a small region of the component will experience the extremes, while the rest is less affected. For example, the heads of Al-Si piston alloys are usually heat treated under a rigorous procedure in their entirety to produce the desired microstructure [144], but it is suggested that the main body of the piston component may undergo a limited degree of stress and thermal attack compared to the top surface of the piston [145, 146]. This may open up an idea to produce a component consisting of different functional parts bonded together, in an attempt to potentially reduce manufacturing cost and make the best of materials. This section outlines the current research into the bonding of aluminium alloys and briefly reviews the advantages and limitations of some frequently used approaches.

2.3.1 Brazing

Brazing is a reliable and economical joining technique which provides a bond between two aluminium alloys using a brazing *filler metal* [147]. As defined by the American Welding Society [148], the working temperature for brazing is above 426ºC, below which the process is defined as *soldering*, and the melting temperature of the filler metal should be slightly below that of any parent metal. Distinguished from welding, brazing only involves the melting of *filler metal* while the parent metal does not melt [147, 149].

The brazing *filler metal* is usually a binary Al-Si alloy (7-13%) with a melting temperature around 575-615ºC [150]. At a properly designed brazing temperature, the molten filler wets the surfaces of the parts to be joined by capillary action [151] and the wetting leads to interatomic contact between the filler and the parent metals, forming a permanent metallic bond between the two parent metals [147].

The advantages of brazing include: it is useful for joining thin walled parts and suitable for large area joints [152, 153]; minimal distortion of the parent materials occurs [147]; it provides a way to bond aluminium alloys to other dissimilar materials such as steel [154], Ti alloys [155] and even ceramics [156]; it can be potentially developed into a mass production method [152].

However, brazing has some limitations. First of all, brazing of aluminium alloys is limited by the availability of suitable filler metals [152]. For example, the Al-Si alloys containing Cu cannot be used as filler metals and parent metals, due to their low liquidus/solidus temperature and the preferential formation of brittle Al-Cu intermetallic compounds [157], which may greatly deteriorate the ductility of both the filler and the parent metals [153, 157-159]; the Al-Si alloys containing Mg are also not brazable due to the enhanced oxide formation and the reduced wettability [147, 150]. Although Germanium [160] and Gallium [161] have proven to be very

useful, but their application is restricted due to the expensive price.

Secondly, the oxidation of Al alloys has to be properly controlled in a brazing process. Researchers have tried to use fluxes [162] to disrupt the initially formed oxide prior to brazing, but the residual flux can significantly reduce the corrosion resistance of brazed joints [163]. In addition, the interim period between oxide removal and brazing must be kept as short as possible, in order to minimize the oxide built-up. Although the use of vacuum brazing or brazing under inert gases may reduce the influence of oxidation [153], the approaches are not practically feasible or economically beneficial for industry.

2.3.2 Friction stir welding

Friction stir welding (FSW) was first invented by *the Welding Institute* (TWI) [164, 165]. As shown in **Figure 2.9**, FSW is a solid state welding method which joins two plate materials by using a rotating tool to generate frictional heat and plastic deformation within the weld zone [166]. It has been shown that within the weld, the rise of temperature (usually around 400ºC) [167] and the intense plastic deformation could result in significant microstructural change [168, 169] and the incorporation of entrained defects [170, 171]. So processing parameters, such as tool traverse speed, rotation speed, tool geometry and tool axial force, must be carefully controlled [164, 166, 172, 173].

It can be seen from the literature that FSW has already been applied to all the major commercial Al alloys, including 2xxx series [174, 175], 5xxx series [176], 6xxx series [169, 177] and 7xxx series [178, 179] Al alloys. FSW of Al alloys has some remarkable advantages over conventional welding methods: it has the absence of melting-related defects and the absence of *filler*-induced problems [166, 180]; it does not rely on specialised welding skills and the process is automated; the strength of the weld can be maintained up to 80% of the parent material [180]. However, as a

fully mechanised technique, FSW is not suitable for joining aluminium alloys with complex shapes [180]; the processing/microstructure relationship has not been comprehensively addressed in the literature; and future work may be needed, particularly to understand how the surface oxides are disrupted and redistributed [181] within the weld zone in a FSW process.

2.3.3 Transient liquid phase bonding

Transient liquid phase (TLP) bonding is a method which uses an interlayer between the surfaces of two components to be joined [182]. The melting temperature of the interlayer is usually lower than that of the parent materials, resulting in the formation of a liquid interlayer once the entire assembly exceeds that temperature [183]. The liquid can then fills the gaps caused by any unevenness of the two surfaces. The assembly is usually isothermally held for a period of time prior to cooling [182], in effect, it is an extended brazing process. Inter-diffusion then occurs between the interlayer and the parent materials [184]. Diffusion may change the composition profile in the contacting regions and result in a widening of the liquid layer [182, 183]. Alternatively, instead of melting itself, the interlayer may react with parent metals to form eutectic phases with lower melting points and this may also induce the melt-back of parent metals [182, 183, 185]. As an example, for joining two Al alloys, a thin Cu layer of a few μm is normally chosen so as to form Al-Cu eutectic liquid at the bond interface [182, 186].

It has been shown that the liquid interlayer can disrupt the oxide films formed on parent metals to some extent [186]. But the planar bond interface which results from equilibrium solidification [182, 183] may still act as a preferential crack propagation path once the assembly is subject to externally applied stresses, in particular shear stresses [187]. An example is present in **Figure 2.10**, which clearly shows a planar bond interface morphology between a 7075 Al alloy and a Ti-6Al-4V alloy produced by TLP using a 22 μm thick Cu interlayer [188]. Recently, Shirzadi and Wallace [189-192] have developed a similar TLP method in which a temperature gradient is

applied across the assembly during solidification of the liquid interlayer, as briefly illustrated in **Figure 2.11**. According to their theory, the use of a temperature gradient produces a non-planar bond interface morphology, providing improved mechanical keying and a better distribution of oxides. It was recommended by Shirzadi and Wallace [190-192] that the magnitude of the temperature gradient should not be large enough to induce dendritic solidification, the associated detrimental effects of which may exceed the benefits.

The advantages of TLP include: it may offer an alternative bonding method for metallic materials which cannot be produced via conventional welding routes [183]; the liquid flow under the influence of capillary forces [183] may eliminate pores within the bond zone without the application of external pressure. TLP also has a few drawbacks: TLP may only be suitable for components with flat surfaces to be joined; unlike brazing, it may destroy the specifically designed microstructure of the parent material by the induced melt-back [185]; brittle intermetallic phases may form along the bond interface during a TLP process in some systems [184]. However, the TLP technique is still promising and the scope of TLP has not yet been fully developed. More experiments are encouraged to identify useful interlayers or systems amenable to TLP.

2.3.4 Casting approaches

From previous sections, it can be inferred that the existing approaches are not suitable for joining Al alloys with complex shapes or to produce near-net shape bonded components. The idea of casting may potentially solve this issue. Unfortunately, little work has been published on the feasibility of any casting-based technique. An interesting technique called *cast-decant-cast* (CDC) which may be relevant here, was developed by University College Dublin [193]. The CDC method involves the casting of two alloys together. During a typical CDC process, as shown in **Figure 2.12**, the first alloy is pumped in to fill the mould but is only allowed to solidify and form a solid skin around the internal surface of the mould before it is decanted, the second alloy is pumped in

to fill the remainder of the mould [194]. The second alloy is usually superheated to allow a slight melt-back of the first alloy and to facilitate the metallic bonding [195]

Similarly, Durrant *et al*. [196] developed a squeeze casting method to incorporate a mild steel inserting to an Al-Si alloy, as shown in **Figure 2.13**. The mild steel insert is normally coated with titanium before casting, resulting in an improved mechanical keying with the Al matrix [196]. Similar methods may have been used by commercial manufacturers to produce Al-Si piston heads with cast iron ring inserts for improved wear resistance [197], as shown in **Figure 2.14**. Processing details are unknown.

In conclusion, it can be seen that casting is potentially suitable for producing near-net shape components with bonded functional parts. It can also be inferred from previous sections that the most significant obstacle to achieve a good bonding between two Al alloys is the formation of oxide films on the surfaces. The oxidation issue also exists even if casting approaches are used. Unfortunately, how the oxide films are disrupted at the bond zone during processing has not been properly addressed in the literature. A comprehensive understanding of the oxidation issue in bonding of Al alloys is therefore needed.

2.4 References

[1] O. Kubaschewski and B. E. Hopkins, *Oxidation of metals and alloys*: Academic Press New York, 1953.

[2] A. Seybolt, "Oxidation of metals," *Advances in Physics*, vol. 12, pp. 1-43, 1963.

[3] E. Verwey and J. De Boer, "Surface oxide films," *Recueil des Travaux Chimiques des Pays-Bas*, vol. 55, pp. 675-687, 1936.

[4] J. Yahalom and T. Hoar, "Galvanostatic anodizing of aluminium," *Electrochimica Acta*, vol. 15, pp. 877-884, 1970.

[5] G. Thompson and G. Wood, "Porous anodic film formation on aluminium," 1981.

[6] R. Furneaux, W. Rigby, and A. Davidson, "The formation of controlled-porosity membranes from anodically oxidized aluminium," *Nature*, vol. 337, pp. 147-149, 1989.

[7] G. Thompson, "Porous anodic alumina: Fabrication, characterization and applications," *Thin solid films*, vol. 297, pp. 192-201, 1997.

[8] C. G. Munger, *Corrosion prevention by protective coatings*: National Association of Corrosion Engineers, 1984.

[9] Z. Fan, Y. Wang, Z. Zhang, M. Xia, H. Li, J. Xu, L. Granasy, and G. Scamans, "Shear enhanced heterogeneous nucleation in some Mg-and Al-alloys," *International Journal of Cast Metals Research*, vol. 22, pp. 318-322, 2009.

[10] Y. Wang, H.-T. Li, and Z. Fan, "Oxidation of aluminium alloy melts and inoculation by oxide particles," *Transactions of the Indian Institute of Metals*, vol. 65, pp. 653-661, 2012.

[11] E. M. Hinton, W. D. Griffiths, and N. R. Green, "Comparison of oxide thickness of aluminium and the effects of selected alloying additions," *Materials Science Forum*, vol. 765, pp. 180-184, 2013.

[12] X. Cao and J. Campbell, "The solidification characteristics of Fe-rich intermetallics in Al-11.5 Si-0.4 Mg cast alloys," *Metallurgical and Materials Transactions A*, vol. 35, pp. 1425-1435, 2004.

[13] J. Campbell, "Entrainment defects," *Materials Science and Technology*, vol. 22, pp. 127-145, 2006.

[14] J. Campbell, "The modeling of entrainment defects during casting," *Simulation of Aluminum Shape Casting Processing: From Alloy Design to Mechanical Properties*, pp. 123-132, 2006.

[15] J. Campbell, "Evidence for entrainment defects," *Materials Science and Technology*, vol. 24, pp. 875-879, 2008.

[16] W. D. Griffiths and N. W. Lai, "Double oxide film defects in cast magnesium alloy," *Metallurgical and Materials Transactions A*, vol. 38A, pp. 190-196, 2007.

[17] R. Raiszadeh and W. D. Griffiths, "The effect of holding liquid aluminum alloys on oxide film content," *Metallurgical and Materials Transactions B*, vol. 42, pp. 133-143, 2011.

[18] W. Griffiths and R. Raiszadeh, "Hydrogen, porosity and oxide film defects in liquid Al," *Journal of materials science*, vol. 44, pp. 3402-3407, 2009.

[19] R. Raiszadeh and W. D. Griffiths, "A method to study the history of a double oxide film defect in liquid aluminum alloys," *Metallurgical and Materials Transactions B*, vol. 37, pp. 865-871, 2006.

[20] D. Dispinar and J. Campbell, "Use of bifilm index as an assessment of liquid metal quality," *International Journal of Cast Metals Research*, vol. 19, pp. 5-17, 2006.

[21] D. Dispinar and J. Campbell, "Effect of casting conditions on aluminium metal quality," *Journal of materials processing technology*, vol. 182, pp. 405-410, 2007.

[22] D. Dispinar and J. Campbell, "Porosity, hydrogen and bifilm content in Al alloy castings," *Materials Science and Engineering: A*, vol. 528, pp. 3860-3865, 2011.

[23] H. Venugopalan and T. DebRoy, "Growth stage kinetics in the synthesis of Al_2O_3/Al composites by directed

oxidation of Al-Mg and Al-Mg-Si alloys," *Journal of the European Ceramic Society,* vol. 16, pp. 1351-1363, 1996.

[24] H. Venugopalan, K. Tankala, and T. DebRoy, "Kinetics of directed oxidation of Al-Mg alloys in the initial and final stages of synthesis of Al_2O_3/Al composites," *Materials Science and Engineering: A,* vol. 210, pp. 64-75, 1996.

[25] H. Venugopalan, K. Tankala, and T. Debroy, "Probing the initial stage of synthesis of Al_2O_3/Al composites by directed oxidation of Al-Mg alloys," *Metallurgical and Materials Transactions B,* vol. 27, pp. 43-50, 1996.

[26] A. S. Nagelberg, "Observations on the role of Mg and Si in the directed oxidation of Al-Mg-Si alloys," *Journal of materials research,* vol. 7, pp. 265-268, 1992.

[27] S. Antolin, A. S. Nagelberg, and D. K. Creber, "Formation of Al_2O_3/metal composites by the directed oxidation of molten aluminum−magnesium−silicon alloys: Part I, microstructural development," *Journal of the American Ceramic Society,* vol. 75, pp. 447-454, 1992.

[28] A. S. Nagelberg, S. Antolin, and A. W. Urquhart, "Formation of Al_2O_3/metal composites by the directed oxidation of molten aluminum−magnesium−silicon alloys: Part II, growth kinetics," *Journal of the American Ceramic Society,* vol. 75, pp. 455-462, 1992.

[29] N. Birks, G. H. Meier, and F. S. Pettit, *Introduction to the high temperature oxidation of metals*: Cambridge University Press, 2006.

[30] P. Kofstad and J. Wiley, *High-temperature oxidation of metals* vol. 584: Wiley New York, 1966.

[31] D. R. Gaskell, *Introduction to the thermodynamics of materials* vol. 2: CRC Press, 2008.

[32] I. Prigogine and P. Van Rysselberghe, "Introduction to thermodynamics of irreversible processes," *Journal of The Electrochemical Society,* vol. 110, pp. 97, 1963.

[33] D. C. Spanner, *Introduction to thermodynamics*: London and New York Academic Press,*1*964.

[34] J. W. Gibbs, *The collected works of J. Willard Gibbs* vol. 1: Yale University Press, 1948.

[35] M. Kaufman, *Principles of thermodynamics*: CRC Press, 2002.

[36] V. Gold, "Glossary of terms used in physical organic chemistry," *Pure and Applied Chemistry,* vol. 55, pp. 1281-1371, 1983.

[37] H. A. Buchdahl, *The concepts of classical thermodynamics*: Cambridge University Press, 2009.

[38] T. L. Hill, *An introduction to statistical thermodynamics*: DoverPublications. com, 1960.

[39] H. J. T. Ellingham, "Reducibility of oxides and sulfides in metallurgical processes," *Journal of the Society of Chemical Industry (London),* vol. 63, pp. 125-133, 1944.

[40] F. Habashi, *Principles of extractive metallurgy* vol. 1: CRC Press, 1969.

[41] A. Atkinson, "Transport processes during the growth of oxide-films at elevated-temperature," *Reviews of Modern Physics,* vol. 57, pp. 437-470, 1985.

[42] E. A. Gulbransen, "The kinetics of oxide film formation on metals and alloys," *Transactions of the Electrochemical Society,* vol. 91, pp. 573-604, 1947.

[43] N. Cabrera and N. F. Mott, "Theory of the oxidation of metals," *Reports on Progress in Physics,* vol. 12, pp. 163-184, 1948.

[44] R. Ghez, "On the Mott−Cabrera oxidation rate equation and the inverse−logarithmic law," *The Journal of Chemical Physics,* vol. 58, pp. 1838-1843, 2003.

[45] F. Fehlner and M. Mott, "Oxidation in the thin-film range," *Paper from Oxidation of Metals and Alloys, ASM, Metals Park* pp. 37-62, 1971.

[46] F. P. Fehlner and N. F. Mott, "Low-temperature oxidation," *Oxidation of Metals,* vol. 2, pp. 59-99, 1970.

[47] C. Wagner, "The cathodic reduction of anions and the anodic oxidation of cations," *Journal of the*

Electrochemical Society, vol. 101, pp. 181-184, 1954.

[48] C. Wagner, "Theoretical analysis of the diffusion processes determining the oxidation rate of alloys," *Journal of the Electrochemical Society,* vol. 99, pp. 369-380, 1952.

[49] D. A. Jelski, L. Nanai, R. Vajtai, I. Hevesi, and T. F. George, "Kinetics of oxide crystal-growth in the transition regime between Cabrera-Mott and Wagner thickness regions," *Materials Science and Engineering :A,* vol. 173, pp. 193-195, 1993.

[50] D. Monceau, R. Peraldi, and B. Pieraggi, "Diffusion and high-temperature oxidation of nickel," *Diffusions in Materials: DIMAT2000, Pts 1 & 2,* vol. 194-1, pp. 1675-1681, 2001.

[51] Z. J. Xu, K. M. Rosso, and S. Bruemmer, "Metal oxidation kinetics and the transition from thin to thick films," *Physical Chemistry Chemical Physics,* vol. 14, pp. 14534-14539, 2012.

[52] E. A. Gulbransen and K. F. Andrew, "Kinetics of the oxidation of chromium," *Journal of the electrochemical society,* vol. 104, pp. 334-338, 1957.

[53] P. Kofstad, "Effect of impurities on the defects in oxides and their relationship to oxidation of metal," *Corrosion,* vol. 24, pp. 379-388, 1968.

[54] D. J. Young, *High temperature oxidation and corrosion of metals* vol. 1: Elsevier, 2008.

[55] R. Prescott and M. Graham, "The formation of aluminum oxide scales on high-temperature alloys," *Oxidation of metals,* vol. 38, pp. 233-254, 1992.

[56] H. Bernstein, "A model for the oxide growth stress and its effect on the creep of metals," *Metallurgical transactions A,* vol. 18, pp. 975-986, 1987.

[57] N. B. Pilling, Bedworth, R. E., "The oxidation of metals at high temperatures," *Journal: Institute of Metals,* vol. 29, p. 4, 1923.

[58] F. Rhines and J. Wolf, "The role of oxide microstructure and growth stresses in the high-temperature scaling of nickel," *Metallurgical Transactions,* vol. 1, pp. 1701-1710, 1970.

[59] R. Bricknell and D. Woodford, "The mechanism of cavity formation during high temperature oxidation of nickel," *Acta Metallurgica,* vol. 30, pp. 257-264, 1982.

[60] G. Wood, "The oxidation of iron-chromium alloys and stainless steels at high temperatures," *Corrosion science,* vol. 2, pp. 173-196, 1962.

[61] C. McBee and J. Kruger, "Nature of passive films on iron-chromium alloys," *Electrochimica Acta,* vol. 17, pp. 1337-1341, 1972.

[62] J. H. Baek and Y. H. Jeong, "Breakaway phenomenon of Zr-based alloys during a high-temperature oxidation," *Journal of Nuclear Materials,* vol. 372, pp. 152-159, 2008.

[63] S. A. Impey, D. J. Stephenson, and J. R. Nicholls, "Mechanism of scale growth on liquid aluminum," *Materials Science and Technology,* vol. 4, pp. 1126-1132, 1988.

[64] H. J. Vanbeek and E. J. Mittemeijer, "Amorphous and crystalline oxides on aluminum," *Thin Solid Films,* vol. 122, pp. 131-151, 1984.

[65] K. Shimizu, G. M. Brown, K. Kobayashi, P. Skeldon, G. E. Thompson, and G. C. Wood, "The early stages of high temperature oxidation of an Al-0.5wt%Mg alloy," *Corrosion Science,* vol. 40, pp. 557-575, 1998.

[66] L. P. H. Jeurgens, W. G. Sloof, F. D. Tichelaar, and E. J. Mittemeijer, "Structure and morphology of aluminium-oxide films formed by thermal oxidation of aluminium," *Thin Solid Films,* vol. 418, pp. 89-101, 2002.

[67] L. P. H. Jeurgens, W. G. Sloof, F. D. Tichelaar, and E. J. Mittemeijer, "Growth kinetics and mechanisms of aluminum-oxide films formed by thermal oxidation of aluminum," *Journal of Applied Physics,* vol. 92, pp. 1649-1656, 2002.

[68] F. Grønlund, *J. Chim. Phys.,* vol. 53, p. 660, 1956.

[69] F. Grønlund and P. J. Møller, "Nucleation control in metal surface oxidation," *Surface Science,* vol. 184, pp. 530-540, 1987.

[70] C. T. Rettner, *Dynamics of gas-surface interactions* vol. 3: Surendra Kumar, 1991.

[71] C. Rettner, D. Auerbach, J. Tully, and A. Kleyn, "Chemical dynamics at the gas-surface interface," *The Journal of Physical Chemistry,* vol. 100, pp. 13021-13033, 1996.

[72] R. K. Hart, "The oxidation of aluminium in dry and humid oxygen atmospheres," *Proceedings of the Royal Society of London Series a-Mathematical and Physical Sciences,* vol. 236, pp. 68-88, 1956.

[73] R. Hart and J. Maurin, "The nucleation and growth of oxide islands on aluminum," *Surface Science,* vol. 20, pp. 285-303, 1970.

[74] I. Olefjord, H. J. Mathieu, and P. Marcus, "Intercomparison of surface-analysis of thin aluminum-oxide films," *Surface and Interface Analysis,* vol. 15, pp. 681-692, 1990.

[75] I. Olefjord and A. Nylund, "Surface-analysis of oxidized aluminum. 2. Oxidation of aluminum in dry and humid atmosphere studied by ESCA, SEM, SAM and EDX," *Surface and Interface Analysis,* vol. 21, pp. 290-297, 1994.

[76] F. Reichel, L. P. H. Jeurgens, and E. J. Mittemeijer, "The role of the initial oxide-film microstructure on the passivation behavior of Al metal surfaces," *Surface and Interface Analysis,* vol. 40, pp. 281-284, 2008.

[77] F. Reichel, L. P. H. Jeurgens, and E. J. Mittemeijer, "The thermodynamic stability of amorphous oxide overgrowths on metals," *Acta Materialia,* vol. 56, pp. 659-674, 2008.

[78] D. W. Aylmore, S. J. Gregg, and W. B. Jepson, "The oxidation of aluminium in dry oxygen in the temperature range 400-650°C," *Journal of the Institute of Metals,* vol. 88, pp. 205-208, 1960.

[79] W. W. Smeltzer, R. R. Haering, and J. S. Kirkaldy, "Oxidation of metals by short circuit and lattice diffusion of oxygen," *Acta Metallurgica,* vol. 9, pp. 880-885, 1961.

[80] W. W. Smeltzer, "Oxidation of aluminum in the temperature range 400-degrees-c-600-degrees-c," *Journal of the Electrochemical Society,* vol. 103, pp. 209-214, 1956.

[81] M. J. Dignam and W. R. Fawcett, "Kinetics and mechanism of oxidation of superpurity aluminum in dry oxygen .2. Growth of crystallites of gamma-alumina," *Journal of the Electrochemical Society,* vol. 113, p. 663, 1966.

[82] A. Beck, M. Heine, E. Caule, and M. Pryor, "The kinetics of the oxidation of Al in oxygen at high temperature," *Corrosion science,* vol. 7, pp. 1-22, 1967.

[83] P. E. Doherty and R. S. Davis, "Direct observation of oxidation of aluminum single-crystal surfaces," *Journal of Applied Physics,* vol. 34, p. 619, 1963.

[84] J. I. Eldridge, R. J. Hussey, D. F. Mitchell, and M. J. Graham, "Thermal-oxidation of single-crystal aluminum at 550ºC," *Oxidation of Metals,* vol. 30, pp. 301-328, 1988.

[85] K. Shimizu, R. C. Furneaux, G. E. Thompson, G. C. Wood, A. Gotoh, and K. Kobayashi, "On the nature of easy paths for the diffusion of oxygen in thermal oxide-films on aluminum," *Oxidation of Metals,* vol. 35, pp. 427-439, 1991.

[86] K. Shimizu, A. Gotoh, K. Kobayashi, G. E. Thompson, and G. C. Wood, "The nucleation sites of gamma-Al_2O_3 crystals in thermal oxide-films on aluminum," *Microscopy of Oxidation,* pp. 144-148, 1992.

[87] L. Backerud, G. Chai, and J. Tamminen, "Solidification characteristics of aluminum alloys. Vol. 2. Foundry alloys," *American Foundrymen's Society,* 1990.

[88] J. Campbell, *Castings*: London Butterworth, 2003.

[89] W. C. Sleppy, "Oxidation of molten high-purity aluminum in dry oxygen," *Journal of the Electrochemical Society,* vol. 108, pp. 1097-1102, 1961.

[90] P. S. Santos, H. S. Santos, and S. Toledo, "Standard transition aluminas. Electron microscopy studies,"

Materials Research, vol. 3, pp. 104-114, 2000.

[91] S. Impey, "The mechanism of dross formation on Al and Al-Mg alloys," PhD Thesis, Cranfield Institute of Technology, 1989.

[92] D. J. Field, G. M. Scamans, and E. P. Butler, "The high-temperature oxidation of Al-4.2 wt pct Mg alloy," *Metallurgical Transactions A,* vol. 18, pp. 463-472, 1987.

[93] K. Kim, "Formation of fine clusters in high-temperature oxidation of molten aluminum," *Metallurgical and Materials Transactions A,* pp. 1-11, 2014.

[94] E. Bergsmark, C. J. Simensen, and P. Kofstad, "The oxidation of molten aluminum," *Materials Science and Engineering :A,* vol. 120, pp. 91-95, 1989.

[95] I. Akagwu, Brooks, R., Quested, P., Fan, Z., Ralph, B.,, "Environmental reaction of liquid aluminium," *Proceedings of the Engineering Doctorate in Environmental Technology,* p. 11, 2003.

[96] L. N. W. Damoah, L. Zhang, and N. F. Adegboyega, "Formation of the solid layer on the top of molten aluminum," 2010.

[97] Z. Fan, Y. Wang, M. Xia, and S. Arumuganathar, "Enhanced heterogeneous nucleation in AZ91D alloy by intensive melt shearing," *Acta Materialia,* vol. 57, pp. 4891-4901, 2009.

[98] J. A. S. Tenorio and D. C. R. Espinosa, "High-temperature oxidation of Al-Mg alloys," *Oxidation of Metals,* vol. 53, pp. 361-373, 2000.

[99] A. J. Brock and M. J. Pryor, "Kinetics of oxidation of aluminum-copper alloys at high temperature," *Journal of the Electrochemical Society,* vol. 117, p. 254, 1970.

[100] A. J. Brock and M. J. Pryor, "Kinetics of oxidation of aluminum-copper alloys in oxygen at high-temperature," *Corrosion Science,* vol. 13, p. 199, 1973.

[101] A. F. Beck, A. J. Brock, and M. J. Pryor, "Oxidation of two-phase aluminum-copper alloys," *Journal of the Electrochemical Society,* vol. 121, pp. 718-720, 1974.

[102] R. Prescott and M. Graham, "The oxidation of iron-aluminum alloys," *Oxidation of Metals,* vol. 38, pp. 73-87, 1992.

[103] Y. Kagawa, T. Chou, S. C. Khatri, and M. J. Koczak, "In-situ observation and modeling of directed oxidation process of Al-Mg-Si alloy," *First International Conference on Processing Materials for Properties,* pp. 1015-1018, 1993.

[104] A. J. Brock and M. J. Pryor, "Kinetics of oxidation of aluminum-zinc alloys," *Journal of the Electrochemical Society,* vol. 125, p. 113, 1978.

[105] A. J. Brock, G. R. Irani, and M. J. Pryor, "The kinetics of the oxidation of aluminum-zinc alloys in oxygen at high-temperature," *Oxidation of Metals,* vol. 15, pp. 77-100, 1981.

[106] S. Becker, A. Rahmel, M. Schorr, and M. Schütze, "Mechanism of isothermal oxidation of the intel-metallic TiAl and of TiAl alloys," *Oxidation of Metals,* vol. 38, pp. 425-464, 1992.

[107] Y. Murakami, M. B. Takeyama, and A. Noya, "Formation processes of the surface oxidized layer on Al-Ti alloy films," *Electronics and Communications in Japan (Part II: Electronics),* vol. 83, pp. 58-66, 2000.

[108] K. Agema and D. Fray, "Preliminary investigation on the deformation behaviour of an oxide scale on molten aluminum," *Department of Materials Science and Metallurgy, University of Cambridge,* 1989.

[109] X. Zhou, G. Thompson, P. Skeldon, G. Wood, K. Shimizu, and H. Habazaki, "Film formation and detachment during anodizing of Al-Mg alloys," *Corrosion Science,* vol. 41, pp. 1599-1613, 1999.

[110] M. H. Zayan, O. M. Jamjoom, and N. A. Razik, "High-temperature oxidation of Al-Mg alloys," *Oxidation of Metals,* vol. 34, pp. 323-333, 1990.

[111] I. A. Kvernes and P. Kofstad, "The oxidation behavior of some Ni-Cr-Al alloys at high temperatures," *Metallurgical Transactions,* vol. 3, pp. 1511-1519, 1972.

[112] G. E. Totten and D. S. MacKenzie, *Handbook of aluminum Vol. 1: Physical metallurgy and processes*: CRC Press, 2003.

[113] M. J. Dignam, "The oxidation of aluminum and certain of its binary alloys below 450°C," *Journal of the Electrochemical Society,* vol. 105, p. 157, 1958.

[114] T. L. Cottrell, *The strengths of chemical bonds*: Butterworths, 1958.

[115] G. R. Wakefield and R. M. Sharp, "The composition of oxides formed on Al-Mg alloys," *Applied Surface Science,* vol. 51, pp. 95-102, 1991.

[116] A. Bahadur, "Behavior of Al-Mg alloys at high-temperature," *Journal of Materials Science,* vol. 22, pp. 1941-1944, 1987.

[117] I. M. Ritchie, J. V. Sanders, and Weickhar.Pl, "Oxidation of a dilute aluminum magnesium alloy," *Oxidation of Metals,* vol. 3, p. 91, 1971.

[118] I. Haginoya and T. Fukusako, "Oxidation of molten Al-Mg alloys," *Transactions of the Japan Institute of Metals,* vol. 24, pp. 613-619, 1983.

[119] K. Surla, F. Valdivieso, M. Pijolat, M. Soustelle, and M. Prin, "Kinetic study of the oxidation by oxygen of liquid Al-Mg 5% alloys," *Solid State Ionics,* vol. 143, pp. 355-365, 2001.

[120] C. Lea and C. Molinari, "Magnesium diffusion, surface segregation and oxidation in Al-Mg alloys," *Journal of Materials Science,* vol. 19, pp. 2336-2352, 1984.

[121] A. K. De, A. Mukhopadhyay, S. Sen, and I. K. Puri, "Numerical simulation of early stages of oxide formation in molten aluminium-magnesium alloys in a reverberatory furnace," *Modelling and Simulation in Materials Science and Engineering,* vol. 12, pp. 389-405, 2004.

[122] C. Lea and J. Ball, "The oxidation of rolled and heat-treated Al-Mg alloys," *Applied Surface Science,* vol. 17, pp. 344-362, 1984.

[123] W. Thiele, "Oxidation of melts of Al and of Al alloys," ed: Aluminum, 1962.

[124] C. Cochran, D. Belitskus, and D. Kinosz, "Oxidation of aluminum-magnesium melts in air, oxygen, flue gas, and carbon dioxide," *Metallurgical Transactions B,* vol. 8, pp. 323-332, 1977.

[125] D. Belitskus, "Oxidation of molten Al-Mg alloy in air, air-SO_2, and air-H_2S atmospheres," *Oxidation of Metals,* vol. 3, pp. 313-317, 1971.

[126] M. Silva, "Oxidation of aluminium-magnesium alloys at elevated temperature in the solid, semi-liquid and liquid states," Brunel University, 1987.

[127] D. Dispinar and J. Campbell, "Critical assessment of reduced pressure test. Part 1: Porosity phenomena," *International Journal of Cast Metals Research,* vol. 17, pp. 280-286, 2004.

[128] D. Dispinar and J. Campbell, "Critical assessment of reduced pressure test. Part 2: Quantification," *International Journal of Cast Metals Research,* vol. 17, pp. 287-294, 2004.

[129] A. Samuel and F. Samuel, "The reduced pressure test as a measuring," *Metallurgical Transactions A,* vol. 24, pp. 1857-1868, 1993.

[130] C. Reilly, N. R. Green, and M. R. Jolly, "Surface oxide film entrainment mechanisms in shape casting running systems," *Metallurgical and Materials Transactions B,* vol. 40, pp. 850-858, 2009.

[131] C. Reilly, N. R. Green, and M. R. Jolly, "Oxide entrainment structures in horizontal running systems," *Shape Casting: 3rd International Symposium 2009,* pp. 71-78, 2009.

[132] X. Dai, X. Yang, J. Campbell, and J. Wood, "Effects of runner system design on the mechanical strength of al-7si-mg alloy castings," *Materials Science and Engineering :A,* vol. 354, pp. 315-325, 2003.

[133] C. Nyahumwa, N. Green, and J. Campbell, "Effect of mold-filling turbulence on fatigue properties of cast aluminum alloys (98-58)," *Transactions of the American Foundrymen's Society,* vol. 106, pp. 215-224, 1998.

[134] M. W. Chase. (1998). *NIST-JANAF thermochemical tables*.

[135] M. A. El-Sayed, H. A. G. Salem, A. Y. Kandeil, and W. D. Griffiths, "Effect of holding time before solidification on double-oxide film defects and mechanical properties of aluminum alloys," *Metallurgical and Materials Transactions B,* vol. 42, pp. 1104-1109, 2011.

[136] R. Raiszadeh and W. D. Griffiths, "The behaviour of double oxide film defects in liquid Al alloys under atmospheric and reduced pressures," *Journal of Alloys and Compounds,* vol. 491, pp. 575-580, 2010.

[137] C. Nyahumwa, N. R. Green, and J. Campbell, "The concept of the fatigue potential of cast alloys," *Journal of the Mechanical Behavior of Materials,* vol. 9, pp. 227-236, 1998.

[138] M. Aryafar, R. Raiszadeh, and A. Shalbafzadeh, "Healing of double oxide film defects in A356 aluminium melt," *Journal of Materials Science,* vol. 45, pp. 3041-3051, 2010.

[139] F. N. Bakhtiarani and R. Raiszadeh, "Healing of double-oxide film defects in commercial purity aluminum melt," *Metallurgical and Materials Transactions B,* vol. 42, pp. 331-340, 2011.

[140] H. T. Larker and R. Larker, "Hot isostatic pressing," *Materials Science and Technology,* 1991.

[141] B. Derby and E. Wallach, "Theoretical model for diffusion bonding," *Metal Science,* vol. 16, pp. 49-56, 1982.

[142] J. Knott, P. R. Beeley, J. R. Griffiths, N. R. Green, C. J. Newton, and J. Campbell, "Commentaries on 'entrainment defects' by J Campbell," *Materials Science and Technology,* vol. 22, pp. 999-1008, 2006.

[143] G. W. Meetham, M. H. Van de Voorde, and M. H. Voorde, *Materials for high temperature engineering applications*: Springer, 2000.

[144] M. Haque and M. Maleque, "Effect of process variables on structure and properties of aluminium–silicon piston alloy," *Journal of Materials Processing Technology,* vol. 77, pp. 122-128, 1998.

[145] A. Sarkar, "Wear of aluminium-silicon alloys," *Wear,* vol. 31, pp. 331-343, 1975.

[146] H. Ye, "An overview of the development of Al-Si-alloy based material for engine applications," *Journal of Materials Engineering and Performance,* vol. 12, pp. 288-297, 2003.

[147] G. Humpston, D. M. Jacobson, G. Humpston, and D. M. Jacobson, *Principles of soldering and brazing*: ASM International, 1993.

[148] Brazing Manual, *American welding society*, 1959.

[149] M. M. Schwartz, *Brazing*: ASM International, 2003.

[150] D. L. Olson, *Asm handbook: Welding, brazing, and soldering* vol. 6: ASM International, 1993.

[151] C. J. Thwaites, *Capillary joining: Brazing and soft-soldering* vol. 2: John Wiley & Sons, 1982.

[152] W. S. Miller, L. Zhuang, J. Bottema, A. Wittebrood, P. De Smet, A. Haszler, and A. Vieregge, "Recent development in aluminium alloys for the automotive industry," *Materials Science and Engineering :A,* vol. 280, pp. 37-49, 2000.

[153] K. F. Dockus, "Method of brazing aluminum parts," ed: Google Patents, 1976.

[154] G. Sierra, P. Peyre, F. D. Beaume, D. Stuart, and G. Fras, "Steel to aluminium braze welding by laser process with Al–12Si filler wire," *Science and Technology of Welding & Joining,* vol. 13, pp. 430-437, 2008.

[155] S. Chang, L. Tsao, Y. Lei, S. Mao, and C. Huang, "Brazing of 6061 aluminum alloy/Ti–6Al–4V using Al–Si–Cu–Ge filler metals," *Journal of Materials Processing Technology,* vol. 212, pp. 8-14, 2012.

[156] K. Suganuma, Y. Miyamoto, and M. Koizumi, "Joining of ceramics and metals," *Annual Review of Materials Science,* vol. 18, pp. 47-73, 1988.

[157] K. Shinozaki and K. Koyama, "Development of Al/Cu dissimilar brazing joint controlled form of intermetallic compound," *Materials science forum,* vol. 539, pp. 4075-4080, 2007.

[158] R. S. Timsit, "Method of brazing aluminum," ed: Google Patents, 1992.

[159] J. Terrill, C. Cochran, and J. Stokes, "Understanding the mechanisms of aluminum brazing," *Welding journal,* vol. 50, 1971.

[160] T. Kayamoto and T. Onzawa, "Development of low melting temperature fillers for aluminium alloys,"

Welding international, vol. 10, pp. 363-369, 1996.

[161] H. Gang, K. Hui, and Z. Pengfei, "Influence of stannum and gallium on vacuum brazing of aluminum and titanium dissimilar alloy," *Aviation Precision Manufacturing Technology*, vol. 4, p. 005, 2001.

[162] M. Jordan and D. Milner, "The removal of oxide from aluminium by brazing fluxes," *Journal of the Institute of Metals*, vol. 85, p. 33, 1956.

[163] Y. Sugiyama, "Brazing of aluminium alloys," *Welding International*, vol. 3, pp. 700-710, 1989.

[164] C. J. Dawes, M. G. Murch, J. C. Needham, E. D. Nicholas, P. Temple-Smith, and W. M. Thomas, "Friction welding," ed: Google Patents, 1995.

[165] O. T. Midling, E. J. Morley, and A. Sandvik, "Friction stir welding," ed: Google Patents, 1998.

[166] C. Dawes, "An introduction to friction stir welding and its development," 1995.

[167] H. Schmidt, J. Hattel, and J. Wert, "An analytical model for the heat generation in friction stir welding," *Modelling and Simulation in Materials Science and Engineering*, vol. 12, p. 143, 2004.

[168] R. Fonda, J. Bingert, and K. Colligan, "Development of grain structure during friction stir welding," *Scripta Materialia*, vol. 51, pp. 243-248, 2004.

[169] Y. S. Sato, H. Kokawa, M. Enomoto, and S. Jogan, "Microstructural evolution of 6063 aluminum during friction-stir welding," *Metallurgical and Materials Transactions A*, vol. 30, pp. 2429-2437, 1999.

[170] Y. Kim, H. Fujii, T. Tsumura, T. Komazaki, and K. Nakata, "Three defect types in friction stir welding of aluminum die casting alloy," *Materials Science and Engineering: A*, vol. 415, pp. 250-254, 2006.

[171] H.-B. Chen, K. Yan, T. Lin, S.-B. Chen, C.-Y. Jiang, and Y. Zhao, "The investigation of typical welding defects for 5456 aluminum alloy friction stir welds," *Materials Science and Engineering: A*, vol. 433, pp. 64-69, 2006.

[172] G. Buffa, J. Hua, R. Shivpuri, and L. Fratini, "Design of the friction stir welding tool using the continuum based fem model," *Materials Science and Engineering: A*, vol. 419, pp. 381-388, 2006.

[173] P. Ulysse, "Three-dimensional modeling of the friction stir-welding process," *International Journal of Machine Tools and Manufacture*, vol. 42, pp. 1549-1557, 2002.

[174] H. R. Shercliff, M. J. Russell, A. Taylor, and T. L. Dickerson, "Microstructural modelling in friction stir welding of 2000 series aluminium alloys," *Mecanique & Industries*, vol. 6, pp. 25-35, 2005.

[175] M. Sutton, B. Yang, A. Reynolds, and R. Taylor, "Microstructural studies of friction stir welds in 2024-T3 aluminum," *Materials Science and Engineering: A*, vol. 323, pp. 160-166, 2002.

[176] M. Peel, A. Steuwer, M. Preuss, and P. Withers, "Microstructure, mechanical properties and residual stresses as a function of welding speed in aluminium aa5083 friction stir welds," *Acta Materialia*, vol. 51, pp. 4791-4801, 2003.

[177] G. Liu, L. Murr, C. Niou, J. McClure, and F. Vega, "Microstructural aspects of the friction-stir welding of 6061-t6 aluminum," *Scripta materialia*, vol. 37, pp. 355-361, 1997.

[178] M. Mahoney, C. Rhodes, J. Flintoff, W. Bingel, and R. Spurling, "Properties of friction-stir-welded 7075 T651 aluminum," *Metallurgical and Materials Transactions A*, vol. 29, pp. 1955-1964, 1998.

[179] C. Rhodes, M. Mahoney, W. Bingel, R. Spurling, and C. Bampton, "Effects of friction stir welding on microstructure of 7075 aluminum," *Scripta materialia*, vol. 36, pp. 69-75, 1997.

[180] P. Threadgill, A. Leonard, H. Shercliff, and P. Withers, "Friction stir welding of aluminium alloys," *International Materials Reviews*, vol. 54, pp. 49-93, 2009.

[181] H. Okamura, K. Aota, M. Sakamoto, M. Ezumi, and K. Ikeuchi, "Behaviour of oxides during friction stir welding of aluminium alloy and their effect on its mechanical properties," *Welding international*, vol. 16, pp. 266-275, 2002.

[182] W. MacDonald and T. Eagar, "Transient liquid phase bonding," *Annual Review of Materials Science*, vol.

22, pp. 23-46, 1992.

[183] W. Gale and D. Butts, "Transient liquid phase bonding," *Science and Technology of Welding & Joining*, vol. 9, pp. 283-300, 2004.

[184] W. Gale and E. Wallach, "Microstructural development in transient liquid-phase bonding," *Metallurgical Transactions A*, vol. 22, pp. 2451-2457, 1991.

[185] G. O. Cook and C. D. Sorensen, "Overview of transient liquid phase and partial transient liquid phase bonding," *Journal of materials science*, vol. 46, pp. 5305-5323, 2011.

[186] Y. Natsume, K. Ohsasa, Y. Tayu, T. Momono, and T. Narita, "Numerical modeling of the transient liquid-phase diffusion bonding process of al using cu filler metal," *ISIJ international*, vol. 43, pp. 1976-1982, 2003.

[187] J. W. Hutchinson, M. Mear, and J. R. Rice, "Crack paralleling an interface between dissimilar materials," *Journal of Applied Mechanics*, vol. 54, pp. 828-832, 1987.

[188] A. AlHazaa, T. Khan, and I. Haq, "Transient liquid phase (TLP) bonding of Al7075 to Ti–6Al–4V alloy," *Materials Characterization*, vol. 61, pp. 312-317, 2010.

[189] A. Shirzadi, H. Assadi, and E. Wallach, "Interface evolution and bond strength when diffusion bonding materials with stable oxide films," *Surface and interface analysis*, vol. 31, pp. 609-618, 2001.

[190] A. Shirzadi and E. Wallach, "Analytical modelling of transient liquid phase (TLP) diffusion bonding when a temperature gradient is imposed," *Acta materialia*, vol. 47, pp. 3551-3560, 1999.

[191] A. Shirzadi and E. Wallach, "New approaches for transient liquid phase diffusion bonding of aluminium based metal matrix composites," *Materials science and technology*, vol. 13, pp. 135-142, 1997.

[192] A. Shirzadi and E. Wallach, "Temperature gradient transient liquid phase diffusion bonding: A new method for joining advanced materials," *Science and Technology of Welding & Joining*, vol. 2, pp. 89-94, 1997.

[193] S. P. Midson and D. J. Browne, "CDC casting," *Advanced Materials & Processes*, vol. 166, pp. 38-40, 2008.

[194] M. Scanlan, D. J. Browne, and A. Bates, "New casting route to novel functionally gradient light alloys," *Materials Science and Engineering: A*, vol. 413, pp. 66-71, 2005.

[195] M. M. Rahvard, M. Tamizifar, M. Boutorabi, and S. G. Shiri, "Effect of superheat and solidified layer on achieving good metallic bond between A390/A356 alloys fabricated by Cast-Decant-Cast process," *Transactions of Nonferrous Metals Society of China*, vol. 24, pp. 665-672, 2014.

[196] G. Durrant, M. Gallerneault, and B. Cantor, "Squeeze cast aluminium reinforced with mild steel inserts," *Journal of materials science*, vol. 31, pp. 589-602, 1996.

[197] RightwayAmerica, "Http://www.Rightwayamerica.Com/products/pistons.Php," 2014.

CHAPTER 3

EXPERIMENTAL DETAILS

3.1 Raw materials

The materials used in the present work are pure Al, Al-5Cu alloy (abbreviation for Al-5wt% Cu alloy, others in the same way), Al-2Mg alloy, Al-0.2Mg alloy. To make up the desired alloy composition, pure Al ingots, pure Mg ingots, and Al-80Cu master alloys were used.

1 kg ingots were prepared each time. In the case of producing an Al-2Mg ingot, 980 g of pure Al was initially melted in a SiC-graphite crucible with a volume of 2 litres and isothermally held at 750ºC within an electric furnace, 20 g of Mg was wrapped tightly with aluminium foil with a thickness of around 16 μm and then gradually immersed into the Al melt. The melt was stirred with a 10 mm thick graphite rod three times, with 10 minutes intervals. The alloy was then carefully poured into an AVON ingot mould and an OES (optical emission spectrometer) mould and left to solidify. Using the same casting procedure, Al-0.2Mg alloy was prepared by mixing pure Al and Al-2Mg together with a 9:1 weight ratio. Al-5Cu alloys were cast by mixing pure Al and Al-80Cu master alloy together with a 15:1 weight ratio.

The chemical compositions of the materials measured from OES samples are given in **Table 3.1**. Before the OES analysis, all specimens were ground down to 2500 grit SiC paper to achieve a smooth and flat surface. Specimens were then cleaned using acetone and methanol to avoid any surface contamination. Measurements were carried out more than 8 times to obtain an average composition value.

3.2 Phase diagram calculations

Equilibrium phase diagrams of Al-Cu and Al-Mg were calculated using MTDATA 5.10 software. The calculations were based on *NPL aluminium database v6.1 – 30 November 2012*. The number of steps was set at 100 and the pressure was set at 101325 pa. The results are shown in **Figures 3.1** and **3.2**. Only the regions of interest on the phase diagrams are highlighted and labelled accordingly. The red line on each phase diagram refers to the alloy composition used in the present work.

3.3 Casting

3.3.1 Electric furnaces

The casting procedure is summarized in **Figure 3.3**. After the ingots were sectioned into small pieces weighing around 100g each. The slugs were re-melted and cast into cylindrical billet-shaped ingots with a 26 mm diameter. The C2 electric furnace (manufacturer: Carbolite; maximum temperature: 1300°C) used is shown in **Figure 3.4**. Each cylindrical billet was further accurately sectioned into disk-shaped slugs of the size 26 mm diameter by 7 mm thickness. The surfaces of disk-shaped slugs were ground down to 4000 grit SiC paper. The disk-shaped slugs were then used for further experiments. The relevant experimental procedure and sample details will be discussed in Chapter 4 (stacking approach) and Chapters 5 and 6 (oxidation studies) accordingly.

3.3.2 Induction melting

Induction heating is a process of heating electrically conducting samples by electromagnetic induction [1]. Eddy currents are generated within the samples and thus the resistance leads to the Joule effect [2], which heats the samples. A mini-CRIM (constrained rapid induction melting) facility was established for use in the highbay lab at the Begbroke Science Park in April 2011, as

shown in **Figure 3.5**. The induction unit has been modified to give a power capacity up to 50 kilowatts. It has been shown by Dai and Jolly [3] that using an induction furnace to melt an alloy can help increase thermal efficiency (lower electricity consumption) up to 67.5%. Meanwhile, induction melting of alloys may add a new facet to foundry practice as the induction produces a specific induction stirring pattern within the melt [1]. In the present work, the induction unit has been used to study how the induction stirring pattern affects the microstructure of castings. Details will be given in Chapter 7.

3.4 Characterization techniques

3.4.1 Macroetching

Macroetching is a standard metallographic method for revealing the macrostructural details of metals or alloys by etching a properly prepared sample surface [4]. It is a good way of providing information on variations in structural features, such as grain size, chemical segregation, dendrites, porosity and cracks [5]. In principle, it is a qualitative and investigatory tool. During the experiment, samples were initially ground down to 4000 grit SiC paper with lubricant water and then immersed into acetone and then methanol to remove any grease, oil or other residue which may cause uneven attack to the surface. The etchant used during the study is Keller's reagent (1.5 ml HCL, 2.5 ml HNO_3, 1.0 ml HF and 95 ml H_2O). Samples were swabbed with the etchant using cotton balls and the progress of etching was closely watched and etching stopped once preferred structural details were revealed. A typical duration for the etching is 10-60 seconds, depending on the chemical compositions of alloys. After etching, the sample was immersed in distilled water for 1 minute and then in methanol for 1 minute. The sample was then dried for 5 minutes using a blow dryer.

3.4.2 Optical microscopy

Optical microscopy (OM) was mainly carried out using a Zeiss microscope (mode: Axioplan 2) with Axiovision v4.8.2 software to examine the microstructures before and after etching. It was also used to assess the quality of polishing for some SEM (scanning electron microscopy) samples. A LINKAM TS1500 hot stage system associated with the Zeiss OM was used to perform an *in situ* observation of the evolution of the surface morphology during heating, melting, and solidification of Al and Al-5Cu. The facility is shown in **Figure 3.6** and the hot stage set-up is illustrated in **Figure 3.7**. In the hot-stage OM experiments, a typical sample is a disk-shaped slug with 3 mm diameter by 1 mm thickness. The slug was polished down to 1 μm diamond suspension before the experiment. A K-type thermocouple was connected to the control unit to indicate the temperature of the sample. Heating/cooling speed was controlled through this unit. The argon/air flush was turned off throughout the experiment. OM images were taken every 5 seconds. The hot-stage OM experimental conditions are summarized in **Table 3.2**.

3.4.3 Scanning electron microscopy (SEM)

JEOL 6300 SEM, JEOL 840A SEM and JEOL 840F SEM (operating at 5 kV) were used during the SEM experiments. For those SEM samples requiring polishing, such as the cross section of a bond, they were prepared by slow saw cutting, grinding, and polishing down to 1 μm diamond suspension, and a further final polishing with distilled water for 10 minutes. Samples were then usually observed at an operating voltage of 20 kV and using a probe current of 1-3 nA. For SEM samples such as oxides or fresh fracture surfaces, samples were either directly introduced into the microscope or coated with a 2 nm Pt film to avoid charging due to poor conductivity.

Both secondary electron (**SE**) imaging and backscattered electron (**BE**) imaging modes were used during the SEM analysis. The SE image gives the topographical information while the BE image

shows contrast between areas with different chemical compositions [6]. Heavy elements (high atomic number, e.g. Cu) backscatter electrons more strongly than light elements (low atomic number, e.g. Al) [7]. So phases containing heavier elements appear brighter in the BE imaging mode (more backscattered electrons signals). This feature may be further explained through the following equation, which shows the scattering coefficient (η – the ratio of the number of backscattered electrons to the number of incident electrons) increases with increasing atomic number Z [8].

$$\eta = -0.0254 + 0.016Z - 1.86\times10^{-4}Z^2 + 8.3\times10^{-7}Z^3 \quad (3.1)$$

SE and BE images were often both taken at each area of interest to provide qualitative information on both topography and composition of interesting microscopic features.

3.4.4 Energy dispersive X-ray analysis (EDX)

Energy dispersive X-ray analysis (EDX) was performed to study the chemical composition of any local features of interest during the SEM analysis. The amount of characteristic X-rays received by the EDX detector was found to be affected by many factors: working distance, accelerating voltage, beam current, electron penetration depth, sample topography, etc. Therefore, experimental conditions were fixed to make sure that all EDX spectra are qualitatively comparable. For each set of EDX spectra, counts are adjusted with respect to the same referencing peak (**Ref**) intensity (usually 2000~4000) at 0.02 KeV. The live time was set as 80 seconds, the dead time percentage was adjusted to be around 30%, and the beam current was set at 3 nA. During the EDX analysis, great care was taken to understand the effect of e-beam sample interaction volume and the effect of local topography. A spectrum is a reflection of all X-ray signals emitted from the interaction volume [9], the size of which is therefore critical to explain the source of elements. A

detailed discussion of this topic will be given in section 3.6. Peaks were labelled according to the literature values of the energies of characteristic X-rays [10].

3.4.5 Thermogravemetric analysis (TGA)

The oxidation kinetics of Al, Al-5Cu, Al-2Mg and Al-0.2Mg were studied using a Perkin Elmer TG/DTA facility to measure the weight gain curves of the alloys while being isothermally held at different holding temperatures. The sensitivity value of the microbalance is 0.1 μg and the weight of each disc-shaped specimen for TGA experiment is around 50 mg with a diameter of 3 mm. The atmosphere was closely controlled using an air flush of 20 cc min^{-1}. The weight gain was recorded every second.

3.4.6 X-ray photoelectron spectroscopy (XPS)

X-ray photoelectron spectroscopy (XPS) analysis was performed in an ion pumped VG Microtech CLAM 4 MCD analyser system. XPS is a powerful quantitative technique used to obtain surface chemistry information (such as elemental compositions, chemical formula, electron states, etc) of materials [11]. In the present work, cylindrical samples with a diameter of 8 mm and a height of 5 mm were irradiated by a beam of X-rays with known energy (both Al Kα and Mg Kα were used in this work). The spectrometer measures the kinetic energy and number of photoelectrons escaping from the top 1~10 nm surface layer of the samples [12]. The photoemission process is illustrated schematically in **Figure 3.8**. The binding energy is a parameter identifying specific electrons (equal to the energy difference between a specific electron state to and the Fermi level [13]). The mathematical relationship between different parameters in XPS studies is expressed as follows

$$E_b = h\nu - E_k - \varphi \tag{3.2}$$

Here E_b and E_k are the binding energy and kinetic energy of the photoelectron, $h\nu$ is the energy of the incident X-ray and φ is the spectrometer work function [12]. An XPS spectrum is a plot of

number of electrons detected (usually presenting as counts per second - CPS) versus the binding energy of electrons detected. Electrons which are excited and escape without energy loss contribute to the characteristic peaks in the XPS spectrum. Those which undergo inelastic scattering resulting in energy loss, contribute to the background of the spectrum [12]. Not all peaks in XPS data are due to the ejection of an electron by direct interaction with an incident photon. The most notable ones are the Auger peaks, and how Auger electrons are produced is also illustrated in **Figure 3.8**: the decay of a more energetic 2s electron to fill the vacant hole at 1s shell which is created due to the knocking out of the 1s electron by incident X-ray; the energy released (2s state to 1s state) can be harnessed by a 2p electron and allows the 2p electron to escape from the vacuum level with a certain kinetic energy [14].

In the present work, wide scan XPS spectra (E_b ranges from 0 to 1100 eV) were mainly used for qualitative analysis to characterise the surface chemistry of oxidized samples and identify the elements present in the oxide layer. Experimental conditions for the acquisition of wide scan spectra are summarized in **Table 3.3**. XPS core levels (such as, Al 2p, O 1s, Mg 2p, etc) were used in conjunction with wide scan to determine the types of oxide phases in the surface oxide layer. Sample details for XPS analysis will be given in Chapters 5 and 6 where the results of XPS studies are discussed. The peak fitting method used throughout the work will be discussed in detail in section 3.7.

3.4.7 X-ray diffraction (XRD)

X-ray diffraction was used to identify the crystallographic phases present in samples. Samples were characterized in a Philips 1810 θ–2θ diffractometer using Cu Kα radiation (λ = 1.5406 Å). Phases were indexed using X'Pert Highscore Plus V2.0 software and its built-in ICDD (International Centre for Diffraction Data) reference patterns [15]. The experimental procedure and details of the reference patterns are given in **Figure 3.9**. Samples were X-rays scanned with

a voltage of 35 kV and a current of 50 mA, the time per step was 1 s and the step size was 0.02˚. When a sample is irradiated by X-rays, not all X-rays will escape from the sample surface. The intensity of X-rays emitted from the sample is a function of the information depth, which is usually quoted as the penetration depth at which the emitted X-ray intensity is around 37% (1/e) of the incident X-ray intensity [16], as shown in **Figure 3.10**. This topic is discussed in **Appendix 3.1**.

3.4.8 Surface topography profiling

A Veeco Dektak 6M stylus profiler was used to profile the surface topography and indicate the surface roughness of oxidized samples. The surface profiler has a resolution in nanometers. The principle of this technique is illustrated in **Figure 3.11**: the surface profiler takes measurements by moving a diamond-tipped stylus over the sample surface and records the vertical movement of stylus due to surface variations. Before the experiment, the bottom surface of a sample was polished down to 1 μm diamond suspension and the sample was placed on a flat stage.

3.5 Oxide extraction

It has been shown that intermetallic phases can be extracted from an Al alloy by dissolving away the α-Al matrix using anhydrous 1-butanol in an argon environment and our group has reported a number papers on using this technique to extract intermetallic phases of interest from different Al alloys [17, 18]. Recently, our group has extended the use of this technique to extract the oxide particles from oxidized samples. The 1-butanol dissolves away the Al matrix (α-Al) through the following chemical reaction:

$$2\ Al + 6\ C_4H_9OH \rightarrow 2\ Al(C_4H_9O)_3 + 3\ H_2$$

This is a redox reaction, C_4H_9OH serves as the oxidant and Al serves as the reductant. Since oxides cannot be further '*oxidized*' (3 moles of electrons have been transferred from Al to H for each mole of Al), oxide products will therefore remain unaffected during the reaction. For each extraction, no more than 0.42 g of material was used. Before the extraction, some filings of pure

Al were added to the 1-butanol before it was refluxed for 3 hours to ensure it was anhydrous. An autoclave was used to facilitate the process, its structure is shown in **Figure 3.12**. All the components were cleaned ultrasonically in deionized water and then dried in an oven at 175ºC. A filter paper with a pore size of 0.2 μm was placed inside the autoclave to collect the extracted oxides. The autoclave was then evacuated, filled with argon and 80 ml of the anhydrous 1-butanol added. The autoclave was sealed and held at 135ºC for around 5 hours to allow complete reaction between the α-Al matrix and the anhydrous 1-butanol. Once completed, the autoclave was dismantled and the filter paper containing the oxide phases was removed.

This novel extraction approach could potentially have two advantages over any existing oxide extraction approaches mentioned in the literature. The use of $HgCl_2$ [1], iodine solution [2], and even bromide solution [3] have been reported, but all of them have safety issues. For example, $HgCl_2$ decomposes to produce poisonous Hg, while iodine must be used in an absolutely dry pure methanol to react with Al, in order to avoid explosion.

3.6 E-beam sample interaction

During the SEM/EDX analysis, the high energy electron beam interacts with the sample to produce a number of signals emitted from the sample surface and create an excitation volume [6]. The *interaction volume* or *excitation volume* is a hemispherical to jug-shaped region with the neck of the jug at the sample surface, as illustrated in **Figure 3.13**.

Understanding the interaction volume during the SEM/EDX analysis is very important as it offers an indication of which depth the characteristic X-rays come from and a scientifically reasonable interpretation of the measured EDX spectrum, as the chemistry within the excitation volume would all potentially contribute to the EDX spectrum. It has been shown that the depth of electron beam penetration into the sample or the volume of e-beam-sample interaction depends on the

acceleration voltage (i.e. electron beam energy), incidence angle, the atomic number and density of the solid sample [19]. Recently, the development of computer technology has made it possible to simulate a large number of the electron trajectories (10,000 to 100,000) within the sample and visualize the interaction volume using a statistical Monte Carlo method.

In the present work, simulations of the interaction volume for different materials used or encountered during the SEM/EDX analysis were performed with the aid of Casino V 2.4.8.1 software [9]. The physics models used during the simulation are illustrated in [9, 20-22], which will not be discussed in detail here. In the present work, the accelerating voltage used on either JEOL 6300 or JSM 840A was in the range of 0-20 kV. The interaction volume values for different interesting materials were simulated according to the actual experimental conditions.

According to the results of simulations shown in **Figures 3.14-3.16**, first of all, taking Al as an example, the depth of the interaction volume increases as the accelerating voltage increases, the depth is 3.7 μm with a 20 kV accelerating voltage. Secondly, the detector take-off angle has an effect on the measured characteristic X-ray intensity. The EDX detectors in the JEOL 6300 SEM and JEOL 840A SEM have a 40˚ take-off angle to the sample surface. From **Figure 3.15** we can calculate the intensity of Al Kα X-rays detected by the detector (at 40˚ take-off angle) is 72.7% of the total intensity of generated X-rays, while when the detector is normal to the sample surface (at 90˚ take-off angle), the detected X-ray intensity is approximately 81.2% of the total intensity. Thirdly, the total generated Al Kα X-ray intensity may not depend on the beam diameter, as shown in **Figure 3.16**. The scale of the interaction volume in terms of the penetration depth (μm) for different materials is summarized in **Figure 3.17**.

3.7 XPS peak fitting methodology

This section discusses the issue of peak fitting in the XPS analysis. A method of assessing the

goodness of fit was developed in the present work by using a combination of different statistics. Whether a fit is good or not can be usually indicated by the coefficient of determination (COD), reduced R-square, or some similar statistics [23]. It is suggested from the present work that great care must be taken when dealing with data consist of closely overlaying peaks and the analysis of the Durbin-Watson statistic [24, 25] should be incorporated. The following content describes an example of O 1s core level fitting to illustrate the issue.

First of all, it should be noted that a peak function is usually a Gaussian function or a Lorentzian function, or even a certain combination of both, depending on the background under the curve [26, 27]. Normally, the C 1s, O 1s, and Al 2p core levels have a flat linear background so Gaussian functions were used throughout the fitting analysis. A peak function can be expressed by the sum of several Gaussian functions after subtracting the background [28] and this is given by

$$y = \sum_i a_i \cdot \exp\left(-\frac{\left(x - c_i\right)^2}{2\sigma_i^2} \right) \tag{3.3}$$

where c_i is the position of the peak centre, a_i is the parameter describing the intensity of the peak, and σ_i is the parameter related to the FMHW (full width at half maximum) of a peak. For an XPS spectrum, taking an O 1s core level scan as an example, the measured result has about 100 pairs of data points (x, y), but the total number of independent parameters for the above equations is usually less than 15 (suppose the curve consists of 4 peaks, then there are 12 parameters to be determined). In this case, the degree of freedom is quite high [29].

In order to illustrate the peak fitting issue mentioned earlier in this section, two different methods, (a) single peak fitting and (b) double peak fitting, of O 1s core level acquired on an oxidized Al sample, were compared in **Figure 3.18**. The fitting parameters are summarized in **Tables 3.4** and **3.5**. Each method of fitting was performed 5 times to obtain the error (deviation) of the fitted parameters.

Providing both methods give the values of COD to be more than 0.99, it is mathematically implied that both of the two fittings are acceptable. The COD of method (a) is even larger than that of method (b) which could possibly suggest that method (a) gives a better fit. However, at second glance, this may not be true. In order to further judge the goodness of fit, residual analysis is then used. The residual value for each point on the curve is defined as

$$R_i = (y_i)_f - (y_i)_m \tag{3.4}$$

Where $(y_i)_f$ is the fitted value and $(y_i)_m$ is the measured value. Firstly, as shown at the top of **Figure 3.19**, residual plots suggests that the method (b) may be a better fit than method (a). Secondly, as shown at the bottom of **Figure 3.19**, lag plots (which are constructed by a normalized $R_i \sim R_{i-1}$ relationship, are used to check the randomness of the data [30]) clearly indicate that there is a non-random structure of residuals using method (a), while a more random structure of residuals is achieved using method (b). Random data should not exhibit any identifiable structure in the lag plot while non-random structure in the lag plot often indicates that the underlying data are not random [30].

Similar to lag plots, the Durbin-Watson test is another method to assess the independence of residuals from the regression analysis. The Durbin-Watson statistic D is defined as:

$$D = \frac{\sum_{i=2}^{n} \left(R_i - R_{i-1}\right)^2}{\sum_{i=1}^{n} R_i^2} \tag{3.5}$$

The Durbin-Watson statistic D is always between 0 and 4 [30]: a value of 2 means there is no autocorrelation in the residuals from the regression analysis; values approaching zero indicate positive autocorrelation; values approaching 4 indicate negative autocorrelation. It is suggested that autocorrelations should be near-zero for randomness and if randomness is not checked then the validity of the fitting becomes suspect [31]. The calculated D values for (a) and (b) are D = 0.08123 and D = 1.67345, suggesting fitting (b) is more reasonable. So the O 1s core level is better

fitted by two peak functions. This is scientifically reasonable because the surface oxide layer may always pick up water molecules to form aluminium hydroxide which would also contribute to the O 1s core level curve. Therefore, in the present work, the Durbin-Watson statistic is always incorporated to have a comprehensive assessment of the XPS peak fitting data (in particular to identify overlapping peaks) and to check the validity of the underlying physical model.

3.8 References

[1] J. Davies and P. Simpson, *Induction heating handbook*: McGraw-Hill London, 1979.

[2] C. Kittel and P. McEuen, *Introduction to solid state physics* vol. 8: Wiley New York, 1986.

[3] X. Dai and M. Jolly, "Potential energy savings by application of the novel crimson aluminium casting process," *Applied Energy,* vol. 89, pp. 111-116, 2012.

[4] H. Keshian, "Development and application of macroetching," *Transactions,* p. 289, 1933.

[5] G. F. Vander Voort, *Metallography, principles and practice*: ASM International, 1984.

[6] D. C. Joy, "Scanning electron microscopy," *Materials Science and Technology,* 1971.

[7] K. Kanaya and S. Okayama, "Penetration and energy-loss theory of electrons in solid targets," *Journal of Physics D: Applied Physics,* vol. 5, p. 43, 1972.

[8] E. Robert, R. Hill, and R. Abbaschian, "Physical metallurgy principles," *PWS-Kent, 3Ed, Boston,* 1992.

[9] D. Drouin, A. R. Couture, D. Joly, X. Tastet, V. Aimez, and R. Gauvin, "Casino v2.42 - a fast and easy-to-use modeling tool for scanning electron microscopy and microanalysis users," *Scanning,* vol. 29, pp. 92-101, 2007.

[10] J. A. Bearden, "X-ray wavelengths," *Reviews of Modern Physics,* vol. 39, pp. 78, 1967.

[11] K. Siegbahn, "Electron spectroscopy-an outlook," *Journal of Electron Spectroscopy and Related Phenomena,* vol. 5, pp. 3-97, 1974.

[12] J. F. Watts and J. Wolstenholme, *An introduction to surface analysis by XPS and AES*: Wiley-VCH, 2003.

[13] T. L. Barr, *Modern escathe principles and practice of X-ray photoelectron spectroscopy*: CRC press, 1994.

[14] C. C. Chang, "Auger electron spectroscopy," *Surface Science,* vol. 25, pp. 53-79, 1971.

[15] J. ICDD, "PDF-2 database," *ICDD Newton Square, PA, USA, release,* vol. 51, 2001.

[16] I. Tomov, "Orientation dependence of the effective depth of X-ray penetration," *Physica Status Solid A-Applied Research,* vol. 98, pp. 43-50, 1986.

[17] S. Kumar, P. Grant, and K. O'Reilly, "Fe bearing intermetallic phase formation in a wrought Al-Mg-Si alloy," *Transactions of the Indian Institute of Metals,* vol. 65, pp. 553-557, 2012.

[18] T. Smith, K. O'Reilly, S. Kumar, and I. Stone, "Influence of grain-refiner addition on the morphology of Fe-bearing intermetallics in a semi-solid processed Al-Mg-Si alloy," *Metallurgical and Materials Transactions A,* vol. 44, pp. 4866-4871, 2013.

[19] P. J. Potts, Cresser, M., *A handbook of silicate rock analysis* vol. 622. Glasgow: London: Blackie, 1987.

[20] D. Drouin, P. Hovington, and R. Gauvin, "Casino: A new Monte Carlo code in C language for electron beam interactions. 2. Tabulated values of the mott cross section," *Scanning,* vol. 19, pp. 20-28, 1997.

[21] P. Hovington, D. Drouin, and R. Gauvin, "Casino: A new Monte Carlo code in C language for electron beam interaction. 1. Description of the program," *Scanning,* vol. 19, pp. 1-14, 1997.

[22] P. Hovington, D. Drouin, R. Gauvin, D. C. Joy, and N. Evans, "Casino: A new Monte Carlo code in C language for electron beam interactions. 3. Stopping power at low energies," *Scanning,* vol. 19, pp. 29-35, 1997.

[23] B. A. Barry and M. D. Morris, *Errors in practical measurement in science, engineering, and technology*: Wiley New York, 1978.

[24] R. Hill and H. Flack, "The use of the Durbin-Watson D statistic in rietveld analysis," *Journal of Applied Crystallography,* vol. 20, pp. 356-361, 1987.

[25] M. Nerlove and K. F. Wallis, "Use of the Durbin-Watson statistic in inappropriate situations," *Econometrica: Journal of the Econometric Society,* pp. 235-238, 1966.

[26] A. E. Hughes and B. A. Sexton, "Curve fitting XPS spectra," *Journal of Electron Spectroscopy and Related*

Phenomena, vol. 46, pp. 31-42, 1988.

[27] E. Ollivier, "XPS peak fitting," *Vide-Science Technique Et Applications*, vol. 52, pp. 53, 1996.

[28] R. Kwok, "XPS peak fitting program for Win95/98 XPSpeak version 4.1," *Department of Chemistry, The Chinese University of Hong Kong*, 2000.

[29] S. L. Meyer, *Data analysis for scientists and engineers*: Wiley, 1975.

[30] I. Hughes, Hase, T., *Measurements and their uncertainties: A practical guide to modern error analysis*: Oxford University Press, 2010.

[31] N. R. Draper and H. Smith, *Applied regression analysis 2nd ed*: New York John Wiley and Sons, 1981.

CHAPTER 4

PROCESSING STUDIES: STACKING APPROACH

4.1 Introduction

In this chapter, the experimental results of the investigation of the Al alloys bonded through a stacking approach are reported. In the stacking approach, two slugs of metals were stacked together and then isothermally held at a given temperature for a certain period of time in an atmosphere. The intention of this study is, firstly, to generate a preliminary understanding of the effect of oxide layers formation on bonding of Al alloys, and secondly, to answer the question of whether the deliberately created '*bi-film*' defect (two oxide layers were in contact with each other by stacking together) would only thickening itself or be somehow disrupted during the bonding process. The quality of bonding in terms of the bond interface morphology and the degree of metallic mixing as a function of holding time were assessed microscopically.

This chapter starts with the characterization of stacked Al/Al-5Cu samples to understand the degree of metallic bonding as a function of time qualitatively. The possible bonding mechanism for the Al/Al-5Cu system is further discussed in detail. Later in this chapter, the results of the stacked Al/Al-2Mg system are presented as a comparison to the stacked Al/Al-5Cu system to preliminarily examine the effects of different alloying elements on bonding from the perspective of oxidation.

4.2 Experimental

The stacking approach refers to the design of a bi-metallic bond formed by stacking two pieces of metals up and down and then holding the stack isothermally at a given temperature for a certain period of time. The geometric size of a stack is illustrated in **Figure 4.1**. The sample details for the stacked Al/Al-5Cu system are summarized in **Table 4.1**. The symbol "/" is used to describe

this stacking design.

In order to minimize the influence of the pre-formed surface oxide layer of each disc-shape sample at the bond interface, surfaces of each sample were ground down to 4000 grit SiC paper before stacking. This sample preparation is used throughout the study, allowing inter-comparability and reproducibility of results. The stacking approach experimental procedure is illustrated in **Figure 4.2**: a stacked sample was first placed in a fitted cylindrical alumina crucible (inner diameter 26 mm; outer diameter 30 mm; height 40 mm; boron nitride spray coated) and then introduced into the preheated electric furnace (preheated up to the desired holding temperature); A relatively low flush speed of air (50 cc min^{-1}) from a gas cylinder was used throughout the experiment to maintain the atmosphere pressure in the furnace chamber. A K-type thermocouple with a 1.5 mm tip diameter was used to monitor the temperature of the stacked sample. Before the experiments, the relative humidity (RH) in the furnace room was measured to be around 5% (presumably the humidity meter functioned well). However, the level of relative humidity inside the furnace chamber at high temperatures (e.g. 750°C) will be somewhat different from that at room temperature. The air from the cylinder may also contain some moisture. It has to be noted that the "air" term used in this chapter does not necessarily mean an absolutely humidity-free atmosphere.

It has been shown in the literature that the oxidation behaviour of Al may be slightly different with the presence of a certain level of humidity. First of all, the most recognized effect of humidity on oxidation of Al (especially liquid Al) is the hydrogen pickup [1]. a liquid Al could react with water vapour to produce hydrogen which is readily soluble in Al through the reaction $2Al\ (g) + 3H_2O\ (g) = Al_2O_3\ (s) + 6H$ (g in l) [2]. Interestingly, it was found by Weigel and Fromm [3] that the initial unbroken and uniform surface oxide film (presumably amorphous) formed on Al could retard the diffusion of H into and out of the melt; once the oxide film was disturbed or broken, the transport of H would be significantly enhanced. Similar observation was reported by Griffiths and

Raiszadeh [4]. The solubility of H in Al increases with temperature [2, 5]. Therefore, the dissolved hydrogen tends to come out of the solution as the melt solidifies, resulting in the formation of hydrogen pores [1]. According to the work by Fox and Campbell [6, 7], it is indicated that oxide films can act as preferential nucleation sites for hydrogen pores. The hydrogen pores around the oxide scale may in turn disrupt the oxide morphology to an unknown extent.

As inferred from the literature, another effect of humidity on oxidation of Al is the formation of aluminium hydroxide (i.e. $Al_2O_3 + H_2O = Al(OH)_3$) on top of an aluminium oxide layer. Morize and Lacombe [8] found that the oxide films formed at room temperature (amorphous aluminium oxide) in humid air (unknown relative humidity) were thicker than those formed in dry air and the oxidation rate increased with increasing humidity. Similar result was reported by Hart [9]. It was then shown by Nylund and Olefjord [10, 11] that aluminium hydroxide (confirmed by XPS) formed on top of aluminium oxide during exposure to a humid atmosphere (80% relative humidity) and they also proposed that the increased oxidation rate observed was probably due to the limited protection property of the hydrated layer [10, 11].

Interestingly, Impey *et al*. [12, 13] reported that the amorphous-to-crystalline aluminium oxide transformation was kinetically slower in the presence of water vapour (unknown relative humidity) than in dry environments. The precise scientific mechanism is still unknown. But it was suggested by the author that the presence of hydroxyl ions or protons may increase the degree of disorder in the amorphous structure and reduce the number of nucleation sites for crystalline oxides.

Identifying the exact effects of humidity on oxidation of Al is undoubtedly necessary as there are always some sources of moisture in foundry practice [1, 14] and it is almost impossible to achieve an absolute dry condition in reality.

4.3 Results and discussion – Stacked Al/Al-5Cu

4.3.1 Cross section – Macrographs

Figures 4.3 (a)-(d) show both the un-etched and etched cross section structures of the Al/Al-5Cu stacks. It is noted that Al-5Cu is more vulnerable to the acid solution than Al. This is because that the θ-$CuAl_2$ phase usually forms along the grain boundaries, the θ-$CuAl_2$ phase renders the grain boundaries anodic to the grain centre, causing rapid grain boundary corrosion [15]. Empirically, it only takes around 15 seconds to reveal the dendritic structure of Al-5Cu while the grain structure of Al is still not fully revealed in such a short time. This opens up a qualitative way of assessing the degree of bonding between Al and Al-5Cu based on the extent of etching.

If the degree of bonding (i.e., metallic mixing) is defined by the percentage of the Cu-rich (dark) across the total cross-sectional area of the Al side, based on image analysis, the values are 9.4%, 12.1%, 100% and 100% for samples *S-0.5*, *S-1*, *S-6* and *S-24*, respectively. If the degree of bonding is defined by the width of metallic mixing zone, the values are 1.5 mm, 3.2 mm, 14 mm and 14 mm respectively. As shown by **Figure 4.3 (d)**, Al and Al-5Cu seem to be fully mixed and the interface of the stacked Al/Al-5Cu is almost macroscopically invisible.

From the observations, longer holding time leads to a greater extent of bonding. As inferred from **Figures 4.3 (a)** and **(b)**, the oxide layers may protect each melt from mixing during initial stages of holding, resulting in a limited degree of bonding. It is hypothesized here that, as the holding time increases, the *barrier layer* (in other words., the *bi-film* layer) become less protective and it could eventually allow a complete metallic mixing between Al and Al-5Cu, as shown by **Figures 4.3 (c)** and **(d)**. Further experiments were then carried out to test the hypothesis.

4.3.2 Cross section – OM studies

Microscopically, as shown in **Figure 4.4**, the local grain structures, in terms of grain size and morphology, are different on the two sides of the interface of sample *S-0.5*, suggesting no significant bonding is achieved in this region and this may be further evidenced by the highlighted grain which looks like it is being intersected by the interface. It was found in the present study that the bond of sample *S-0.5* was relatively weak and the interface might already be cracked through during the sample preparation stage (cutting, polishing, etc), as revealed by the large interfacial gap between Al and Al-5Cu.

Figures 4.5 (a) and **(b)** show more similar grain structures on both sides of the stacked Al/Al-5Cu sample *S-1*, suggesting some degree of metallic mixing of the two melts at this region. However, **Figures 4.5 (c)** and **(d)** show obviously two different grain structures on the Al side and Al-5Cu side, suggesting little mixing of the two melts at this region. **Figure 4.6** is a composite panoramic overview of the cross-section of the sample *S-1*. The image is generated by stitching more than 300 OM micrographs using a Microsoft Image Composite Editor (ICE) software [16]. The composite image is particularly useful as it reveal the overall structure without losing detail. According to **Figure 4.6**, a possible mixing mechanism is graphically illustrated: the cracking of oxide scales could lead to the flow of the Al-5Cu melt into the Al side.

Figures 4.7 (a)-(c) show the bond interface microstructure of the stacked Al/Al-5Cu sample *S-6*, similar grain and dendritic features on the Al and Al-5Cu sides confirm the mixing of the two melts during the isothermal holding process. **Figure 4.7 (c)** shows two individual grains across the interface and grains are intercepted by the interfacial gap. Similar to the results from the sample *S-1*, it is indicated by **Figure 4.8** that the fracture of oxide layer could lead to the metallic mixing of Al and Al-5Cu.

For sample *S-24*, it can be seen from **Figure 4.3 (d)** that the bond interface is almost macroscopically invisible, but still microscopically visible, as suggested by **Figure 4.9**.

To sum up, it can be seen from previous results that the fracture of the *bi-film* layer could allow the metallic mixing in a stacked Al/Al-5Cu sample and the extent of mixing is hypothesized to be somewhat a function of holding time.

4.3.3 SEM/EDX studies

The intention of the work described in this section is, firstly, to understand how cracks are formed in the oxide scale, and secondly, to identify other possible bonding mechanisms.

Figure 4.10 is a pair of SE and BE images showing the bond interface structure of stacked Al/Al-5Cu sample *S-6*. The interface position is highlighted by yellow arrows. It is noted in this figure that metallic mixing is achieved in this sample, as suggested by the similar microstructure feature and the observation that Cu-rich intermetallic phases are present on the Al side, as highlighted by red arrows.

Figure 4.11 shows a pair of SE and BE images suggesting the entrapment of metal with a width of around 40 μm between the Al and Al-5Cu, the entrapped metal is highlighted by yellow arrows. Quantified EDX results are summarized in **Figures 4.12 (a)-(c)**. It is possible that melt could move through the cracks in the oxide layer and the presence of entrapped metal between the oxide layers not only facilitates the wetting of the two oxide layers but may also become a "*bridge*" connecting Al and Al-5Cu and providing an indirect way of metallic mixing, as shown schematically in **Figure 4.13**. In addition, as shown in **Figure 4.14**, some crystalline-like oxide phases with the size of around 1-2 μm are observed at the bond interface. Oxide phases usually appear bright in SE imaging mode because of the poor-conductivity causing electrons charging

and they usually appear dark in BE imaging mode because of the low atomic number of oxygen [17]. The combination of SEM and EDX analysis has proven to be very useful for identifying any oxide phases [18]. The EDX results are summarized in **Figures 4.15 (b)** and **(c)**, clearly suggesting they are aluminium oxides.

Figures 4.16-4.19 show the results of SEM/EDX studies from the sample *S-24*. Similar to the observations in the sample *S-6*, **Figure 4.16** shows that crystalline-like oxide phases have formed locally at the bond interface, as highlighted by the yellow circles. EDX results (in particular P4 and P7 in **Figure 4.17**) suggest that they are aluminium oxides. As shown in **Figures 4.18** and **4.19**, the crystalline-like aluminium oxides formed on both sides at the interface have a total thickness of around 5 μm. Interestingly, as highlighted by the red arrow in **Figure 4.20**, a region of the *bi-film* layer seems to be completely healed without the presence of any crack-like feature. EDX results are given in **Figure 4.21**, consistent with previous observations. It has been shown by Griffiths *et al*. [19-21] that the entrapped air within a double oxide film pocket could be gradually consumed by reaction with the surrounding melt and the oxide films may bond together to some degree. The observed result in this study also provides direct evidence showing that the healing of oxide films is possible.

Another interesting phenomenon observed in the present work is the local fracture of the *bi-film* layer at the edge of a crystalline-like oxide, as shown in **Figures 4.22** and **4.23** (EDX results). During the bonding process, the rigid crystalline-like oxide in the continuous bi-film layer is unlikely to deform in the same way and at the same time as the rest of the layer, this could lead to a significant build-up of local stress, in particular at the peripheries of the oxide crystals. Cracking provides a route to release the stresses [22] and metallic mixing could be further facilitated through these easy channels during the bonding process.

4.3.4 Effect of gravity

If Al-5Cu was stacked on the top of Al, it is called a **stacked Al-5Cu/Al**. (Al/Al-5Cu when Al is on top of Al-5Cu). It can be seen from **Figure 4.24** that, for the stacked Al-5Cu/Al sample which was held at 750°C for 1 h, there is almost a complete mixing of Al and Al-5Cu and the grain structures on both sides are similar. This observation may be explained by the effect of *gravity segregation* of the Cu-rich melt.

The density of Al melts depends significantly on the density of alloying elements [1]. The density of Cu is approximately three times more than that of Al [23]. In the present work, for the stacked Al-5Cu/Al sample, the Cu-rich melt on the Al-5Cu side would easily sink down to the Al side and mix with the Al melt due to gravity, providing cracks (easy channels) are present within the *bi-film* layer. Instead, as for the stacked Al/Al-5Cu sample, it is difficult for the Cu-rich melt to overcome the gravity force and climb upwards, so the metallic mixing proceeds slower than that in the stacked Al-5Cu/Al sample. The gravity segregation of Cu in Al melts has also been recognized in other studies. Recently, Liotti *et al*. [24, 25] have used synchrotron X-ray and optical *in situ* measurement to analyse some solidification phenomenon, such as dendrites fragmentation in an Al-15Cu alloy under a Pulsed Electro Magnetic Field (PEMF) and the gravity segregation of Cu was directly observed. Similarly, Rerko *et al*. [26] has studied how the gravity segregation of Cu affects the grain structure of Al-Cu alloys during solidification.

4.3.5 Bonding mechanism

To understand the bonding mechanism, first of all, it should be noted that each stacked Al/Al-5Cu sample will undergo three distinctive stages during the stacking experiment: melting, isothermal holding, and solidification. How would each stage affects the bonding specifically?

4.3.5.1 Melting stage

Let us first consider the physical phenomenon of melting a single piece of Al slug. **Figure 4.25** shows the appearance of an Al sample before (left) and after (right) melting and re-solidifying. The sample was initially placed in an alumina boat crucible, melted and held at 750ºC for 1 h, then air-cooled down to room temperature. It is interesting to note that the slug still holds its shape after the process, indicating that the oxide layer at the surface of the melt has some degree of strength and can actually hold the melt in place. During the melting stage, the oxide layer is subject to significant topographical reconstruction and stress accumulation due to different thermal expansion coefficients and elasticity [22]. It is therefore not surprising that microcracks always exist within the oxide layer formed on a metal [27, 28]. These cracks could become easy channels for metallic mixing due to the capillarity effect [29], which may cause the Al-5Cu melt flow upwards in this case. Although how much the melting stage contributes to the degree of bonding cannot be quantified, it is certainly not a dominating factor. If it were, as each stacked Al/Al-5Cu sample would go through the same melting stage, then each stack would have the similar degree of bonding, regardless of how long it is held at liquid state.

4.3.5.2 Holding stage

It is obvious from previous results that the isothermal holding time plays a significant role in determining the degree of metallic bonding during the stacking process. As we know, liquid is mixed more quickly through thermal convection than through thermal diffusion [30]. In this case, as the temperature shall be constant throughout the molten stack and the condition was deliberately maintained to be isothermal, so the thermal convection within the molten stack may be somewhat limited. Meanwhile, how fast would the Cu diffusion profile reach 7 mm (thickness of the Al disc)? The diffusivity of Cu in a liquid Al is quoted from the work by Du *et al*. [31] as

$$D = 1.06\times10^{-7}\exp\left(-\frac{24000}{RT}\right) \qquad \text{(Unit: } m^2\ s^{-1}\text{)} \qquad (4.1)$$

Taking T = 1023 K (750°C), the diffusivity is calculated to be $D = 6.31\times10^{-9}$ $m^2\ s^{-1}$. Assuming a one directional diffusion model (only up and down) [32], the diffusion distance is approximated as

$$x \approx \sqrt{2Dt} \tag{4.2}$$

Taking x = 7 mm (thickness of the Al disc), the time t, which is the time for Cu diffusion profile to reach 7 mm, is calculated to be around 3800 s, a little bit more than 1 h. This value is reasonable. As we can see from **Figure 4.3** that for the *S-1* sample, although there is around 12.1% of Al side being occupied by the Cu-rich melt, the upward flow of Cu must overcome the gravity force and the actual time required to allow the Cu diffusion profile to reach 7 mm by thermal diffusion is therefore longer than the calculated value. However, if Al-5Cu is on top of the Al, according to previous discussions, the time to reach the complete mixing is greatly affected by the gravitational flow of Cu-rich melt instead of thermal diffusion. As discussed previously in section 4.3.3 and also summarized in **Figure 4.26**, another feature of the time effect is that, during the holding stage, as the holding time increases, the breaking of the *bi-film* layer occurs due to the formation of crystalline-like oxides, generating more cracks (easy channels).

4.3.5.3 Solidification stage

The thermal mismatch (different thermal expansion coefficients between metal and oxide) during solidification can be estimated using the following equation [33]

$$\sigma \approx E_o \Delta T \left(\alpha_o - \alpha_m\right) \tag{4.3}$$

Here α is the linear thermal expansion coefficient for oxide or metal, ΔT is the degree of supercooling and E_o is the elastic modulus of the oxide, and σ is the internal stress arising from the discrepancy in α_o and α_m. As α_o is usually less than α_m, so a compressive stress is always present within the oxide scale during cooling. From **Equation 4.3**, it can be inferred that the faster the cooling, the more internal thermal stress generated. Cracking of the oxide scale is an effective way to release the stress [22].

Although the solidification time is relatively short (empirically around 5 minutes), the possibility of having some degree of metallic mixing in this stage cannot be ruled out. For example, in the case of the stacked Al-5Cu/Al (Al-5Cu is on top of Al), when Al solidifies the Al-5Cu melt could flow through cracks generated by thermal mismatch stress and shrinkage during solidification of Al. But the amount of the Al-5Cu melt that can go through these channels in this stage is extremely difficult to quantify.

On the other hand, in the case of the stacked Al/Al-5Cu system, the Al-5Cu melt would preferentially remain at the Al-5Cu side, so even if the *bi-film* layer is disrupted to have more cracks in this stage, the metallic mixing has to be achieved mainly through thermal diffusion of Cu, as the up flow of the Cu-rich melt needs to overcome the gravity force. But again, it has to be admitted that it is very difficult to determine exactly how solidification could affect the degree of bonding in this stacking approach. During solidification, the release of latent heat could potentially bring in thermal convection within the stack which may facilitate the flow of melt to an unknown extent. There is a lack of direct evidence to substantiate the described hypothesis, perhaps an *in situ* observation or tracer element marking experiment may be helpful.

4.4 Results and discussion – Stacked Al/Al-2Mg

This section presents the results and discussion of the stacked Al/Al-2Mg system, in particular the oxidation issues involved in bonding of Al and Al-2Mg. Several interesting findings from the present work will be introduced here, but a more rigorous analysis of the mechanism behind all these phenomena will be given in Chapter 6, where the oxidation studies of the Al-Mg-O_2 system are described in detail. The results and discussion will be correlated back to here again. The sample details in this section are given in **Table 4.2**.

4.4.1 SEM/EDX studies

As can be seen from **Figure 4.27**, the interface is microscopically rough with some metal entrapment (highlighted by yellow arrows) with widths up to 20 μm between Al and Al-2Mg. As highlighted by red arrows, some oxide-like phases have formed at the bond interface, in particular along the Al-2Mg side of the interface. Similar features are shown in **Figure 4.28**. EDX point analysis of interested areas was performed and the quantified results are presented in **Figure 4.29**. The compositions in weight percentage are calculated for P1 and P2. The results suggest that Mg has migrated to the Al side and there is a certain degree of metallic mixing. It is also noted that the matrix composition of Mg on the Al-2Mg side is slightly less than the original bulk Mg composition (Al-2wt% Mg). As revealed by P3 and P4 in **Figure 4.29**, Mg-rich oxides have formed at the interface. The atomic ratio for Mg, Al and O was calculated with respect to Mg (which is 1). Although the quantified results suggest that the Mg-rich oxides may be $MgAl_2O_4$, it is still so far unclear and hard to tell exactly what these Mg-rich oxides comprise of. This question will be addressed further in the following discussion and also in Chapter 6.

Figures 4.30-4.32 are pairs of SE and BE images showing a bond interface morphology of the stacked Al/Al-2Mg sample *M-6* similar to that observed in *M-1*. However, as indicated by **Figure 4.30**, the Mg-rich oxide layer on the Al-2Mg side is more continuous with a thickness of around 2 μm. In addition, as highlighted in **Figure 4.31**, the interface has actually healed at this location with the presence of some scattered oxide particles with an average size of 1.2 μm, suggesting a possible oxidation mechanism: the formation of Mg-rich oxides by reducing the pre-formed aluminium oxide layers, the original aluminium oxide layer serves as a substrate and Mg-rich oxides form at the expense of it. The detailed oxidation mechanism will be discussed in Chapter 6. **Figure 4.32** also shows a scattered distribution of oxide particles at the interface zone. Some of these oxides particles are well embedded within the matrix and facetted. The EDX results are shown in **Figure 4.33** and the quantified results in terms of the atomic ratio are listed. It is noted

that the composition of these facetted oxides is close to the stoichiometric oxide $MgAl_2O_4$. Meanwhile, as shown in **Figure 4.34**, there is a possible metallic mixing mechanism for the stacked Al/Al-2Mg system: the fracture of the *bi-film* layer causing the metallic mixing through the generated channel.

Figure 4.35 comprises pairs of SE and BE images showing the interface microstructure of the stacked Al/Al-2Mg sample *M-24*. It is observed that the *bi-film* layer is healed in some regions and oxide particles are present there. This may suggest another possible metallic mixing mechanism: melts could flow through the space between these oxide particles as a result of capillarity [29]. Meanwhile, it is noted that the oxide layer formed on the Al-2Mg side (around 2-4 μm) is thicker than that in sample *M-6*, suggesting the effect of time on the oxide growth. Interestingly, as can be seen from **Figure 4.36**, there are many facetted oxide particles with sizes of around 1-5 μm assembling into a continuous oxide layer and also embedded elsewhere in the matrix. EDX analysis has been performed on these features and the results are shown in **Figures 4.37** and **4.38**, suggesting these facetted oxide particles are highly likely to be $MgAl_2O_4$.

First of all, as we recall from Chapter 3, the interaction volume for $MgAl_2O_4$, calculated using the experimental conditions in the present work, is around 3 μm. Secondly, as the surface of the SEM sample is flat, there should be little topography-induced effects on the intensity of X-rays counted by the EDX detector installed on the microscope. Thirdly, according to **Figures 4.37** and **4.38**, the average size of the facetted oxide particle size is around 4 μm, larger than the interaction volume for $MgAl_2O_4$. Therefore, the chemistry of the oxide particles calculated from the EDX spectra should be very close to the actual chemistry. According to the above EDX results, we can see good consistency and the facetted oxide particles are highly likely to be $MgAl_2O_4$ and the Mg-rich oxide layer formed on the Al-2Mg side mainly consists of $MgAl_2O_4$. As indicated by **Figure 4.38**, the $MgAl_2O_4$ shows a typical {111}-like faceting interface with the matrix. This is because

that $MgAl_2O_4$ and α-Al have the same crystal structure (fcc) and only a lattice misfit of 1.4% [34], it is easy to obtain a cube-on-cube orientation relationship between $MgAl_2O_4$ and α-Al on the close-packed planes. Similar observation has been reported by Wang *et al*. [34], who also found a common epitaxial relationship (111) [110] $MgAl_2O_4$ // (111) [110] α-Al.

4.4.2 Bonding mechanism

According to previous results and discussion, there are at least two possible bonding mechanisms occurring in the stacked Al/Al-2Mg samples: first of all, the formation of Mg-rich oxides at the bond interface disrupts the *bi-film* layer and leads to both melt entrapment and fracture of the *bi-film* layer, melts mix through the generated cracks; second, in the stacked Al/Al-2Mg samples which had been held for a longer time (up to 24 h), the *bi-film* layer could be healed locally and the space between the crystalline-like oxide particles serve as microchannels for metallic mixing.

4.5 Concluding remarks

According to the current investigation, it has to be admitted that the stacking approach may have some limitations, as it does not help get a clean bond interface, and the process requires a complete melting of the parent materials, which could take a lot of energy. Precaution must also be taken to avoid complete mixing of two melts during the process. Despite its exploratory nature, the study has still gone some way towards enhancing our understanding of the bonding of Al alloys and the results show the central importance of oxide formation at the bond interface and its subsequent behaviour during the bonding process. This study has also thrown up some aspects which may be in need of further investigation, such as the factors controlling the oxide growth, etc. The issue of oxidation itself is an intriguing topic.

4.6 References

[1] J. Campbell, *Castings*: London Butterworth, 2003.

[2] W. Opie and N. Grant, "Hydrogen solubility in aluminum and some aluminum alloys," *Trans. AIME*, vol. 188, pp. 1237-1247, 1950.

[3] J. Weigel and E. Fromm, "Determination of hydrogen absorption and desorption processes in aluminum melts by continuous hydrogen activity measurements," *Metallurgical Transactions B*, vol. 21, pp. 855-860, 1990.

[4] W. D. Griffiths and R. Raiszadeh, "Hydrogen, porosity and oxide film defects in liquid Al," *Journal of Materials Science*, vol. 44, pp. 3402-3407, 2009.

[5] J. Scully, G. Young Jr, and S. Smith, "Hydrogen solubility, diffusion and trapping in high purity aluminum and selected Al-base alloys," *Materials science forum*, vol. 331, pp. 1583-1600, 2000

[6] S. Fox and J. Campbell, "Visualisation of oxide film defects during solidification of aluminium alloys," *Scripta materialia*, vol. 43, pp. 881-886, 2000.

[7] S. Fox and J. Campbell, "Liquid metal quality," *International Journal of Cast Metals Research*, vol. 14, pp. 335-340, 2002.

[8] P. Morize and P. Lacombe, "Chimie physique-etude de loxydation de laluminium par lair, a la temperature ordinaire par la mesure du potentiel de dissolution," *Comptes rendus hebdomadaires des séances de l'académie des sciences*, vol. 222, pp. 658-659, 1946.

[9] R. K. Hart, "The oxidation of aluminium in dry and humid oxygen atmospheres," *Proceedings of the Royal Society of London Series a-Mathematical and Physical Sciences*, vol. 236, pp. 68-88, 1956.

[10] I. Olefjord and A. Nylund, "Surface-analysis of oxidized aluminum. 2. Oxidation of aluminum in dry and humid atmosphere studied by ESCA, SEM, SAM and EDX," *Surface and Interface Analysis*, vol. 21, pp. 290-297, 1994.

[11] A. Nylund and I. Olefjord, "Surface analysis of oxidized aluminium. 1. Hydration of Al_2O_3 and decomposition of $Al(OH)_3$ in a vacuum as studied by ESCA," *Surface and Interface analysis*, vol. 21, pp. 283-289, 1994.

[12] S. A. Impey, D. J. Stephenson, and J. R. Nicholls, "Mechanism of scale growth on liquid aluminum," *Materials Science and Technology*, vol. 4, pp. 1126-1132, 1988.

[13] S. Impey, "The mechanism of dross formation on Al and Al-Mg alloys," PhD Thesis, Cranfield Institute of Technology, 1989.

[14] E. Howard, *Modern foundry practice*: Philosophical Library, 1959.

[15] E. McCafferty, *Introduction to corrosion science*: Springer, 2010.

[16] http://research.microsoft.com/en-us/um/redmond/groups/ivm/ice/.

[17] D. C. Joy, *Scanning electron microscopy*: Wiley-VCH, 2003.

[18] J. M. Lameille, E. Buiret, and C. Berthier, "The scanning electron microscopy (SEM) and energy dispersive X-ray spectroscopy (EDS) for the study of the high temperature oxidation mecanisms." *Microscopy and Microanalysis*, vol. 9, pp. 634-635, 2003.

[19] R. Raiszadeh and W. Griffiths, "A method to study the history of a double oxide film defect in liquid aluminum alloys," *Metallurgical and Materials Transactions B*, vol. 37, pp. 865-871, 2006.

[20] R. Raiszadeh and W. Griffiths, "A semi-empirical mathematical model to estimate the duration of the atmosphere within a double oxide film defect in pure aluminum alloy," *Metallurgical and Materials Transactions B*, vol. 39, pp. 298-303, 2008.

[21] W. Griffiths and R. Raiszadeh, "Hydrogen, porosity and oxide film defects in liquid Al," *Journal of materials science*, vol. 44, pp. 3402-3407, 2009.

[22] P. Kofstad and J. Wiley, *High-temperature oxidation of metals* vol. 584: Wiley New York, 1966.

[23] H. E. Boyer and H. E. Boyer, *Metal handbook*: American Society of Metals., 1960.

[24] E. Liotti, A. Lui, R. Vincent, S. Kumar, Z. P. Guo, T. Connolley, M. Hart, L. Arnberg, R. H. Mathiesen, and P. S. Grant, "A synchrotron X-ray radiography investigation of induced dendrite fragmentation in Al-15wt% Cu," in *Materials Science Forum*, 2013, pp. 210-214.

[25] E. Liotti, A. Lui, R. Vincent, S. Kumar, Z. Guo, T. Connolley, I. Dolbnya, M. Hart, L. Arnberg, and R. Mathiesen, "A synchrotron X-ray radiography study of dendrite fragmentation induced by a pulsed electromagnetic field in an Al-15Cu alloy," *Acta Materialia*, vol. 70, pp. 228-239, 2014.

[26] R. Rerko, H. de Groh, and C. Beckermann, "Effect of melt convection and solid transport on macrosegregation and grain structure in equiaxed Al-Cu alloys," *Materials Science and Engineering: A*, vol. 347, pp. 186-197, 2003.

[27] A. Csanady, A. Barna, and P. B. Barna, "Direct observation and investigation of the oxidation of aluminum in the transmission electron-microscope," *Oxidation of Metals*, vol. 13, pp. 245-254, 1979.

[28] P. E. Doherty and R. S. Davis, "Direct observation of oxidation of aluminum single-crystal surfaces," *Journal of Applied Physics*, vol. 34, p. 619, 1963.

[29] E. W. Washburn, "The dynamics of capillary flow," *Physical review*, vol. 17, p. 273, 1921.

[30] R. K. Zeytounian, *Convection in fluids: A rational analysis and asymptotic modelling* vol. 90: Springer, 2009.

[31] Y. Du, Y. Chang, B. Huang, W. Gong, Z. Jin, H. Xu, Z. Yuan, Y. Liu, Y. He, and F.-Y. Xie, "Diffusion coefficients of some solutes in fcc and liquid Al: Critical evaluation and correlation," *Materials Science and Engineering: A*, vol. 363, pp. 140-151, 2003.

[32] J. Crank, *The mathematics of diffusion*: Oxford university press, 1979.

[33] P. Kofstad, *High-temperature oxidation of metals* vol. 584: Wiley New York, 1966.

[34] Y. Wang, H.-T. Li, and Z. Fan, "Oxidation of aluminium alloy melts and inoculation by oxide particles," *Transactions of the Indian Institute of Metals*, vol. 65, pp. 653-661, 2012.

CHAPTER 5

OXIDATION STUDIES: THE Al-Cu-O_2 SYSTEM

5.1 Introduction

Based on the observations described in Chapter 4, we know that the oxide *bi-film* layer is a physical barrier to prevent metallic bonding and it evolves microscopically with increasing holding time. It is felt that a more in-depth understanding of the oxide formation itself is needed. A few questions then arise: How does the oxide grow? How will the oxide layer behave microscopically during melting and solidification? Is it possible to create a universal oxidation model for Al alloys? Only through a detailed investigation to gain adequate knowledge of oxidation shall we be able to tailor the oxide as a function of temperature and time and to better design the proper processing conditions for bonding of Al alloys. So this chapter gives details of the work investigating the oxidation mechanisms for dilute Al-Cu binary alloys, using an Al-5Cu alloy as the model system and pure Al as the control.

It should be noted that the results shown in this chapter only focus on metal-oxygen reactions. Theoretically, some highly reactive metals, such as Al and Mg, may also react with other gases in the environment. For example, as discussed in Chapter 2, Al could react with nitrogen to form AlN. Mg can also react with nitrogen to produce Mg_3N_2 [1, 2]. In the present work, as the atmosphere condition is maintained during the experiments (no depletion of oxygen), the oxides will always form preferentially than nitrides from a perspective of thermodynamics, as briefly discussed in **Appendix 5.1**. It is also indicated that the nitrides may only emerge in an oxygen-depleted environment. The results in Chapters 5 and 6 also indicate that AlN and Mg_3N_2 were not present in the surface oxide scales, which is consistent with the thermodynamic prediction.

In this chapter, Section 5.2.1 addresses the issue of oxidation from a perspective of

thermodynamics by considering the Gibbs free energy change associated with different oxidation reactions. Section 5.2.2 describes some preliminary experimental results of the study of the Al-5Cu alloy in terms of its typical as-cast microstructure and phase transformation behaviours. Sections 5.2.3 and 5.2.4 describe the study of the nature of the oxide scale in terms of its roughness, composition and morphology and some particular "*patterning*" features. Section 5.2.5 then presents the results of SEM/EDX studies which show the structure and morphology of the oxide scale at a microscopic level. Section 5.2.6 focuses on the XPS studies and section 5.2.7 gives details of results of oxidation kinetics studies. Section 5.3 presents further discussion of the oxidation mechanisms occurring through a comprehensive analysis of the oxide scale evolution during different oxidation stages.

5.2 Results and discussion

5.2.1 Thermodynamics calculations

Oxidation of metals is a thermodynamically and kinetically complex process, and the presence of oxide-forming alloying elements in a metal may significantly modify its oxide growth mechanism [3]. As shown in Chapter 2, the favourability of a particular oxidation reaction at any given temperature depends on its amount of reduction in Gibbs free energy.

For comparison of different oxidation reactions, the one which lowers the total Gibbs free energy most could proceed preferentially [4]. This section focuses on the thermodynamic analysis of the Al-Cu-O_2 system carried out in the present work, specifically in two aspects: (1) the calculation of Gibbs free energy change for each possible dry atmospheric oxidation reaction as a function of alloy composition and oxidizing temperature; (2) the construction of stability diagrams [4] which show the conditions under which an oxide will be reduced to its metal.

It has to be noted that the thermodynamics analysis described in this section is only thermodynamic in nature and it ignores reaction kinetics: the oxidation reaction which is predicted to be favourable may actually proceed very slowly. Oxidation is a far more complex process and how it is treated depends on different situations.

5.2.1.1 Gibbs free energy functions

For the Al-Cu-O_2 system, metal oxides can be produced through the following reactions. For the ease of comparison, the stoichiometric coefficient of O_2 is normalized to one in each reaction.

A. $4/3Al + O_2 = 2/3Al_2O_3$ (Reaction A)

B. $4Cu + O_2 = 2Cu_2O$ (Reaction B)

C. $2Cu + O_2 = 2CuO$ (Reaction C)

The standard free energy change for each reaction as a function of temperature is estimated in the form of $\Delta G^{\circ}(T) = a + bT + cT\ln T$ using the method described in **Appendix 5.2** as follows:

A. $\Delta G^{\circ}(T) = -1099621 + 148.60T + 7.82T\ln T$ (Unit: J mol^{-1}) (5.1)

B. $\Delta G^{\circ}(T) = -345590 + 223.92T - 10.05T\ln T$ (Unit: J mol^{-1}) (5.2)

C. $\Delta G^{\circ}(T) = -318006 + 302.42T - 16.97T\ln T$ (Unit: J mol^{-1}) (5.3)

According to section 2.2.1, the Gibbs free energy change for a reaction which occurs at a non-standard state is affected by the chemical activities of reacting species [5], as shown by **Equation 2.5** in Chapter 2. The non-standard Gibbs free energy change for reactions A, B and C are expressed as

A. $\Delta G(T) = -1099621 + 148.60T + 7.82T\ln T - RT\ln\left(\frac{a_{O_2}\cdot a_{Al}^{4/3}}{a_{Al_2O_3}^{2/3}}\right)$ (5.4)

B. $\Delta G(T) = -345590 + 223.92T - 10.05T\ln T - RT\ln\left(\frac{a_{O_2}\cdot a_{Cu}^{4}}{a_{Cu_2O}^{2}}\right)$ (5.5)

C. $\Delta G(T) = -318006 + 302.42T - 16.97T\ln T - RT\ln\left(\frac{a_{O_2}\cdot a_{Cu}^{2}}{a_{CuO}^{2}}\right)$ (5.6)

In the present work, the chemical activities of Al, Cu, O_2 and metal oxides are estimated under three assumptions: it is assumed that oxygen gas behaves ideally and its activity equals to the ratio between the oxygen partial pressure and the standard pressure 1 atm [6]. (Note: P_{O2} is used as an expression for a_{O2} throughout further discussion); it is assumed that the binary Al-Cu alloy forms an ideal solution and the activities of Al and Cu are equal to their mole fractions (i.e. $a_{Al} = X_{Al} = 1 - X_{Cu}$ and $a_{Cu} = X_{Cu}$); the activities of metal oxides are assumed to be 1, as it is suggested that these oxides are nearly immiscible with each other in the temperature range relevant to the present work (which is 20-1100ºC) [7].

These assumptions are made for two reasons: a lack of experimentally measured thermodynamic data for the Al-Cu system in the literature and ease of mathematical manipulation. Therefore, **Equations 5.4-5.6** can be further simplified as a function of oxygen activity P_{O2} and Cu mole fraction X_{Cu}:

A. $\Delta G(T) = -1099621 + 148.60T + 7.82T\ln T - RT\ln\left(P_{O_2}\cdot(1-X_{Cu})^{4/3}\right)$ (5.7)

B. $\Delta G(T) = -345590 + 223.92T - 10.05T\ln T - RT\ln\left(P_{O_2}\cdot X_{Cu}^{4}\right)$ (5.8)

C. $\Delta G(T) = -318006 + 302.42T - 16.97T\ln T - RT\ln\left(P_{O_2}\cdot X_{Cu}^{2}\right)$ (5.9)

5.2.1.2 $\Delta G(T)$ plots

$\Delta G(T)$ plots are used to assess the favourability of each oxidation at different temperatures by fixing P_{O2} and X_{Cu}. **Figure 5.1** is a 2D plot showing the ΔG versus T relationship in a dry air condition (with P_{O2} = 0.21, and X_{Cu} is around 0.0215 for the Al-5Cu alloy). **Figure 5.2** is a 3D plot showing ΔG profile as a function of both X_{Cu} and T (with P_{O2} = 0.21). It can be inferred from these plots that Al_2O_3 is the most thermodynamically favourable metal oxide in the Al-5Cu alloy, or any standard commercial Al alloys (at most 10wt% Cu (4.4mol%) in 2xxx series alloys [8]), or even the $CuAl_2$ intermetallic (32.9mol% Cu), as the reduction in free energy for reaction A is

around one order of magnitude more than for the other reactions at the interested ranges of X_{Cu} and T.

These predications are in keeping with observations in the literature. According to the work by Son *et al*. [9], a $CuAl_2$ thin film will only undergo oxidation to Al_2O_3 at 580ºC; it has been shown by Garcia-Vergara *et al*. [10] that no CuO or Cu_2O has been observed in the anodic oxide film formed on an Al-4.14wt%Cu (Al-1.77mol%Cu alloy), but Cu has an influence on the morphology of the oxide film [10, 11]. On the other hand, according to the work by Wu *et al.* [12], Al_2O_3 was found in an oxidized Cu alloy containing ~2wt% Al (5mol% Al) in the temperature range 800-1000°C and similarly, Soleimanpour *et al*. [13] reported the presence of Al_2O_3 in a Cu alloy containing Al as low as 0.37wt% (0.88mol% Al) at 950°C, suggesting the preferred growth of Al_2O_3 over copper oxides even at such low levels of Al.

It can be seen that adding Cu into Al would not inhibit the preferential oxidation of Al thermodynamically. The oxidation behaviour of pure Al and the Al-5Cu binary alloy in terms of the oxidation products are highly likely to be the same, purely based on the thermodynamic analysis in the present work as well as the implications from the literature.

5.2.1.3 Stability diagram 1: lnP_{O2} versus T

The lnP_{O2} versus T plot is used to give the conditions under which the oxides (Al_2O_3, Cu_2O, and CuO) dissociate into metal. **Figure 5.3** is a stability diagram constructed based on **Equations 5.7-5.9** (let $\Delta G(T) = 0$ and $X_{Cu} = 0.0215$). The plot shows the oxygen dissociation pressure as a function of temperature. It indicates that the oxides become less stable at higher temperatures (higher oxygen dissociation pressure). Interestingly, the oxygen dissociation pressure of Al_2O_3 is estimated to be around 5×10^{-185} Pa at 25°C, as a similar value of 1.5×10^{-185} Pa is deduced from the results shown by Wu *et al*. [12]. This implies that Al will always pick up oxygen to form Al_2O_3

and the oxide will remain stable, given that it is impossible to have an environment with such a low oxygen partial pressure in practice.

5.2.1.4 Stability diagram 2: $\ln P_{O2}$ versus X_{Cu}

Figure 5.4 is a stability diagram constructed by letting $\Delta G(T) = 0$ and $T = 1023$ K in **Equations 5.7-5.9**. It shows the oxygen dissociation pressure as a function of Cu mole fraction X_{Cu} at a fixed temperature of 750ºC. It is inferred that for Al-Cu alloys with a Cu composition below 0.1mol% (around 0.24wt%), the formation of Cu_2O or CuO is almost impossible in dry air, because the oxygen dissociation pressure of either Cu_2O or CuO is higher than 0.21 atm. Meanwhile, Cu_2O and CuO are predicted to be stable in dry air at 750°C, suggesting the likely formation of Cu_2O and CuO in the Al-5Cu alloy. In fact, this is consistent with the implication from **Figure 5.1** that the reactions B and C are also thermodynamically spontaneous (free energy reduction). But again, as discussed previously, because the amount of free energy reduction for reaction A is far more than those of reactions B and C, the formation of Al_2O_3 is more likely.

To sum up, although the thermodynamic analysis described in section 5.2 is subject to the accuracy and credibility of Gibbs free energy values quoted from various databases as well as the assumptions made, at least it allows us to ascertain the conditions under which given oxidation products are feasible.

5.2.2 Microstructure of Al-5Cu

This section presents results on the investigation of the Al-5Cu alloy in terms of its microstructure, solidification and phase transformation behaviour. The composition of Cu in this alloy is very close to commercial 2xxx wrought Al alloys [14], which are widely used in the aerospace and automotive industries [15]. The addition of Cu to Al lowers the melting point of the Al solid solution and leads to the precipitation of θ-$CuAl_2$ phase at room temperature [16]. The θ-$CuAl_2$ phase has high optical contrast with the Al matrix and is readily visible in microscopes [17, 18].

The equilibrium phase diagram of Al-5Cu was calculated using MTDATA software, as shown in **Figure 3.1**. The equilibrium phases for an Al-5Cu binary alloy are α-Al and θ-$CuAl_2$ precipitates. The eutectic phase (α-Al + θ-$CuAl_2$) is also often observed in as-cast hypoeutectic Al-Cu alloys [16]. Differential Scanning Calorimetry (DSC) was carried out to confirm the presence of this transformation behaviour on melting. In this study, the difference in heat flow between the sample and a reference was observed to determine any phase transition stage. The results are shown in **Figure 5.5**. It is noted that Al-5Cu starts to melt at around 548ºC (eutectic temperature) and the curve is featured by a small endothermic peak centred at 550ºC and a broad peak centred at 660ºC.

Figure 5.6 is a pair of SE and BE images showing the fracture surface topography of an as-cast Al-5Cu alloy. First of all, it can be seen that the microstructure of the Al-5Cu consists of cored dendrites of α-Al with θ-$CuAl_2$ at grain boundaries or in interdendritic regions. As illustrated by **Figure 5.7**, the presence of brittle θ-$CuAl_2$ at boundaries makes the alloy very susceptible to intergranular corrosion and intergranular cracking [19, 20]. The equilibrium θ-$CuAl_2$ phase is incoherent with the α-Al matrix and they have significantly different stiffness and thermal expansion coefficients, etc [21], which make the interface between θ-$CuAl_2$ and α-Al a favourable crack initiation site and propagation path [20]. As also observed in **Figure 5.6**, it is interesting to note that junctions between three grains tend to maintain an approximate 120°/120°/120° relationship, this is a result of an equilibrium balance of grain boundary tensions at a three grain junction [22, 23]. Meanwhile, it is found in the present work that there is a good interconnectivity of the θ-$CuAl_2$ network in the as-cast Al-5Cu, as shown in **Figure 5.8**, further suggesting the cored dendritic structure of α-Al. The intermetallic phases were extracted using the methods described in Chapter 3.

5.2.3 Surface oxide film – dendritic patterning

From earlier discussion, it was noted that as-cast Al-5Cu usually has a cored dendritic structure with $CuAl_2$ phases at the grain boundaries. One of the topographic features of the oxide layer formed on Al-5Cu samples observed in the present work is "***dendritic patterning***". During casting, fresh Al-5Cu melt is exposed to the air and an oxide skin quickly develops on the surface. Normally, in the early stages, the thickness of the oxide layer is unlikely to grow enough to make the oxide layer become mechanically rigid [24]. In such a case, the oxide layer is very thin in nature and it is easily bent and deformed and thus follows the topography of the dendrites. It was suggested by Bubar and Vermilyear [25] that thin aluminium oxide films less than 10 nm in thickness exhibit good ductility.

In the present work, as shown in **Figure 5.9**, the surface topography of the as-cast Al-5Cu sample follows its dendritic structure and varies with cooling rate during solidification: a cooling rate of 40 K min^{-1} leads to the formation of dendrites with around 30 µm secondary arm spacing and 100 K min^{-1} leads to the formation of dendrites with around 5 µm secondary arm spacing.

In addition, a DEKTAK surface profiler was used to further investigate this "***dendritic patterning***" feature. Al samples and Al-5Cu samples were oxidized at 750ºC for 1 h and 6 h to study the influence of oxidizing time on surface roughness. Prior to heat treatment, samples were polished down to 1µm diamond suspension and a flat and uniformly rough surface is achieved, see **Figure 5.10 (a)**. **Figure 5.10 (b)** shows that both Al and Al-5Cu have similar levels of roughness after polishing. **Figure 5.10 (c)** presents the different surface roughness conditions for Al and Al-5Cu after being oxidized in air for 1 h: this is because that the relatively thin and ductile oxide layer formed on Al-5Cu (1 h oxidation) tends to copy the pattern of the dendritic structure during solidification and the dendritic structure of Al-5Cu contributes significantly to the larger height change during the DEKTAK analysis. Interestingly, according to **Figure 5.10 (d)**, Al and Al-5Cu

samples have similar surface roughness: this is because the oxide layer can become thick and rigid after a longer period of holding time and it is less likely to deform during solidification. So dendritic patterning may only exist when the oxide layer is thin and ductile. **Figure 5.11** shows OM micrographs clearly showing such effect, as highlighted by red circle, a piece of fragmented rectangular oxide film with a size of around 1.5 mm by 0.6 mm floats on the Al-5Cu melt and it does not copy the dendritic structure, as compared with its surrounding area. By implication, this piece of oxide must be thicker than the surrounding oxide.

5.2.4 Hot-stage OM studies

As discussed in Chapter 4, the stacked Al/Al-5Cu sample will undergo three distinct stages during the stacking approach: melting, holding, and solidification. In the present work, hot-stage OM studies were performed to directly observe the microstructure development of the surface oxide layer formed on Al or Al-5Cu during a *re-melting* process. The experimental procedure was described in Chapter 3. For Al, the results of *in situ* observation of the surface oxide film evolution during the re-melting process are shown in **Figure 5.12**. The evolution of surface topography can be represented by five successive stages. ***Stage 1*** **–** highlighted by black boxes: sample temperature rises, grain boundary region starts to melt at 600ºC; ***Stage 2*** – highlighted by red boxes: the oxide layer thickens and becomes increasingly rough and wrinkled; ***Stage 3*** – highlighted by blue boxes: the sample is completely liquid and the oxide layer keeps thickening; ***Stage 4*** – highlighted by yellow boxes: during cooling, the oxide layer deforms to accommodate the formation of grain structure; ***Stage 5*** – highlighted by green boxes: the oxide layer copies the new grain structure of Al. It can be seen from these images that grain boundaries melt first and thus grooves form. Similar features were also observed by Allen et al. [26]. This is because the grain boundaries of Al were often enriched with impurity elements, such as Fe, Si, Zn, Mg, etc, and these alloying elements lower the melting point of Al [27]. Thermodynamically, impurity elements segregate to grain boundaries as an attempt to reduce the total free energy of the system

[28]. Kinetically, the grain boundaries serve as short-circuit diffusion paths for impurity atoms [29], they prefer to move along grain boundaries and provide a drag force on grain boundaries motion [30]. The topic of segregation will be discussed again in Chapter 6.

For Al-5Cu, the surface oxide film evolution is similar to that observed for Al, as shown in **Figure 5.13**. It is also noted in the present work that $CuAl_2$ intermetallics are in different locations before melting compared to after solidification, as highlighted by purple (before) and red lines (after).

During the experiment, it was found that the temperature calibration of the hot stage was not very accurate and the temperature measured from the control unit is somewhat overvalued and the deviation from the actual temperature of the samples is at least 10ºC, as suggested by the image labelled 670ºC in **Figure 5.12**, where the Al seemed not to be as completely melted as it should be.

5.2.5 SEM/EDX studies

In this section, the SEM/EDX studies of differently oxidized Al and Al-5Cu samples are described, in terms of oxide morphology and chemistry.

5.2.5.1 750ºC

Figure 5.14 presents two pairs of SE and BE images showing the oxide layer morphology of an Al-5Cu sample which was oxidized at 750ºC for 1h in dry air. The oxide layer exhibits a wrinkled morphology suggesting its ductile nature. It look likes that the oxide layer *"acts"* independently from the melt underneath, as contrasted by a regular cored microstructure from BE images. Interestingly, as highlighted by yellow arrows in **Figure 5.14 (b)**, two rigid oxide island-like pieces with the diameters of around 80 μm become pinning points from which the oxide film deforms during solidification. The observed result seems consistent with the results from hot-

stage OM studies described in section 5.2.4.

Figures 5.15 – 5.17 presents the results of Al samples which were oxidized for longer periods (12h, 24h and 48h). First of all, it can be noted that the number of crystalline-like oxides increases as the oxidation time is extended. In the present work, prior to oxidation experiments, the surfaces of samples were deliberately ground with 800 grit size SiC paper to study whether the oxides would preferentially nucleate and grow along the scratches to form "straight lines"-like oxide morphologies. Accord to the current results, instead of growing along scratches, the crystalline-like oxides tend to nucleate and grow locally to form small circular-shaped islands around 10-100 μm. Similar oxide morphology was observed by Doherty and Davis [31] and Eldridge *et al.* [32]. Meanwhile, as suggested by **Figure 5.18**, secondary crystals can grow on existing islands and the primary oxide island consists of small faceted crystalline particles and they grow through a "*ledge*" mechanism so as to reduce surface energy [33]. The "*ledge*" growth mechanism will be discussed in detail in section 5.2.5.3. EDX analysis was performed on the island-like oxides and the result is given in **Figure 5.19**. They are identified as aluminium oxide. The lower atomic ratio between Al and O from the matrix position is probably due to the interaction volume issue, as characteristic Al Kα X-rays may also come from the metal beneath the oxide layer. XRD analysis of the oxidized sample was tried but not successful. This is probably due to the low volume fraction of the crystalline oxides compared to the bulk. Hinton and Griffiths have recently used glancing XRD to successfully identify the oxide formed on high purity Al at 750ºC after 3h of oxidation as consisting of crystalline γ-Al_2O_3 [34]. This suggests that the crystalline-like oxide observed in the present work may be γ-Al_2O_3 as well. **Figure 5.20** shows the cross sectional view of the oxidized Al sample (750ºC 12 h). Faceted crystalline-like oxides, with the thickness of around 5μm, penetrating into the metal were observed. According to Wang *et al*. [35], the crystalline (γ-Al_2O_3) oxides formed at 750ºC after 4h of oxidation in air were also morphologically faceted. Similar observations were also reported by Doherty and Davis [36] who studied the solid state oxidation

of Al and found that the crystalline oxides grow inwardly and epitaxially into the metal with a preferential relationship (110) [110] γ-Al_2O_3 // (111) [110] Al.

Figures 5.21-24 show the oxide layer morphology developed on Al-5Cu samples oxidized at 750ºC for a series of times and the observed oxides are similar to those on Al: the number of island-like oxides increases with oxidizing time; the crystalline oxides grow locally at the beginning and then agglomerate to eventually cover the whole surface; the crystalline oxide grows by a *ledge* mechanism.

Interestingly, **Figure 5.25** shows an oxide island can be as large as 45 μm, as highlighted by the red circle. In addition, the lower-right BE image in **Figure 5.25** provides evidence for Al-Cu intermetallic (bright contrast) trapped within the crystalline oxide-island. This might be a result of a possible oxide-island growth mechanism: individual oxide crystals agglomerate to form oxide islands and there are gaps between them, the melt may flow and get trapped in the gaps, and the continuous consumption of Al to form Al_2O_3 increases the Cu composition in the trapped melt locally and the Al-Cu intermetallic is thus formed. **Figure 5.26** shows the EDX analysis performed on an oxidized Al-5Cu sample, the features are similar to those observed on the oxidized Al sample.

5.2.5.2 950ºC

Figures 5.27 and **5.28** show the powdery morphology of the oxide scale formed on Al-5Cu at 950ºC for 48h. During the experiments, it was found that oxides could be easily scraped from the samples (powdery morphology, the oxides were loosely attached to the metal). Therefore, some of the scraped oxides were collected and mounted on carbon adhesive tabs. As noted in **Figures 5.27** and **5.28**, the oxides have two different morphologies, which may refer to the "*dry*" side and the "*wet*" side of a surface oxide film. By definition, the "*dry*" side refers to the oxide/air interface,

while the "*wet*" side is used to describe the melt-wetted metal/oxide interface which may consist of different microstructural features (e.g. oxide crystals, intermetallics) [37-40]. As shown in **Figures 5.27 (a)** and **(b)**, the oxide layer shows a macroscopically smooth and uniform topography (scratches from polishing are observed), which is similar to a typical *dry* side morphology [38, 39]. Macrocracks are also observed, but they may have formed during the scraping process (the issue associated with the scraping technique is that it may destroy the oxide film mechanically to an unknown extent, Chapter 6 will present a novel extraction method to obtain a view of the wetted side of a surface oxide film and details will be given there). Meanwhile, according to **Figures 5.27 (c) and (d)**, the oxides show a blossom-like morphology and consists of fine oxide-like particles, implying a view of the wetted side. **Figures 5.27 (c)** and **(d)** were deliberately taken at different focal lengths. It is noted that some areas are out of focus, probably suggesting different penetration depths of these oxides into the melts. From **Figure 5.28**, it can be seen that voids around 1-2 μm were observed at the crystalline-like oxide layer, suggesting a non-protective feature. Oxygen may readily flow through these voids and react with the melt at the metal/oxide interface.

Figure 5.29 is a collection of images showing the scraped oxides from an oxidized Al sample (950ºC, 48 h), the morphology is similar to that of Al-5Cu: faceted steps and ledges were found on the oxide/air interface; the layer thickens by a *ledge* mechanism while at the metal/oxide interface individual oxide-islands grow inwardly.

As shown in **Figure 5.30**, analysis of the *ledge* grow mechanism observed in the present work suggests the crystalline-like oxides, at least the external part of the oxide scale, has an fcc structure, as does γ-Al_2O_3. Specifically, 2D growth ledges are identified for the growth of an fcc crystalline phase and the crystal planes and directions are labelled. The 2D nucleation energy barrier on a flat surface [41] is quoted as $\Delta G^*_{2D} = \pi\varepsilon^2 / \Delta\mu$, where $\Delta\mu$ is the driving force for nucleation and ε is

the edge free energy, which is zero for an atomically rough surface and positive for an atomically smooth surface. In addition, twin plane reentrant edge mechanism of growth was also observed. Reentrant edges are formed as an easy site for growth [42]. The nucleation barrier in this mechanism [41] is given by $\Delta G^*_{TPRE} = \frac{\pi\varepsilon^2}{\Delta\mu}\left(\frac{\theta - \sin\theta\cos\theta}{\pi}\right)$. θ was observed here to be 141.06°, which is consistent with an fcc structure (e.g., γ-Al_2O_3) when the twin plane is (111), in this case $\Delta G_{TPRE}^* \approx 0.63\,\Delta G_{2D}^*$, suggesting the edges in the particular reentrant troughs are more favoured growth sites.

Figure 5.31 shows the XRD traces of the scraped oxides collected from the oxidized Al and Al-5Cu samples. Diffraction references are taken from [43-45]. Oxides scraped from 4 identical samples were initially placed in an Agate mortar. Ethanol was added into the mortar and the oxides were then ground. The solution was then transferred to a flat based beaker with a filter paper placed in the middle. After drying, the oxides were mounted on a silicon chip to be examined by XRD. In the present work, the analysis indicates that the oxides developed on Al and Al-5Cu at 950ºC for 48 h consisted of both γ-Al_2O_3-like (there is a humps-like shape in the background around 2θ = 45.5º, which may indicate a structure intermediate between the amorphous state and completely crystalline γ-Al_2O_3, as suggested by the work from Vernon [46]) and α-Al_2O_3 oxides (also identified using TEM analysis, results are shown in section 5.3.4). This is consistent with the work by Trunov *et al.* [47, 48] and Venugopalan *et al.* [49-51], who found traces of α-Al_2O_3 forming in the temperature range 850-1100ºC. A detailed discussion of this topic and the oxidation mechanism will be given in section 5.3.

5.2.6 XPS studies

5.2.6.1 Wide scan

Samples analysed by XPS in this study are summarized in **Table 5.1**. A typical XPS sample is a

cylindrical-shaped sample with diameter 8 mm by 4 mm thick. Wide scans were used to determine the chemistry of the surface oxide qualitatively. **Figure 5.32** shows the wide scan spectra from ***A1-AP***, ***A1-R1***, ***A1-R6*** and ***Al-R24***. All peaks are labelled according to reference [52]. As discussed in section 3.4.6, a wide XPS spectrum consists of XPS peaks characteristic of binding energies, induced Auger peaks (such as C KLL and O KLL) and a stepped background. First of all, carbon is observed in all spectra. This is because that an adventitious carbon film is usually present on any air-exposed sample, even small exposure to air could generate such a thin carbonaceous film [53]. This film is usually comprised of a variety of hydrocarbon species (C-C, C-H, etc), and sometimes with both singly and doubly bonded oxygen atoms (C-OH, C=O, etc) [52]. Detailed scans of C 1s core level confirms the presence of such species, the results will be shown in section 5.2.6.2. Secondly, it is noted that the aluminium oxide forms on top of all samples, as indicated by the strong peaks of O 1s and O KLL in all spectra. For ***Al-R1***, ***Al-R6***, *and* ***A1-R24*** samples which were oxidized in air for certain periods of time, it is expected that a relatively thick aluminium oxide layer has formed on the surface. For as-polished ***Al-AP***, once exposed to oxygen-containing environment, a natural amorphous oxide layer would rapidly form with a thickness of a few nanometers [54, 55]. In the present study, this is further confirmed by the detailed scan of Al 2p core level on sample ***Al-AP***, the result will be shown in section 5.2.6.2.

XPS is a very surface sensitive technique with an information depth around 10 nm [53]. As suggested by **Figure 5.32**, small amounts of chloride-like impurities (NaCl, KCl, etc) were identified. During the XPS sample preparation stage, four identical Al cylinder-shaped samples were initially polished down to 1μm diamond suspension and cleaned in distilled water (not able to remove all chlorides and surface contamination!). Three out of the four samples were then oxidized for different periods of time. The first XPS analysis was performed on ***Al-AP***. Since the sample was not cleaned thoroughly, chloride-like surface contamination was deposited on the surface, which made the interpretation of the XPS spectra very difficult, especially for the sake of

quantitative analysis. Therefore, ***Al-AP*** was then thoroughly re-cleaned using acetone and methanol and immediately introduced into the XPS chamber to minimize surface contamination, but still it was not possible to avoid the carbon contamination (everywhere! air, vacuum chamber …).

These chloride-like impurities remain on the top of the aluminium oxide layer, as indicated by the results from ***Al-R1***, ***Al-R6*** and ***Al-R24***. Because of this limitation, the results from wide XPS spectra are only used to show which elements are present in the oxide layer and not to quantify the oxides, as originally intended.

Meanwhile, depth profiling was attempted to analyse the composition profile across the surface oxide layer. There are two ways of performing compositional depth profiling in XPS analysis. One is non-destructive analysis using angle resolved electron spectroscopy [53]. In this case, samples are irradiated by X-rays at different take-off angles. The principle is based on the Beer-Lambert law [56]. The change of take-off angle changes the sampling depth so the top layer (oxide)/underlying matrix (metal) signal ratio varies according to take-off angle as a result [53]. Another destructive approach is to use ion bombardment to sputter the sample surface at a certain current for a period of time and then analyse the chemistry (XPS spectrum) after each bombardment [53]. The efficiency of this technique depends on the condition of the vacuum chamber, stability of the ion beam source, and sputter yield of the sample [53, 57].

This study reports an attempt at using the destructive ion beam bombardment to study the chemistry depth profile of the oxidized Al samples. During the study, argon ion bombardment experiments were performed on ***Al-AP***, ***Al-R1***, and ***Al-R6*** for two purposes. Firstly, ion bombardment with a current of 300 nA was used to investigate whether contamination (chloride-like impurities, carbon, etc) was just external substances depositing on the surface or whether they

had been incorporated within the oxide layers during oxidation. As shown in **Figures 5.33-5.35**, carbonaceous contaminations were significantly removed after bombardment for ***Al-AP*** (2 minutes), ***Al-R1*** (2 minutes) and ***Al-R6*** (4 minutes in total). It is noted that the bombardment resulted in argon being implanted in the surface. Ar 2p and Ar 2s peaks are observed accordingly. For the ***Al-R1*** sample, peak areas under Na 1s and Cl 2s were also reduced significantly after being bombarded for only 4 minutes. Therefore, the chloride-like species found were highly unlikely to be part of the aluminum oxide layer.

However, the depth profiling experiment was eventually unsuccessful. It can be seen that the oxygen peaks (O 1s, O KLL, etc) do not change at all. It may be the case that the vacuum condition in the analysing chamber is not good enough and contains a certain level of air and hence the bombardment not only implanted argon, but also oxygen into the surface. Meanwhile, even at an extremely low oxygen pressure condition (e.g 10^{-100} atm, as shown in previous thermodynamics calculations in section 5.2), Al would pick up any oxygen to form aluminium oxide: it is absolutely IMPOSSIBLE to prevent the formation of aluminium oxide in practice.

Similarly, three Al-5Cu samples were oxidized at 750°C for 1h, 6h and 24h respectively. One Al-5Cu sample (sample code: ***Al-5Cu-AP***) was used as a reference. **Figure 5.36** shows their XPS wide scan spectra. Al peaks (Al 2p, Al 2s) and oxygen peaks (O 1s, O 2s, and O KLL) are present in all four samples, confirming the formation of aluminium oxide. Cu 2p peaks gradually diminish as oxidation time increases, indicating that Cu is not part of the surface oxide. The result is consistent with the prediction from thermodynamics calculations, previous SEM/EDX results and XRD analysis.

5.2.6.2 Core levels

(a) C 1s

As shown in **Figure 5.37**, the C 1s core levels peaks were fitted using Gaussian functions. The centre of C 1s elemental peak (C-C, C-H) was fixed as 284.8 eV and peak positions of other core levels XPS spectra were then shifted with respect to this value. The fittings indicate the presence of other carbon species containing oxygen in the adventitious film and also suggest that carbon bonding with each oxygen atom causes a shift of approximately 1.5 eV to higher binding energy [58].

(b) O 1s

As shown in **Figure 5.38**, the O 1s core levels were fitted with Gaussian functions. According to the database [52], the fittings indicate the O in Al_2O_3 contributes to the O 1s peak, together with a small amount of O from absorbed water. It has been found that the absorbed water usually react with Al_2O_3 to form $Al(OH)_3$, once the oxide layer is exposed to a humid environment [59]. First of all, for ***Al-AP***, ***Al-R1***, ***Al-R6***, and ***Al-R24***, the O 1s (Al_2O_3) peak positions are 532.62 eV, 532.65 eV, 532.61 eV and 532.60 eV respectively, and they all show a well-resolved spectral line located at 532.65 ± 0.05 eV binding energy. The O 1s peaks in this range are attributed to the Al_2O_3 lattice oxygen [60-62]. The broad featured O 1s peaks in the range of 534-534.5 eV are assigned as a mixture of hydrated oxygen and these types of oxygen species are usually associated with the absorbed O^-, OH^-, H_2O, etc or from the hydrated lattice (hydroxyl ions) and the contamination layer [60, 63-65]. The Durbin-Watson statistics of the O 1s core level fitting in ***Al-AP***, ***Al-R1***, ***Al-R6*** and ***Al-R24*** are 1.763, 1.834, 1.812 and 1.645 respectively, suggesting a good randomness for the residual values of fitting. Secondly, the fittings of O 1s core level for the samples ***Al-5Cu-AP***, ***Al-5Cu-R1***, ***Al-5Cu-R6***, ***Al-5Cu-R24*** show similar patterns to those of oxidized Al samples. For ***Al-5Cu-AP***, ***Al-5Cu-R1***, ***Al-5Cu-R6*** and ***Al-5Cu-R24***, the fitted O 1s peak positions are 532.65 eV, 532.65 eV, 532.63 eV and 532. 69 eV respectively and they all show a well-resolved spectral line located at 532.65 ± 0.05 eV binding energy, suggesting the same type of oxide formed as that on oxidized Al samples. The Durbin-Watson statistics of the O 1s core level fitting in ***Al-5Cu-AP***,

Al-5Cu-R1, ***Al-5Cu-R6*** and ***Al-5Cu-R24*** is 1.892, 1.794, 1.937 and 1.745 respectively, again suggesting a good randomness for the residual values of fitting.

(c) Al 2p

The Al 2p peak from un-reacted elemental Al usually has a spectra line of approximately 72.8 eV and the Al 2p peak would be shifted to higher binding energy around 75.8 eV due to the oxidation of Al which causes the transfer of electrons from aluminium to oxygen [60]. As the information depth during the XPS is approximately 10 nm, Al 2p photoelectrons emitted from elemental Al beneath any oxide layer less than 10 nm would be recorded [66]. When the oxide is thicker than 10 nm, only the Al 2p photoelectrons emitted from Al_2O_3 would appear on the spectra, as shown by **Figure 5.39**. For ***Al***, ***Al-R1***, ***Al-R6*** and ***Al-R24***, the fitted Al 2p peaks are all located at a well-defined spectral line of 75.80 ± 0.05 eV. They are at 75.83 eV, 75.81 eV, 75.79 eV and 75.81 eV with Durbin-Watson statistic values of 1.854, 1.922, 1.868 and 1.813 respectively. The Al_2O_{3-x}-like Al 2p peak represents the deviation from the stoichiometric Al_2O_3 due to the incomplete oxidation of Al, suggesting a low coordination number of Al in the oxide structure close to the metal/oxide interface [67]. The intermediate peaks are located at a spectral line of 73.50 ± 0.12 eV. Because the aluminium suboxides Al_2O and AlO exist only in the gaseous states and the solid state oxides would decompose into Al and Al_2O_3 below 1050ºC (Al_2O) and 1600ºC (AlO) [68-70]. So the broad intermediate peak is attributed to the transition region between the elemental Al and the aluminium oxide layer instead of the existence of any suboxides. The peak area under the lower binding energy Al 2p elemental peak and the higher binding energy Al 2p oxide peak can be used to quantify the thickness of the oxide layer. The calculation is given in section 5.3.1.

Similarly, for ***Al-5Cu***, ***Al-5Cu-R1***, ***Al-5Cu-R6*** and ***Al-5Cu-R24***, the fitted Al 2p peaks are all located at a well-defined spectral line of 75.80 ± 0.05 eV. They are 75.83 eV, 75.84 eV, 75.82 eV and 75.82 eV with Durbin-Watson statistic values of 1.763, 1.912, 1.871 and 1.773 respectively.

From all of the XPS results discussed above, it is inferred that Cu does not affect the chemistry of the oxide formed on Al-5Cu and the oxide chemistry is similar to the oxide formed on Al, at least the oxide chemistry within the top 10 nm region. Fitting results from wide scan, O 1s core levels and Al 2p core levels suggest the oxide is aluminium oxide. This conclusion is consistent with previous results in this study and is also in agreement with previous observations from the literature [71-73].

5.2.7 Kinetics of oxidation

According to previous experimental results, it is shown that Al and Al-5Cu have similar oxidation progression paths. The goal of this study was to further compare the oxidation of Al and Al-5Cu kinetically using thermogravemetric analysis (TGA). For all TGA experiments, the oxidation time scale used was 1h. The weight gain Δm versus time t curves (TGA curves) are useful in two aspects: first, TGA curves can be used to show whether the oxide growth kinetics obey some rate laws (linear [74], parabolic [75], etc); second, if the TGA curves can be described by rate equations such as $\Delta m = A \cdot t$ and $(\Delta m)^2 = A \cdot t$, as the rate coefficient A usually obeys an Arrhenius relationship $A = A_0 \cdot \exp(-Q/RT)$ [76, 77], then the oxidation activation energy Q can be estimated using the TGA data.

5.2.7.1 Al

Figure 5.40 shows the kinetics curves for Al in the temperature range 450-950°C. It can be seen that the oxidation rate is a strong function of temperature.

(a) 450-650°C

In the temperature range 450-650°C, the Al solid state oxidation kinetics exhibit parabolic-like progression and this may suggest a protective oxide layer forming [78, 79]. This behaviour was

also reported by Gulbransen and Wysong [80] who found that Al exhibits a parabolic growth law in the temperature range 350-450ºC, and by Smeltzer [81] who found that the oxide growth rate of Al was best fitted with a parabolic law in the temperature range 400-600ºC.

Parabolic equations have been used to fit these curves and an adjusted *R*-square method [82] was used to assess the quality of fit (the closer to 1, the better quality). The results are summarized in **Table 5.2**. From the table, it is mathematically implied that the kinetics curves can be well described by parabolic laws. In addition, as shown in **Figure 5.41**, the oxidation activation energy is estimated to be 62 ± 3 kJ mol^{-1} and the Al oxidation rate coefficient in the temperature range 450-650°C is therefore approximately given by

$$R_{Al} = 2.3\times10^{-7} \exp\left(-\frac{62000}{RT}\right) \qquad \text{(Unit: mg } cm^{-2}\ s^{-1}\text{)} \tag{5.10}$$

The value calculated in the present work is smaller than the value of 95.4 kJ mol^{-1} reported by Gulbransen and Wysong [80] as well as the value of 155.6 kJ mol^{-1} reported by Smeltzer [81]. Although the actual reason is unknown, the discrepancy is probably due to different experimental conditions: Gulbransen and Wysong [80] performed their work using oxygen of unspecified purity, Smeltzer [81] used dry oxygen, while dry air is used in the present work. This implies that oxygen partial pressure might affect the oxide growth kinetics of Al.

(b) 750-950°C

In the temperature range 750-950°C, it can be seen that the oxidation kinetics are best described by linear rate equations. Similar results were also reported by Akagwu *et al*. [83]. As Al is in the liquid state in this temperature range, the linear behaviour could result from a non-protective oxidation mechanism [3]. Linear equations have been used to fit these curves and the results are summarized in **Table 5.3**. In addition, as shown in **Figure 5.42**, the oxidation activation energy is estimated to be 178 ± 42 kJ mol^{-1} and the oxidation rate coefficient is approximately given by

$$R_{Al} = 45.2 \exp\left(-\frac{178000}{RT}\right) \qquad \text{(Unit: mg cm}^{-2}\text{ s}^{-1}\text{)} \qquad (5.11)$$

There are no significant results available in the literature, particularly on the oxide growth kinetics of Al (matching the 1h oxidation time scale in this study). Therefore, it is not possible to compare this activation energy to those found by other researchers.

5.2.7.2 Al-5Cu

(a) 450-650°C

For Al-5Cu, the weight gain curves as a function of time and temperature are shown in **Figure 5.43**. It can be seen that Al-5Cu exhibits similar oxidation kinetics to Al, suggesting that the addition of Cu may not introduce new oxidation mechanisms. In the temperature range 450-650°C, the oxidation kinetics of Al-5Cu are faster than those of Al during an oxidation period of 1h. The curves are not well represented by simple parabolic equations, as indicated by the lower adjusted *R*-square values shown in **Table 5.4**. The Arrhenius plot is shown in **Figure 5.44**. The oxidation activation energy is estimated to be 71.6 ± 25.4 kJ mol^{-1} and the rate equation (based on parabolic fittings) is given by

$$R_{Al\text{-}5Cu} = 3\times10^{-6} \exp\left(-\frac{71600}{RT}\right) \qquad \text{(Unit: mg cm}^{-2}\text{ s}^{-1}\text{)} \qquad (5.12)$$

It is recalled from the literature that the solid state oxidation of Al is controlled either the inward diffusion of oxygen or outward diffusion of Al, which can be described by classic parabolic rate equations [84-89]. In the case of Al-5Cu, it is implied from the work by Brock and Pryor [71, 72] that doping of Cu to the aluminium oxide could alter its defects structure and potentially result in a change in the oxidation kinetics and so the oxidation kinetics of Al-5Cu may not exhibit typical parabolic behaviour, as suggested by the present work. This topic will be discussed again in section 5.3.2.

(b) 750-950°C

In the temperature range 750-950°C, it is noted that the liquid state oxidation kinetics of Al-5Cu are also well described by linear rate equations. The fitted parameters are summarized in **Table 5.5**. The Arrhenius plot in this temperature range is shown in **Figure 5.45**. The activation energy is estimated to be 152.5 ± 10.7 kJ mol^{-1} and the overall rate equation is approximately given by

$$R_{\text{Al-5Cu}} = 28.2 \exp\left(-\frac{152500}{RT}\right) \qquad \text{(Unit: mg cm}^{-2}\text{ s}^{-1}\text{)} \tag{5.13}$$

To sum up, it can be seen from previous results and discussion that Al and Al-5Cu show similar oxidation kinetics in the temperature range 450-950ºC within a time scale of 1h. In particular, the solid state oxidation kinetics for Al and Al-5Cu can be described by parabolic rate equations while liquid state oxidation kinetics for Al and Al-5Cu are featured by linear rate laws. Besides, breakaway oxidation was not observed in the present work. According to the results shown by Impey *et al*. [90], the breakaway oxidation of Al occurs primarily due to the mechanical breakdown caused by the γ-Al_2O_3 to α-Al_2O_3 phase transformation which is associated with a 24% reduction in oxide volume. Impey *et al*. [90, 91] also found that the incubation period of breakaway oxidation at 750ºC to be around 5h. Similarly, Hinton *et al*. [34, 92] found that breakaway oxidation did not occur until after 3h of oxidation at 750ºC and no α-Al_2O_3 was present after 1h of oxidation. The current result is therefore consistent with the literature.

5.3 Oxidation mechanism

This section is an attempt to establish a more fundamental understanding of the oxidation process for the Al-Cu-O_2 system by bringing together results from the present work and some existing findings from the literature.

5.3.1 Amorphous oxide

It is generally agreed in the literature that a continuous amorphous aluminium oxide layer would firstly form on fresh surfaces of Al or dilute Al alloys [54, 55, 87, 93, 94]. The amorphous structure

probably derives from the less ordered atomic arrangement in the surface region than in the bulk (amorphous melt in the case of liquid oxidation) [37], on which the oxide nucleates and grows. Alternatively, the amorphous nature of the initial surface oxide layer may be explained from a perspective of thermodynamics: Jeurgen *et al*. [94, 95] proposed that the amorphous aluminium oxide is more thermodynamically stable than crystalline γ-Al_2O_3 below a critical thickness of a few nanometers and this is mainly due to the lower interfacial energy at the metal/oxide interface which could compensate for the excess bulk free energy of the amorphous structure. In the present work, an XPS technique was used to determine the thickness of such amorphous layers on Al and Al-5Cu.

The Al 2p core level XPS spectra from Al and Al-5Cu are shown in **Figure 5.46**. To calculate the thickness, the following equation proposed by Strohmeier [61] is used

$$d = \lambda_o \sin\theta \ln\left(\frac{N_m\lambda_m}{N_o\lambda_o}\cdot\frac{I_o}{I_m}+1\right) \tag{5.14}$$

Here I_o and I_m are the intensity (in terms of peak area, the value was calculated using the software Origin 8.0) under the Al 2p oxide peak and the Al 2p metallic peak respectively. For Al-AP, I_o and I_m are 7601.76 and 1568.07 respectively. For Al-5Cu-AP, I_o and I_m are 6670.46 and 1260.42 respectively. N_m and N_o are the volume densities of Al atoms in the metal and the Al_2O_3 oxide respectively, and N_m/N_o = 1.5 [53, 61, 96] . λ_m and λ_o are the inelastic mean free path (IMFPs) of the metal and the oxide [97, 98]. The IMFP values were obtained using a set of predictive equations (designated TPP-2M) proposed by Tanuma *et al*. [99]. The values are calculated with the help of the NIST Standard reference database 71 [97]. The database is based on the TPP-2M equations. As Mg Kα X-rays (1253.6 eV) were used in this experiment, the IMFP values for Al and Al_2O_3 are calculated to be λ_m = 2.22 nm and λ_o = 2.71 nm, using the TPP-2M equations. The θ in **Equation 5.14** is the take−off angle (sin θ = 1 in this experiment). Therefore, taking the numbers described above, Equation 5.14 can be simplified to

$$d = 2.71\ln\left(1.23\cdot\frac{I_o}{I_m}+1\right) \tag{5.15}$$

So the thicknesses of the oxide layers calculated using **Equation 5.15** are 5.26 nm (***Al-AP***) and 5.46 nm (***Al-5Cu-AP***) respectively.

It should be noted that there are various sources of error in these calculations. Firstly, the stoichiometry of the aluminum oxide layer is assumed such that N_m/N_o = 1.5, in fact, the real N_m/N_o value is slightly less than 1.5 as the average coordination number of Al in amorphous alumina is lower than that in the stoichiometric crystalline Al_2O_3 [100, 101]. Secondly, the plasmon losses from Al 2p core level peaks have not been considered. Electrons lose certain amounts of energy during transit through the metal and oxide as part of the emission process [62]. The plasmon losses could influence the ratio of peak intensities to an unknown extent. These features are recommended to be characterized by reflection electron energy-loss spectroscopy [102, 103]. Thirdly, according to the TTP-2M equations, the IMFP value of a material is related to its density ρ [98]. The theoretical density of the stoichiometric γ-Al_2O_3 (3.67 g/cm^3) is used in this analysis. Actually, it has been shown that the density of the amorphous oxide is less than that of the stoichiometric crystalline oxide [93, 100, 101].

5.3.2 Effect of doping with Cu

(a) Amorphous oxide growth stage

Dignam [86, 87, 104] reported that compared to Al, an addition of 1.51wt% Cu would increase the growth rate of amorphous oxide in the temperature range 250-450ºC. Brock and Pryor [71, 72] reported an increase in Cu content resulted in an increase in the amorphous oxide thickening rate in the temperature range 475-575ºC. Meanwhile, the XPS analysis in the present work indicates s a thicker oxide layer formed on Al-5Cu. (though not sufficiently persuasive as only one test was carried out…). In order to understand the underlying physics, a defects reaction model is proposed

in the present work.

First of all, the amorphous aluminium oxide lacks long-range order but do have short-range order [54, 94, 105-107] and point defects (vacancies, interstitials, etc) also exist in this structure [108, 109]. It has been suggested that the amorphous aluminium oxide is best described by a distorted fcc packing of O atoms while partially bonded Al ions occupy the octahedral and tetrahedral interstitial sites [67]. This structure is close to the γ-Al_2O_3 crystal structure [67, 110]. The only difference in crystallography is that the amorphous structure has a lower averaging Al coordination number (CN) than that in the γ-Al_2O_3 crystal structure [100], in other words, the amorphous structure is featured by the metal excess and oxygen deficiency (Al_2O_{3-x}). It has been shown that Al has different coordination numbers in the amorphous structure and they are AlO_4 ($^{[4]}$Al), AlO_5 ($^{[5]}$Al) and AlO_6 ($^{[6]}$Al) [111]. The fraction of five coordinated Al is usually used to describe the magnitude of disorder in amorphous structure [111]. According to the NMR results reported by Lee *et al*. [101], amorphous to crystalline transformation is accompanied by the ordering of AlO_4 and AlO_6 network through the reaction $2^{[5]}Al=^{[4]}Al+^{[6]}Al$.

Secondly, as shown by **Figure 5.47**, two possible doping mechanisms are proposed based on Kröger-Vink defects reaction theories [112]: a Cu atom can occupy an Al vacancy site through the **Reactions 5.16** and **5.17**; a Cu atom can substitute an Al lattice site (oxide) and eject an Al interstitial atom through the **Reactions 5.18** and **5.19**

$$\mathrm{Cu} + V_{\mathrm{Al}}''' \rightarrow \mathrm{Cu}'_{\mathrm{Al}} + 2\mathrm{e}' \tag{5.16}$$

$$\mathrm{Cu} + V_{\mathrm{Al}}''' \rightarrow \mathrm{Cu}''_{\mathrm{Al}} + \mathrm{e}' \tag{5.17}$$

$$\mathrm{Cu} + \mathrm{Al}^{x}_{\mathrm{Al}} \rightarrow \mathrm{Cu}'_{\mathrm{Al}} + \mathrm{Al}_{\mathrm{i}}''' + 2\mathrm{e}' \tag{5.18}$$

$$\mathrm{Cu} + \mathrm{Al}^{x}_{\mathrm{Al}} \rightarrow \mathrm{Cu}''_{\mathrm{Al}} + \mathrm{Al}_{\mathrm{i}}''' + \mathrm{e}' \tag{5.19}$$

Which reactions are likely to occur? It has been shown in the literature [87, 95, 105, 113-115] that

the growth of the amorphous aluminium oxide layer at high temperatures is controlled by the outward diffusion of Al ions, and the vacancies density is a lot smaller than that in the crystalline structure, due to the excess of partially bonded Al ions [100, 101]: since Al ions are relatively easy to move through the amorphous oxide structure [95, 114, 116], any vacancies sites will be quickly occupied by free Al interstitial ions. So the vacancy-filling mechanism is highly unlikely. Considering **Reactions 5.18** and **5.19**, Cu atoms enter onto Al lattice sites as substitutes, this would lead to the formation of more Al interstitials ions, enhancing the diffusivity of Al ions and the amorphous oxide layer thickening rate. So the substitution mechanism is more likely to occur in the amorphous structure. Cu sits substitutionally in the amorphous oxide structure and the doping of Cu leads to an enhanced amorphous oxide layer thickening rate.

(b) Crystalline oxide growth

The exact effect of doping with Cu on the crystalline oxides growth is actually unknown. Brock and Pryor [71, 72] reported an increase in dielectric constant and reduction in ionic conductivity (reduced number of Al cation vacancies) of the crystalline γ-Al_2O_3 formed on Al-Cu alloys, compared to the oxides formed on Al. This might be explained using **Reactions 5.16** and **5.17** mentioned earlier in this section: Cu atoms filling Al vacancies. But there is a lack of experimental data in the literature to reach an agreement and this topic is beyond the scope of this thesis.

5.3.3 γ-Al_2O_3 and α-Al_2O_3

Previous results and discussion have suggested that for both Al and Al-5Cu alloy, crystalline γ-Al_2O_3 phase forms at a later oxidation stage from the crystallization of an amorphous layer. Thermodynamically, the energy state of the amorphous oxide is expected to be slightly higher than the crystalline γ-Al_2O_3 as the atomic structure of γ-Al_2O_3 is more organized [54, 94, 117]. So there always exists a volumetric Gibbs free energy driving force associated with such a transition. As shown previously, the crystalline γ-Al_2O_3 grows into oxide islands heterogeneously on the

surface at ridge-like sites, preferentially with a ledge mechanism; microscopically, the crystalline oxides also grow inwardly into the metal at 950ºC, and growth rate at this temperature is featured by a linear rate law, suggesting a non-protective behaviour during oxidation.

It is generally accepted that the cubic spinel structure γ-Al_2O_3 would transform into the hexagonal close-packed structure α-Al_2O_3 (Rhombohedral structure, hexagonal packing of oxide anions while cations occupying 2/3 of the octahedral interstitial sites [118]) at the temperatures above 850°C when the formation conditions are favourable [119]. α-Al_2O_3 is the most stable form of alumina as it has the lowest Gibbs free energy of formation compared to other transition aluminas (γ, θ, δ, κ, etc) [45]. Therefore, there always existing a thermodynamic driving force for transformation of γ-Al_2O_3 to α-Al_2O_3. In agreement with the literature [119-121], this phase transformation behaviour is also observed in the present work, as indicated by previous XRD results.

In the present work, TEM analysis was further used to identify the presence of α-Al_2O_3 in the oxide layers developed on Al and Al-5Cu at 950ºC in air after 48h. TEM samples were prepared using the following method: a 10 ml Agate pestle and mortar set supplied by Cole-Parmer Instrument was used; the mortar was initially filled with 1 ml ethanol, oxides were then scraped from the samples directly into the mortar, a further 2 ml ethanol was added and oxides were then ground for 10 minutes. A glass pipette was used to transfer the prepared solution into a 10 ml glass vial. An ultrasonic process was adopted to disperse the oxides uniformly in the solution. Another glass pipette was used to transfer two drops of the solution onto a 300 mesh Cu grid which had a carbon film attached (supplied by Agar scientific, product no. S147-3). The TEM sample was then examined using a JEOL 2000F at an accelerating voltage of 100 kV. **Figures 5.48** and **5.49** display the TEM micrographs of plate-like α-Al_2O_3 oxides and their diffraction patterns. However, the stripped oxides were severely ground and crushed during the sample preparation stage and the

original morphology of an individual oxide crystal is therefore not maintained.

The phase transformation of γ-Al_2O_3 to α-Al_2O_3 can be expressed using the following reaction

$$\gamma\text{-}Al_2O_3 \rightarrow \alpha\text{-}Al_2O_3 \tag{5.20}$$

The change of Gibbs free energy associated with this reaction is calculated using the method shown in **Appendix 5.2** as

$$\Delta G(T) = -17037.3 + 35.54T + 5.43T\ln T \quad (\text{J mol}^{-1}) \tag{5.23}$$

It can be seen that the change of Gibbs free energy ΔG is negative in the temperature range 25-1000°C. A kinetic model is proposed to explain why this phase transformation is so difficult at low temperatures, as shown in **Appendix 5.3** as a reference (this is beyond the scope of study, just for my personal interest).

5.3.4 Implications for bonding

In the present work, it is found that the degree of metallic bonding between Al and Al-5Cu is a function of holding time. Similar behaviour was also observed by Bakhtiarani and Raiszadeh [122] who found the extent of bonding between two identical commercial pure Al blocks (Al/Al bond) increased gradually with holding time. From the results in Chapter 4, it is known that cracks formed on the oxide layers provide necessary paths for the melt to diffuse through and cracks develop preferentially at the peripheries of the crystalline oxides. From the results in Chapter 5, it is further implied that the oxide layer formed on an Al melt or Al-5Cu is not protective and the oxide layer becomes powdery (porous) after a pro-longed period due to the formation of crystalline oxides γ-Al_2O_3 and α-Al_2O_3, resulting in generation of more channels to allow metallic mixing. As suggested by Impey *et al*. [90], the γ-Al_2O_3 to α-Al_2O_3 phase transformation is accompanied by a 24% reduction in volume of the oxide, so the induced tensile stresses could further facilitate the fracture of the oxide. Considering the stacking approach described in Chapter 4, the use of a long holding time could increase the degree of metallic mixing but may also

introduce a detrimental effect (mechanically) by the formation of crystalline oxides at the bond interface. This needs to be taken into account whenever trying to design proper processing conditions for bonding of Al alloys.

5.4 Concluding remarks

The current results have added to our understanding of the oxidation mechanism of pure Al and Al-Cu alloys, in particular liquid state oxidation mechanism. Generally speaking, the oxidation behaviour of Al-5Cu is similar to that of Al, in terms of oxide morphology, chemistry, growth kinetics and overall oxidation progression paths. The methodology of investigation learned from this work can be applied to study other systems and the knowledge generated is hoped to form a basis for future studies of bonding and add to a growing body of literature on oxidation of Al alloys.

5.5 References

[1] H. Scholz and P. Greil, "Nitridation reactions of molten Al-(Mg, Si) alloys," *Journal of materials science*, vol. 26, pp. 669-677, 1991.

[2] F. Czerwinski, "Oxidation characteristics of magnesium alloys," *JOM*, vol. 64, pp. 1477-1483, 2012.

[3] O. Kubaschewski and B. E. Hopkins, *Oxidation of metals and alloys*: Academic Press New York, 1953.

[4] N. Birks, G. H. Meier, and F. S. Pettit, *Introduction to the high temperature oxidation of metals*: Cambridge University Press, 2006.

[5] D. R. Gaskell, *Introduction to the thermodynamics of materials* vol. 2: CRC Press, 2008.

[6] K. Denbigh, *The principles of chemical equilibrium*: Cambridge University Press Cambridge, 1966.

[7] M. Diemer, A. Neubrand, K. P. Trumble, and J. Rödel, "Influence of oxygen partial pressure and oxygen content on the wettability in the copper–oxygen–alumina system," *Journal of the American Ceramic Society*, vol. 82, pp. 2825-2832, 1999.

[8] Handbook, *Aluminum and aluminum alloys*: ASM International, 1993.

[9] K. A. Son, N. Missert, J. C. Barbour, J. Hren, R. G. Copeland, and K. G. Minor, "Growth and oxidation of thin film Al_2Cu," *Journal of the Electrochemical Society*, vol. 148, pp. 260-263, 2001.

[10] S. Garcia-Vergara, K. El Khazmi, P. Skeldon, and G. Thompson, "Influence of copper on the morphology of porous anodic alumina," *Corrosion science*, vol. 48, pp. 2937-2946, 2006.

[11] G. Thompson, "Porous anodic alumina: Fabrication, characterization and applications," *Thin solid films*, vol. 297, pp. 192-201, 1997.

[12] J. J. Wu, Y. Zhang, Y. T. Shen, G. B. Li, and T. Q. Lei, "Internal oxidation of Cu-Al alloy," *Journal of Materials Science & Technology*, vol. 15, pp. 444-448, 1999.

[13] A. Soleimanpour, P. Abachi, and K. Purazrang, "Wear behaviour of in situ Cu-Al_2O_3 composites produced by internal oxidation of as cast alloys," *Tribology-Materials, Surfaces & Interfaces*, vol. 3, pp. 125-131, 2009.

[14] G. E. Totten and D. S. MacKenzie, *Handbook of aluminum (Vol. 1)*: CRC Press, 2003.

[15] W. S. Miller, L. Zhuang, J. Bottema, A. Wittebrood, P. De Smet, A. Haszler, and A. Vieregge, "Recent development in aluminium alloys for the automotive industry," *Materials Science and Engineering :A*, vol. 280, pp. 37-49, 2000.

[16] L. Backerud, G. Chai, and J. Tamminen, "Solidification characteristics of aluminum alloys. Vol. 2. Foundry alloys," *American Foundrymen's Society*, p. 266, 1990.

[17] D. L. Baty, R. A. Tanzilli, and R. W. Heckel, "Solution kinetics of $CuAl_2$ in an Al-4Cu alloy," *Metallurgical Transactions*, vol. 1, pp. 1651-1656, 1970.

[18] G. Chadwick, "Solidification of $CuAl_2$-Al eutectic alloys," *J Inst Met*, vol. 91, pp. 169-173, 1963.

[19] T. Kobayashi, "Strength and fracture of aluminum alloys," *Materials Science and Engineering: A*, vol. 280, pp. 8-16, 2000.

[20] G. V. Narayana, V. Sharma, V. Diwakar, K. S. Kumar, and R. Prasad, "Fracture behaviour of aluminium alloy 2219-T87 welded plates," *Science and Technology of Welding & Joining*, vol. 9, pp. 121-130, 2004.

[21] Y. Grin, F. R. Wagner, M. Armbrüster, M. Kohout, A. Leithe-Jasper, U. Schwarz, U. Wedig, and H. Georg von Schnering, "$CuAl_2$ revisited: Composition, crystal structure, chemical bonding, compressibility and raman spectroscopy," *Journal of Solid State Chemistry*, vol. 179, pp. 1707-1719, 2006.

[22] D. Brandon, "The structure of high-angle grain boundaries," *Acta Metallurgica*, vol. 14, pp. 1479-1484, 1966.

[23] D. McLean, *Grain boundaries in metals*: Clarendon Press, 1957.

[24] D. T. Read, Y.-W. Cheng, R. R. Keller, and J. D. McColskey, "Tensile properties of free-standing aluminum thin films," *Scripta Materialia,* vol. 45, pp. 583-589, 2001.

[25] S. Bubar and D. Vermilyea, "Deformation of passive films," *Journal of The Electrochemical Society,* vol. 114, pp. 882-885, 1967.

[26] C. Allen, K. O'reilly, B. Cantor, and P. Evans, "Intermetallic phase selection in 1xxx Al alloys," *Progress in Materials Science,* vol. 43, pp. 89-170, 1998.

[27] J. E. Hatch, *Aluminum: Properties and physical metallurgy*: ASM International, 1984.

[28] M. De Hass and J. T. M. De Hosson, "Grain boundary segregation and precipitation in aluminium alloys," *Scripta materialia,* vol. 44, pp. 281-286, 2001.

[29] A. Austin and N. Richard, "Grain-boundary diffusion," *Journal of Applied Physics,* vol. 32, pp. 1462-1471, 2004.

[30] J. W. Cahn, "The impurity-drag effect in grain boundary motion," *Acta metallurgica,* vol. 10, pp. 789-798, 1962.

[31] P. E. Doherty and R. S. Davis, "Direct observation of oxidation of aluminum single-crystal surfaces," *Journal of Applied Physics,* vol. 34, p. 619, 1963.

[32] J. I. Eldridge, R. J. Hussey, D. F. Mitchell, and M. J. Graham, "Thermal-oxidation of single-crystal aluminum at 550ºC," *Oxidation of Metals,* vol. 30, pp. 301-328, 1988.

[33] D. A. Porter, Easterling, K. E., *Phase transformations in metals and alloys*: CRC Press, 1992.

[34] E. Hinton, W. D. Griffiths, N. R. Green, "Oxidation of Al alloys," *The EPSRC centre for innovative manufacturing in liquid metal engineering report 2012,* pp. 31, 2012.

[35] Y. Wang, H.-T. Li, and Z. Fan, "Oxidation of aluminium alloy melts and inoculation by oxide particles," *Transactions of the Indian Institute of Metals,* vol. 65, pp. 653-661, 2012.

[36] P. Doherty and R. Davis, "Direct observation of the oxidation of aluminum single-crystal surfaces," *Journal of Applied Physics,* vol. 34, pp. 619-628, 2004.

[37] J. Campbell, *Castings*: London Butterworth, 2003.

[38] J. Campbell, "Entrainment defects," *Materials Science and Technology,* vol. 22, pp. 127-145, 2006.

[39] X. Cao and J. Campbell, "The solidification characteristics of Fe-rich intermetallics in Al-11.5Si-0.4Mg cast alloys," *Metallurgical and Materials Transactions A,* vol. 35, pp. 1425-1435, 2004.

[40] S. Fox and J. Campbell, "Visualisation of oxide film defects during solidification of aluminium alloys," *Scripta materialia,* vol. 43, pp. 881-886, 2000.

[41] P. Bennema, Hurle, D. T. J., *Handbook of crystal growth (vol. 1)*: Elsevier, 1993.

[42] J. Faust Jr and H. John, "The growth of semiconductor crystals from solution using the twin-plane reentrant-edge mechanism," *Journal of Physics and Chemistry of Solids,* vol. 25, pp. 1407-1415, 1964.

[43] M. Jellinek and I. Fankuchen, "X-ray diffraction examination of gamma alumina," *Industrial & Engineering Chemistry,* vol. 37, pp. 158-163, 1945.

[44] F. Mirjalili, L. C. Abdullah, H. Mohamad, A. Fakhru'l-Razi, A. Dayang Radiah, and R. Aghababazadeh, "Process for producing nano-alpha-alumina powder," *ISRN Nanotechnology,* vol. 2011, 2011.

[45] P. S. Santos, H. S. Santos, and S. Toledo, "Standard transition aluminas. Electron microscopy studies," *Materials Research,* vol. 3, pp. 104-114, 2000.

[46] E. Verwey, "Electrolytic conduction of a solid insulator at high fields the formation of the anodic oxide film on aluminium," *Physica,* vol. 2, pp. 1059-1063, 1935.

[47] M. A. Trunov, M. Schoenitz, and E. Dreizin, "Effect of polymorphic phase transformations in alumina layer on ignition of aluminium particles," *Combustion Theory and Modelling,* vol. 10, pp. 603-623, 2006.

[48] M. A. Trunov, M. Schoenitz, X. Zhu, and E. L. Dreizin, "Effect of polymorphic phase transformations in

Al_2O_3 film on oxidation kinetics of aluminum powders," *Combustion and Flame*, vol. 140, pp. 310-318, 2005.

[49] H. Venugopalan and T. DebRoy, "Growth stage kinetics in the synthesis of Al_2O_3/Al composites by directed oxidation of Al-Mg and Al-Mg-Si alloys," *Journal of the European Ceramic Society*, vol. 16, pp. 1351-1363, 1996.

[50] H. Venugopalan, K. Tankala, and T. DebRoy, "Kinetics of directed oxidation of Al-Mg alloys in the initial and final stages of synthesis of Al_2O_3/Al composites," *Materials Science and Engineering :A*, vol. 210, pp. 64-75, 1996.

[51] H. Venugopalan, K. Tankala, and T. Debroy, "Probing the initial stage of synthesis of Al_2O_3/Al composites by directed oxidation of Al-Mg alloys," *Metallurgical and Materials Transactions B*, vol. 27, pp. 43-50, 1996.

[52] D. Briggs, Seah, M. P., *Practical surface analysis: Auger and X-ray photoelectron spectroscopy vol. 1*: Wiley, 1990.

[53] J. F. Watts and J. Wolstenholme, *An introduction to surface analysis by XPS and AES*: Wiley-VCH, 2003.

[54] P. C. Snijders, L. P. H. Jeurgens, and W. G. Sloof, "Structural ordering of ultra-thin, amorphous aluminium-oxide films," *Surface Science*, vol. 589, pp. 98-105, 2005.

[55] F. Reichel, L. P. H. Jeurgens, and E. J. Mittemeijer, "The thermodynamic stability of amorphous oxide overgrowths on metals," *Acta Materialia*, vol. 56, pp. 659-674, 2008.

[56] D. Calloway, "Beer-lambert law," *Journal of Chemical Education*, vol. 74, p. 744, 1997.

[57] D. Leinen, A. Fernandez, J. Espinos, J. Holgado, and A. González-Elipe, "An XPS study of the mixing effects induced by ion bombardment in composite oxides," *Applied surface science*, vol. 68, pp. 453-459, 1993.

[58] T. L. Barr and S. Seal, "Nature of the use of adventitious carbon as a binding energy standard," *Journal of Vacuum Science & Technology A*, vol. 13, pp. 1239-1246, 1995.

[59] A. Nylund and I. Olefjord, "Surface analysis of oxidized aluminium. 1. Hydration of Al_2O_3 and decomposition of $Al(OH)_3$ in a vacuum as studied by ESCA," *Surface and Interface analysis*, vol. 21, pp. 283-289, 1994.

[60] J. F. Moulder, J. Chastain, and R. C. King, *Handbook of X-ray photoelectron spectroscopy*: Physical Electronics Eden Prairie, 1995.

[61] B. R. Strohmeier, "An ESCA method for determining the oxide thickness on aluminum-alloys," *Surface and Interface Analysis*, vol. 15, pp. 51-56, 1990.

[62] I. Olefjord and A. Nylund, "Surface-analysis of oxidized aluminum. 2. Oxidation of aluminum in dry and humid atmosphere studied by ESCA, SEM, SAM and EDX," *Surface and Interface Analysis*, vol. 21, pp. 290-297, 1994.

[63] P. Marcus, C. Hinnen, and I. Olefjord, "Determination of attenuation lengths of photoelectrons in aluminum and aluminum-oxide by angle-dependent X-ray photoelectron-spectroscopy," *Surface and Interface Analysis*, vol. 20, pp. 923-929, 1993.

[64] E. Panda, L. P. H. Jeurgens, and E. J. Mittemeijer, "The initial oxidation of Al-Mg alloys: Depth-resolved quantitative analysis by angle-resolved X-ray photoelectron spectroscopy and real-time in situ ellipsometry," *Journal of Applied Physics*, vol. 106, 2009.

[65] C. R. Werrett, D. R. Pyke, and A. K. Bhattacharya, "XPS studies of oxide growth and segregation in aluminium-silicon alloys," *Surface and Interface Analysis*, vol. 25, pp. 809-816, 1997.

[66] M. Alexander, G. Thompson, X. Zhou, G. Beamson, and N. Fairley, "Quantification of oxide film thickness at the surface of aluminium using XPS," *Surface and interface analysis*, vol. 34, pp. 485-489, 2002.

[67] G. Gutiérrez and B. Johansson, "Molecular dynamics study of structural properties of amorphous Al_2O_3," *Physical Review B,* vol. 65, p. 104202, 2002.

[68] H. Wriedt, "The Al-O (aluminum-oxygen) system," *Journal of Phase Equilibria,* vol. 6, pp. 548-553, 1985.

[69] R. F. Porter, P. Schissel, and M. G. Inghram, "A mass spectrometric study of gaseous species in the Al-Al_2O_3 system," *The Journal of Chemical Physics,* vol. 23, pp. 339-342, 2004.

[70] L. Brewer and A. W. Searcy, "The gaseous species of the Al-Al_2O_3 system1, 2, 3," *Journal of the American Chemical Society,* vol. 73, pp. 5308-5314, 1951.

[71] A. J. Brock and M. J. Pryor, "Kinetics of oxidation of aluminum-copper alloys at high temperature," *Journal of the Electrochemical Society,* vol. 117, p. 254, 1970.

[72] A. J. Brock and M. J. Pryor, "Kinetics of oxidation of aluminum-copper alloys in oxygen at high-temperature," *Corrosion Science,* vol. 13, p. 199, 1973.

[73] A. F. Beck, A. J. Brock, and M. J. Pryor, "Oxidation of two-phase aluminum-copper alloys," *Journal of the Electrochemical Society,* vol. 121, pp. 718-720, 1974.

[74] A. Atkinson, "Transport processes during the growth of oxide-films at elevated-temperature," *Reviews of Modern Physics,* vol. 57, pp. 437-470, 1985.

[75] H. Hindam and D. Whittle, "Microstructure, adhesion and growth kinetics of protective scales on metals and alloys," *Oxidation of Metals,* vol. 18, pp. 245-284, 1982.

[76] A. Frost and R. Pearson, "Kinetics and mechanism," *The Journal of Physical Chemistry,* vol. 65, pp. 384-384, 1961.

[77] K. J. Laidler, "The development of the arrhenius equation," *Journal of Chemical Education,* vol. 61, p. 494, 1984.

[78] P. Kofstad and J. Wiley, *High-temperature oxidation of metals*: Wiley New York, 1966.

[79] A. Fromhold Jr, "Parabolic growth law for coherent oxides," *The Journal of Chemical Physics,* vol. 41, pp. 509-514, 2004.

[80] E. A. Gulbransen and W. S. Wysong, "Thin oxide films on aluminum," *Journal of Physical and Colloid Chemistry,* vol. 51, pp. 1087-1103, 1947.

[81] W. W. Smeltzer, "Oxidation of aluminum in the temperature range 400-600ºC," *Journal of the Electrochemical Society,* vol. 103, pp. 209-214, 1956.

[82] J. R. Taylor, *An introduction to error analysis: The study of uncertainties in physical measurements*: University science books, 1997.

[83] I. Akagwu, Brooks, R., Quested, P., Fan, Z. and Ralph, B., "Environmental reaction of liquid aluminium," *Proceedings of the Engineering Doctorate in Environmental Technology,* p. 11, 2003.

[84] A. F. Beck, M. A. Heine, E. J. Caule, and M. J. Pryor, "Kinetics of oxidation of Al in oxygen at high temperature," *Corrosion Science,* vol. 7, p. 1, 1967.

[85] M. J. Dignam, "Oxide films on aluminum. 2. Kinetics of formation in oxygen," *Journal of the Electrochemical Society,* vol. 109, pp. 192-198, 1962.

[86] M. J. Dignam and W. R. Fawcett, "Kinetics and mechanism of oxidation of superpurity aluminum in dry oxygen. 2. Growth of crystallites of gamma-alumina," *Journal of the Electrochemical Society,* vol. 113, p. 663, 1966.

[87] M. J. Dignam, W. R. Fawcett, and H. Bohni, "Kinetics and mechanism of oxidation of superpurity aluminum in dry oxygen. 1. Apparatus description and growth of amorphous oxide," *Journal of the Electrochemical Society,* vol. 113, p. 656, 1966.

[88] E. A. Gulbransen, "The kinetics of oxide film formation on metals and alloys," *Transactions of the Electrochemical Society,* vol. 91, pp. 573-604, 1947.

[89] D. A. Jelski, L. Nanai, R. Vajtai, I. Hevesi, and T. F. George, "Kinetics of oxide crystal-growth in the transition regime between Cabrera-Mott and Wagner thickness regions," *Materials Science and Engineering :A,* vol. 173, pp. 193-195, 1993.

[90] S. A. Impey, D. J. Stephenson, and J. R. Nicholls, "Mechanism of scale growth on liquid aluminum," *Materials Science and Technology,* vol. 4, pp. 1126-1132, 1988.

[91] S. Impey, "The mechanism of dross formation on Al and Al-Mg alloys," PhD thesis, Cranfield Institute of Technology, 1989.

[92] E. M. Hinton, W. D. Griffiths, and N. R. Green, "Comparison of oxide thickness of aluminium and the effects of selected alloying additions," *Materials Science Forum,* vol. 765, pp. 180-184, 2013.

[93] H. J. Vanbeek and E. J. Mittemeijer, "Amorphous and crystalline oxides on aluminum," *Thin Solid Films,* vol. 122, pp. 131-151, 1984.

[94] L. P. H. Jeurgens, W. G. Sloof, F. D. Tichelaar, and E. J. Mittemeijer, "Thermodynamic stability of amorphous oxide films on metals: Application to aluminum oxide films on aluminum substrates," *Physical Review B,* vol. 62, pp. 4707-4719, 2000.

[95] L. P. H. Jeurgens, W. G. Sloof, F. D. Tichelaar, and E. J. Mittemeijer, "Structure and morphology of aluminium-oxide films formed by thermal oxidation of aluminium," *Thin Solid Films,* vol. 418, pp. 89-101, 2002.

[96] R. C. Weast, "Handbook of chemistry and physics," *The American Journal of the Medical Sciences,* vol. 257, p. 423, 1969.

[97] C. J. Powell, Jablonski, A., *NIST electron inelastic-mean-free-path database - version 1.2*. Gaithersburg, MD: National Institute of Standards and Technology, 2010.

[98] J. Ashley, C. Tung, and R. Ritchie, "Electron inelastic mean free paths and energy losses in solids: I. Aluminum metal," *Surface Science,* vol. 81, pp. 409-426, 1979.

[99] S. Tanuma, C. J. Powell, and D. R. Penn, "Proposed formula for electron inelastic mean free paths based on calculations for 31 materials," *Surface Science,* vol. 192, pp. 849-857, 1987.

[100] S. P. Adiga, P. Zapol, and L. A. Curtiss, "Atomistic simulations of amorphous alumina surfaces," *Physical Review B,* vol. 74, p. 062264, 2006.

[101] S. K. Lee, S. B. Lee, S. Y. Park, Y. S. Yi, and C. W. Ahn, "Structure of amorphous aluminum oxide," *Physical Review Letters,* vol. 103, p. 095504, 2009.

[102] P. Jiricek, I. Bartos, J. Zemek, and W. S. M. Werner, "Reflection electron energy loss spectroscopy of aluminum," *Surface Science,* vol. 604, pp. 1006-1009, 2010.

[103] R. Stefani, B. Befeno, and R. Allet, "A quantitative approach to electron-energy loss spectroscopy on aluminum and silicon in the reflection mode," *Scanning Electron Microscopy,* pp. 601-606, 1984.

[104] M. J. Dignam, "The oxidation of aluminum and certain of its binary alloys below 450ºC," *Journal of the Electrochemical Society,* vol. 105, p. 157, 1958.

[105] L. P. H. Jeurgens, W. G. Sloof, F. D. Tichelaar, and E. J. Mittemeijer, "Composition and chemical state of the ions of aluminium-oxide films formed by thermal oxidation of aluminium," *Surface Science,* vol. 506, pp. 313-332, 2002.

[106] H. Momida, S. Nigo, G. Kido, and T. Ohno, "Effect of vacancy-type oxygen deficiency on electronic structure in amorphous alumina," *Applied Physics Letters,* vol. 98, p. 042102, 2011.

[107] L. Aleshina, E. Nikitina, and A. Fofanov, "Short-range order in amorphous aluminum oxides," *Crystallography Reports,* vol. 42, pp. 836-842, 1997.

[108] P. Puri, *Multi scale modeling of ignition and combustion of micro and nano aluminum particles*: ProQuest, 2008.

[109] C. Shek, T. Gu, G. Lin, and J. Lai, "Positron lifetime study of vacancy-type defects in amorphous and polycrystalline nanometer-sized alumina," *Applied Physics A,* vol. 66, pp. 413-418, 1998.

[110] M. Prokhorskii, A. Fofanov, L. Aleshina, and E. Nikitina, "Structure of amorphous oxide Al_2O_3: Results of a molecular-dynamics experiment," *Crystallography Reports,* vol. 49, pp. 631-634, 2004.

[111] S. K. Lee, S. Y. Park, Y. S. Yi, and J. Moon, "Structure and disorder in amorphous alumina thin films: Insights from high-resolution solid-state NMR," *Journal of Physical Chemistry C,* vol. 114, pp. 13890-13894, 2010.

[112] F. Kröger and H. Vink, "Relations between the concentrations of imperfections in crystalline solids," *Solid state physics,* vol. 3, pp. 307-435, 1956.

[113] N. Cabrera and N. F. Mott, "Theory of the oxidation of metals," *Reports on Progress in Physics,* vol. 12, pp. 163-184, 1948.

[114] L. P. H. Jeurgens, W. G. Sloof, F. D. Tichelaar, and E. J. Mittemeijer, "Growth kinetics and mechanisms of aluminum-oxide films formed by thermal oxidation of aluminum," *Journal of Applied Physics,* vol. 92, pp. 1649-1656, 2002.

[115] M. J. Dignam, "Oxide films on aluminum. 1. Ionic conduction and structure," *Journal of the Electrochemical Society,* vol. 109, pp. 184-191, 1962.

[116] F. Reichel, L. P. H. Jeurgens, and E. J. Mittemeijer, "The effect of substrate orientation on the kinetics of ultra-thin oxide-film growth on al single crystals," *Acta Materialia,* vol. 56, pp. 2897-2907, 2008.

[117] K. Shimizu, A. Gotoh, K. Kobayashi, G. E. Thompson, and G. C. Wood, "The nucleation sites of gamma-Al_2O_3 crystals in thermal oxide-films on aluminum," *Microscopy of Oxidation,* pp. 144-148, 1992.

[118] R. H. Doremus, "Diffusion in alumina," *Journal of Applied Physics,* vol. 100, p. 101301, 2006.

[119] C. J. P. Steiner, Hasselma.Dp, and R. M. Spriggs, "Kinetics of gamma-to-alpha alumina phase transformation," *Journal of the American Ceramic Society,* vol. 54, pp. 412, 1971.

[120] K. Okada, A. Hattori, T. Taniguchi, A. Nukui, and R. N. Das, "Effect of divalent cation additives on the gamma Al_2O_3-to-alpha Al_2O_3 phase transition," *Journal of the American Ceramic Society,* vol. 83, pp. 928-932, 2000.

[121] M. I. F. Macedo, C. A. Bertran, and C. C. Osawa, "Kinetics of the gamma to alpha alumina phase transformation by quantitative X-ray diffraction," *Journal of Materials Science,* vol. 42, pp. 2830-2836, 2007.

[122] F. N. Bakhtiarani and R. Raiszadeh, "Healing of double-oxide film defects in commercial purity aluminum melt," *Metallurgical and Materials Transactions B,* vol. 42, pp. 331-340, 2011.

CHAPTER 6

OXIDATION STUDIES: THE Al-Mg-O_2 SYSTEM

6.1 Introduction

6.1.1 Objectives

Mg is the main alloying element in commercial 5xxx series wrought Al alloys, Al-Mg alloys have excellent corrosion resistance and Mg improves the mechanical properties of Al [1]. However, Mg can be readily selectively oxidized during melting or casting due to its higher affinity for oxygen than Al [2]. The formation of magnesium rich oxides and the loss of Mg may cause undesirable effects during downstream processing. The intention of this work is to understand the oxidation mechanisms of Al-Mg alloys, particularly of molten Al-Mg alloys, in terms of oxidation thermodynamics, growth kinetics and oxide microstructures.

6.1.2 Scope of this chapter

Section 6.2.1 discusses the Gibbs free energy change of each oxidation reaction in the Al-Mg-O_2 system as a function of temperature and Mg composition, and the Mg vapour pressure as a function of temperature. Section 6.2.2 describes the effect of Mg composition on the order of thermodynamic favourability for different oxides. Section 6.2.3 presents the results of SEM/EDX studies of oxidized Al-Mg samples. Section 6.2.4 gives details of the XPS studies and section 6.2.5 addresses the oxidation kinetics. Section 6.3 brings all the current results and the literature together to discuss the oxidation mechanisms in Al-Mg alloys in detail.

6.2 Results and discussion

6.2.1 Thermodynamics calculations

The following is a list of all possible chemical reactions in the Al-Mg-O_2 system [3, 4]. In can be

seen that MgO may form from either a *direct reaction* between Mg and O_2 or through a *reduction reaction* between Mg and Al_2O_3, and MgO to $MgAl_2O_4$ transformation can take place with the presence of Al or Al_2O_3.

$$2\mathrm{Mg}(s,l,g)+\mathrm{O_2}(g)\rightarrow 2\mathrm{MgO}(s) \quad (6.1a)$$

$$4/3\mathrm{Al}(s,l)+\mathrm{O_2}(g)\rightarrow 2/3\mathrm{Al_2O_3}(s) \quad (6.2a)$$

$$1/2\mathrm{Mg}(s,l,g)+\mathrm{Al}(s,l)+\mathrm{O_2}(g)\rightarrow 1/2\mathrm{MgAl_2O_4}(s) \quad (6.3a)$$

$$3\mathrm{Mg}(s,l,g)+\mathrm{Al_2O_3}(s)\rightarrow 3\mathrm{MgO}(s)+2\mathrm{Al}(s,l) \quad (6.4a)$$

$$\mathrm{MgO}(s)+2\mathrm{Al}(s,l)+3/2\mathrm{O_2}(g)\rightarrow \mathrm{MgAl_2O_4}(s) \quad (6.5a)$$

$$\mathrm{MgO}(s)+\mathrm{Al_2O_3}(s)\rightarrow \mathrm{MgAl_2O_4}(s) \quad (6.6a)$$

6.2.1.1 Gibbs free energy functions

The standard free energy change associated with each reaction as a function of temperature (unit: J mol^{-1}) is calculated using the method described in **Appendix 5.2**. The temperature is in the range 300-1300 K (27-1027ºC).

$$\Delta G^{\circ}(T) = -1193268 + 95.68T + 16.28T\ln T \quad (6.1b)$$

$$\Delta G^{\circ}(T) = -1099621 + 148.60T + 7.82T\ln T \quad (6.2b)$$

$$\Delta G^{\circ}(T) = -1142545 + 110.10T + 12.98T\ln T \quad (6.3b)$$

$$\Delta G^{\circ}(T) = -123433 - 43.84T + 7.25T\ln T \quad (6.4b)$$

$$\Delta G^{\circ}(T) = -1688560 + 172.35T + 17.83T\ln T \quad (6.5b)$$

$$\Delta G^{\circ}(T) = -22086 - 15.01T + 0.66T\ln T \quad (6.6b)$$

In practice, the reactants are not always at standard state and they are normally dissolved in solutions, so the chemical activities of different phases must be taken into consideration. **Equations 6.1b-6.6b** are therefore modified to

$$\Delta G(T) = \Delta G^o(T) + RT \ln\left(\frac{a_{MgO}^2}{a_{Mg}^2 P_{O_2}}\right) \quad (6.1c)$$

$$\Delta G(T) = \Delta G^o(T) + RT \ln\left(\frac{a_{Al_2O_3}^{2/3}}{a_{Al}^{4/3} P_{O_2}}\right) \quad (6.2c)$$

$$\Delta G(T) = \Delta G^o(T) + RT \ln\left(\frac{a_{MgAl_2O_4}^{1/2}}{a_{Mg}^{1/2} a_{Al} P_{O_2}}\right) \quad (6.3c)$$

$$\Delta G(T) = \Delta G^o(T) + RT \ln\left(\frac{a_{MgO}^3 a_{Al}^2}{a_{Mg}^3 a_{Al_2O_3}}\right) \quad (6.4c)$$

$$\Delta G(T) = \Delta G^o(T) + RT \ln\left(\frac{a_{MgAl_2O_4}}{a_{MgO} a_{Al}^2 P_{O_2}^{3/2}}\right) \quad (6.5c)$$

$$\Delta G(T) = \Delta G^o(T) + RT \ln\left(\frac{a_{MgAl_2O_4}}{a_{MgO} a_{Al_2O_3}}\right) \quad (6.6c)$$

First of all, assuming the oxygen gas behaves ideally, the partial pressure of oxygen in air is therefore proportional to its fraction, which is around 0.21 atm (Note: P_{O2} is used as an expression for a_{O2} throughout further discussion). In fact, the Al or Mg would theoretically react with all gas phases present, e.g. reacting with nitrogen to form nitrides [5], but the amount of reduction in Gibbs free energy of these metal-gas reactions are approximately one order of magnitude smaller than that of the metal-oxygen reactions, making them thermodynamically less favourable and negligible when oxygen is readily available [6, 7].

Secondly, as it has been suggested by Alper *et al*. [8] , Salas *et al*. [9] and Valdez *et al*. [10] that Al_2O_3, MgO and $MgAl_2O_4$ are nearly immiscible in each other in the temperature range 25-1000ºC, the chemical activities of these oxides are therefore assumed equal to 1 throughout the analysis.

Thirdly, according to the classical principles of thermodynamics [11-14] , the chemical activity of Mg is given by

$$a_{Mg} = \gamma \cdot X_{Mg} \quad (6.7)$$

Where γ is the activity coefficient and X_{Mg} is the Mg mole fraction in the system. In the present work, the chemical activity of Mg has been calculated differently in two situations (solid Al-Mg alloys and liquid Al-Mg alloys). First of all, at temperatures above 650°C (normally liquid Al-Mg), the activity coefficient γ as a function of Mg mole fraction X_{Mg} and temperature is quoted from Salas *et al*. [9] as

$$\ln \gamma_{Mg} = -\frac{225.52}{T}\left(1 - X_{Mg}\right)^2 + 0.4016\left(1 - \frac{1073.15}{T}\right) \quad (6.8)$$

Figure 6.1 is a plot based on **Equations 6.7** and **6.8**, showing the Mg chemical activity as a function of Mg mole fraction in the temperature range 25-950°C. It can be seen that **Equation 6.8** is only suitable for liquid Al-Mg alloys, because Salas *et al*. [9] derived the equation using the thermodynamic data from the work by Tiwari [15] who only reported the thermodynamic properties of liquid Al-Mg alloys (0.027-95.50 atomic% Mg). **Figure 6.1** also indicates a slight negative deviation from ideal behaviour (especially when $X_{Mg} < 0.5$) in the case of liquid Al-Mg alloys, similar result was reported by Saunders [16]. Meanwhile, it is also noted in **Figure 6.1** that when X_{Mg} is equal to 1, the chemical activity of Mg is not equal to 1, suggesting **Equation 6.8** may not be applicable for Al-Mg systems with extremely high Mg mole fractions (above 0.96). But it seems that the difference in Gibbs free energy is negligible when X_{Mg} is higher than 0.96 (approximately 0.3 kJ/mol deviation from ideal behaviour). So **Equation 6.8** is used for the calculation of Mg chemical activity at temperatures above 650ºC in the present work.

Second, at temperatures not higher than 650°C (normally solid Al-Mg), the chemical activity of Mg is assumed equal to X_{Mg} (ideal solution), due to the lack of thermodynamic data in the literature.

Meanwhile, the results from Murray [17], Bhatt and Garg [18], and Saunders [16] have suggested that the Al chemical activity in the Al-Mg system can be approximated as ideal and it can be calculated using Raoult's law [14].

$$a_{\mathrm{Al}} = X_{\mathrm{Al}} = 1 - X_{\mathrm{Mg}} \tag{6.9}$$

Bringing **Equations 6.1c-6.6c** and **6.7-6.9** together, it is inferred that ΔG is a function of Mg mole fraction and temperature which can be represented by

$$\Delta G = \Delta G\left(X_{\mathrm{Mg}}, T\right) \tag{6.10}$$

In the present work, the ΔG plots are used to understand which oxide has the most thermodynamic favourability at different combinations of Mg mole fraction and temperature. Results will be discussed in section 6.2.2.

6.2.1.2 Mg vapour pressure

It has been shown by Bloch *et al*. [19] that Mg can vaporize into individual Mg atoms at temperatures above 200°C. The presence of the Mg gas phase could enhance the Mg chemical activity and change the thermodynamics locally. It is therefore necessary to know the Mg vapour pressure at different temperatures. The vapour pressure of Mg can be calculated using the Gibbs free energy change function of the following reaction

$$\mathrm{Mg}(s,l) \rightarrow \mathrm{Mg}(g) \tag{6.11a}$$

The Gibbs free energy change function (unit: J mol^{-1}) for this reaction is calculated as

$$\Delta G^{\circ}(T) = 155860 - 253.40T + 19.20T \ln T \tag{6.11b}$$

$$\Delta G(T) = \Delta G^{\circ}(T) + RT \ln\left(\frac{P_{\mathrm{Mg}}}{P^{\circ}}\right) \tag{6.12}$$

When $\Delta G = 0$, **Reaction 6.11a** reaches an equilibrium and **Equation 6.12** is modified to

$$\ln\left(\frac{P_{\mathrm{Mg}}}{P^{\circ}}\right) = -\frac{18747}{T} - 2.31\ln T + 30.48 \tag{6.13}$$

where P_{Mg} is the Mg vapour pressure and P^{o} is the reference pressure (atmospheric pressure in this case). **Figure 6.2** is a plot constructed using **Equation 6.13**, showing the Mg vapour pressure as a function of temperature in the range 300-1300 K (27-1027ºC). In the present work, using the above method, it is estimated that Mg has a high vapour pressure up to more than 2.14 kPa at 750ºC

while the vapour pressure of Al is only around 0.14 kPa. So it is reasonable to assume that the influence of Al gas phase is negligible in such system. Similar suggestion was also given by Damoah *et al*. [20].

6.2.2 Effect of Mg composition

Previously in the literature, Haginoya and Fukusako [21], and Ritchie *et al*. [22] have attempted to explain their observations of MgO and $MgAl_2O_4$ in the oxide scales from a perspective of thermodynamics. But they did not take the chemical activities of Mg, Al and O_2 into consideration and simply used the standard Gibbs free energy change of each reaction to compare thermodynamic tendencies, which is a little inappropriate. In the present work, **Equations 6.1c-6.3c** are therefore plotted to understand which oxide is the most thermodynamically stable at different combinations of Mg mole fraction and temperature. **Figures 6.3-6.12** show the Gibbs free energy change profiles of the oxides Al_2O_3, $MgAl_2O_4$ and MgO as a function of X_{Mg} at a specific temperature.

First of all, it can be seen that MgO becomes the most favourable once in excess of a critical Mg mole fraction (defined as $\boldsymbol{C_{Mg}}$) and $MgAl_2O_4$ becomes the most favourable below this critical Mg composition (highlighted by the green dash lines). Al_2O_3 becomes the most favourable when the Mg mole fraction is below at least 0.0002 (highlighted by the purple dash lines). The critical Mg mole percentage (0-100%) is approximately 0.0001% at 25ºC, 0.01% at 150ºC, 0.08% at 250ºC, 0.15% at 350ºC, 0.6% at 450ºC, 1.2% at 550ºC, 2.0% at 650ºC, 4.0% at 750ºC, 6.0% at 850ºC and 7.5% at 950ºC. It is noted that C_{Mg} increases with temperature, as shown in **Figure 6.13**. Below 400ºC, C_{Mg} does not vary very much with increasing temperature and it is less than 1%. Above 400ºC, C_{Mg} increases approximately linearly with temperature, suggesting an increased thermodynamic favourability of $MgAl_2O_4$ at high temperatures.

The results also suggest that MgO is the most favourable oxide when the Mg mole fraction is more than 0.1 in the temperature range 25-950ºC. This is consistent with the observations reported by Wakefield and Sharp [23] that oxide formed at 430°C in an Al-10Mg alloy consists of almost entirely MgO. In fact, according to the summary shown in **Table 6.2** at the end of this Chapter, the results of thermodynamics calculations in the present work are somewhat reasonably predictive and are in agreement with most of the experimental results reported in the literature.

6.2.3 SEM/EDX studies

SEM and EDX have been combined to study the oxide scales formed on Al-Mg alloys in terms of oxide morphology and chemistry. As discussed in Chapter 5, the surface of an oxidized sample is usually microscopically rough, the interpretation of EDX results is therefore always associated with the specific conditions (such as local topography, interaction volume size, etc) in which the spectrum was obtained. For the SEM/EDX studies, Al-2Mg and Al-0.2Mg were used.

6.2.3.1 Al-2Mg – wrinkled morphology

Figure 6.14 shows the surface oxide layer morphology of an Al-2Mg sample which was oxidized at 750ºC in air for 1 h. It can be seen that the surface oxide layer has a wrinkled morphology with snake-like ridges. **Figure 6.15** is an overview of such an oxide layer morphology. As highlighted by the white arrows, cauliflower-like bulges with sizes of around 10 μm are observed. From **Figure 6.16**, it can be seen that these cauliflower-like bulges are agglomerates of spherical-like crystalline oxides less than 1 μm in diameter, which protrude out of the oxide layer. EDX analysis was performed on these features. As shown in **Figure 6.16 (b)**, EDX spectra of these features (P1-P3) suggests they are richer in both Mg and O, compared to the main oxide chemistry (P4).

EDX analysis has been used widely to identify MgO and $MgAl_2O_4$ oxides [24, 25], which are two of the important oxides in the Al-Mg-O_2 system. Ideally, the stoichiometric weight ratio of Mg to

O in MgO and $MgAl_2O_4$ is 1.5 and 0.375 respectively. It has been suggested that if the Mg/O ratio is less than 0.4, the oxide is highly likely to be $MgAl_2O_4$-rich oxide, if the Mg/O ratio is more than 1, the oxide consists of a high percentage of pure MgO [25]. But again, the conditions of the EDX analysis must be taken into account, including the topography, interaction volume, etc, in order to avoid misinterpretation of the results.

From **Figure 6.16 (b)**, the Mg/O weight ratio for spectra P1-P3 are 1.30, 1.01, and 1.36 respectively, suggesting the cauliflower-like bulges are highly likely to contain MgO. The chemistry of the main oxide, as indicated by P4, is more certainly an average chemistry from both the oxide layer and the metal underneath: for $MgAl_2O_4$, the Mg/Al weight ratio is around 0.44, in this case, the Mg/Al ratio is only 0.34, implying that X-ray signals are also coming from the metallic Al beneath the oxide layer. Similar results are shown in **Figure 6.17**, demonstrating the consistency of the chemistry in different structural features.

Figure 6.18 shows the cross section of the oxidized Al-2Mg alloy. Firstly, it can be seen that the surface oxide layer is actually a composite layer: consisting of pores, Mg-rich oxide, metals, etc. Secondly, it is noted that each pore is coated with an oxide layer with a thickness of around 100 nm, as indicated by yellow arrows. Protruding bulges are also identified, as highlighted by the blue arrows.

Figure 6.18 indicates that this composite oxide layer is around 3 μm in thickness. From the SEM/EDX results of the stacked Al/Al-2Mg sample *M-24* (24h oxidation) in Chapter 4, there is an $MgAl_2O_4$-like layer covering the Al-2Mg alloy with a similar thickness of around 3-5 μm, as shown in **Figure 4.35**. It is likely that this spinel layer is transformed from the composite oxide layer structure shown in **Figure 6.18**. The MgO to $MgAl_2O_4$ transformation has been suggested by Haginoya and Fukusako [21], Impey *et al*. [26] and Venugopalan *et al*. [27]. In the present work,

as discussed in sections 6.2.1 and 6.2.2, after a long period of oxidation time, the consumption of Mg to form MgO may lower the surface Mg composition to a level where spinel becomes the most favourable oxide to form. It is therefore hypothesized here that the oxidation of the Al-Mg alloys may proceed in the MgO - to - $MgAl_2O_4$ order.

6.2.3.2 Al-0.2Mg – nodule morphology

Figures 6.19 (a)-(c) (SE images) and **Figure 6.19 (d)** (BE image) show the surface oxide layer morphology of an Al-0.2Mg sample which was also oxidized at 750ºC for 1 h. The oxide layer consists of 1-2 μm crystalline particles, exhibiting an overall "*nodule*" morphology and powdery topography. From **Figure 6.20**, these loosely packed particles containing Mg and O with an average weight ratio of around 0.52, indicating a possible combination of both MgO and $MgAl_2O_4$.

Figure 6.21 shows the surface topography of the oxidized Al-0.2Mg sample. Cracks even as wide as up to 400 μm were observed in this powdery layer and the metal below was exposed. This is not surprising as during solidification, significant thermal stress builds up in the oxide scale [6], cracking is an effective way to release the stress. Interestingly, as can be seen from **Figure 6.22**, the fresh exposed metal is quickly covered by a new deformable and ductile thin oxide layer. As highlighted by yellow arrows, it can be inferred that, during solidification, the metal contracts and the oxide layer gets wrinkled and folded, this could lead to the entrainment of surface solid substances (e.g. oxide particles) between these wrinkles and folds. This may provide an evidence for Campbell's entrainment theory [28]. From **Figure 6.23**, the chemistry at the exposed metal indicates an average Mg weight concentration of 0.95%, which is higher than the initial bulk Mg composition (0.2wt%), suggesting the preferential segregation of Mg to the surface region during oxidation. The topic of segregation will be discussed in section 6.3.2.1. As suggested by the EDX results in **Figures 6.23** and **6.24**, these 1-2 μm nodule-like oxide particles mainly comprise $MgAl_2O_4$.

Figures 6.25 and **6.26** show the effect of surface treatments on oxidation. The surface was deliberately coarsely ground with 120 grit SiC paper. The morphology of the powdery layer is similar but the layer is rougher microscopically. This is probably due to the increased surface area and oxides are easier to nucleate and grow on ridges or junctions with the aid of local stress energy [7, 29]. The mechanism is shown by the sketch in **Figure 6.27**.

6.2.3.3 Extracted oxides

In the present work, a novel method is introduced to directly observe the morphology of the "*wet*" side of an oxide layer (the metal/oxide interface) and the "dry" side of an oxide layer (the oxide/air interface) by using the extraction method described in Chapter 3. The intention of this work is to capture the structure of the surface oxide scale at the very beginning stage (a few minutes) of oxidation.

During the experiment, an Al-2Mg or Al-0.2Mg sample were initially heated to 750ºC and the surface oxide was then carefully skimmed away using a K-type thermocouple probe with tip diameter of 1 mm. This would allow the oxidation progress to be set back to the start and expose fresh melt to the atmosphere. As confirmed experimentally by Impey *et al*. [26, 30], the mechanical skimming would not introduce any new oxide formation, it only resets the oxidation progress starting with a freshly exposed melt.

In the present work, we were not able to quantify the preferential segregation and oxidation of Mg during the heating up stage and thus it is difficult to know what is happening at the initial stage of oxidation using only the previous results. So the skimming was used to reset the oxidation back to the very start. The oxidation proceeds firstly by the formation of an amorphous aluminium oxide layer on the melt [31]. The skimmed sample was then isothermally held at 750ºC for around 10

minutes. After extraction, electronically conductive disc-shaped carbon adhesive tabs were pressed on to cylindrical stubs with a 12.5 mm diameter and a 10 mm height. Extracted oxides were scrapped from the dried filter onto these tabs and then coated with a platinum film of thickness ~ 2 nm before SEM examination.

Figure 6.28 is an SE image showing the *dry* side (the oxide/air interface) morphology of the oxide layer formed on an Al-0.2Mg sample. It is very interesting to notice the formation of spherical nanoparticles averaging between 30-600 nm in diameter. The growth of these nanoparticles causes microcracks around the particles averaging 1-3 μm long within the continuous oxide layer. **Figure 6.28** also suggests that nanoparticles may initially nucleate at the metal/oxide interface and within the initial amorphous oxide layer, and then grow towards the oxide/air interface. This is consistent with the model proposed by Shimizu *et al*. [32] and Zayan [33] that MgO forms and cracks the initial formed aluminium oxide layer in the early stage of oxidation (usually in a time less than 5 minutes). This mechanism is further supported by the XPS results described in section 6.2.4. A detailed description of the mechanism will be given in section 6.3.3.

Figure 6.29 (a) is an SE image showing the *wet* side morphology of the oxide layer formed on the same sample, which is featured by a complex microstructure consisting of both oxides and intermetallic-like substances). It is noted that the *wet* side of the oxide layer also consists of spherical nanoparticles: at the area where P1 was taken, the averaging particle size is around 1 μm; where P2 was taken, the averaging particle size is less than 400 nm. This suggests that the oxides grow preferentially in local regions instead of growing uniformly everywhere. The chemistry of these particles indicates that the oxides mainly consist of MgO, as suggested qualitatively by the EDX spectra in **Figure 6.29 (b)**. As also can be seen from **Figure 6.30**, these MgO-like nanoparticles can form clusters of diameter up to 8 μm.

Figure 6.31 shows the morphology of both sides of the oxide layer formed on Al-0.2Mg which was held for only 5 minutes after skimming. It looks like the *dry* side of the oxide layer is mostly intact while oxide-like particles have already nucleated and grown on the *wet* side. Similarly, **Figure 6.32** shows the distinctive features of the *dry* side and the *wet* side of an oxide layer formed on an Al-2Mg sample. It can be seen that oxides have formed at the metal/oxide interface with a flower-like wavy morphology and 100-200 nm oxide particles have grown within the oxide layer towards the *dry* side.

6.2.4 XPS studies

The intention of XPS studies is, firstly, to understand what type of oxide forms naturally on fresh surfaces of Al-Mg alloys, and secondly, to confirm the transformation of aluminium oxide to MgO within the oxide scale, as suggested by the SEM/EDX results. XPS analysis was performed on ***Al-AP*** (as polished pure Al sample), ***Al-2Mg-AP*** (as polished Al-2Mg sample), ***Al-2Mg-R1*** (Al-2Mg sample oxidized at 750˚C in air for 1h) and ***Al-2Mg-R6*** (Al-2Mg sample oxidized at 750˚C in air for 6h). Two different X-ray sources (Al Kα and Mg Kα) were used during the experiments. All XPS peaks were labelled according to references [34, 35].

6.2.4.1 Wide scan

Figure 6.33 shows that the surface oxide formed on ***Al-AP*** and ***Al-2Mg-AP*** is aluminium oxide, as indicated by the presence of Al 2p & Al 2s peaks and the absence of Mg 2p & Mg 2s peaks. While the surface oxide formed on ***Al-2Mg-R1*** and ***Al-2Mg-R6*** is magnesium oxide, as confirmed by the presence of Mg 2p & Mg 2s peaks and the absence of Al 2p & Al 2s peaks. The results imply that aluminium oxide is the first oxide naturally formed on free surfaces of dilute Al-Mg alloys. This is further confirmed by XPS results shown in section 6.2.4.2. A possible qualitative explanation for this finding may be established based on Cabrera-Mott theory [36]: when the oxide layer is thinner than 5 nm, an electric field of approximately 1 or 2 volts is established across the

oxide layer and the kinetics of oxide growth are controlled by the outward transport of metal ions [36]: the trivalent Al ions (Al^{3+}) simply move faster to the oxide/air interface to bond with oxygen than divalent Mg ions (Mg^{2+}) under the same electric field.

Figure 6.34 shows the wide scan XPS spectra acquired with Al Kα X-ray, whose energy (1486.6 eV) is higher than that of Mg Kα X-ray (1253.6 eV). It has been shown that Mg KLL is very sensitive to Al Kα [34]. In the present work, Mg Auger peaks (Mg KLL) are not observed in the spectra of ***Al-AP*** and ***Al-2Mg-AP***, suggesting a near complete absence of Mg in the surface oxide layer; while Mg KLL peaks are clearly identified in the spectra of ***Al-2Mg-R1*** and ***Al-2Mg-R6***, suggesting the formation of Mg-rich oxide layer on the top surface. Given the fact that the depth of information of XPS analysis is around 10 nm [37], it can be concluded that magnesium oxide is the main oxide formed on ***Al-2Mg-R1*** and ***Al-2Mg-R6***, at least the external part of the oxide layer; while the top surface oxide of ***Al-AP*** and ***Al2Mg-AP*** is aluminium oxide.

Interestingly, the O 1s "*ghost*" peak is observed in the spectra of ***Al-2Mg-R1*** and ***Al-2Mg-R6***. This type of peak is identified as a magnesium induced "*ghost*" peak [38]. When a sample containing Mg is irradiated with Al Kα X-rays, photoelectrons interact with the sample to produce Mg Kα. Mg Kα can cause further emission of photoelectrons. In the present work, the binding energy of these Mg Kα induced O 1s photoelectrons is observed at approximately 766 eV, as highlighted in **Figure 6.34**. This is because the kinetic energy of the induced O 1s photoelectrons is approximately 1253.6 eV – 532.5 eV (O 1s binding energy) = 721.1 eV so they would appear at around 1486.6 eV - 721.1 eV = 765.5 eV in the spectrum.

6.2.4.2 Core levels

(a) Al 2p

A detailed scan of the Al 2p core level was then performed to calculate the thickness of the

aluminium oxide layer formed on the ***Al-2Mg-AP*** sample. The results are shown in **Figure 6.35**. Both curves were fitted with Gaussian functions. In the present work, the elemental Al 2p peaks are located at a binding energy of 72.82 eV for Mg Kα irradiation and 72.81 eV for Al Kα irradiation. The oxide Al 2p peaks are located at binding energies of 75.86 eV (Mg Kα) and 75.88 eV (Al Kα). The ratio of the areas under the fitted elemental Al 2p peak and the oxide Al 2p peak is 1:6.45 (using Mg Kα) and 1:5.57 (using Al Kα), respectively. It is noted that the ratio is slightly higher in the Al Kα irradiated sample. This is due to the higher X-ray energy (Al Kα - 1453.6 eV), causing more emission of photoelectrons from the metal underneath. The feature is further identified during the analysis of O 1s core levels, as will be shown in **Figure 6.36**. Based on **Equation 5.15** described in Chapter 5, the thickness of the aluminium oxide layer formed on ***Al-2Mg-AP*** is calculated to be 5.9 nm (using Mg Kα) and 5.6 nm (using Al Kα).

(b) O 1s

The O 1s peaks were fitted with Gaussian functions. In the present work, as shown in **Figure 6.36**, the O 1s peaks at 530.01 eV (***Al-2Mg-R1***, Mg Kα) and 529.98 eV (***Al-2Mg-R6***, Mg Kα) are attributed to the O from MgO, while the O 1s peaks at higher binding energies of 532.18 eV (***Al-2Mg-R1***, Mg Kα) and 532.20 eV (***Al-2Mg-R6***, Mg Kα) are attributed to the O from the hydroxide species, $Mg(OH)_2$. It has been shown that $Mg(OH)_2$ forms naturally on the MgO layer once the sample is exposed to a humid environment and even after short periods of exposure to a humid atmosphere, the sample surfaces could form an appreciable level of $Mg(OH)_2$ [39]. Similarly, the O 1s core levels XPS spectra under Al Kα irradiation were fitted with Gaussian functions. In the present work, the MgO O 1s peaks are at 530.02 eV (***Al-2Mg-R1***) and 530.01 eV (***Al-2Mg-R1***) and the $Mg(OH)_2$ O 1s peaks are at 532.16 eV (***Al-2Mg-R6***) and 532.15 eV (***Al-2Mg-R6***). It can be seen that fitted MgO O 1s peaks are all located at a spectral line of 530.00 ± 0.02 eV and $Mg(OH)_2$ O 1s peaks are all located at a spectral line of 532.20 ± 0.05 eV. The results clearly prove the presence of only MgO at the top surface (at least first 10 nm range) of ***Al-2Mg-R1*** and ***Al-***

2Mg-R6. Whilst, only Al_2O_3 is identified in the ***Al-2Mg-AP*** sample with the O 1s peak located in the range 532.65 ± 0.05 eV, suggesting the first naturally formed oxide layer on Al-2Mg alloy is aluminium oxide. At the same time, since the energy of Al Kα X-rays is higher than Mg Kα X-rays, Al Kα X-rays generates information from a greater sample depth than Mg Kα X-rays, the ratio of MgO/$Mg(OH)_2$ quantified from the spectra varies with the energy of X-ray used. From the data in **Figure 6.36**, the intensity ratio for MgO and $Mg(OH)_2$ changes from 1:2.01 to 1:1.78 for sample ***Al-2Mg-R1***. Similarly, the ratio changes from 1:1.98 to 1:1.45 for sample ***Al-2Mg-R6***.

It can be seen from the above results that aluminium oxide transforms to MgO in the external part of the oxide scale after the Al-2Mg was oxidized. Similarly, Lea and Ball [40] found that aluminium oxide initially formed on an Al-2.5Mg alloy and MgO entirely covered the surface after 1 h oxidation at 600°C.

(c) Mg 2p

Mg 2p core levels were also analysed to confirm the presence of MgO on ***Al-2Mg-R1*** and ***Al-2Mg-R6***. As shown in **Figure 6.37**, Mg 2p peaks are all located within the range 51.2 ± 0.2 eV and broad peaks at higher binding energies of 53.5 ± 0.5 eV are attributed to $Mg(OH)_2$. The width of, and intensities under, the $Mg(OH)_2$ Mg 2p peaks may be related to the levels of hydration. The absence of Mg 2p peaks for ***Al-2Mg-AP*** is due to the formation of aluminium oxide instead of MgO, this is consistent with previous results and also the work by Panda *et al*. [31, 41, 42] who found the absence of the Mg 2p signal from an Al-1.1Mg sample which was oxidized in pure oxygen at 400 K for 6000 s. Panda *et al*. [31] proposed a complex thermodynamics model to show that amorphous γ-Al_2O_3 is more thermodynamically favourable than amorphous MgO or amorphous $MgAl_2O_4$ on the Al-Mg substrate (at least 0-50% Mg) for temperatures below 610 K due to its lower interfacial energy with the Al-Mg metal substrate, further suggesting the preferential formation of aluminium oxide at the beginning stage of oxidation.

To sum up, based on previous results and discussion, it may be reasonably concluded that (1) the as-polished Al-2Mg alloy is naturally covered with an aluminium oxide layer with a thickness of around 5 nm at room temperature; (2) MgO is essentially present in the external part of the oxide film thermally grown on Al-2Mg samples and it is prone to hydration.

6.2.5 Kinetics of oxidation

The goal of this section of the work was to assess the oxidation (1h oxidation time) kinetically using thermogravemetric analysis (TGA). Samples were polished according to the standard surface preparation described in Chapter 3. In the present work, the results indicate that the oxidation kinetics of Al-Mg alloys is affected by both oxidizing temperature and alloy composition.

Figure 6.38 shows the oxidation kinetics curves of Al-2Mg and Al-0.2Mg. It can be seen that there is a linear-like behaviour in the temperature range of 750-950°C, particularly in the later stage of oxidation (approximately after 600 seconds). This may suggest that there are some non-protective characteristics of the oxide scale. In this temperature range, the alloys are in the liquid state. In the temperature range of 450-650°C, the oxidation growth also shows linear progression in the later stage (approximately after 2400 seconds). However, for both alloys, parabolic-like behaviour is observed during the earlier stage of oxidation (before 600s), probably indicating some degree of protectiveness of the initially formed oxide structure.

Breakaway oxidation [43] is not observed in this study (in the case of 1h oxidation time), the overall oxidation kinetics of Al-Mg alloys may be best described by a ***para-linear*** growth law: the initial stage shows a parabolic-like progression and then the oxidation gradually progresses linearly. Similar behaviour was observed by Lea and Ball [40] who found that an Al-2.5Mg alloy exhibited a para-linear growth rate (1h time, dry air) at 500°C. Meanwhile, Tenorio and Espinosa [44]

reported para-linear oxide growth behaviour (1h time, dry air) for an AA5182 alloy (around 4.5wt% Mg) in the temperature range 400-800°C. The present findings are consistent with their results.

According to previous results and discussion, the preferential oxidation of Mg causes development of cracks within the scale and the oxide scale is featured by either a wrinkled morphology with localised protruding cauliflower-like oxide islands (Al-2Mg) or nodule morphology with loosely packed oxide particles (Al-0.2Mg): the oxide scale is not a continuously protective layer. As shown by TGA results, in the later stage of oxidation (after 2400s), the weight gain curves for Al-0.2Mg and Al-2Mg are almost linear, indicating the rate-controlling process may be the reaction between Mg and O_2, rather than the diffusion of any species [7], as both Mg and O_2 may easily flow through the porously structured oxide scale.

The weight gain curves as a function of time between 2400s and 3600s were fitted linearly and plotted using Arrhenius equations to estimate the oxidation activation energy. The results are summarized in **Figure 6.39** and **Table 6.1**. For Al-2Mg, the oxidation rate equations in the temperature range of 450-650˚C and 750-950˚C are calculated as

$$R_{\text{Al-2Mg}} = 0.53\exp\left(-\frac{85400}{RT}\right) \quad \text{(Linear stage, 450-650˚C, mg cm}^{-2}\text{ s}^{-1}\text{)} \qquad (6.14)$$

$$R_{\text{Al-2Mg}} = 1.3\times10^{-3}\exp\left(-\frac{37200}{RT}\right) \quad \text{(Linear stage, 750-950˚C, mg cm}^{-2}\text{ s}^{-1}\text{)} \qquad (6.15)$$

For Al-0.2Mg, the oxidation rate equations in the temperature range of 450-650˚C and 750-950˚C are given by

$$R_{\text{Al-0.2Mg}} = 3.6\times10^{-3}\exp\left(-\frac{63900}{RT}\right) \quad \text{(Linear stage, 450-650˚C, mg cm}^{-2}\text{ s}^{-1}\text{)} \qquad (6.16)$$

$$R_{\text{Al-0.2Mg}} = 1.2\times10^{-3}\exp\left(-\frac{53500}{RT}\right) \quad \text{(Linear stage, 750-950˚C, mg cm}^{-2}\text{ s}^{-1}\text{)} \qquad (6.17)$$

According to **Figure 6.39**, the oxidation rate for Al-2Mg is faster than that for Al-0.2Mg at all

temperatures, suggesting the accelerating effect of Mg on the oxidation of Al. Meanwhile, it is noted that the Arrhenius plots for both Al-2Mg and Al-0.2Mg (not obvious) consist of two parts, having two different activation energies: for Al-2Mg, one of them refers to an oxidation activation energy of 85.4 kJ mol^{-1} for the solid state Al-2Mg and the other refers to a lower oxidation activation energy of 37.2 kJ mol^{-1} for the liquid state Al-2Mg; for Al-0.2Mg, the activation energy is calculated to be 63.9 kJ mol^{-1} in the temperature of 450-650˚C and 53.5 kJ mol^{-1} in the temperature range of 750-950˚C. This clearly suggests a kinetic advantage for liquid state oxidation. Similar results were reported by Tenório and Espinosa [44], and Jin *et al*. [45] who also estimated the activation energy to be around 50-100 kJ mol^{-1} using a modified Chou model [46].

To sum up, the actual reason for the observed overall para-linear growth law is unknown, as discussed later in section 6.3.1, it may be a result of inward diffusion of oxygen, possibly the inward diffusion of O_2 molecules through a porously structured oxide scale. The proposed mathematical model of the para-linear growth law is shown in **Appendix 6.1**.

6.3 Oxidation mechanism

According to previous results and discussion, the oxidation mechanism of molten Al-Mg alloys is suggested as follows: the Al-Mg melt is initially covered by an amorphous aluminium oxide skin; MgO particles then form through a *direct* reaction mechanism between inwardly diffused oxygen molecules and Mg gas, as well as a *reduction* reaction mechanism between the dissolved Mg in the amorphous structure and the oxygen from the initially formed aluminium oxide; the depletion of Mg favours the growth of $MgAl_2O_4$ at later stages of oxidation.

6.3.1 Inward diffusion of oxygen

Unlike Cu, Mg, which has a higher oxygen affinity, may simply react with oxygen to form the MgO crystal structure instead of undergoing a series of defect reactions in the pre-formed

aluminium oxide layer. It is recognized from the previous SEM/EDX results that MgO particles nucleate at the metal/oxide interface and grow towards the oxide/air interface, a possible consequence of an inward ionic diffusion of oxygen across the amorphous oxide layer, as suggested by various researchers [22, 33, 47, 48]. If this is the case, the oxidation rate should be directly related to the number of oxygen vacancies in the aluminium oxide scale. Mg may dope the aluminium oxide through the following reaction

$$Mg + V_{Al}''' \rightarrow Mg_{Al}' + 2e' \tag{6.18}$$

The electrons and oxygen vacancies annihilate at the oxide/air interface, as described by **Reaction 6.19**. This reaction also indicates the effect of oxygen pressure on defects within the oxide scale.

$$V_O^{\bullet\bullet} + 2e' + \frac{1}{2}O_2 \rightarrow O_x^x \tag{6.19}$$

Overall, **Reactions 6.18** and **6.19** result in a decrease in both Al vacancies and oxygen vacancies. Therefore, as suggested by Olefjord and Karlsson [49], the oxidation rate should be lowered due to the doping of Mg. However, as indicated by the present work, and the results from Hinton *et al*. [50], Field *et al*. [51], Impey *et al*. [26], and Lea and Ball [40], Al-Mg alloys usually show increased oxidation rates. This is probably because the doping effect is insignificant, compared to the preferential formation of MgO which contributes to the overall weight gain of the scale. In fact, it is suggested here that oxygen in the MgO comes mostly from inwardly diffused **molecular O_2**.

TEM results from Shimizu *et al*. [52], and Doherty and Davis [53] have proven the presence of micro-cracks developed in the amorphous layer at temperatures above 450ºC. This is highly likely as during the heating-up period, tensile or compressive stress could accumulate due to the different thermal expansion coefficients of the amorphous layer and metal matrix. Cracking is a way of stress relief. At high temperatures, as it get thicker, the amorphous layer becomes more brittle and it is easier to develop cracks within the oxide scale. Molecular O_2 may directly diffuse through the cracks in the amorphous layer to react with fresh metal at the metal/oxide interface. According to the kinetic theory of gases [54], the mean free path of oxygen molecules (the average inter-

molecule distance) can be estimated using the following equation.

$$\lambda = \frac{RT}{\sqrt{2}\pi d^2 N_A P} \tag{6.20}$$

where R is the gas constant, T is the temperature, d is the mean diameter of an oxygen molecule (around 0.3 nm [54]), N_A is the Avogadro constant and P is the pressure, which is 1 atm in this case. For example, taking T = 1023 K (750ºC), λ is calculated to be around 0.35 μm. As shown in **Figure 6.28**, some cracks observed are even up to 1 μm, which could act as easy diffusion channels for O_2 molecules. The O_2 molecules could easily flow through these channels. Eldridge *et al*. [29] also reported the oxygen inward transport through micro-channels and porosity to the metal/oxide interface at temperatures above 450°C by using ^{18}O/SIMS technique, clearly supporting the above mechanism.

6.3.2 Mg segregation and evaporation

From my point of view, oxidation studies of the Al-Mg-O_2 system are more complicated than other systems. First of all, Mg atoms readily segregate at the surface through rapid grain boundary diffusion especially at temperatures above 200ºC [55]. It has been shown that the level of Mg at the surface could be increased to 35 at% for an Al-0.005Mg alloy at 800˚C [56]. Secondly, Mg has a high vapour pressure. The evaporation of Mg could lead to the loss of Mg and the direct reaction between Mg gas phase and oxygen. This causes depletion of Mg and may influence the surface Mg content to an unknown extent. The following subsections will address each kinetic process separately and attempt to understand how they affect the overall oxidation behaviour of Al-Mg alloys.

6.3.2.1 Segregation

Thermodynamically, it has been shown that Mg atoms segregate to free surfaces or grain boundaries as an attempt to reduce the free energy of the system [57-59]. Meanwhile, the presence

of large solute atoms (Mg atom 12% larger than Al atom) sets up a strain field in the bulk and it can be relieved by preferentially sitting at a free surface, where the coordination number is low and there is excess free volume [60, 61]. So the size effect provides another driving force for Mg to segregate to the surface in Al-Mg alloys. Kinetically, some researchers believe that the surface segregation of Mg is mainly due to the fast diffusivity of Mg along the grain boundaries of α-Al and Mg atoms are rapidly delivered to the free surface via these paths [55, 58, 62, 63].

It has been shown by the Langmuir-McLean theory [1] that the segregation kinetics can be described by an Arrhenius type equation in terms of a segregation energy

$$\frac{x_s}{1-x_s} = \frac{x_b}{1-x_b}\exp\left(\frac{G}{RT}\right) \tag{6.21}$$

where x_s refers to the equilibrium solute composition in the surface region (a few atomic layers) and x_b refers to the equilibrium solute composition in the bulk, and G is the free energy of segregation. If the segregation energy is positive, then solute atoms segregate at the free surface to reduce the total Gibbs free energy, and vice versa [64]. The exponential term is usually regarded as an enrichment ratio, which is predicted to be around 1-10 in the case of Al-Mg alloys [40, 55]. However, this equation may only be applied to solid state segregation and there is currently no widely accepted segregation theory for liquid metal, and it could be far more complicated than a simple equation can explain. Even if **Equation 6.21** is correct, the segregation free energy still needs to be determined, which is expected to be approximately 20-50 kJ mol^{-1} [19, 58, 63, 65]. But it is likely that there is already some degree of Mg segregation occurring during the heating up period when the Al-Mg is still in the solid state.

6.3.2.2 Evaporation

Because Mg has high vapour pressure at elevated temperatures and the evaporation of Mg is a characteristic phenomenon of Al-Mg alloys and Mg alloys [27, 66, 67]. The effect has been treated numerically by Venugopalan *et al*. [27, 66, 67] and De *et al*. [68] and it has been shown that the

evaporation kinetics can play a dominant role in determining the overall oxide growth kinetics.

In particular for Al-Mg alloys with Mg compositions above 20wt%, the evaporation of Mg has been readily detected with the walls of the crucible being found to be coated with MgO as a result of direct reaction between Mg vapour and oxygen [69-72]. This is further confirmed in the present work, as shown in **Figure 6.40**. A pure Mg slug of around 40 mg was oxidized at 750ºC and it can be seen that the cylindrical alumina crucible was eventually coated with white MgO powder, clearly suggesting the evaporation of Mg occurring at high temperatures. Using **Equation 6.20**, the mean free path of Mg atoms is around 0.3 μm, implying that the Mg vapour could also easily flow through the porously structured oxide scale.

According to the work by Wu *et al*. [73], the evaporation kinetics may not be dominant if dilute Al-Mg alloys are oxidized in air. It has been suggested that a local equilibrium may be established between the evaporation and recondensing kinetics of Mg during the oxidation. Loss of Mg through reaction with oxygen will reduce the Mg partial pressure in the environment, evaporation of '*new*' Mg atoms into the environment occurs in order to maintain this equilibrium. The time to reach equilibrium may depend on the temperature and the environment (open or closed). The degree of loss of Mg through evaporation may be limited in a closed environment. In fact, the formation of a continuous amorphous γ-Al_2O_3 layer at the early stage of oxidation may offer some degree of protectiveness and prevent the loss of Mg. Even at later stages when other oxide scale starts to form, the composite oxide scale still could serve as a barrier saturated with Mg vapour, and the Mg partial pressure could be maintained in equilibrium with the melt solution locally around the oxide scale. This argument is similar to that suggested by Lea and Molinari [55]: i.e. that the evaporation and segregation kinetics of Mg are the dominant kinetic processes in vacuum while segregation and oxidation kinetics are the dominant kinetic processes in air.

6.3.3 Formation of MgO and $MgAl_2O_4$

This section mainly focuses on the growth mechanisms of MgO and $MgAl_2O_4$ in the Al-Mg-O_2 system.

6.3.3.1 MgO

The growth of MgO during the early stages of oxidation is possible via two chemical reactions

$$Mg + \frac{1}{2}O_2 \rightarrow MgO \tag{6.22}$$

$$Mg + \frac{1}{3}\gamma\text{-}Al_2O_3(\text{amorphous}) \rightarrow MgO + \frac{2}{3}Al \tag{6.23}$$

Reaction 6.22 is a direct reaction where Mg reacts with oxygen to produce MgO. **Reaction 6.23** is a reduction reaction where Mg reacts with the existing amorphous aluminium oxide structure to produce MgO and Al. In order to compare which reaction is more thermodynamically favourable, the change in Gibbs free energy ΔG for each reaction is compared via the parameter $\Delta\boldsymbol{\delta} = \Delta G_{6.22} - \Delta G_{6.23}$, if $\Delta\boldsymbol{\delta}$ is less than zero, it means that **Reaction 6.22** has a larger reduction in free energy per mole of Mg consumed, and vice versa. As shown in **Figure 6.41**, the direct reaction between Mg and O_2 is always the most favourable in the temperature range 300-1300 K (27-1027ºC) in air.

However, the oxygen in MgO may also come from the amorphous aluminium oxide, particularly in oxygen-deficient conditions. First of all, **Reaction 6.23** is still thermodynamically feasible due to the reduction in free energy, and as shown in **Figure 6.41**, it becomes more thermodynamically favourable as the oxygen content decreases. This is consistent with the work reported by Goldstein and Dresner [74], who used Auger Electron Spectroscopy (AES) to study the growth of MgO while heating an Al-1Mg sample at 450ºC for 5 minutes in 10^{-5} torr O_2. They found that the oxide-state Mg (the Mg from MgO) started to appear and increase within the naturally formed Al_2O_3 layer and there was also a decreased oxide-state Al signal (the Al from Al_2O_3) and an increased metal-state Al, clearly suggesting the occurrence of the reduction mechanism at low oxygen pressures.

Secondly, as can be seen from **Figure 6.28**, there are some regions where MgO nanoparticles grow without the presence of microcracks around, and it looks like these MgO nanoparticles nucleate and grow within the amorphous structure, as there may be some degree of oxygen deficiency at the very beginning of oxidation. Thirdly, as experimentally proven by Guillot *et al*. [75], Mg could diffuse into the amorphous structure to form Mg-O bonds. The result from Nylund *et al*. [76] also shows the presence of Mg^{2+} in the interior region of amorphous γ-Al_2O_3 layer which may suggests the diffusion of Mg^{2+} from the metal/oxide interface into the amorphous γ-Al_2O_3 layer. Meanwhile, the results reported by Scamans *et al*. [51, 77] also suggest the formation of MgO through the reaction between the dissolved Mg and the amorphous structure.

From previous discussion, the MgO growth mechanism observed in the present work can be illustrated in **Figure 6.42**. During the early stages of oxidation, MgO particles grow beneath (Mg directly reacts with inwardly diffused oxygen at the metal/oxide interface) or within the amorphous layer (reduction reaction). The difference in the PB ratios of MgO (0.81) and Al_2O_3 (1.28) different [78] leads to the generation of interface elastic strain [79]. As the particles further coarsen, the stress builds up and eventually cracks are generated to release the strain energy [80]. Once the protective amorphous layer starts to fail, more O_2 molecules can enter through the cracks to facilitate the formation of MgO particles. MgO particles form preferentially around channels, holes and pores, as these paths are rich in the flow of O_2 and Mg vapour. Due to the increased availability of oxygen and Mg vapour, the oxidation process may gradually be dominated by the direct reaction between Mg vapour and O_2, and the effect of the reduction mechanism is gradually minimized. This could eventually result in a porously structured oxide scale.

6.3.3.2 $MgAl_2O_4$

It is known from previous results and discussion that $MgAl_2O_4$ is the main oxidation product for oxidation over longer periods and for alloys with low Mg composition. From previous discussion,

it is known that the surface segregation and evaporation of Mg lead to the preferential formation of MgO during the initial stages of oxidation, even if the bulk Mg composition may favour the growth of $MgAl_2O_4$ thermodynamically. As MgO particles grow, their surroundings become depleted of Mg and $MgAl_2O_4$ may start to nucleate and grow through the following reactions, as discussed in section 6.2.1.

$$Mg + 2Al + 2O_2 \rightarrow MgAl_2O_4 \quad (6.24)$$

$$MgO + 2Al + \frac{3}{2}O_2 \rightarrow MgAl_2O_4 \quad (6.25)$$

$$MgO + Al_2O_3 \rightarrow MgAl_2O_4 \quad (6.26)$$

According to the work by Haginoya and Fukusako [21] who studied the oxidation behaviour of a series of Al-Mg alloys at 750ºC, they found an initial increase in MgO quantity and then a gradual decrease after reaching a maximum, and eventually there is a steady accumulation of $MgAl_2O_4$. This clearly shows the formation of $MgAl_2O_4$ at the expense of MgO. A similar effect was identified by Impey *et al*. [26, 30]. Shimizu *et al*. [32] also found there was a thinning of the amorphous layer to compensate for the formation of $MgAl_2O_4$ during the oxidation of an Al-0.5Mg alloy, this indicates the possibility of **Reaction 6.26**. In the present work, similar to the results in Chapter 4 and previous SEM/EDX results, **Figure 6.43** shows the presence of MgO and $MgAl_2O_4$ in both Al-2Mg and Al-0.2Mg after oxidation for 1h. As can be seen from **Table 6.2**, which is a summary of some representative similar studies reported in the literature, the oxide products are usually a mixture of MgO and $MgAl_2O_4$, especially for Al-Mg alloys with Mg bulk composition below 4wt% (around 4.5 mol% Mg).

Table 6.2 – Selected studies of Al-Mg alloys oxidation available in literature.

T (°C)	Alloy (wt. %)	P_{O2} (a_{O2})	Time scale	Oxides detected	Reference
400	Al-1%Mg - film	P=1	1 h	MgO	[22]
400	Al-4.2%Mg	P=0.21	1 h	MgO	[51]
400	Al-0.8%Mg	P=0.21	1 h	MgO	[81]
400	Al-2.5%Mg	P=0.21	1 h	MgO	[81]
430	Al-10%Mg	P=0.21	1 h	MgO	[23]
475	Al-5%Mg - film	$P=10^{-4}$	30 min	MgO + $MgAl_2O_4$	[77]
480	Al-4.2%Mg	P=0.21	15 min	MgO	[51]
500	Al-1%Mg - film	P=1	30 min	MgO + $MgAl_2O_4$	[22]
520	Al-4.2%Mg	P=0.21	1 h	MgO	[51]
550	Al-3%Mg	P=1	55 h	MgO + $MgAl_2O_4$	[82]
550	Al-0.4%Mg	P=0.21	90 h	MgO + $MgAl_2O_4$	[48]
550	Al-2%Mg	P=0.21	90 h	MgO + $MgAl_2O_4$	[48]
550	Al-5%Mg	P=0.21	90 h	MgO	[33]
577	Al-0.05%Mg	P=0.21	30 min	MgO + $MgAl_2O_4$	[83]
577	Al-0.1%Mg	P=0.21	30 min	MgO + $MgAl_2O_4$	[83]
600	Al-0.8%Mg	P=0.21	1 h	MgO	[81]
600	Al-2.5%Mg	P=0.21	1 h	MgO	[81]
655	Al-0.03%Mg	Unknown	Unknown	MgO	[84]
700	Al-0.7%Mg	P=1	3 h	$MgAl_2O_4$	[85]
700	Al-5%Mg	P=1	30 min	MgO	[86]
730	Al-7Si+0.35Mg	P=0.21	3 h	MgO + Al_2O_3	[87]
750	Al-10%Mg	P=0.21	3 h	MgO + $MgAl_2O_4$	[21]
750	Al-4%Mg	P=0.21	70 h	MgO + $MgAl_2O_4$	[88]
750	**Al-2%Mg**	**P=0.21**	**1 h**	**MgO + $MgAl_2O_4$**	**Current work**
750	Al-0.5%Mg	P=0.21	48 h	MgO + $MgAl_2O_4$	[81]
750	**Al-0.2%Mg**	**P=0.21**	**1 h**	**MgO + $MgAl_2O_4$**	**Current work**
800	Al-3%Mg	P=0.21	1 h	MgO + γ-Al_2O_3	[89]
850	Al-0.005%Mg	P=1	20 h	MgO + α-Al_2O_3	[88]
950	Al-0.005%Mg	P=1	20 h	α-Al_2O_3	[88]
1118	Al-5%Mg	P=0.035	10 min	MgO	[27, 66, 67]
1118	Al-5%Mg	P=0.42	10 min	MgO	[27, 66, 67]

6.3.4 Implications for bonding

A few implications for bonding may be inferred from the oxidation studies of the Al-Mg-O_2 system. First of all, the preferential formation of Mg-rich oxides on Al-Mg alloys leads to a porously structured oxide scale. These hard and brittle Mg-rich oxide particles could potentially jeopardize the integrity of the bond interface and reduce the bond durability. Secondly, even if the *bi-film* like bond interface were healed completely using the stacking approach and the interface were microscopically continuous without the presence of crack-like defects, the bond would still be weak due to humidity attack and cannot subsequently be used in humid environments, as MgO is prone to hydration. Generally speaking, for the sake of successful bonding, Al alloys containing high Mg are not recommended as parent materials.

6.4 Concluding remarks

The oxidation of Al-Mg alloys shows strong preferential oxidation of Mg into MgO and $MgAl_2O_4$ in the oxide scale. The addition of Mg to Al will prevent the formation of aluminium oxide thermodynamically. Following the initially formed amorphous aluminium oxide layer, MgO is usually the second oxide appearing in the scale. Further oxidation causes the depletion of Mg and the formation of $MgAl_2O_4$ dominates over MgO. Kinetically, the oxidation is rationalized by para-linear laws. Microscopically, in particular during the initial stage of oxidation, the morphology of the oxide layer develops from an early compact and protective uniform amorphous layer to a loosely structured oxide scale with agglomerates of MgO particles. The outer surface of the atmospherically oxidized Al-2Mg alloy is covered entirely by MgO as confirmed by XPS studies.

6.5 References

[1] L. F. Mondolfo, *Aluminum alloys: Structure and properties* vol. 5: London Butterworths, 1976.

[2] R. C. Weast, M. J. Astle, and W. H. Beyer, *CRC handbook of chemistry and physics* vol. 69: CRC press, 1988.

[3] D. Weirauch, "Interfacial phenomena involving liquid metals and solid oxides in the Mg-Al-O system," *Journal of Materials Research,* vol. 3, pp. 729-739, 1988.

[4] D. G. Kim, J. Kaneko, and M. Sugamata, "Preferential oxidation of Mg in mechanically alloyed Al-Mg-O based systems," *JIM, Materials Transactions,* vol. 36, pp. 305-311, 1995.

[5] R. Raiszadeh, W. Griffiths, "A method to study the history of a double oxide film defect in liquid aluminum alloys," *Metallurgical and Materials Transactions B,* vol. 37, pp. 865-871, 2006.

[6] O. Kubaschewski and B. E. Hopkins, *Oxidation of metals and alloys*: London Butterworths, 1953.

[7] N. Birks, G. H. Meier, and F. S. Pettit, *Introduction to the high temperature oxidation of metals*: Cambridge University Press, 2006.

[8] A. Alper, R. McNally, P. Ribbe, and R. Doman, "The system MgO-$MgAl_2O_4$," *Journal of the American Ceramic Society,* vol. 45, pp. 263-268, 1962.

[9] O. Salas, H. Ni, V. Jayaram, K. C. Vlach, C. G. Levi, and R. Mehrabian, "Nucleation and growth of Al_2O_3/metal composites by oxidation of aluminum-alloys," *Journal of Materials Research,* vol. 6, pp. 1964-1981, 1991.

[10] M. Valdez, K. Prapakorn, A. W. Cramb, and S. Seetharaman, "A study of the dissolution of Al_2O_3, MgO and $MgAl_2O_3$ particles in a CaO-Al_2O_3-SiO_2 slag," *Steel research,* vol. 72, pp. 291-297, 2001.

[11] D. C. Spanner, *Introduction to thermodynamics*: London and New York Academic Press, 1964.

[12] M. Kaufman, *Principles of thermodynamics*: CRC Press, 2002.

[13] D. R. Gaskell, *Introduction to the thermodynamics of materials* vol. 2: CRC Press, 2008.

[14] H. A. Buchdahl, *The concepts of classical thermodynamics* vol. 1: Cambridge University Press, 2009.

[15] B. L. Tiwari, "Thermodynamic properties of liquid Al-Mg alloys measured by the EMF method," *Metallurgical Transactions A,* vol. 18, pp. 1645-1651, 1987.

[16] N. Saunders, "A review and thermodynamic assessment of the Al-Mg and Mg-Li systems," *CALPHAD,* vol. 14, pp. 61-70, 1990.

[17] J. L. Murray, "The Al-Mg system," *Bulletin of Alloy Phase Diagrams,* vol. 3, pp. 60-74, 1982.

[18] Y. Bhatt and S. Garg, "Thermodynamic study of liquid aluminum-magnesium alloys by vapor pressure measurements," *Metallurgical Transactions B,* vol. 7, pp. 271-275, 1976.

[19] J. Bloch, D. J. Bottomley, J. G. Mihaychuk, H. M. Vandriel, and R. S. Timsit, "Magnesium surface segregation and its effect on the oxidation rate of the (111) surface of Al-1.45at%Mg," *Surface Science,* vol. 322, pp. 168-176, 1995.

[20] L. N. W. Damoah, L. Zhang, and N. F. Adegboyega, "Formation of the solid layer on the top of molten aluminum," 2010.

[21] I. Haginoya and T. Fukusako, "Oxidation of molten Al-Mg alloys," *Transactions of the Japan Institute of Metals,* vol. 24, pp. 613-619, 1983.

[22] I. M. Ritchie, J. V. Sanders, and P. Weickhar, "Oxidation of a dilute aluminum magnesium alloy," *Oxidation of Metals,* vol. 3, p. 91, 1971.

[23] G. R. Wakefield and R. M. Sharp, "The composition of oxides formed on Al-Mg alloys," *Applied Surface Science,* vol. 51, pp. 95-102, 1991.

[24] M. Aryafar, R. Raiszadeh, and A. Shalbafzadeh, "Healing of double oxide film defects in A356 aluminium melt," *Journal of Materials Science,* vol. 45, pp. 3041-3051, 2010.

[25] F. N. Bakhtiarani and R. Raiszadeh, "The behaviour of double oxide film defects in Al-4.5wt%Mg melt," *Journal of Materials Science,* vol. 46, pp. 1305-1315, 2011.

[26] S. A. Impey, D. J. Stephenson, and J. R. Nicholls, "Mechanism of scale growth on liquid aluminum," *Materials Science and Technology,* vol. 4, pp. 1126-1132, 1988.

[27] H. Venugopalan, K. Tankala, and T. Debroy, "Probing the initial stage of synthesis of Al2O3/al composites by directed oxidation of al-mg alloys," *Metallurgical and Materials Transactions B,* vol. 27, pp. 43-50, 1996.

[28] J. Campbell, "Entrainment defects," *Materials Science and Technology,* vol. 22, pp. 127-145, 2006.

[29] J. I. Eldridge, R. J. Hussey, D. F. Mitchell, and M. J. Graham, "Thermal-oxidation of single-crystal aluminum at 550°C," *Oxidation of Metals,* vol. 30, pp. 301-328, 1988.

[30] S. Impey, "The mechanism of dross formation on Al and Al-Mg alloys," PhD Thesis, Cranfield Inst. of Technology, 1989.

[31] E. Panda, L. P. H. Jeurgens, and E. J. Mittemeijer, "The initial oxidation of Al-Mg alloys: Depth-resolved quantitative analysis by angle-resolved X-ray photoelectron spectroscopy and real-time *in situ* ellipsometry," *Journal of Applied Physics,* vol. 106, 2009.

[32] K. Shimizu, G. M. Brown, K. Kobayashi, P. Skeldon, G. E. Thompson, and G. C. Wood, "The early stages of high temperature oxidation of an Al-0.5wt%Mg alloy," *Corrosion Science,* vol. 40, pp. 557-575, 1998.

[33] M. H. Zayan, "Model for nonprotective oxidation of al-mg alloys," *Oxidation of Metals,* vol. 34, pp. 465-472, 1990.

[34] D. Briggs, Seah, M. P., *Practical surface analysis: Auger and X-ray photoelectron spectroscopy* vol. 1. Chichester: Wiley, 1990.

[35] J. F. Moulder, J. Chastain, and R. C. King, *Handbook of X-ray photoelectron spectroscopy*: Physical Electronics Eden Prairie, 1995.

[36] N. Cabrera and N. F. Mott, "Theory of the oxidation of metals," *Reports on Progress in Physics,* vol. 12, pp. 163-184, 1948.

[37] J. F. Watts and J. Wolstenholme, *An introduction to surface analysis by XPS and AES*: Wiley-VCH, 2003.

[38] C. Klauber, "Refinement of magnesium and aluminium kα X-ray source functions," *Surface and interface analysis,* vol. 20, pp. 703-715, 1993.

[39] W. Giauque and R. Archibald, "The entropy of water from the third law of thermodynamics. The dissociation pressure and calorimetric heat of the reaction $Mg(OH)_2 = MgO + H_2O$," *Journal of the American Chemical Society,* vol. 59, pp. 561-569, 1937.

[40] C. Lea and J. Ball, "The oxidation of rolled and heat-treated Al-Mg alloys," *Applied Surface Science,* vol. 17, pp. 344-362, 1984.

[41] E. Panda, L. P. H. Jeurgens, and E. J. Mittemeijer, "Growth kinetics and mechanism of the initial oxidation of Al-based Al-Mg alloys," *Corrosion Science,* vol. 52, pp. 2556-2564, 2010.

[42] E. Panda, L. P. H. Jeurgens, G. Richter, and E. J. Mittemeijer, "The amorphous to crystalline transition of ultrathin (Al,Mg)-oxide films grown by thermal oxidation of AlMg alloys: A high-resolution transmission electron microscopy investigation," *Journal of Materials Research,* vol. 25, pp. 871-879, 2010.

[43] H. Evans, A. Donaldson, and T. Gilmour, "Mechanisms of breakaway oxidation and application to a chromia-forming steel," *Oxidation of Metals,* vol. 52, pp. 379-402, 1999.

[44] J. A. S. Tenorio and D. C. R. Espinosa, "High-temperature oxidation of Al-Mg alloys," *Oxidation of Metals,* vol. 53, pp. 361-373, 2000.

[45] F. Jin, Q. Luo, B. Zhou, and Q. Li, "Modeling investigation of the oxidation kinetics of copper and aluminum alloys," *Advanced Materials Research,* vol. 402, pp. 17-21, 2012.

[46] K. C. Chou, "A kinetic model for oxidation of Si-Al-O-N materials," *Journal of the American Ceramic*

Society, vol. 89, pp. 1568-1576, 2006.

[47] I. Olefjord and A. Karlsson, "Aluminium technology," *The Institute of Metals, London, p383,* 1986.

[48] M. H. Zayan, O. M. Jamjoom, and N. A. Razik, "High-temperature oxidation of Al-Mg alloys," *Oxidation of Metals,* vol. 34, pp. 323-333, 1990.

[49] I. Olefjord and A. Karlsson, "Surface analysis of aluminium foil," *Aluminium Technology,* vol. 86, pp. 383-391, 1986.

[50] E. M. Hinton, W. D. Griffiths, and N. R. Green, "Comparison of oxide thickness of aluminium and the effects of selected alloying additions," *Materials Science Forum,* vol. 765, pp. 180-184, 2013.

[51] D. J. Field, G. M. Scamans, and E. P. Butler, "The high-temperature oxidation of Al-4.2wt%Mg alloy," *Metallurgical Transactions A,* vol. 18, pp. 463-472, 1987.

[52] K. Shimizu, R. C. Furneaux, G. E. Thompson, G. C. Wood, A. Gotoh, and K. Kobayashi, "On the nature of easy paths for the diffusion of oxygen in thermal oxide-films on aluminum," *Oxidation of Metals,* vol. 35, pp. 427-439, 1991.

[53] P. E. Doherty and R. S. Davis, "Direct observation of oxidation of aluminum single-crystal surfaces," *Journal of Applied Physics,* vol. 34, p. 619, 1963.

[54] W. Kauzmann, *Kinetic theory of gases*: Courier Dover Publications, 2012.

[55] C. Lea and C. Molinari, "Magnesium diffusion, surface segregation and oxidation in Al-Mg alloys," *Journal of Materials Science,* vol. 19, pp. 2336-2352, 1984.

[56] E. Bergsmark, C. J. Simensen, and P. Kofstad, "The oxidation of molten aluminum," *Materials Science and Engineering: A,* vol. 120, pp. 91-95, 1989.

[57] J. J. Burton and E. S. Machlin, "Prediction of segregation to alloy surfaces from bulk phase-diagrams," *Physical Review Letters,* vol. 37, pp. 1433-1436, 1976.

[58] X. Y. Liu, P. P. Ohotnicky, J. B. Adams, C. L. Rohrer, and R. W. Hyland, "Anisotropic surface segregation in Al-Mg alloys," *Surface Science,* vol. 373, pp. 357-370, 1997.

[59] M. Seah, "Quantitative prediction of surface segregation," *Journal of Catalysis,* vol. 57, pp. 450-457, 1979.

[60] H. Ehrenreich and F. Spaepen, *Solid state physics*: Academic Press, 2001.

[61] C. Kittel and P. McEuen, *Introduction to solid state physics* vol. 8: Wiley New York, 1986.

[62] R. C. Picu and D. Zhang, "Atomistic study of pipe diffusion in Al-Mg alloys," *Acta Materialia,* vol. 52, pp. 161-171, 2004.

[63] D. T. L. van Agterveld, G. Palasantzas, and J. T. M. De Hosson, "Magnesium surface segregation and oxidation in Al-Mg alloys studied with local probe scanning auger-scanning electron microscopy," *Applied Surface Science,* vol. 152, pp. 250-258, 1999.

[64] A. R. Miedema, "Surface segregation in alloys of transition-metals," *Zeitschrift Fur Metallkunde,* vol. 69, pp. 455-461, 1978.

[65] F. Esposto, C.-S. Zhang, P. Norton, and R. Timsit, "Segregation of mg to the surface of an Al-Mg single crystal alloy and its influence on the initial oxidation at room temperature," *Surface science,* vol. 302, pp. 109-120, 1994.

[66] H. Venugopalan and T. DebRoy, "Growth stage kinetics in the synthesis of Al_2O_3/Al composites by directed oxidation of Al-Mg and Al-Mg-Si alloys," *Journal of the European Ceramic Society,* vol. 16, pp. 1351-1363, 1996.

[67] H. Venugopalan, K. Tankala, and T. DebRoy, "Kinetics of directed oxidation of Al-Mg alloys in the initial and final stages of synthesis of Al_2O_3/Al composites," *Materials Science and Engineering:A,* vol. 210, pp. 64-75, 1996.

[68] A. K. De, A. Mukhopadhyay, S. Sen, and I. K. Puri, "Numerical simulation of early stages of oxide formation

in molten aluminium-magnesium alloys in a reverberatory furnace," *Modelling and Simulation in Materials Science and Engineering*, vol. 12, pp. 389-405, 2004.

[69] F. Czerwinski, "The oxidation behaviour of an AZ91D magnesium alloy at high temperatures," *Acta Materialia*, vol. 50, pp. 2639-2654, 2002.

[70] F. Czerwinski, "The oxidation of magnesium alloys in solid and semisolid states," *Magnesium Technology 2003*, pp. 39-42, 2003.

[71] F. Czerwinski, "Factors affecting the oxidation nature of magnesium alloys," *JOM*, vol. 56, pp. 29-31, 2004.

[72] F. Czerwinski, "The early stage oxidation and evaporation of Mg-9%Al-1%Zn alloy," *Corrosion Science*, vol. 46, pp. 377-386, 2004.

[73] G. Wu, Galano, M., O'Reilly, K., "A basic study on evaporation kinetics in Al-Mg alloys (unpublished short report, still incomplete)," 2013.

[74] B. Goldstein and J. Dresner, "Growth of MgO films with high secondary electron emission on Al-Mg alloys," *Surface Science*, vol. 71, pp. 15-26, 1978.

[75] J. Guillot, N. Valle, E. Maitre, S. Verdier, and H. N. Migeon, "Investigation on the magnesium segregation in low-magnesium aluminium alloys," *Surface and Interface Analysis*, vol. 42, pp. 735-738, 2010.

[76] A. Nylund, K. Mizuno, and I. Olefjord, "Influence of Mg and Si on the oxidation of aluminum," *Oxidation of Metals*, vol. 50, pp. 309-325, 1998.

[77] G. M. Scamans and E. P. Butler, "Insitu observations of crystalline oxide formation during aluminum and aluminum-alloy oxidation," *Metallurgical Transactions A*, vol. 6, pp. 2055-2063, 1975.

[78] N. B. Pilling, Bedworth, R. E., "The oxidation of metals at high temperatures," *Journal: Institute of Metals*, vol. 29, p. 4, 1923.

[79] P. Kofstad and J. Wiley, *High-temperature oxidation of metals* vol. 584: Wiley New York, 1966.

[80] E. A. Gulbransen, "The kinetics of oxide film formation on metals and alloys," *Transactions of the Electrochemical Society*, vol. 91, pp. 573-604, 1947.

[81] O. Ozdemir, J. E. Gruzleski, and R. A. L. Drew, "Effect of low-levels of strontium on the oxidation behavior of selected molten aluminum-magnesium alloys," *Oxidation of Metals*, vol. 72, pp. 241-257, 2009.

[82] W. W. Smeltzer, "Oxidation of an aluminum-3 percent magnesium alloy in the temperature range 200-550°C," *Journal of the Electrochemical Society*, vol. 105, pp. 67-71, 1958.

[83] H. Leighly Jr and A. Alam, "The oxidation of dilute alloys of magnesium in aluminium," *Journal of Physics F: Metal Physics*, vol. 14, p. 1573, 1984.

[84] S. Dobiński and M. Niesluchowski, "Selective oxidation of aluminium alloys," *Nature*, vol. 144, pp. 510-511, 1939.

[85] Y. Wang, H.-T. Li, and Z. Fan, "Oxidation of aluminium alloy melts and inoculation by oxide particles," *Transactions of the Indian Institute of Metals*, vol. 65, pp. 653-661, 2012.

[86] K. Surla, F. Valdivieso, M. Pijolat, M. Soustelle, and M. Prin, "Kinetic study of the oxidation by oxygen of liquid Al-Mg 5% alloys," *Solid State Ionics*, vol. 143, pp. 355-365, 2001.

[87] S. Miresmaeili, "Oxidation of liquid Al-7Si alloys containing strontium and magnesium," *Metal 2005*, pp. 223-231.

[88] D. Belitsku, "Oxidation of molten Al-Mg alloy in air, air-SO_2, and air-H_2S atmospheres," *Oxidation of Metals*, vol. 3, pp. 313-317, 1971.

[89] M. Silva, "Oxidation of aluminium-magnesium alloys at elevated temperature in the solid, semi-liquid and liquid states," Brunel University, 1987.

CHAPTER 7

PROCESSING STUDIES: DOUBLE-POURING APPROACH

7.1 Introduction

The oxidation behaviour of Al-Cu and Al-Mg alloys as a function of alloy composition, temperature and time has been discussed in previous chapters. Al and Al-5Cu were used again here. In the present work, a *double-pouring* approach was developed to produce an Al/Al-5Cu bimetallic composite. The interface microstructure of a double-poured Al/Al-5Cu sample was compared with that of the stacked Al/Al-5Cu samples to gain an understanding of how external agitation affects the bonding between Al and Al-5Cu and the evolution of oxide films during processing.

There are two reasons to conduct the study on this topic. First, bimetallic composites consisting of two alloys/composites bonded together have drawn serious attention recently due to the combination of properties of two base materials [1] and the versatility to cope with extreme conditions [2]. As discussed in Chapter 2, there are several approaches for the production of bonded bimetallic composites, such as transient liquid phase bonding [3], brazing [4, 5] and friction stir welding [6, 7]. However, components with complex geometries may not be produced using the above approaches. These methods are only suitable for manufacturing bimetallic plates [8], rods [9], or other shape-limited products [10]. As also mentioned in Chapter 2, casting one metal on to or around the base metal allows to produce a near-net shape component with a complex geometry and the use of casting reduces industrial expenses and increases productivity [11-13]. Unfortunately, little work has been reported in the literature. Second, the interface microstructure between two Al alloys to be bonded during processing is scientifically interesting. As discussed in previous chapters, an amorphous aluminium oxide layer rapidly forms on the surface of Al once in contact with air. The chemically and thermally stable oxide *bi-film* layer acts as a physical

barrier preventing metallic bonding. Metallic bonding is achieved only when the oxide layers have either been dissolved or disrupted between two metals.

Guentner and Sahm [14, 15] firstly studied a multi-pouring method to produce graded Al composites reinforced with SiC particles. In this method, slurries with different compositions were poured into a mould sequentially and the authors found that the gradation across the interface strongly depends on the solid fraction of the first cast alloy before pouring of the second alloy. However, they did not recognize the influence of the oxide layer formation on the interface microstructure. In the present work, an approach termed as "*double-pouring*" has been used to attempt casting an Al/Al-5Cu bimetallic composite and its interface microstructure has been characterized to understand the bonding mechanism.

7.2 Results and discussion

7.2.1 Processing details

Slugs of pure Al (~99.99%) and Al-5Cu binary alloy were initially melted and isothermally held inside two cylindrical alumina crucibles separately at 750°C in an electric resistance furnace. After the top solid dross layer had been skimmed, liquid Al-5Cu was then poured steadily into a cylindrical graphite mould (height: 80 mm; diameter: 40 mm) which had been preheated to 400ºC. The Al-5Cu was then left to cool and solidify. Liquid Al was finally filled gradually on top of the partially solidified Al-5Cu, as illustrated in **Figure 7.1**. The casted bimetallic composite was air cooled to room temperature.

7.2.2 Bond interface

A local region with a well-bonded interface morphology between Al and Al-5Cu was observed after macroetching, as shown in **Figure 7.2**. This stitched cross-sectional view from multiple OM

micrographs suggests metallic bonding was achieved between the Al and the Al-5Cu after the processing. In the present work, it was also found that the Al-5Cu showed much quicker response to the etchant than the Al. As discussed in Chapter 4, this is probably due to the presence of θ-$CuAl_2$ phase at the grain boundaries, which causes rapid grain boundary corrosion during the etching process [16]. The degree of mixing between the Al and the Al-5Cu could therefore be assessed qualitatively by the optical contrast between the Cu-rich zone and the Cu-deficient zone. The width of the bond zone is estimated to be around 100 μm according to **Figure 7.2**.

Figure 7.3 is a BE image showing the well-bonded interface morphology between Al and Al-5Cu. As indicated by **Figure 7.3**, the Cu gradation behaviour within the α-Al matrix across the interface from the Al-5Cu side to the Al side was assessed using an EDX line scan analysis. It is noted that the Cu composition within the α-Al matrix decreases from 0.99% to almost 0% across the interface from the Al-5Cu side to the Al side. The gradation of Cu across the bond interface could be well fitted by a sigmoid logistic function as

$$y = \frac{y_0}{1+\exp\left[k\cdot\left(x-x_c\right)\right]} \tag{7.1}$$

This function has been widely used to describe the span and the gradient of an "*S-shape*" curve [17]. In this case, y_0 is the concentration of Cu in α-Al matrix on the Al-5Cu side far away from the bond zone, k is a factor indicating the width of bond zone, x is the relative distance to zero point and x_c is the relative position of the interface to zero point. The fitted results are summarized in **Table 7.1**. Based on EDX results, the width of the bond zone is estimated to be around 120 μm, similar to the result obtained from the OM image analysis. It is expected that the value y_0 shall not be equal to 5% due to solute partitioning during solidification which leads to the preferential segregation of Cu at cell boundaries [18-20] (usually in the form of θ-$CuAl_2$). The preferential segregation of Cu at cell boundaries causes the depletion of Cu at the centre [21]. As shown in **Figure 7.3**, the other EDX line scan was performed to assess gradient of Cu from the centre of a

cell to an adjacent cell across the boundary. It can be seen that that the Cu composition profile may be well fitted with a Gauss Function, suggesting the diffusive nature of Cu from high composition regions to low composition regions.

Meanwhile, the bumpy (wavy) non-planar un-bonded interface morphology with the presence of the "crack-like" defects sandwiched between Al and Al-5Cu was also observed in the double-poured Al/Al-5Cu sample, as shown in **Figure 7.4**. It is inferred that a 100% metallic bonding cannot be achieved using the *double-pouring* approach. Based on the results and discussion from previous chapters, it is known that either liquid Al or semi-solid Al-5Cu is coated with a naturally-formed oxide layer before getting in contact; a complete metallic bonding may only be achieved when these oxide layers are disrupted or dissolved.

7.2.3 Fracture surfaces

SEM/EDX study on fracture surfaces confirmed the presence of oxide *bi-film* defects at the interface and these defects provide easy crack propagation paths. The crack propagated along the bond interface. **Figure 7.5** is a pair of butterfly symmetric images showing the fracture surfaces of the *double-poured* Al/Al-5Cu sample. It is noted that a *bi-film* defect at the interface was split into two halves on both sides. These defects at the bond interface are points of stress concentration and detrimental to the bond strength. Meanwhile, according to **Figure 7.6** (in particular S1), the presence of Cu (2.49%) suggests the bonding is achieved between Al and Al-5Cu in that region.

7.2.4 Bonding mechanism

As shown in **Figure 7.7**, the bonding mechanism is proposed as follows: initially, each metal will be coated with a thin layer of oxide; secondly, hot liquid Al will increase the local temperature at the interface and the liquid (Al)/semi-solid (Al-5Cu) interface is pushed down as a result of partial melt-back of the solidified Al-5Cu; thirdly, severe turbulence and thermal convection help disrupt

and rupture the oxide into small pieces in the form of *bi-film* defects which are discontinuously distributed along the bond interface. Therefore, 100% metallic bond is not possible due to the presence of *bi-film* defects which prevent any further metallic bonding. During the fracture analysis, these defects are subject to stress concentration and *bi-film* defects are split into two halves. As suggested by a finite element method (FEM) simulation shown in **Figure 7.8**, when the *double-poured* Al/Al-5Cu is subject to a tensile force, stress would accumulate significantly around the *bi-film* defects at the bond interface.

7.2.5 Suggestions for improved bonding

As discussed previously, using the *double-pouring* approach, the obstacle to achieve a 100% metallic bonding is the presence of discontinuous *bi-film* defects at bond interface. From the oxidation studies in Chapter 5, we know that it is absolutely impossible to prevent the oxide formation on Al alloys in practice. In the present work, two secondary processing methods are suggested to be undertaken to minimize the detrimental effect of *bi-film* defects at bond interface and potentially improve the efficiency of the *double-pouring* approach.

The current author [22] reports a result on how a controlled induction stirring pattern re-distribute oxide *bi-film* defects to the top surface due to their buoyancy in the melt. A well-controlled further induction stirring after the *double-pouring* process is suggested to be used to improve the bond structure by relocating the *bi-film* defects from the interface to the surface, as illustrated in the **Figure 7.9**.

In the *double-pouring* approach, the processing time is only a few minutes. According to previous results and discussion in Chapter 5, the oxide films formed on molten Al and Al-5Cu may still be soft in nature and stay amorphous. Applying a pressure during the solidification of the *double-poured* Al/Al-5Cu may help stitch the *bi-film* defects by introducing adequate plastic deformation

within the *bi-film* pockets and this could increase the total effective metallic bonding area. The idea is illustrated in **Figure 7.10**.

7.3 Other approaches

7.3.1 Squeeze casting

As discussed in section 7.2.5, the use of squeeze casting could potentially improve the bond and it is an interesting topic worthwhile to explore further. In the present work, a squeeze casting method was attempted to produce an Al based bimetallic composite.

The set-up of the squeeze casting mould is shown in **Figure 7.11**. First of all, cylindrical Al billet with a diameter of 80 mm and a height of 20 mm was initially isothermally placed within the mould at 350ºC and 400 g of Al-5Cu slug was melt at 750ºC in an extra crucible. After the surface dross was skimmed, liquid Al-5Cu was then poured onto the solid Al billet. A pressure of 10 tonnes was applied for 15 minutes during the solidification. This pressure is enough to disrupt any oxide layer as the strength of an aluminium oxide layer is averaged around 400 MPa [23]. The experiment was performed with the help of Dr B. Liu in the Advanced Materials Centre for Aerospace and Aeronautics at Shanghai Jiao Tong University.

Macroscopically, it can be seen from **Figure 7.12** that a uniform and clean bond interface is achieved. Microscopically, as shown in **Figure 7.13**, the bond interface is free from crack-like defects. However, it was found that the bond is relatively weak at the positions close to the wall of the mould, cracks have formed during the sample preparation, as shown in **Figure 7.14**. It is inferred that there is no significant interface reaction occurring at these regions. As the heat may be released quickly through the relatively cold steel mould, the observed un-bonded morphology is probably due to the chilling of the Al-5Cu melt around the solid Al together with surface oxide

layers on both Al and Al-5Cu. Similar observation was also reported by Durrant *et al*. [24]. In the present work, the melt-back of Al did occur, as suggested by the wavy feature of the interface, but because of the chilling effect (the relatively cold Al serves as a chill), Al and Al-5Cu might immediately solidify and the metallic mixing was significantly prohibited. At the edge of the interface, there was probably only solid-solid contact before the application of pressure. This could lead to a degradation of bond strength. It is therefore proposed that Al could be pre-heated to a higher temperature than 350ºC to minimize the chilling effect (allow a greater degree of melt-back), or use die coatings to reduce the mould/casting interfacial heat-transfer [25].

To summarize, using the squeeze casting approach, the superheated Al-5Cu melt could cause the melt-back of a limited area of surface region of the solid Al billet, the applied pressure brings two materials into close contact and stitches the *bi-film* defects at the interface. Although there is a certain degree of the melt-back of the solid base material, this method could reduce the change of microstructure of the solid to a minimum while it offers a clean bond interface, if the chilling effect can be kept to a minimum. Meanwhile, the processing time is short enough to ensure the oxidation progress being confined in early stages (amorphous oxide layer). Therefore, the use of squeeze casting is potentially promising in particular to obtain metallic bonding between a liquid Al alloy and a solid Al alloy without altering the microstructure of the base solid drastically.

7.3.2 Extrusion bonding

In the present work, an extrusion bonded 6082Al-NQX (NQX: the aberration for Al nanoquasicrystalline alloy) sample was characterized using SEM/EDX. Recently, Galano, Audebert, and Rounthwaite have successfully produced bulk Al based NQX via an extrusion route [26-29]. In this method, NQX powders were initially put into a 6082 aluminium can with an outer diameter of 50.5 mm, an inner diameter of 43.5 mm and a height of 100 mm. The whole unit was then extruded together into a bar with around a diameter of 14 mm at an extrusion temperature of

375°C. The extrusion ratio is around 13:1. The progress is briefly illustrated in **Figure 7.15**.

An Al-Fe-Cr-Nb NQX alloy extruded bar was characterized in this study, in particular the bond interface between the NQX alloy and the aluminium. The bar was produced by Rounthwaite and Galano [26]. Interestingly, it can be seen that the interface is free from crack-like defects and it has a diffuse interface like morphology, as shown in **Figures 7.16** and **7.17**. The wavy feature of the bond interface clearly suggests good metallic contact between 6082 Al and NQX. EDX line scan was attempted to estimate the width of bonding zone. From **Figure 7.18**, it may only be concluded that the bonding zone is less than 100 μm, due to the limited resolution of the EDX composition profile. Since the averaging size of the NQX powders used is around 50-75 μm, so the bonding zone covers approximately one or two layers of NQX particles, suggesting the microstructure of the extruded NQX alloy is not disturbed to a great extent.

To conclude, although the processing approaches discussed in this thesis have some limitations, they have all potential for future development, at least all these studies have offered some insights on how to design a proper Al alloys bonding approach in different situations, and also a greater scientific understanding of the role of oxidation in bonding Al alloys.

7.4 References

[1] R. M. Jones, *Mechanics of composite materials*: CRC Press, 1998.

[2] I. Beyerlein, N. Mara, J. Wang, J. Carpenter, S. Zheng, W. Han, R. Zhang, K. Kang, T. Nizolek, and T. Pollock, "Structure–property–functionality of bimetal interfaces," *JOM*, vol. 64, pp. 1192-1207, 2012.

[3] G. O. Cook and C. D. Sorensen, "Overview of transient liquid phase and partial transient liquid phase bonding," *Journal of materials science*, vol. 46, pp. 5305-5323, 2011.

[4] K. F. Dockus, "Method of brazing aluminum parts," ed: Google Patents, 1976.

[5] R. S. Timsit, "Method of brazing aluminum," ed: Google Patents, 1992.

[6] M. Mahoney, C. Rhodes, J. Flintoff, W. Bingel, and R. Spurling, "Properties of friction-stir-welded 7075 T651 aluminum," *Metallurgical and Materials Transactions A*, vol. 29, pp. 1955-1964, 1998.

[7] C. Rhodes, M. Mahoney, W. Bingel, R. Spurling, and C. Bampton, "Effects of friction stir welding on microstructure of 7075 aluminum," *Scripta materialia*, vol. 36, pp. 69-75, 1997.

[8] W. Suxia and Z. Shengguo, "Study on the interface of bimetallic plate produced by explosive welding-hot rolling," *Journal of Iron and Steel Research*, vol. 3, 1995.

[9] A. Mamalis, A. Szalay, N. Vaxevanidis, and D. Manolakos, "Fabrication of bimetallic rods by explosive cladding and warm extrusion," *Journal of Materials Processing Technology*, vol. 83, pp. 48-53, 1998.

[10] M. Paramsothy, N. Srikanth, and M. Gupta, "Solidification processed Mg/Al bimetal macrocomposite: Microstructure and mechanical properties," *Journal of Alloys and Compounds*, vol. 461, pp. 200-208, 2008.

[11] J. Campbell, *Castings*: London Butterworth, 2003.

[12] M. Scanlan, D. J. Browne, and A. Bates, "New casting route to novel functionally gradient light alloys," *Materials Science and Engineering: A*, vol. 413, pp. 66-71, 2005.

[13] S. P. Midson and D. J. Browne, "CDC casting," *Advanced Materials & Processes*, vol. 166, pp. 38-40, 2008.

[14] A. Guentner, J. Schaedlich-Stubenrauch, and P. Sahm, "Casting technique for the production of functional gradient materials by controlled mould filling, Part II," *Aluminium -Dusseldorf then Isernhagen-*, vol. 73, pp. 630-637, 1997.

[15] A. Guentner, J. Schaedlich-Stubenrauch, and P. Sahm, "Casting technique for the production of functonal gradient materials by controlled mould filling, Part I," *Aluminium -Dusseldorf then Isernhagen-*, vol. 73, pp. 531-536, 1997.

[16] A. Garner, Tromans, D, "Direct observation of intergranular corrosion in Al-4wt%Cu alloy," *Corrosion*, vol. 35, pp. 55-60, 1979.

[17] M. I. Jordan, "Why the logistic function? A tutorial discussion on probabilities and neural networks," ed: Citeseer, 1995.

[18] D. Poirier, K. Yeum, and A. Maples, "A thermodynamic prediction for microporosity formation in aluminum-rich Al-Cu alloys," *Metallurgical Transactions A*, vol. 18, pp. 1979-1987, 1987.

[19] R. Rerko, H. de Groh, and C. Beckermann, "Effect of melt convection and solid transport on macrosegregation and grain structure in equiaxed Al-Cu alloys," *Materials Science and Engineering: A*, vol. 347, pp. 186-197, 2003.

[20] J. E. Spinelli, D. M. Rosa, I. L. Ferreira, and A. Garcia, "Influence of melt convection on dendritic spacings of downward unsteady-state directionally solidified Al-Cu alloys," *Materials Science and Engineering: A*, vol. 383, pp. 271-282, 2004.

[21] G. Chadwick, "Solidification of $CuAl_2$-Al eutectic alloys," *J Inst Met*, vol. 91, pp. 169-173, 1963.

[22] G. Wu, K. O'Reilly, and M. Galano, "Characterization of casting defects in aluminium alloys," *Advanced Materials Research*, vol. 430, pp. 984-987, 2012.

[23] M. K. Tripp, C. Stampfer, D. C. Miller, T. Helbling, C. F. Hermann, C. Hierold, K. Gall, S. M. George, and V. M. Bright, "The mechanical properties of atomic layer deposited alumina for use in micro- and nano-electromechanical systems," *Sensors and Actuators a-Physical*, vol. 130, pp. 419-429, 2006.

[24] G. Durrant, M. Gallerneault, and B. Cantor, "Squeeze cast aluminium reinforced with mild steel inserts," *Journal of materials science*, vol. 31, pp. 589-602, 1996.

[25] C. Hallam and W. Griffiths, "A model of the interfacial heat-transfer coefficient for the aluminum gravity die-casting process," *Metallurgical and materials transactions B*, vol. 35, pp. 721-733, 2004.

[26] N. Rounthwaite, "Development of bulk nanoquasicrystalline alloys for high strength elevated temperature applications," DPhil thesis, University of Oxford, 2012.

[27] M. Galano, F. Audebert, A. G. Escorial, I. C. Stone, and B. Cantor, "Nanoquasicrystalline Al-Fe-Cr-based alloys. Part II. Mechanical properties," *Acta Materialia*, vol. 57, pp. 5120-5130, 2009.

[28] M. Galano, F. Audebert, I. C. Stone, and B. Cantor, "Nanoquasicrystalline Al-Fe-Cr-based alloys. Part I: Phase transformations," *Acta Materialia*, vol. 57, pp. 5107-5119, 2009.

[29] F. Audebert, M. Galano, C. T. Rios, H. Kasama, M. Peres, C. Kiminami, W. Botta, and C. Bolfarini, "Nanoquasicrystalline Al-Fe-Cr-Nb alloys produced by powder metallurgy," *Journal of Alloys and Compounds*, vol. 577, pp. 650-657, 2013.

CHAPTER 8

CONCLUSIONS AND FUTURE DEVELOPMENT

8.1 Summary

The project aims to understand the role of oxidation in bonding of aluminium alloys using casting-related approaches. As a new project with no prior research to build upon, it started with the experiments by stacking two pieces of metals together at different conditions and then assessed the bond interface microscopically to reveal the bonding mechanism might involve. It was found that metallic bonding is achieved only when the oxide films become disrupted, either through external mechanical agitation or intrinsic stress accumulation. The understanding of the oxide formation is therefore crucial and scientifically interesting as the knowledge achieved would help tailor the oxide in castings and offer suggestions to the design of bonding approaches. Therefore, the project moved on to focus more on probing the oxidation mechanisms of some typical binary Al alloys both experimentally and theoretically using a combination of techniques. A research methodology is recommended based on the knowledge learned during the course of study. As shown by **Figure 8.1**, it is suggested that a comprehensive knowledge of the oxidation mechanism of a system may be unveiled until all the three aspects are resolved. This matrix may allow drawing a complete assessment of the effect of different factors controlling the oxide growth. Finally, some large scale processing facilities were used to conduct some research on the design of casting approaches to bond Al alloys.

8.2 Conclusions

8.2.1 Processing studies

All of these approaches have technical difficulties which still need to be overcome and scientific areas which require further understanding, but all have potential. The significant conclusions from the studies on processing are summarized as follows.

1. In the stacking approach, the *bi-film* layer is a physical barrier which prevents metallic mixing. Specifically, in the stacked Al/Al-5Cu system, metallic bonding is achieved by the diffusive flow of Al-5Cu melt through cracks within the oxide scale. Gravity plays a dominate role in determining the degree of metallic mixing. In the stacked Al/Al-2Mg system, metallic bonding is achieved by the flow of Al-2Mg melt through either cracks or the space between scattered $MgAl_2O_4$ crystals.
2. In the *double-pouring* approach, metallic bonding is achieved and the bond zone is around 100 μm. The bond interface is featured by the presence of *bi-film* defects. The crack-like defects align discontinuously at the bond interface.
3. In the squeeze casting approach, metallic bonding between a liquid Al-5Cu and a solid Al is achieved through a certain level of the melt-back of solid Al at the interface and by the effect of the applied pressure on stitching oxide *bi-film* defects.
4. In the extrusion bonding approach, metallic bonding between an Al-Fe-Cr-Nb nano-quasicrystalline alloy and a commercial 6082 Al alloy is achieved. The bond interface is microscopically rough without the presence of crack-like defects. The interface zone is less than 100 μm.

8.2.2 Oxidation studies

1. Thermodynamically, in the case of commercial Al-Cu alloys, the formation of Al_2O_3 always dominates over Cu_2O and CuO in the temperature range of 25-1000°C. In the case of Al-Mg-O_2 system, the formation of MgO or $MgAl_2O_4$ always dominates over Al_2O_3 when Mg surface composition is above 0.02mol% in the temperature range of 25-1000°C. High Mg content favours the growth of MgO. Specifically, in the temperature range of 25-450°C, the formation of MgO dominates over $MgAl_2O_4$ when Mg is above 0.6mol%; at 550°C, this critical composition increases up to 1.2mol%, and 4.0mol% at 750°C, and around 7.5mol% at 950°C; when Mg mole fraction is above 0.1, MgO dominates over $MgAl_2O_4$ at any temperature within 25-1000°C.

2. Kinetically, temperature has a strong effect on the oxidation kinetics of Al alloys. Higher temperatures accelerate the oxidation process. In the case of the Al-Cu-O_2 system: in the temperature of 450-650°C, the oxidation kinetics of Al exhibit protectiveness and parabolic progression and Al-5Cu shows a pseudo-parabolic oxidation behaviour. The oxidation activation energies for Al and Al-5Cu are in the range 50-100 kJ mol^{-1}. In the temperature range of 750-950°C, the oxidation kinetics of both Al and Al-5Cu is well represented by linear rate equations with calculated oxidation activation energies in the range 150-200 kJ mol^{-1}. The overall oxidation kinetics of Al-0.2Mg and Al-2Mg are well described by a para-linear model: the initial stage shows parabolic progression then gradually proceeds linearly. The oxidation activation energy is in the range of 50-100 kJ mol^{-1} and decreases as temperature increases.

3. The thickness of the amorphous aluminium oxide layer formed on as-polished Al, Al-5Cu or Al-2Mg at room temperature is around 5 nm.

4. In the case of Al-Cu-O_2 system, dry atmospheric oxidation of molten Al or Al-5Cu proceeds by the sequence: amorphous γ-Al_2O_3 to crystalline γ-Al_2O_3 to crystalline α-Al_2O_3. The doping of Cu increases the amorphous layer thickening rate by generating more Al interstitials; the initial amorphous oxide layer is ductile and could copy the dendritic structure of Al-5Cu; the crystalline γ-Al_2O_3 grows through a *ledge* mechanism; the crystalline α-Al_2O_3 grows inwardly into the melt.

5. In the case of Al-Mg-O_2 system, dry atmospheric oxidation of molten dilute Al-Mg alloys proceeds by the sequence: amorphous γ-Al_2O_3 to MgO to $MgAl_2O_4$. The preferential segregation of Mg and evaporation of Mg favors the growth of MgO initially. MgO particles preferentially nucleate and grow at the metal/oxide interface. The morphology of the oxide layer develops from early compact and protective uniform γ-Al_2O_3 amorphous layer to loosely scaled structure with agglomeration of MgO particles. $MgAl_2O_4$ grows mainly at the cost of MgO in later stages of oxidation.

8.3 Implications for bonding

Based on what have been discovered in the present wok so far, some implications for bonding of Al alloys may be proposed:

1. Al alloys containing a high level of Mg and other similar reactive elements are not suitable choices for the sake of obtaining well-bonded Al joints. The Mg would segregate at the bond surface and the preferential growth of MgO and $MgAl_2O_4$ causes the discontinuity at the bond interface which jeopardizes the bond interface mechanically. The hard magnesium-rich oxide film is also hygroscopic and prone to hydration and it is detrimental if the bond is exposed to humid atmospheres.
2. Cu would not affect the overall kinetics thermodynamically. Al alloys containing a small level of Cu (e.g. <1%) may also exhibit improved mechanical properties due to solution hardening and precipitation hardening. But a high level of Cu (e.g > 4wt%) may cause the formation of eutectic phases and the segregation of Cu in the formation of brittle θ-$CuAl_2$ intermetallic at bond interface. So the cooling condition in terms of temperature gradient within the bonded alloys must be carefully controlled.
3. Aluminium oxide films show better adhesion to the metal substrate and the harmless ductile amorphous layer is only a few nanometres and can be easily stitched or healed under pressure. A short processing time is suggested to be adopted to ensure the oxidation progress does not proceed far enough to allow any micro-chemical change within the oxide layer.
4. The chilling of the melt around/on the target metal may reduce the degree of interface reaction, resulting in less metallic bonding. It is suggested that the target metal is superheated to allow some melt-back, which could further help break the surface oxide layers to become individual fragments under applied pressure.

8.4 Future development

It is impossible to cover every interested area of research exhaustively, but the oxidation studies and processing studies in the present work have helped understand the role of oxidation in bonding of Al alloys. Theoretically, the effect of other alloying elements on the oxidation mechanism of Al, such as Si, Fe, Cr, Ti, etc, can be predicted based on thermodynamics, but the experimental studies are always immensely significant and interesting to help strengthen our understanding. Besides, as for the processing studies, all of the approaches described in this thesis have limitations, but are potentially useful. From my point of view, I think the following research areas are scientifically worthwhile for future development.

1. The development of Al-Fe-Cr based nanoquasicrystalline alloys have been shown to exhibit enhanced mechanical properties at elevated temperatures. These alloys will be potentially used as automotive components, such as piston heads. So its oxidation behaviour, in particular high temperature oxidation behaviour is of ultimate importance technologically. The oxidation studies of Al nanoquasicrystalline alloy could offer insights into its high temperature oxidation and even corrosion behaviour to help design any bonding approach for this material.
2. The study of effect of humidity on oxidation of Al alloys may also be interesting. As it is expected that the oxidation reactions would be changed thermodynamically with the presence of humidity, the reactions with H_2O must be considered. The products of aqueous oxidation also include hydrogen, which can dissolve readily in the metal. In addition, the incorporation of hydroxyl ions into the oxide lattice structure may also change the defects chemistry of the oxide, influencing the diffusivity of metal cations and oxygen anions. In foundry practice, the knowledge of such topic may help understand the melt dross formation mechanism and potentially how to improve melt cleanliness.
3. The squeeze casting method shows vast potential for future development. Further research on optimizing the processing parameters, interface reaction, identifying suitable interlayers or new alloy systems may be needed.

Appendix 3.1

X-ray penetration depth

According to the Beer-Lambert law [1], the intensity of X-rays *I* after travelling a distance *x* within a material is given by

$$I = I_0 \exp(-\mu \cdot \rho \cdot x) \quad (1)$$

Where μ ($cm^2\ g^{-1}$) is the linear mass attenuation coefficient and ρ ($g\ cm^{-3}$) is the density of the material. For a compound or a solution, the mass attenuation coefficient is calculated by

$$\mu = \sum_i \mu_i \cdot C_i \quad (2)$$

Where C_i is the concentration of the element *i* in the sample [2, 3]. As shown in **Figure 1**, the distance *x* which X-ray travels in the sample can be expressed by the penetration depth d_p by the following relationship

$$2 \cdot \frac{d_p}{\sin\theta} = x \quad (3)$$

Assume $I = I_0/e$ (the intensity of X-ray decreases to 37%), combining **Equations 1 and 3**, it can be deduced that

$$d_p = \frac{\sin\theta}{2 \cdot \mu \cdot \rho} \quad (4)$$

It can be seen from **Equation 4** that the information depth is also a function of incidence angle and it is a maximum when θ = 90°. As Cu Kα X-rays were used in the present work, the linear mass attenuation coefficient of materials encountered during the work are quoted from the reference [2], maximum penetration depth (when θ = 90°) for 37% emission and that for 1% emission were calculated and summarized accordingly in **Table 1**.

The intention of the above analysis is to understand the size of the top surface region which would contribute to the XPS spectrum. As the errors of the mass attenuation coefficient and density values are unknown, the values of penetration depth are only obtained here as the calculated results with three decimal places. The deviation of the values are therefore unknown.

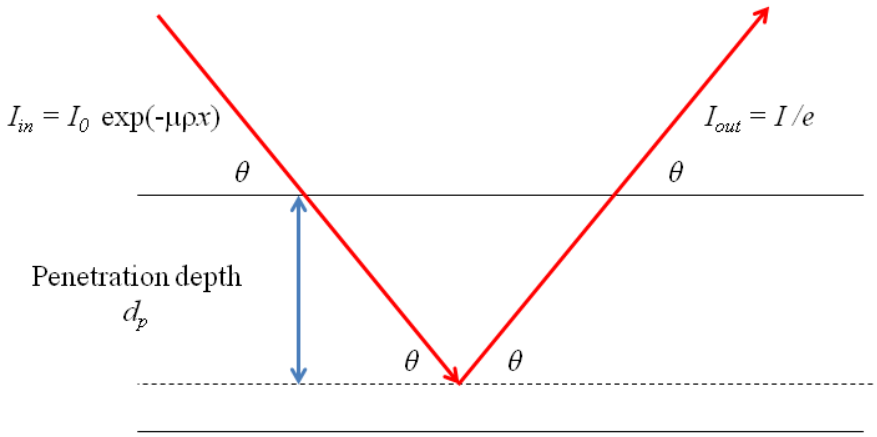

Figure 1 - Diagram showing the X-ray penetrating through a thickness of d_p and the intensity of the emitted X-ray is degraded by a factor 1/e.

Table 1 - Calculated X-ray Penetration depths for different materials.

Material	μ (cm^2/g)	ρ (g/cm^3)	d (37% emission, µm)	d (1% emission, µm)
Al	48.600	2.700	38.104	175.475
Mg	38.600	1.738	74.530	343.225
Cu	53.000	8.960	10.529	48.488
Al-5Cu	48.820	2.796	36.630	168.687
Al-2Mg	48.400	2.670	38.691	178.180
Al-0.2Mg	48.580	2.697	38.162	175.743
$CuAl_2$	50.979	4.360	22.495	103.595
Al_2O_3	31.136	3.950	40.655	187.222
MgO	27.842	3.580	50.163	231.011
$MgAl_2O_4$	30.203	3.640	45.480	209.442

References

[1] J. Mitschele, "Beer-Lambert law," *Journal of Chemical Education*, vol. 73, pp. 260-261, 1996.

[2] J. H. Hubbell, Seltzer, S. M., "Tables of X-ray mass attenuation coefficients and mass energy-absorption coefficients," *National Institute of Standards and Technology*, 2004.

[3] H. W. Thummel, "Principles of multicomponent analysis with electron and beta radiation. 3. Determination of effective mass attenuation coefficient of mixtures of substances," *Isotopenpraxis*, vol. 13, pp. 155-160, 1977.

Appendix 3.2

Crystallography Open Database (COD)

Besides the references from the COD, Santos *et al*. [1] is also referenced.

Al - 2300250

Formula	- Al -
Calculated formula	- Al -
Title of publication	Phase behaviour and thermoelastic properties of perdeuterated ammonia hydrate and ice polymorphs from 0 to 2GPa
Authors of publication	Fortes, A. D.; Wood, I. G.; Vočadlo, L.; Knight, K. S.; Marshall, W. G.; Tucker, M. G.; Fernandez-Alonso, F.
Journal of publication	Journal of Applied Crystallography
Year of publication	2009
Journal volume	42
Journal issue	5
Pages of publication	846 - 866
a	4.03702 ± 0.00012 Å
b	4.03702 Å
c	4.03702 Å
α	90°
β	90°
γ	90°
Cell volume	65.793 ± 0.002 $Å^3$
Number of distinct elements	1
Hermann-Mauguin symmetry space group	F m -3 m
Hall symmetry space group	-F 4 2 3
Has coordinates	Yes
Has disorder	No
Has F_{obs}	No

Mg - 9008506

Formula	- Mg -
Calculated formula	- Mg2 -
Title of publication	Second edition. Interscience Publishers, New York, New York Hexagonal closest packed, hcp, structure
Authors of publication	Wyckoff, R. W. G.
Journal of publication	Crystal Structures
Year of publication	1963
Journal volume	1
Pages of publication	7 - 83
a	3.20927 Å
b	3.20927 Å
c	5.21033 Å
α	90°
β	90°
γ	120°
Cell volume	46.474 $Å^3$
Number of distinct elements	1
Hermann-Mauguin symmetry space group	P 63/m m c
Hall symmetry space group	-P 6c 2c
Has coordinates	Yes
Has disorder	No
Has F_{obs}	No

$\alpha-Al_2O_3$ - 1000017

Chemical name	Aluminium oxide
Mineral name	Corundum
Formula	- Al2 O3 -
Calculated formula	- Al2 O3 -
Title of publication	Ruby structure peculiarities derived from X-ray data. Localization of chromium atoms and electron deformation density
Authors of publication	Tsirelson, V G; Antipin, M Y; Gerr, R G; Ozerov, R P; Struchkov, Y T
Journal of publication	Physica Status Solidi, Sectio A: Applied Research
Year of publication	1985
Journal volume	87
Pages of publication	425 - 433
a	4.7606 ± 0.0005 Å
b	4.7606 ± 0.0005 Å
c	12.994 ± 0.001 Å
α	90°
β	90°
γ	120°
Cell volume	255 $Å^3$
Number of distinct elements	2
Hermann-Mauguin symmetry space group	R -3 c :H
Hall symmetry space group	-R 3 2"c
Residual factor for all reflections	0.063
Has coordinates	Yes
Has disorder	No
Has F_{obs}	No

γ−Al_2O_3 - 2015530

Common name	Gamma Alumina
Formula	- Al2.67 O4 -
Calculated formula	- Al2.6653 O4 -
Title of publication	γ-Alumina: a single-crystal X-ray diffraction study
Authors of publication	Ľubomír Smrčok; Vratislav Langer; Jan Křesťan
Journal of publication	Acta Crystallographica Section C
Year of publication	2006
Journal volume	62
Journal issue	9
Pages of publication	i83 - i84
a	7.9382 ± 0.0001 Å
b	7.9382 ± 0.0001 Å
c	7.9382 ± 0.0001 Å
α	90°
β	90°
γ	90°
Cell volume	500.226 ± 0.011 $Å^3$
Cell temperature	173 ± 2 K
Ambient diffraction temperature	173 ± 2 K
Number of distinct elements	2
Hermann-Mauguin symmetry space group	F d -3 m :2
Hall symmetry space group	-F 4vw 2vw 3
Has coordinates	Yes
Has disorder	No
Has F_{obs}	Yes

MgO – 1000054

Chemical name	Magnesium oxide
Mineral name	Periclase
Formula	- Mg O -
Calculated formula	- Mg O -
Title of publication	X-Ray Determination of Electron-Density Distributions in Oxides, Mg O, Mn O, Co O, and Ni O, and Atomic Scattering Factors of their Constituent Atoms
Authors of publication	Sasaki, S; Fujino, K; Takeuchi, Y
Journal of publication	Proceedings of the Japan Academy
Year of publication	1979
Journal volume	55
Pages of publication	43 - 48
a	4.217 ± 0.001 Å
b	4.217 ± 0.001 Å
c	4.217 ± 0.001 Å
α	90°
β	90°
γ	90°
Cell volume	75 $Å^3$
Number of distinct elements	2
Hermann-Mauguin symmetry space group	F m -3 m
Residual factor for all reflections	0.0126
Has coordinates	Yes
Has disorder	No
Has F_{obs}	No

$MgAl_2O_4$ - 9001367

Mineral name	Spinel
Formula	- Al2 Mg O4 -
Calculated formula	- Al16 Mg8 O32 -
Title of publication	A time-of-flight neutron powder diffraction study of MgAl2O4 at temperatures up to 1273 K sample UC, T = 923 K
Authors of publication	Peterson, R. C.; Lager, G. A.; Hitterman, R. L.
Journal of publication	American Mineralogist
Year of publication	1991
Journal volume	76
Pages of publication	1455 - 1458
a	8.12508 Å
b	8.12508 Å
c	8.12508 Å
α	90°
β	90°
γ	90°
Cell volume	536.393 $Å^3$
Ambient diffraction temperature	923 K
Number of distinct elements	3
Hermann-Mauguin symmetry space group	F d -3 m :2
Hall symmetry space group	-F 4vw 2vw 3
Has coordinates	Yes
Has disorder	No
Has F_{obs}	No

$CuAl_2$ – 9012196

Mineral name	Khatyrkite
Formula	- Al2 Cu -
Calculated formula	- Al8 Cu4 -
Title of publication	Refinement of the crystal structure of tetragonal Al2Cu Locality: synthetic
Authors of publication	Meetsma, A.; de Boer, J. L.; van Smaalen, S.
Journal of publication	Journal of Solid State Chemistry
Year of publication	1989
Journal volume	83
Pages of publication	370 - 372
a	6.067 Å
b	6.067 Å
c	4.877 Å
α	90°
β	90°
γ	90°
Cell volume	179.515 $Å^3$
Number of distinct elements	2
Hermann-Mauguin symmetry space group	I 4/m c m
Hall symmetry space group	-I 4 2c
Has coordinates	Yes
Has disorder	No
Has F_{obs}	No

References

[1] P. S. Santos, H. S. Santos, and S. Toledo, "Standard transition aluminas. Electron microscopy studies," *Materials Research*, vol. 3, pp. 104-114, 2000.

Appendix 5.1

Nitrides formation from air: a thermodynamic perspective

(a) AlN formation from air

For a gas mixture containing only N_2 and O_2 with 1 atm pressure

a1. Nitride formation: $\mathrm{Al}+\frac{1}{2}\mathrm{N_2}\rightarrow \mathrm{AlN}$

In the temperature range 300-1300 K:

$$\Delta G^{\circ}(T) = -312144 + 15.37T + 12.36T\ln T \qquad \text{(J/mol Al)} \qquad (1)$$

$$\Delta G(T) = \Delta G^{\circ}(T) + RT\left(\frac{a_{\mathrm{AlN}}}{a_{\mathrm{N_2}}^{1/2}a_{\mathrm{Al}}}\right) \qquad (2)$$

If the values of AlN chemical activity and Al chemical activity are assumed equal to 1, and nitrogen behaves ideally, the above equation can be expressed as

$$\Delta G(T) = \Delta G^{\circ}(T) + RT\left(\frac{1}{X_{\mathrm{N_2}}^{1/2}}\right) \qquad (3)$$

The Gibbs free energy is a function of temperature and nitrogen mole fraction $X_{N2.}$

a2. Oxide formation: $\mathrm{Al}+\frac{3}{4}\mathrm{O_2}\rightarrow\frac{1}{2}\mathrm{Al_2O_3}$

In the temperature range 300-1300 K:

$$\Delta G^{\circ}(T) = -824716 + 111.45T + 5.87T\ln T \qquad \text{(J/mol Al)} \qquad (4)$$

$$\Delta G(T) = \Delta G^{\circ}(T) + RT\left(\frac{a_{\mathrm{Al_2O_3}}^{1/2}}{a_{\mathrm{O_2}}^{3/4}a_{\mathrm{Al}}}\right) \qquad (5)$$

If the values of Al_2O_3 chemical activity and Al chemical activity are assumed equal to 1, and oxygen behaves ideally, the above equation can be expressed as

$$\Delta G(T) = \Delta G^{\circ}(T) + RT\left(\frac{1}{X_{\mathrm{O_2}}^{3/4}}\right) \qquad (6)$$

The Gibbs free energy is a function of temperature and oxygen mole fraction $X_{O2.}$ As $X_{\mathrm{N_2}} + X_{\mathrm{O_2}} = 1$ in this case (Dalton's law and Raoult's law), Equation 3 can be further expressed as

$$\Delta G(T) = \Delta G^{\circ}(T) + RT\left(\frac{1}{\left(1-X_{\mathrm{O_2}}\right)^{1/2}}\right) \qquad (7)$$

Therefore, it can be seen from Equations 6 and 7 that Gibbs free energy profiles for both reactions is a function of temperature and oxygen mole fraction.

For example, T = 1023 K (750°C), the Gibbs free energy profiles are shown in **Figure 1**. It is noted that the formation of Al_2O_3 surpass the formation of AlN thermodynamically almost for any oxygen mole fraction value above 10^{-30}. Therefore, by implication from thermodynamics alone, at 1023 K, the formation of AlN may only occurs after all of the oxygen is consumed.

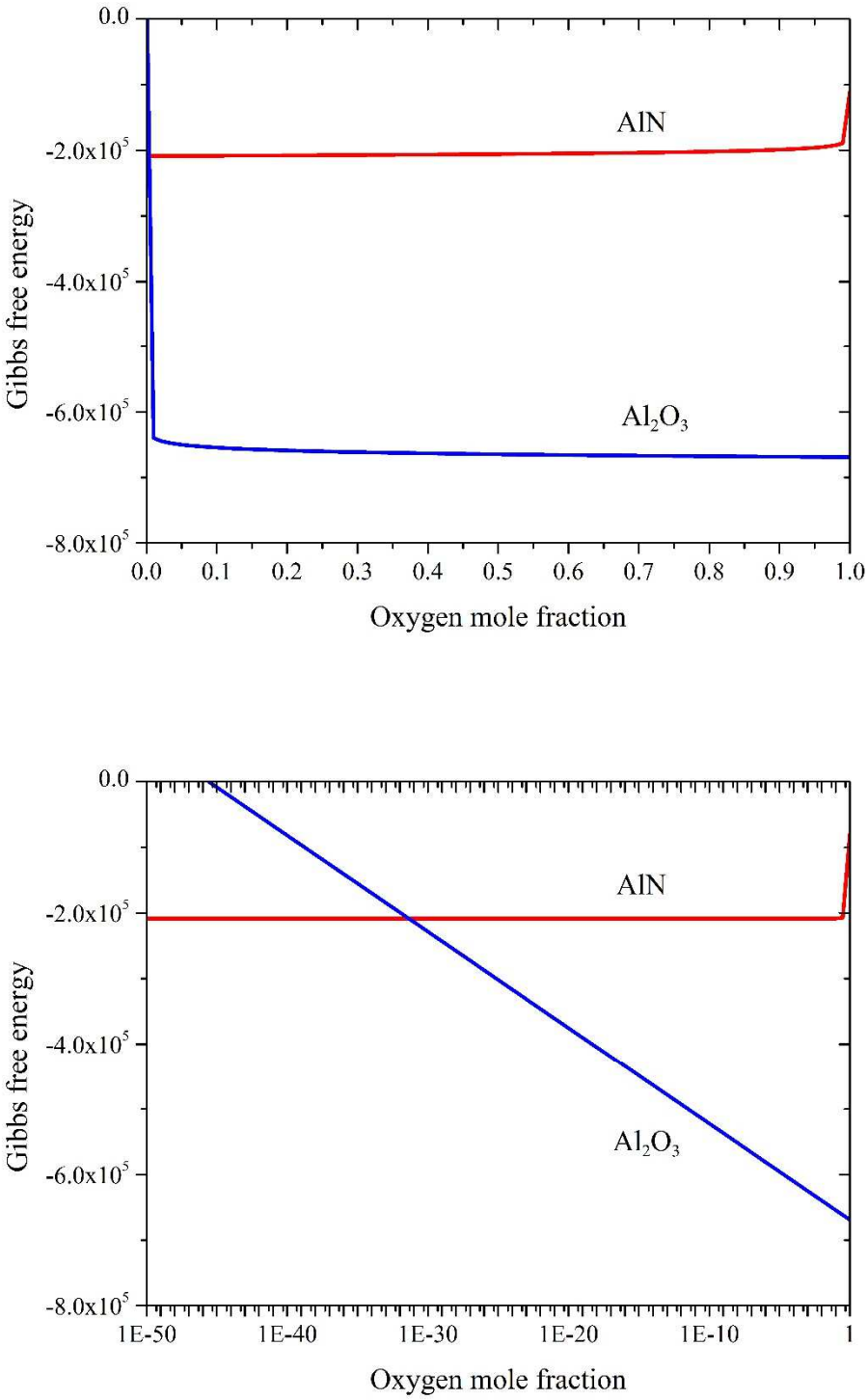

Figure 1 – Gibbs free energy (J/mol Al) profiles of AlN formation (red) and Al_2O_3 formation (blue) as a function of oxygen mole fraction at 750°C.

(b) Mg_3N_2 formation from air

For a gas mixture containing only N_2 and O_2 with 1 atm pressure

b1. Nitride formation: $\mathrm{Mg}+\frac{1}{3}\mathrm{N_2}\rightarrow\frac{1}{3}\mathrm{Mg_3N_2}$

In the temperature range 300-1300 K:

$$\Delta G^{\circ}(T) = -148156 - 10.12T + 10.56T\ln T \qquad \text{(J/mol Mg)} \qquad (8)$$

$$\Delta G(T) = \Delta G^{\circ}(T) + RT\left(\frac{a_{\mathrm{Mg_3N_2}}^{1/3}}{a_{\mathrm{N_2}}^{1/3}a_{\mathrm{Mg}}}\right) \qquad (9)$$

If the values of Mg_3N_2 chemical activity and Mg chemical activity are assumed equal to 1, and nitrogen behaves ideally, the above equation can be expressed as

$$\Delta G(T) = \Delta G^{\circ}(T) + RT\left(\frac{1}{X_{\mathrm{N_2}}^{1/3}}\right) \qquad (10)$$

The Gibbs free energy is a function of temperature and nitrogen mole fraction X_{N2}.

b2. Oxide formation: $\mathrm{Mg}+\frac{1}{2}\mathrm{O_2}\rightarrow\mathrm{MgO}$

In the temperature range 300-1300 K:

$$\Delta G^{\circ}(T) = -596634 + 47.84T + 8.14T\ln T \qquad \text{(J/mol Mg)} \qquad (11)$$

$$\Delta G(T) = \Delta G^{\circ}(T) + RT\left(\frac{a_{\mathrm{MgO}}}{a_{\mathrm{O_2}}^{1/2}a_{\mathrm{Mg}}}\right) \qquad (12)$$

If the values of MgO chemical activity and Mg chemical activity are assumed equal to 1, and oxygen behaves ideally, the above equation can be expressed as

$$\Delta G(T) = \Delta G^{\circ}(T) + RT\left(\frac{1}{X_{\mathrm{O_2}}^{1/2}}\right) \qquad (13)$$

The Gibbs free energy is a function of temperature and oxygen mole fraction X_{O2}. As $X_{\mathrm{N_2}} + X_{\mathrm{O_2}} = 1$ in this case (Dalton's law and Raoult's law), Equation 10 can be further expressed as

$$\Delta G(T) = \Delta G^{\circ}(T) + RT\left(\frac{1}{\left(1 - X_{\mathrm{O_2}}\right)^{1/3}}\right) \qquad (14)$$

Therefore, it can be seen from Equations 13 and 14 that Gibbs free energy profiles for both reactions is a function of temperature and oxygen mole fraction.

For example, T = 1023 K (750°C), the Gibbs free energy profiles are shown in **Figure 2**. It is noted that the formation of MgO surpass the formation of Mg_3N_2 thermodynamically almost for any oxygen mole fraction value above 10^{-30}. Therefore, by implication from thermodynamics alone, at 1023 K, the formation of Mg_3N_2 may only occurs after all of the oxygen is consumed.

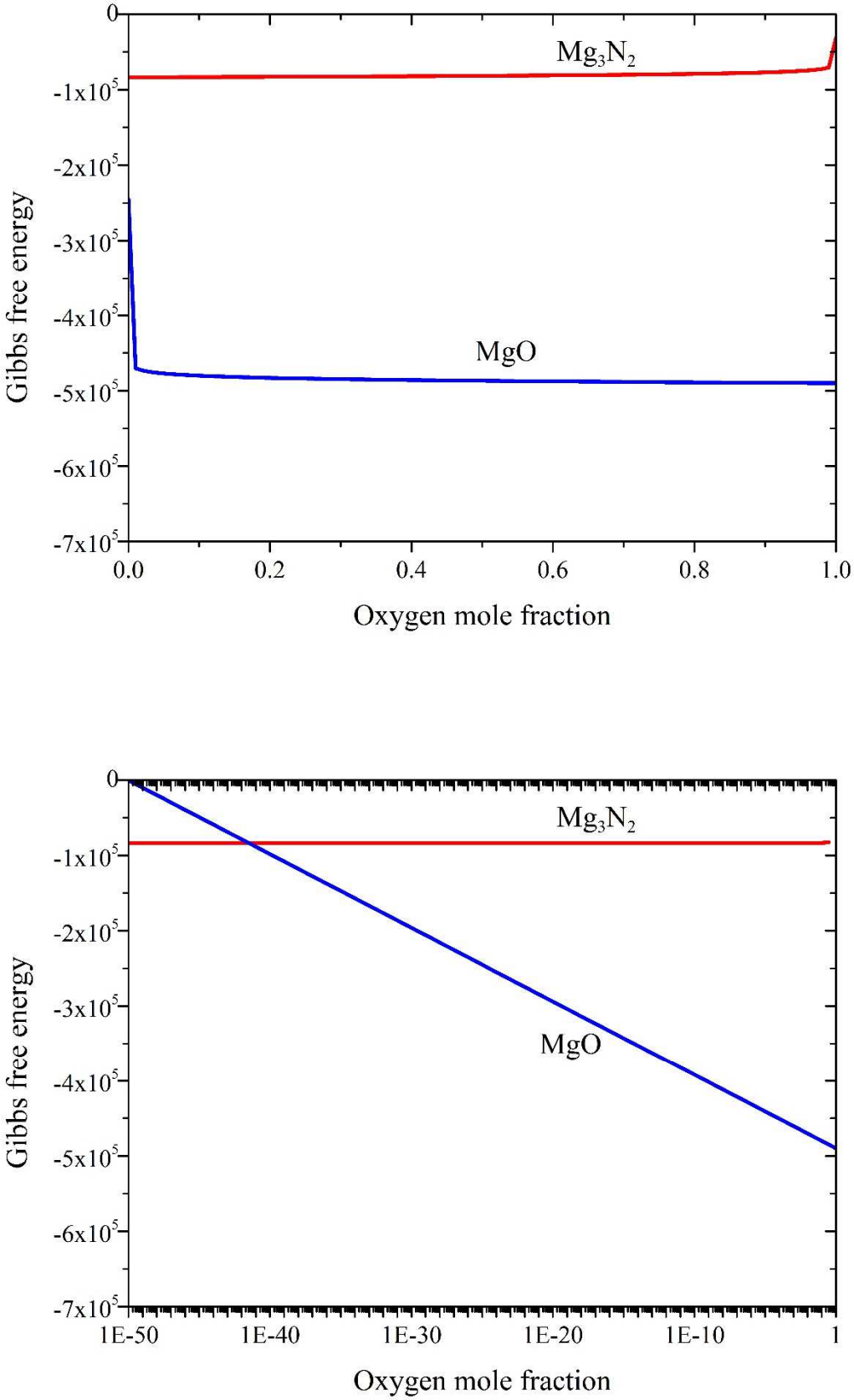

Figure 2 - Gibbs free energy (J/mol Mg) profiles of Mg_3N_2 formation (red) and MgO formation (blue) as a function of oxygen mole fraction at 750°C.

Appendix 5.2

The Gibbs free energy change of a chemical reaction as a function of temperature

1. Why $\Delta G^o(T) = A + BT + CT\ln T$?

For a chemical reaction at a constant atmospheric pressure

Reactant **1** + Reactant **2** + ••• + Reactant ***i*** = Product **1** + Product **2** + ••• + Product ***j***

The term $\Delta G^o(T)$ defines the Gibbs free energy reduction/increment at temperature T if the reaction proceeds completely. It can be calculated by

$$\Delta G^o = \sum_{products} n_i \bar{G}_i - \sum_{reactants} n_j \bar{G}_j \qquad \text{(Equation 1)}$$

$$\bar{G}_i = \mu_i, \bar{G}_j = \mu_j \qquad \text{(Equation 2)}$$

Where Gibbs free energy per mole for a component *i* equals to its chemical potential μ_i (in the case of pure state), and ΔG^o equals to the sum of Gibbs free energy of all products *j* minus the sum of Gibbs free energy of all reactants *i*. If $\Delta G^o<0$, the chemical reaction can proceed spontaneously; If $\Delta G^o=0$, the chemical reaction is at equilibrium; If $\Delta G^o>0$, the chemical reaction can only proceed with external energy inputs. At temperature *T*, the Gibbs free energy of a specie can be expressed by its definition $G = H - TS$ [1].

$$\bar{G}_T = \bar{H}_T - T\bar{S}_T \qquad \text{(Equation 3)}$$

Where the enthalpy term is calculated through $\bar{H}_T = \bar{H}_{298K} + \int_{298K}^{T} C_p dT$ and the entropy term is calculated through $\bar{S}_T = \bar{S}_{298K} + \int_{298K}^{T} \frac{C_p}{T} dT$ [1]. Since the heat capacity C_p (at constant pressure) does not vary too much with respect to temperature *T* [2], it is assumed to be constant in the present work, so does most of work in the literature [3]. Equation 3 can be further modified as

$$\bar{G}_T = \bar{H}_{298K} + C_p(T - 298) - T\left(\bar{S}_{298K} + C_p(\ln T - \ln 298)\right)$$

$$\bar{G}_T = a + bT + cT\ln T \qquad \text{(Equation 4)}$$

Where *a*, *b* and *c* are numerical coefficients. Equation 4 is also termed the Gibbs free energy of a specie to a stable element reference state (SER) [4]. Combining Equation 1 and Equation 4, the term $\Delta G^o(T)$ can be finally expressed by

$$\Delta G^o(T) = A + BT + CT\ln T \qquad \text{(Equation 5)}$$

The original expression for Gibbs free energy of a specie as a function of temperature (which is derived by statistical thermodynamics) [3] is given in terms of infinite series as

$$\bar{G}_T = a + bT + cT\ln T + dT^2 + eT^3 + f/T + \cdots \qquad \text{(Equation 5)}$$

Usually only the first two or three terms are needed, as used by many researchers to calculate phase diagrams (in particular CALPHAD) [3, 5]. As also indicated by **Figure 1**, the use of first three terms is already enough to give a near perfect (suggested by R-square value) fit for the Gibbs free energy data quoted from NIST [6].

2. How to get *A*, *B* and *C*?

The first step is to obtain the Gibbs free energy values for each specie using the NIST thermochemical table [6]. Values of species at different temperatures are summarized in **Table 1**, **2**, and **3**. The second step is to calculate the ΔG^o at each temperature *T* using Equation 1. The third step is to plot the 11 pairs of dots (T, ΔG^o) and fit the dots by Equation 5. An example is shown in **Figure 1**, where the Gibbs free energy function of the reaction $4\mathrm{Cu} + \mathrm{O}_2 \rightarrow 2\mathrm{Cu}_2\mathrm{O}$ is obtained using such method. The quality of fitting is also assessed using residual analysis.

References

[1] H. A. Buchdahl, *The concepts of classical thermodynamics*: Cambridge University Press, 2009.

[2] T. L. Hill, *An introduction to statistical thermodynamics*: DoverPublications. com, 1960.

[3] R. J. Tilley, *Understanding solids: The science of materials*: John Wiley & Sons, 2004.

[4] G. Bozzolo, R. D. Noebe, and P. B. Abel, *Applied computational materials modeling: Theory, simulation and experiment*: Springer, 2007.

[5] N. Saunders and A. P. Miodownik, *CALPHAD: A comprehensive guide* vol. 1: Elsevier, 1998.

[6] M. W. Chase, *NIST-JANAF thermochemical tables*, 1998.

Table 1 – Summary of Gibbs free energy data in the case of Al-Cu-O_2 system (Unit kJ mol^{-1})

T (K)	Al_2O_3	Cu_2O	CuO	γ-Al_2O_3	α-Al_2O_3
300	-1581.696	-147.745	-128.120	-1563.273	-1581.696
400	-1550.226	-140.092	-118.875	-1532.001	-1550.226
500	-1518.718	-132.484	-109.785	-1500.804	-1518.718
600	-1487.319	-124.944	-100.851	-1469.815	-1487.319
700	-1456.059	-117.478	-92.056	-1439.054	-1456.059
800	-1424.931	-110.087	-83.387	-1408.504	-1424.931
900	-1393.908	-102.767	-74.830	-1378.128	-1393.908
1000	-1361.437	-95.517	-66.375	-1346.370	-1361.437
1100	-1328.286	-88.331	-58.012	-1313.990	-1328.286
1200	-1295.228	-81.208	-49.730	-1281.757	-1295.228
1300	-1262.264	-74.144	-41.520	-1249.668	-1262.264

Table 2 - Summary of Gibbs free energy data in the case of Al-Mg-O_2 system (Unit kJ mol^{-1})

T (K)	MgO	γ-Al_2O_3	$MgAl_2O_4$	α-Al_2O_3
300	-568.745	-1563.273	-2175.861	-1581.696
400	-557.898	-1532.001	-2134.626	-1550.226
500	-547.078	-1500.804	-2093.365	-1518.718
600	-536.312	-1469.815	-2052.230	-1487.319
700	-525.600	-1439.054	-2011.255	-1456.059
800	-514.930	-1408.504	-1970.433	-1424.931
900	-504.289	-1378.128	-1929.739	-1393.908
1000	-492.952	-1346.370	-1886.914	-1361.437
1100	-481.399	-1313.990	-1843.219	-1328.286
1200	-469.844	-1281.757	-1799.239	-1295.228
1300	-458.291	-1249.668	-1756.239	-1262.264

Table 3 - Summary of Gibbs free energy data for Al, Mg and O_2

(Unit kJ mol^{-1})

T (K)	Mg(ref)	Mg(l)	Mg(g)	Al(ref)	O_2(g, ref)
300	0	4.252	112.307	0	0
400	0	3.932	100.780	0	0
500	0	3.403	89.387	0	0
600	0	2.731	78.122	0	0
700	0	1.955	66.981	0	0
800	0	1.107	55.961	0	0
900	0	0	45.062	0	0
1000	0	0	35.000	0	0
1100	0	0	25.283	0	0
1200	0	0	15.690	0	0
1300	0	0	6.209	0	0

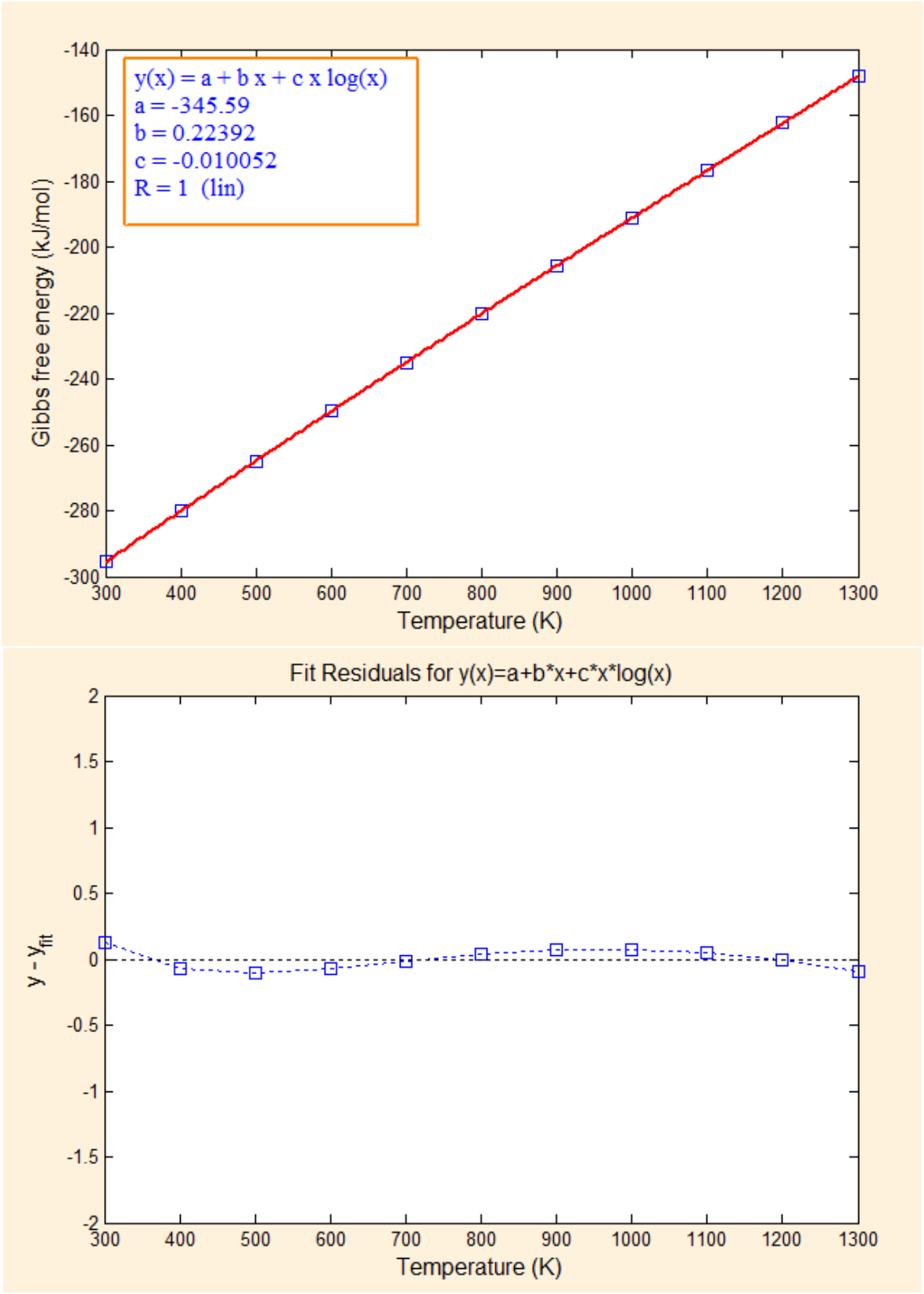

Figure 1 - Fitting report for $4Cu + O_2 \rightarrow 2Cu_2O$

Appendix 5.3

A qualitative model to explain the stability of γ-Al_2O_3 at low temperatures and why γ-Al_2O_3 to α-Al_2O_3 occurs usually at temperatures above 850ºC

1. The γ-Al_2O_3 to α-Al_2O_3 phase transformation energy barrier

The kinetics of γ-Al_2O_3 to α-Al_2O_3 phase transformation have been studied by several researchers. But the results are contradictory. Steiner *et al*. [1] reported a linear relationship between the fraction of α-Al_2O_3 and time of transformation with an activation energy of 485.3 kJ mol^{-1}. Clark and White [2] found the kinetics of the transformation of the first 50% γ-Al_2O_3 to α-Al_2O_3 was best described by a logarithmic law and reported an activation energy of 331 kJ mol^{-1}. Shelleman *et al*. [3] reported an activation energy of 431 kJ mol^{-1} while Macedo *et al*. [4] used quantitative X-ray diffraction analysis and found the activation energy to be 201 kJ mol^{-1} and that the phase transformation was best described by a sigmoid kinetic law. Mcardle and Messing [5] found a high activation energy of 578 kJ mol^{-1}. The discrepancies between these results are probably due to different experimental conditions, including different synthesis methods for α-Al_2O_3, different conditions of starting materials, different impurity levels, different mechanical or thermal pre-treatments, etc. For example, as shown by the work from Okada *et al*. [6], extrinsic dopants could affect the defect chemistry of γ-Al_2O_3, which may lead to an accelerating effect (Cu^{2+}, Mn^{2+}, etc), a retarding effect (Ca^{2+}, Ba^{2+}, etc) or little or no effect on the phase transformation (Mg^{2+}, Zn^{2+}, Ni^{2+}, Co^{2+}, etc). Based on previous literature results, an average value of **405.26 kJ mol^{-1}** is calculated.

2. Amorphous γ-Al_2O_3 to crystalline γ-Al_2O_3 phase transformation energy barrier

First of all, it is known from the literature that the crystallization process is accelerated with increasing temperature and the growth law at this stage is close to a linear relationship [7]. Data from Snijders *et al*. [8] were used to calculate the activation energy of the amorphous-to-crystalline phase transition using a pure Al sample. According to the work by Snijder *et al*., the degree of crystallization in (percentage %), under the same oxidation conditions (1.33×10^{-4} pa pure oxygen, oxidation time t = 500 s), was different at each temperature in the temperature range of 200-500°C, implying the rate kinetics is a function of temperature. Therefore, based on their data, an Arrhenius plot has been constructed and is presented in **Figure 1**. The calculated phase transformation activation energy is around **10.7** kJ mol^{-1}, this value is surprisingly one order of magnitude lower than the values reported in the literature. According to the literature review in Chapter 2, the average activation energy of the oxidation at this stage (amorphous-to-crystalline) is around 200 kJ mol^{-1} [9-13]. The crystallization process has been shown to be limited by the inward diffusion of oxygen during the formation of crystalline γ-Al_2O_3 [11]. However, most researchers obtain this value indirectly from weight gain curves of the oxidation processes. In fact,

the reaction rate obtained from weight gain curve is a reflection of multi-kinetics processes. So it may not be appropriate to directly correlate the value obtained from TGA experiments to the actual crystallization energy barrier. On the other hand, the activation energy **10.7 kJ mol^{-1}** which is calculated based on the data from Snijders *et al*. [8] is more acceptable as the authors use XPS (surface sensitive) to study the shift in chemical bonding states of Al and O in a ONLY few nm size oxide layer on a Al substrate.

Gibbs free energy profile (kinetic path) of the amorphous to γ-Al_2O_3 to α-Al_2O_3 phase transformation (the evolution of oxidation products) is plotted quantitatively in **Figure 2**. It is indicated that even if there is a reduction in free energy for a particular transition, atoms must also gain sufficient thermal energy to overcome the relevant energy barrier. So for example, suppose there is a thick crystalline γ-Al_2O_3 oxide layer existing at room temperature and then γ-Al_2O_3 to α-Al_2O_3 transition would be thermodynamically favourable. However, the transition will not eventually occur due to the big kinetic energy barrier of around 400 kJ mol^{-1}.

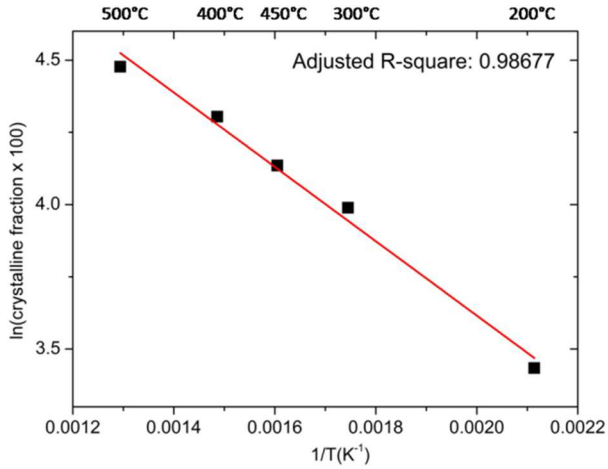

Figure 1 - Arrhenius plot indicating the amorphous-to-crystalline transition activation energy.

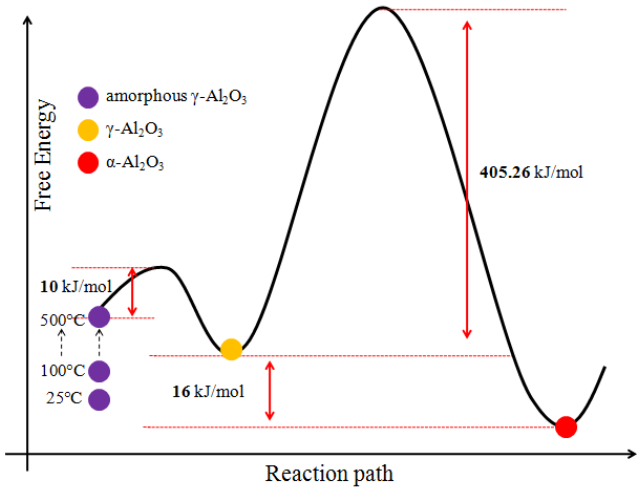

Figure 2 – Plot showing the kinetic reaction path together with the values of energy barriers associated with each oxide transition in the Al-Cu-O_2 system

References

[1] C. J. P. Steiner, Hasselma.Dp, and R. M. Spriggs, "Kinetics of gamma-to-alpha alumina phase transformation," *Journal of the American Ceramic Society,* vol. 54, pp. 412, 1971.

[2] P. W. Clark, White, J., "Some aspects of sintering," *Trans. Brit. Ceram. Soc,* vol. 49, pp. 305-333, 1950.

[3] R. A. Shelleman, G. L. Messing, and M. Kumagai, "Alpha-alumina transformation in seeded boehmite gels," *Journal of Non-Crystalline Solids,* vol. 82, pp. 277-285, 1986.

[4] M. I. F. Macedo, C. A. Bertran, and C. C. Osawa, "Kinetics of the gamma to alpha-alumina phase transformation by quantitative X-ray diffraction," *Journal of Materials Science,* vol. 42, pp. 2830-2836, 2007.

[5] J. L. Mcardle and G. L. Messing, "Transformation, microstructure development, and densification in alpha-Fe_2O_3-seeded boehmite-derived alumina," *Journal of the American Ceramic Society,* vol. 76, pp. 214-222, 1993.

[6] K. Okada, A. Hattori, T. Taniguchi, A. Nukui, and R. N. Das, "Effect of divalent cation additives on the gamma-Al_2O_3-to-alpha-Al_2O_3 phase transition," *Journal of the American Ceramic Society,* vol. 83, pp. 928-932, 2000.

[7] D. W. Aylmore, S. J. Gregg, and W. B. Jepson, "The oxidation of aluminium in dry oxygen in the temperature range 400-650°C," *Journal of the Institute of Metals,* vol. 88, pp. 205-208, 1960.

[8] P. C. Snijders, L. P. H. Jeurgens, and W. G. Sloof, "Structural ordering of ultra-thin, amorphous aluminium-oxide films," *Surface Science,* vol. 589, pp. 98-105, 2005.

[9] A. F. Beck, M. A. Heine, E. J. Caule, and M. J. Pryor, "Kinetics of oxidation of Al in oxygen at high temperature," *Corrosion Science,* vol. 7, p. 1, 1967.

[10] M. J. Dignam, "Oxide films on aluminum. 2. Kinetics of formation in oxygen," *Journal of the Electrochemical Society,* vol. 109, pp. 192-198, 1962.

[11] M. J. Dignam and W. R. Fawcett, "Kinetics and mechanism of oxidation of superpurity aluminum in dry oxygen. 2. Growth of crystallites of gamma-alumina," *Journal of the Electrochemical Society,* vol. 113, p. 663, 1966.

[12] E. A. Gulbransen, "The kinetics of oxide film formation on metals and alloys," *Transactions of the Electrochemical Society,* vol. 91, pp. 573-604, 1947.

[13] W. C. Sleppy, "Oxidation of molten high-purity aluminum in dry oxygen," *Journal of the Electrochemical Society,* vol. 108, pp. 1097-1102, 1961.

Appendix 6.1

Derivation of a para-linear kinetic model in the Al-Mg-O_2 system

In early theories of metal oxidation, the growth of an oxide film is controlled by the diffusion of both ionic and electronic charged species across the film. It is known from the work that the solid layer at the top of molten dilute Al-Mg alloys begins with the formation of a thin oxide layer to cover the surface of the melt. Oxidation starts by the absorption of oxygen molecules onto the metal surface, then the nucleation of oxide islands, and finally the formation of a thin continuous amorphous oxide layer. As the oxidation proceeds, the kinetics is generally controlled by either the transport of either oxygen anions or metal cations through the oxide film. If the oxide layer is completely uniform and protective. The thickening of such layer can be described by a **parabolic rate** equation. If the oxide layer is no longer protective, oxygen molecules could directly diffuse to the metal/oxide interface and the growth kinetics is well represented by a **para-linear rate** equation. The underlying mathematics can be illustrated by the Deal-Grove Model [1], which is usually used to describe the thermal oxidation kinetics of Si.

First of all, the oxide layer is relatively thin, it is assumed that there is a *linear* gradient of oxygen concentration across the oxide layer. According to Fick's first law, the diffusion flux of molecular oxygen J_{O2} is expressed as

$$J_{O_2} = D\left(\frac{C_{o/a} - C_{m/o}}{x}\right) \tag{1}$$

Where $C_{o/a}$ and $C_{m/o}$ are the concentrations of molecular oxygen at the oxide/air interface and the metal/oxide interface respectively. Mg is readily available at the metal/oxide interface due to the segregation kinetics, the reaction rate is limited by the concentration of oxygen. The reaction flux (growth of oxide) is approximated as

$$J_{\text{oxide}} = k_1 \cdot C_{m/o} \tag{2}$$

Where k_1 is a reaction rate constant. At steady state, the two fluxes should be the same. Combining Equations 1 and 2, the concentration of molecular oxygen at the metal/oxide interface is given by

$$C_{m/o} = \frac{DC_{o/a}}{D + k_1 \cdot x} \tag{3}$$

As the growth rate of oxide is proportional to the reaction flux

$$\frac{dx}{dt} = k_2 \cdot J_{\text{oxide}} \tag{4}$$

Combining Equation 2, 3, and 4 together, the following equations are obtained.

$$\left(k_1 DC_{\text{o/a}}\right)\cdot dt = \left(k_2 D + k_1 k_2 x\right)\cdot dx \tag{5}$$

$$\int_0^t \left(k_1 DC_{\text{o/a}}\right)\cdot dt = \int_{x_0}^{x} \left(k_2 D + k_1 k_2 x\right)\cdot dx \tag{6}$$

$$t = \frac{k_1 k_2 \cdot x^2 + 2k_2 D\cdot x + \left(-2k_2 D x_0 - k_1 k_2 x_0^2\right)}{2k_1 DC_{\text{o/a}}} \tag{7}$$

Equation 7 can be further simplified into

$$t = A\cdot x^2 + B\cdot x + C \tag{8}$$

It can be seen from Equation 8 that the growth of oxide is represented by a para-linear equation.

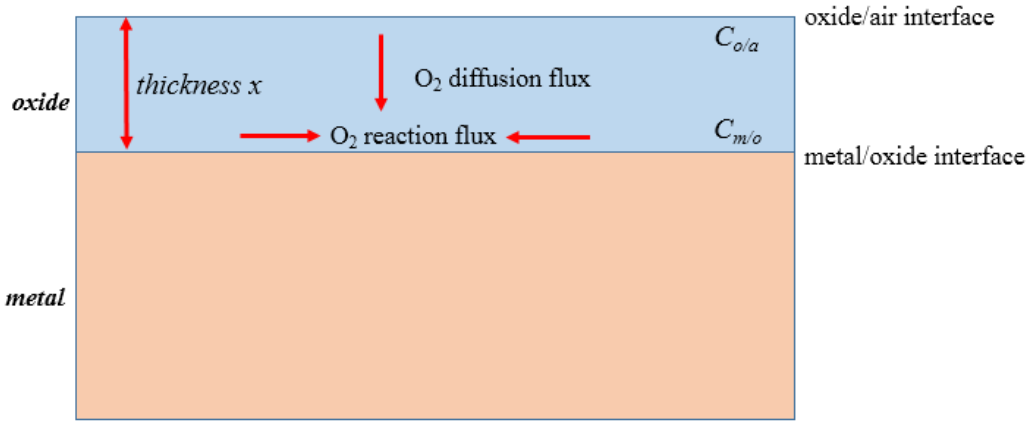

Figure 1 – Schematic diagram showing the construction of the para-linear kinetic model

References

[1] B. E. Deal and A. Grove, "General relationship for the thermal oxidation of silicon," *Journal of Applied Physics*, vol. 36, pp. 3770-3778, 1965.

Figure 2.1 – Ellingham diagram [1] showing the thermodynamic tendency of different metal-gas reactions as a function of temperature and pressure.

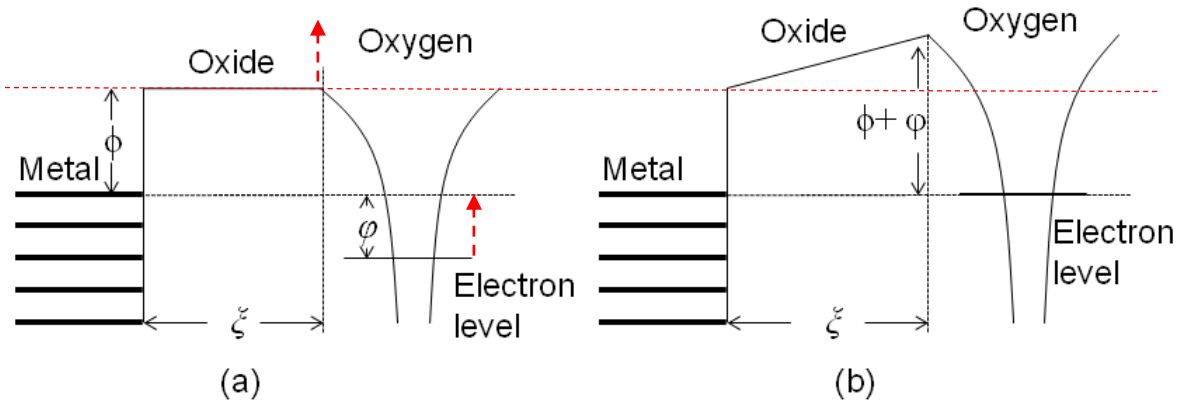

Figure 2.2 – Diagrams showing energy levels in the metal and oxide (a) before and (b) after the exchange of electrons – Cabrera-Mott theory [2]: first of all, oxygen atoms are absorbed on the surface of the oxide film and become traps for electron transferred from the metal by quantum-mechanical tunnelling or by thermionic emission. It was assumed that before the transport of electrons from metal to oxygen, the empty electron energy levels of the absorbed oxygen atoms are below the Fermi level in the metal. The transfer of electrons to oxygen atoms to form oxygen ions raises the energy level up to the metal Fermi level. A potential drop across the oxide film is produced at equilibrium and its value is around one to two volts. Since the oxide film is very thin (2-20 nm), the electric field is sufficiently strong to allow the activated jump of metal ions from the metal/oxide interface to the outside surface of oxide film.

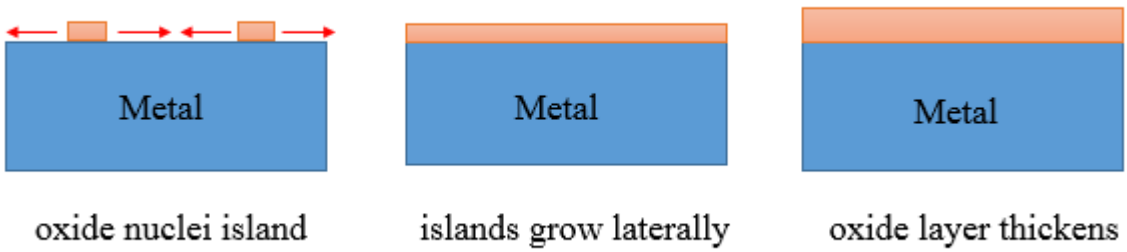

Figure 2.3 – Diagram showing the amorphous oxide layer growth model proposed by Grønlund [3].

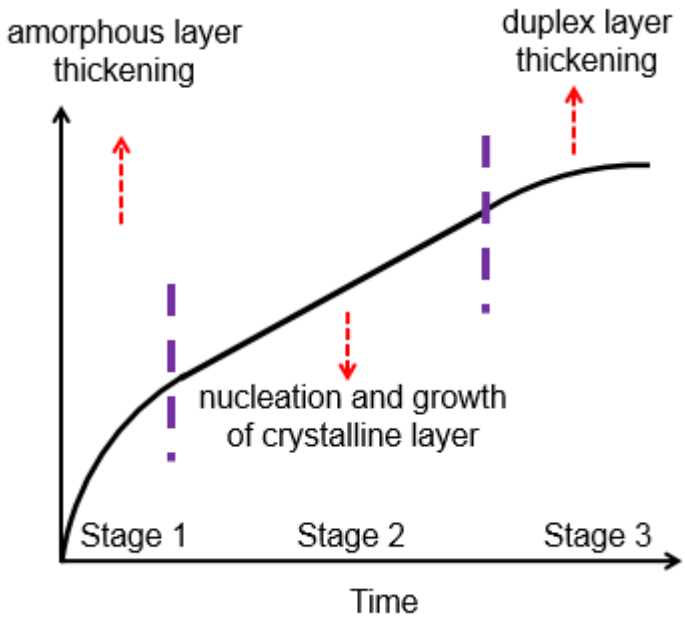

Figure 2.4 – Plot showing the high temperatures oxidation kinetics pattern for pure Al, as suggested by Aylmore *et al*. [4].

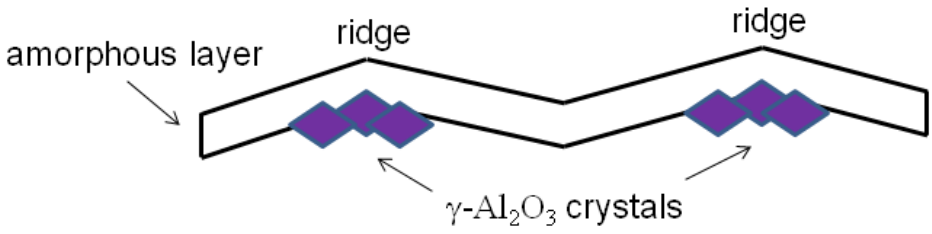

Figure 2.5 – Diagram showing the crystalline γ-Al_2O_3 growth beneath the amorphous layer and preferentially nucleate at ridge sites, as suggested by Shimizu *et al*. [5, 6].

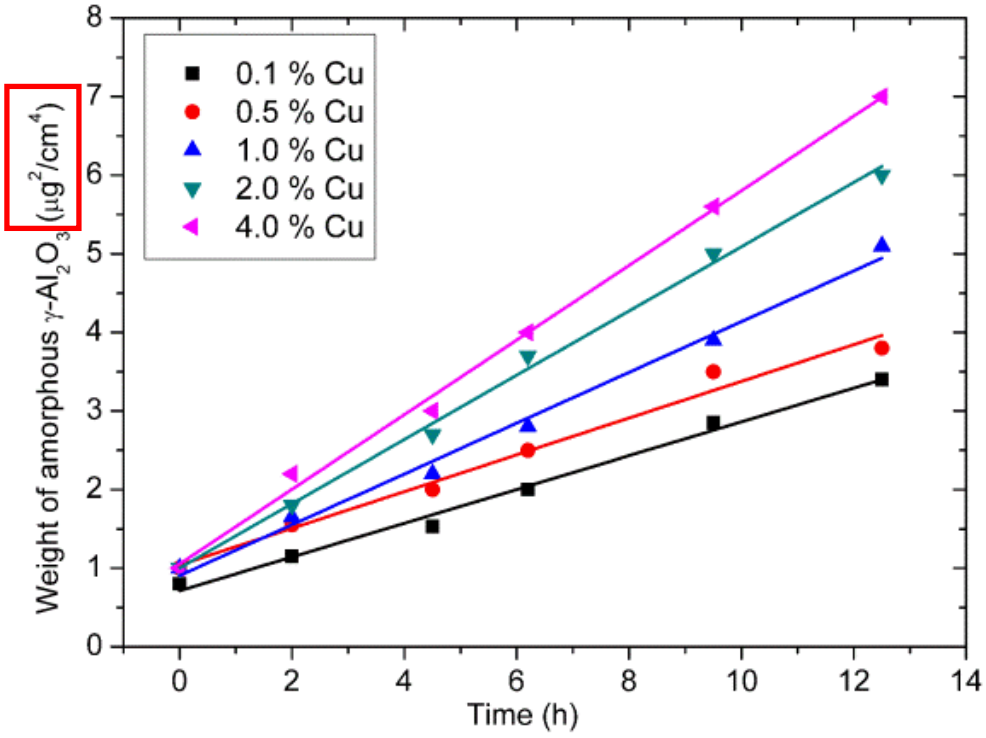

Figure 2.6 – Reconstructed plots showing the weight gain of amorphous γ-Al_2O_3 on different Al-Cu alloys Data from Brock and Pryor [7].

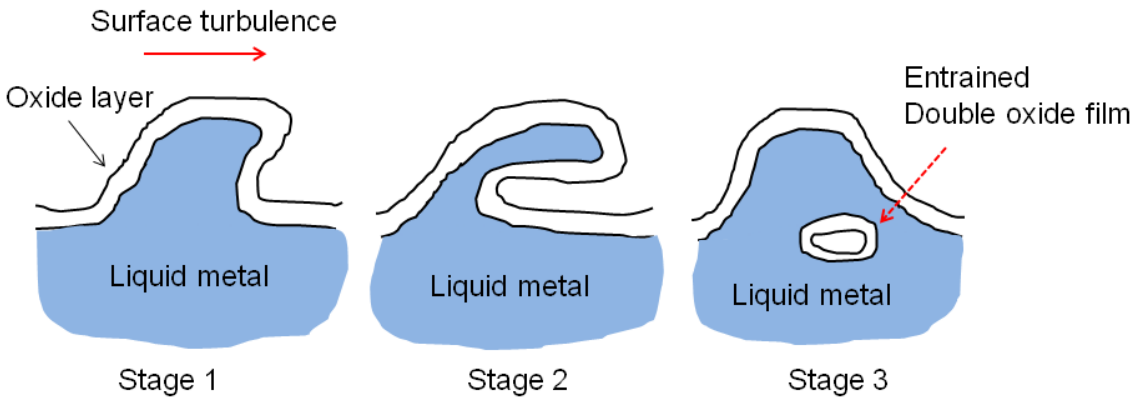

Figure 2.7 – Diagram showing the formation mechanism of an entrained double oxide film. (Image reconstructed according to [8, 9])

Figure removed due to copyright reasons

Figure 2.8 – SE images of opposed fracture surfaces of an Al-11Si-0.6Fe alloy showing the oxide bi-film split into its folded halves. Image from [9, 10].

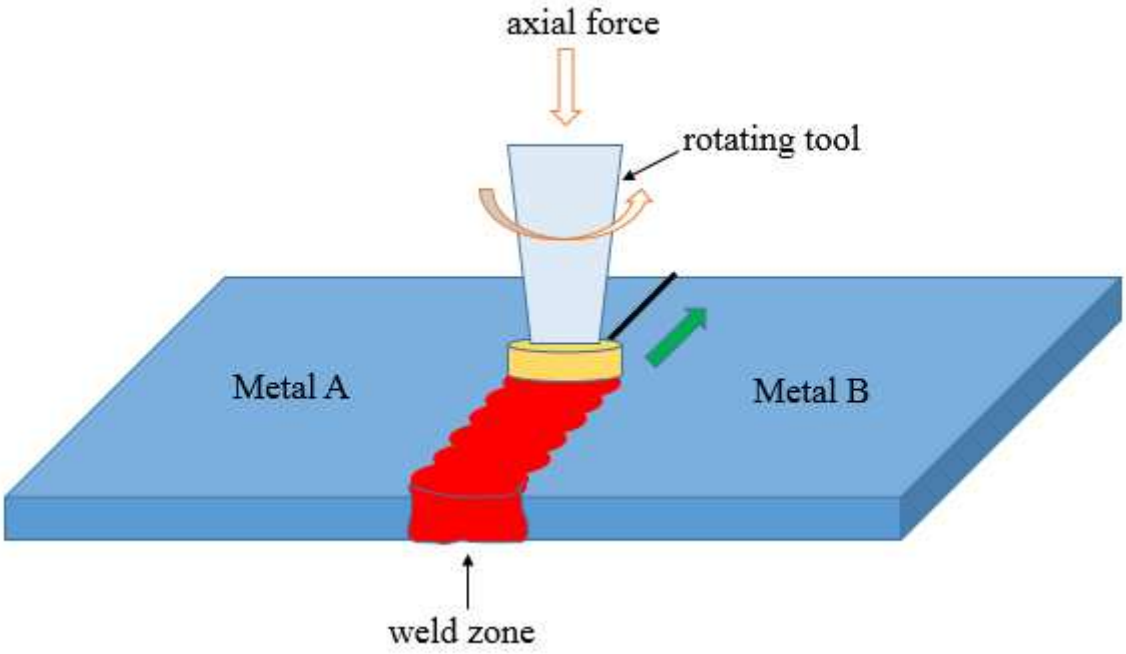

Figure 2.9 – Diagram illustrating the principle of a friction stir welding process (FSW).

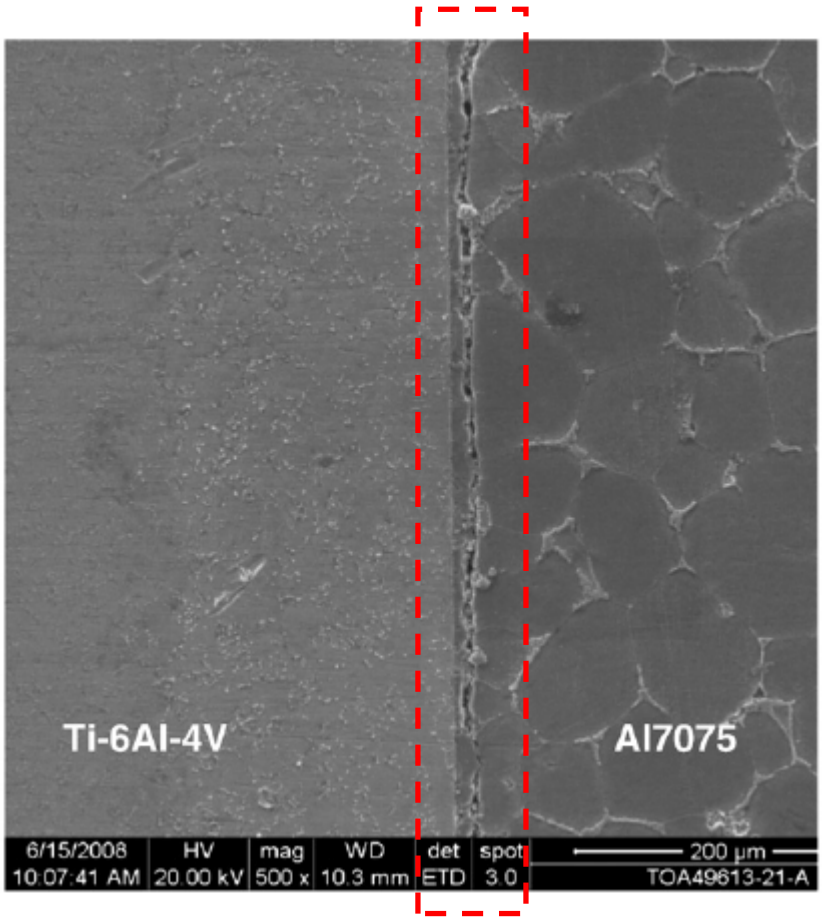

Figure 2.10 – SE image showing the interface morphology of a TLP bonded Ti-6Al-4V/Al7075 joint. Image from [11]. (With permission from Elsevier)

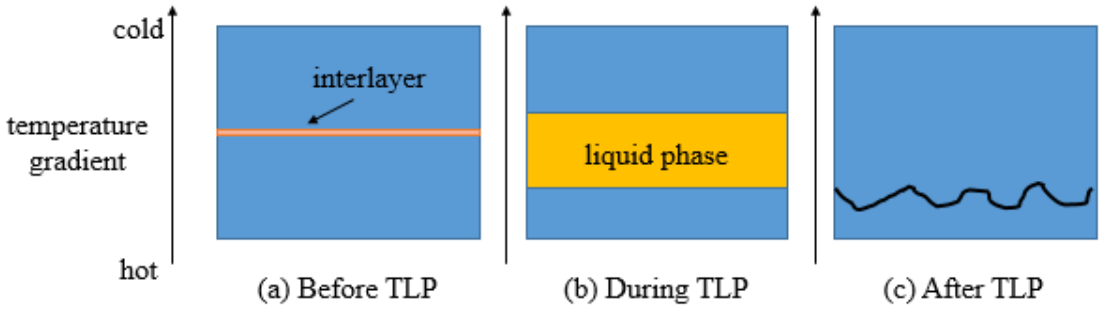

Figure 2.11 – Diagram showing a temperature-gradient TLP process.

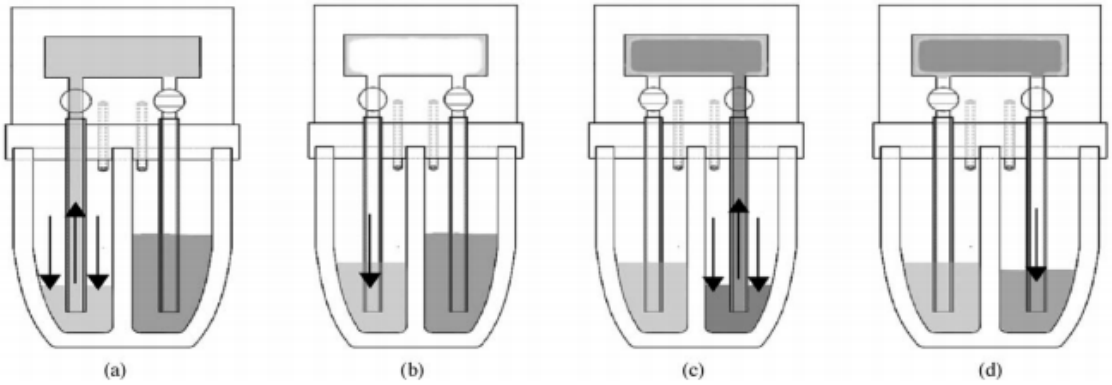

Figure 2.12 – Diagram showing the typical casting sequence (from a to d) of a CDC process. Image from [12]. (With permission from Elsevier)

Figure removed due to copyright reasons

Figure 2.13 – Diagram showing the squeeze casting process. Image from [13].

Figure removed due to copyright reasons

Figure 2.14 – Diagram showing the squeeze casted Al-Si piston with cast iron ring groove reinforcement.

References – Chapter 2 Figures

[1] H. J. T. Ellingham, "Reducibility of oxides and sulfides in metallurgical processes," *Journal of the Society of Chemical Industry (London)*, vol. 63, pp. 125-133, 1944.

[2] N. Cabrera and N. Mott, "Theory of the oxidation of metals," *Reports on Progress in Physics*, vol. 12, p. 163, 1949.

[3] F. Grønlund, *J. Chim. Phys.*, vol. 53, p. 660, 1956.

[4] D. Aylmore, S. Gregg, and W. Jepson, "The oxidation of aluminium in dry oxygen in the temperature range 400-650°C," *Journal of the Institute of Metals*, vol. 88, 1960.

[5] K. Shimizu, A. Gotoh, K. Kobayashi, G. E. Thompson, and G. C. Wood, "The nucleation sites of gamma-Al_2O_3 crystals in thermal oxide-films on aluminum," *Microscopy of Oxidation*, pp. 144-148, 1992.

[6] K. Shimizu, R. C. Furneaux, G. E. Thompson, G. C. Wood, A. Gotoh, and K. Kobayashi, "On the nature of easy paths for the diffusion of oxygen in thermal oxide-films on aluminum," *Oxidation of Metals*, vol. 35, pp. 427-439, 1991.

[7] A. J. Brock and M. J. Pryor, "Kinetics of oxidation of aluminum-copper alloys in oxygen at high-temperature," *Corrosion Science*, vol. 13, p. 199, 1973.

[8] J. Campbell, *Castings*: London Butterworth, 2003.

[9] J. Campbell, "Entrainment defects," *Materials Science and Technology*, vol. 22, pp. 127-145, 2006.

[10] X. Cao and J. Campbell, "The solidification characteristics of Fe-rich intermetallics in Al-11.5 Si-0.4 Mg cast alloys," *Metallurgical and Materials Transactions A*, vol. 35, pp. 1425-1435, 2004.

[11] A. AlHazaa, T. Khan, and I. Haq, "Transient liquid phase (TLP) bonding of Al7075 to Ti–6Al–4V alloy," *Materials Characterization*, vol. 61, pp. 312-317, 2010.

[12] M. Scanlan, D. J. Browne, and A. Bates, "New casting route to novel functionally gradient light alloys," *Materials Science and Engineering: A*, vol. 413, pp. 66-71, 2005.

[13] G. Durrant, M. Gallerneault, and B. Cantor, "Squeeze cast aluminium reinforced with mild steel inserts," *Journal of materials science*, vol. 31, pp. 589-602, 1996.

Table 3.1 – Chemical compositions (in weight %) of the ingots.

Ingots name	Mg	Si	Fe	Cu	Al
Al	-	0.03 ± 0.01	0.04 ± 0.02	-	99.93 ± 0.03
Al-5Cu	-	0.04 ± 0.02	0.05 ± 0.02	4.97 ± 0.03	94.94 ± 0.07
Al-2Mg	2.02 ± 0.01	0.02 ± 0.01	0.02 ± 0.02	-	97.94 ± 0.05
Al-0.2Mg	0.21 ± 0.02	0.03 ± 0.01	0.05 ± 0.02	-	99.71 ± 0.05

Table 3.2 – Experimental conditions used for the hot-stage OM analysis.

Material	Temperature	Heating speed	Cooling speed
Al	30°C~750°C	40°C min^{-1}	100°C/min
	750°C	Hold 5 min	
Al-5Cu	30°C~750°C	40°C min^{-1}	100°C/min
	750°C	Hold 5 min	

Table 3.3 – XPS wide scan experimental conditions.

X-ray	Energy	Step size (eV)	Pass energy (eV)	Dwell time (s)	BE scale (eV)
Mg Kα	1253.6	1.00122	20	0.1	0 - 1100
Al Kα	1486.6	1.00122	20	0.1	0 - 1100

Table 3.4 – Fitted parameters using a single peak - method (a).

Peak 1	Centre	Area	Width
O 1s as Al_2O_3 like	532.37 ± 0.12	76420.22 ± 530.31	2.15 ± 0.03
Height	Coefficient of determination (COD)	Reduced Chi Square	
28312.31 ± 201.39	0.998 ± 0.002	162232.10 ± 1334.85	

Table 3.5 – Fitted parameters using double peaks - method (b).

Peak	Centre	Area	Width
O 1s as Al_2O_3 like	532.35 ± 0.09	70170.52 ± 462.23	2.01 ± 0.02
O 1s - (H_2O) like	533.01 ± 0.13	7513.23 ± 109.54	1.94 ± 0.03
Height	Coefficient of determination (COD)	Reduced Chi Square	
27803.58 ± 253.53	0.991 ± 0.003	10968.08 ± 267.82	
3085.69 ± 120.39			

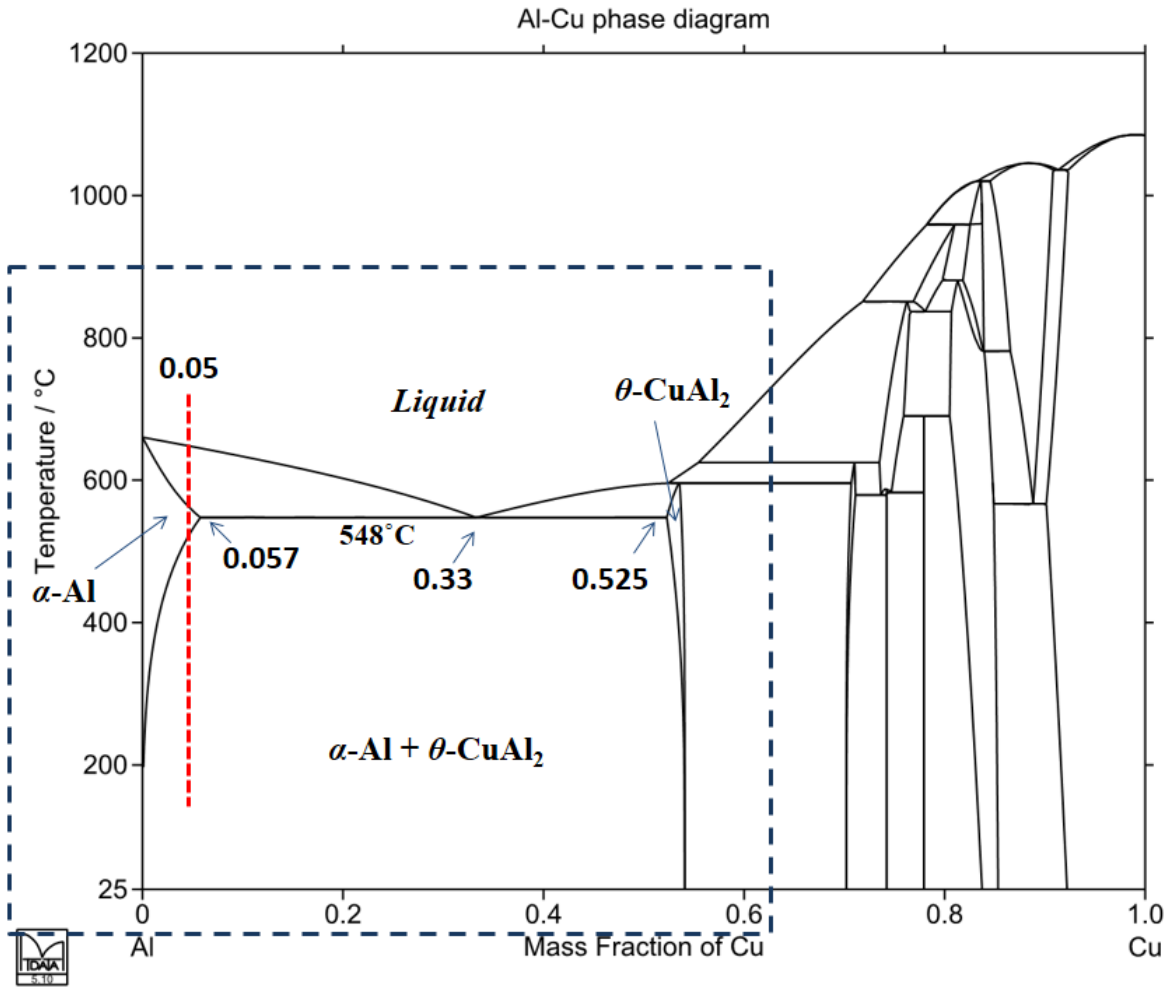

Figure 3.1 – Calculated equilibrium phase diagram for the Al-Cu system.

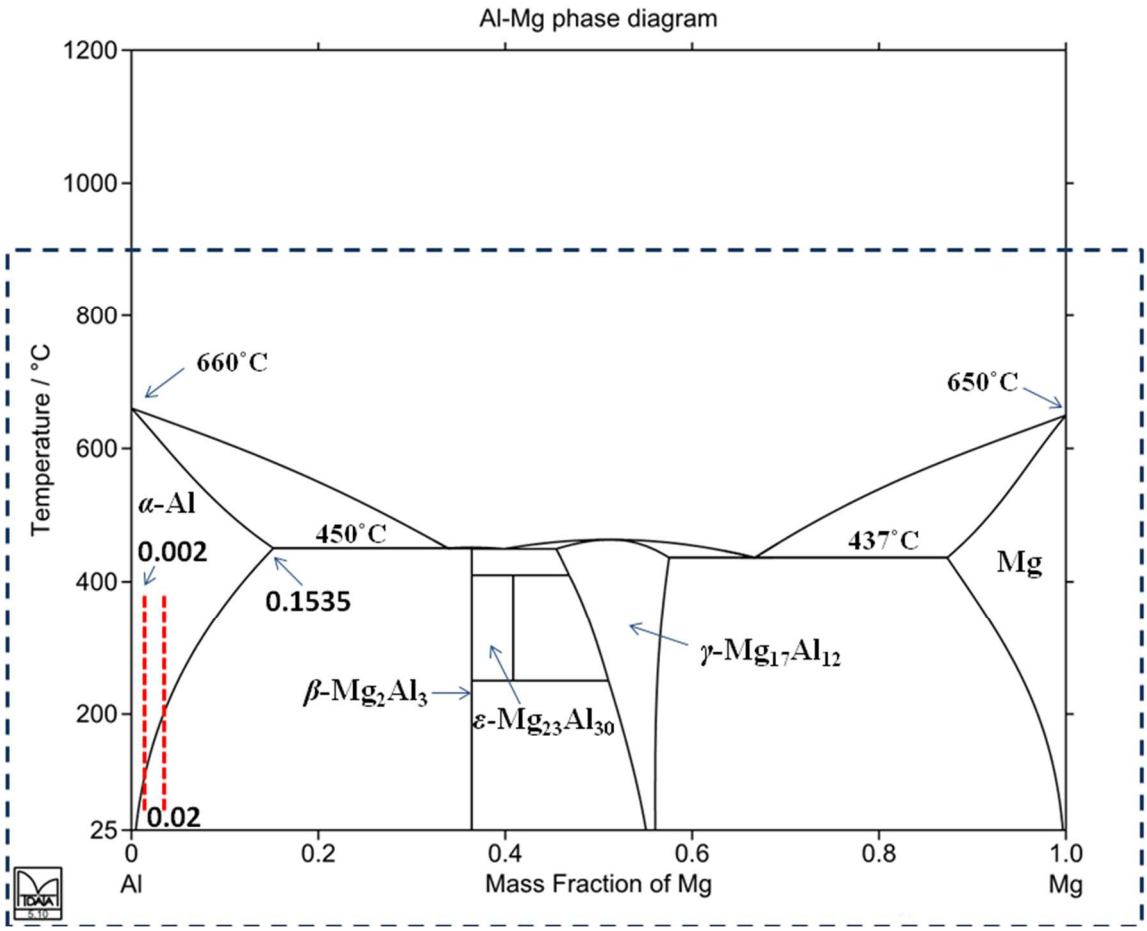

Figure 3.2 – Calculated equilibrium phase diagram for the Al-Mg system

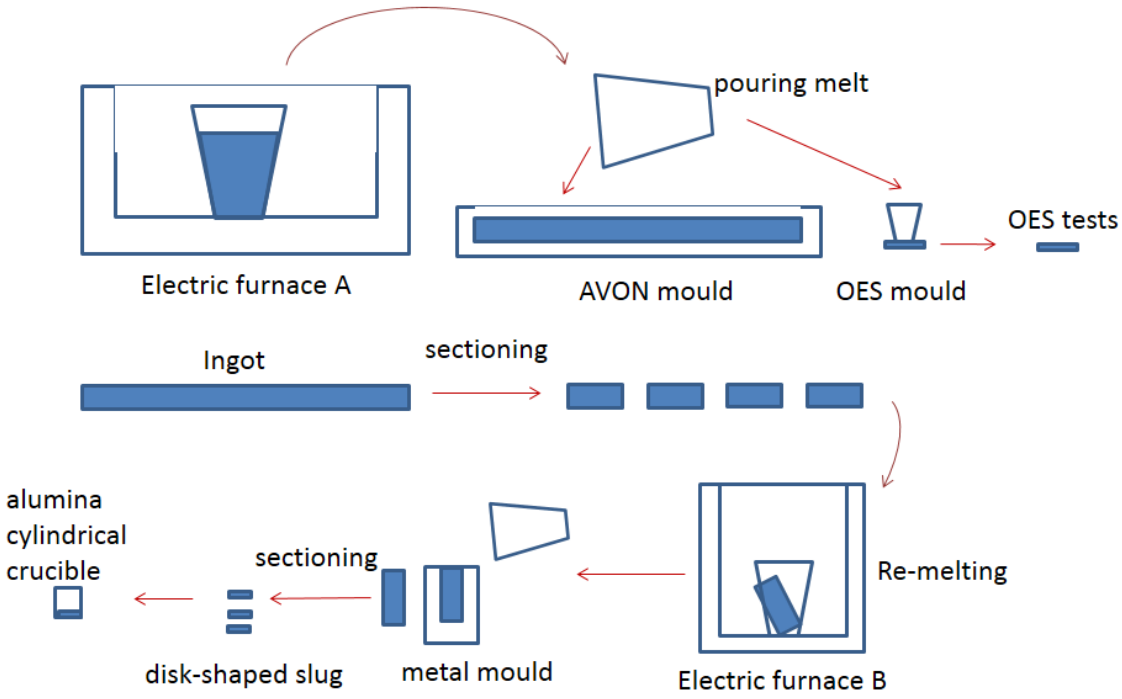

Figure 3.3 – Diagram showing the casting procedure used for producing cylindrical billets (diameter around 26 mm) in the present work.

Figure 3.4 – The C2 Carbolite electric furnace facility used in the present work.

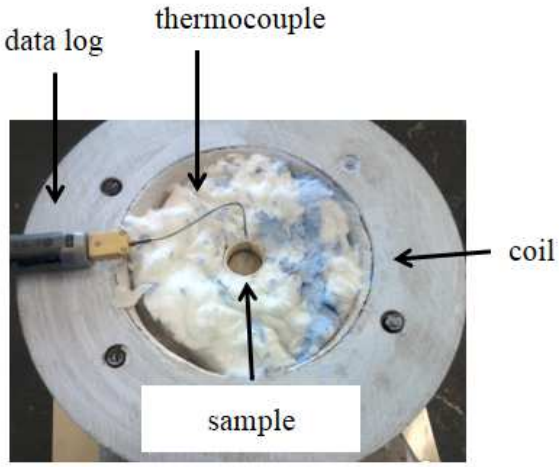

Figure 3.5 – The mini-CRIM furnace facility used in the present work and a top view of the associate induction coil system.

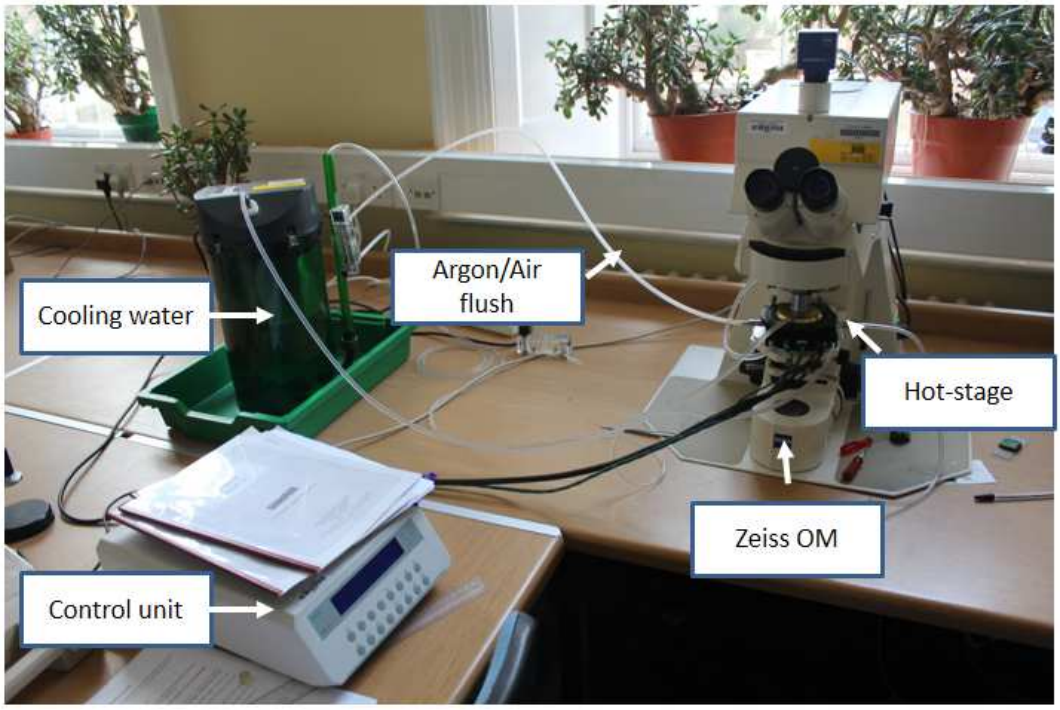

Figure 3.6 – Photo showing the LINKAM TS1500 hot stage system and Zeiss OM.

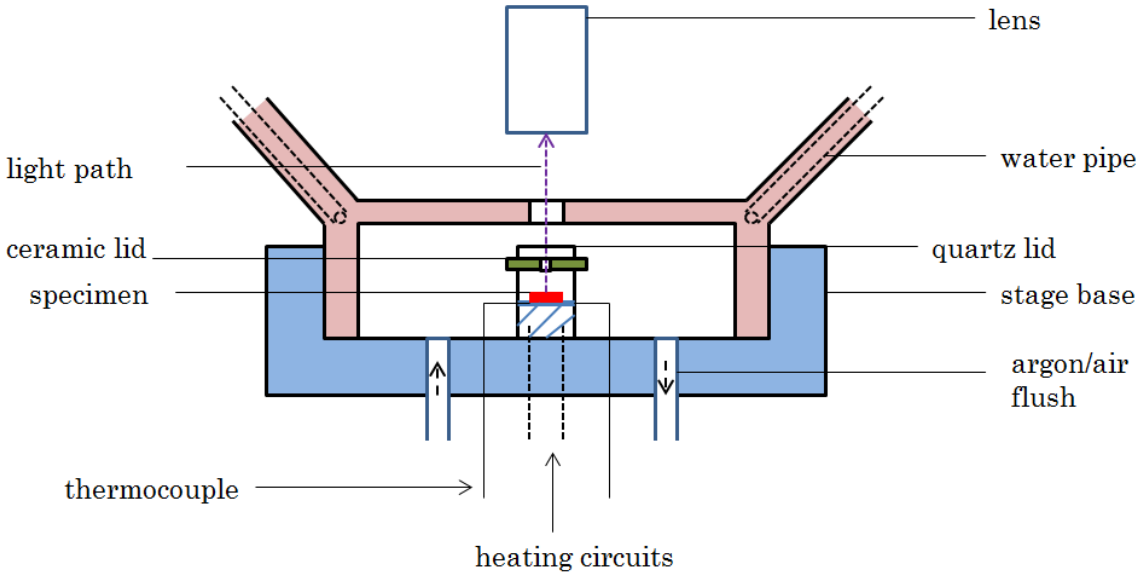

Figure 3.7 – Diagram showing the cross section view of the hot-stage system.

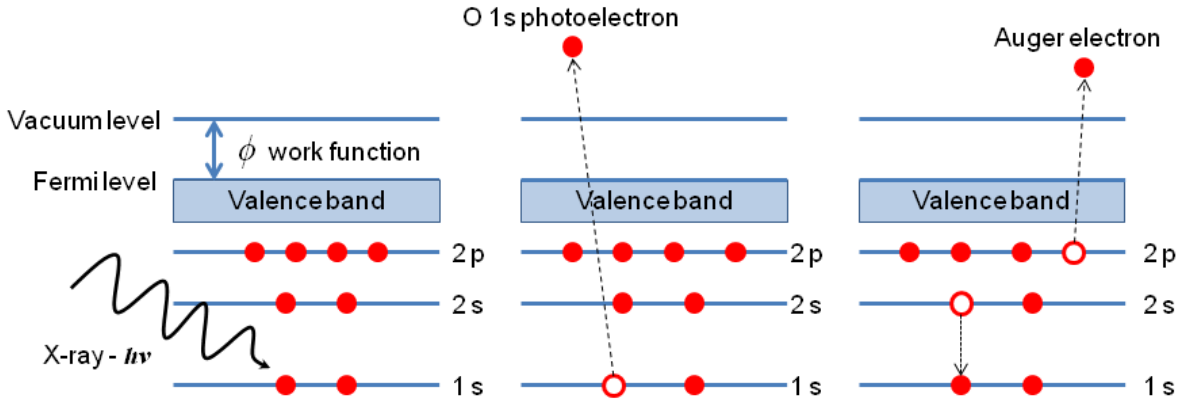

Figure 3.8 – Diagram showing the principle of the XPS photoelectron emission and the Auger electron emission process.

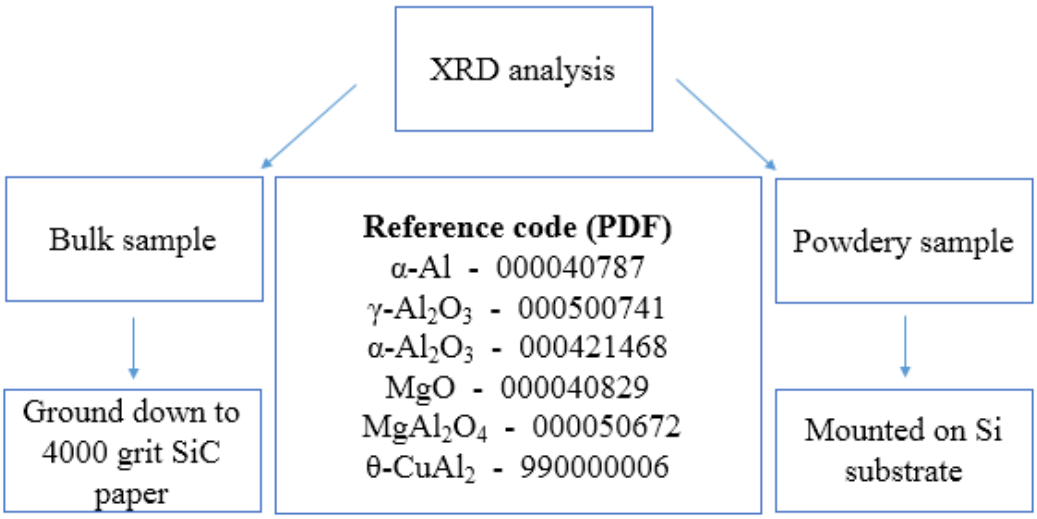

Figure 3.9 – XRD analysis sample preparation and XRD patterns quoted from the X'Pert Highscore software database.

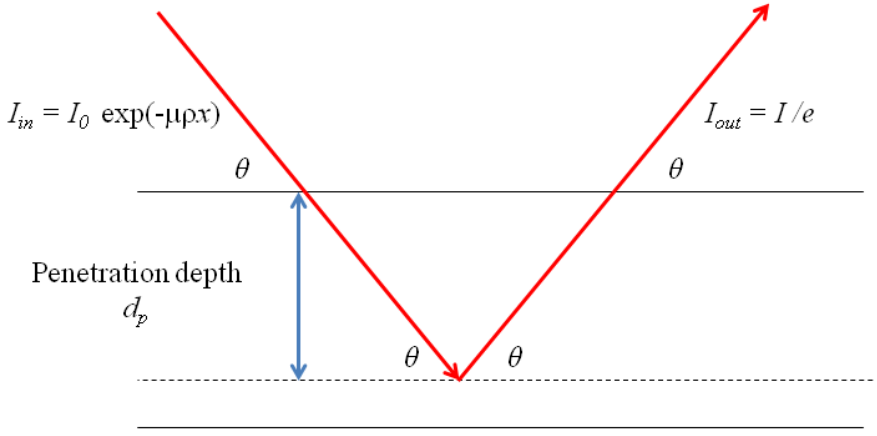

Figure 3.10 – Diagram showing the X-ray penetrating through a thickness of d_p and the intensity of the emitted X-ray is degraded by a factor 1/e.

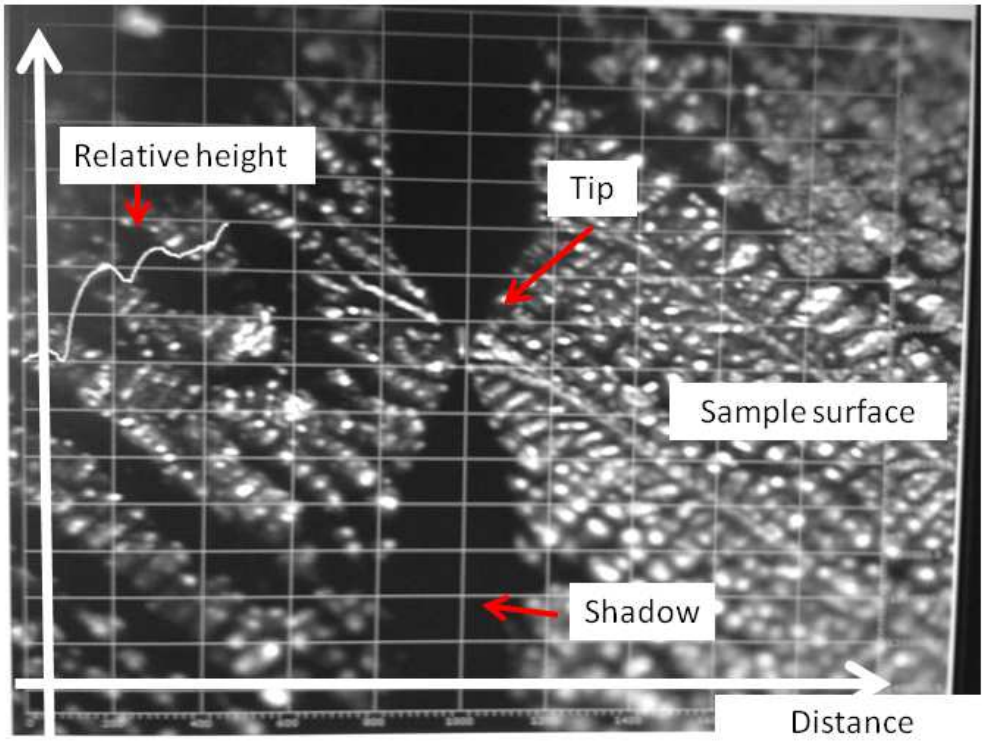

Figure 3.11 – Image showing the Dektak surface profiler working principle.

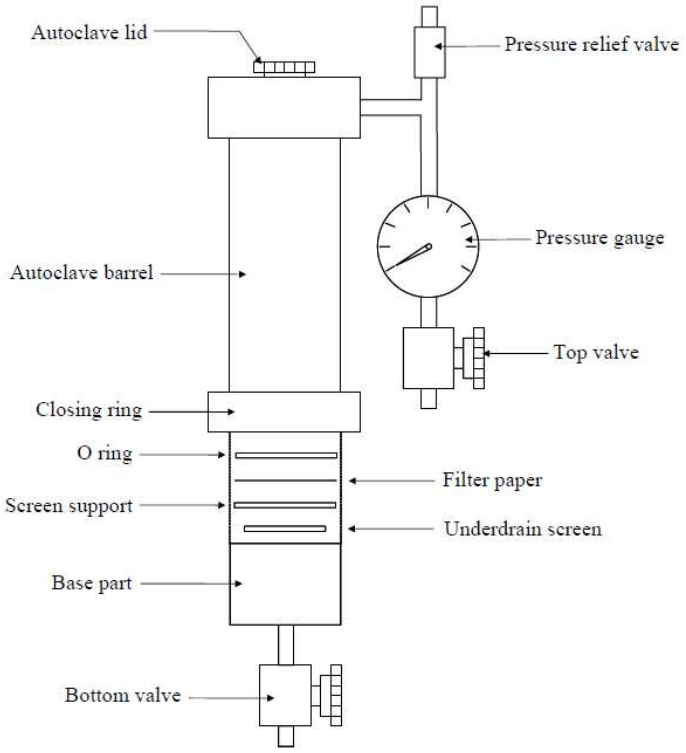

Figure 3.12 – Diagram showing the set-up of an autoclave.

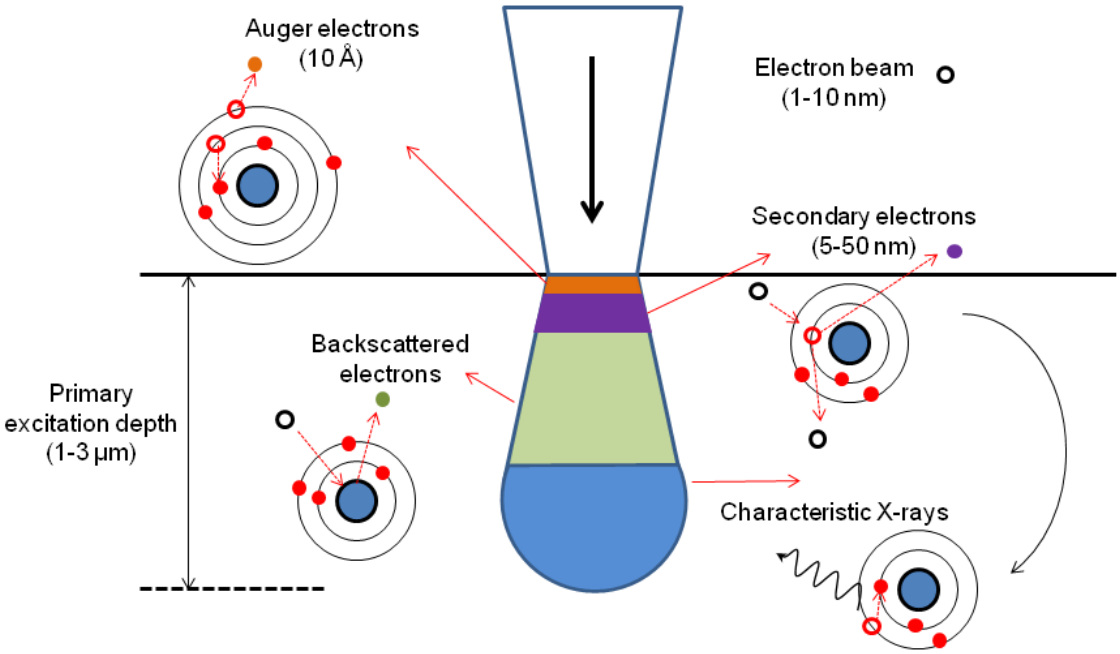

Figure 3.13 – Diagram illustrating the concept of the e-beam ~ sample interaction and how different signals are generated.

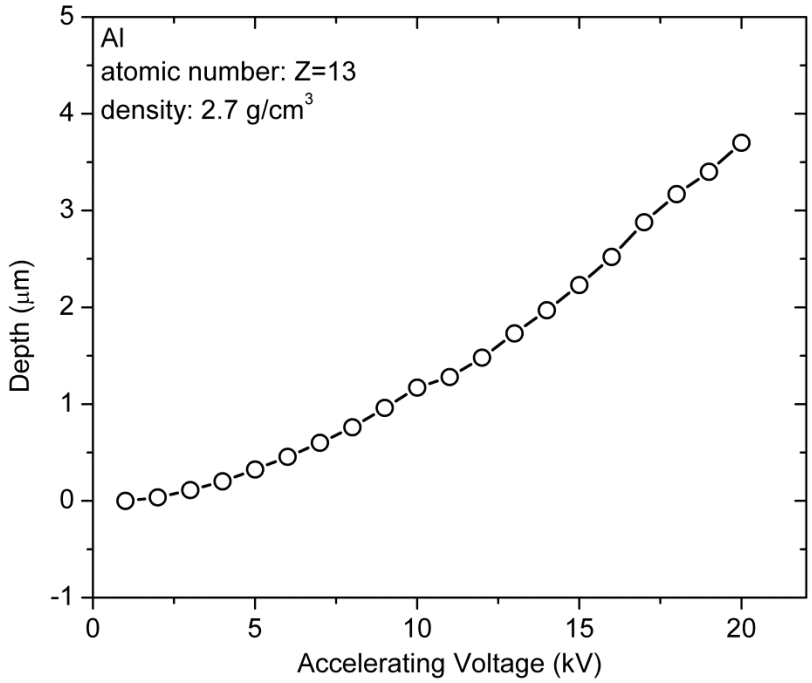

Figure 3.14 – Plot showing the calculated depth of the primary excitation volume as a function of the accelerating voltage for Al (20,000 electron trajectories simulated, incidence angle 0˚)

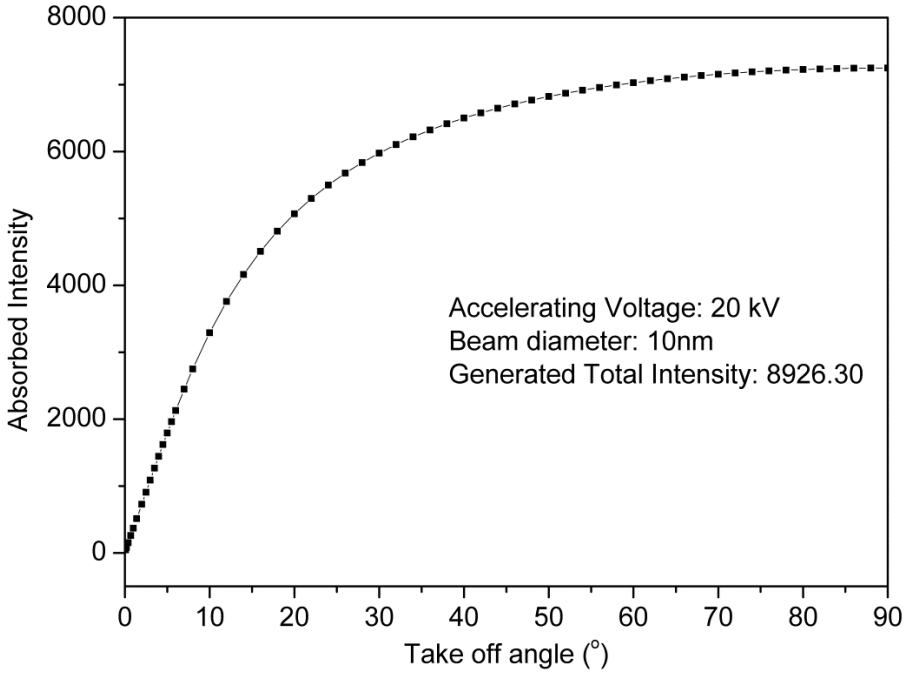

Figure 3.15 – Plot showing the calculated absorbed intensity value of Al Kα X-rays as a function of EDX detector take off angle (20,000 electron trajectories simulated, incidence angle 0˚)

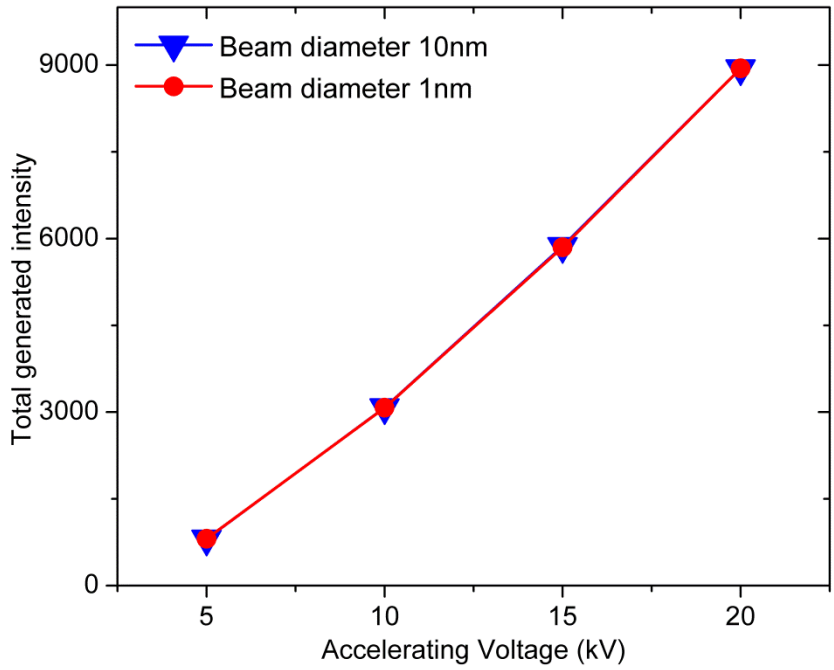

Figure 3.16 – Plot showing the total generated Al Kα X-ray intensity as a function of accelerating voltage using different beam diameters (20,000 electron trajectories simulated, incidence angle 0˚)

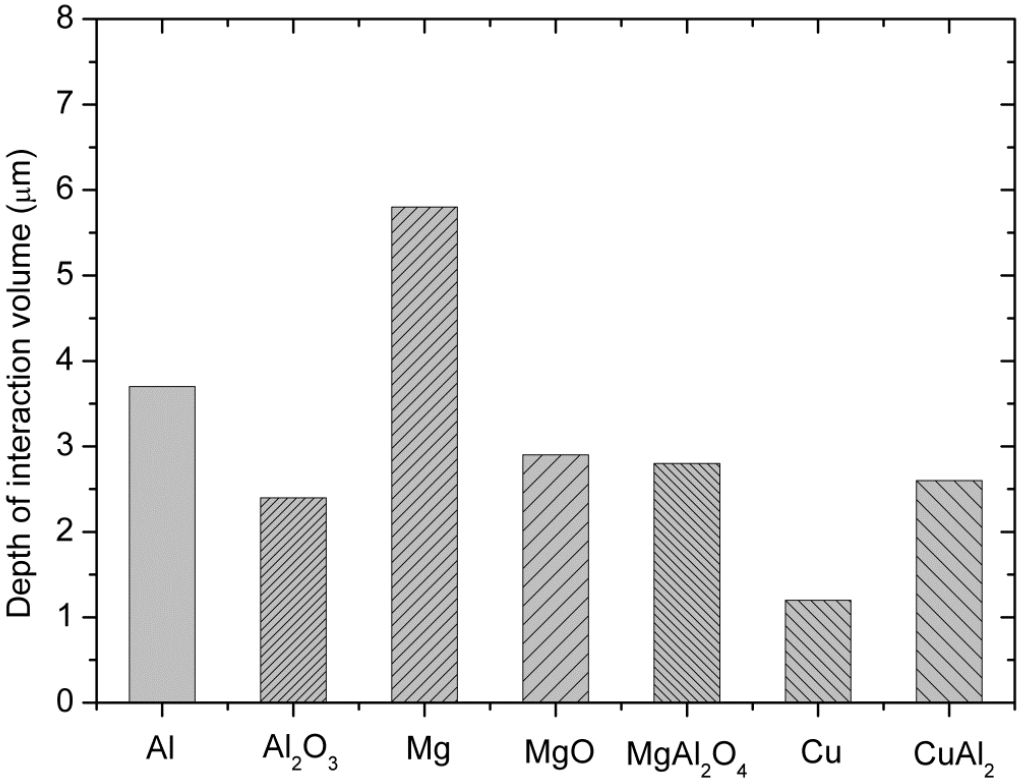

Figure 3.17 – Summary of the results of simulations of the scale of the interaction volume for different phases encountered in the present work.

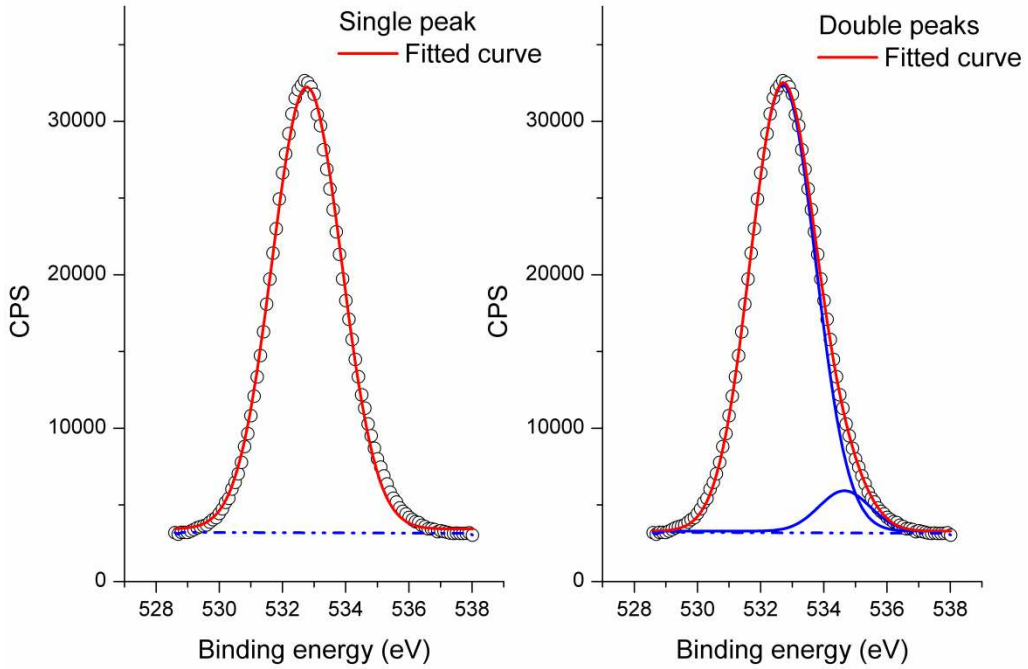

Figure 3.18 – Plots showing Gaussian functions fitted curves for the O 1s core level measured on an oxidized Al sample using two methods.

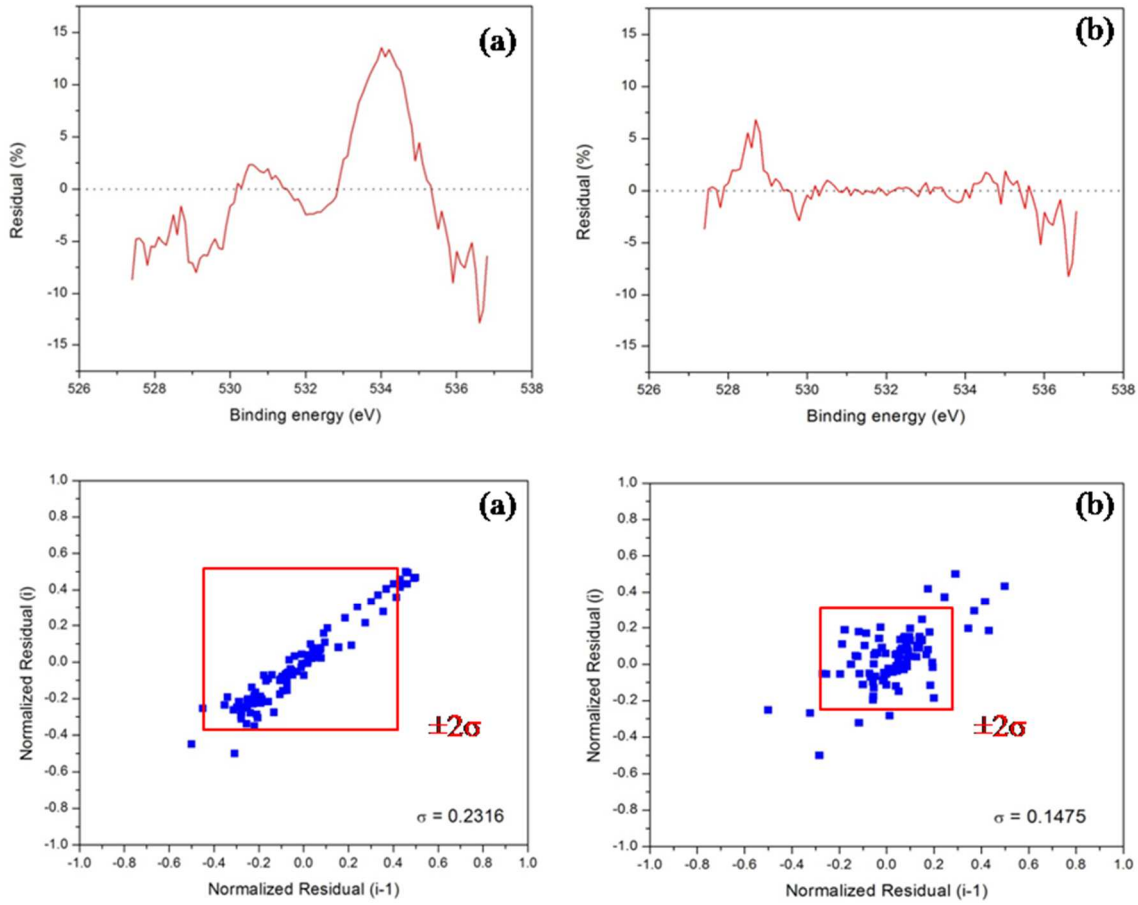

Figure 3.19 – Residual plots and lag plots of the O 1s core level XPS peak fittings for the two different methods (a) and (b).

Table 4.1 – Sample details of the stacked Al/Al-5Cu system.

Sample code	Holding temperature (ºC)	Holding time (h)	Cross section view
S-0.5	750	0.5	Al / Al-5Cu
S-1	750	1	Al / Al-5Cu
S-6	750	6	Al / Al-5Cu
S-24	750	24	Al / Al-5Cu

Table 4.2 – Sample details of the stacked Al/Al-2Mg system.

Sample code	Holding temperature (ºC)	Holding time (h)	Cross section view
M-1	750	1	Al / Al-2Mg
M-6	750	6	Al / Al-2Mg
M-24	750	24	Al / Al-2Mg

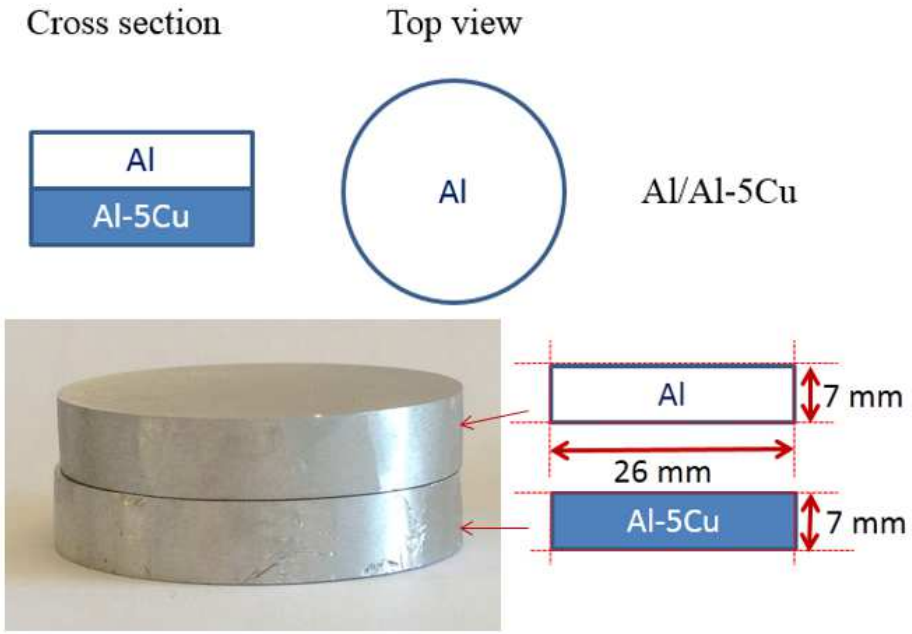

Figure 4.1 – Diagram showing the geometric size of a typical stacked Al/Al-5Cu sample.

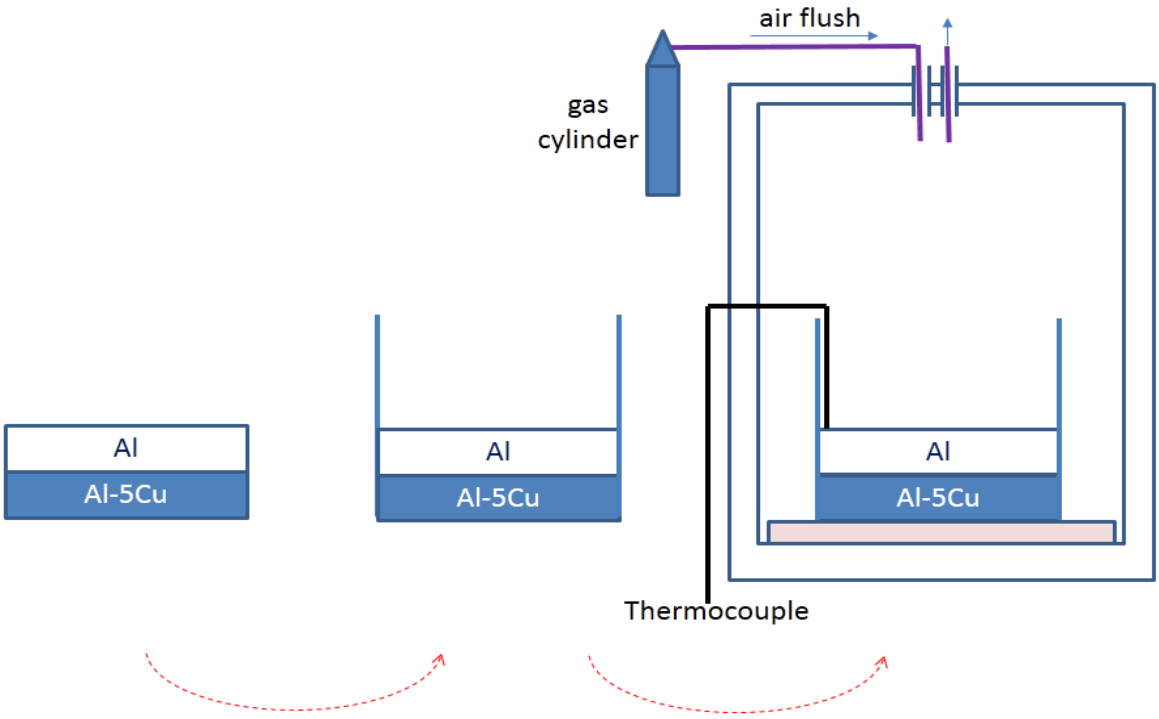

Figure 4.2 – Diagram briefly showing the typical experimental procedure in the stacking approach.

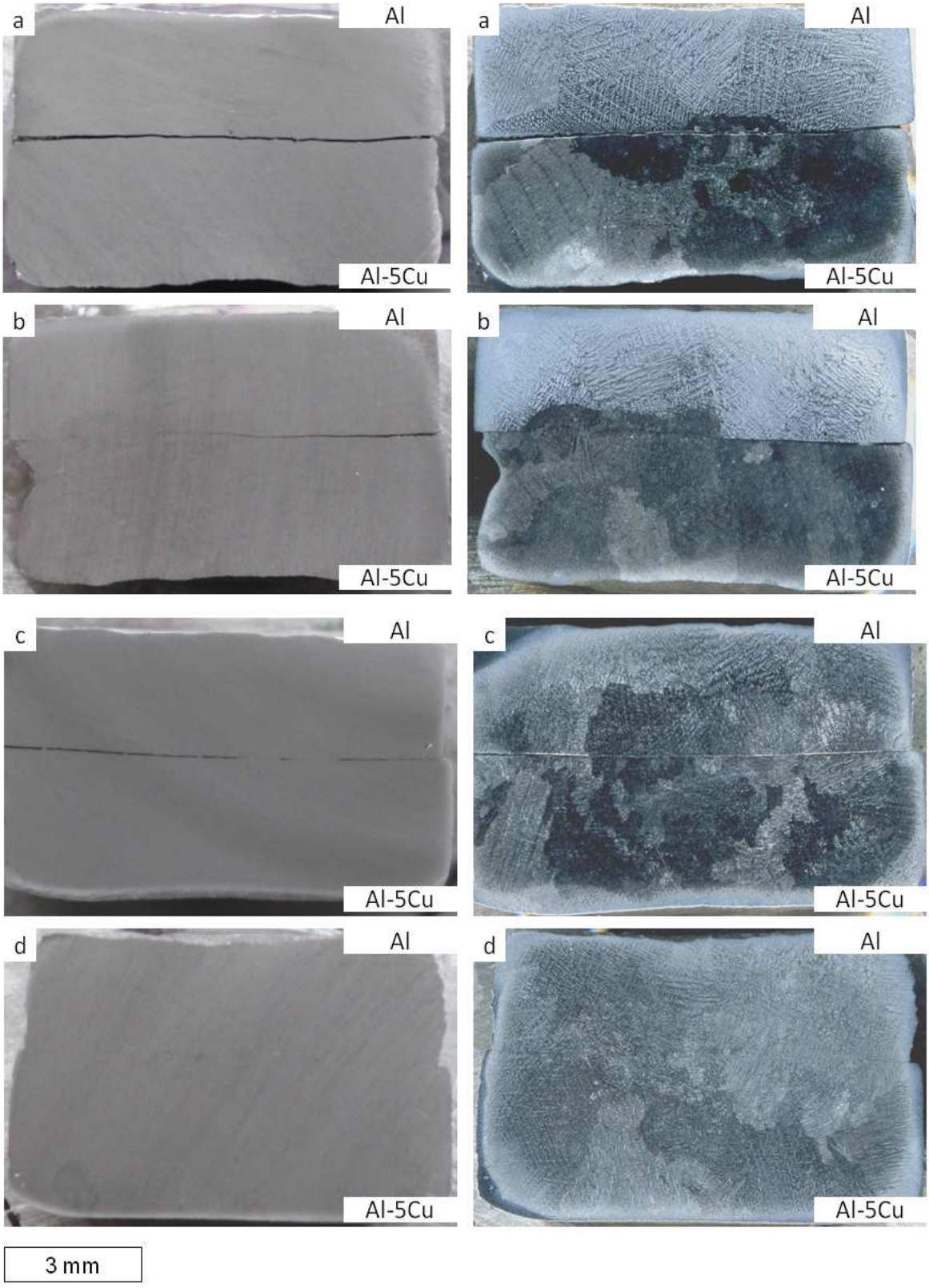

Figure 4.3 – Macrographs showing the cross section structure of the stacked Al/Al-5Cu samples before (left) and after (right) macroetching (a) *S-0.5* (b) *S-1* (c) *S-6* (d) *S-24*.

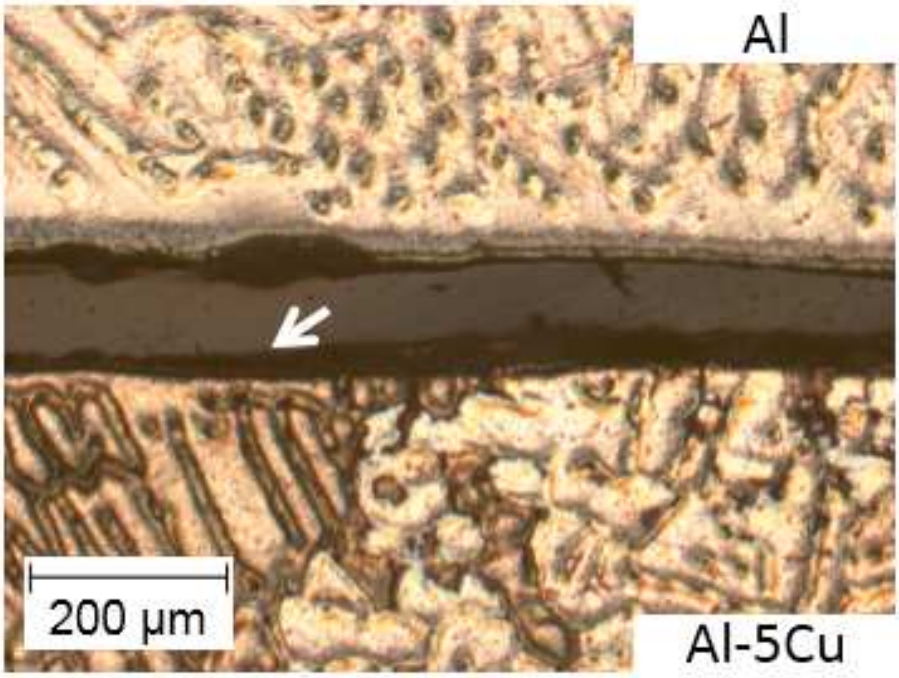

Figure 4.4 – OM image showing the interface microstructure of the stacked Al/Al-5Cu sample *S-0.5*.

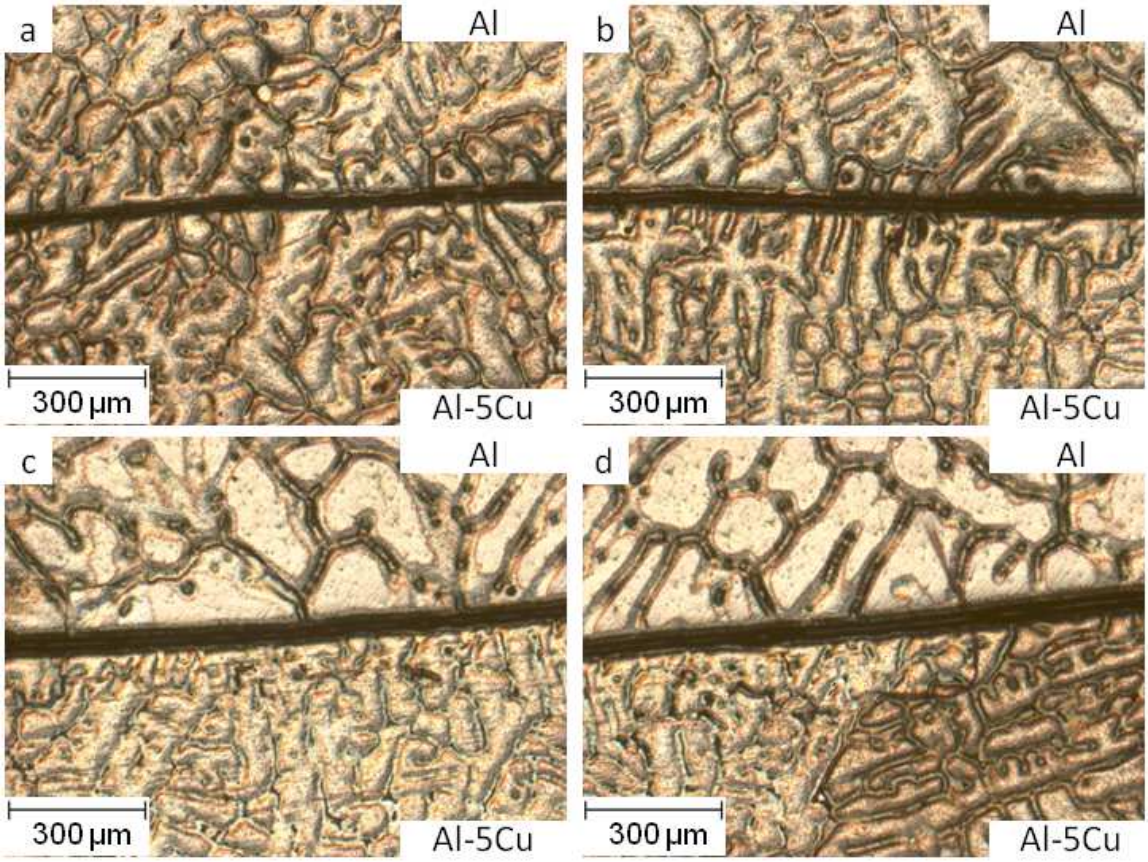

Figure 4.5 – OM images showing the interface microstructure of the stacked Al/Al-5Cu sample *S-1*.

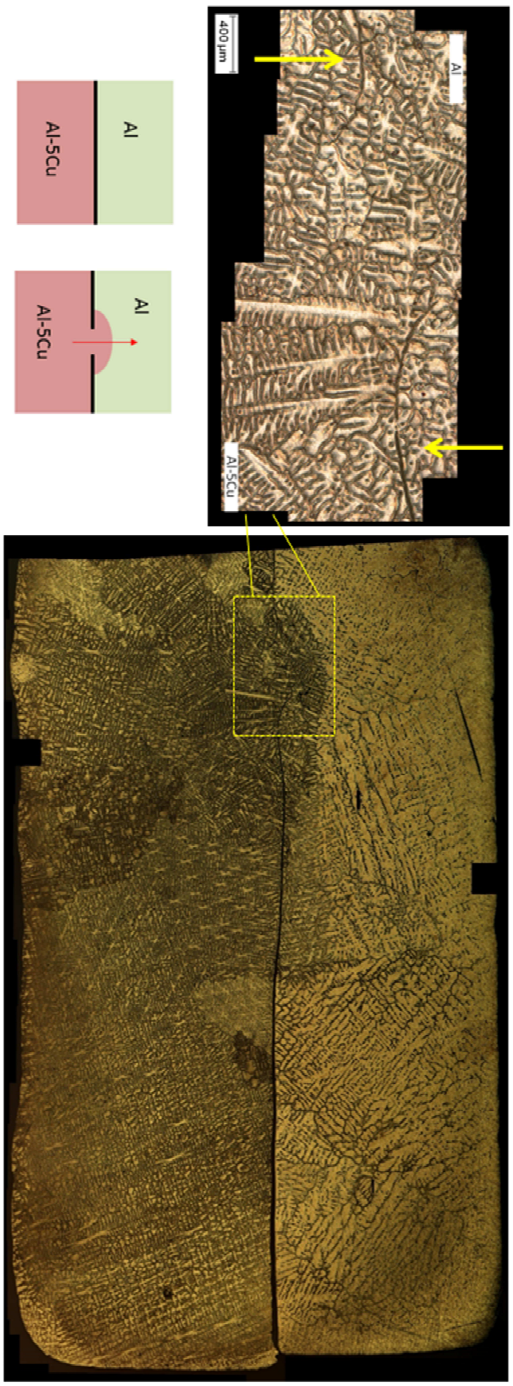

Figure 4.6 – Stitched panoramic view showing the interface microstructure of the stacked Al/Al-5Cu sample *S-1*, revealing the mixing of Al-5Cu melt to the Al side through a crack

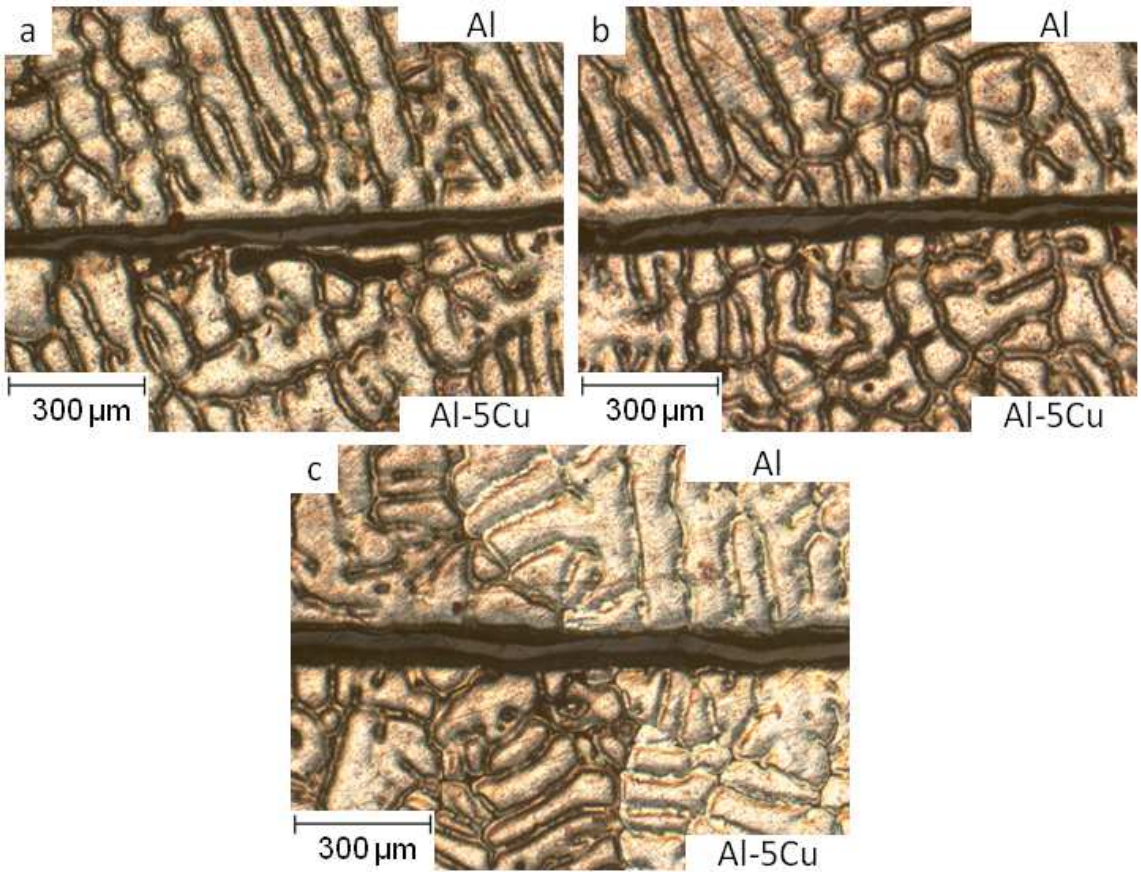

Figure 4.7 – OM images showing the interface microstructure of the stacked Al/Al-5Cu sample *S-6*.

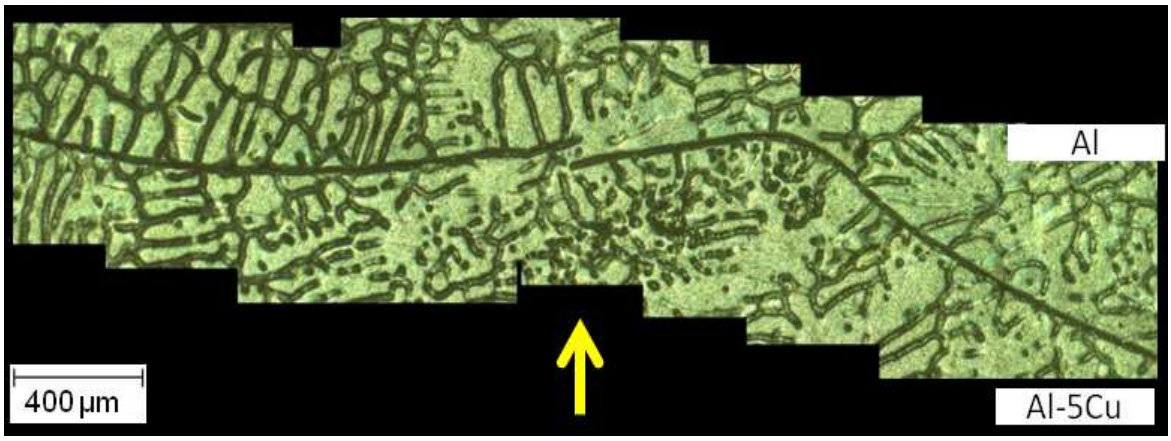

Figure 4.8 – Local stitched panoramic view showing the interface microstructure of the stacked Al/Al-5Cu sample *S-6* and the yellow arrow indicates the fracture of the oxide scale.

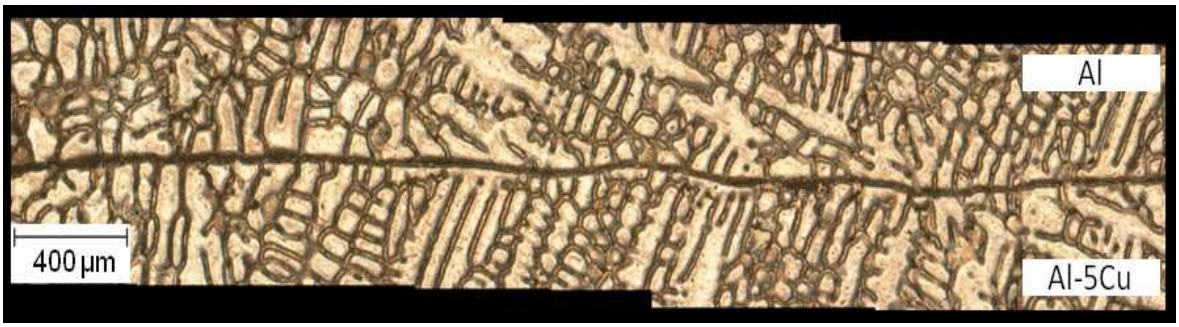

Figure 4.9 – Local stitched panoramic view image showing the interface microstructure of the stacked Al/Al-5Cu sample *S-24*.

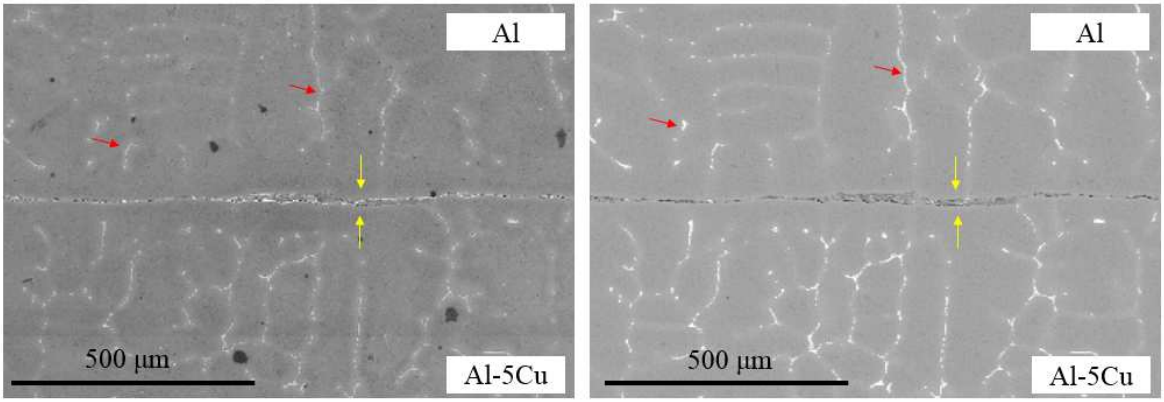

Figure 4.10 – A pair of SE and BE images showing the interface microstructure of the stacked sample *S-6*.

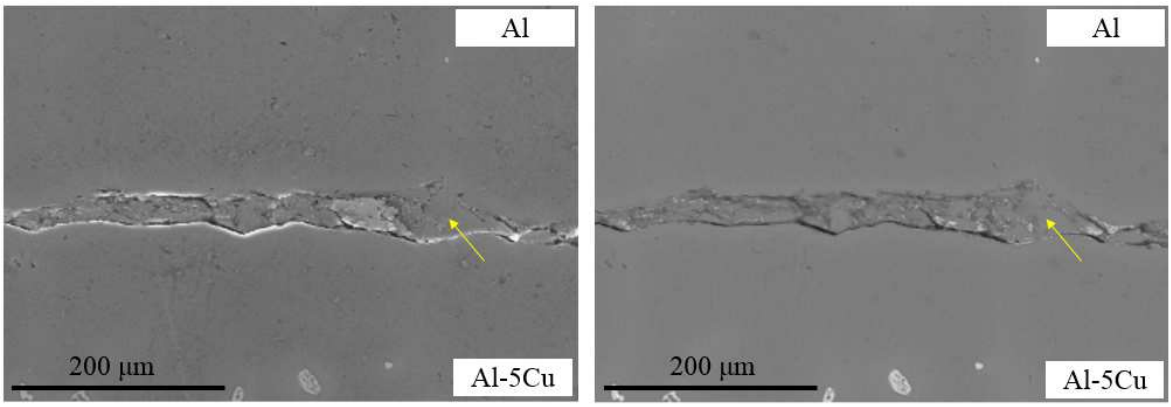

Figure 4.11 – A pair of SE (left) and BE (right) images showing the entrapment of metal at the interface of the stacked sample *S-6*.

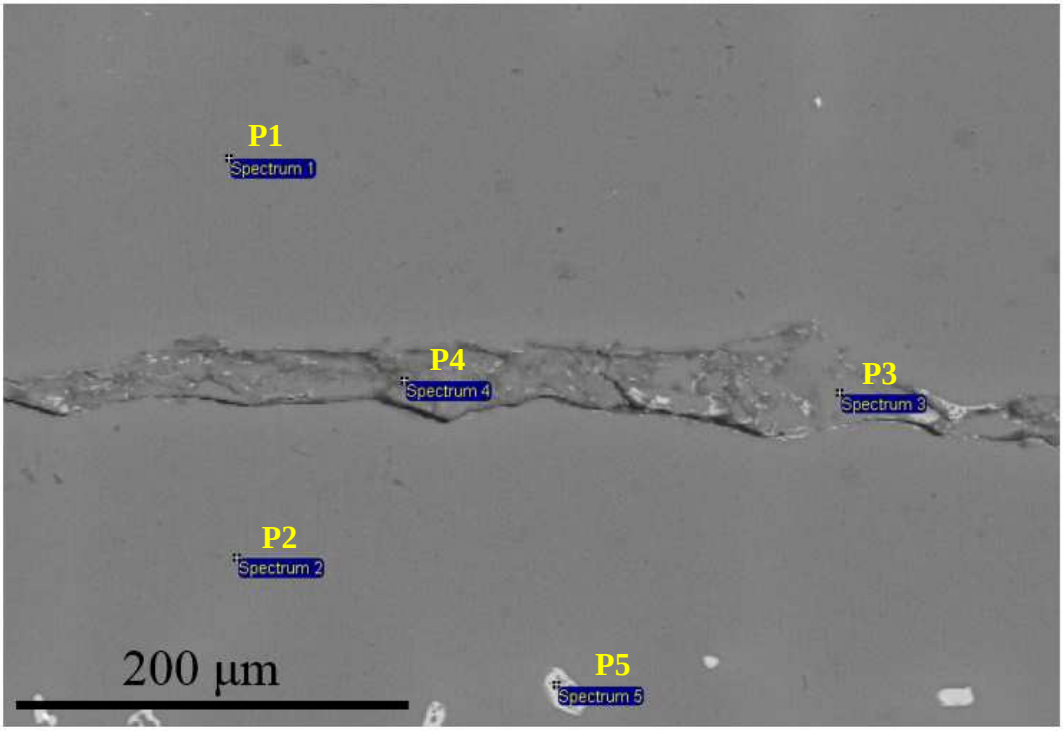

Figure 4.12 (a) – BE image showing the EDX point analysis performed at the interface region in the stacked sample *S-6*.

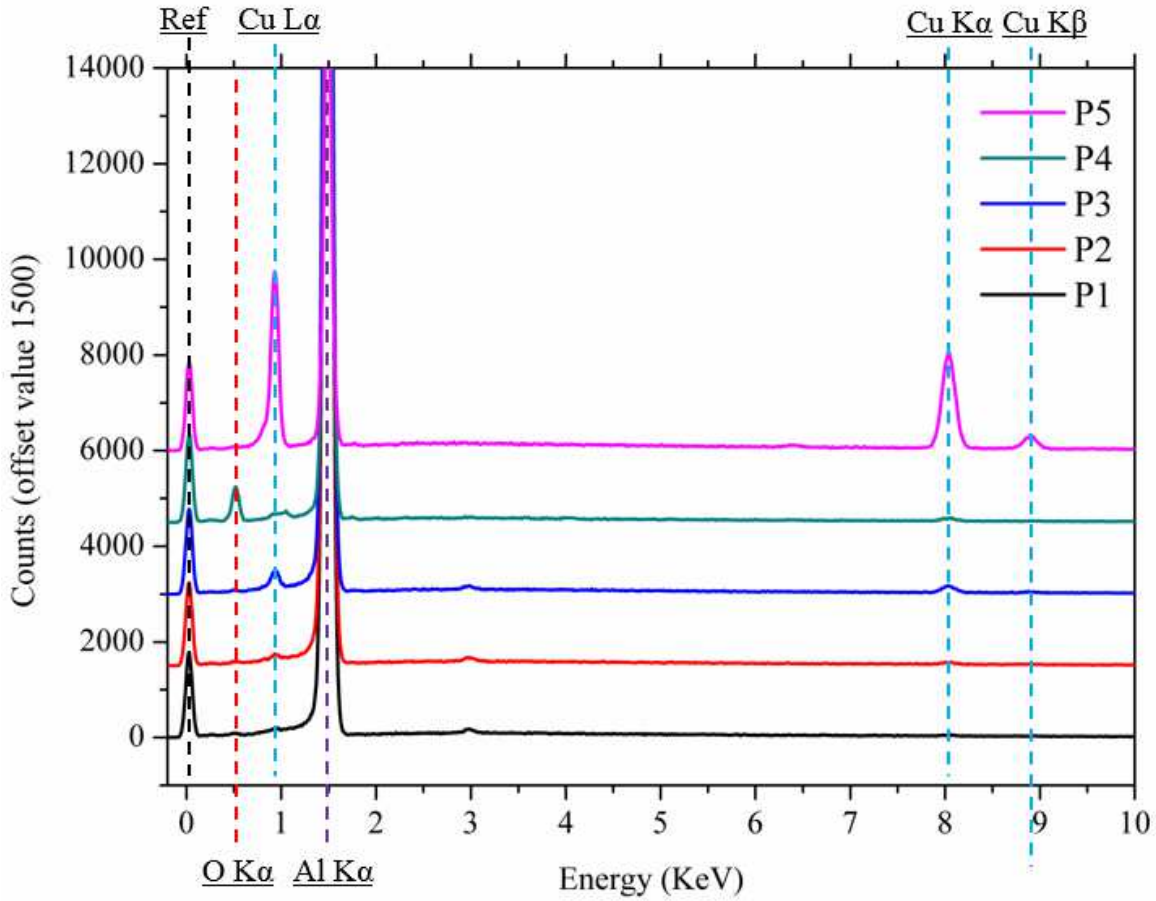

Figure 4.12 (b) – Measured EDX spectra from the positions shown in Figure 4.12 (a).

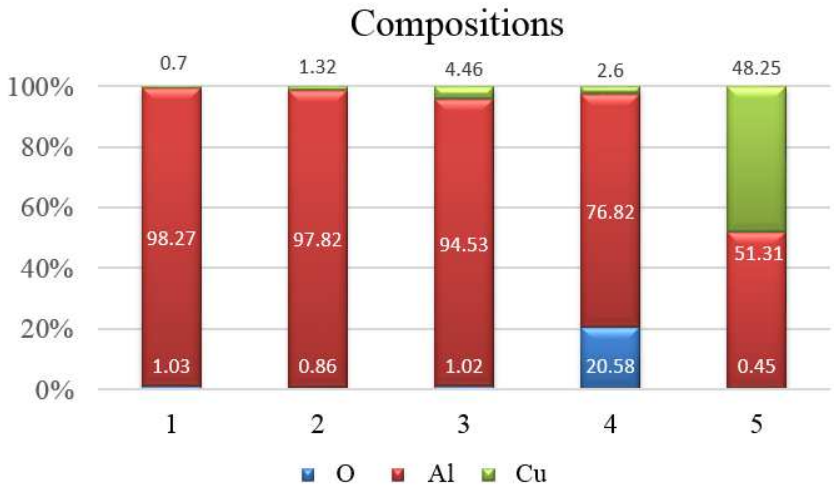

Figure 4.12 (c) – Quantified weight percentage results of the EDX spectra shown in Figure 4.12 (b).

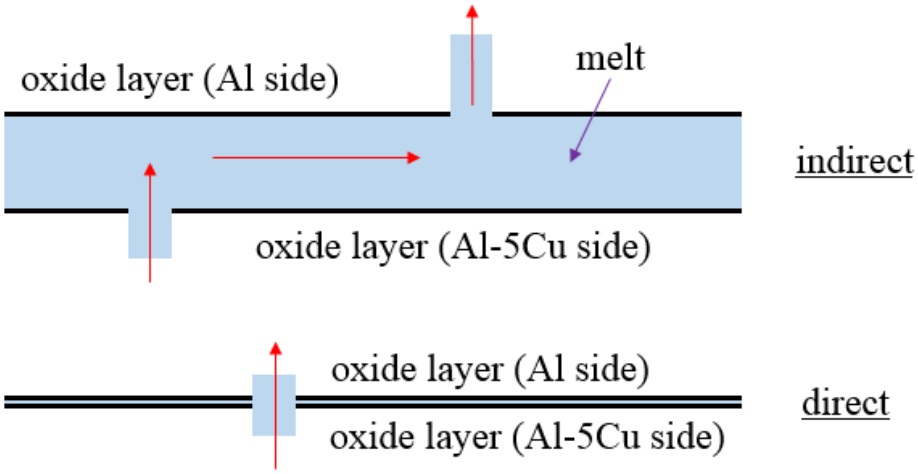

Figure 4.13 – Diagram illustrating a possible indirect way of metallic mixing in the stacked Al/Al-5Cu system.

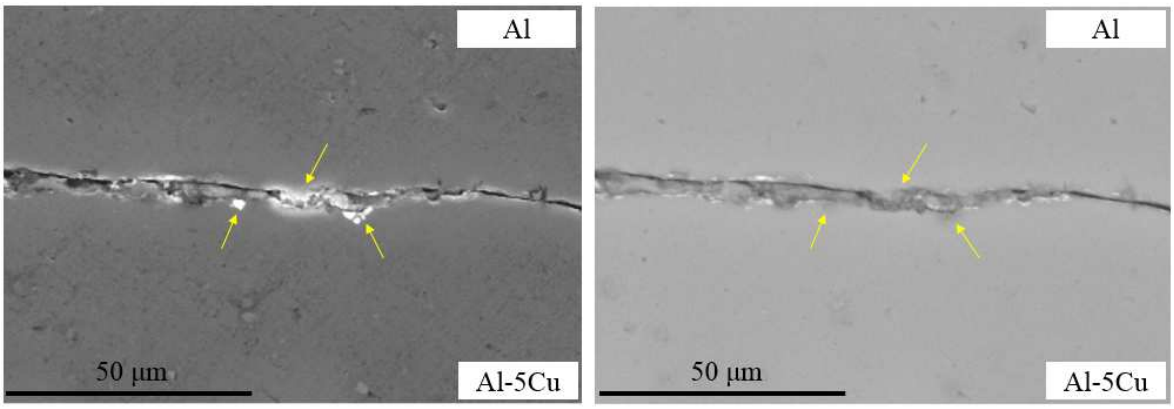

Figure 4.14 – A pair of SE (left) and BE (right) showing the oxide crystalline phases observed at the bond interface in the stacked sample *S-6*

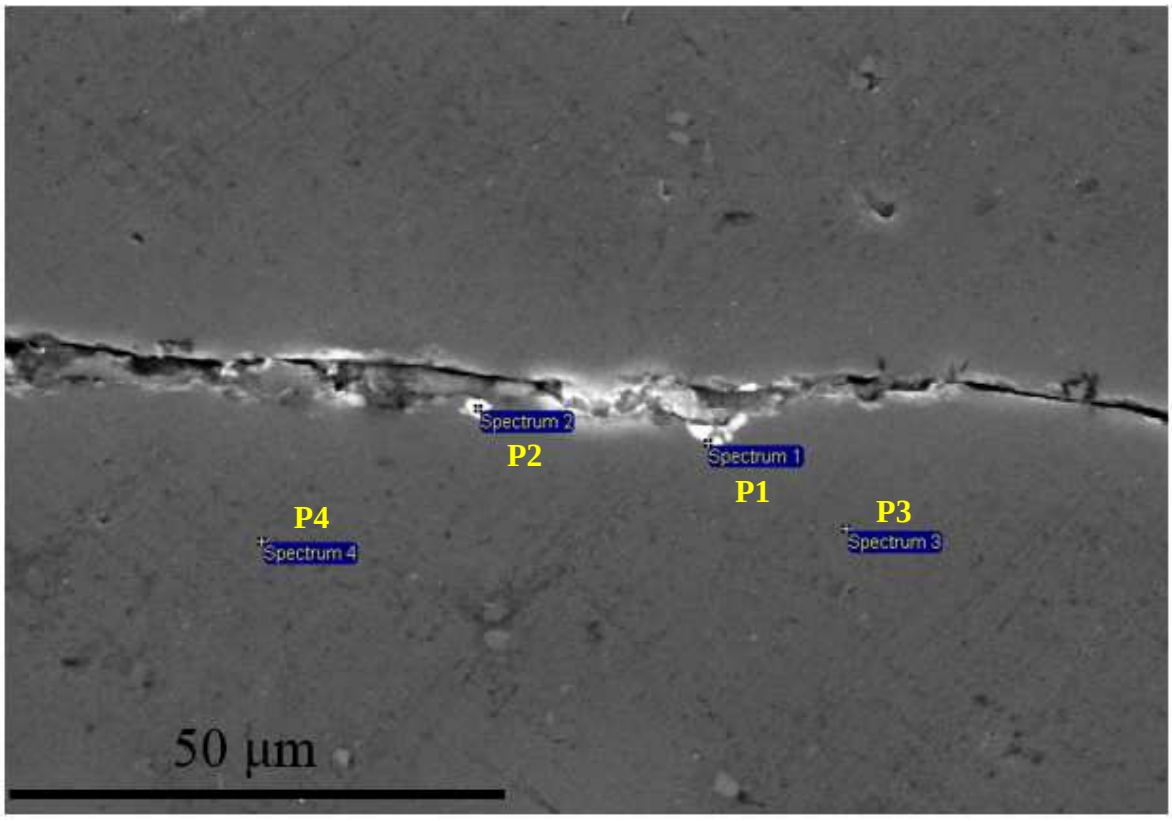

Figure 4.15 (a) – SE image showing the EDX analysis performed on the oxide phases at the bond interface and the matrix.

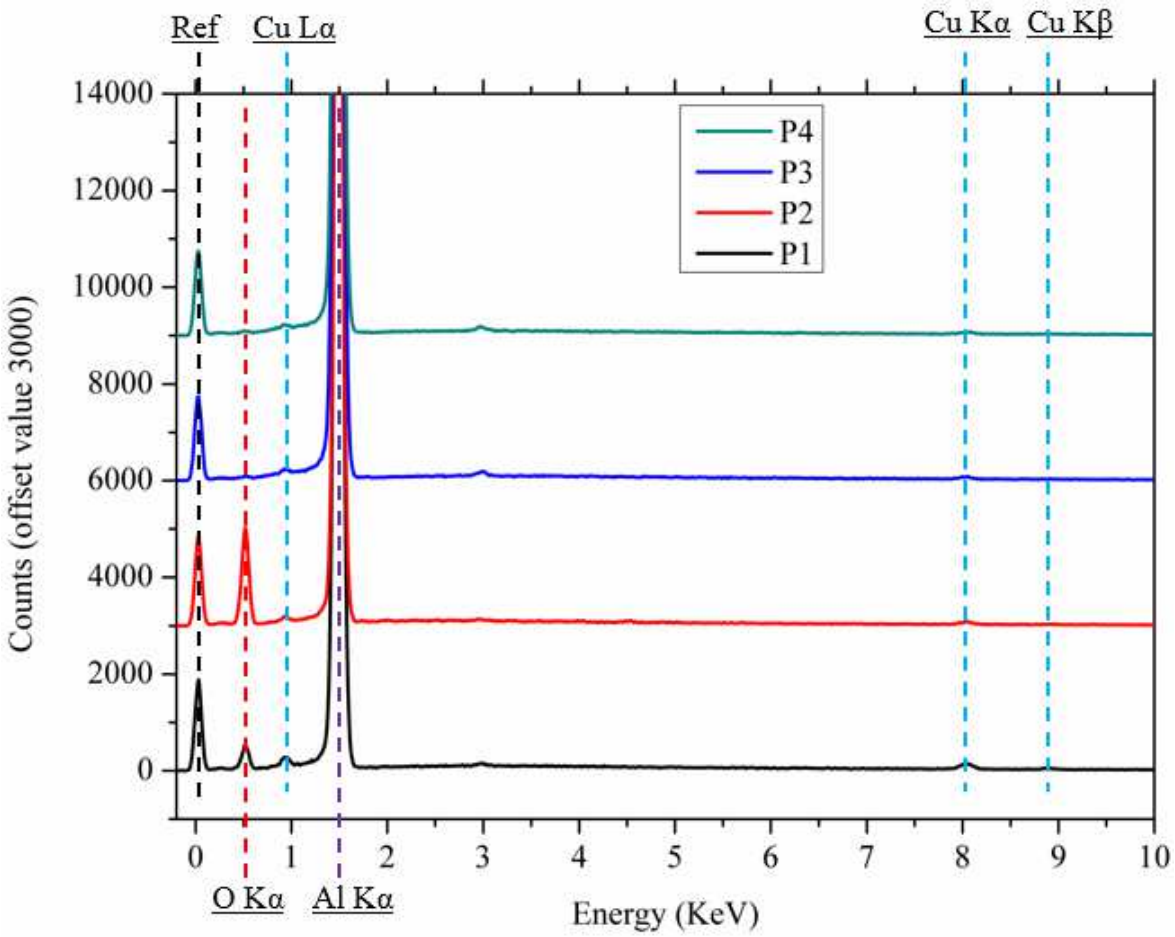

Figure 4.15 (b) – Measured EDX spectra from the positions shown in Figure 4.15 (a).

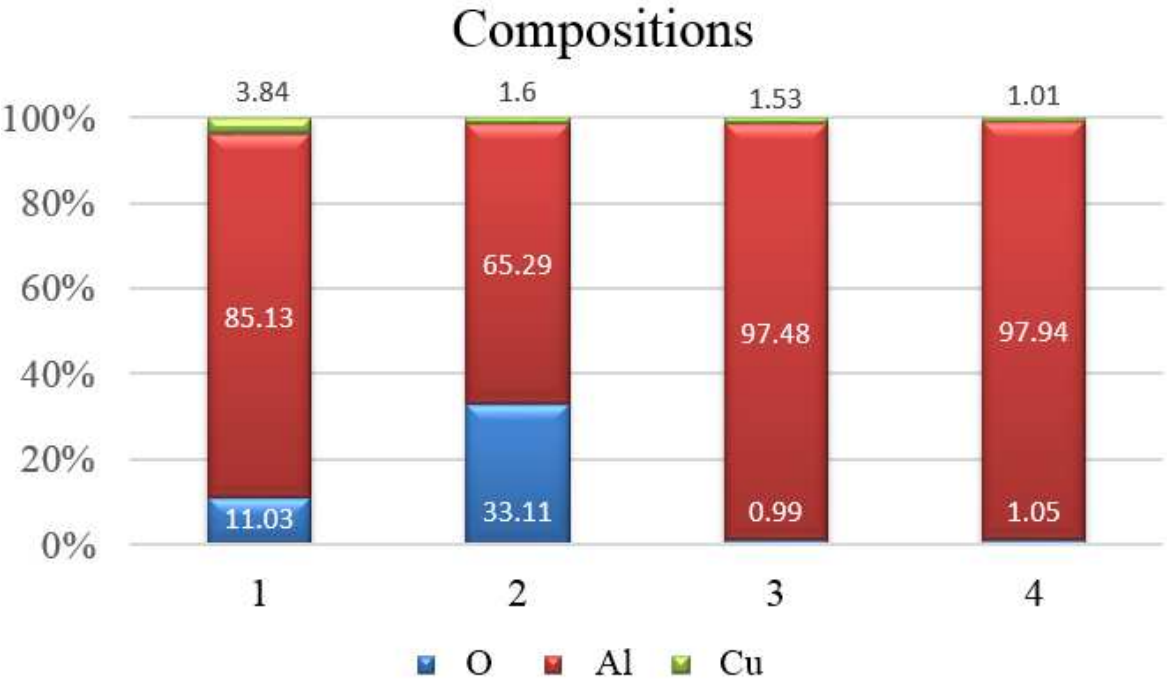

Figure 4.15 (c) – Quantified weight percentage results of the EDX spectra shown in Figure 4.15 (b).

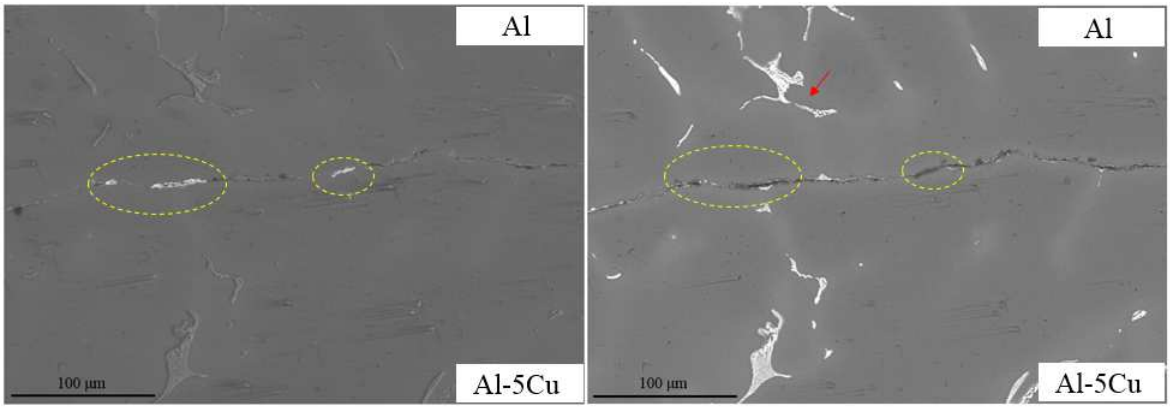

Figure 4.16 – A pair of SE and BE images showing the oxide crystalline phases observed at the bond interface in the stacked sample *S-24*.

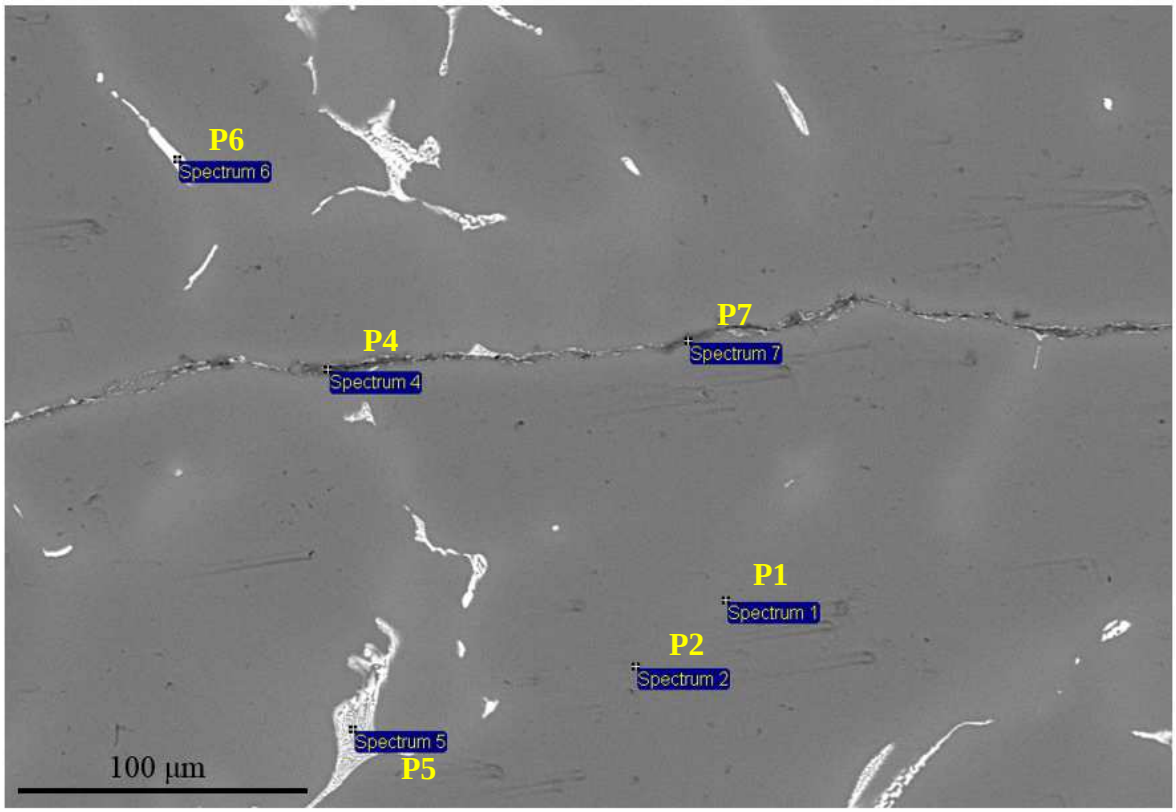

Figure 4.17 (a) – SE image showing the EDX analysis performed on the oxide phases at the bond interface, Cu-rich intermetallic phase and the matrix in sample *S-24*. (P3 was not successful because of some interruption during the experiments…)

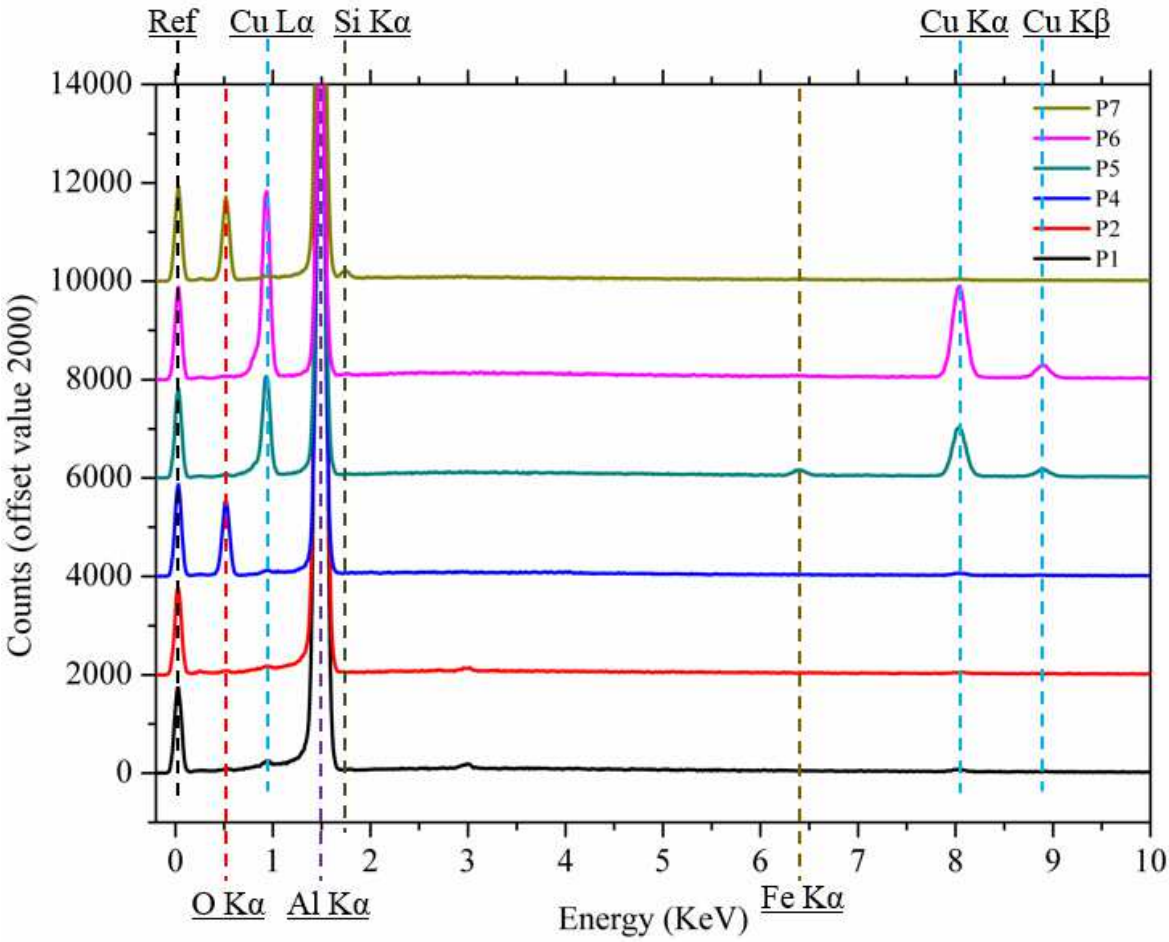

Figure 4.17 (b) – Measured EDX spectra at the points shown in Figure 4.17 (a). The quantified EDX results in terms of atomic ratio are P1 - $Al_{99.23}Cu_{0.67}$; P2 - $Al_{99.61}Cu_{0.39}$; P4 - $Al_2O_{2.04}$; P5 - $CuAl_{4.51}$; P6 - $CuAl_{2.12}$; P7 - $Al_2O_{2.05}$.

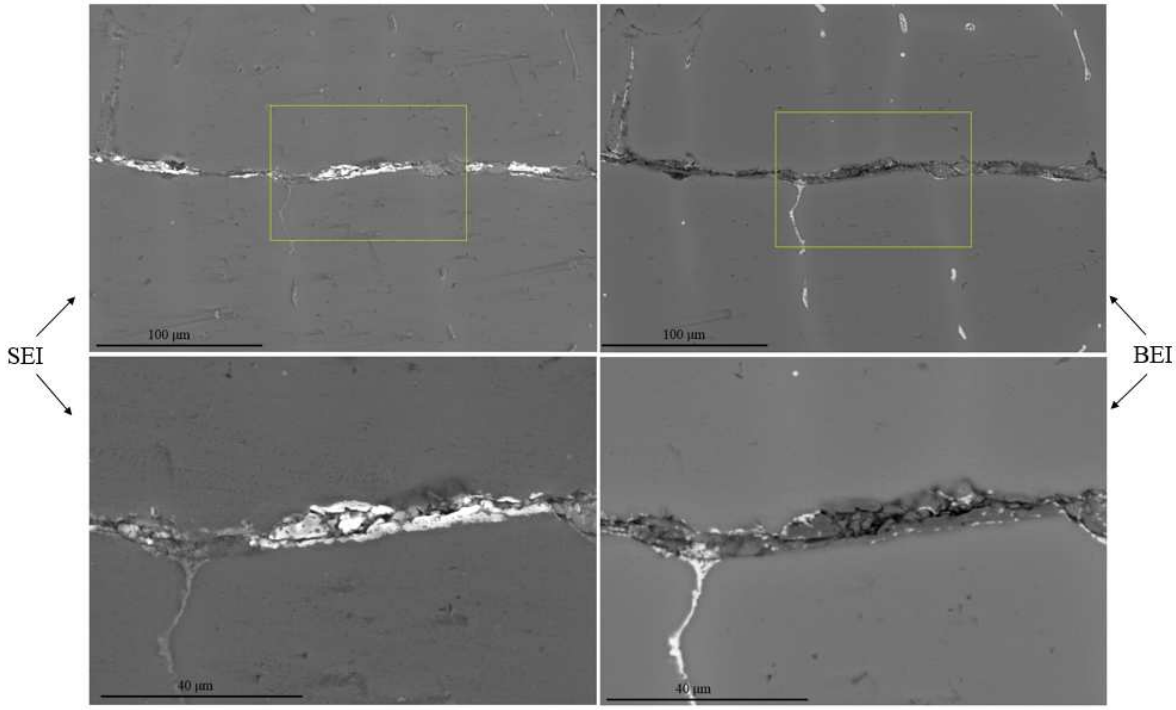

Figure 4.18 – Two pairs of SE and BE images showing the oxide crystalline phases observed at the bond interface in the stacked sample *S-24*.

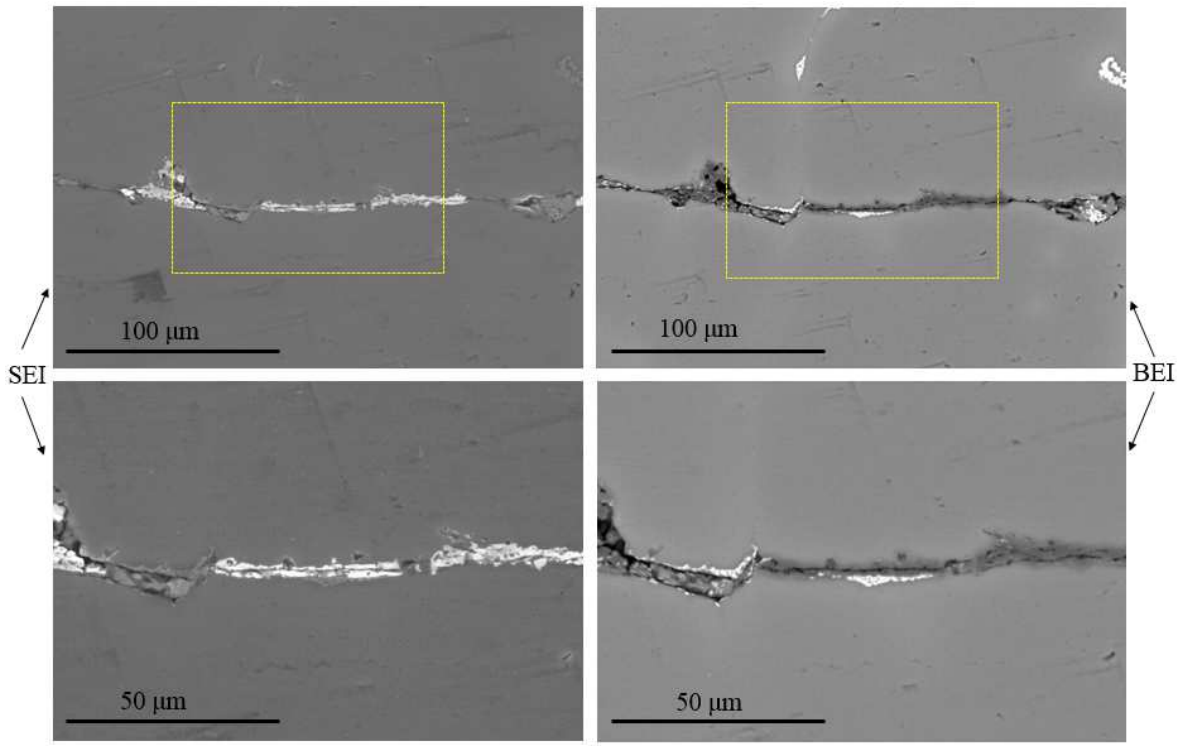

Figure 4.19 – Two pairs of SE and BE images showing the oxide crystalline phases observed at the bond interface. Oxides have formed on both the Al and Al-5Cu sides of the stacked sample *S-24*.

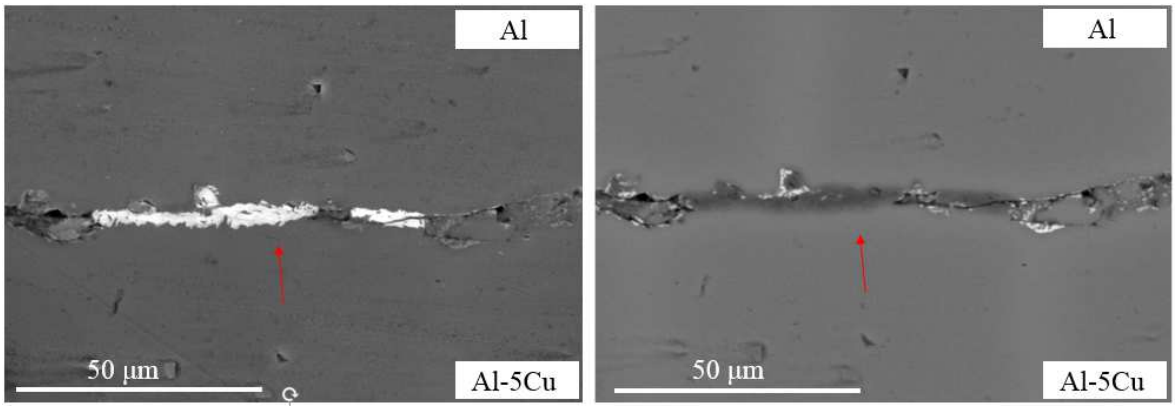

Figure 4.20 – A pair of SE and BE showing the presence of crystalline-like oxide phases at the bond interface, Al and Al-5Cu are bonded through the healing of the oxide films (sample *S-24*).

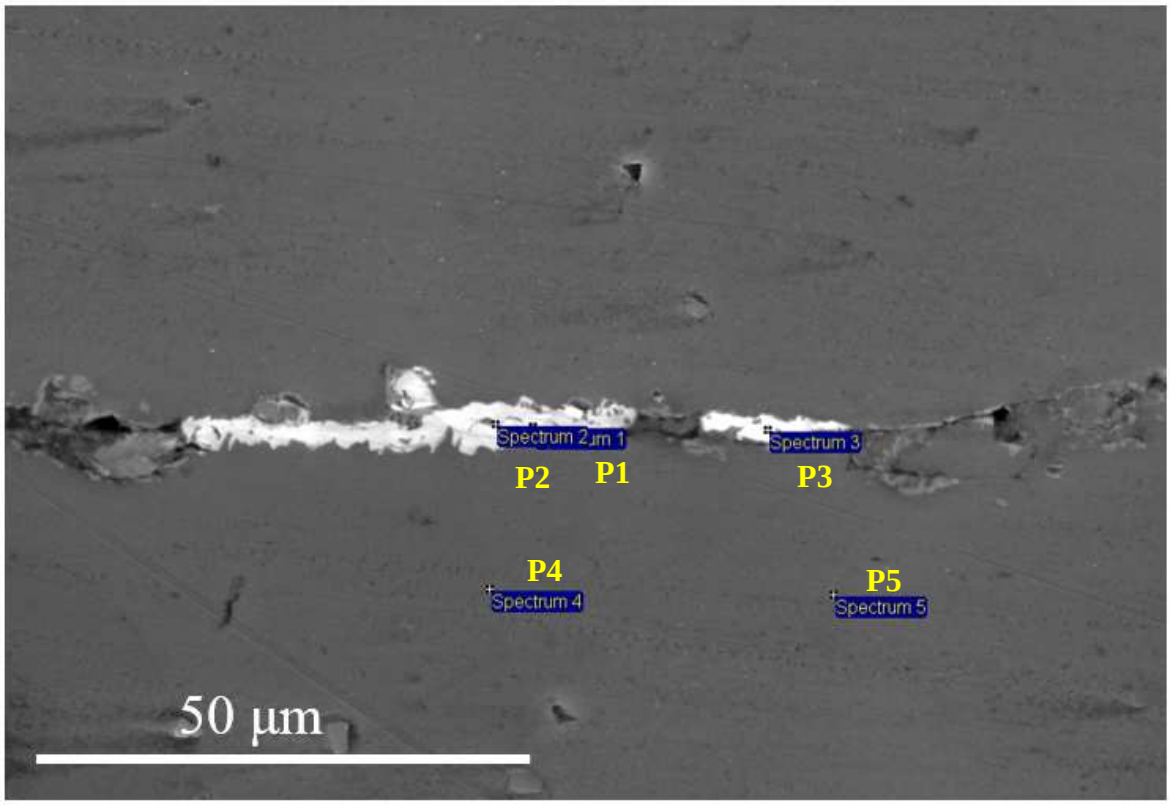

Figure 4.21 (a) – SE image showing the EDX analysis performed at the location of crystalline-like oxide phases and on the Al-5Cu side away from the interface (sample *S-24*).

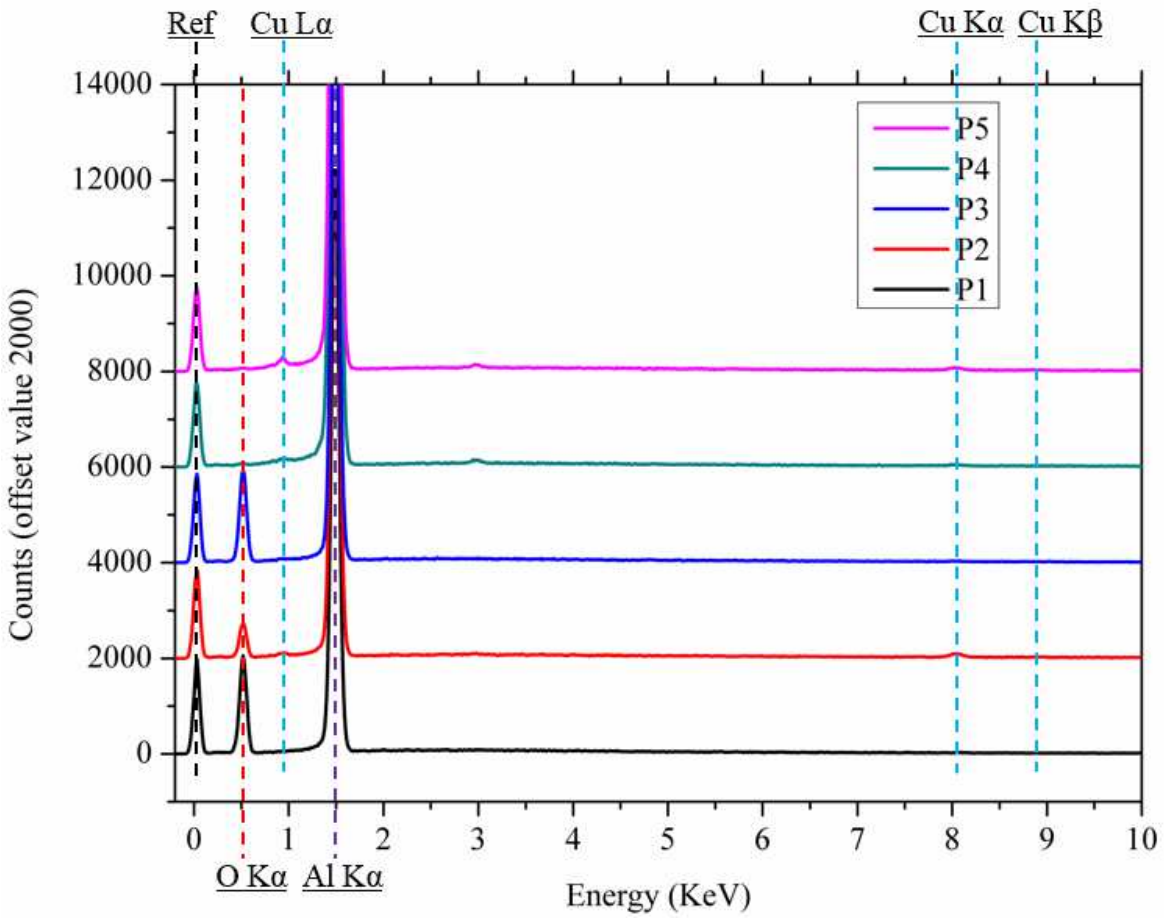

Figure 4.21 (b) – Measured EDX spectra at the points shown in Figure 4.21 (a) and the quantified EDX results in terms of atomic ratio are P1 - $Al_2O_{2.51}$, P2 - $Al_2O_{1.32}Cu_{0.04}$, P3 - $Al_2O_{2.31}$, P4 - $Al_{99.12}Cu_{0.88}$, P5 - $Al_{98.73}Cu_{1.27}$.

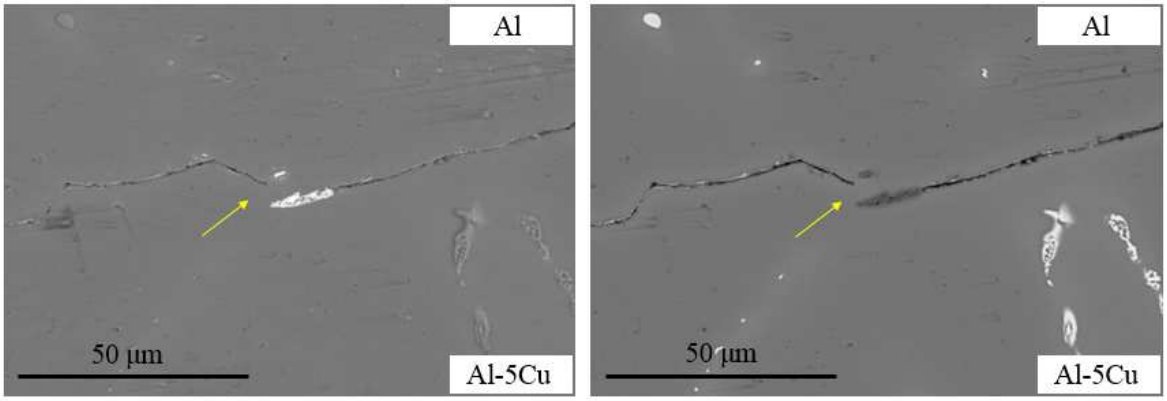

Figure 4.22 – A pair of SE and BE images showing the presence of crystalline-like oxide phases at the bond interface and the bi-film layer fractured at the edge of the oxide (sample *S-24*)

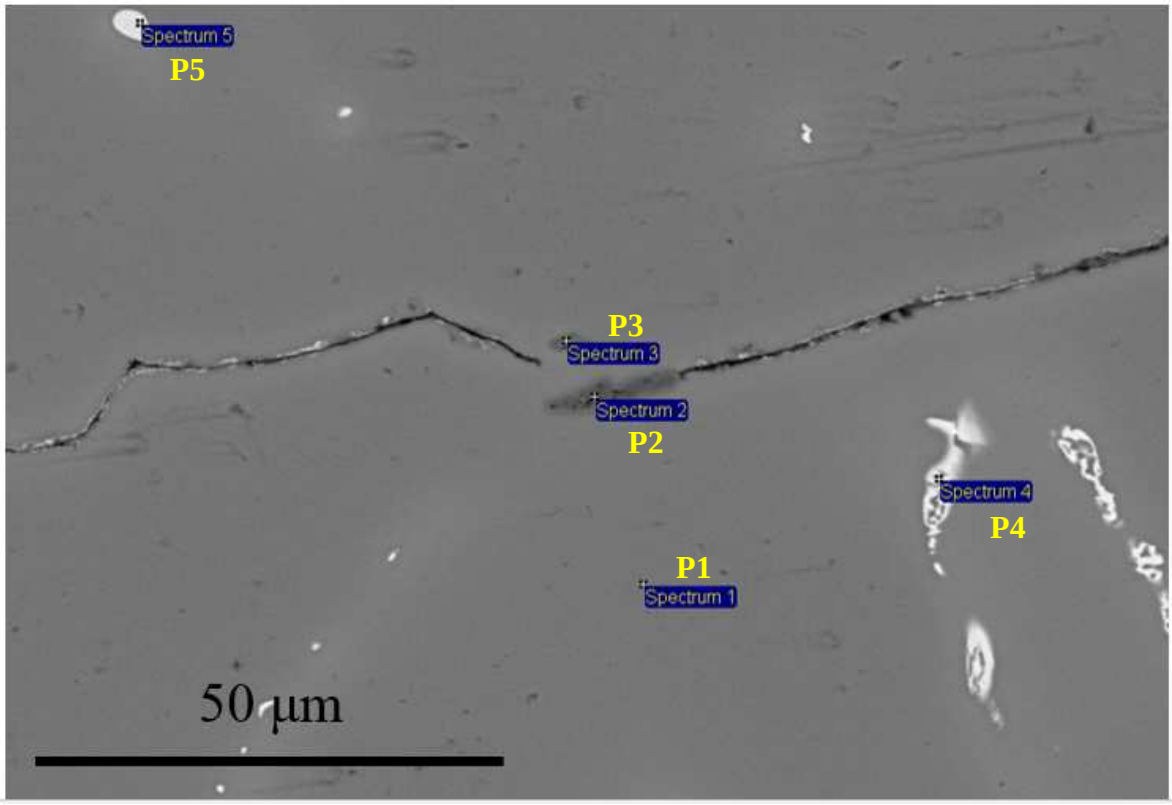

Figure 4.23 (a) – SE image showing the EDX point analysis performed at the interested features (sample *S-24*)

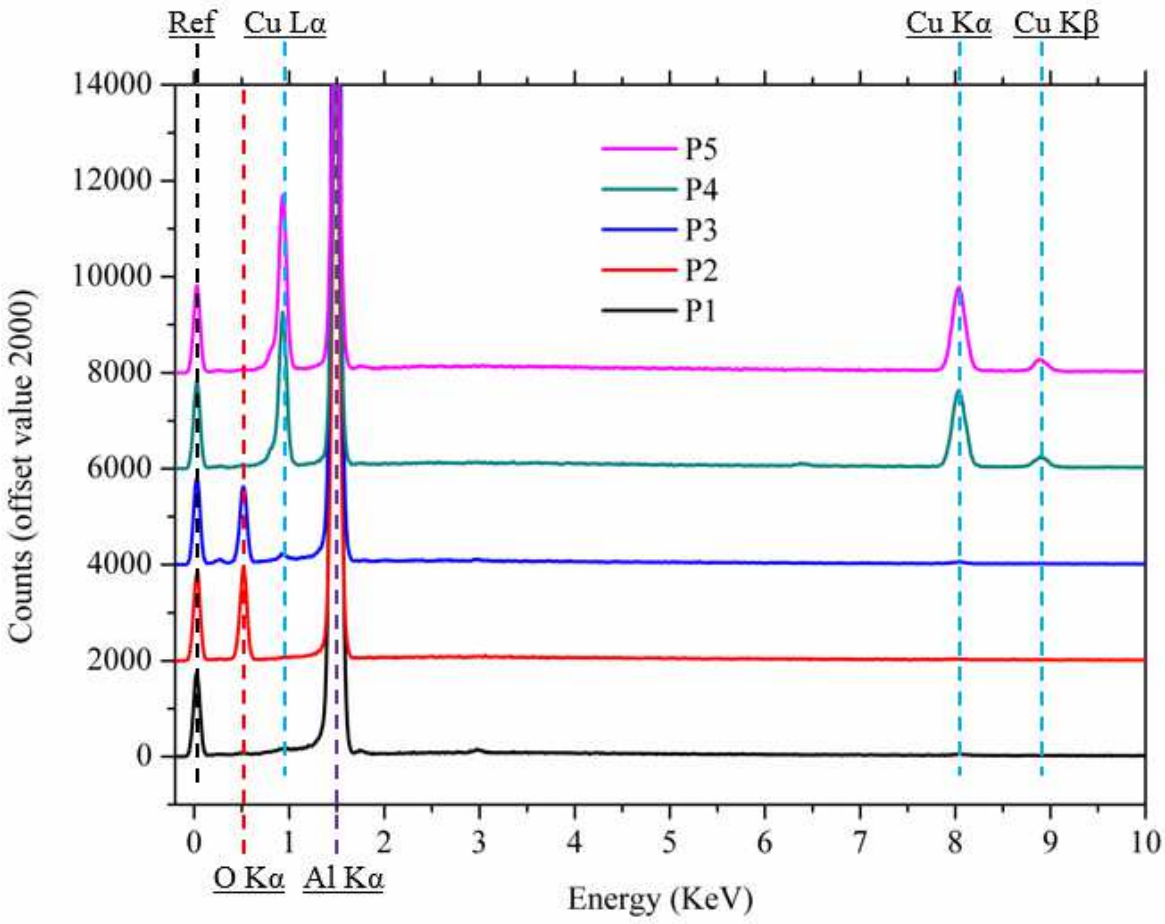

Figure 4.23 (b) – Measured EDX spectra at the points shown in Figure 4.23 (a). The quantified EDX results in terms of atomic ratio are P1 - $Al_{99.82}Cu_{0.18}$, P2 - $Al_2O_{2.29}$, P3 - $Al_2O_{1.55}$, P4 - $CuAl_{2.68}$, P5 - $CuAl_{2.47}$.

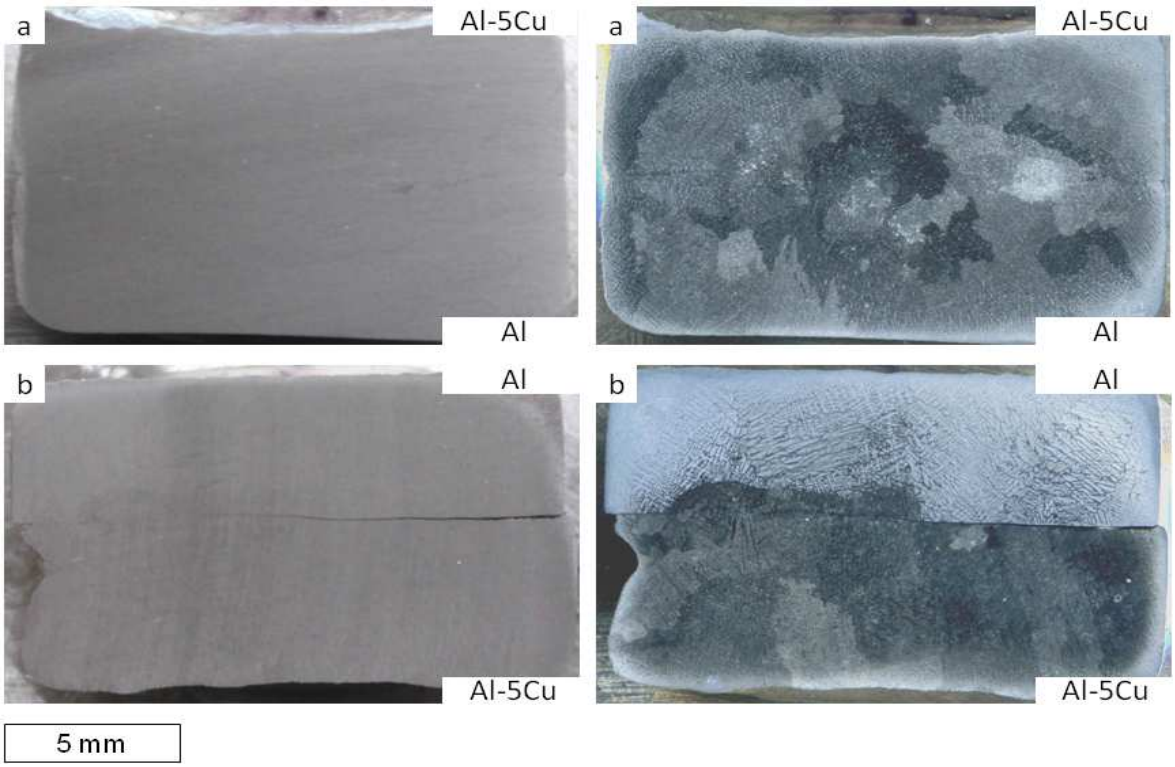

Figure 4.24 – Pairs of macrographs showing the cross section structure of the stacked Al-5Cu/Al (a) and the stacked Al/Al-5Cu (b). Both of the stacks were held at 750°C for 1h.

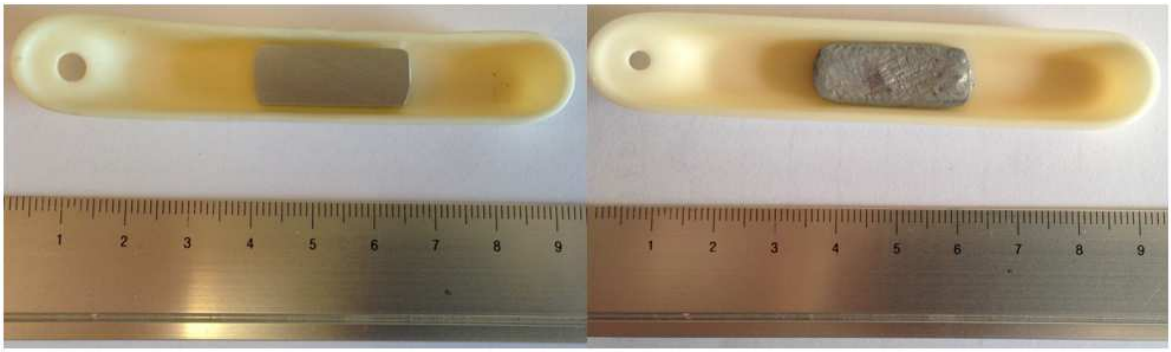

Figure 4.25 – Macrographs showing the outside appearance of an Al slug before (left) and after (right) melting and re-solidifying.

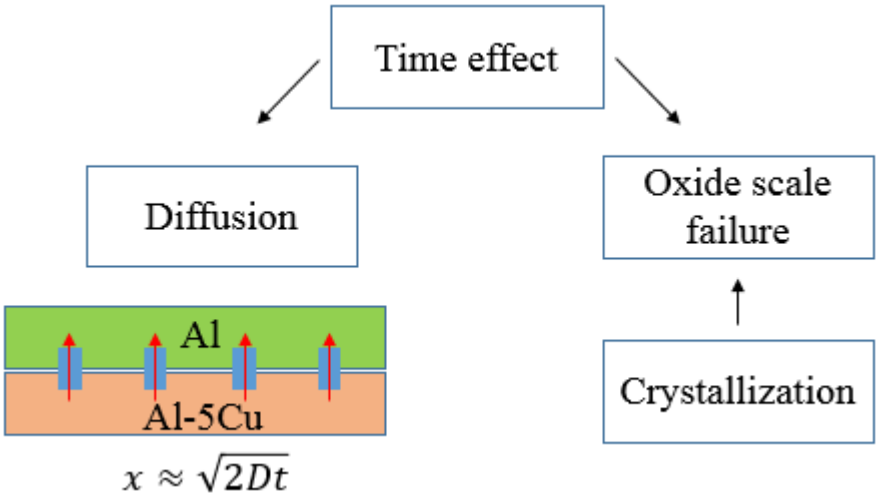

Figure 4.26 – Diagram showing the two main processes occurring during the isothermal holding stage in the stacking approach: diffusion causes the upward flow of Al-5Cu melt through easy channels and the diffusion distance is time-dependent. Oxide phase crystallization causes the failure of oxide scale and the protectiveness of the *bi-film* barrier layer is reduced as time goes by.

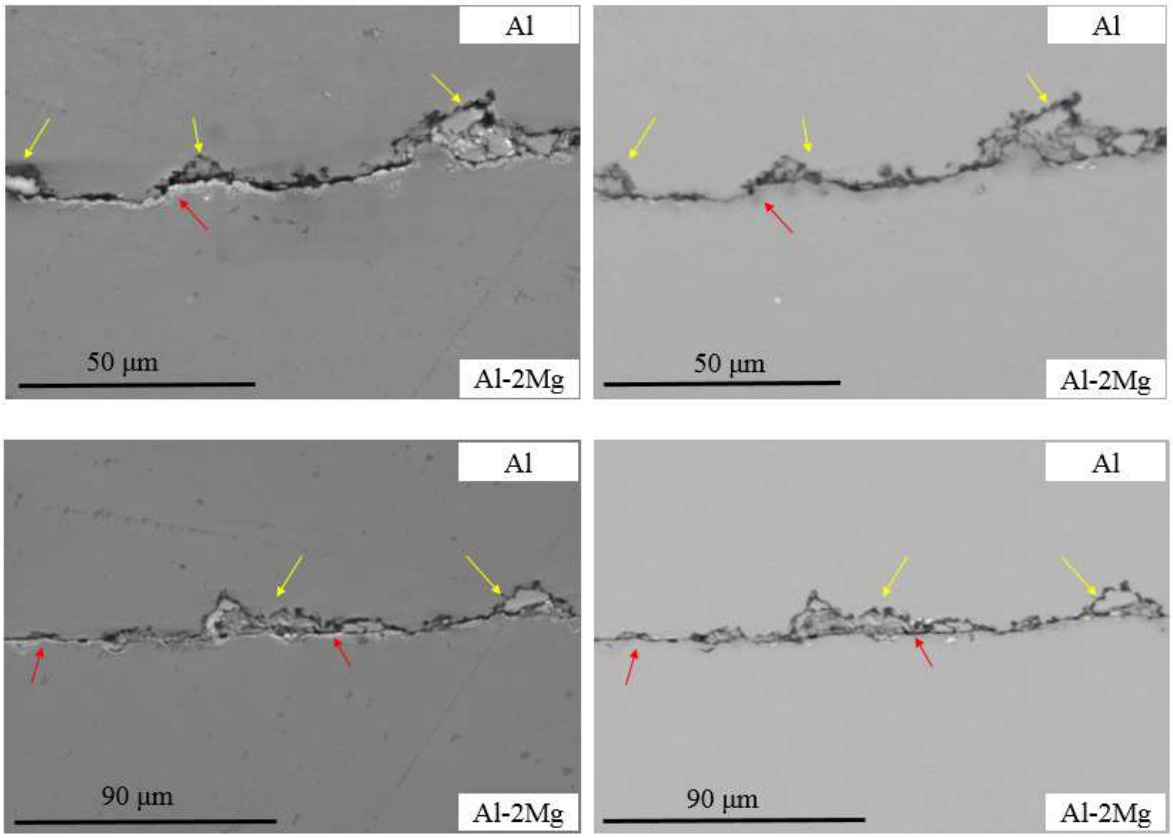

Figure 4.27 – Two pairs of SE and BE images showing the bond interface microstructure of the stacked Al/Al-2Mg sample *M-1*.

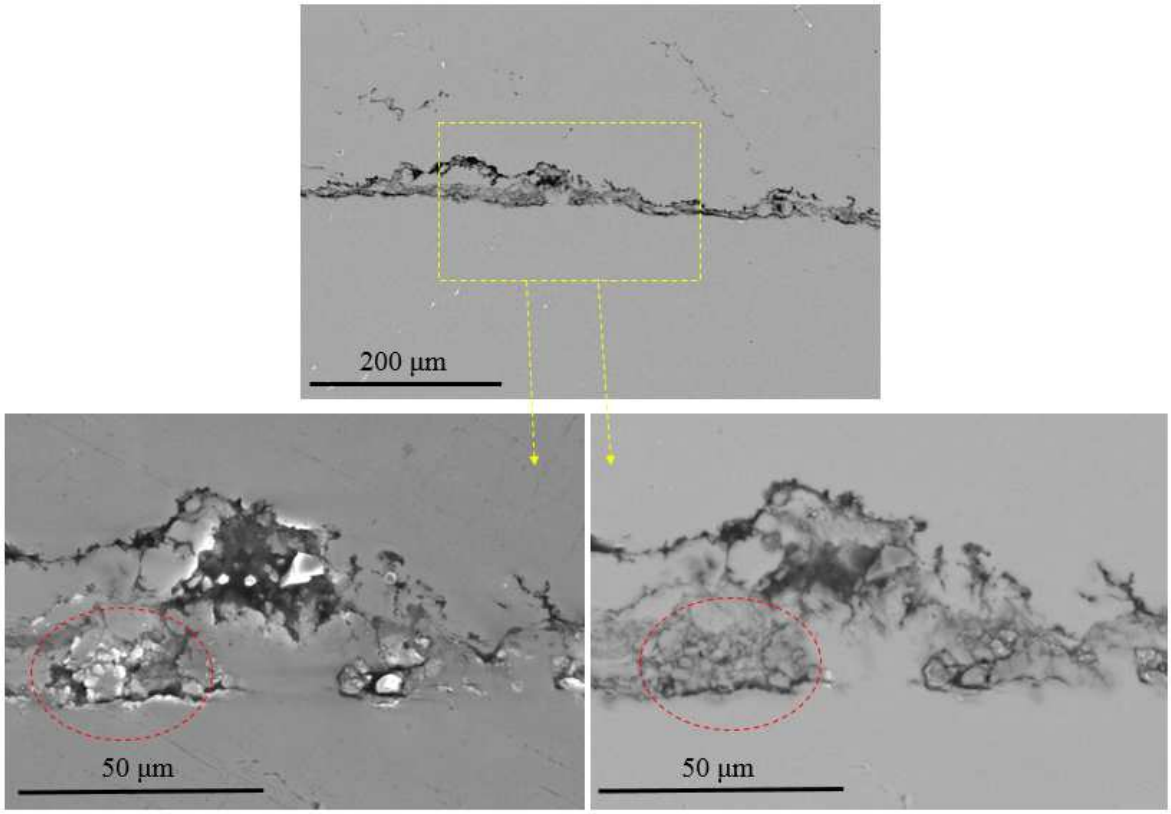

Figure 4.28 – BE image at low magnification and a pair of SE and BE images taken at high magnification showing the rough interface morphology observed in the stacked Al/Al-2Mg sample *M-1*.

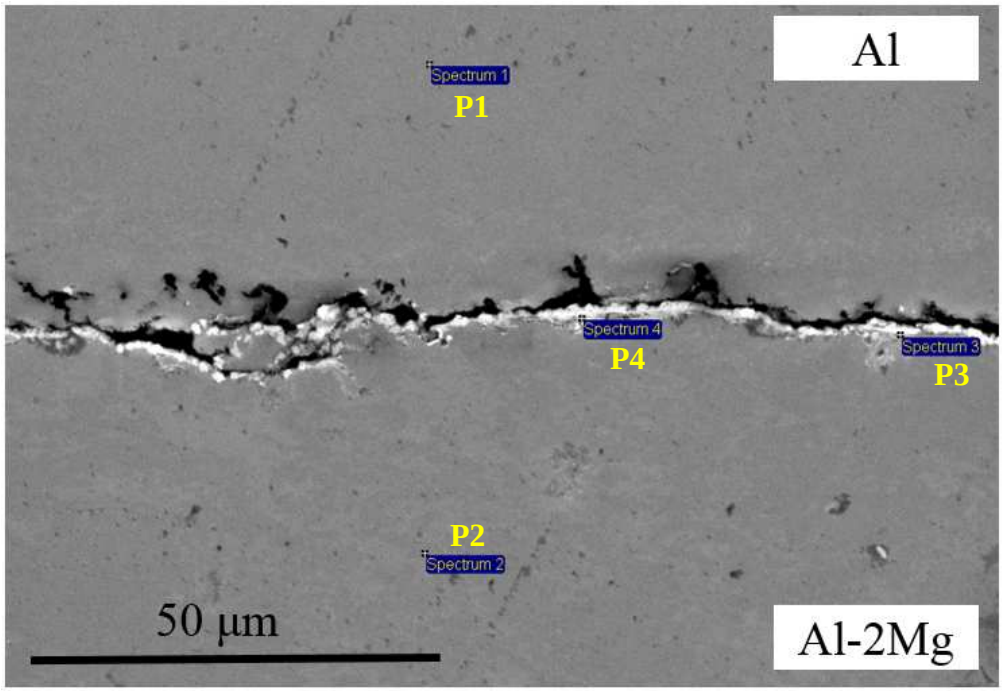

Figure 4.29 (a) – SE image showing the presence of oxide-like particles at the bond interface and EDX point analysis was performed.

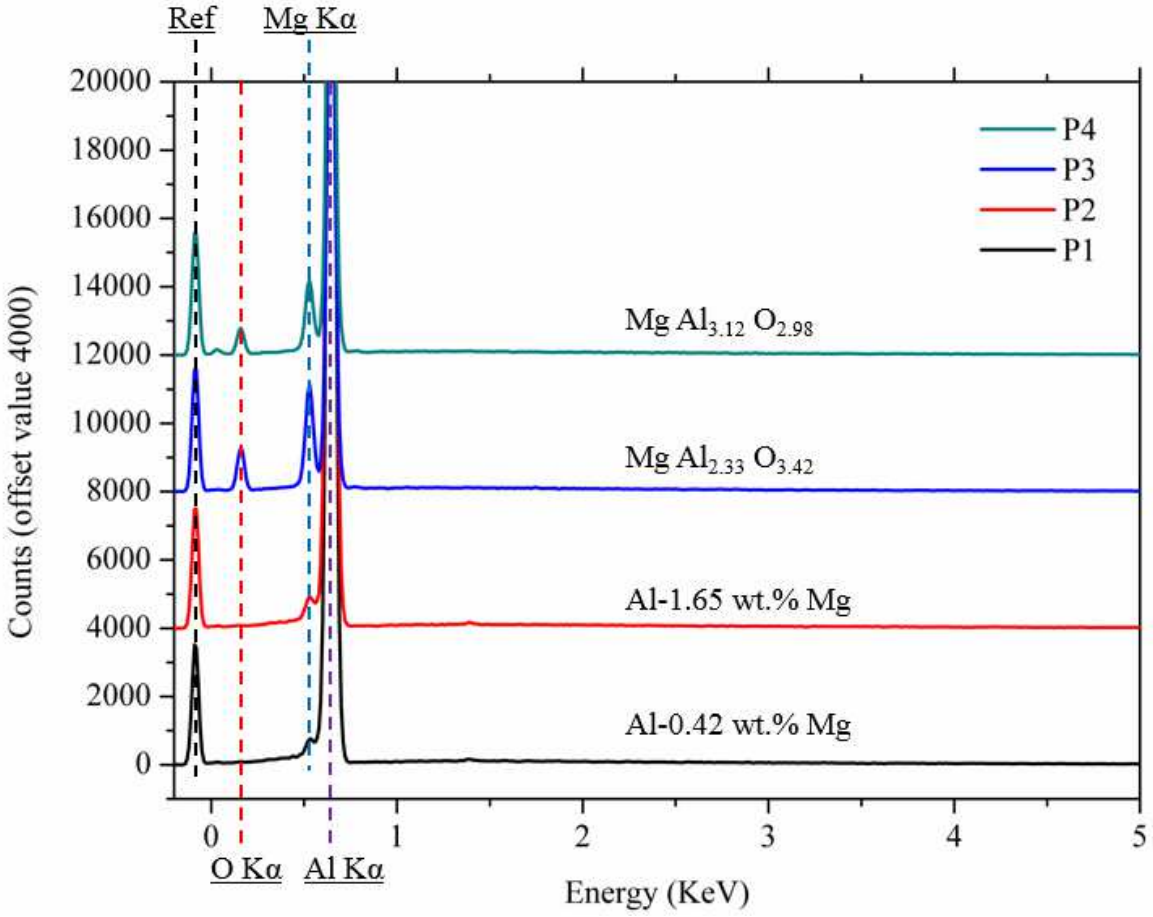

Figure 4.29 (b) – Measured EDX spectra and quantified results in terms of atomic ratio (P3 and P4) and weight ratio (P1 and P2).

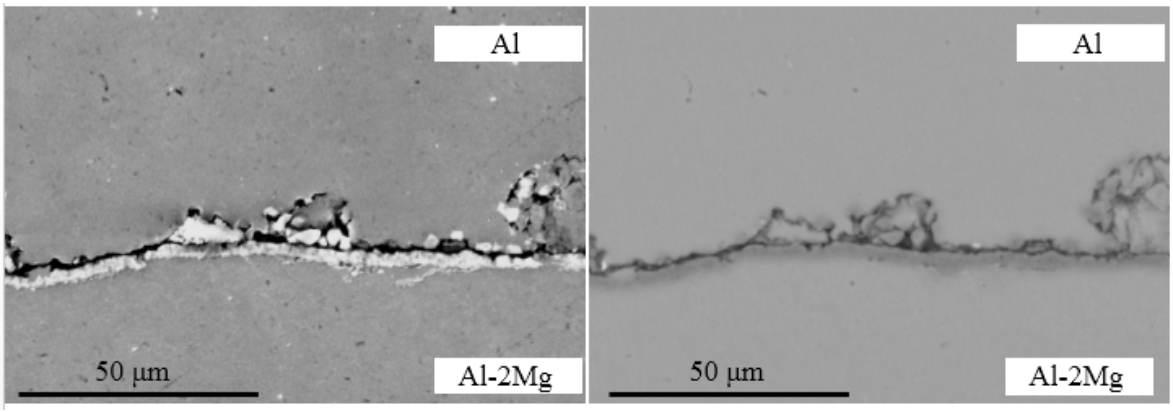

Figure 4.30 – A pair of SE and BE images showing the bond interface morphology observed in the stacked Al/Al-2Mg (sample *M-6*).

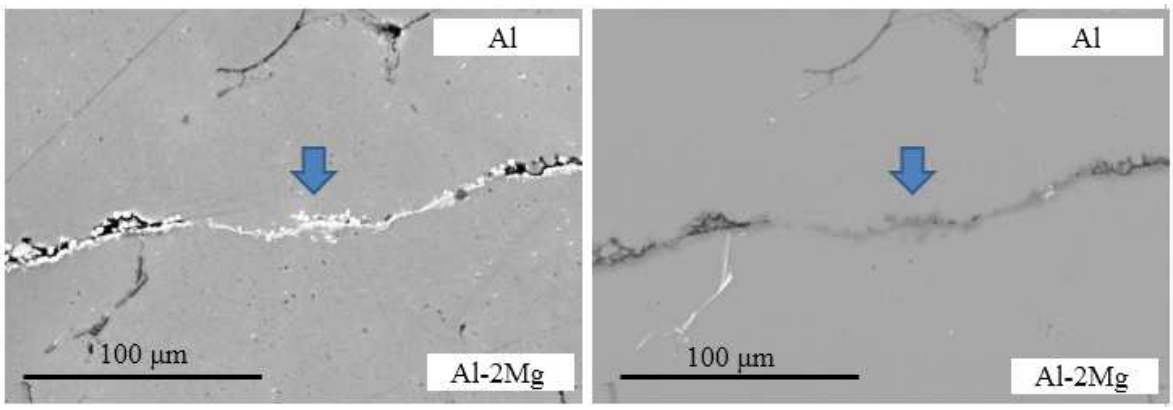

Figure 4.31 – A pair of SE and BE images showing the healing of the bi-film layer at the bond interface (sample *M-6*).

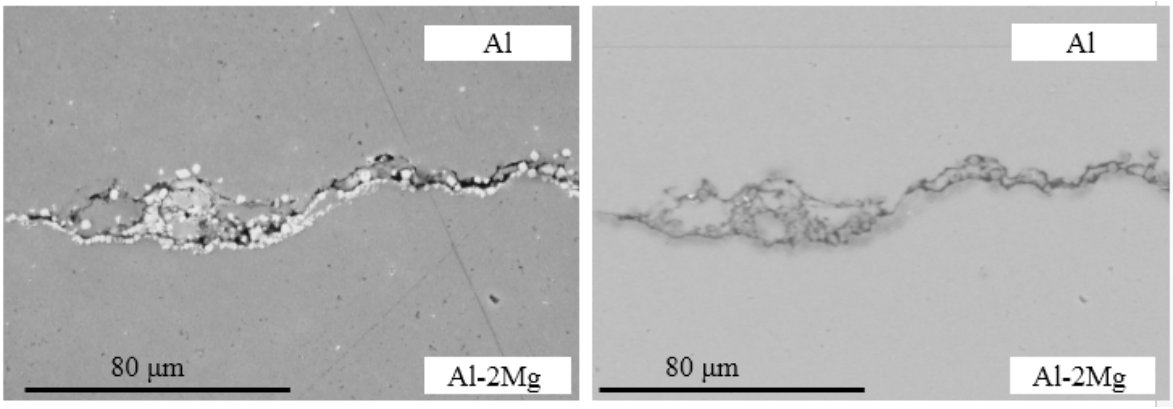

Figure 4.32 – A pair of SE and BE images showing the scattered oxide phases along the non-planar bond interface (sample *M-6*).

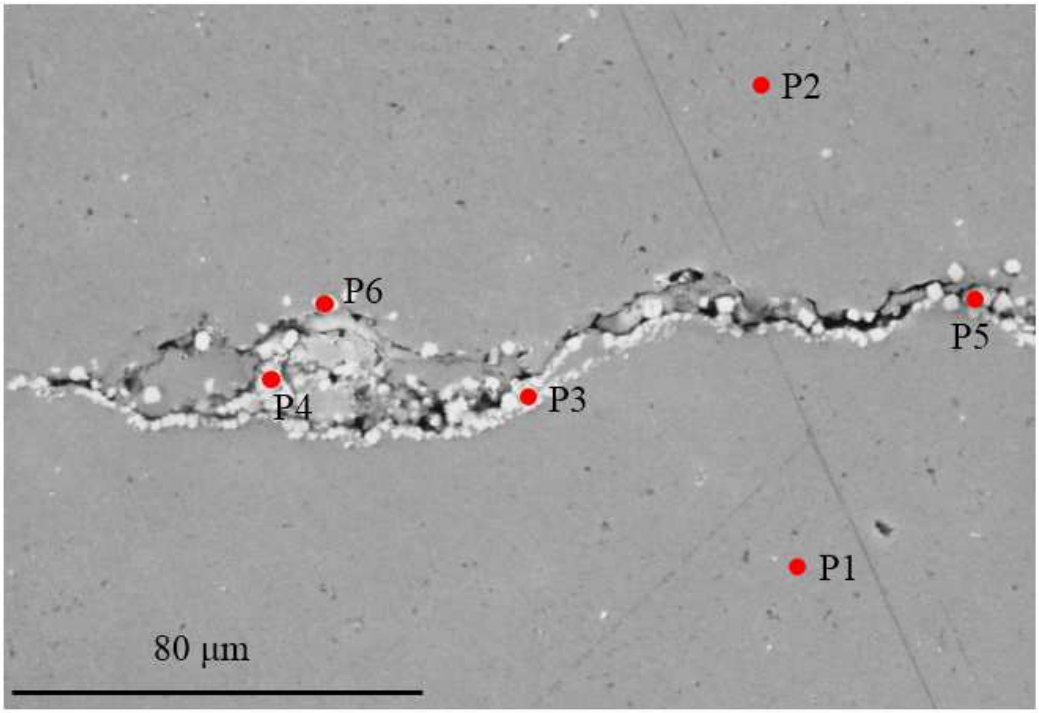

Figure 4.33 (a) – SE image showing the scattered oxide phases along the non-planar bond interface and EDX analysis was performed (sample M-6).

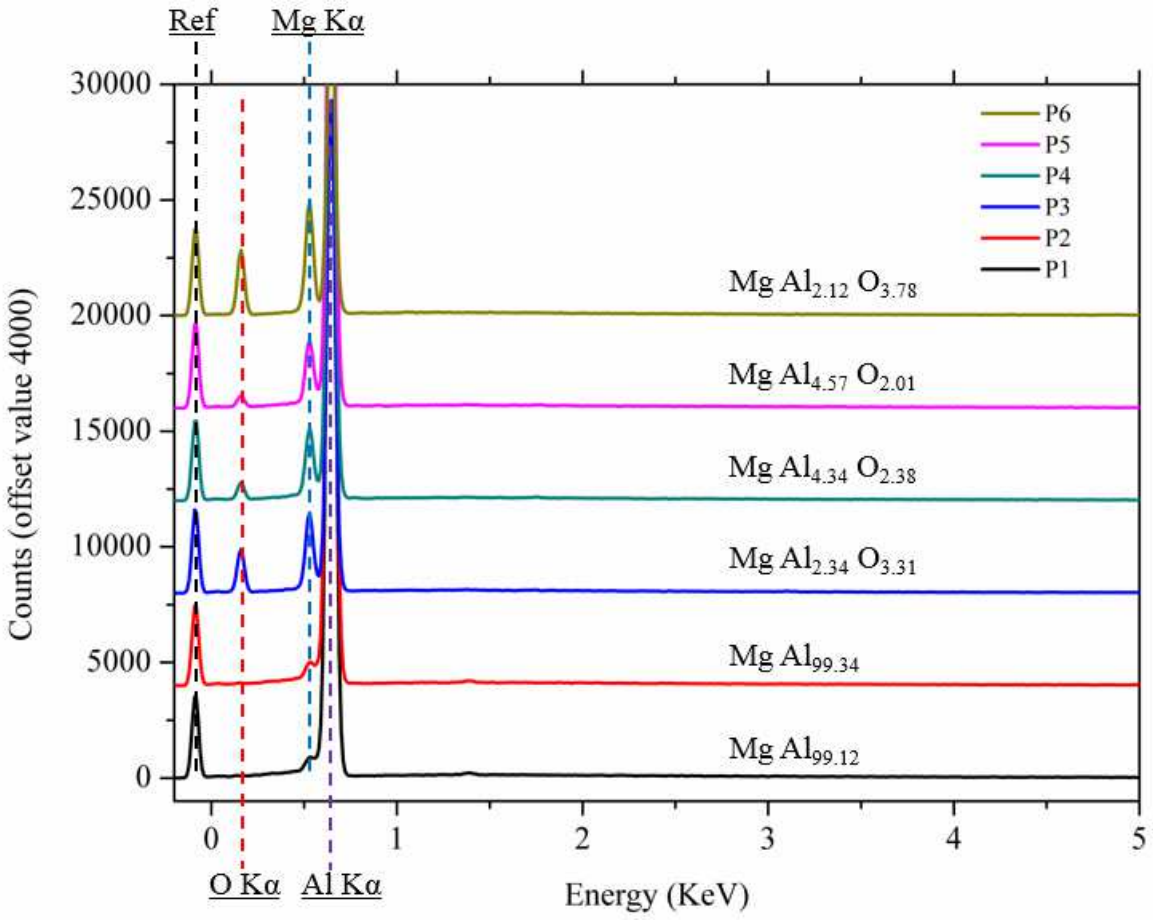

Figure 4.33 (b) – Measured EDX spectra (P1-P6 in Figure 4.33 (a)) and the quantified results in terms of atomic ratio.

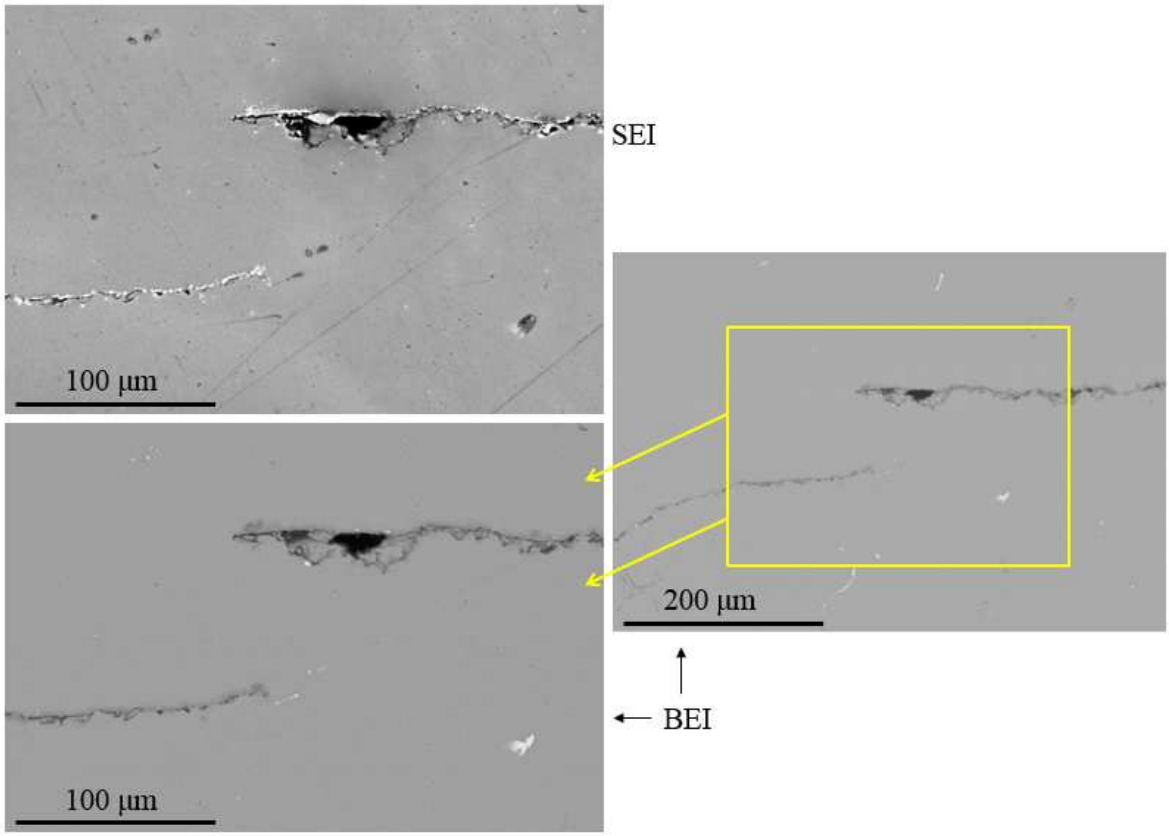

Figure 4.34 – SE and BE images showing the fracture of the bi-film layer leading to the direct metallic bonding between Al and Al-2Mg (sample *M-6*).

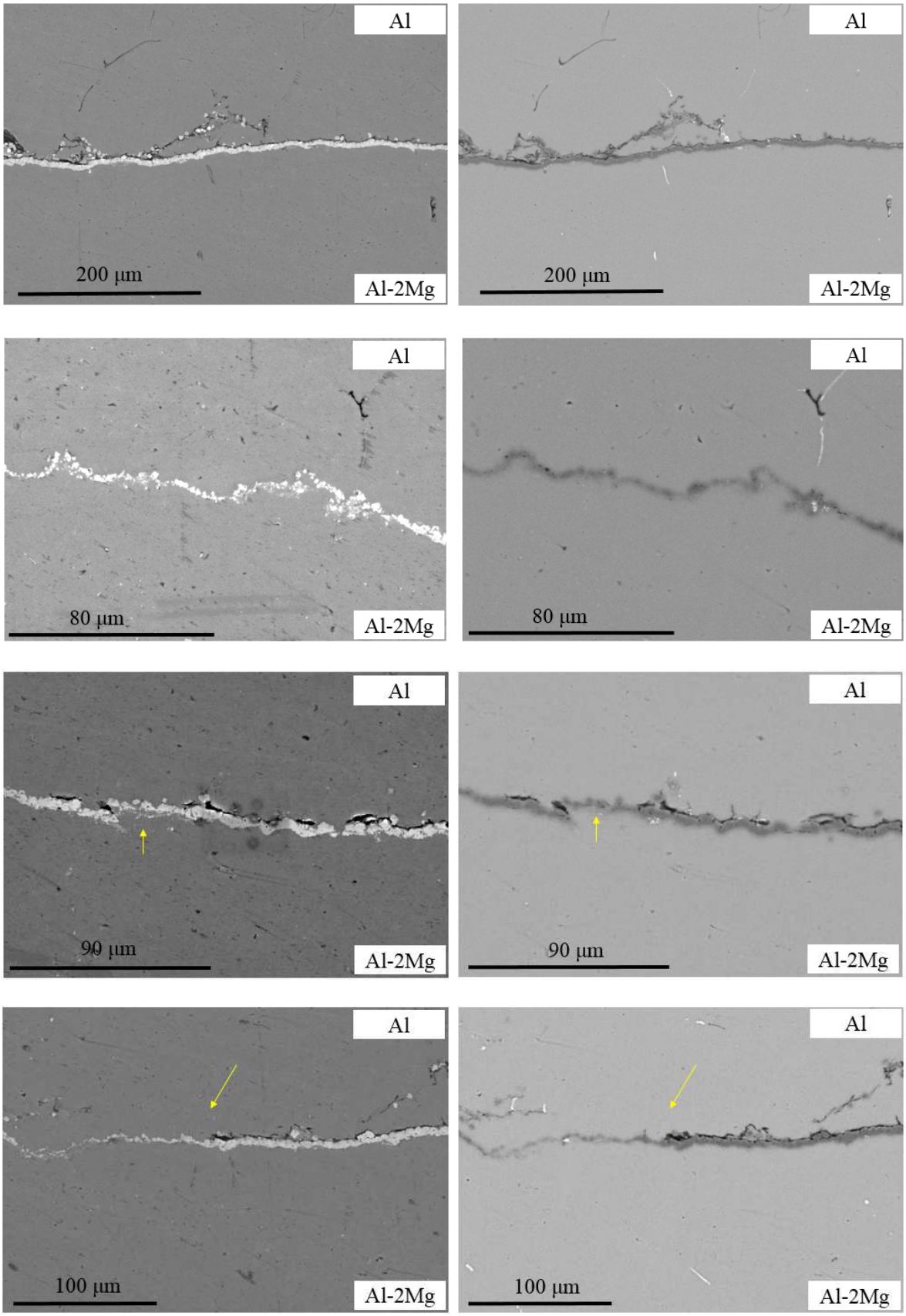

Figure 4.35 – Pairs of SE and BE images showing a thicker Mg-rich oxide layer on the Al-2Mg side and the complete healing of the bi-film layer in some places with the presence of scattered oxide particles (sample *M-24*).

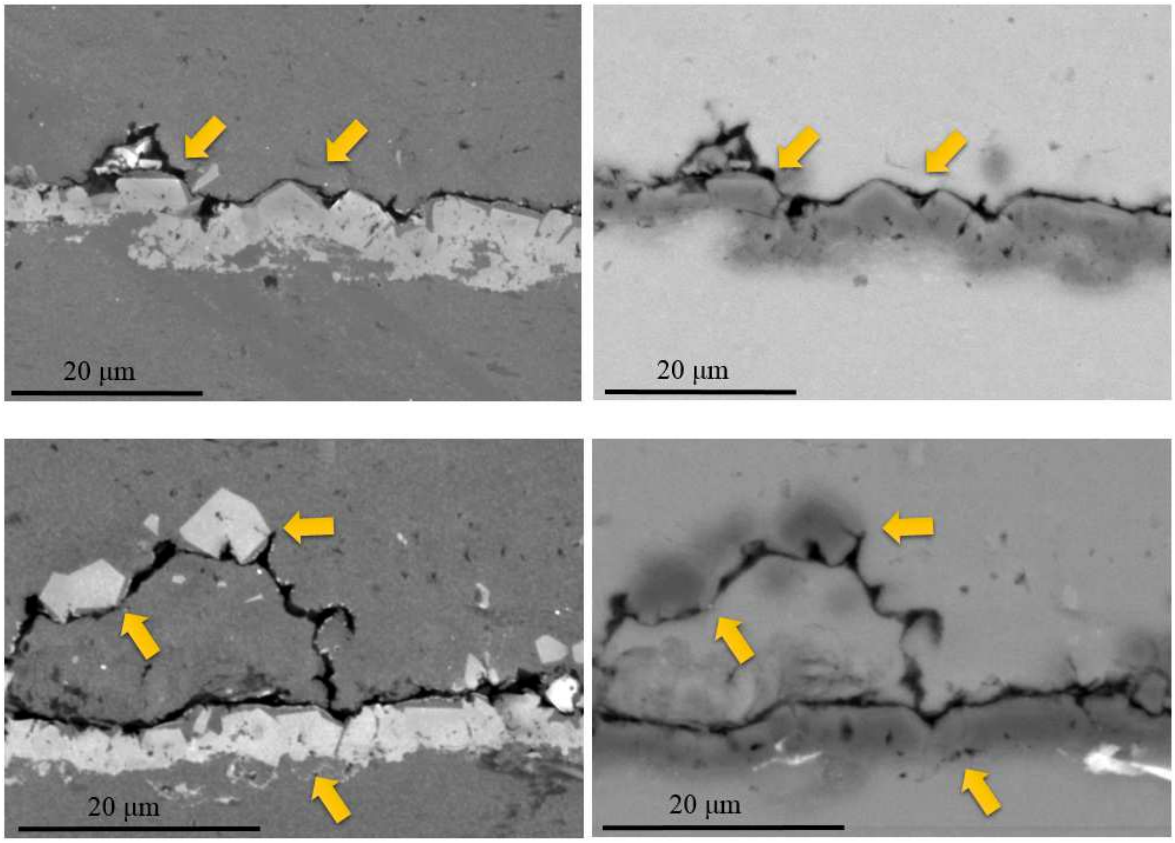

Figure 4.36 – Pairs of SE and BE images showing the facetted oxide particles at the bond interface. The oxide layer consisting of facetted oxide particles has a thickness of 2-3 µm (sample *M-24*).

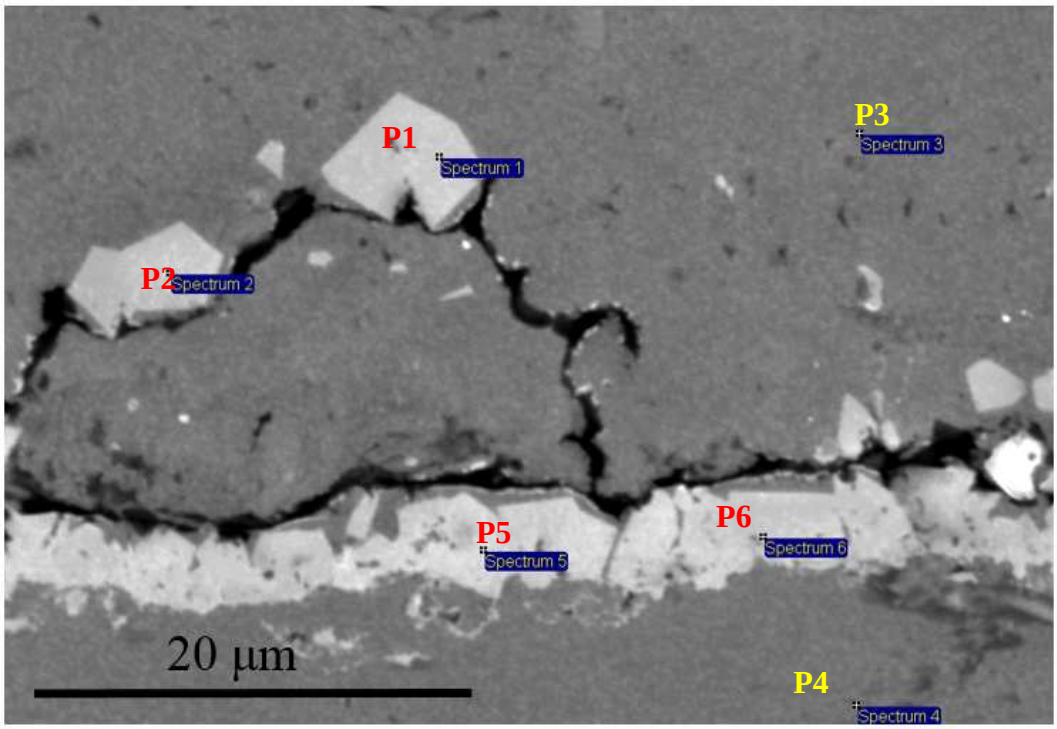

Figure 4.37 (a) – SE image showing the facetted $MgAl_2O_4$-like oxide crystals at the bond interface and an $MgAl_2O_4$-like layer on the Al-2Mg side. EDX point analysis was performed on these features (sample *M-24*).

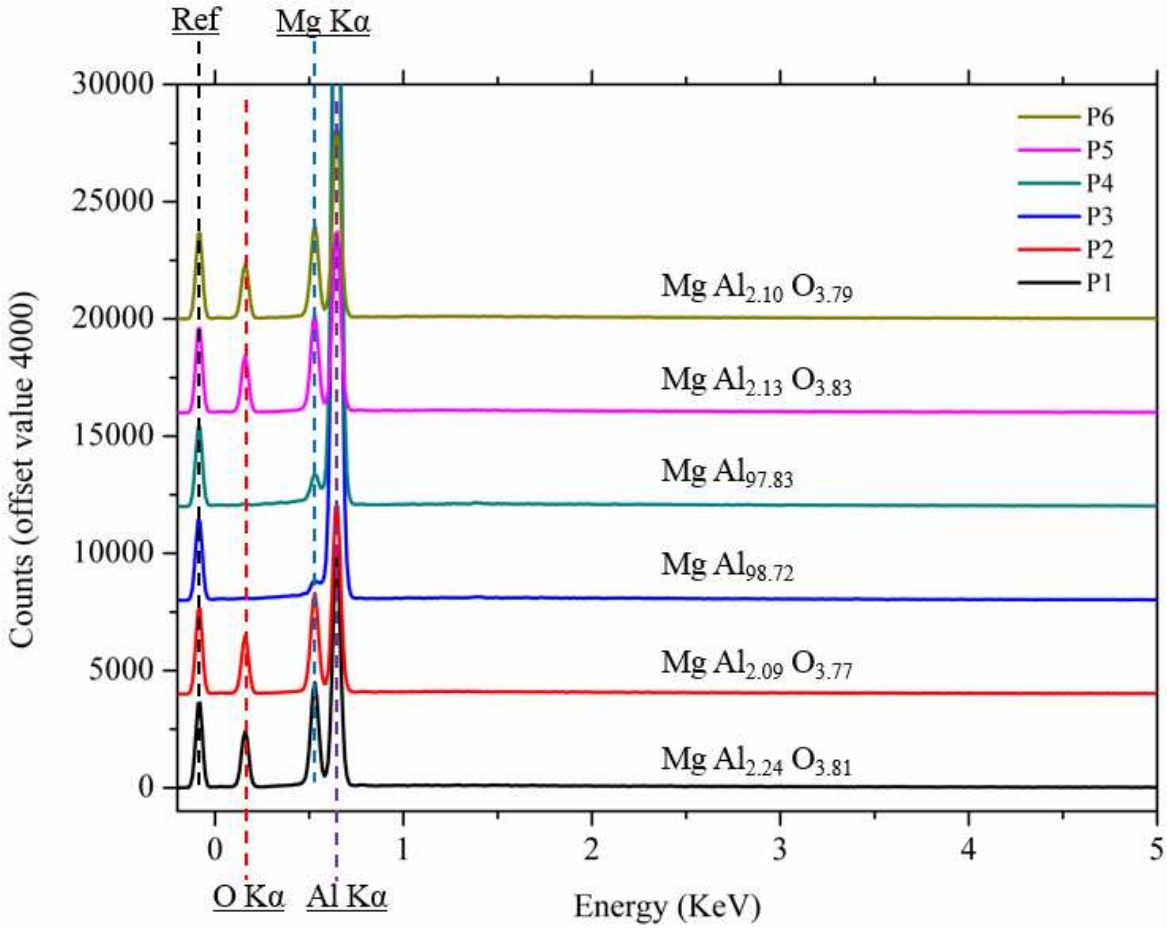

Figure 4.37 (b) – Measured EDX spectra 1-6 as shown in Figure 4.37 (a) and the quantified results in terms of the atomic ratio, clearly suggesting the faceting oxide to be $MgAl_2O_4$ (sample *M-24*).

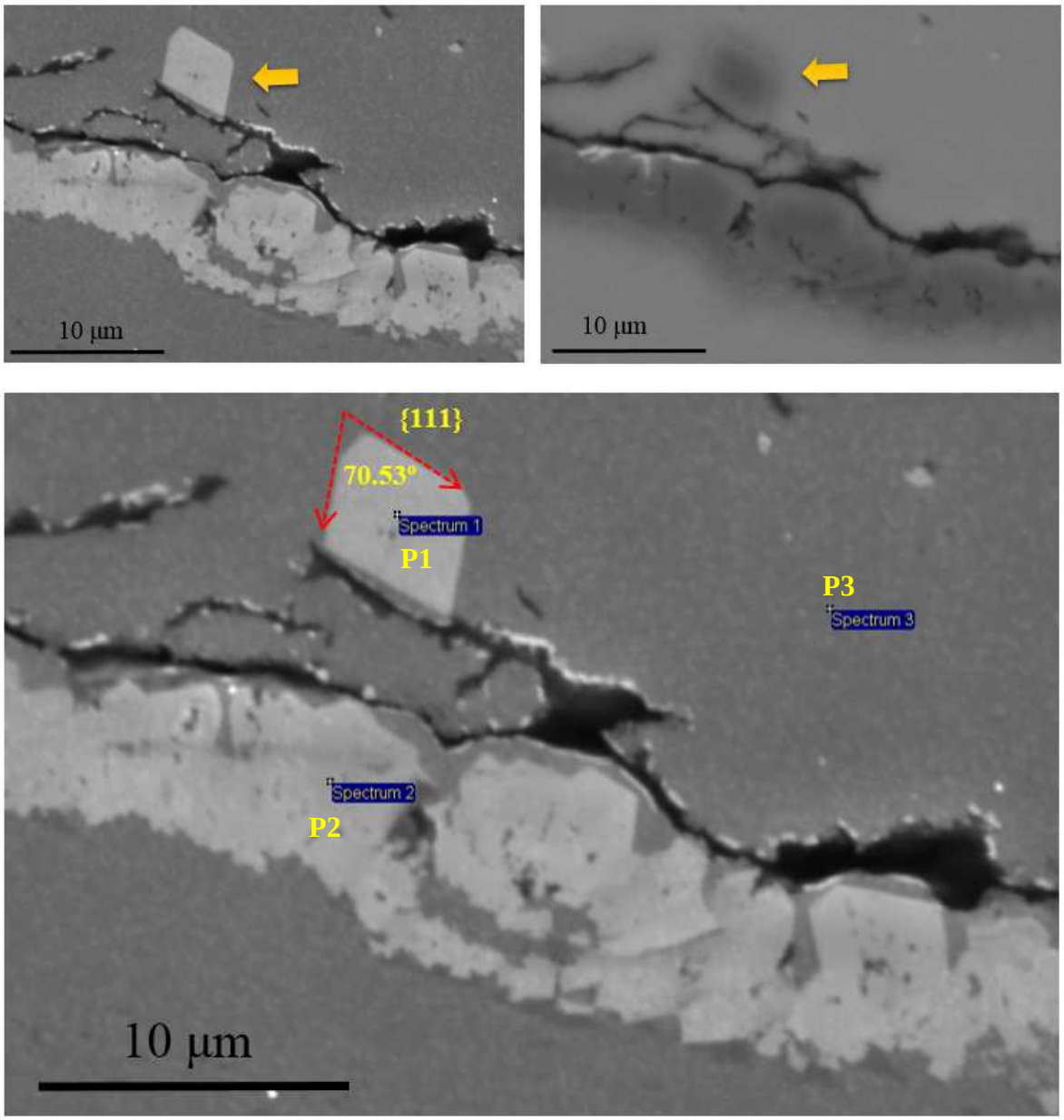

Figure 4.38 (a) – SE and BE images showing the facetted $MgAl_2O_4$-like oxide crystals at the bond interface and an $MgAl_2O_4$-like layer on the Al-2Mg side. The crystal was labelled to possibly have an {111} low index plane. EDX point analysis was also performed on these features (sample *M-24*).

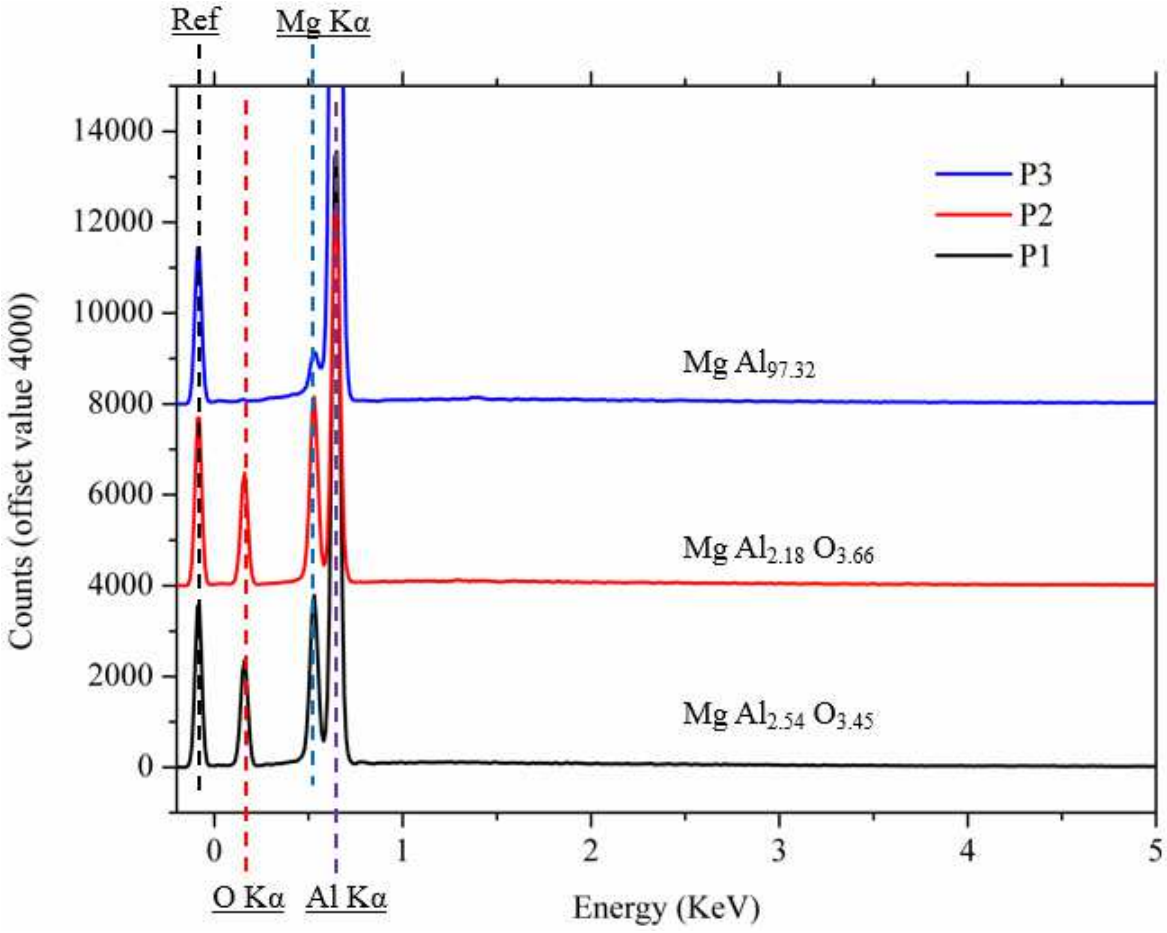

Figure 4.38 (b) – Measured EDX spectra 1-3 as shown in Figure 4.38 (a) and the quantified results in terms of the atomic ratio, clearly suggesting the faceting oxide to be $MgAl_2O_4$. The result is consistent (sample *M-24*).

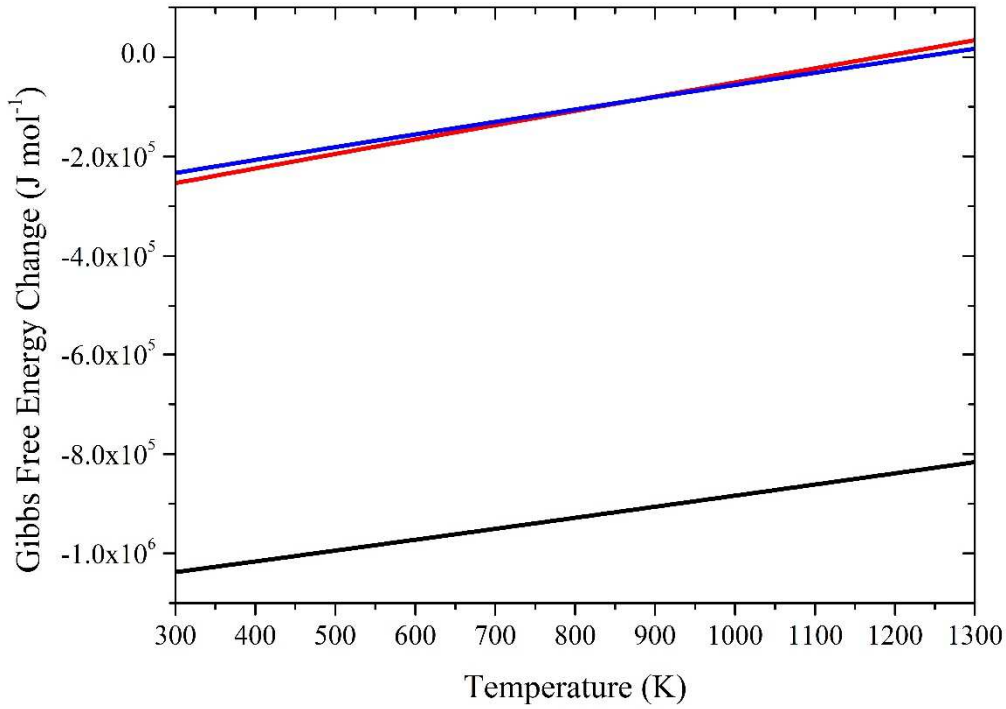

Figure 5.1 – Plot showing the free energy change as a function of temperature for Reactions A (black), B (red) and C (blue), given that X_{Cu} = 0.0215 (Al-5wt%Cu alloy).

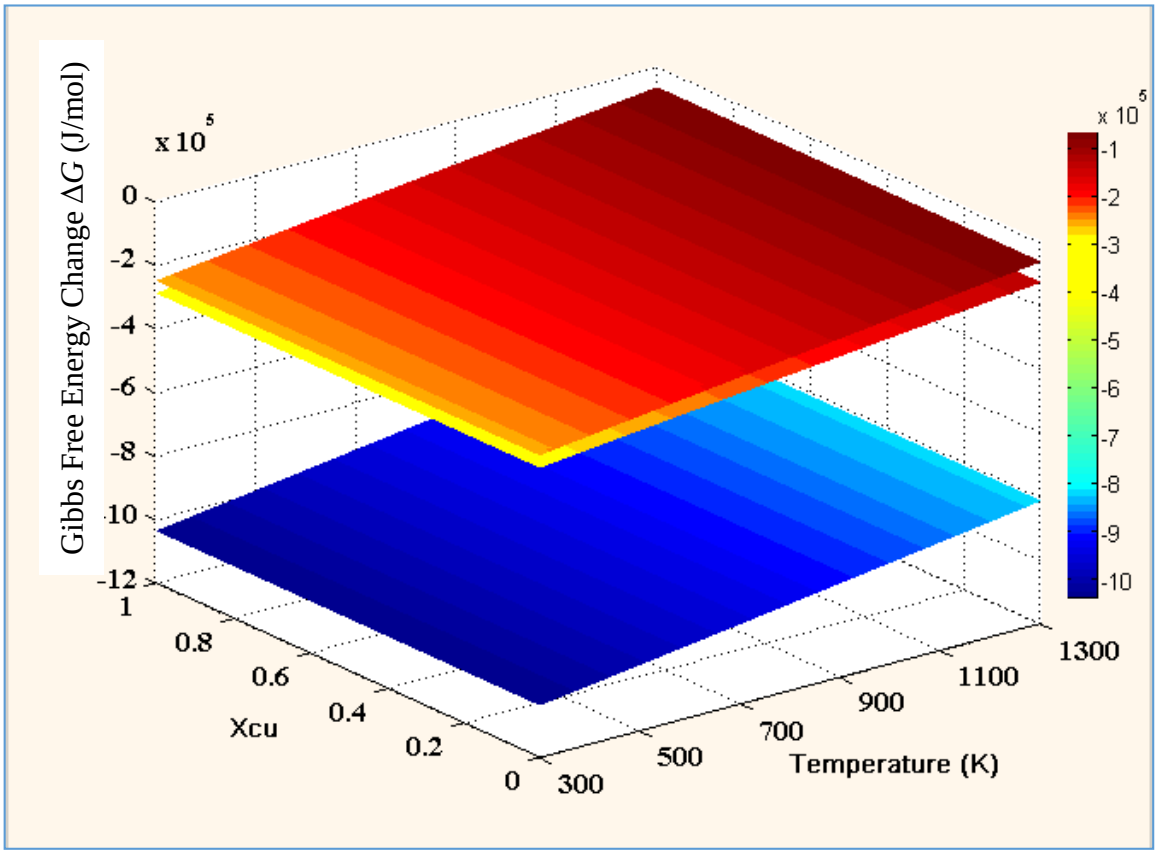

Figure 5.2 – 3D plot showing the free energy surface profile for Reactions A, B, C as a function of mole fraction X_{Cu} and T.

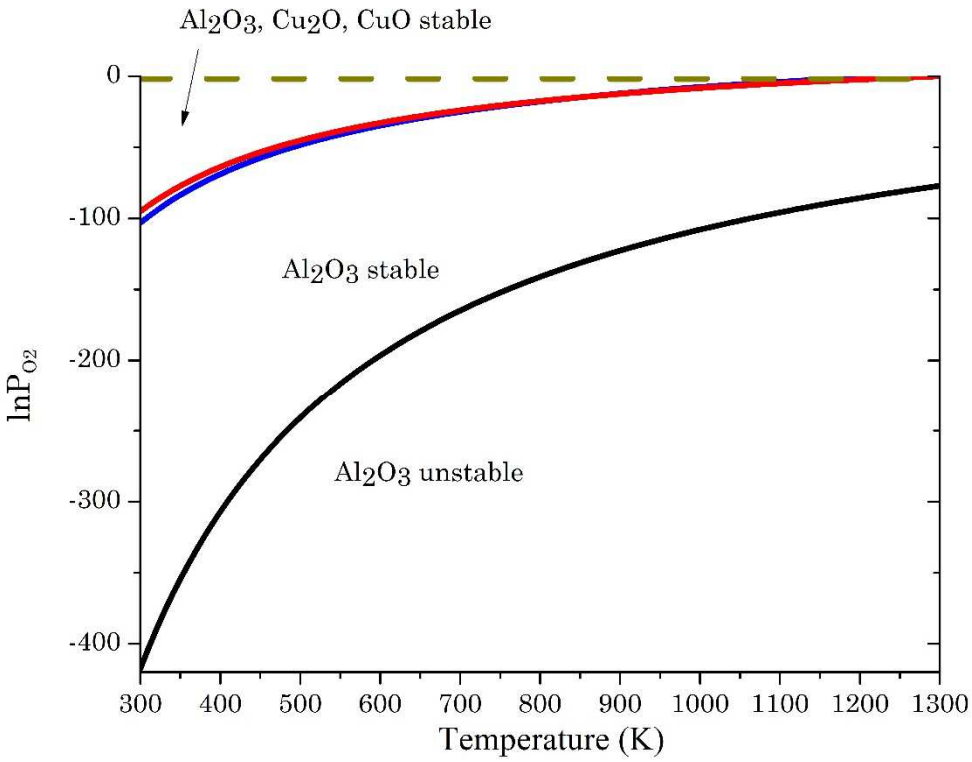

Figure 5.3 – Stability diagram of the Al-Cu-O_2 system showing the dissociation pressure as a function of temperature for Al_2O_3 (black), Cu_2O (blue) and CuO (red) when X_{Cu} = 0.0215 (In the case of an Al-5Cu alloy). Dry air condition (dash dark yellow line) is highlighted as a reference.

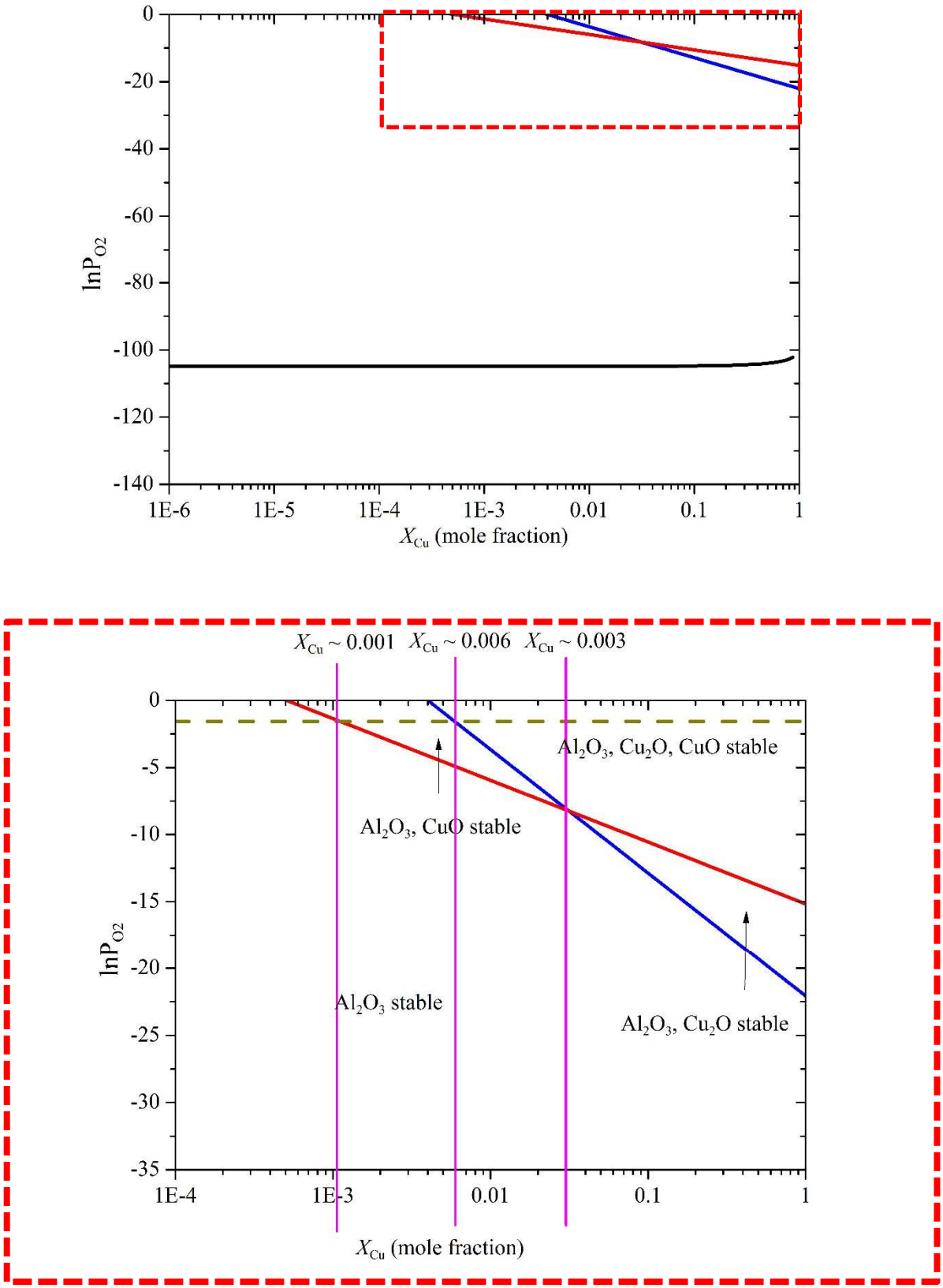

Figure 5.4 – Stability diagram showing the dissociation pressure as a function of Cu mole fraction at the temperature 750°C. Dry air condition (dash dark yellow line) is highlighted as a reference.

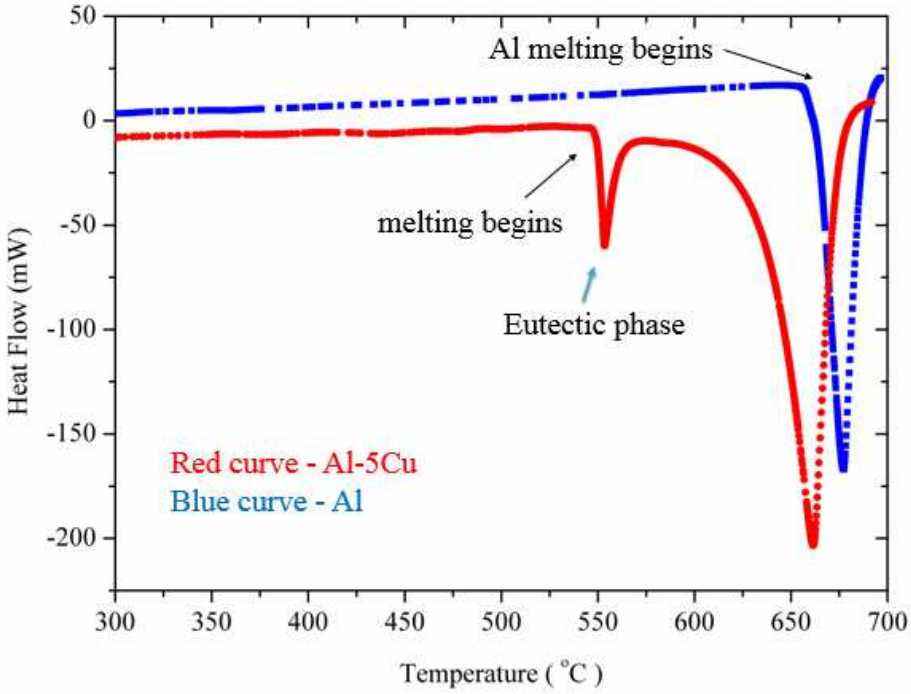

Figure 5.5 – DSC curves of Al-5Cu and Al obtained at a heating rate of 40° C min^{-1}.

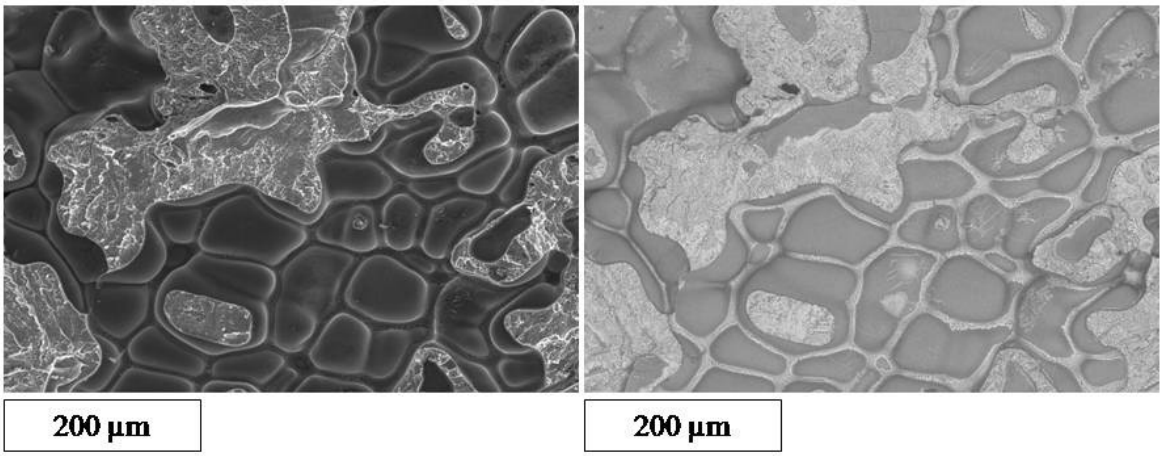

Figure 5.6 – A pair of SE and BE images showing the fracture surface topography of an as-cast Al-5Cu alloy

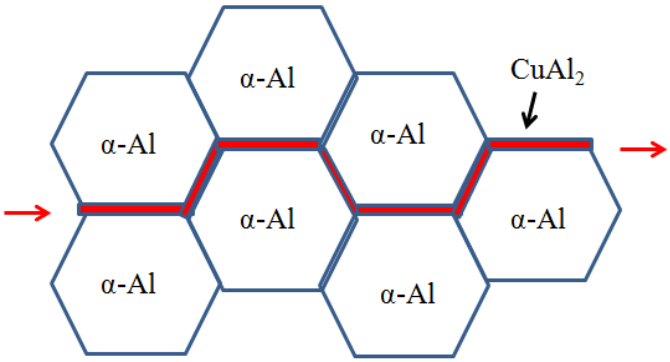

Figure 5.7 – Diagram illustrating the crack prorogation along the cell boundaries

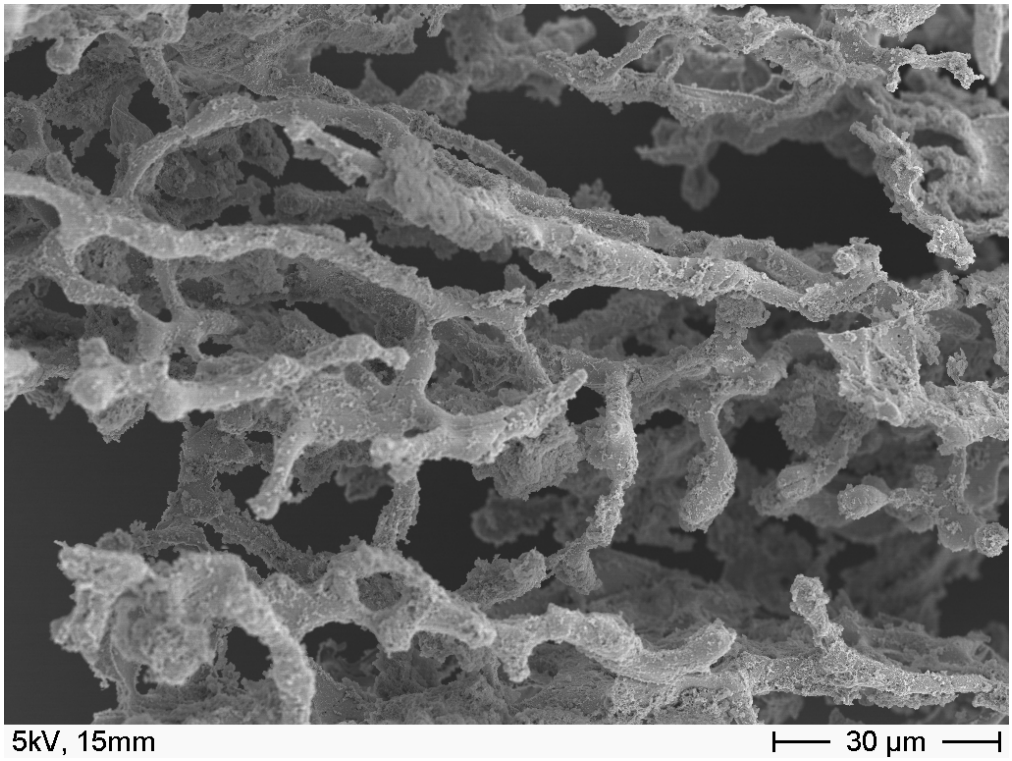

Figure 5.8 – SE Image showing the interconnected network of $CuAl_2$. The intermetallic phase was extracted by dissolving the Al matrix.

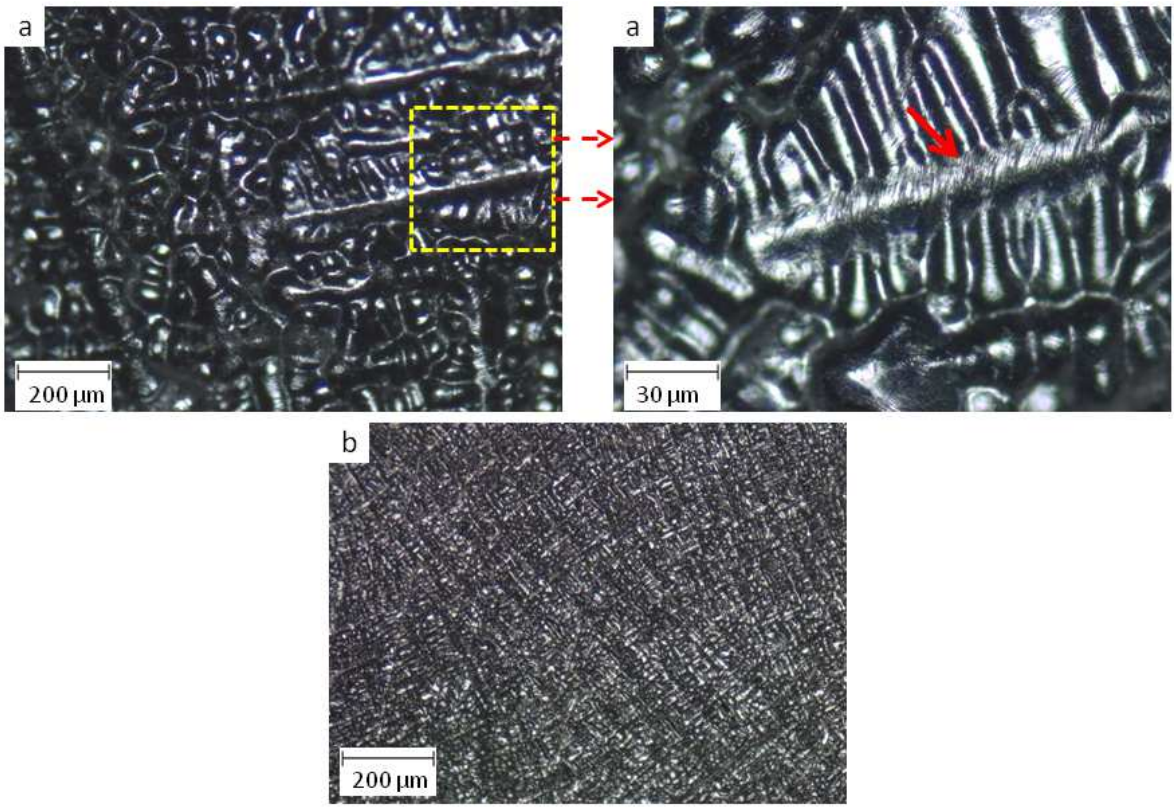

Figure 5.9 – OM images showing the surface topography of the as-cast Al-5Cu (a) slow cooling at a rate of 40 K min^{-1} (b) fast cooling at a rate of 100 K min^{-1}

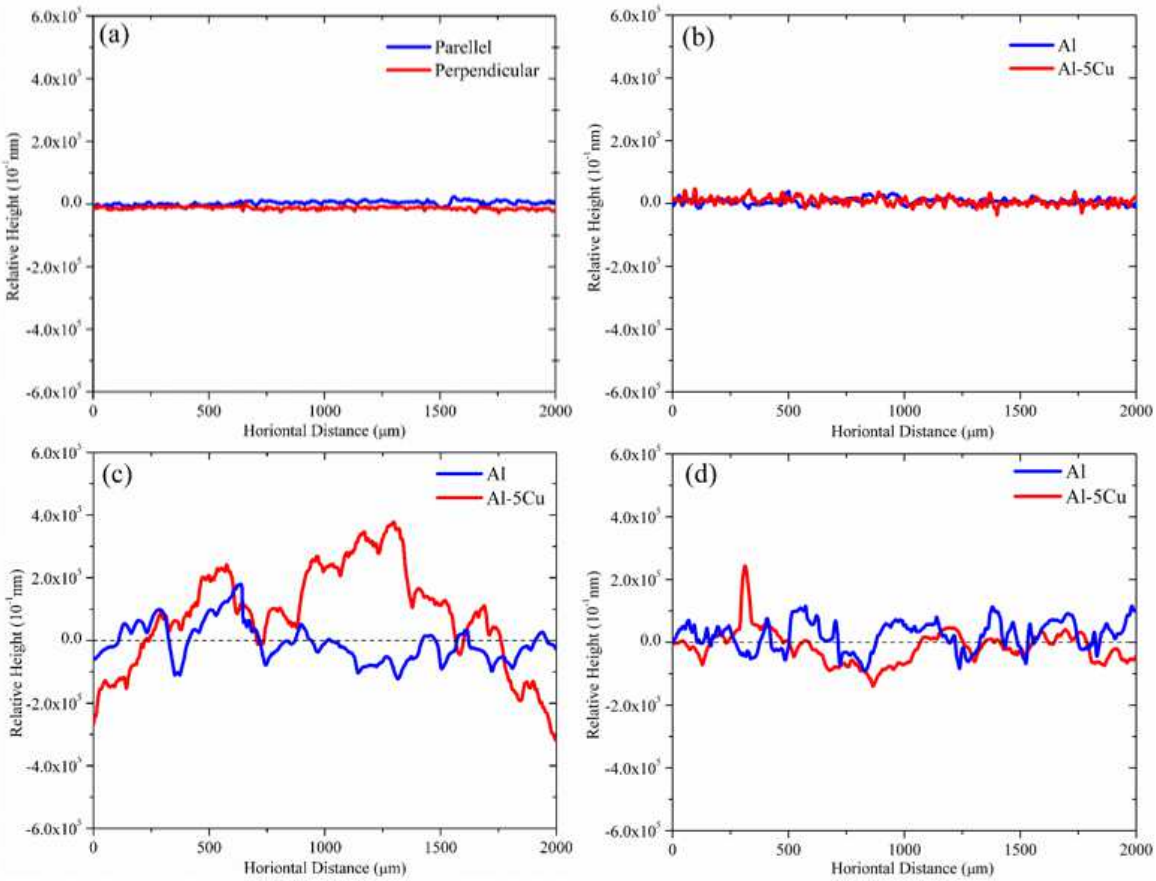

Figure 5.10 – Plots showing the DEKTAK surface roughness profiles on surfaces of different samples (a) as polished Al (b) as polished Al and Al-5Cu (c) oxidized Al and Al-5Cu – 750ºC 1 h (d) oxidized Al and Al-5Cu – 750ºC 6 h.

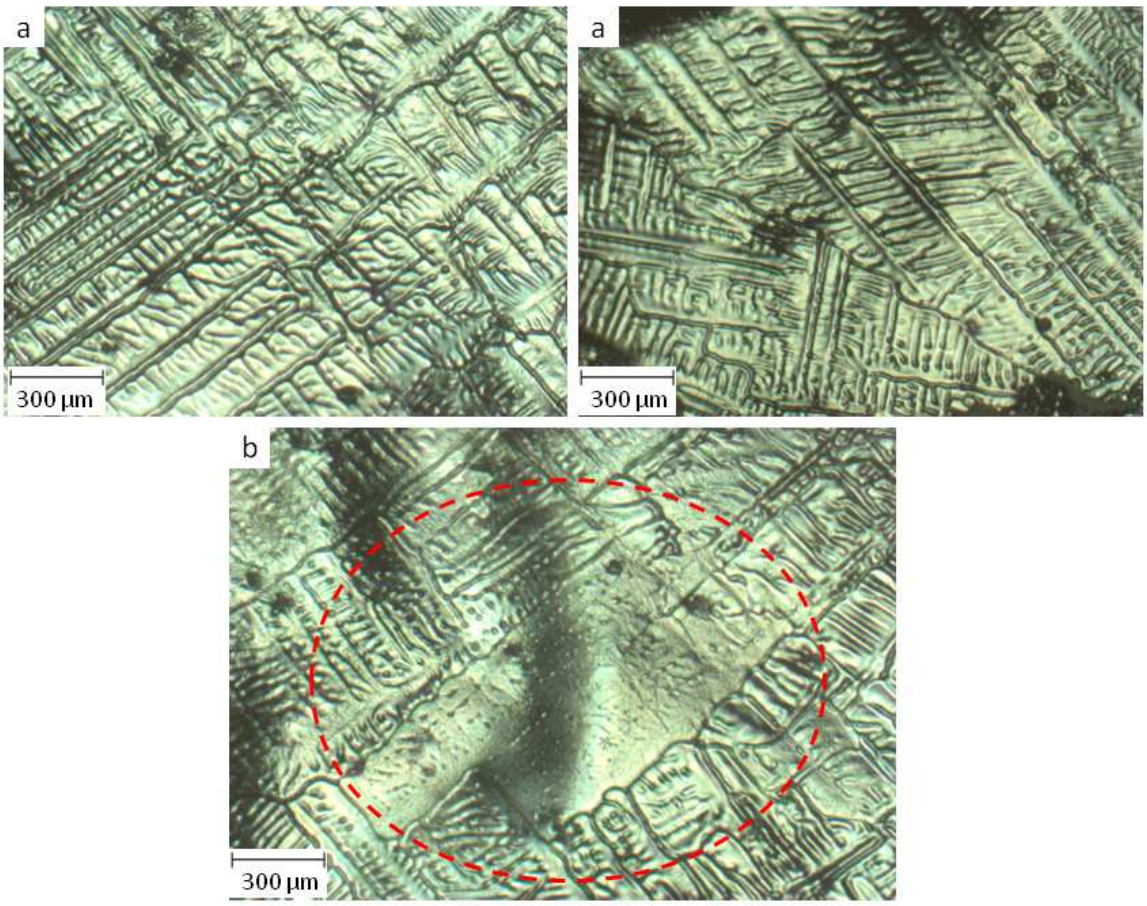

Figure 5.11 – OM images showing the dendritic patterning observed in as-cast Al-5Cu

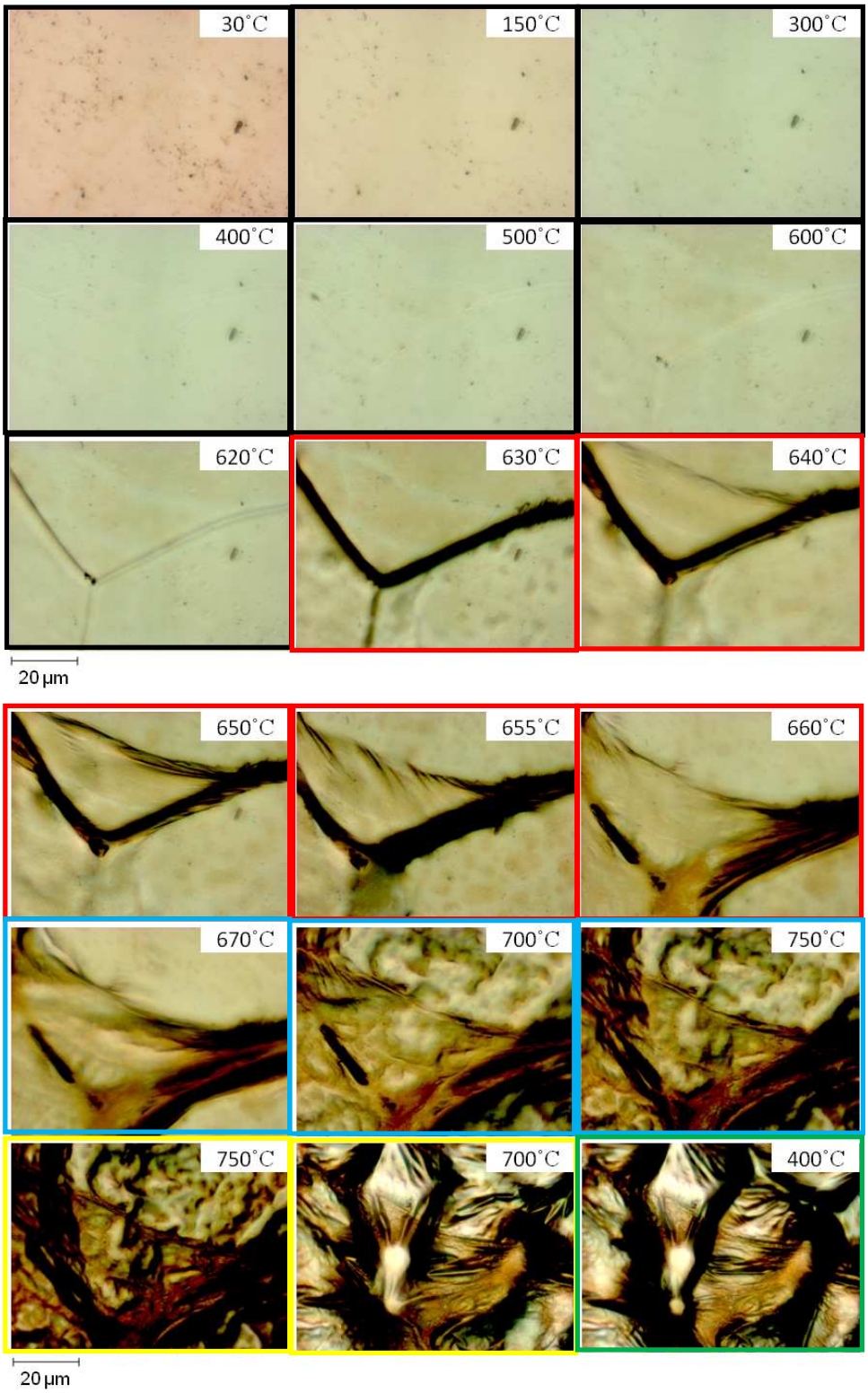

Figure 5.12 – OM images showing the surface oxide layer evolution during the hot-stage OM experiment at different temperatures, pure Al sample

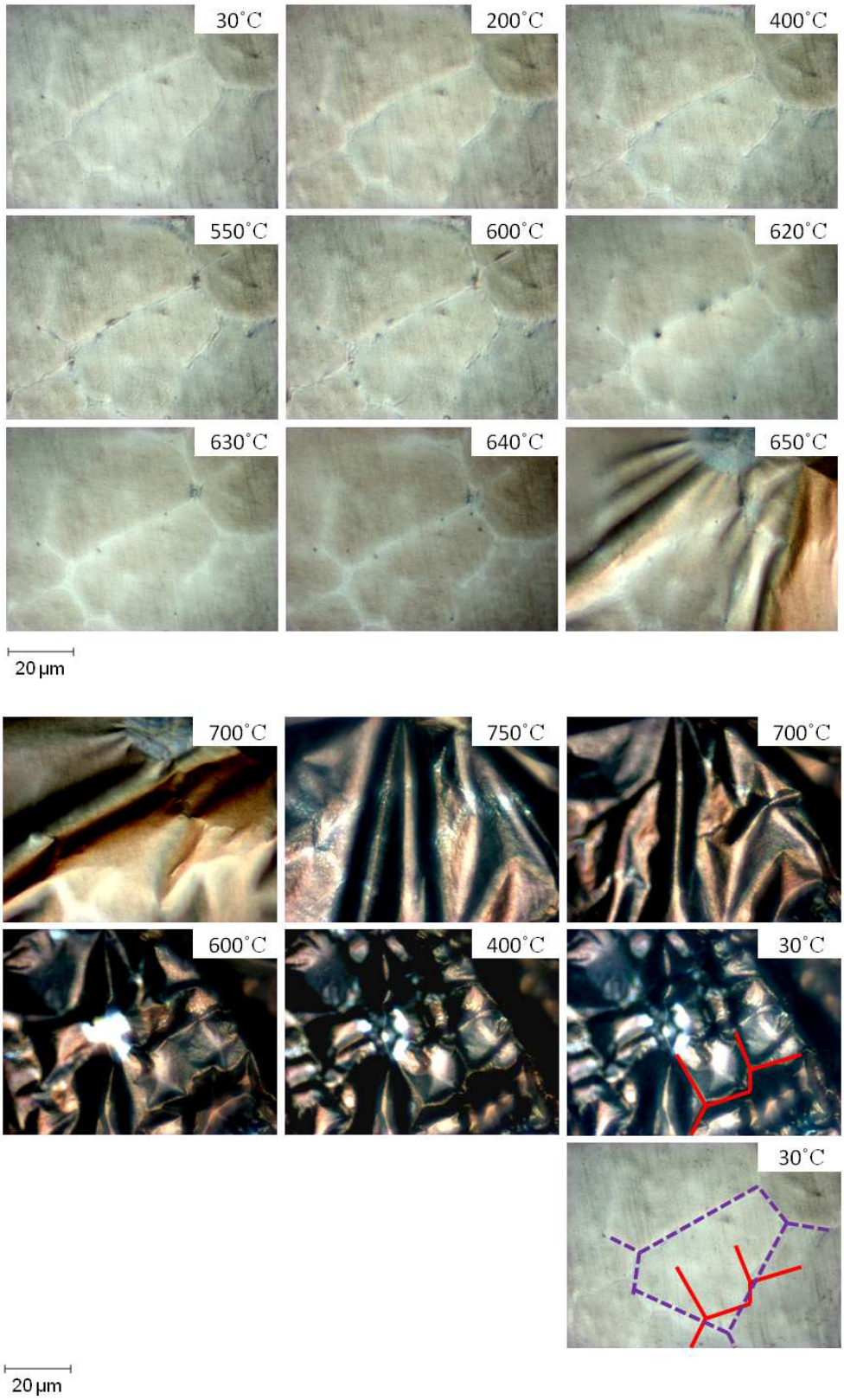

Figure 5.13 – OM images showing the surface oxide layer evolution during the hot-stage OM experiment at different temperatures, Al-5Cu sample

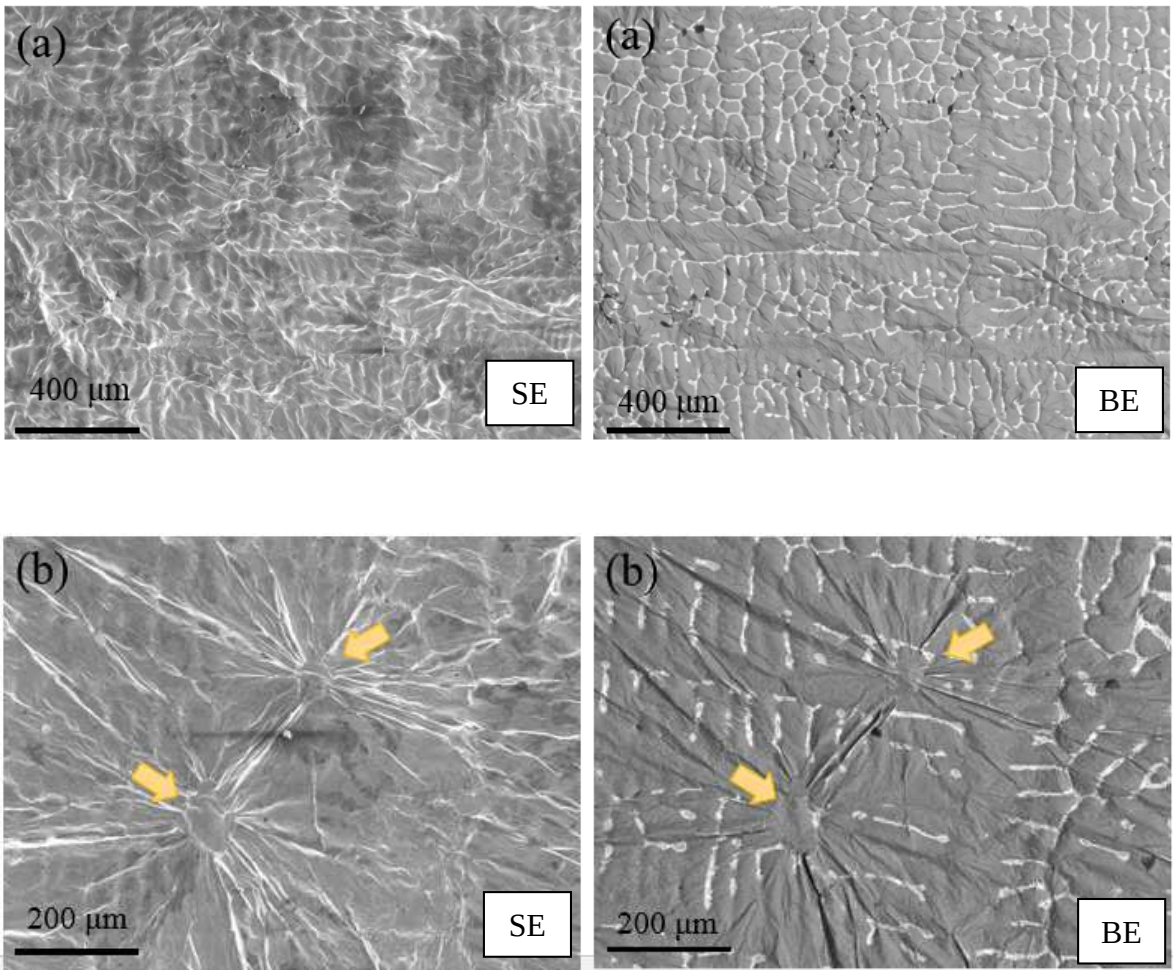

Figure 5.14 – Pairs of SE and BE images showing the oxide layer morphology of an oxidized Al-5Cu sample (750° C, 1 h)

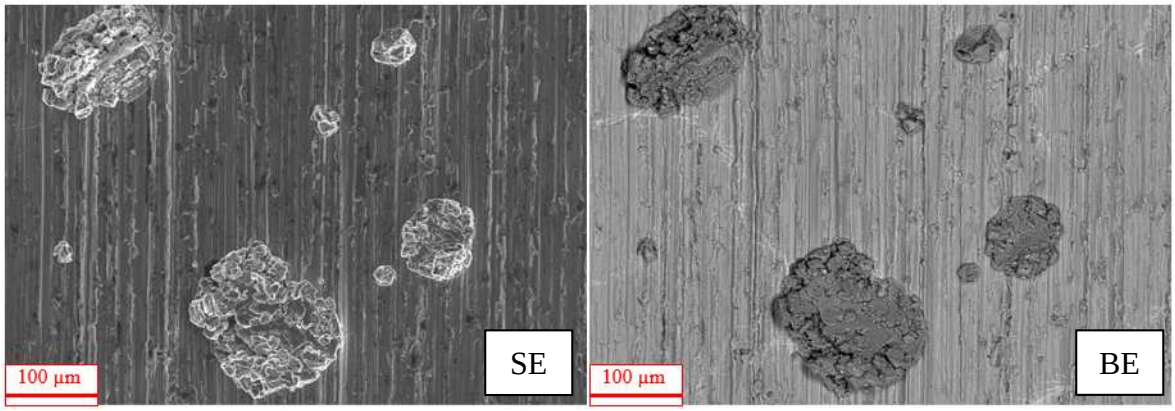

Figure 5.15 – A pair of SE and BE images showing the oxide layer morphology of an oxidized Al sample 750ºC 12 h.

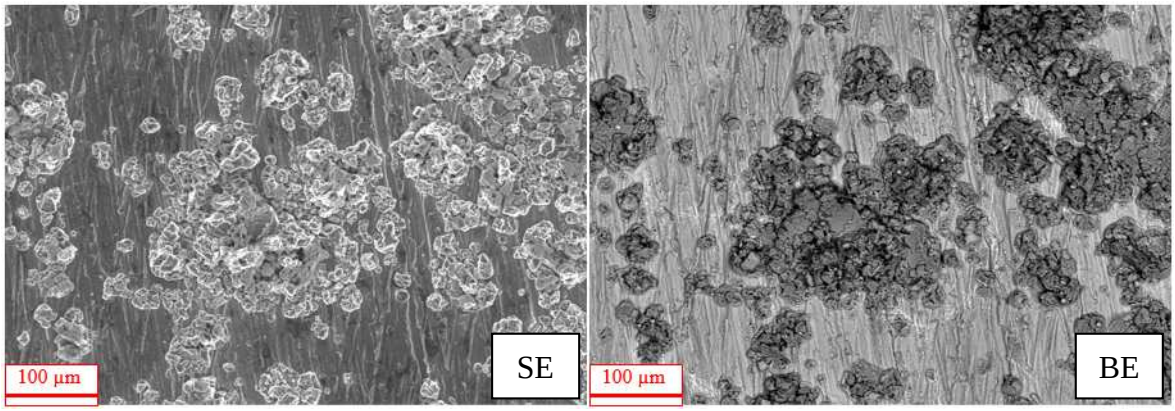

Figure 5.16 – A pair of SE and BE images showing the oxide layer morphology of an oxidized Al sample 750ºC 24 h

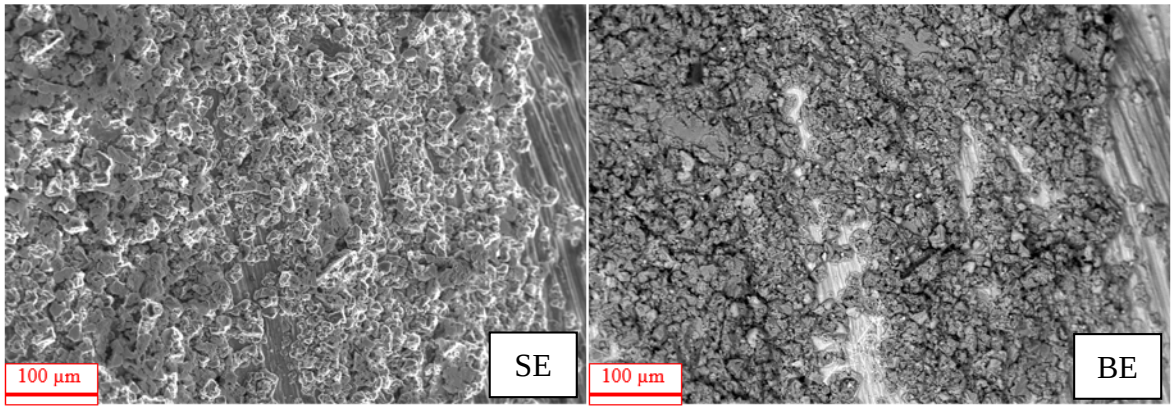

Figure 5.17 – A pair of SE and BE images showing the oxide layer morphology of an oxidized Al sample 750ºC 48 h.

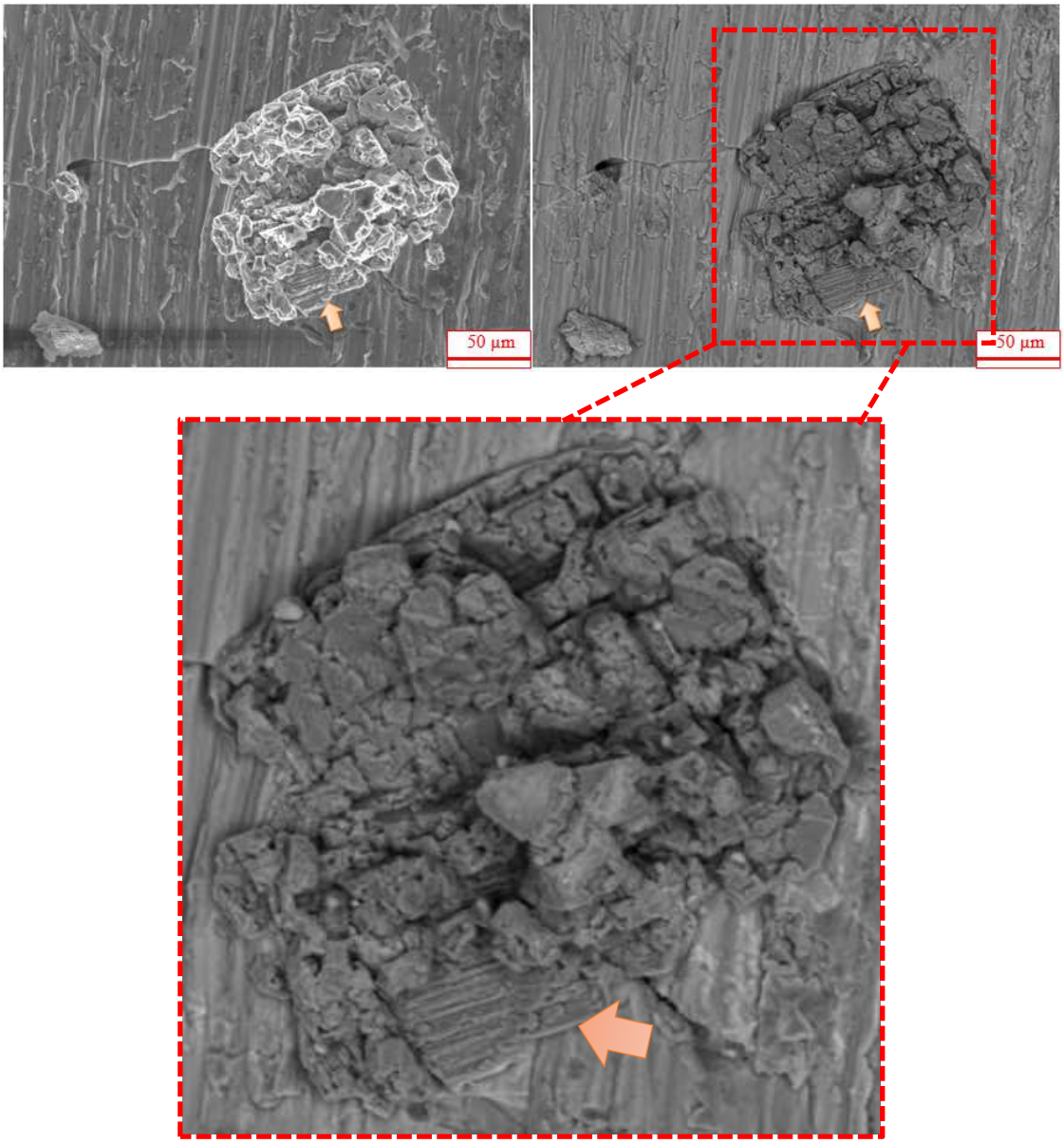

Figure 5.18 – A pair of SE and BE images showing the oxide layer morphology of an oxidized Al sample 750ºC 12 h

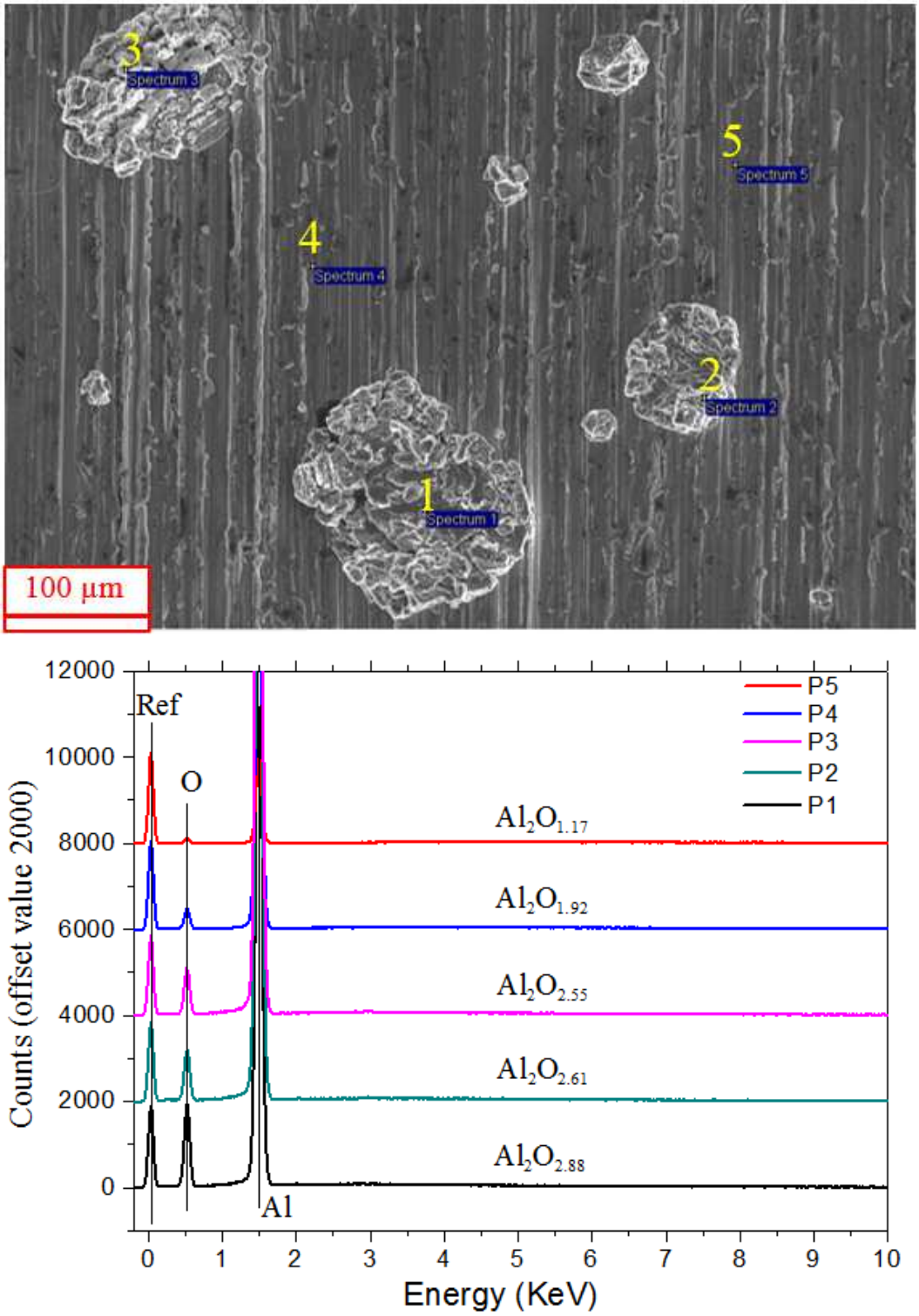

Figure 5.19 – EDX analysis showing the chemistry of the island-like crystalline oxide agglomerates.

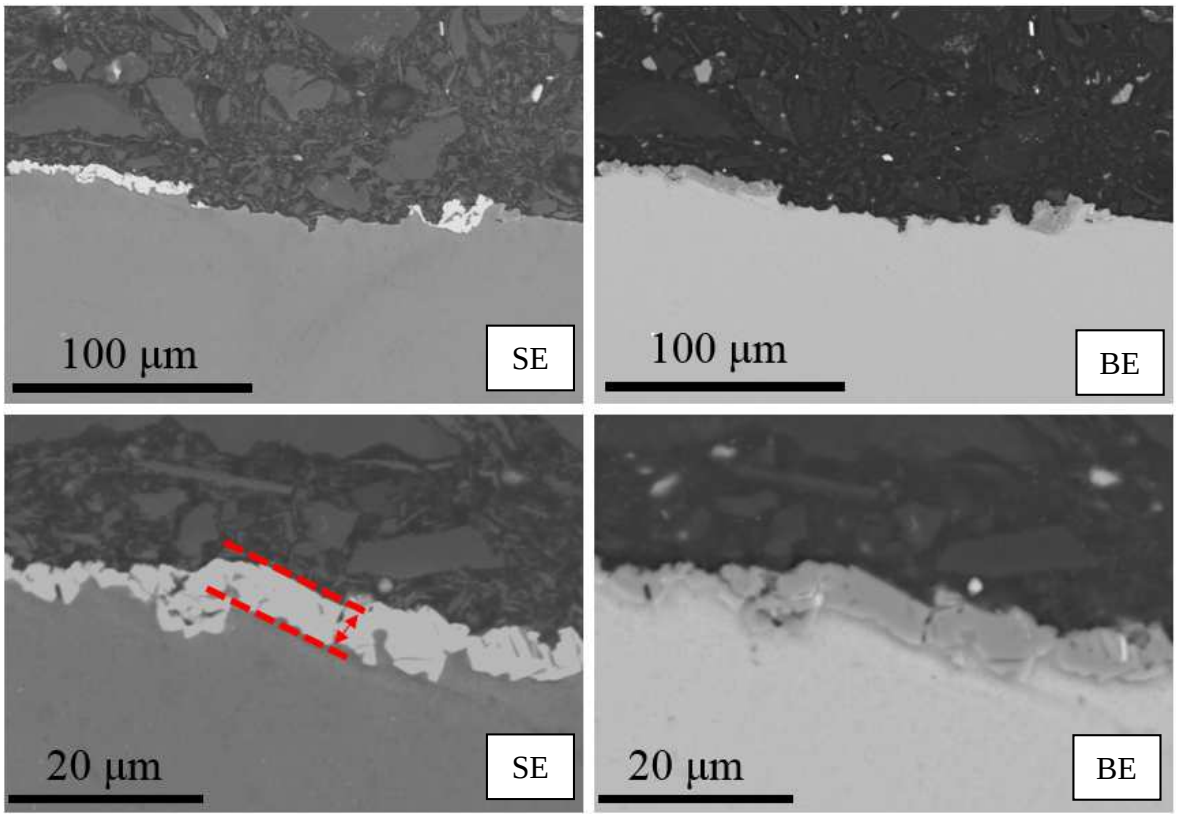

Figure 5.20 – Pairs of SE and BE images showing the cross sectional view of the oxidized Al sample 750ºC 12 h.

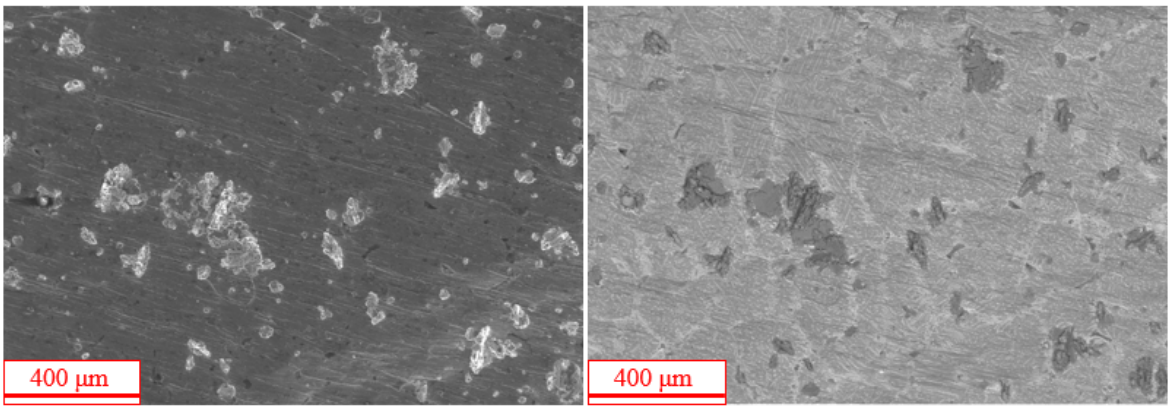

Figure 5.21 – A pair of SE (left) and BE (right) showing the oxide layer morphology of an oxidized Al-5Cu sample 750°C 12 h.

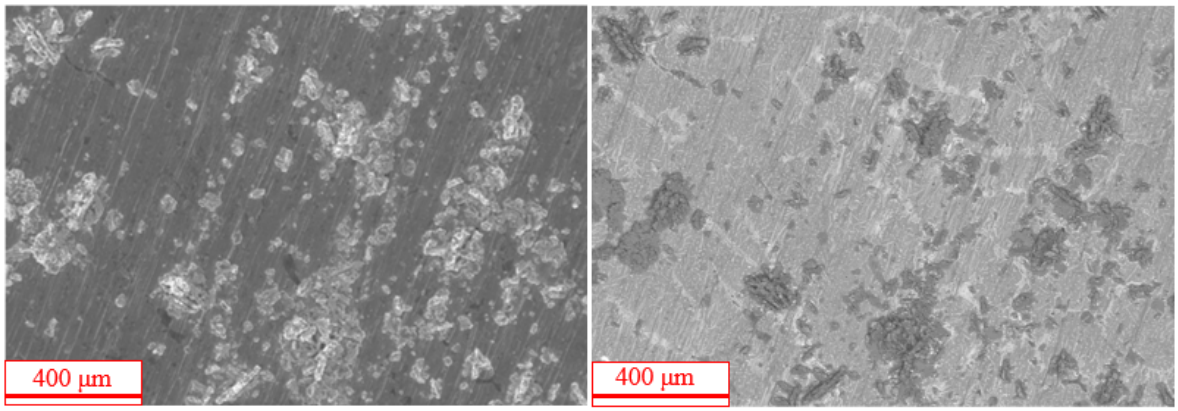

Figure 5.22 – A pair of SE (left) and BE (right) showing the oxide layer morphology of an oxidized Al-5Cu sample 750°C 24 h.

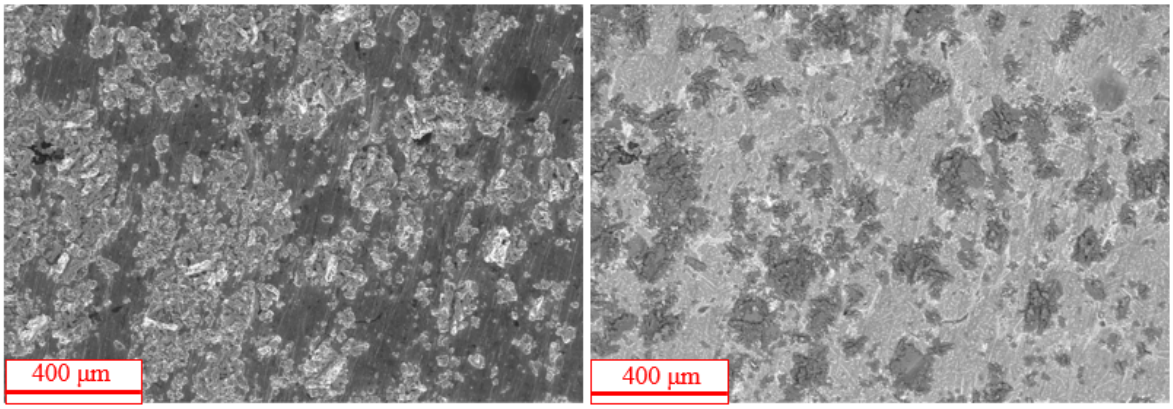

Figure 5.23 – A pair of SE (left) and BE (right) showing the oxide layer morphology of an oxidized Al-5Cu sample 750°C 48 h.

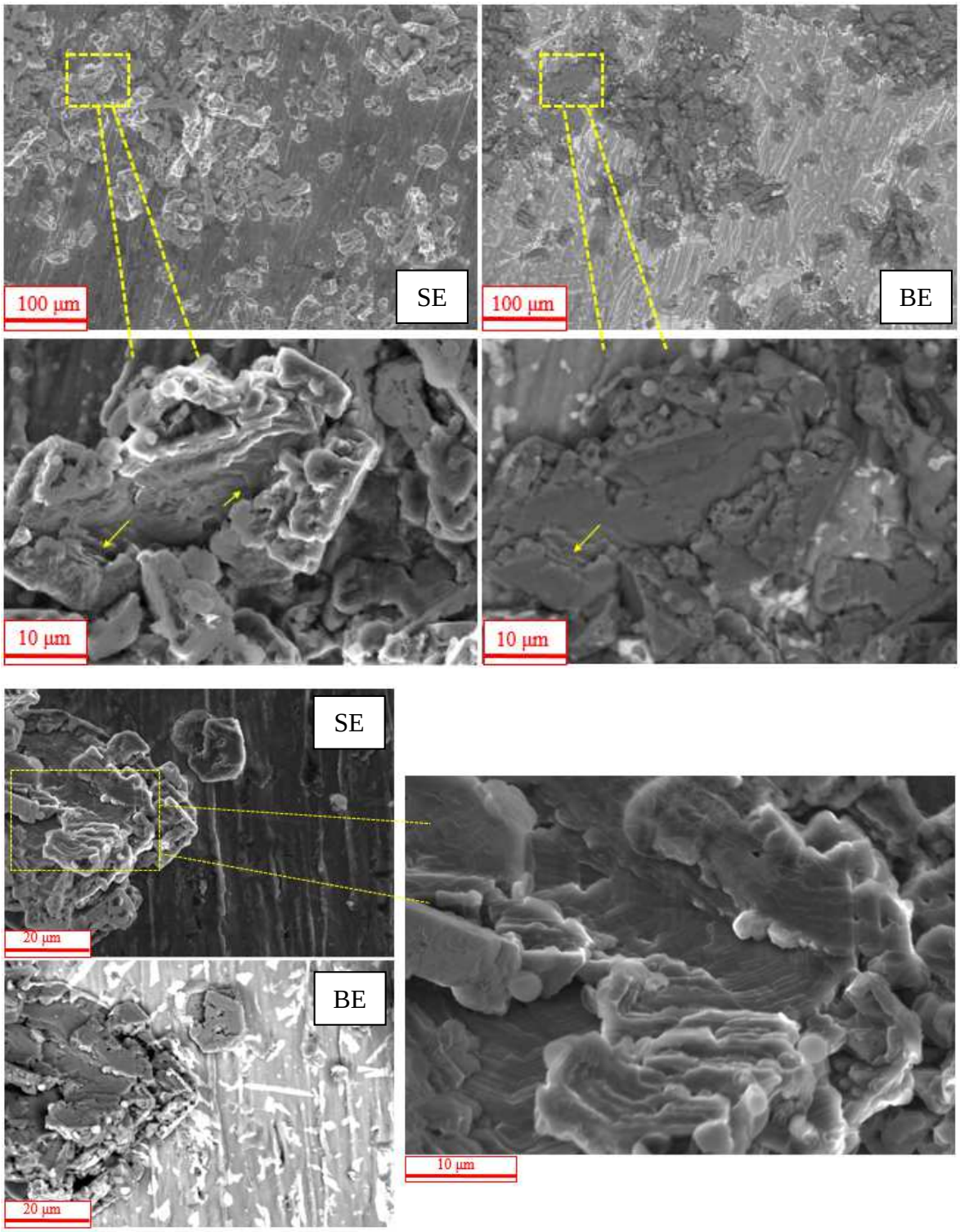

Figure 5.24 – Pairs of SE and BE images indicating a *ledge* growth mechanism of the crystalline oxides.

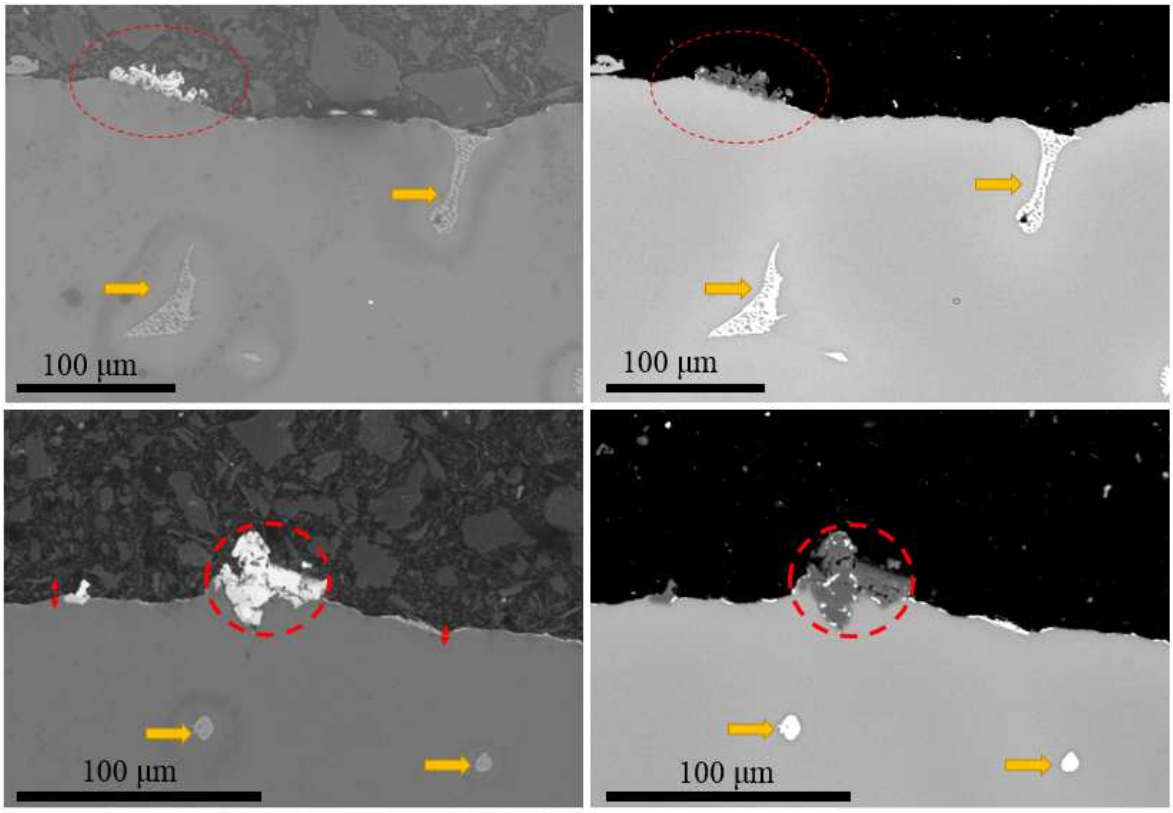

Figure 5.25 – Pairs of SE (left) and BE (right) images showing the cross sectional view of the oxidized Al-5Cu sample 750ºC 12 h.

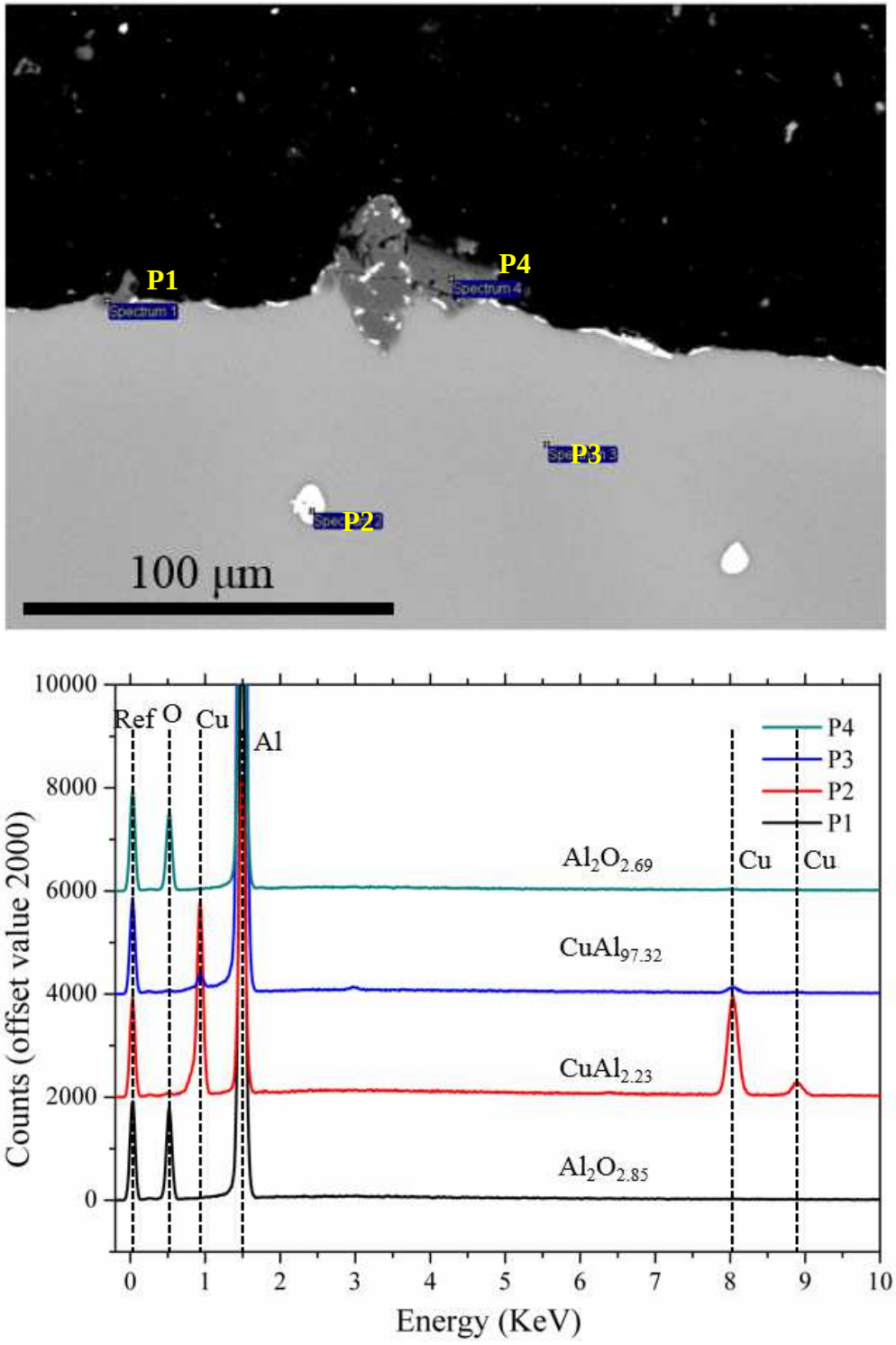

Figure 5.26 – EDX analysis showing the chemistry of different phases.

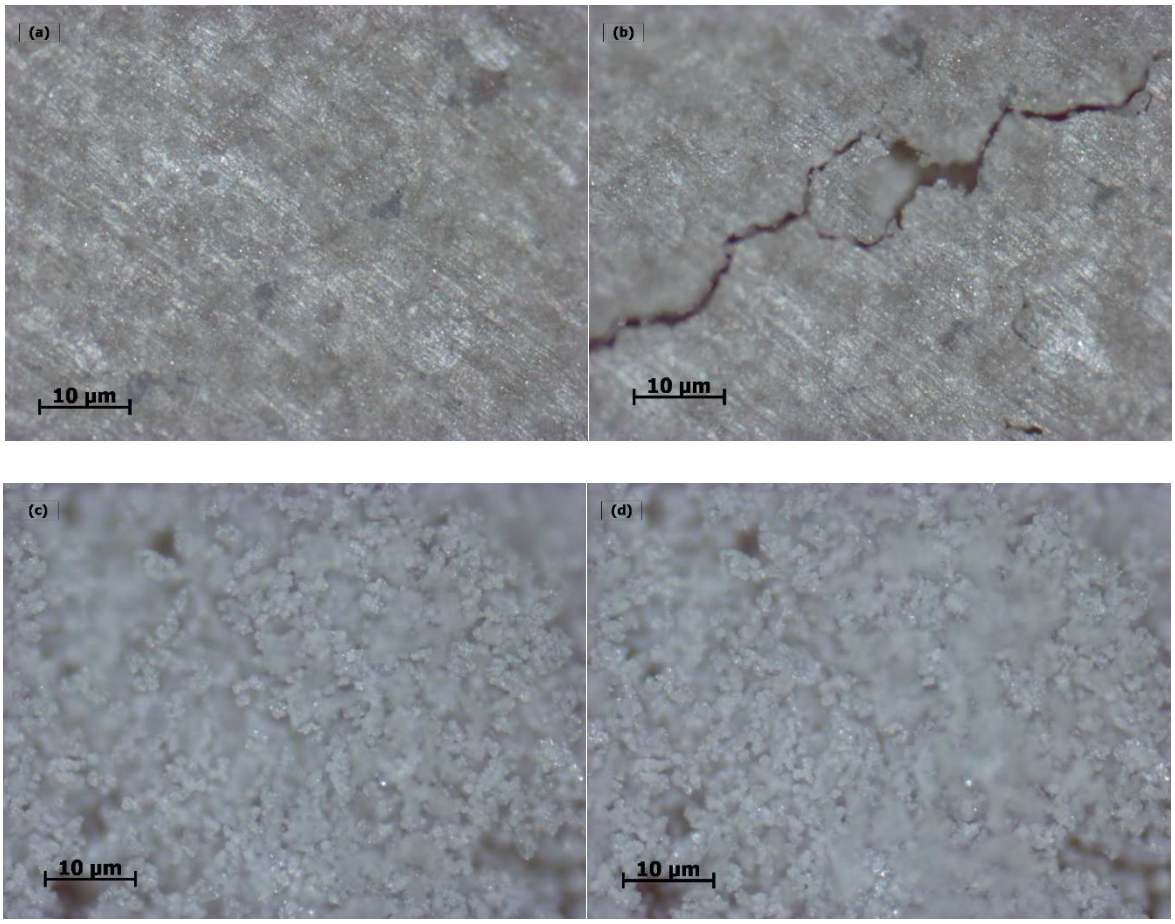

Figure 5.27 – OM images showing the dry side (a-b) and the wet side (c-d) morphology of the oxide layer formed on an Al-5Cu sample oxidized at 950ºC for 48 h.

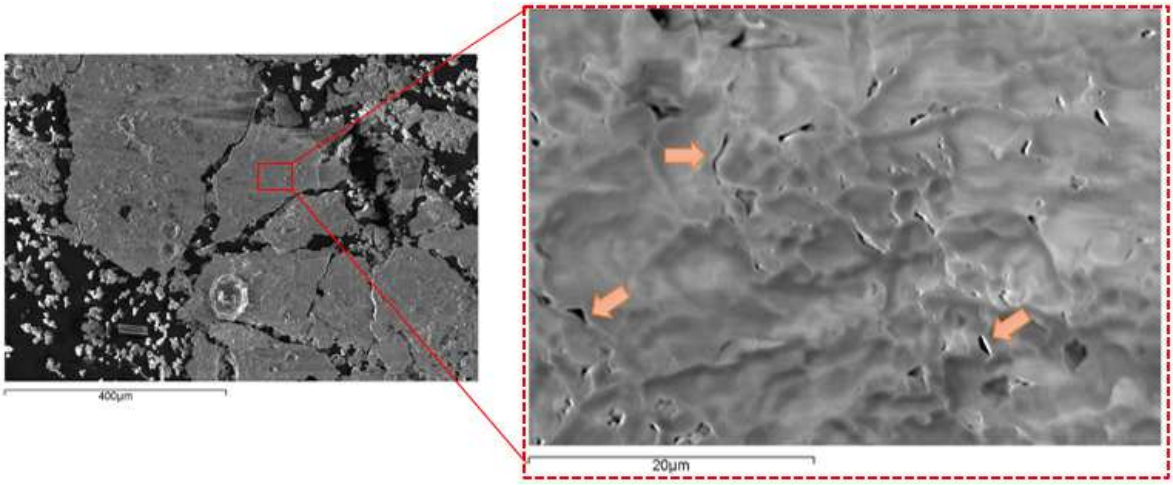

(a)

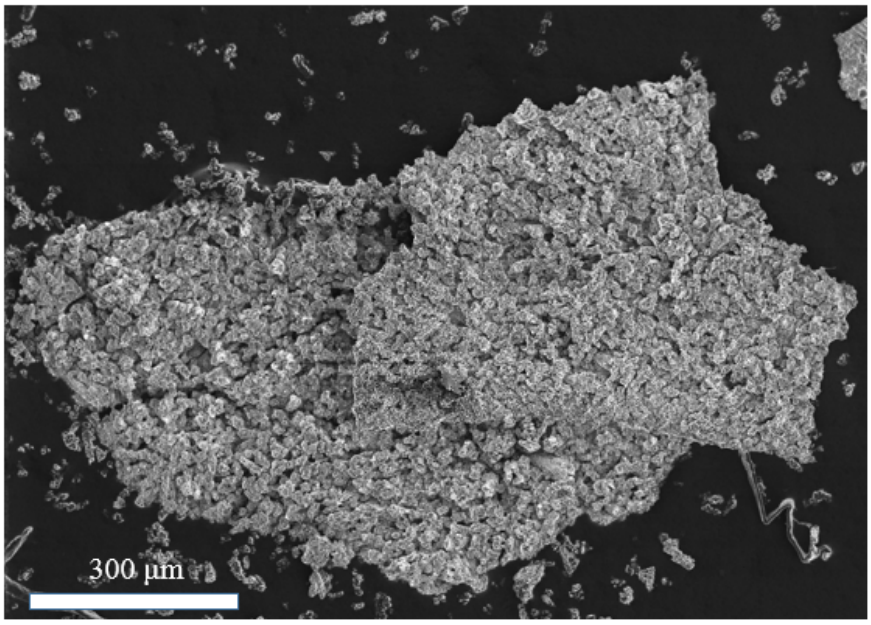

(b)

Figure 5.28 – SE images showing the dry side (a) and the wet side (b) morphology of the oxide layer formed on an Al-5Cu sample oxidized at 950ºC for 48 h.

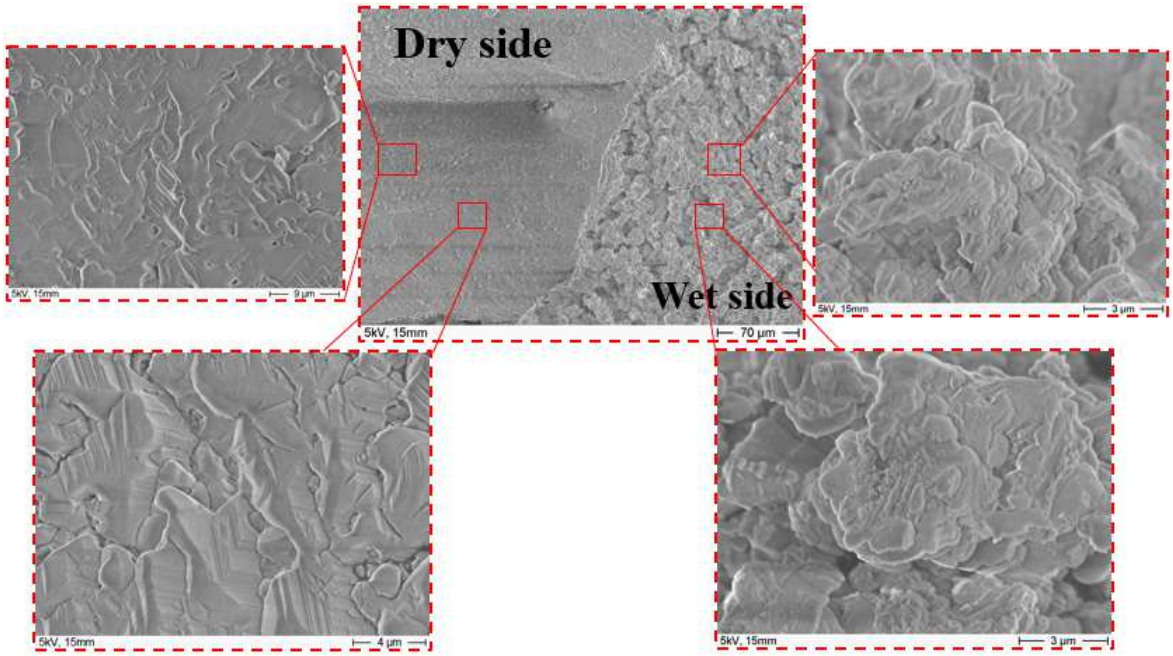

Figure 5.29 – SE images showing morphology of the oxide layer formed on an Al sample oxidized at 950°C for 48 h.

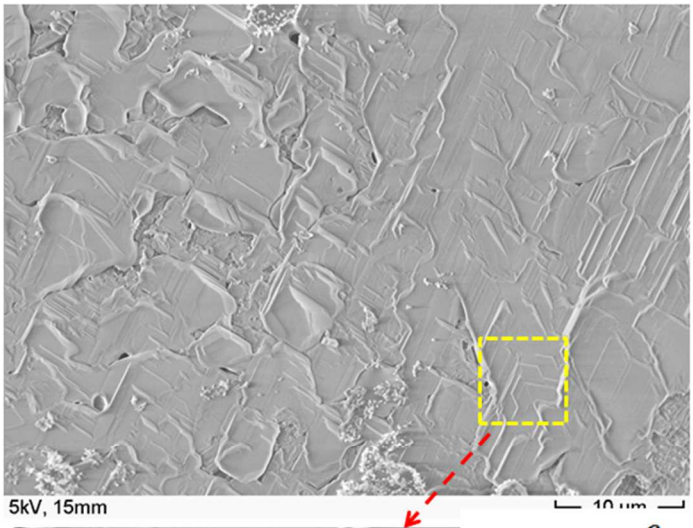
5kV, 15mm
10 µm

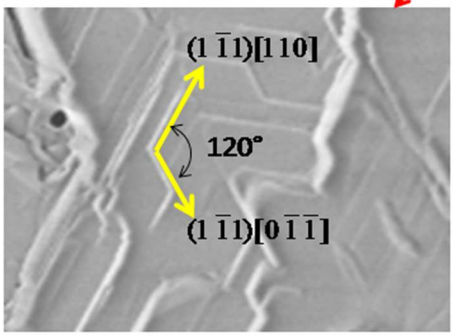
(1 $\bar{1}$ 1)[1 1 0]
120°
(1 $\bar{1}$ 1)[0 $\bar{1}$ $\bar{1}$]

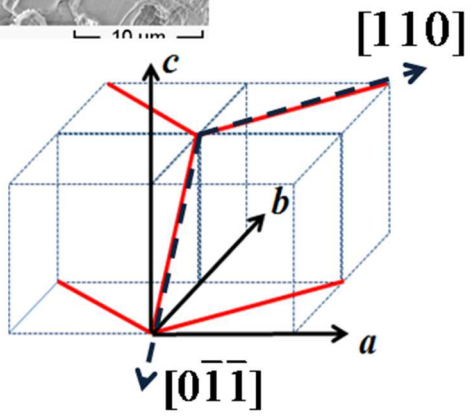
[1 1 0]
c
b
a
[0 $\bar{1}$ $\bar{1}$]

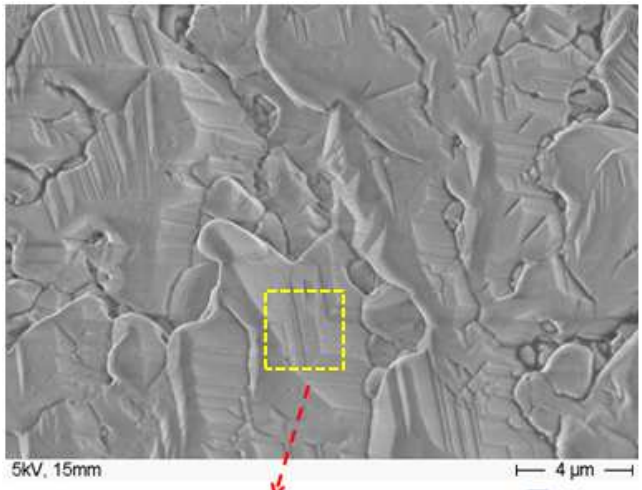
5kV, 15mm
4 µm

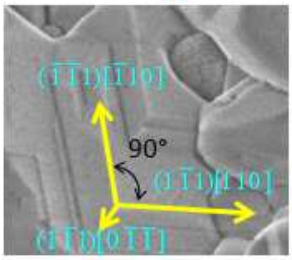
90°

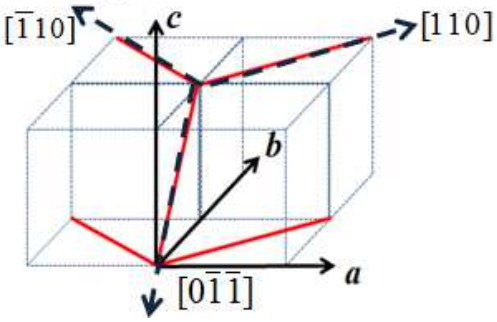
[$\bar{1}$ 1 0]
c
[1 1 0]
b
a
[0 $\bar{1}$ $\bar{1}$]

Overleaf

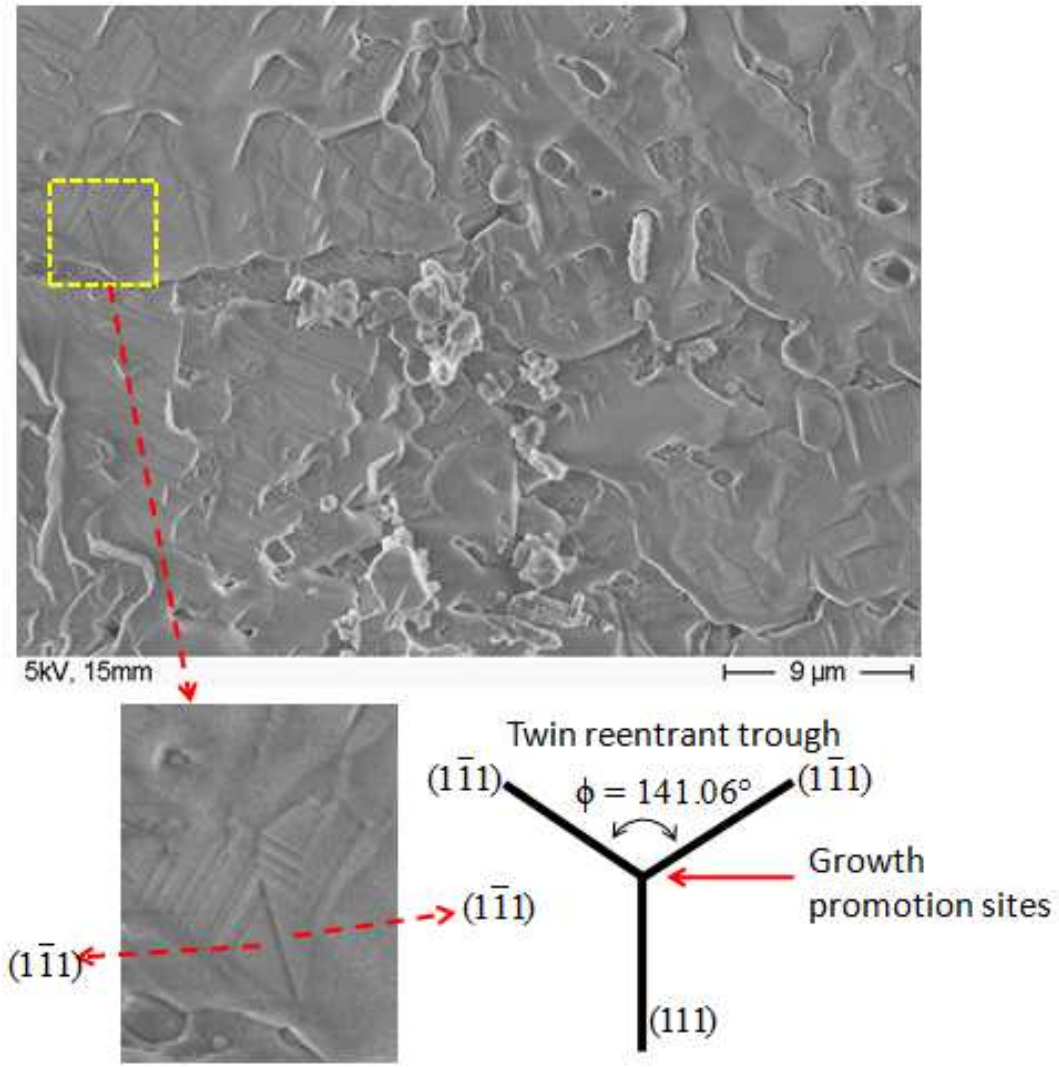

Figure 5.30 – SEI images showing the facetted ledges observed at the oxide/air interface and a 2D growth and twin re-entrant growth mechanism are observed.

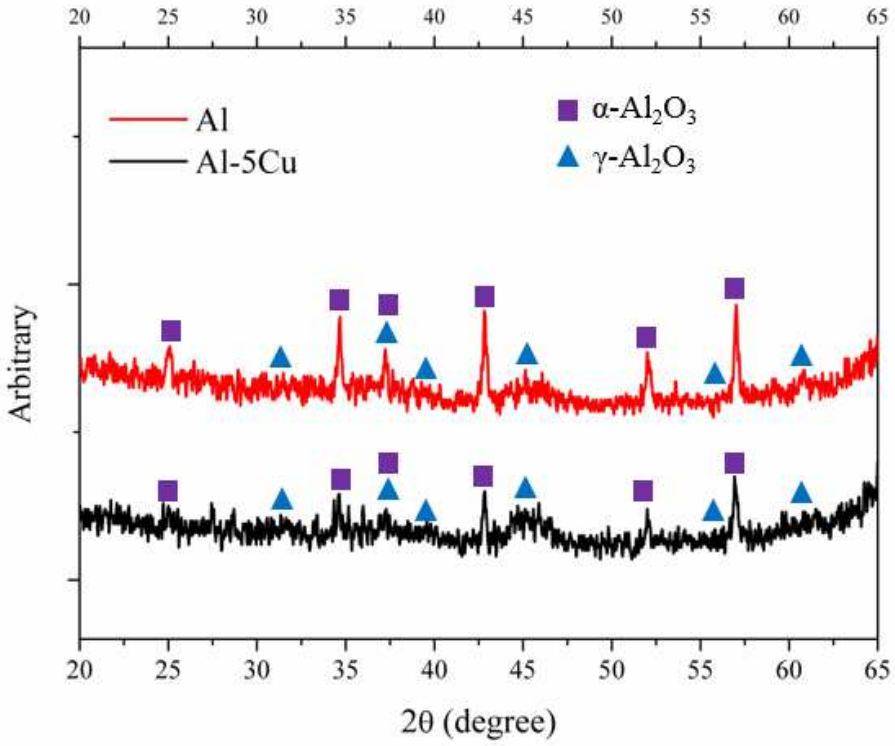

Figure 5.31 – XRD traces of the oxides scraped from the Al and Al-5Cu samples which were oxidized at 950ºC for 48 h.

Table 5.1 - Sample details of XPS analysis in this Chapter

Sample Codes	As polished	1 h oxidation	6 h oxidation	24 h oxidation
Al	***Al-AP***	***Al-R1***	***Al-R6***	***Al-R24***
Al-5Cu	***Al-5Cu-AP***	***Al-5Cu-R1***	***Al-5Cu-R6***	***Al-5Cu-R24***

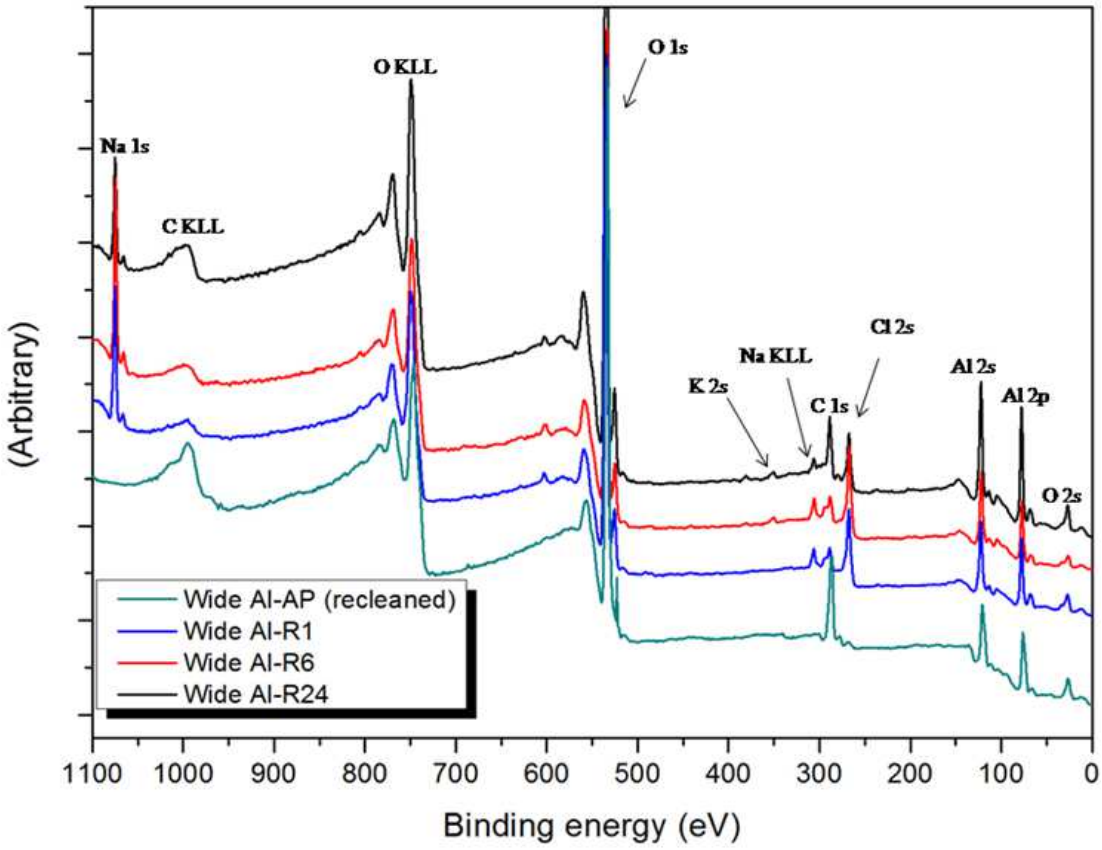

Figure 5.32 – Wide scan XPS spectra acquired in *Al-AP, Al-R1, Al-R6, and Al-R24*

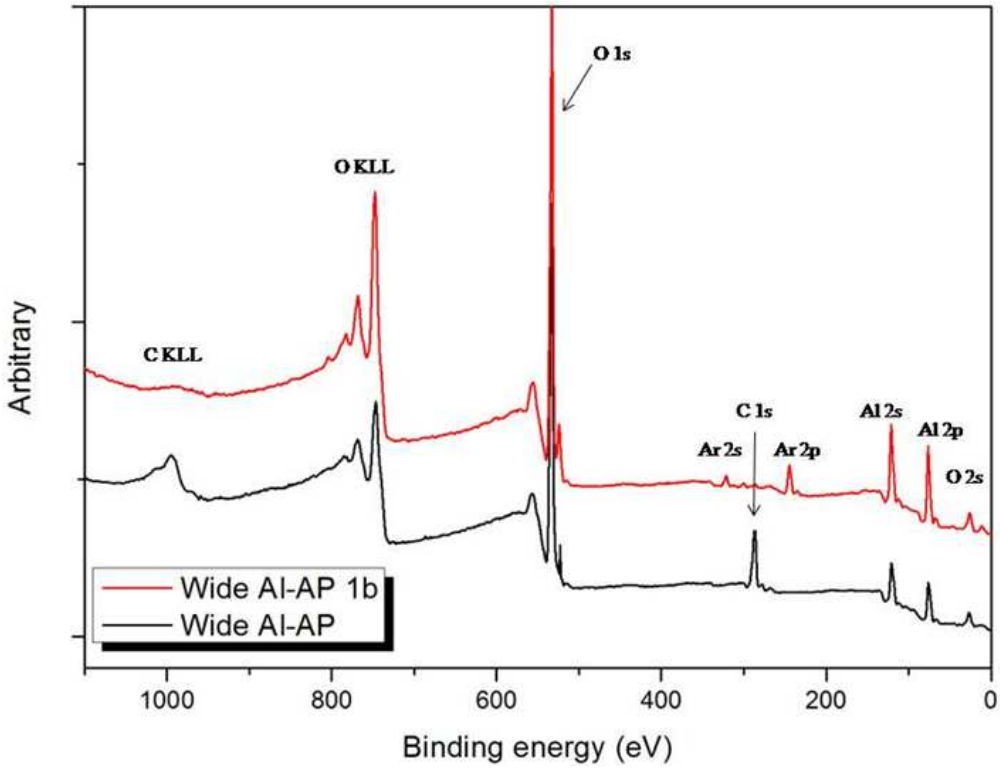

Figure 5.33 – Wide scan XPS spectra acquired in sample Al-AP and Al-AP 1b (after one bombardment experiment)

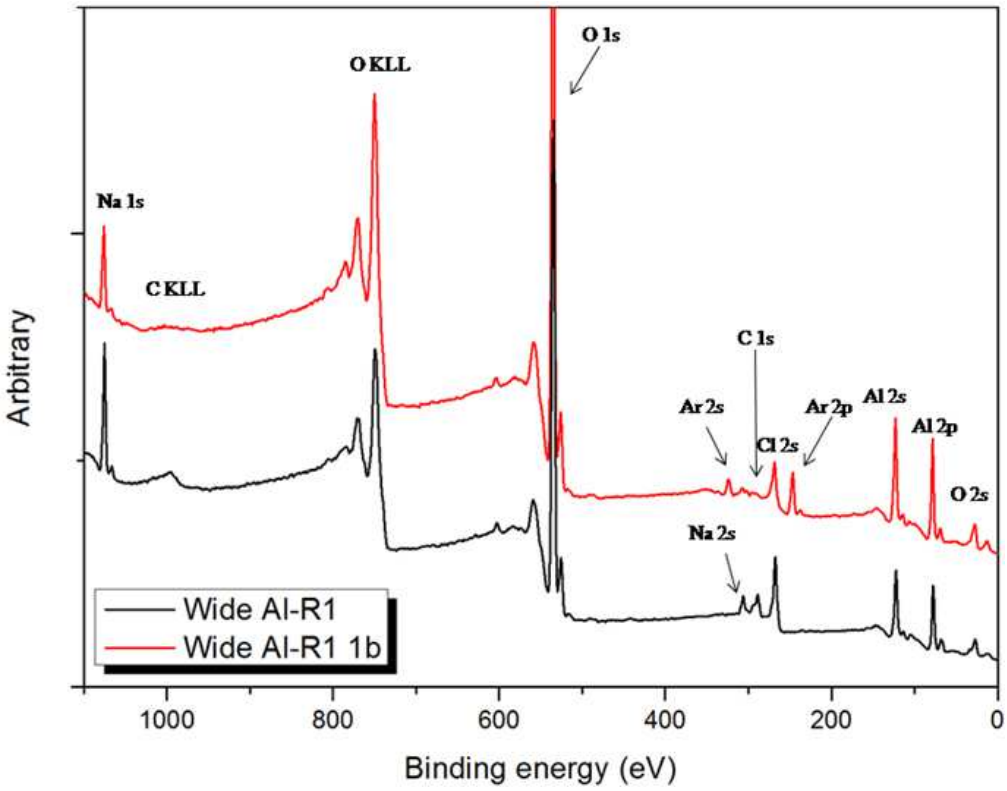

Figure 5.34 – Wide scan XPS spectra acquired in sample *Al-R1* and *Al-R1* 1b (after one bombardment experiment)

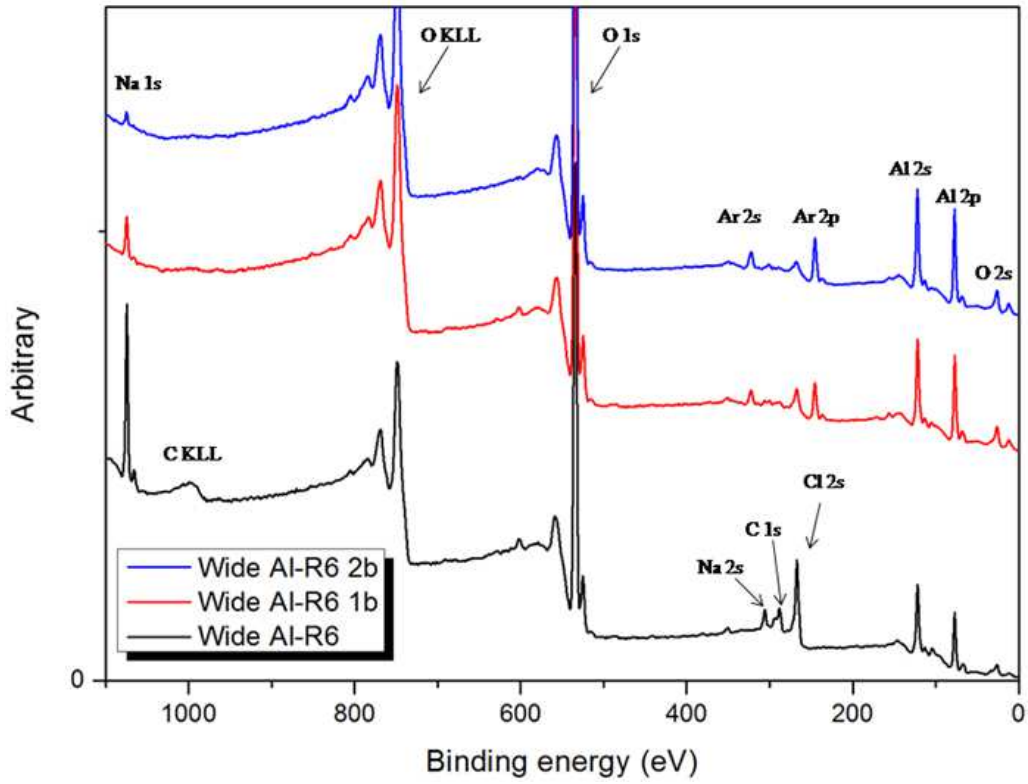

Figure 5.35 – Wide scan XPS spectra acquired in sample Al-R6, Al-R6 1b and 2b (after two bombardment experiments).

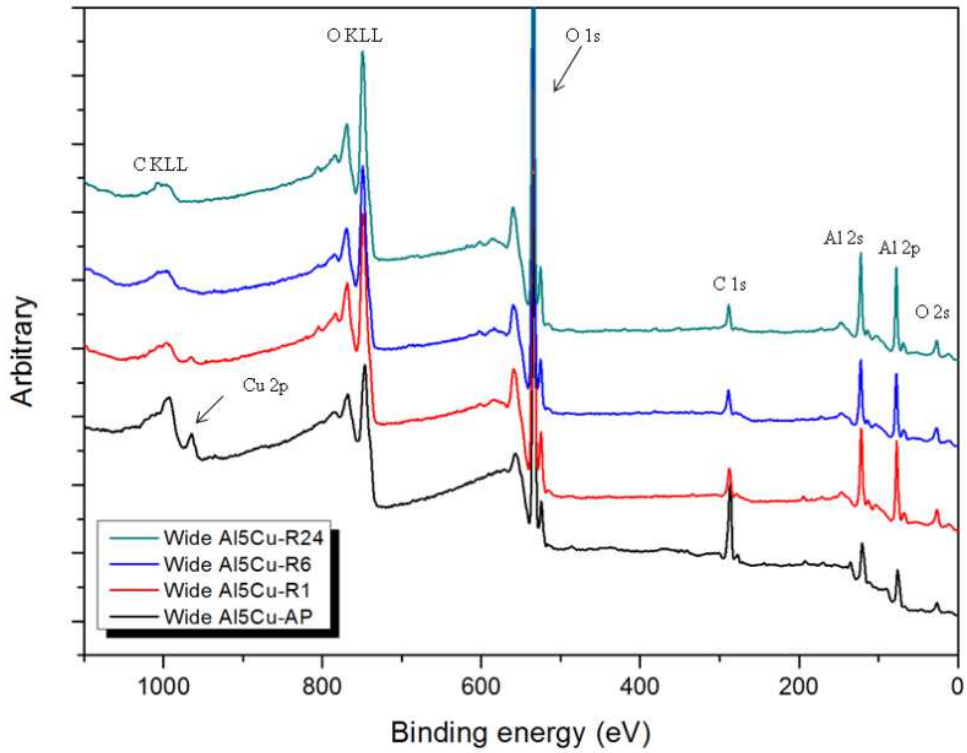

Figure 5.36 – Wide scan XPS spectra acquired in *Al-5Cu-AP, Al-5Cu-R1, Al-5Cu-R6* and *Al-5Cu-R24*.

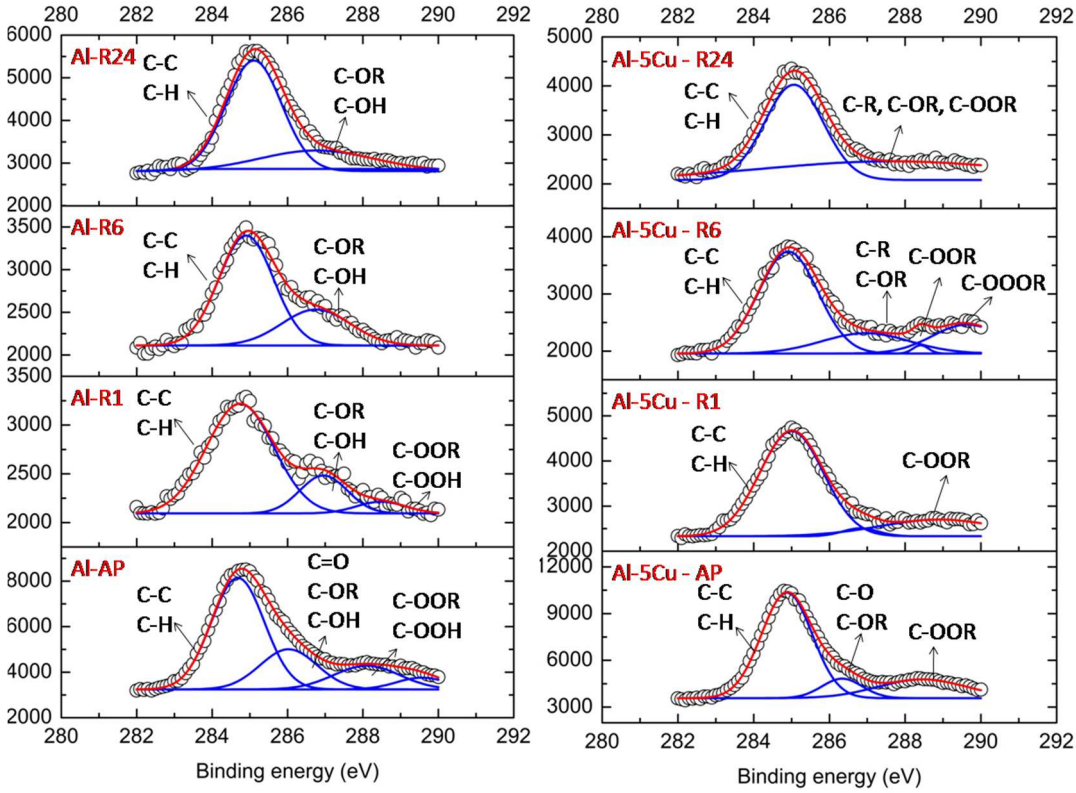

Figure 5.37 – C 1s core levels acquired in all XPS samples.

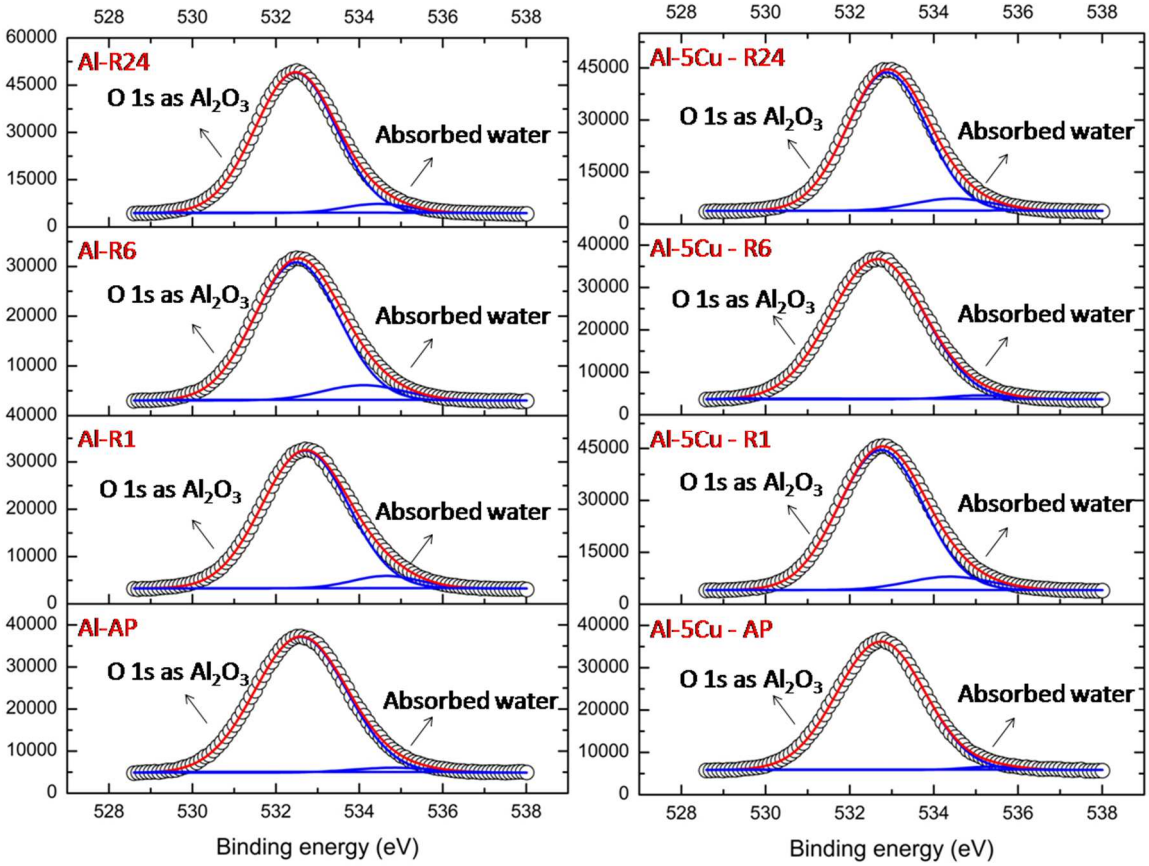

Figure 5.38 – O 1s core levels acquired in all XPS samples.

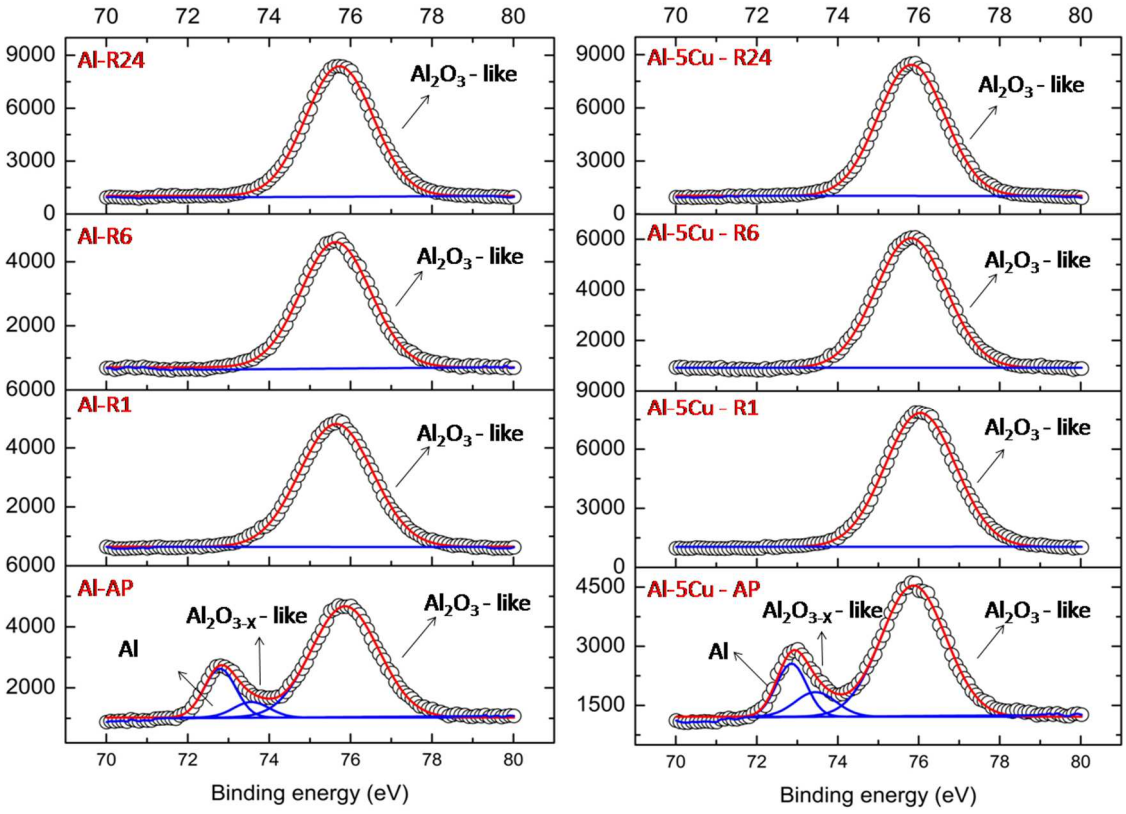

Figure 5.39 – Al 2p core levels acquired in all XPS samples.

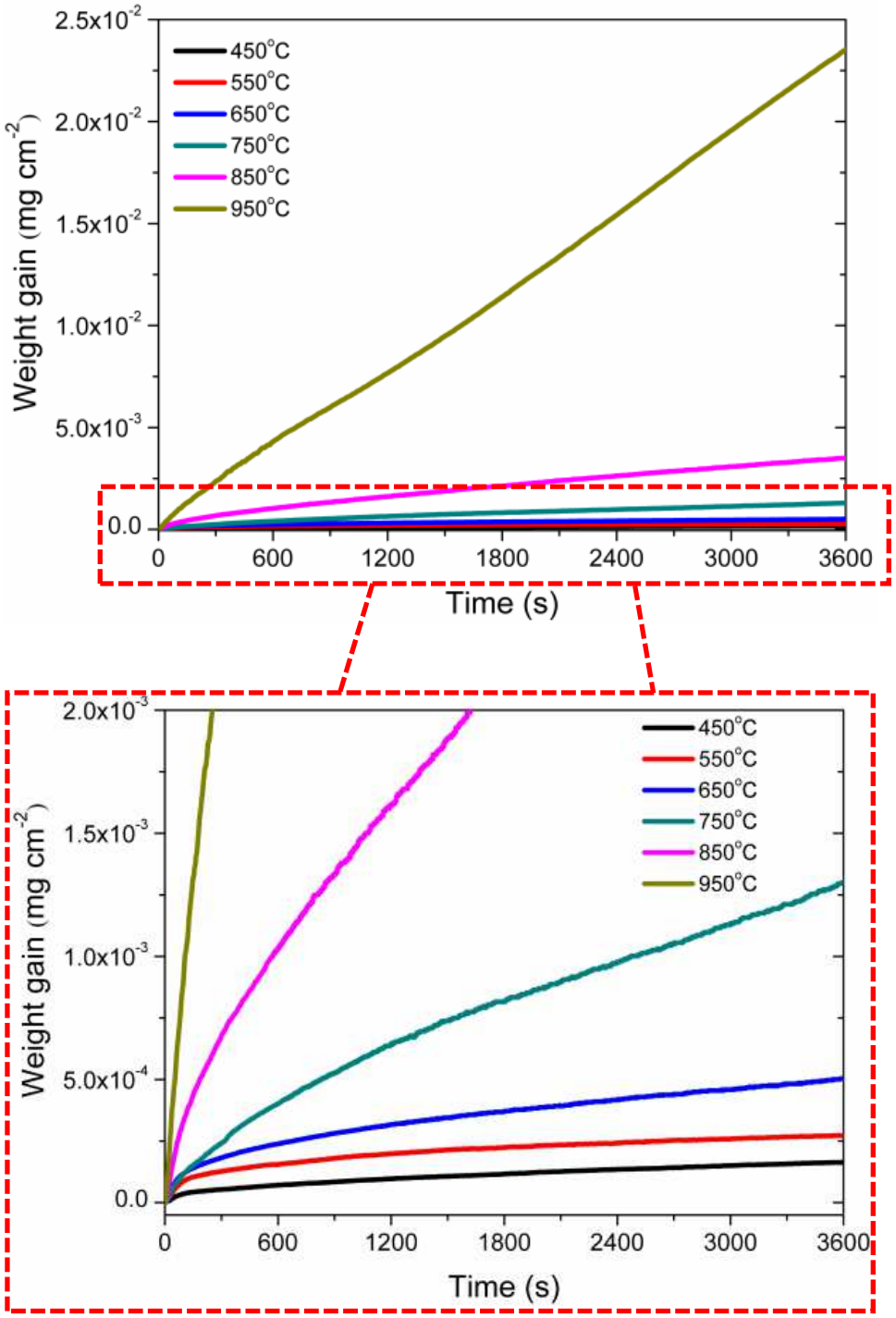

Figure 5.40 – Kinetics curves of the oxidation of Al at different temperatures.

Temperature (˚C)	$y^2 = A \cdot t$ (parameter A)	Adj. R-square
450	7.9501e-12	0.99493
550	2.5790e-11	0.91303
650	7.5001e-11	0.97281

Table 5.2 - Summarized fitting results for oxidation kinetics studies of Al in the temperature range 450-650ºC.

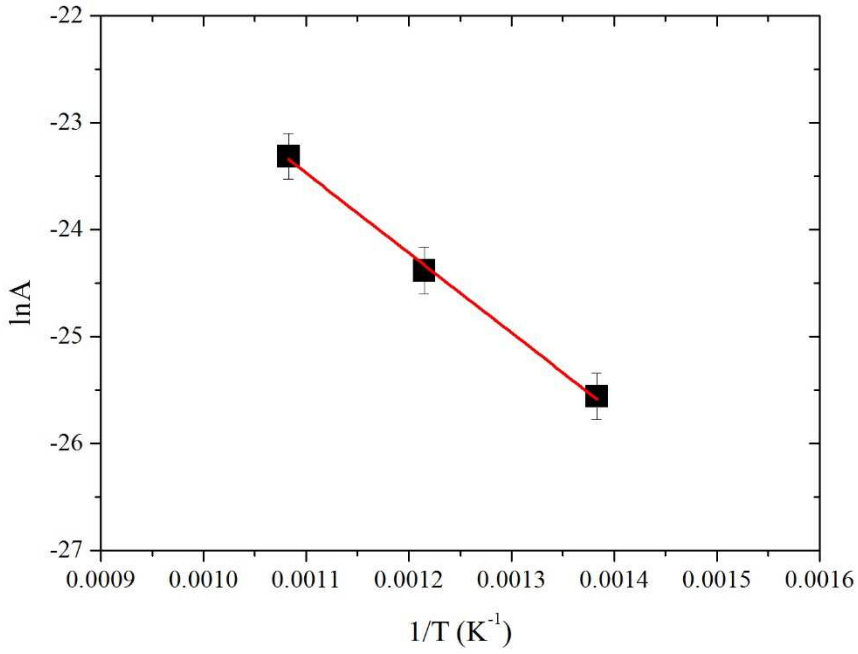

Figure 5.41 – Arrhenius plots of the oxidation kinetics of Al in the temperature range 450-650ºC.

Temperature (˚C)	$y = A \cdot t$ (parameter A)	Adj. R-square
750	2.6651e-7	0.99842
850	7.3982e-7	0.99921
950	6.7903e-6	0.99986

Table 5.3 - Summarized fitting results for oxidation kinetics studies of Al in the temperature range 750-950ºC.

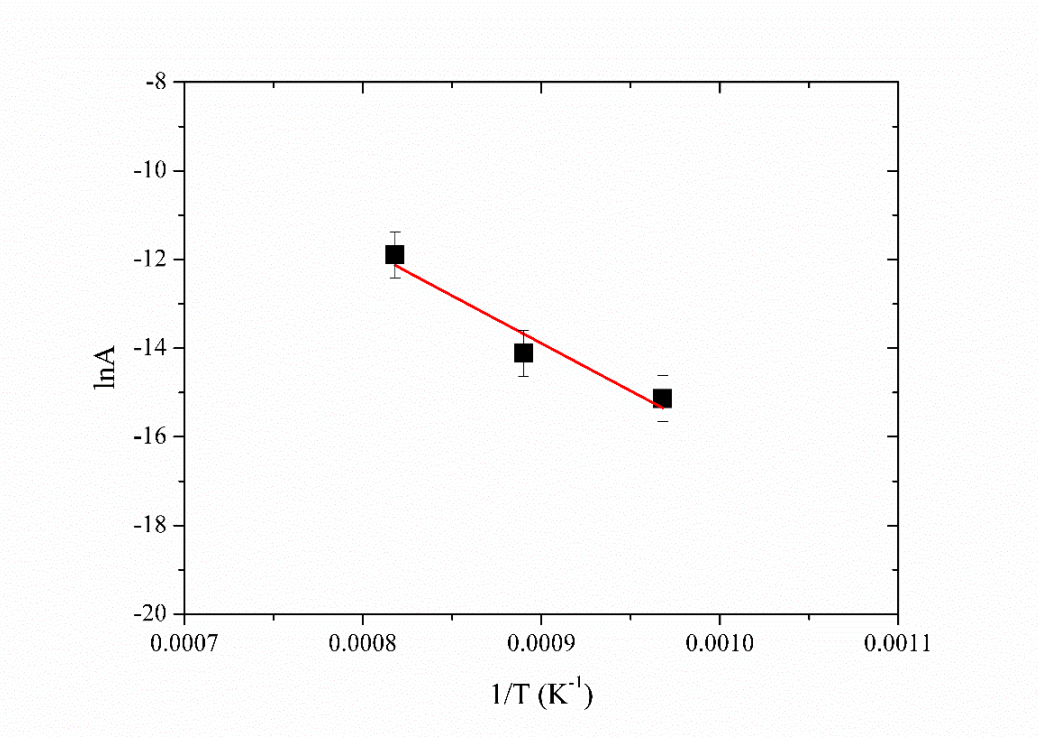

Figure 5.42 –Arrhenius plots of the oxidation kinetics of Al in the temperature range 750-950ºC.

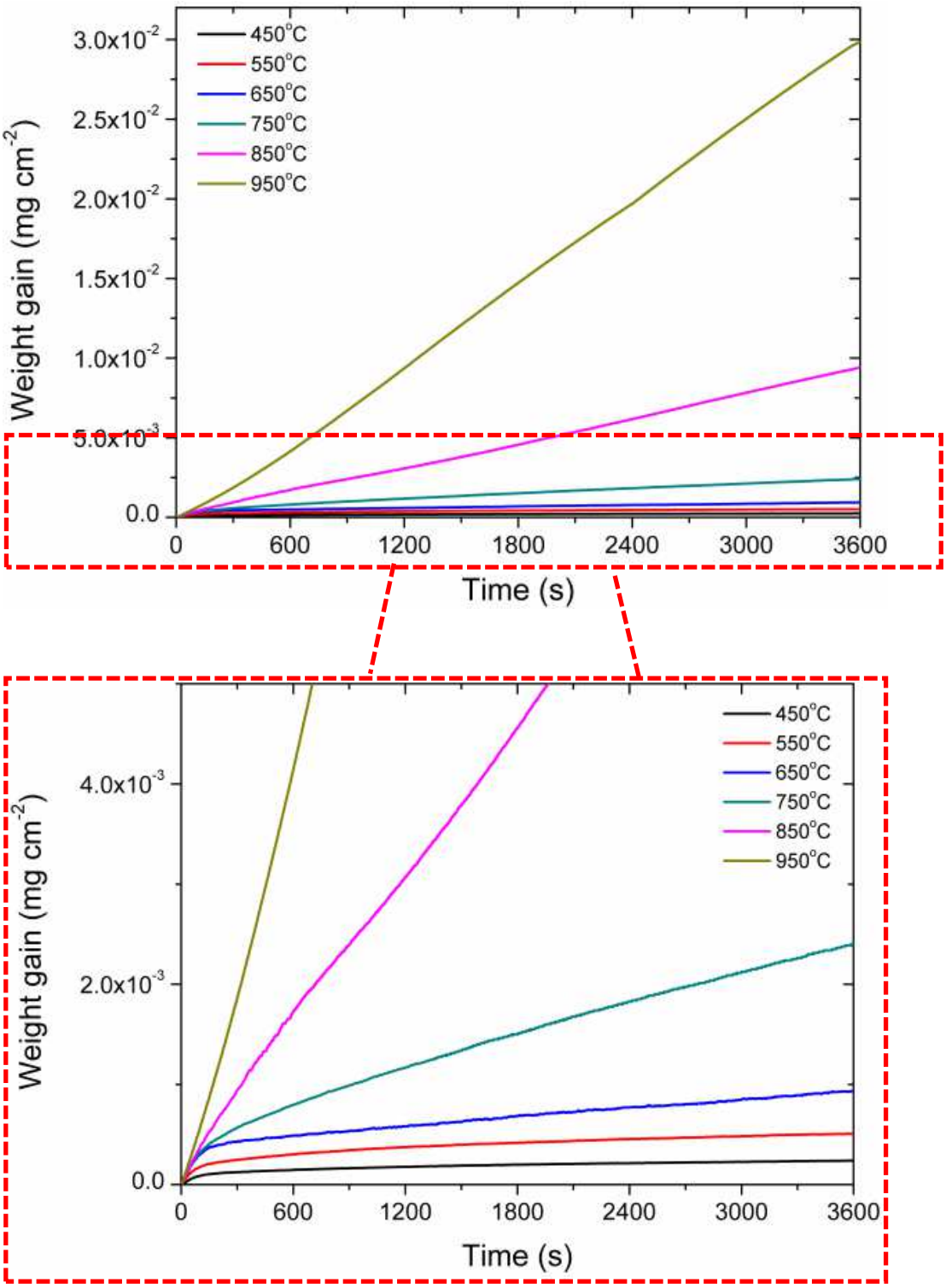

Figure 5.43 –Kinetics curves of the oxidation of Al-5Cu at different temperatures.

Temperature (˚C)	$y^2 = A \cdot t$ (parameter A)	Adj. R-square
450	2.0192e-11	0.88373
550	9.0249e-11	0.89518
650	2.5933e-10	0.87646

Table 5.4 - Summarized fitting results for oxidation kinetics studies of Al-5Cu in the temperature range 450-650ºC.

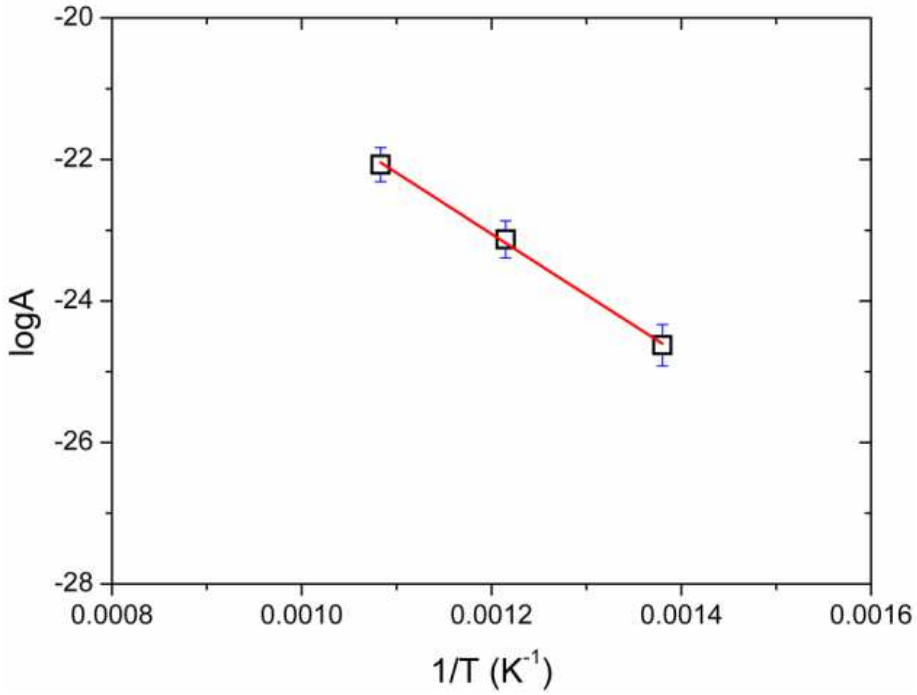

Figure 5.44 – Arrhenius plots showing different activation energies in temperature ranges 450-650ºC.

Temperature (˚C)	$y = A \cdot t$ (parameter A)	Adj. R-square
750	5.4969e-7	0.99911
850	2.7095e-6	0.99983
950	8.5668e-6	0.99951

Table 5.5 - Summarized fitting results for oxidation kinetics studies of Al-5Cu in the temperature range 750-950ºC.

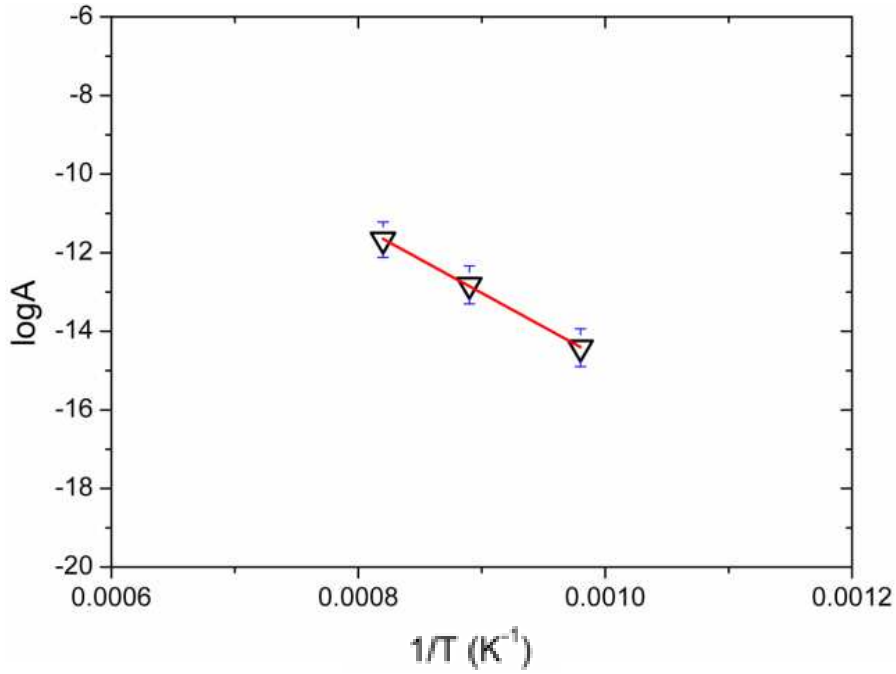

Figure 5.45 –Arrhenius plots showing different activation energies in temperature ranges 750-950ºC.

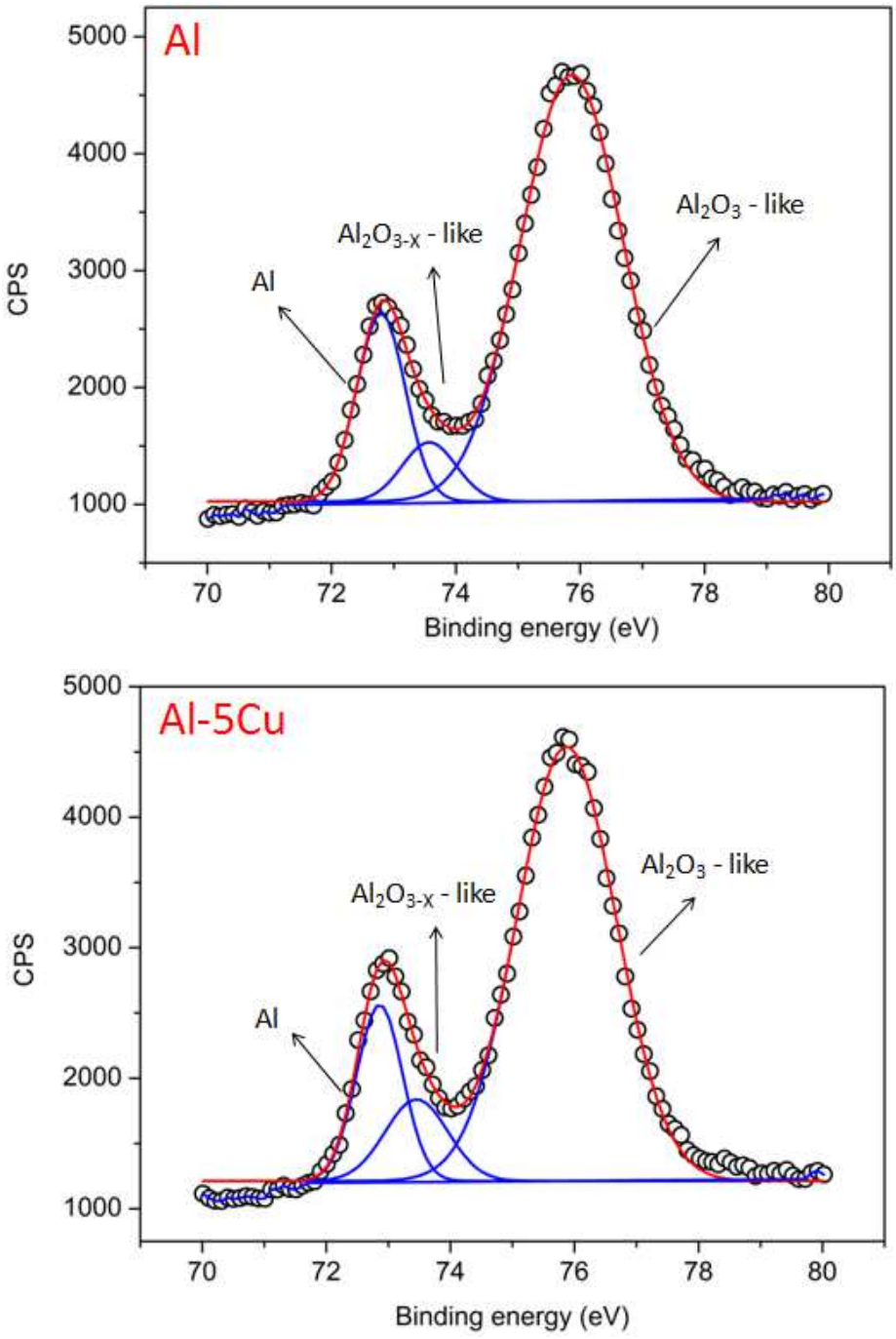

Figure 5.46 – Al 2p core levels acquired in Al-AP and Al-5Cu-AP.

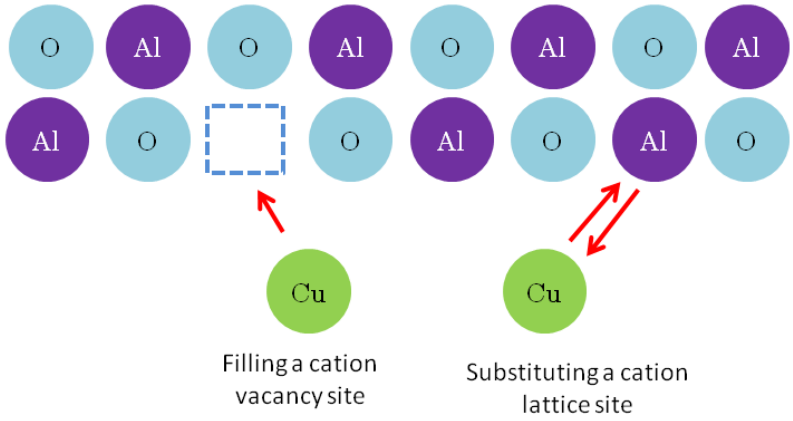

Figure 5.47 – Diagram showing the defects reaction model used to explain the effect of doping with Cu.

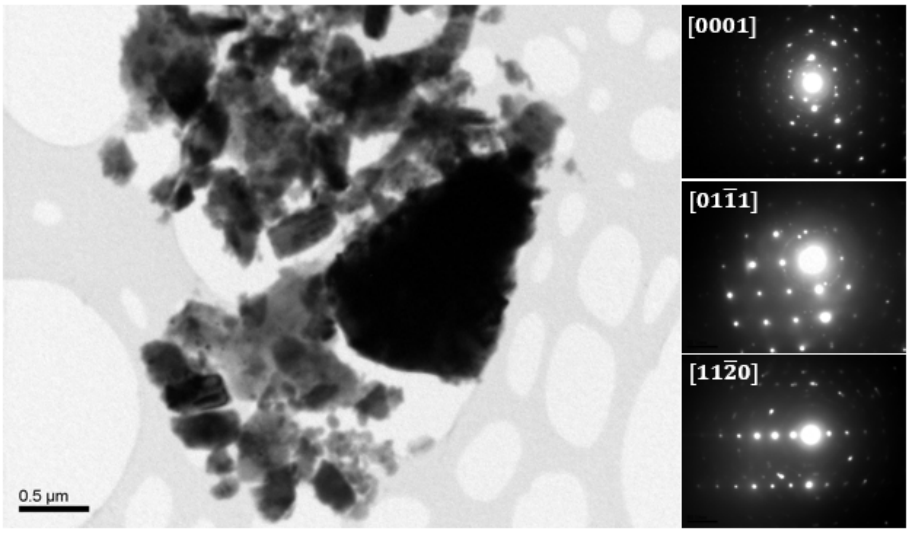

Figure 5.48 – TEM image and diffraction patterns of the stripped oxide from Al (950º C, 48h).

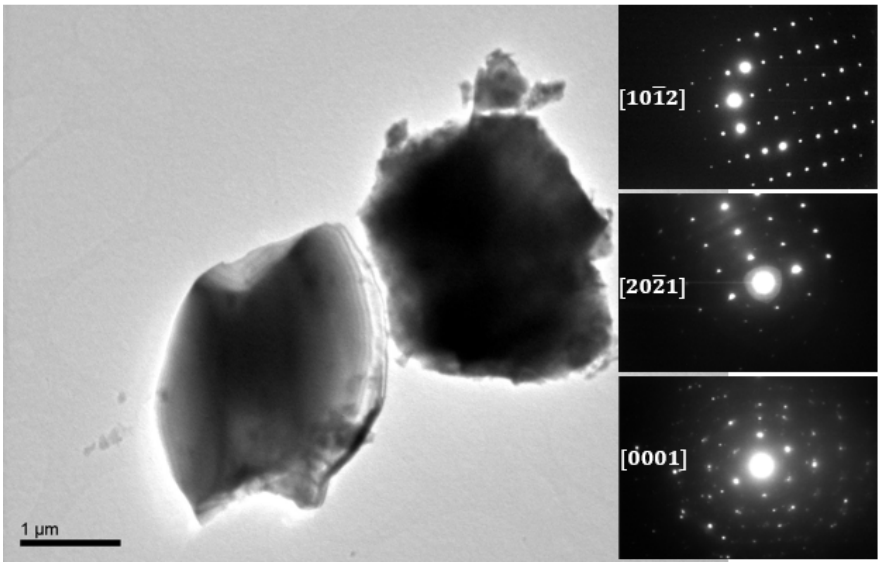

Figure 5.49 – TEM image and diffraction patterns of the stripped oxide from Al (950º C, 48h).

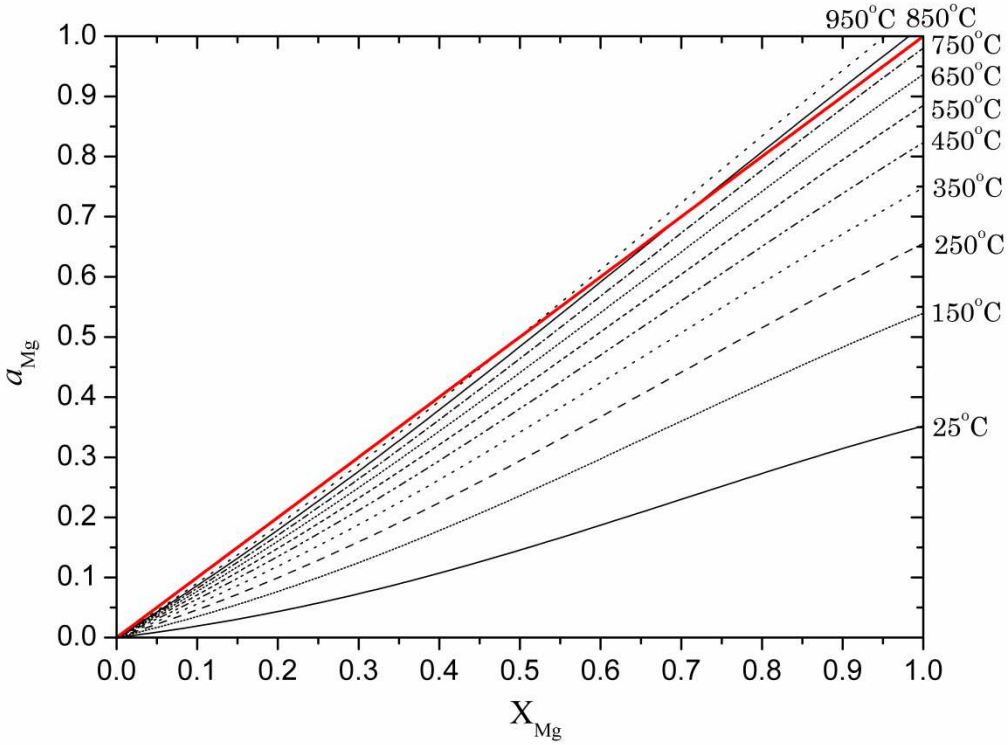

Figure 6.1 – Plots showing the Mg chemical activity as a function of Mg mole fraction at different temperatures. It clearly indicates that Equation 6.8 is only suitable for liquid Al-Mg alloys. There is a slight negative deviation from ideal behaviour in the temperature range 650-950°C, especially for dilute liquid Al-Mg alloys. In the present work, in the case of solid Al-Mg alloys (not higher than 650°C), the chemical activity of Mg is assumed equal to X_{Mg}.

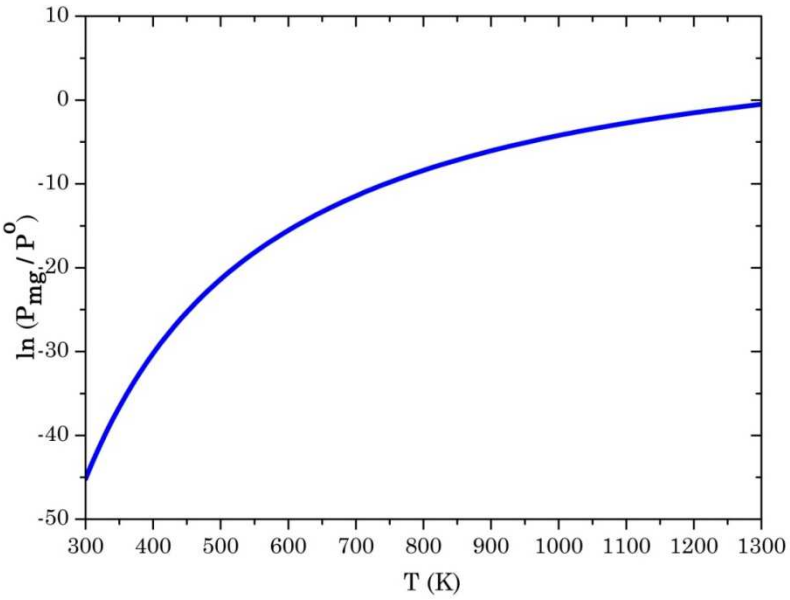

Figure 6.2 – Plot showing the Mg vapour pressure (in terms of activity) as a function of temperature.

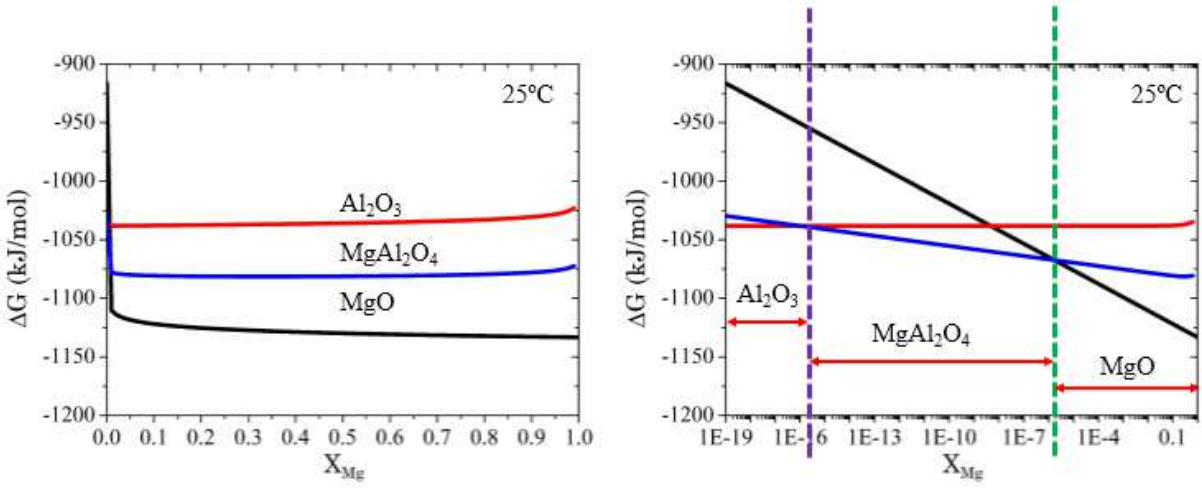

Figure 6.3 – Plot showing the Gibbs free energy change profile of different oxides as a function of Mg mole fraction at 25°C.

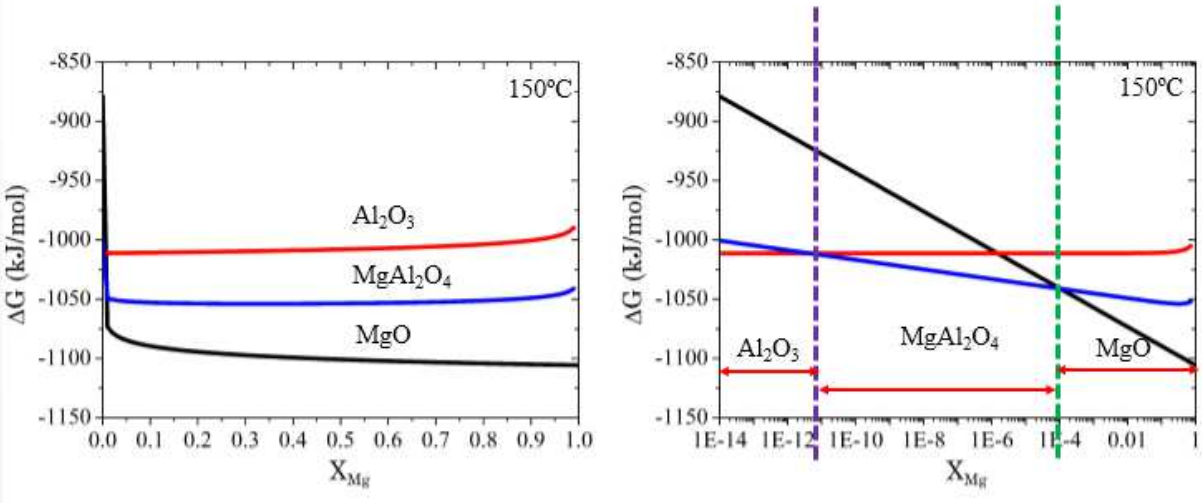

Figure 6.4 – Plot showing the Gibbs free energy change profile of different oxides as a function of Mg mole fraction at 150°C.

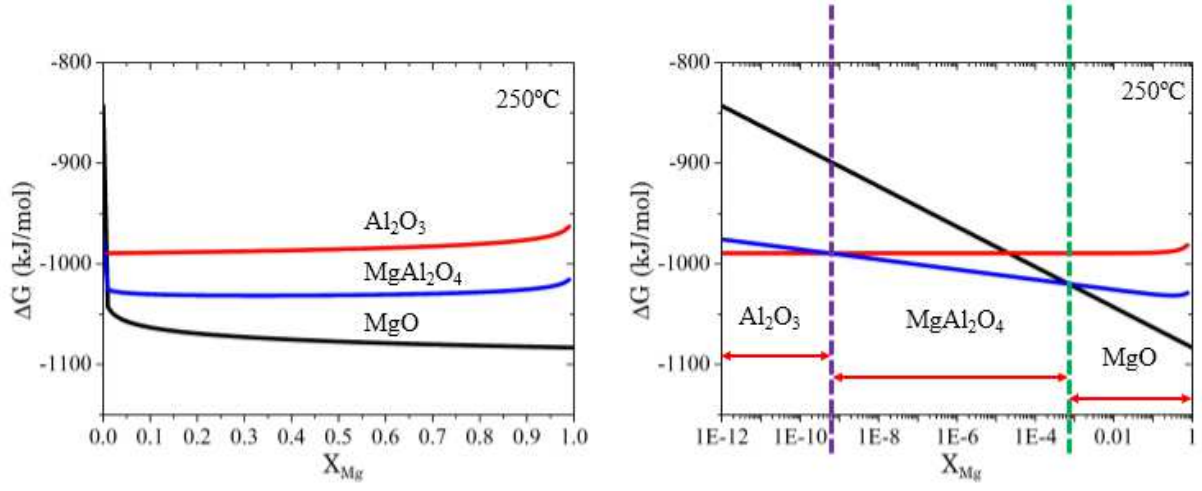

Figure 6.5 – Plot showing the Gibbs free energy change profile of different oxides as a function of Mg mole fraction at 250°C.

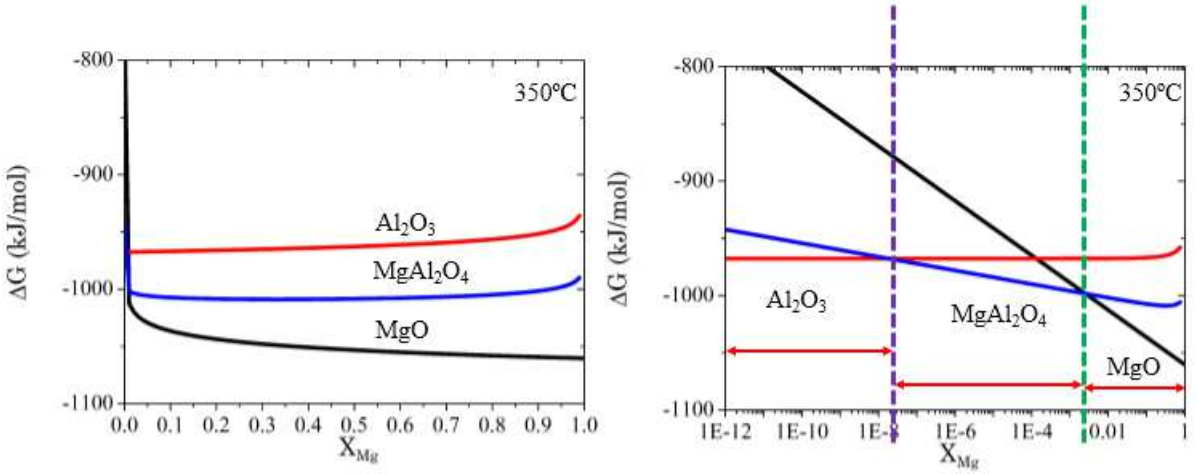

Figure 6.6 – Plot showing the Gibbs free energy change profile of different oxides as a function of Mg mole fraction at 350ºC.

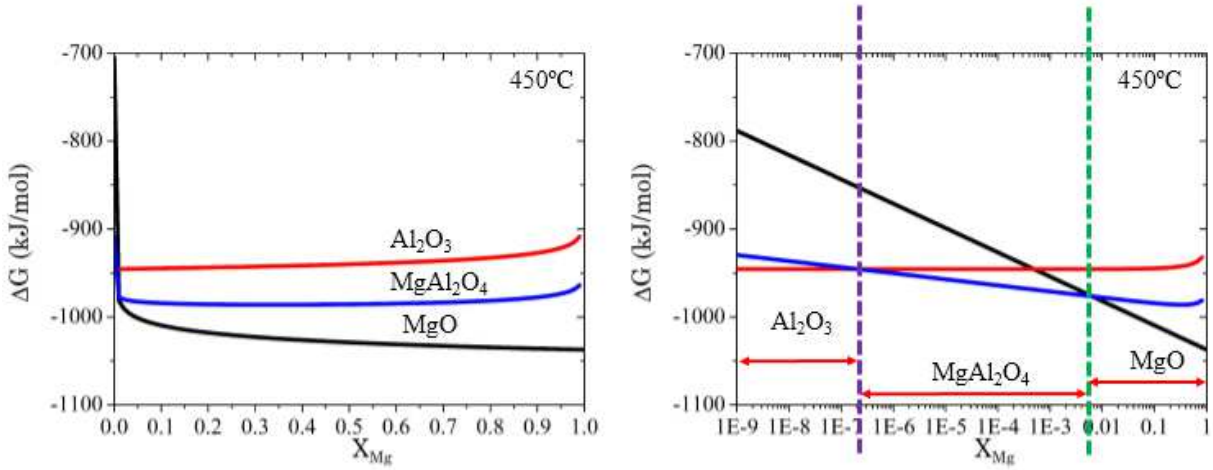

Figure 6.7 – Plot showing the Gibbs free energy change profile of different oxides as a function of Mg mole fraction at 450ºC.

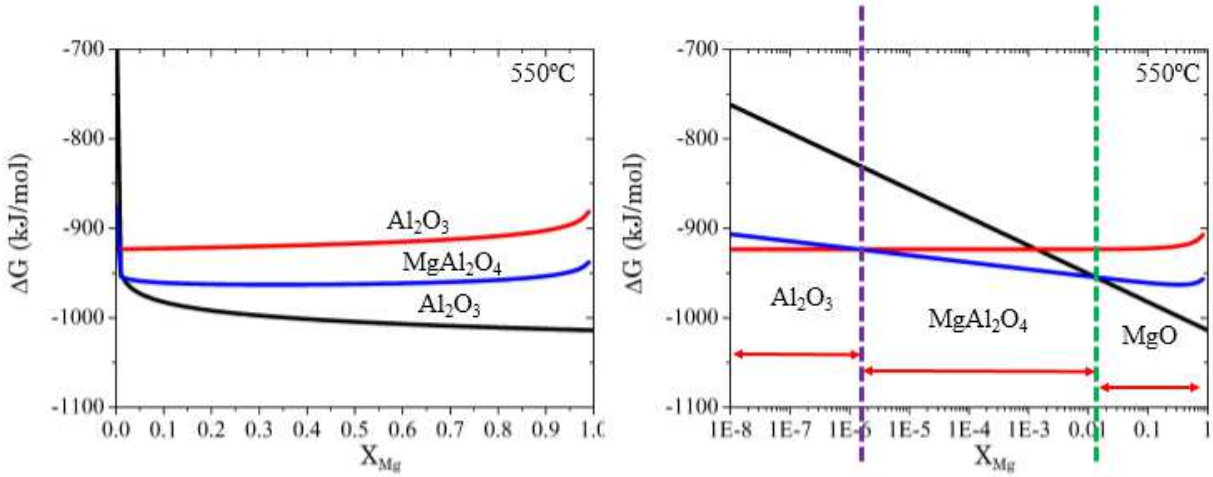

Figure 6.8 – Plot showing the Gibbs free energy change profile of different oxides as a function of Mg mole fraction at 550ºC.

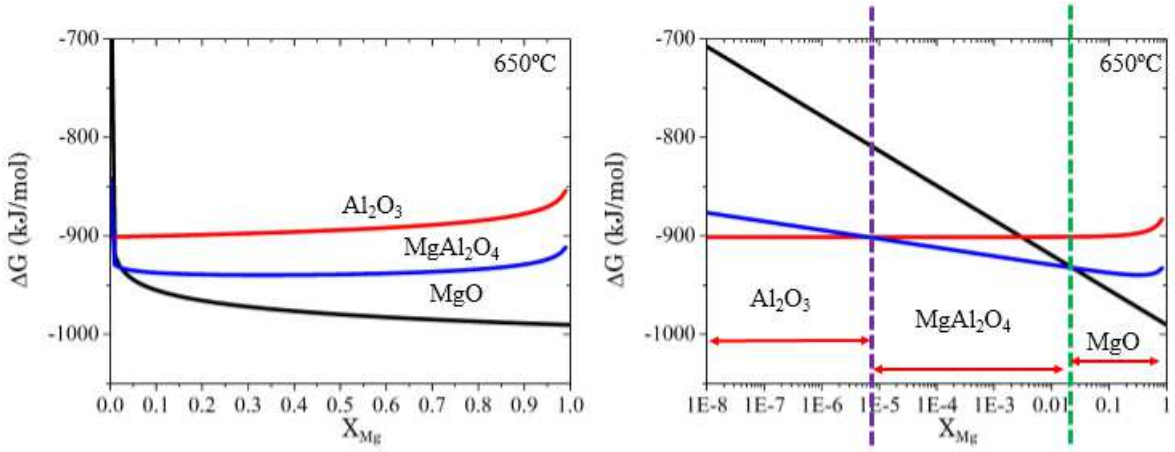

Figure 6.9 – Plot showing the Gibbs free energy change profile of different oxides as a function of Mg mole fraction at 650°C.

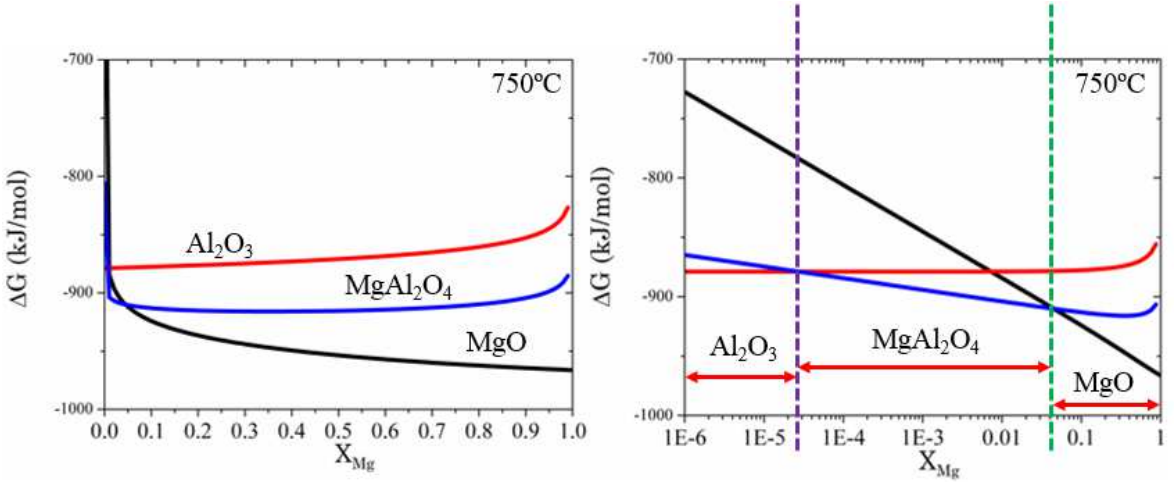

Figure 6.10 – Plot showing the Gibbs free energy change profile of different oxides as a function of Mg mole fraction at 750°C.

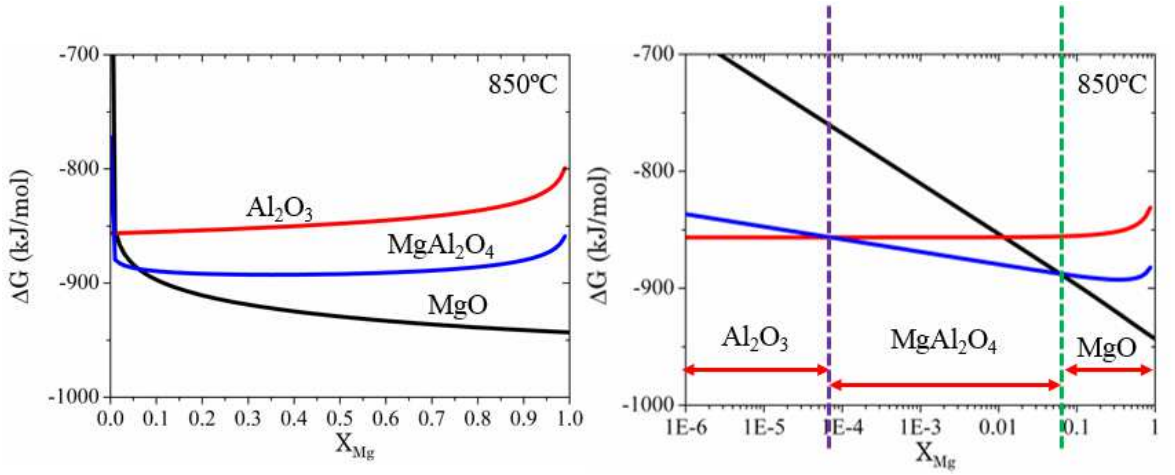

Figure 6.11 – Plot showing the Gibbs free energy change profile of different oxides as a function of Mg mole fraction at 850°C.

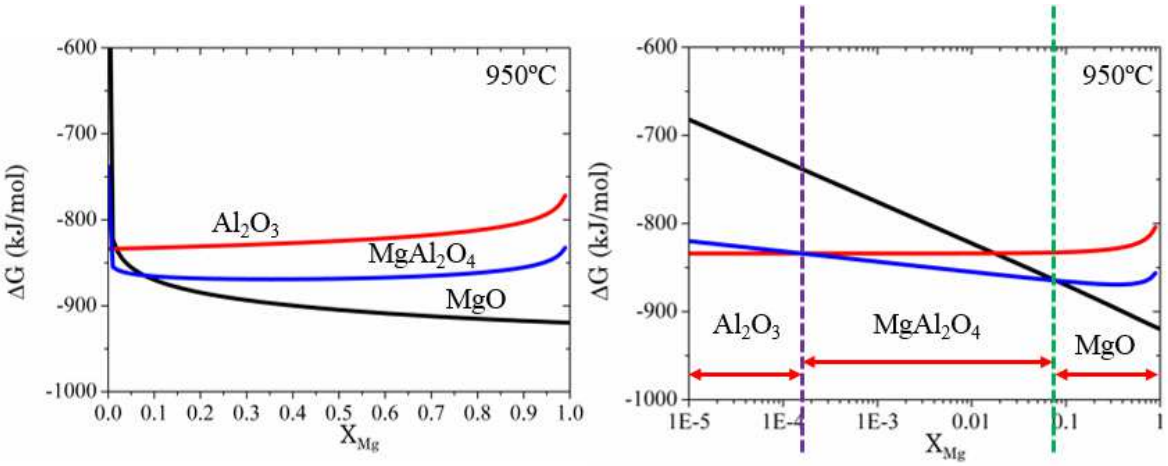

Figure 6.12 – Plot showing the Gibbs free energy change profile of different oxides as a function of Mg mole fraction at 950°C.

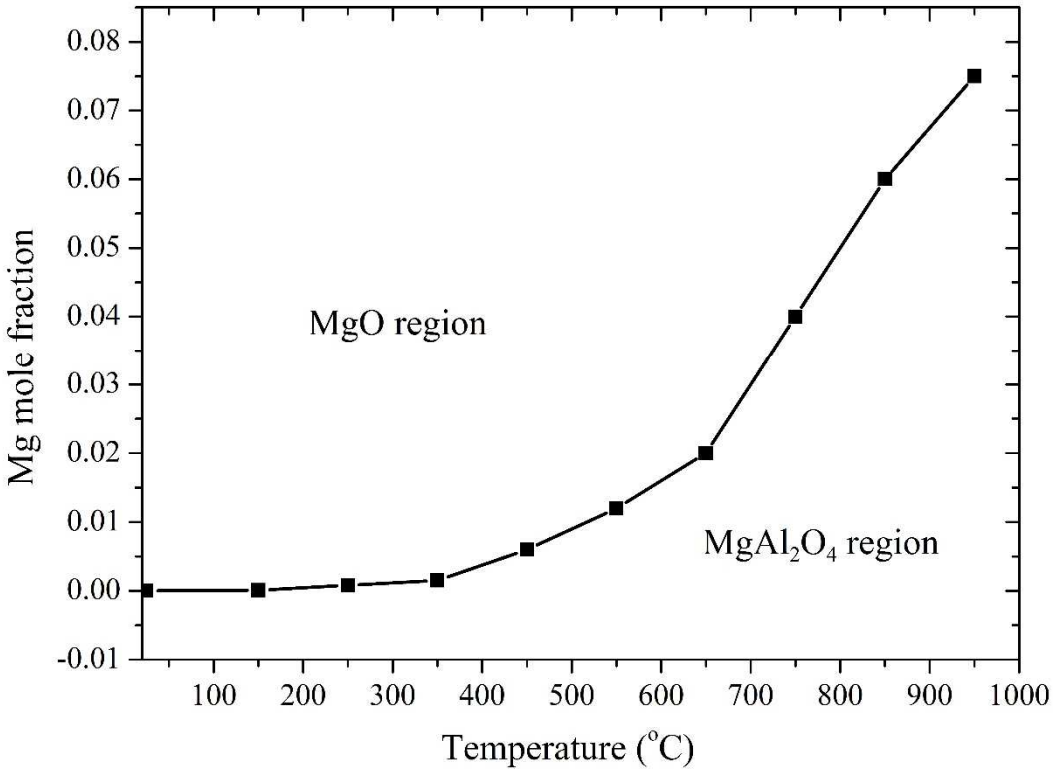

Figure 6.13 – Plot showing the critical Mg mole fraction (range: 0-1) C_{Mg} as a function of temperature in the range of 25-950°C.

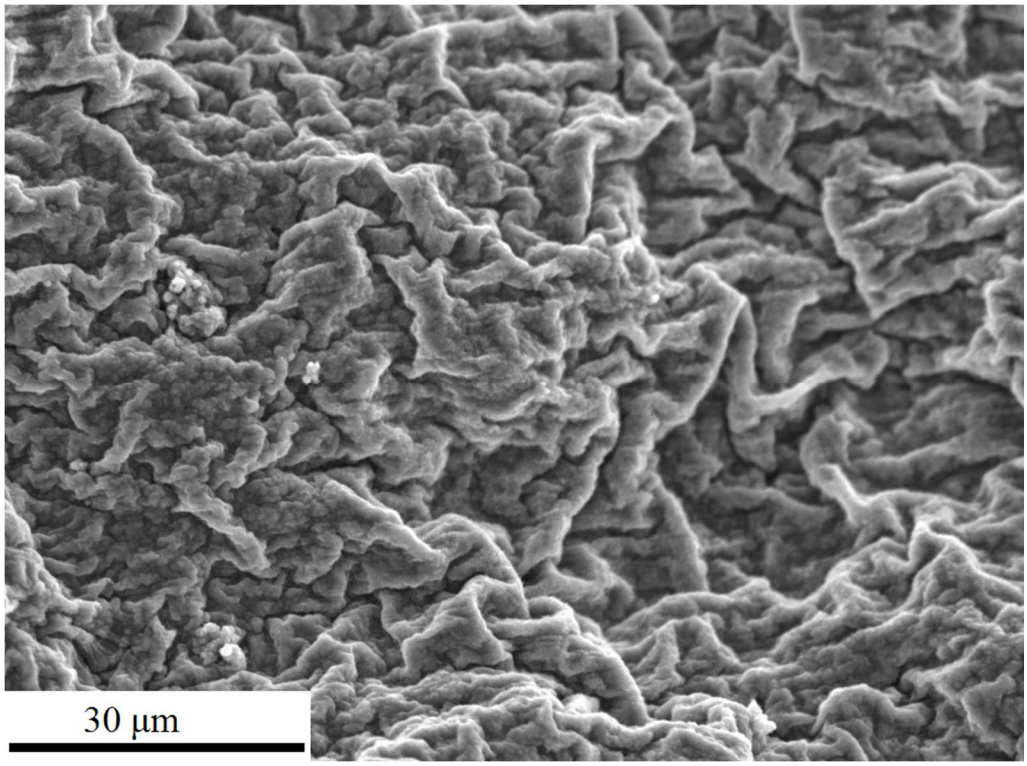

Figure 6.14 – SE image showing the wrinkled morphology of the oxide layer formed on an Al-2Mg alloy (750°C, 1h, dry air).

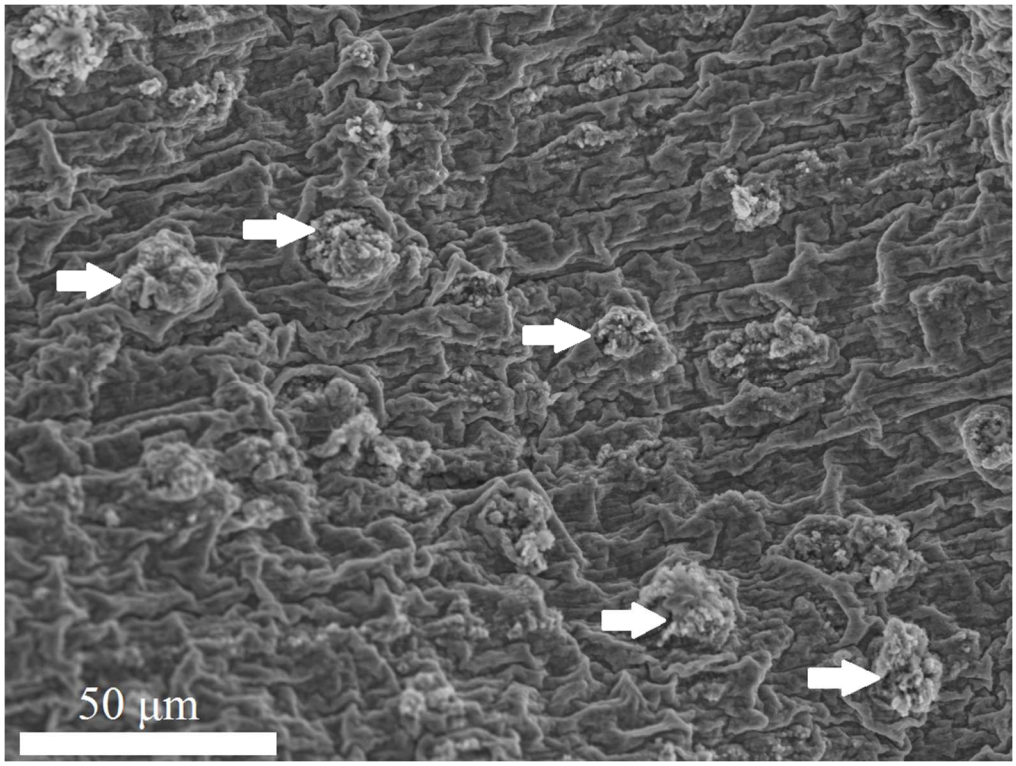

Figure 6.15 – SE image showing the cauliflower-like oxide bulges formed on an Al-2Mg alloy (750°C, 1h, dry air).

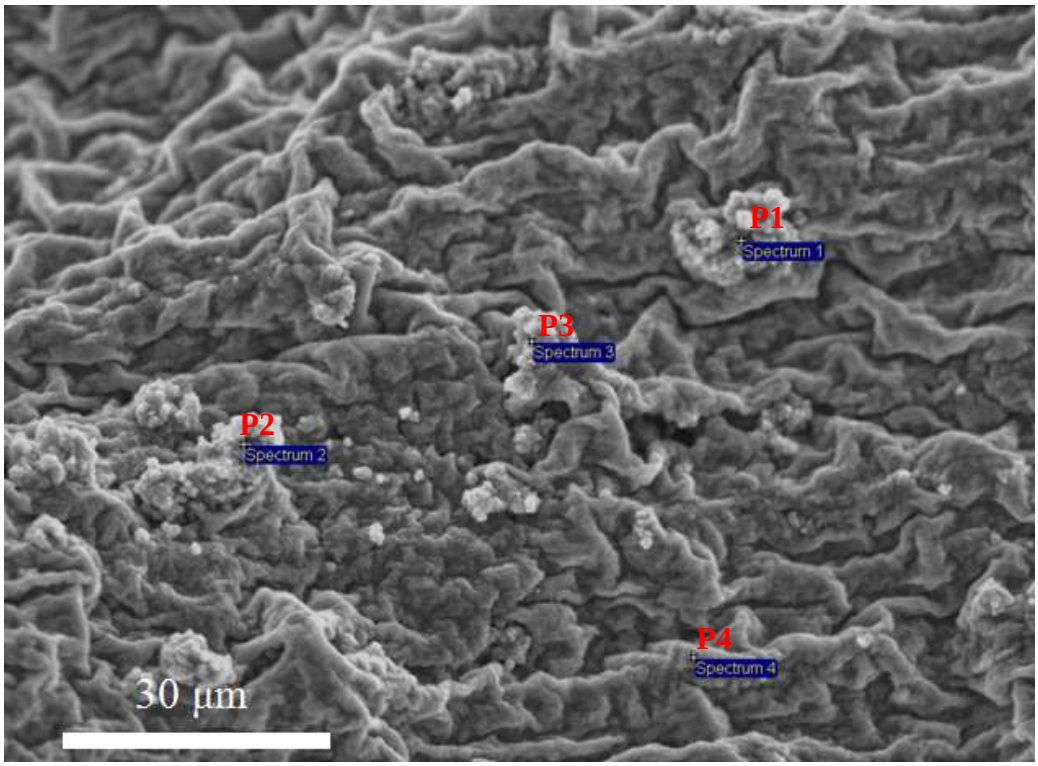

Figure 6.16 (a) – SE image showing the cauliflower-like oxide bulges consisting of fine crystalline oxides

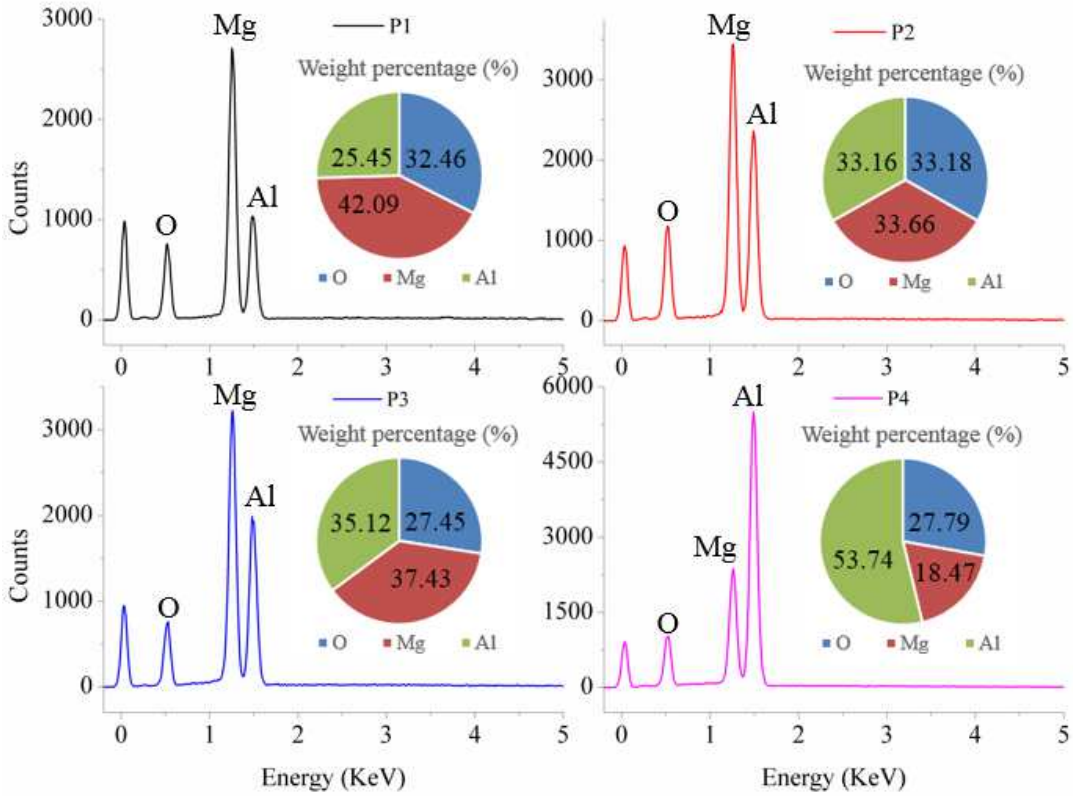

Figure 6.16 (b) – Quantified EDX results and EDX spectra corresponding to Figure 6.16 (a)

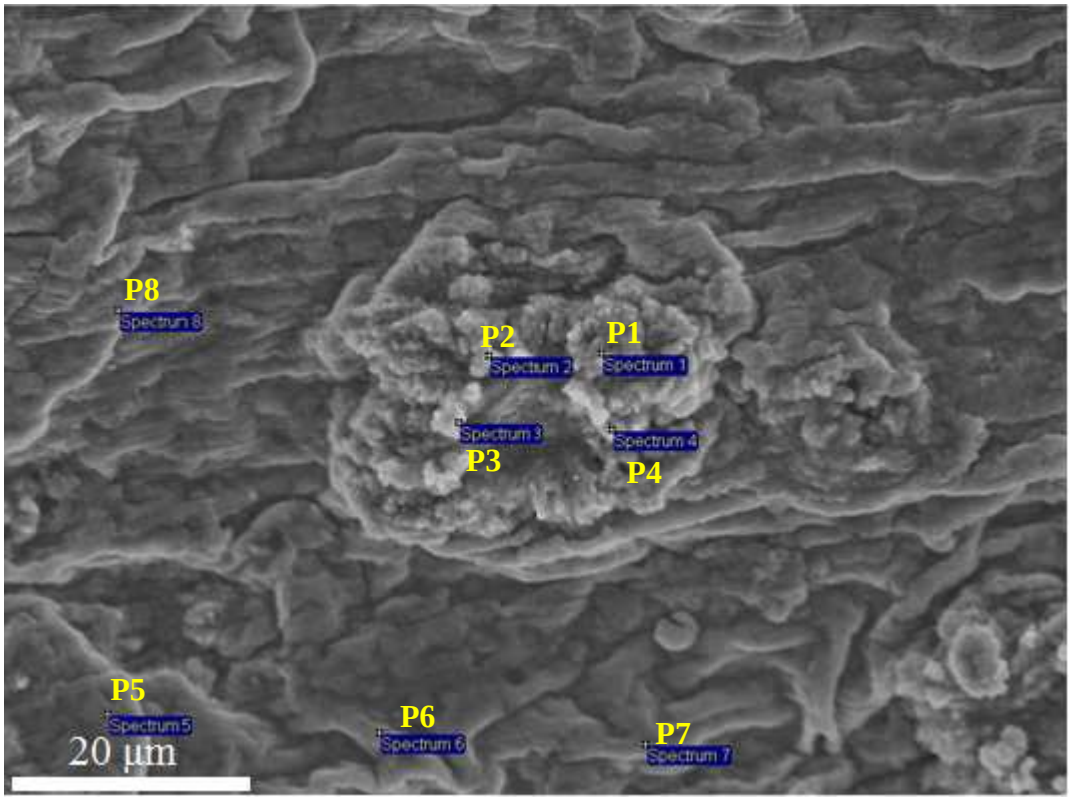

Figure 6.17 – (a) SE image showing the cauliflower-like oxide bulge consisting of fine crystalline oxides and (b) EDX analysis (overleaf).

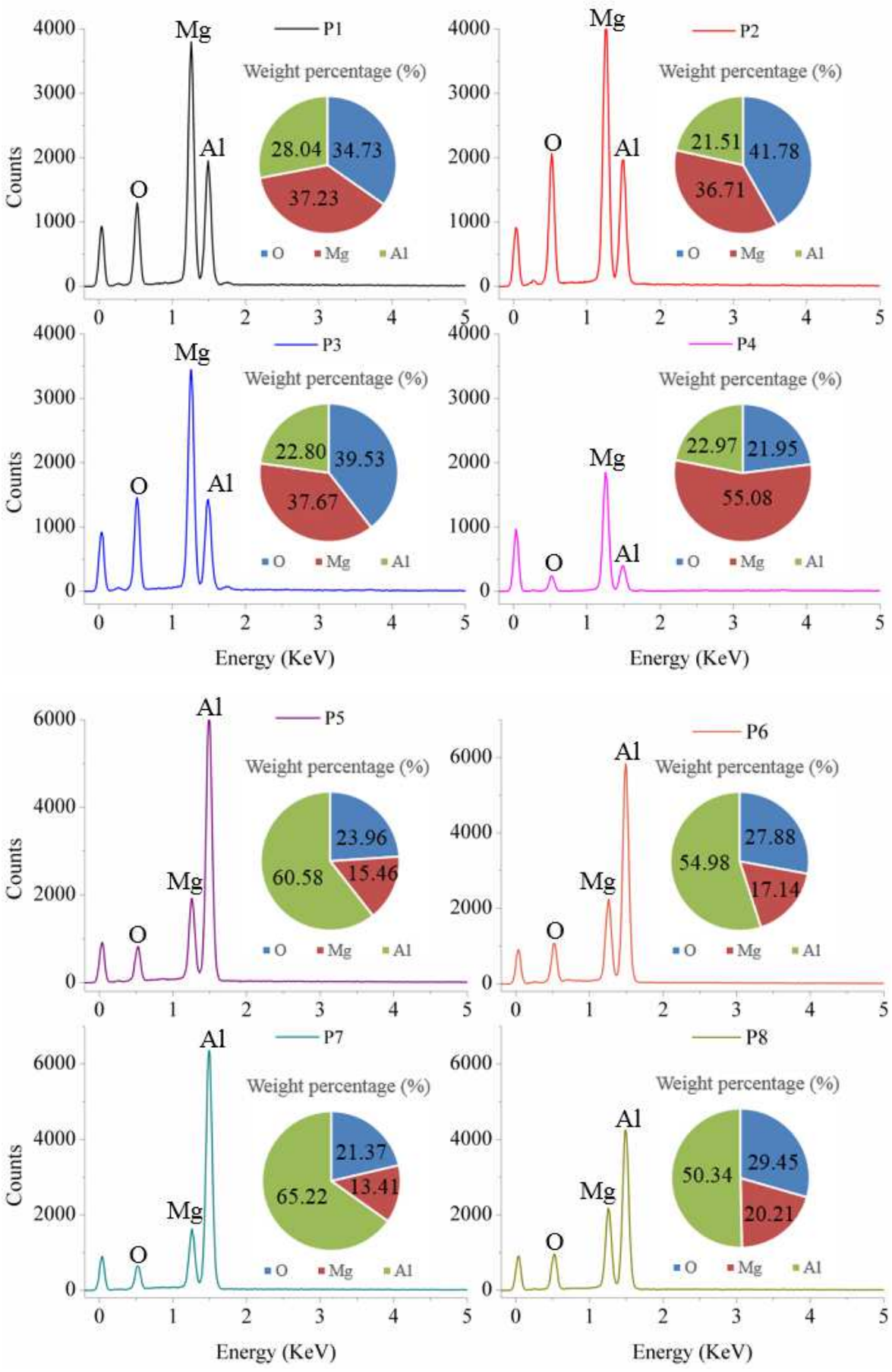

Figure 6.17 (b) – Quantified EDX results and EDX spectra

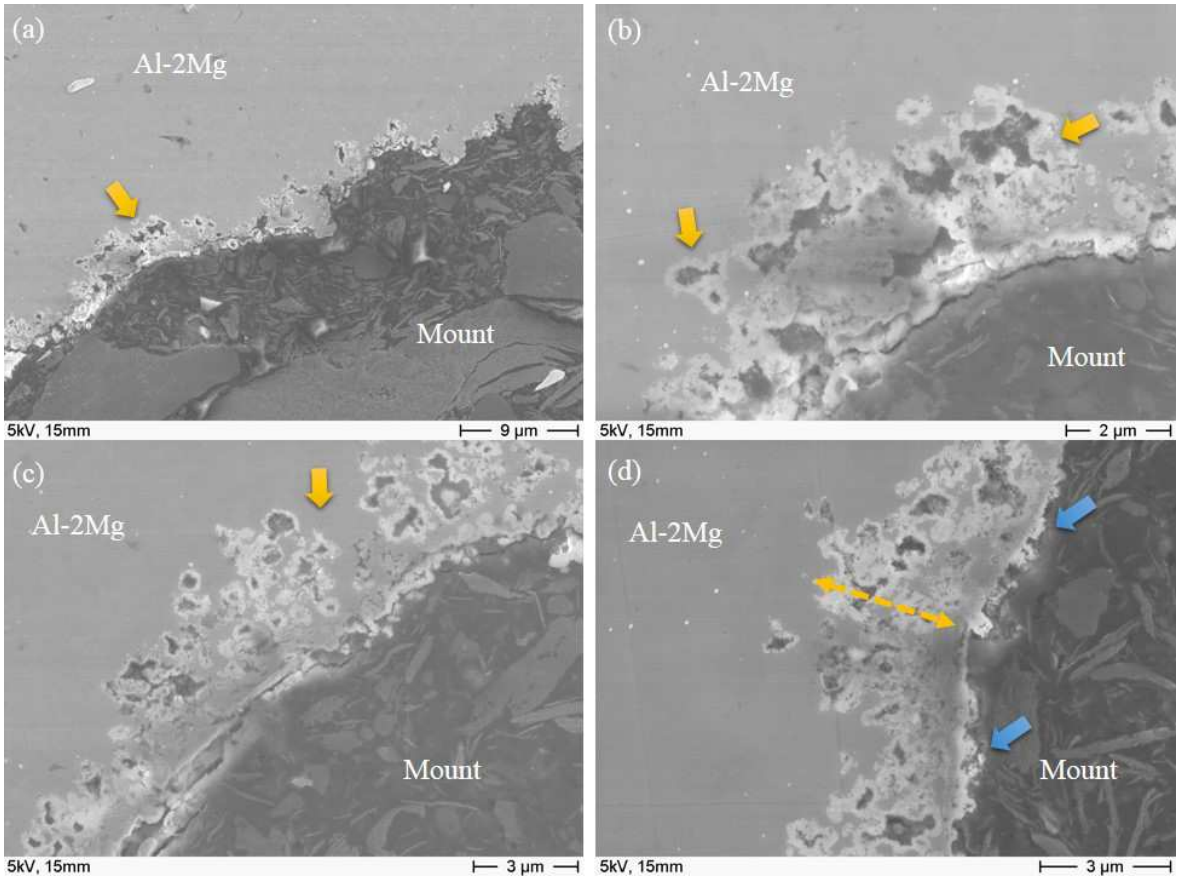

Figure 6.18 – SE image showing the cross sectional morphology of an oxidized Al-2Mg

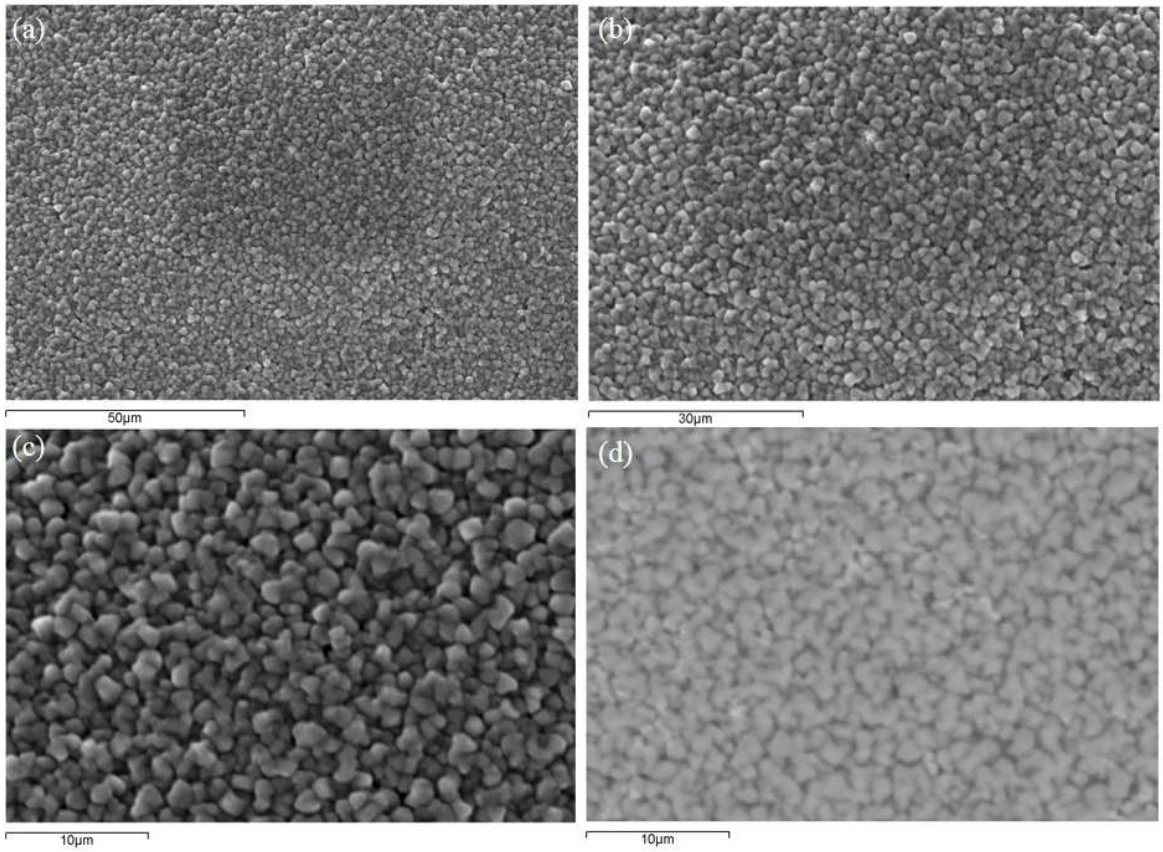

Figure 6.19 – Images showing the topography and morphology of the surface oxide layer on an Al-0.2Mg sample (750ºC, 1h, dry air) (a-c) SE image (d) BE image

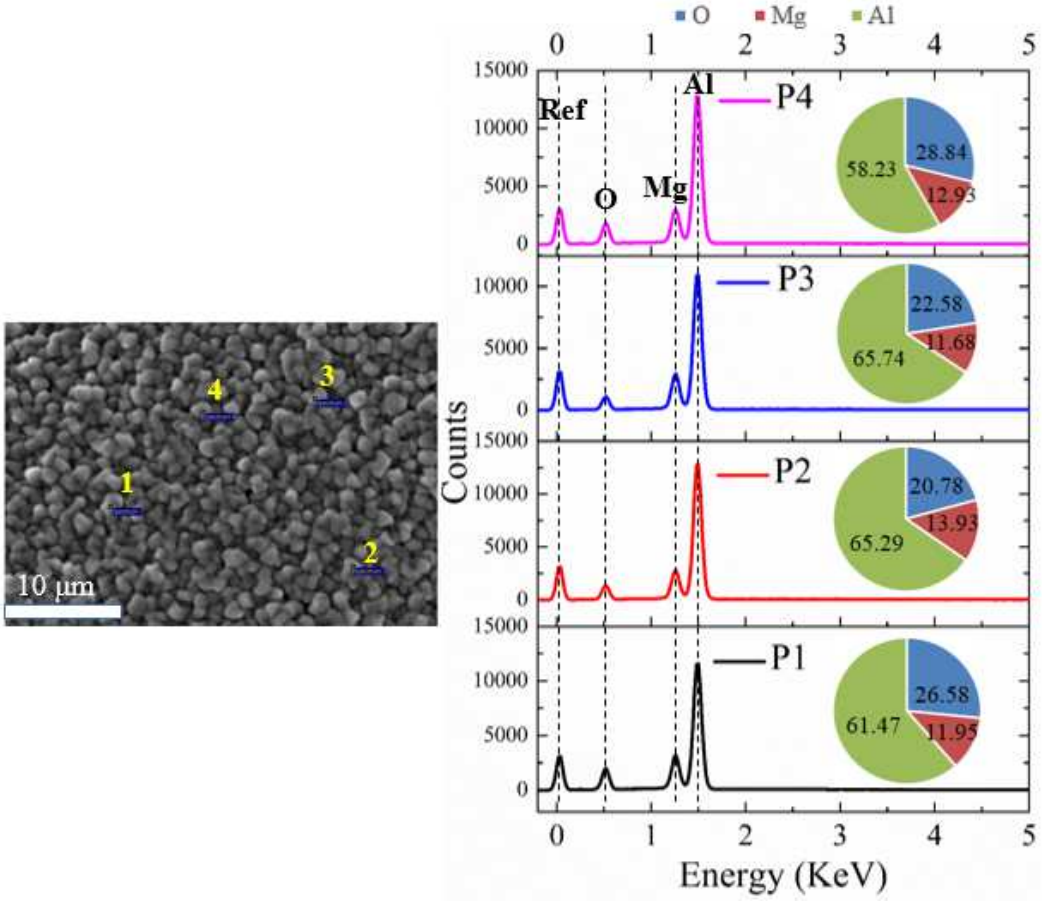

Figure 6.20 – EDX analysis on crystalline-like oxide particles.

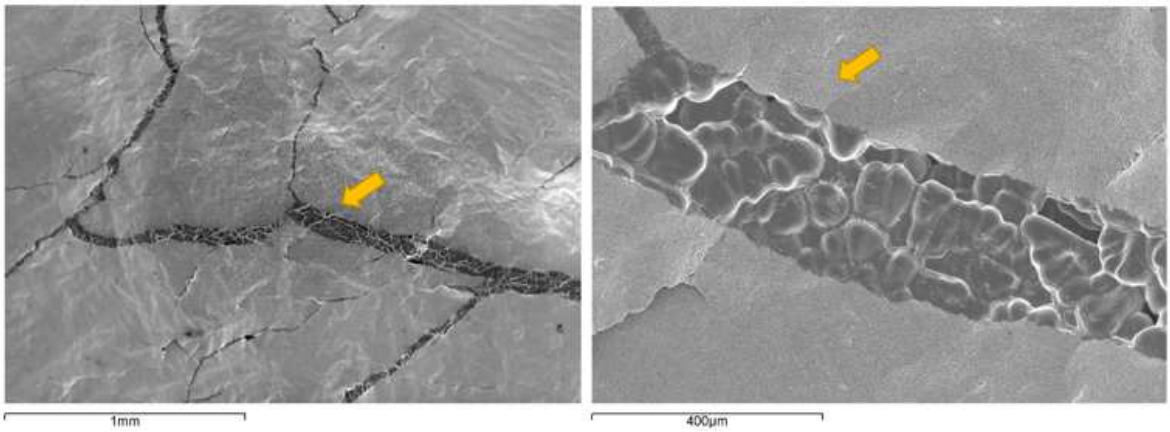

Figure 6.21 – SE Images showing the fracture of the oxide layer and the exposure of metal.

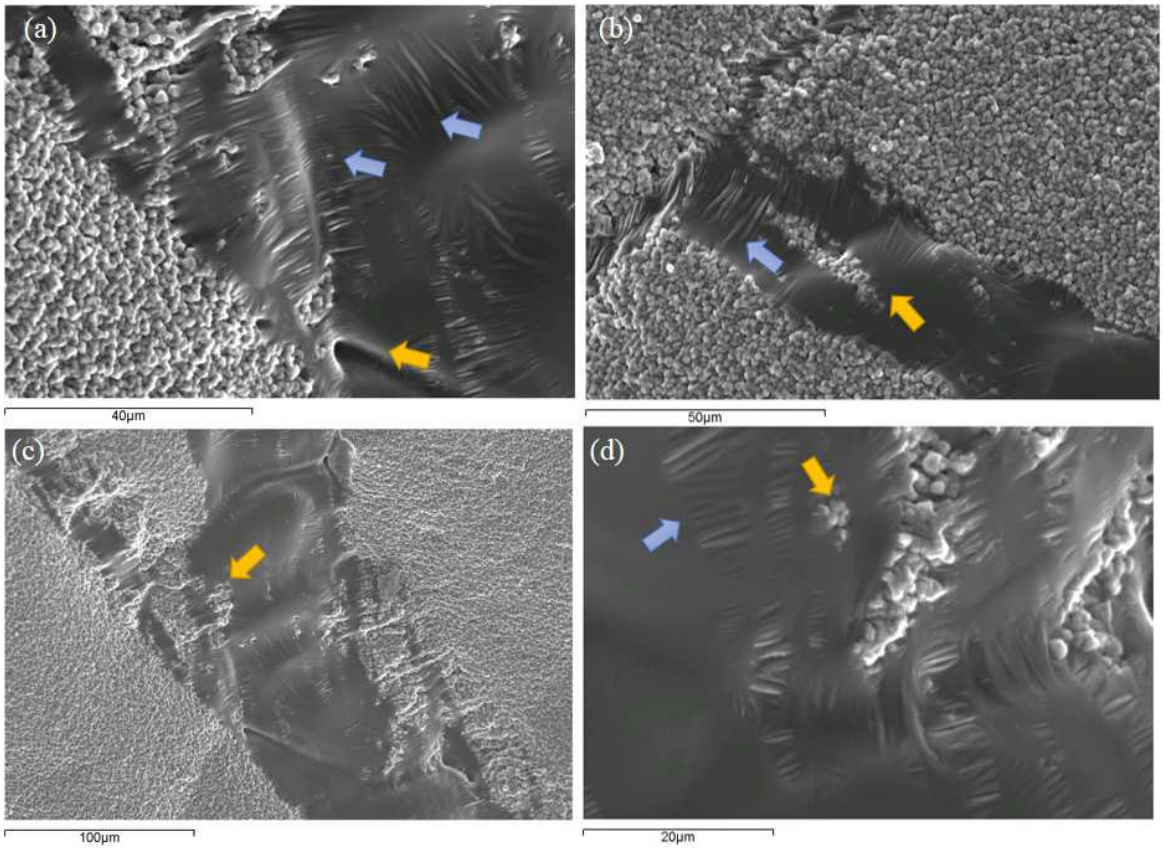

Figure 6.22 – SE images showing the entrapment of oxide particles observed in an oxidized Al-0.2Mg sample

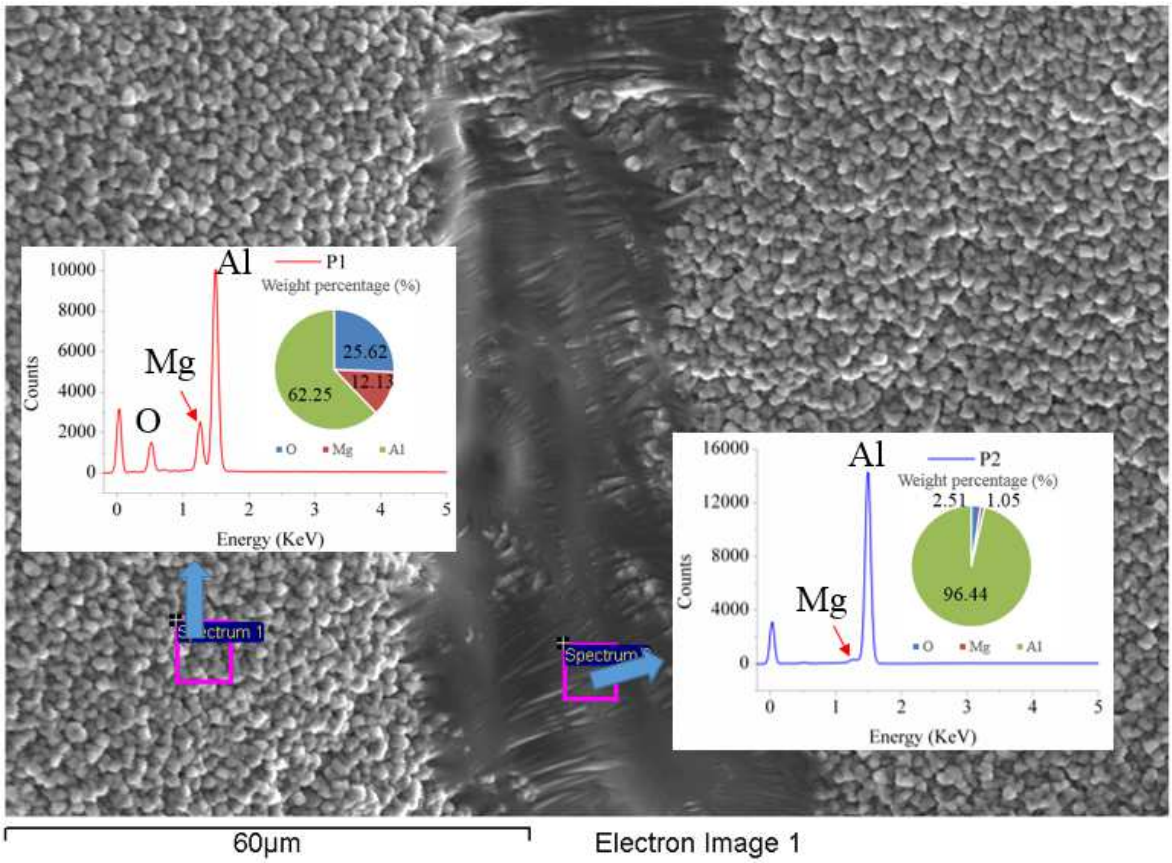

Figure 6.23 – EDX analysis on oxides and the exposed metal. (Al-0.2Mg, 1h, 750°C)

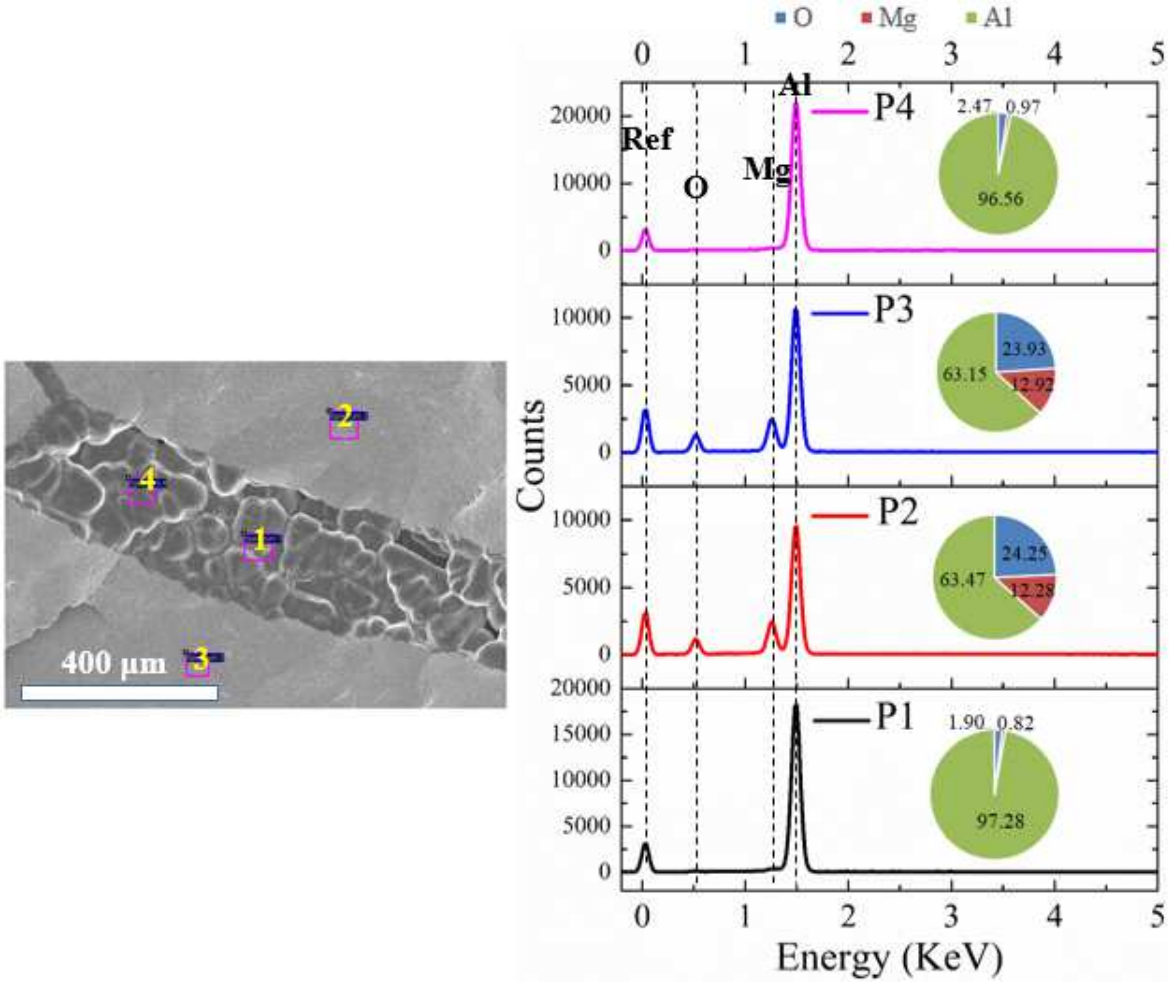

Figure 6.24 – Four EDX area analysis on oxides and the exposed metal.

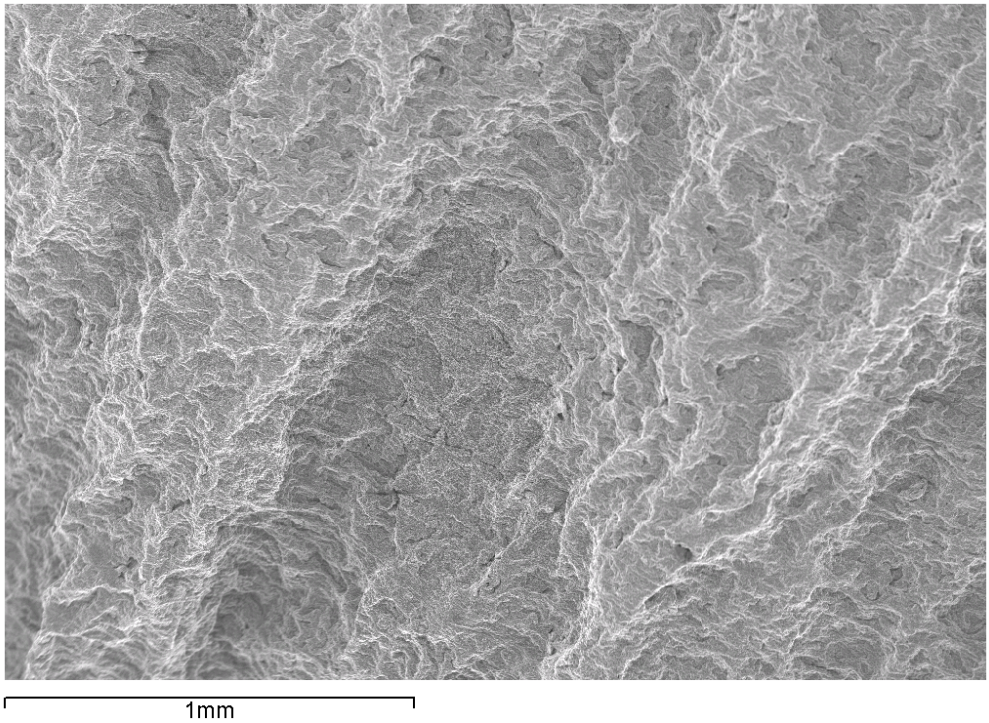

Figure 6.25 – SE image showing the topography and morphology of the surface oxide layer of an Al-0.2Mg sample which was ground to 120 grit SiC paper prior to oxidation (750^{o} C 1h dry air)

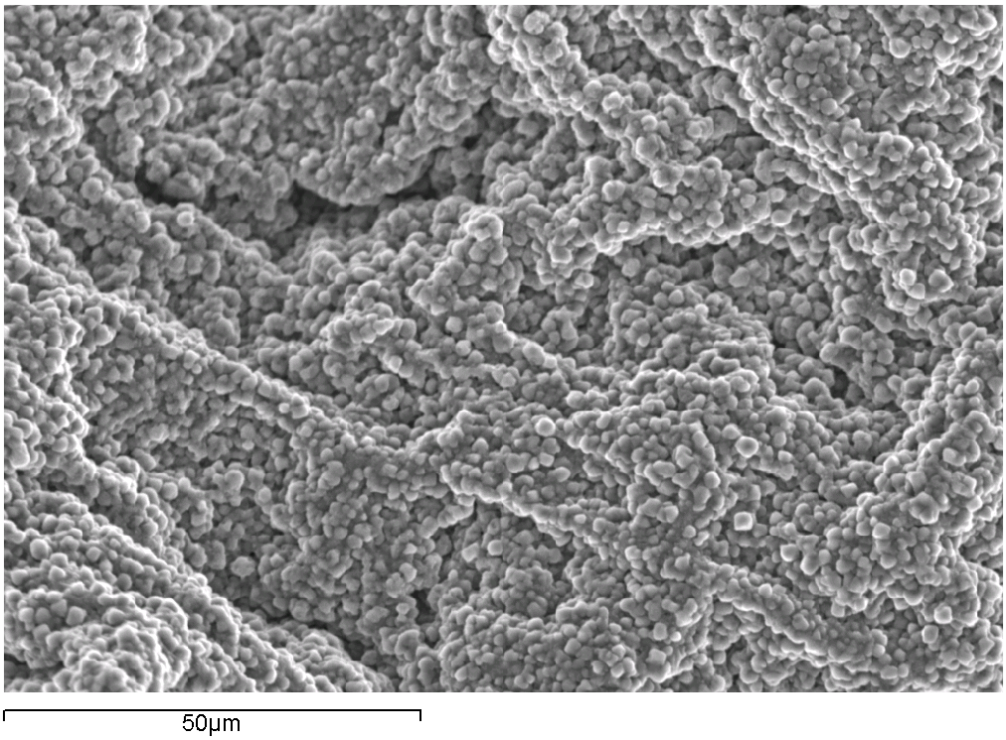

Figure 6.26 – SE image showing the topography and morphology of the surface oxide layer of an Al-0.2Mg sample which was ground to 120 grit SiC paper prior oxidation (750^{o} C 1h dry air)

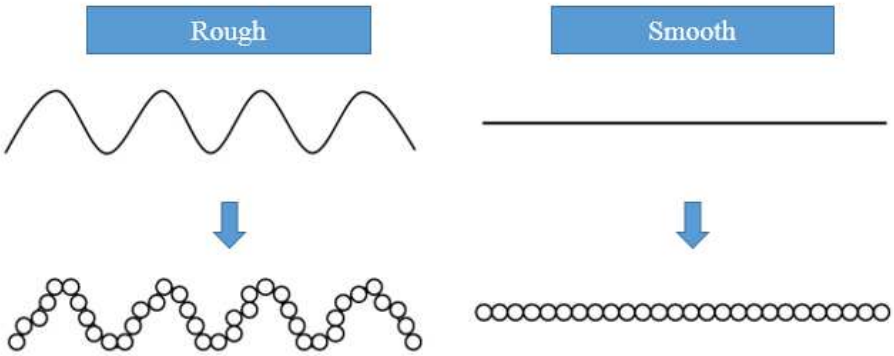

Figure 6.27 – Diagram illustrating the effect of surface pre-treatment prior to oxidation experiments.

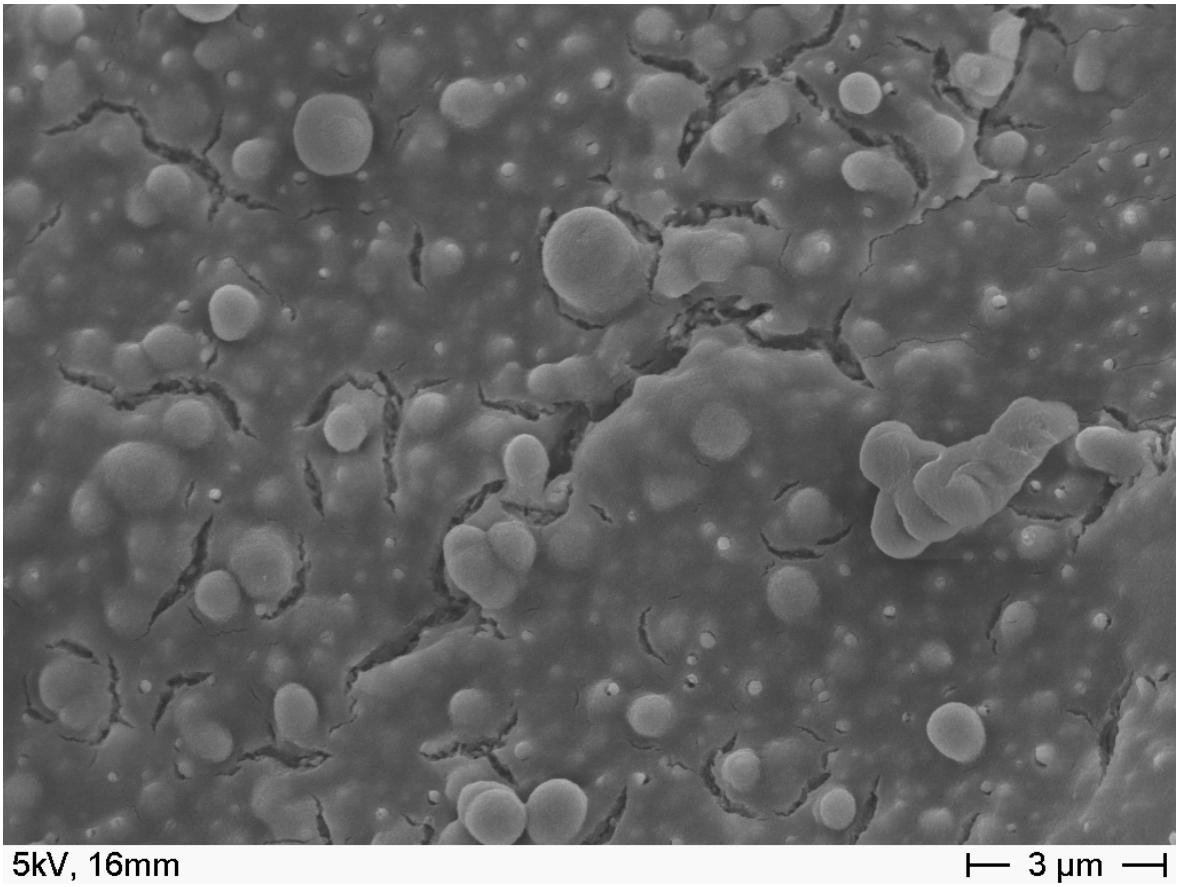

Figure 6.28 – SE image showing morphology of the *dry* side of the extracted oxide layer from an oxidized Al-0.2Mg sample (750ºC, 10 minutes after skimming)

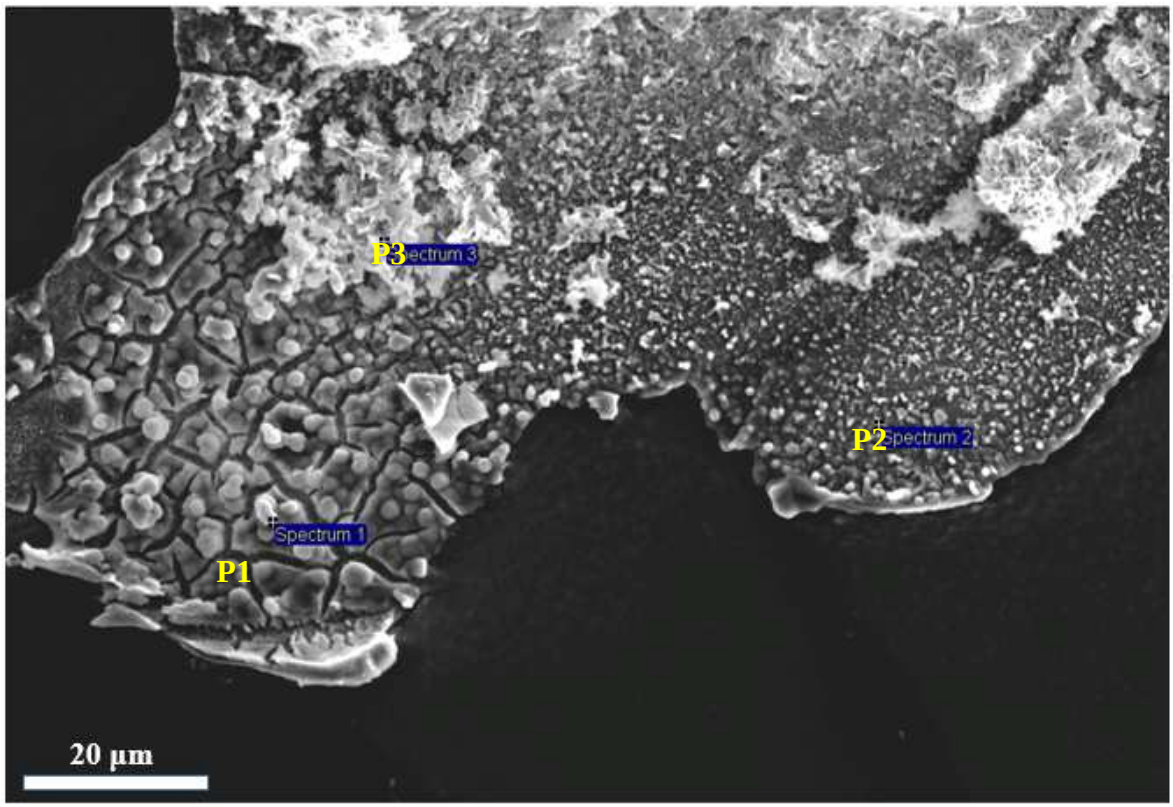

Figure 6.29 (a) – SE image showing morphology of the *wet* side of the extracted oxide layer from an oxidized Al-0.2Mg sample (750^{o} C, 10 minutes after skimming).

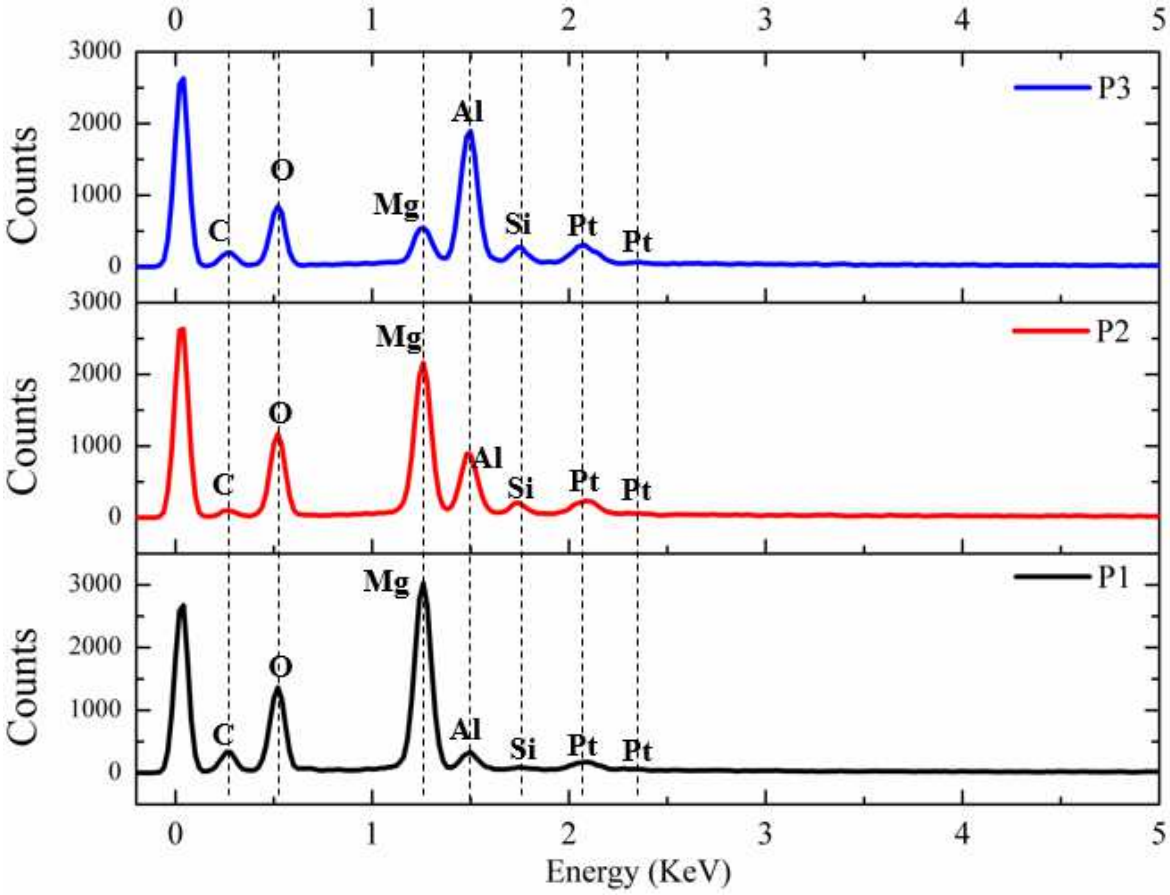

Figure 6.29 (b) – EDX spectra illustrating the chemistry of the extracted oxide, corresponding to Figure 6.29 (a).

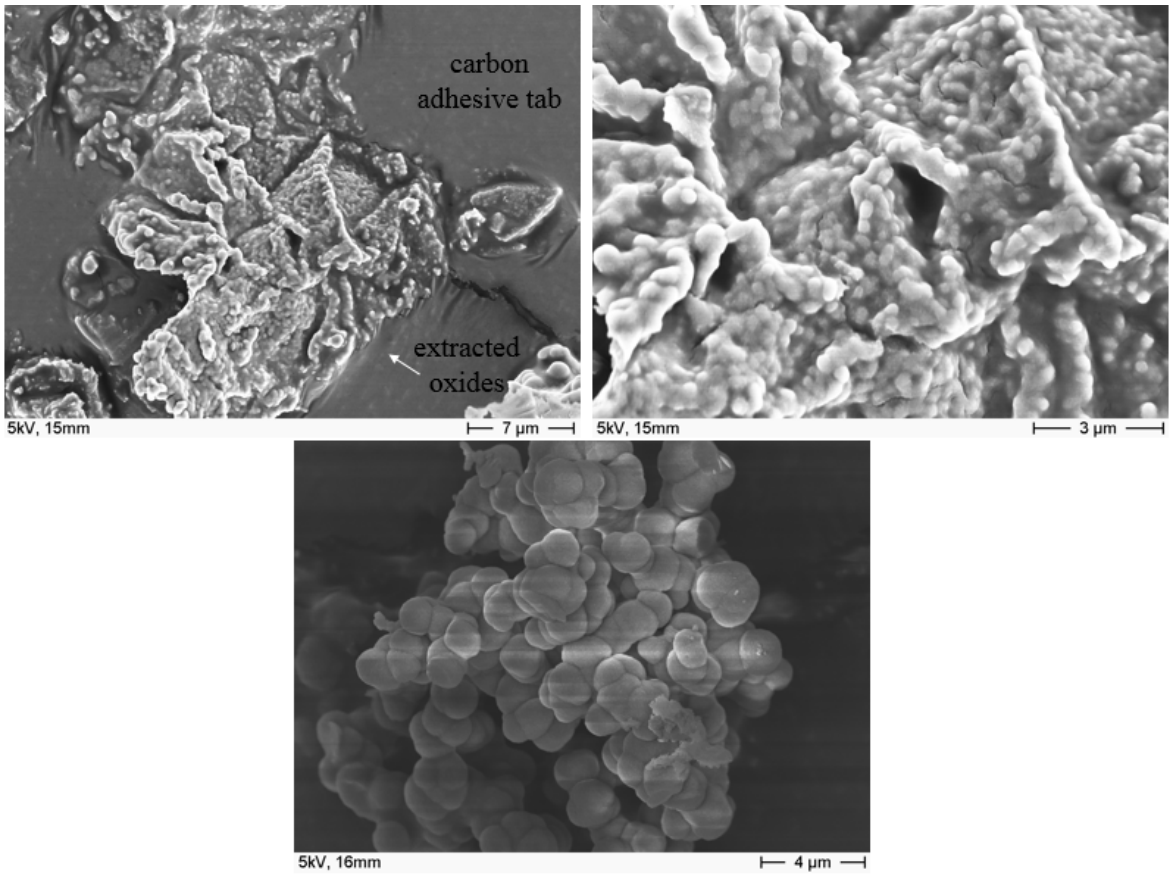

Figure 6.30 – SE image showing the agglomeration of MgO nanoparticles to form clusters.

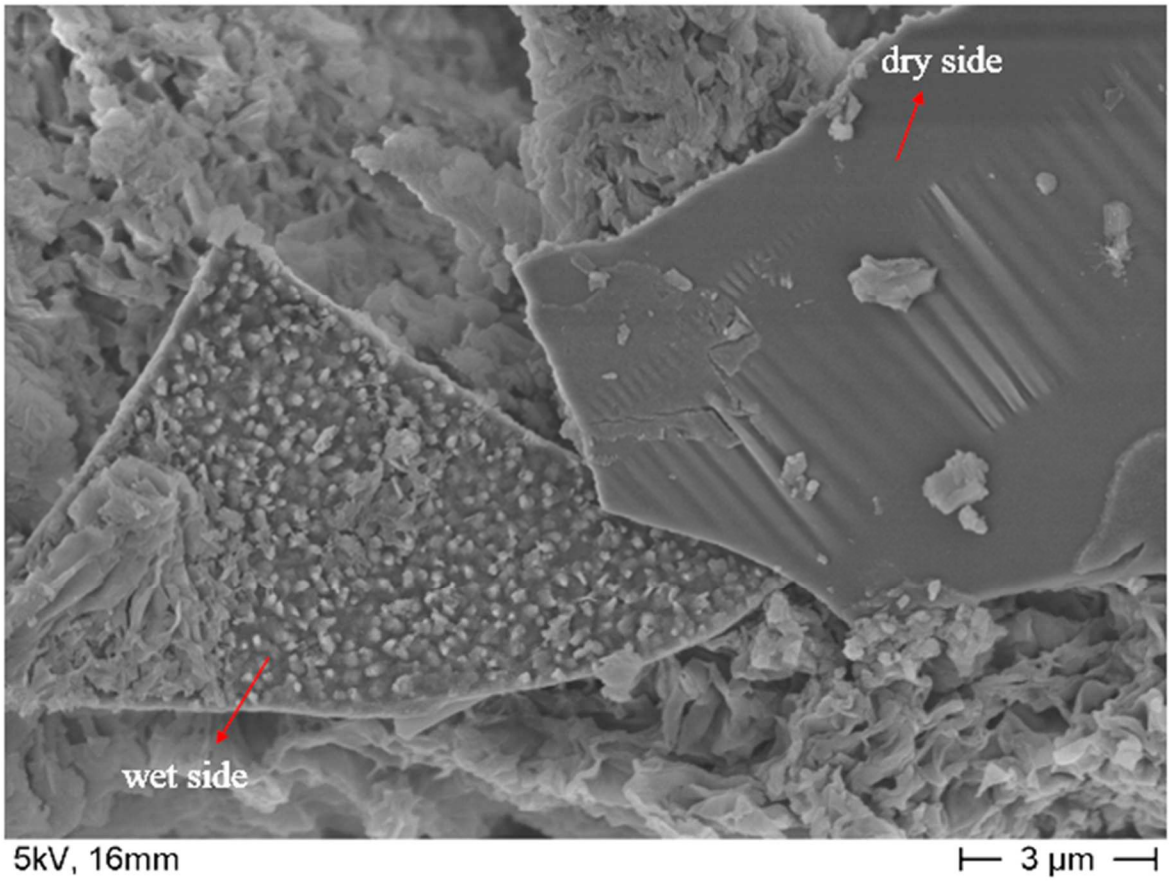

Figure 6.31 – SE image showing the extracted oxide layer formed on an Al-0.2Mg sample which was held at 750°C for only 5 minutes after skimming.

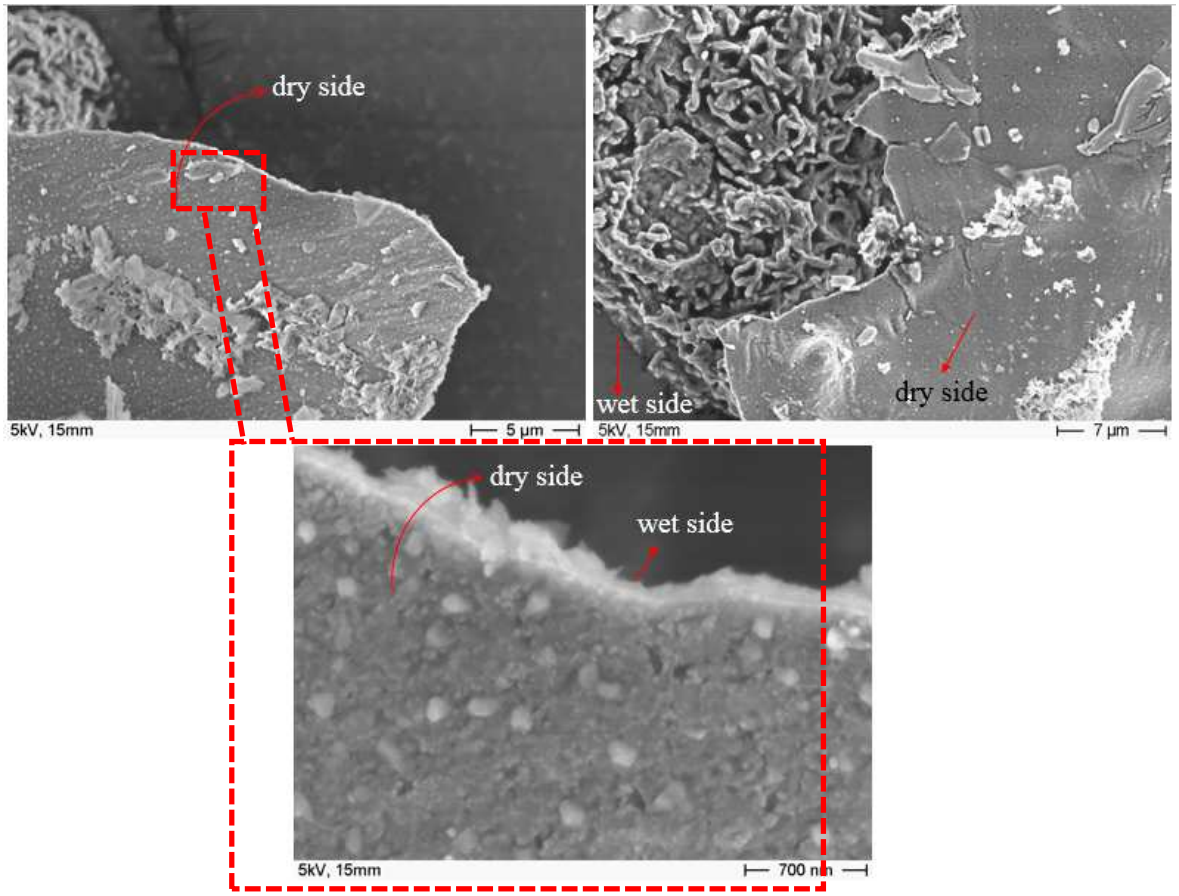

Figure 6.32 – SE images showing the extracted oxide layer formed on an Al-2Mg sample (750°C, 10 minutes after skimming)

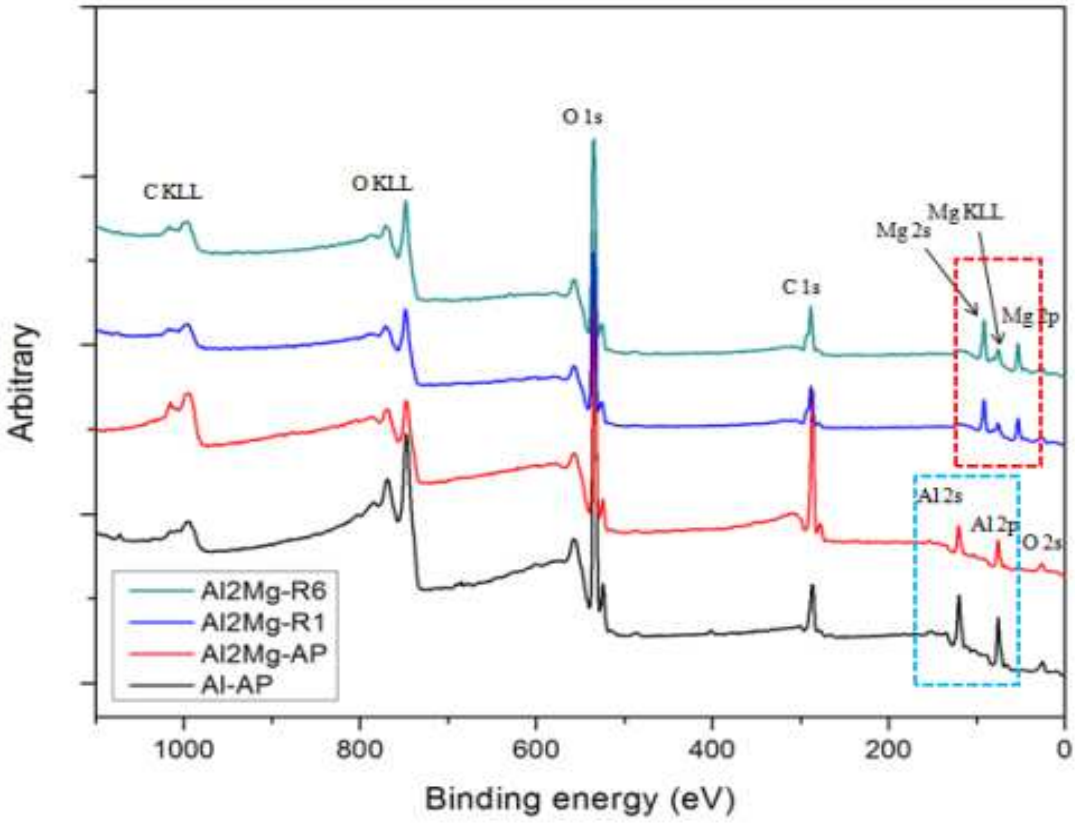

Figure 6.33 – Wide scan XPS spectra acquired using Mg Kα X-ray source.

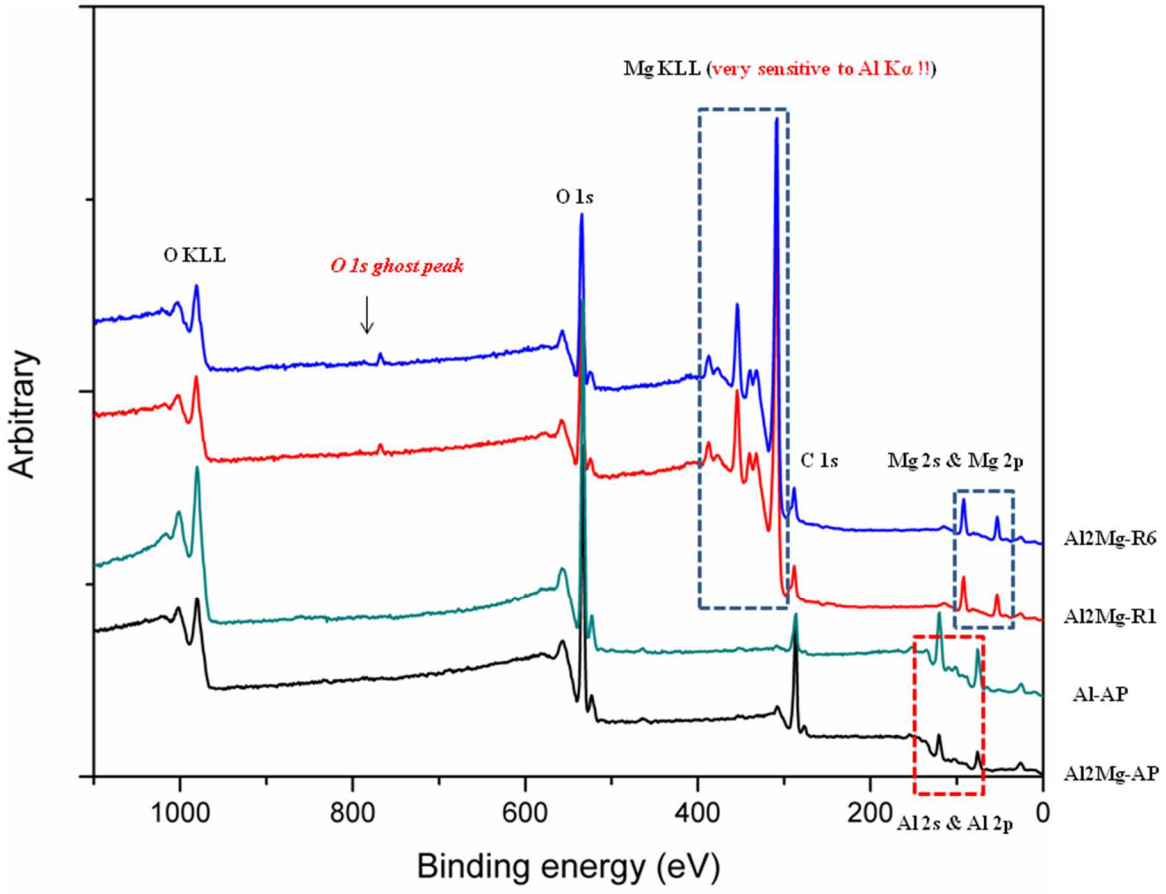

Figure 6.34 – Wide scan XPS spectra acquired using Al Kα X-ray source.

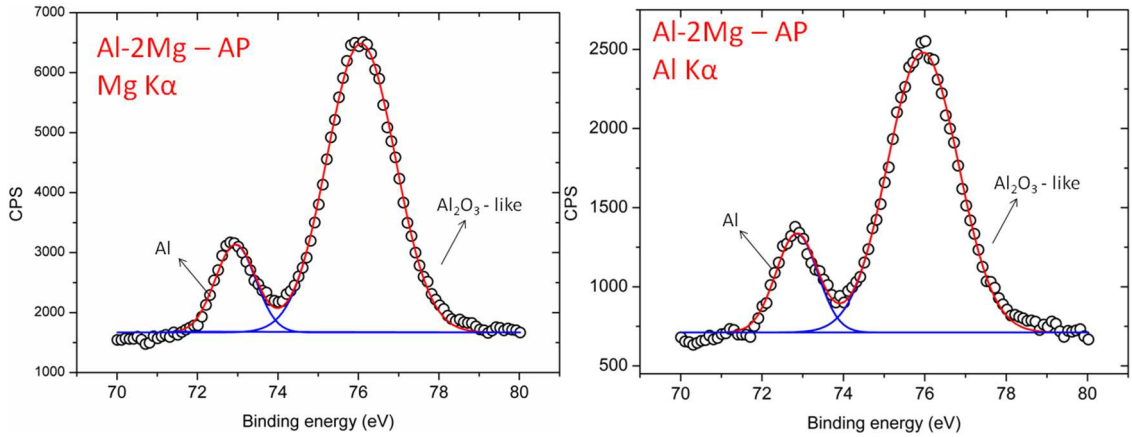

Figure 6.35 – The Al 2p core level spectra acquired from the *Al-2Mg-AP* sample (left – Mg Kα X-ray; right – Al Kα X-ray)

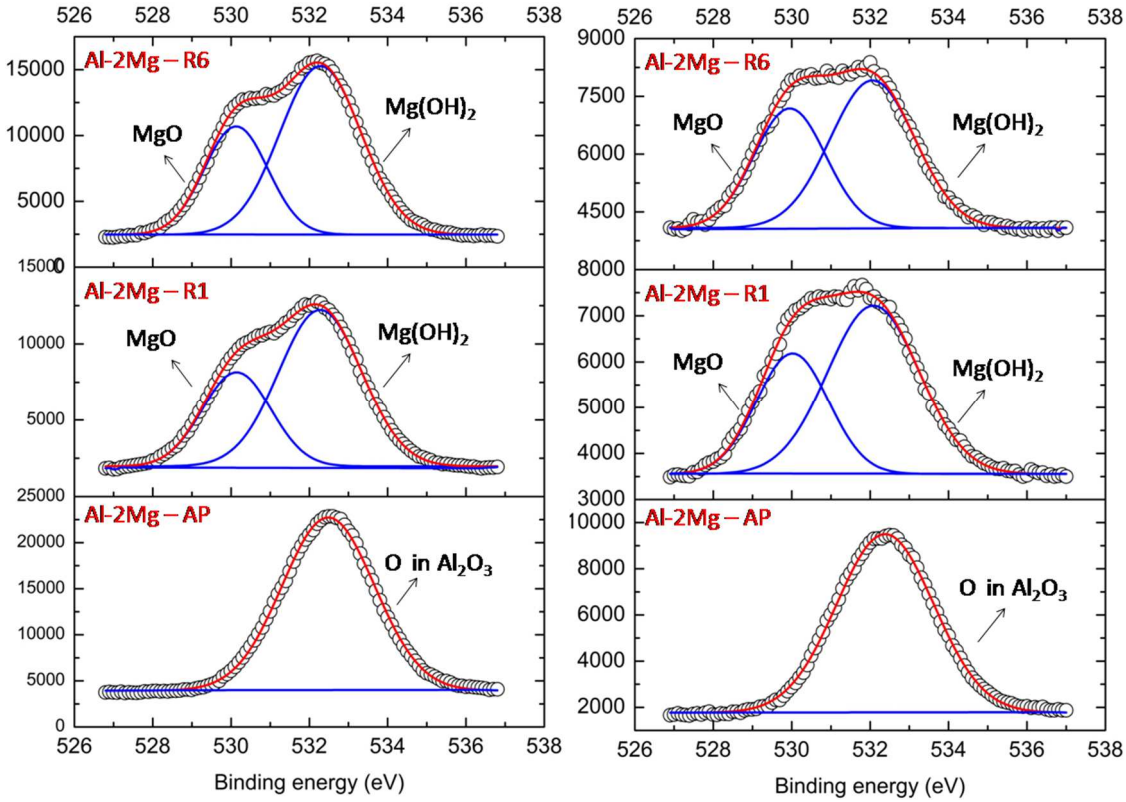

Figure 6.36 – The O 1s core level spectrum acquired from different Al-2Mg samples (left – Mg Kα X-ray; right – Al Kα X-ray)

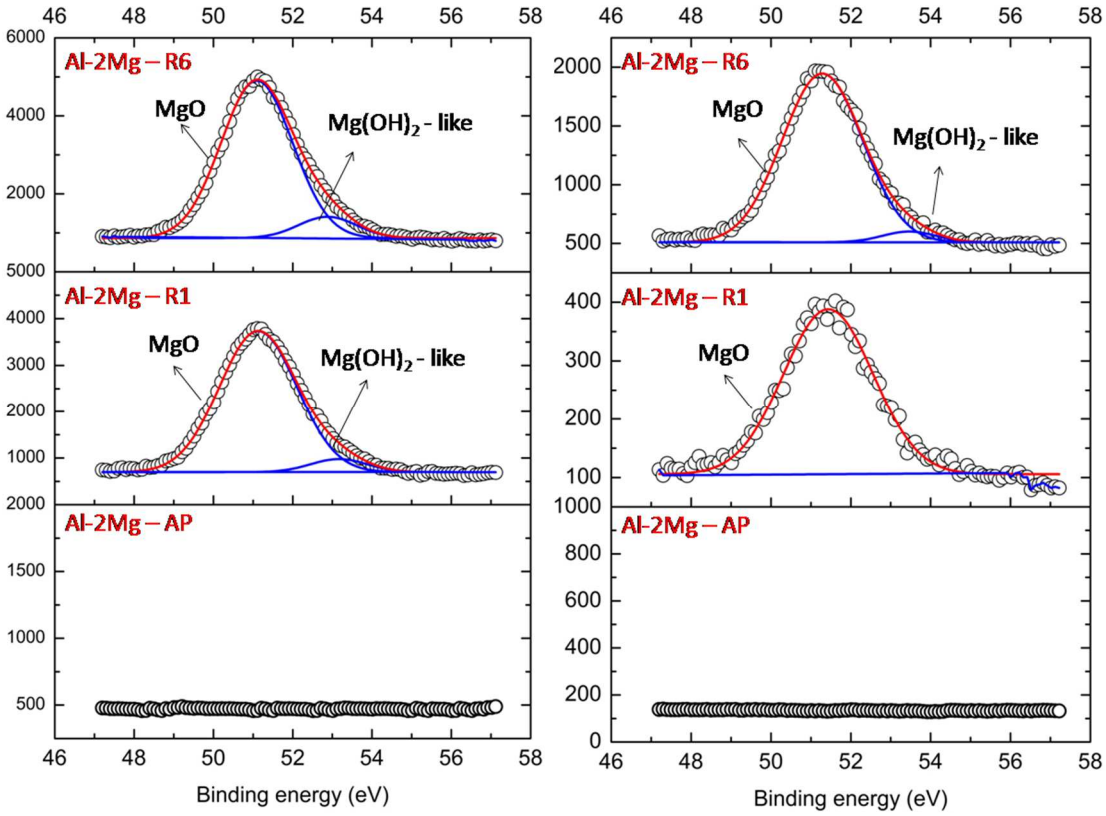

Figure 6.37 – The Mg 2p core level spectrum acquired from different Al-2Mg samples (left – Mg Kα X-ray; right – Al Kα X-ray)

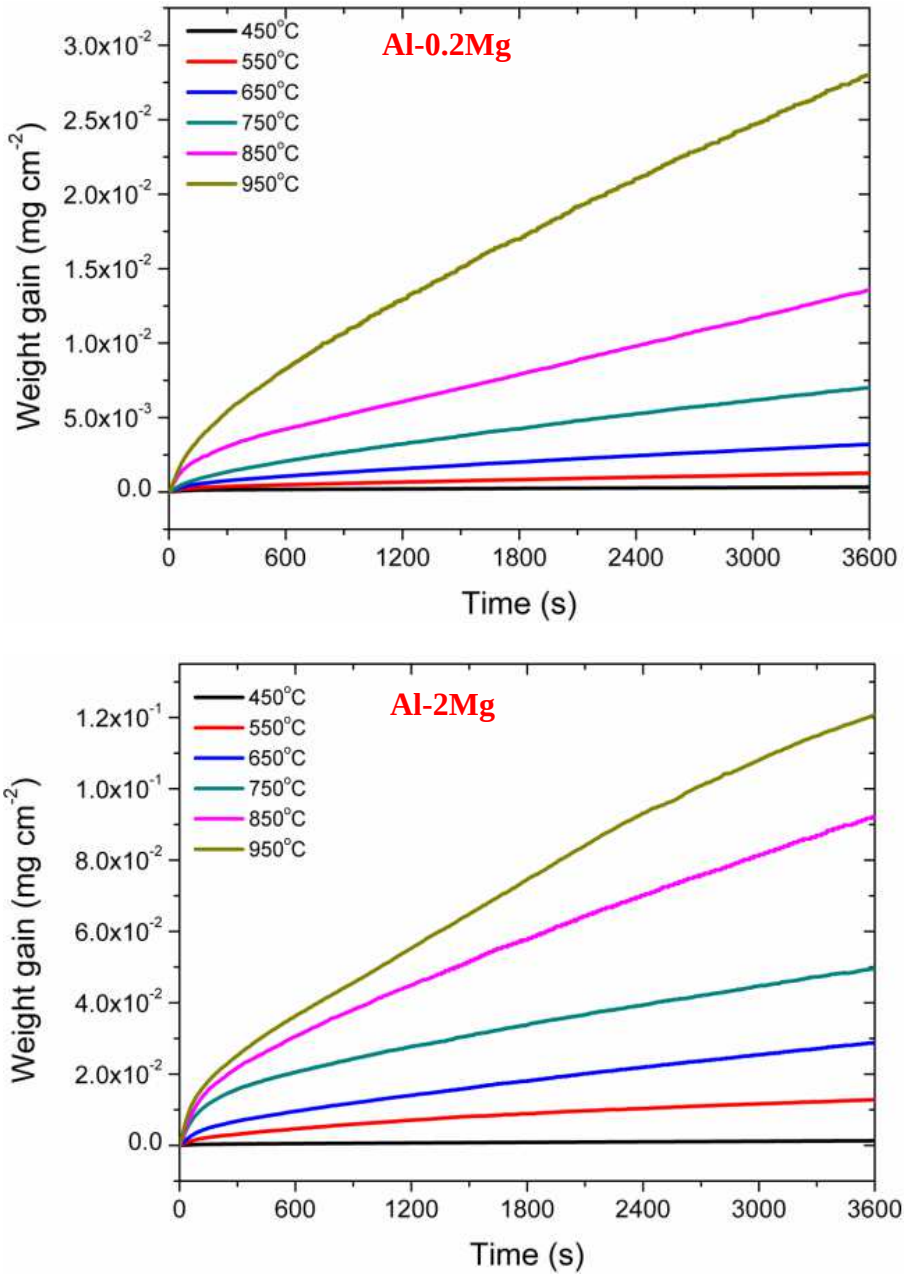

Figure 6.38 – Oxidation kinetics curves for Al-0.2Mg and Al-2Mg.

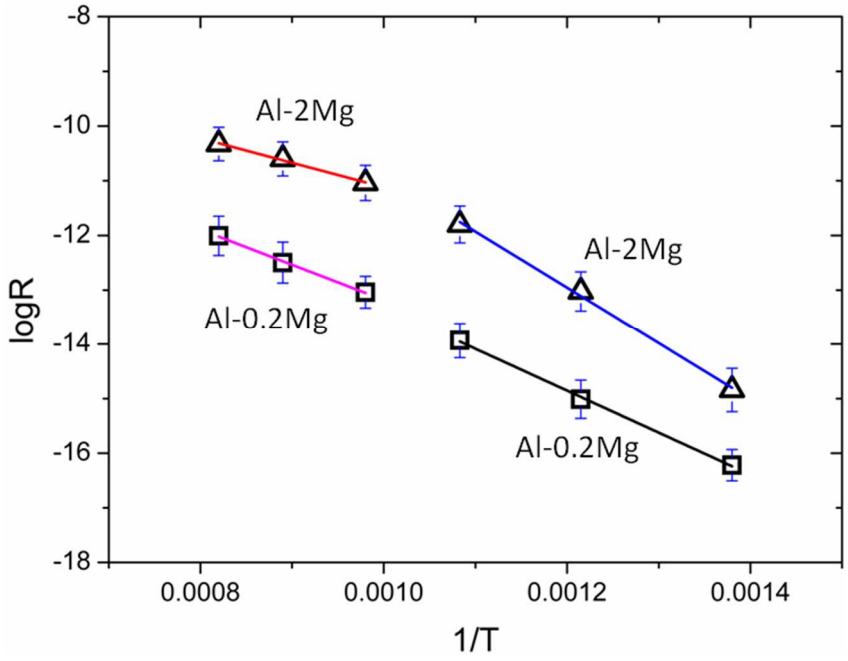

Figure 6.39 – Arrhenius plots showing the linear stage oxidation rate as a function of temperature.

Table 6.1 - Summarized fitting data for the Arrhenius plots show in Figure 6.39

	Al-2Mg		Al-0.2Mg	
Temperature range (˚C)	Activation energy (kJ mol^{-1})	Adj. R-square	Activation energy (kJ mol^{-1})	Adj. R-square
450-650	**85.4**	0.99542	**63.9**	0.99788
750-950	**37.2**	0.99156	**53.5**	0.99618

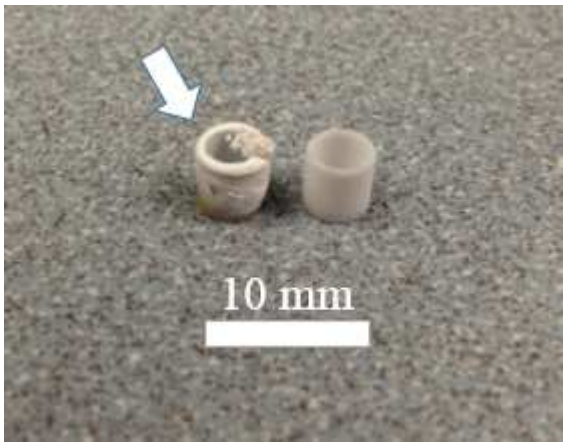

Figure 6.40 – Photograph showing that the walls of an alumina crucible were coated with MgO powder after a pure Mg sample was oxidized at 750ºC for 1 h.

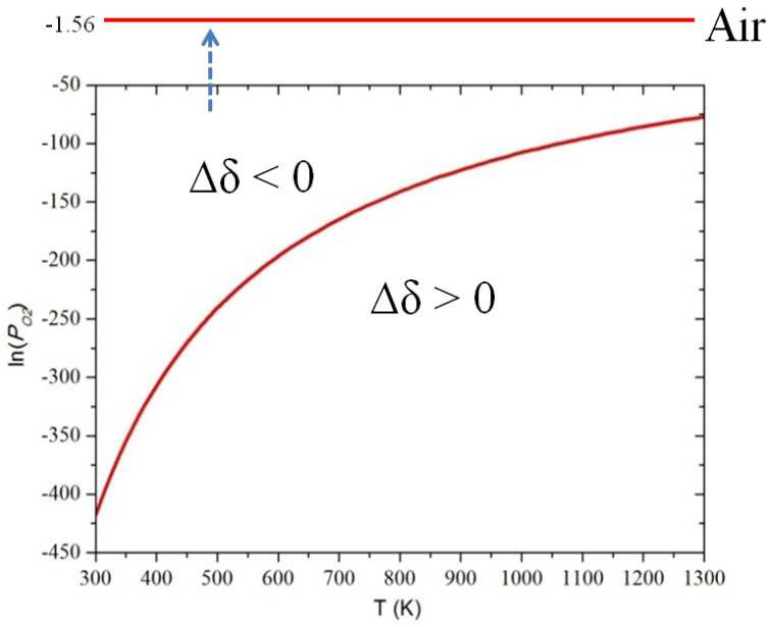

Figure 6.41 – Plot indicating the conditions of oxygen partial pressure and temperature under which the direct reaction and reduction reaction are equally favourable (Red curve).

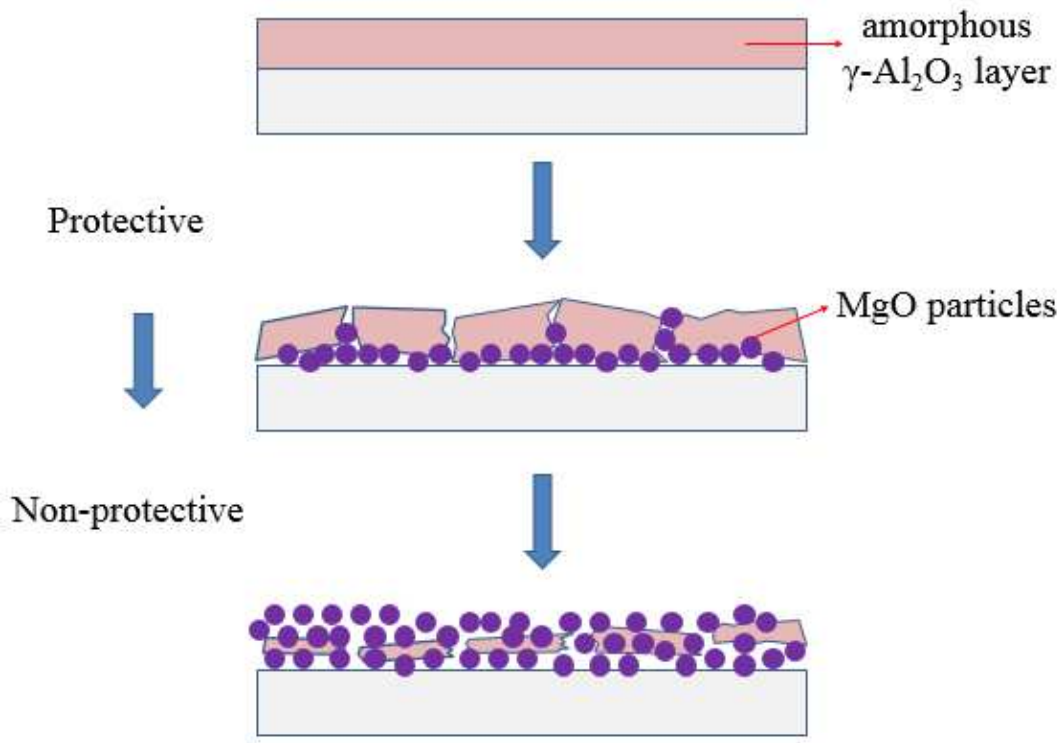

Figure 6.42 – Diagram showing the non-protective growth of MgO on Al-Mg alloys.

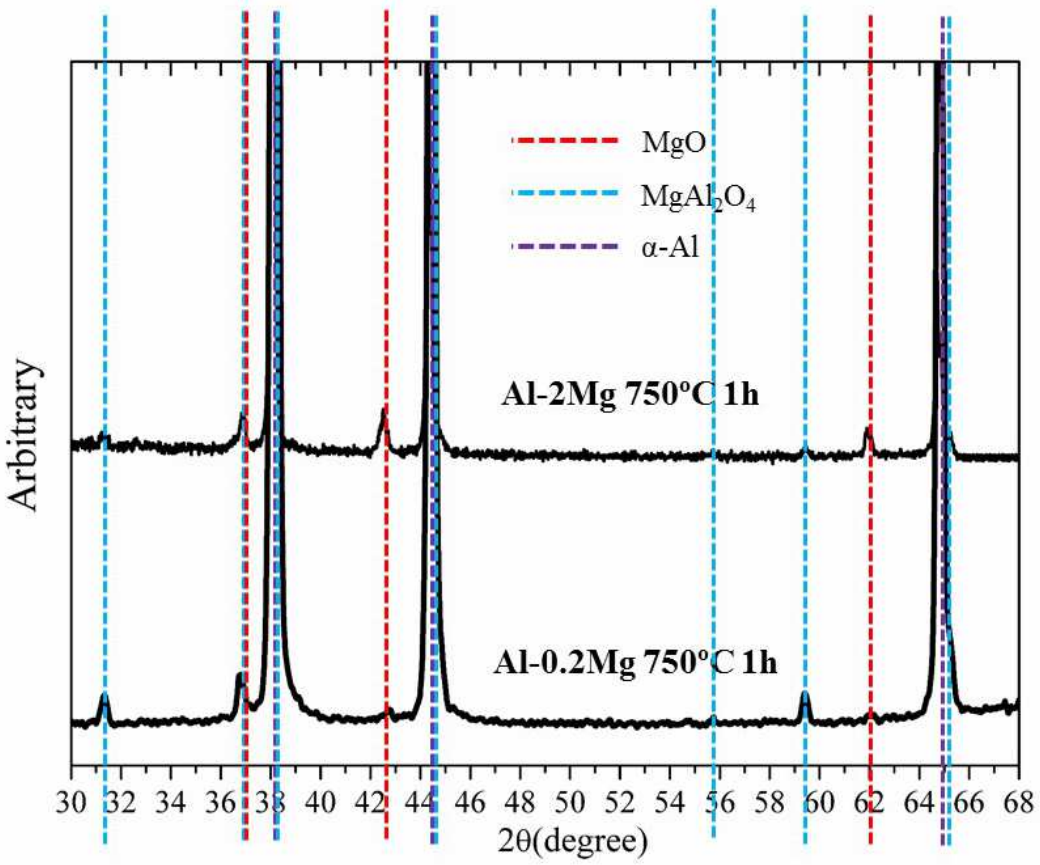

Figure 6.43 – XRD results showing the presence of both MgO and $MgAl_2O_4$ in oxidized Al-2Mg and Al-0.2Mg.

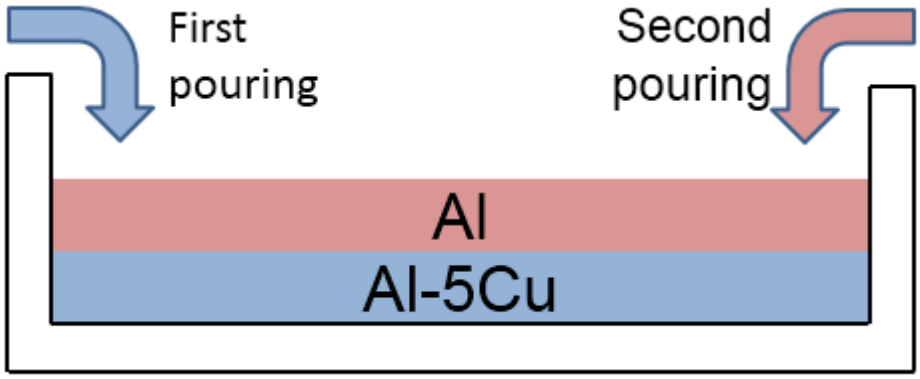

Figure 7.1 – Diagram briefly showing the *double-pouring* approach.

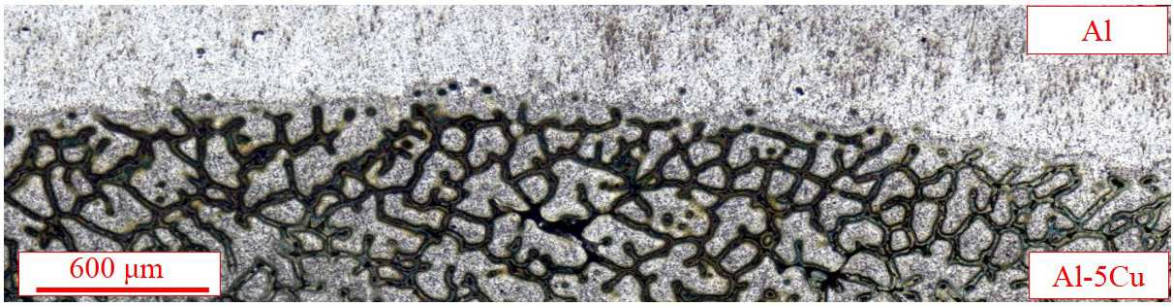

Figure 7.2 – OM image showing the well-bonded interface morphology of the double-poured Al/Al-5Cu.

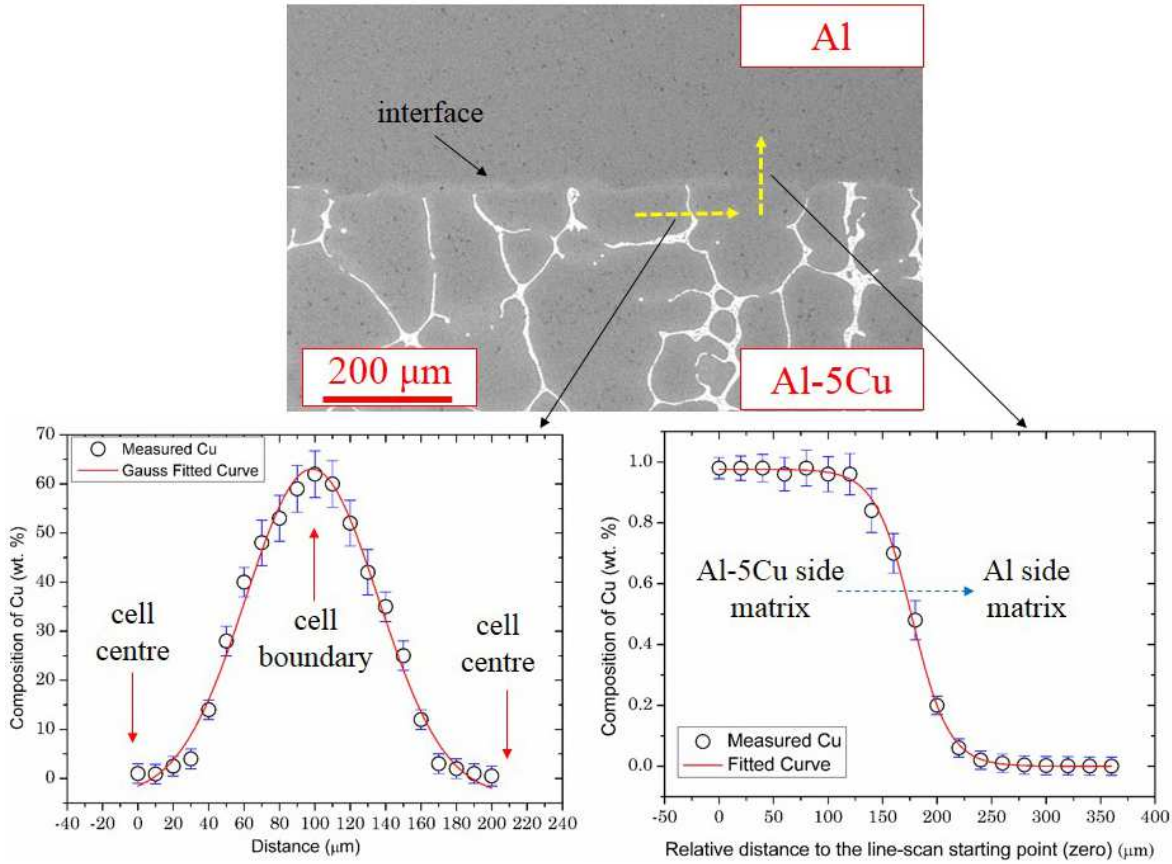

Figure 7.3 – BE image showing the well-bonded interface morphology and EDX line scan analysis was performed accordingly (highlighted by yellow dash lines).

Table 7.1 Fitted results of the EDX line scan profile across the bond interface from the Al-5Cu side to Al side.

Parameters	Value	Error
y_0 (%)	0.9855	0.0046
k	0.0591	0.0017
x_c (µm)	177.031	0.6965
Adj. R-square	0.99955	

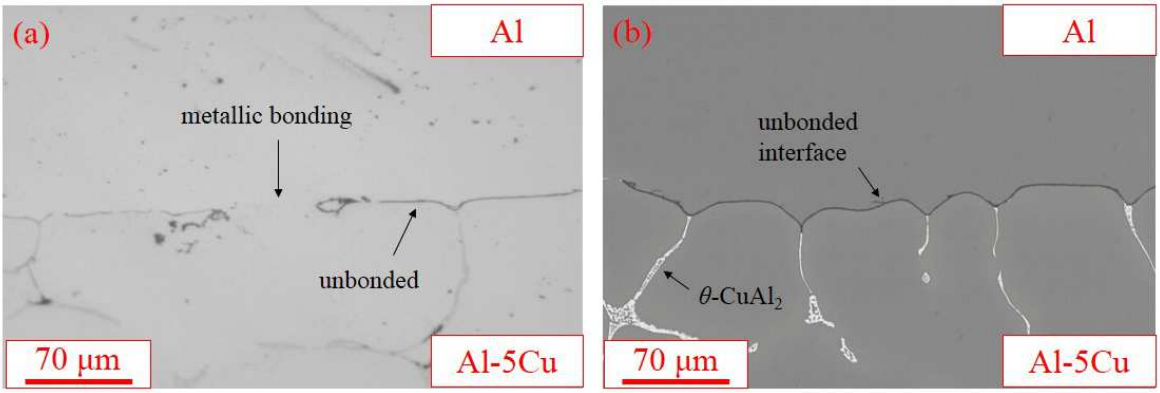

Figure 7.4 – OM image (left) and BE image (right) showing the bumpy (wavy) un-bonded bond interface observed in the double-poured Al/Al-5Cu.

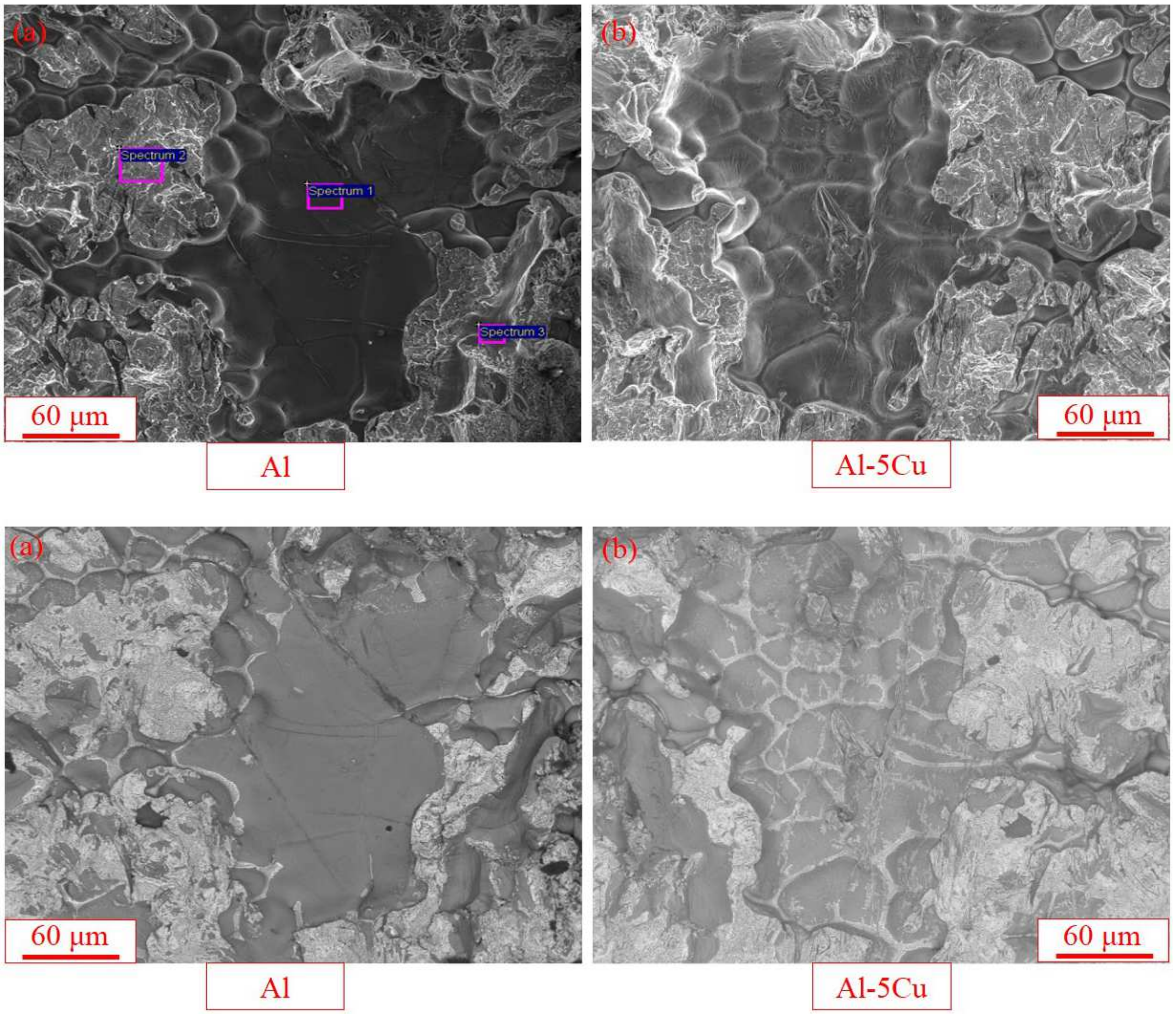

Figure 7.5 – Pairs of SE (up) and BE (down) images showing the fracture surface morphology on both Al-5Cu side and Al side, indicating the *bi-film* pocket was split into two halves.

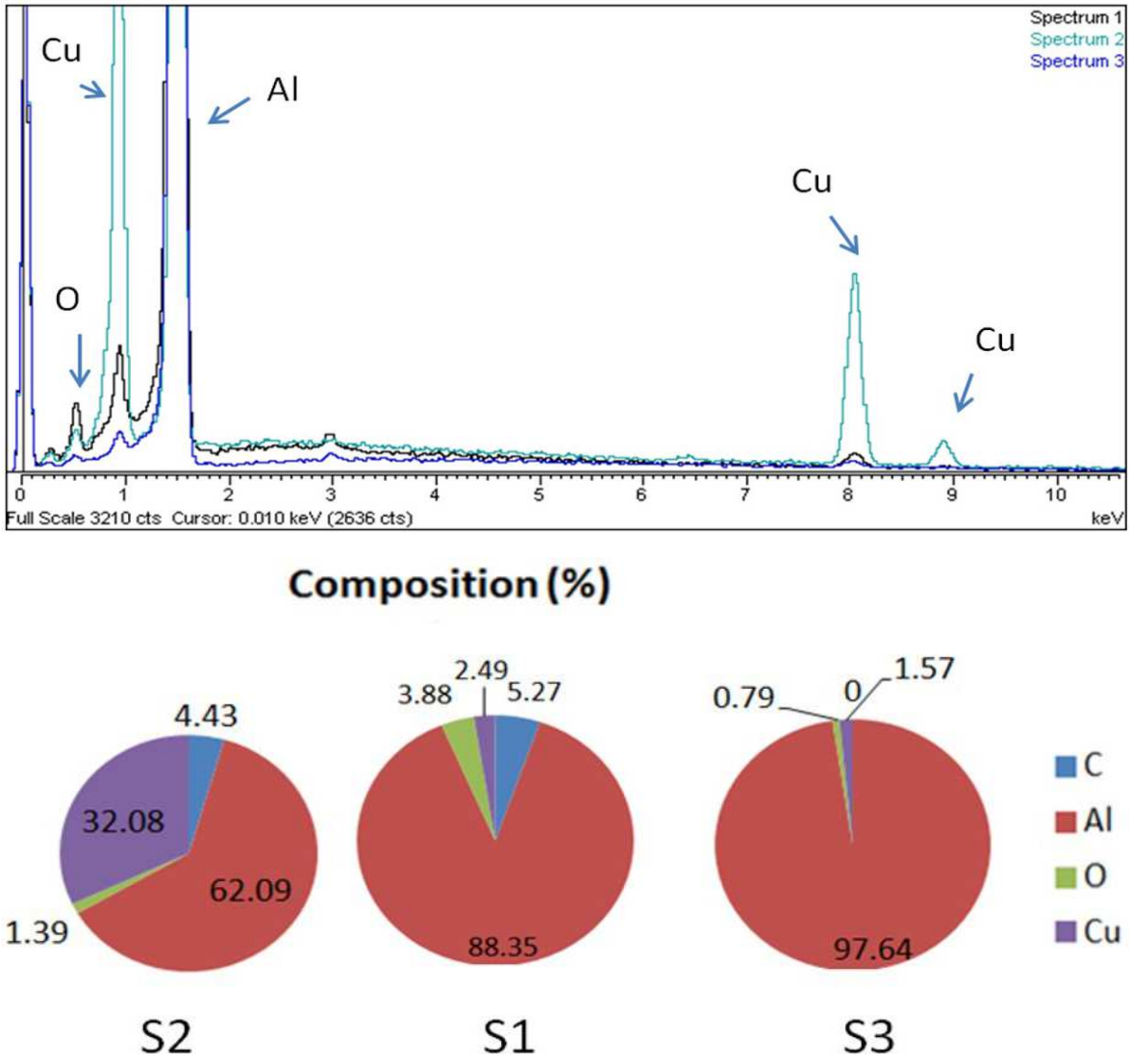

Figure 7.6 – EDX spectra and quantified EDX results of the scanned points shown in Figure 7.5

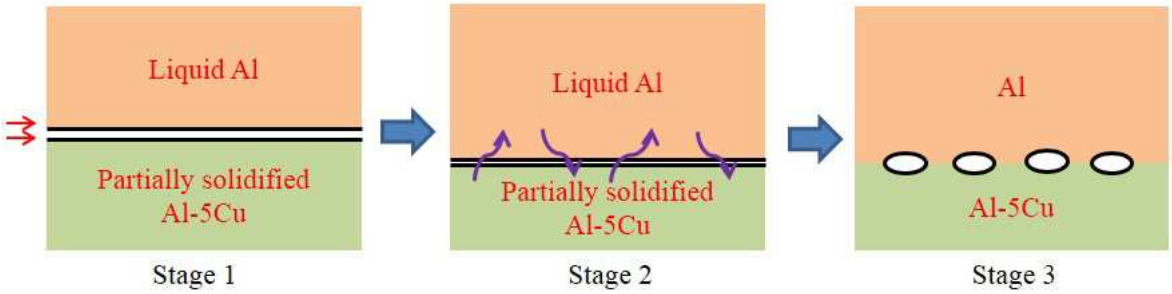

Figure 7.7 – Diagram illustrating the bonding mechanism between Al and Al-5Cu using the double-pouring approach.

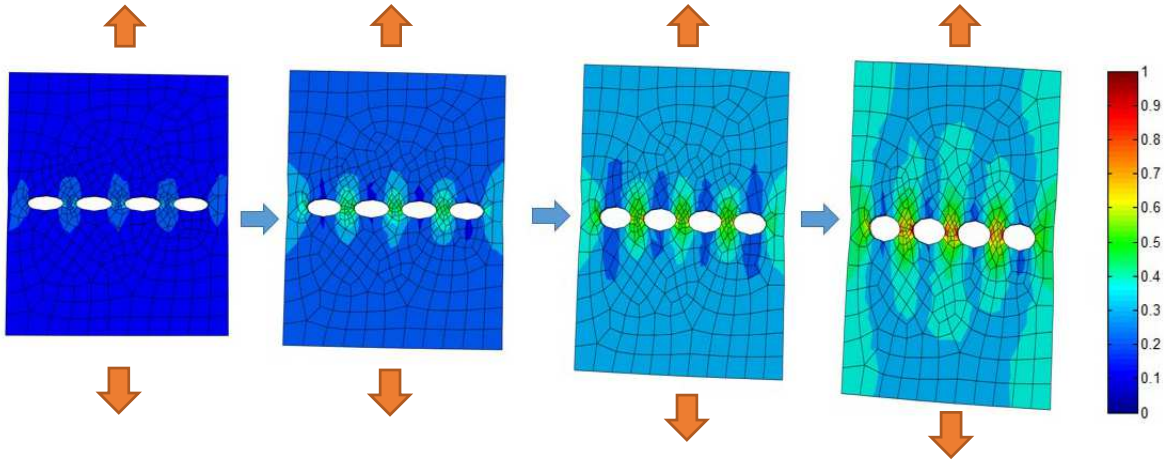

Figure 7.8 – Diagram showing the stress concentration around the bi-film defects at the interface once subject to an external tensile force. The diagram is obtained using the software Abaqus Student Version 6.10.

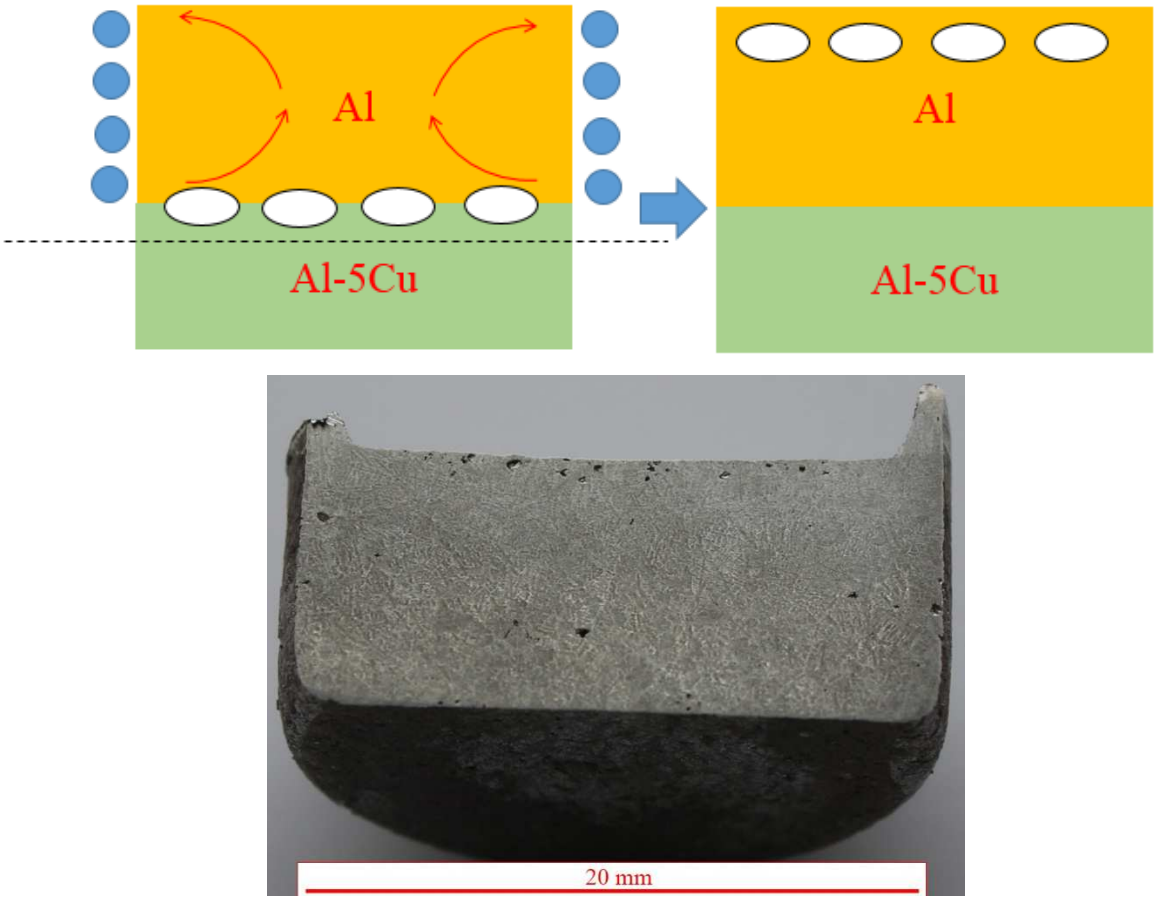

Figure 7.9 – Diagram and a macrograph illustrating the induction stirring pattern generated within the melt could help push the buoyant *bi-film* defects to the top surface region.

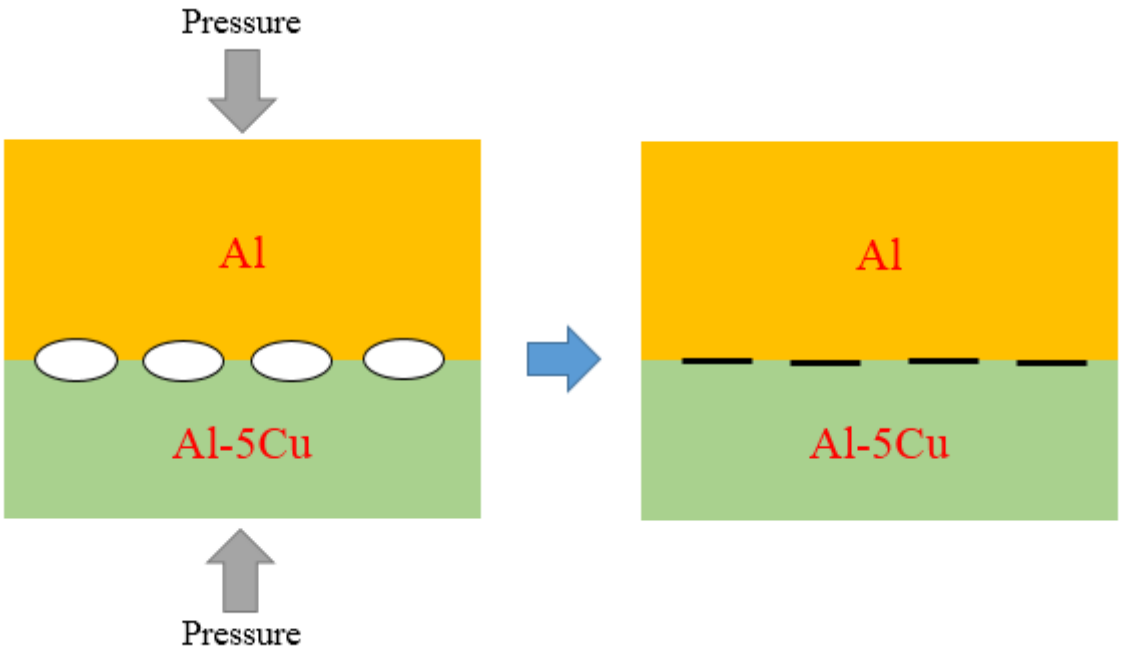

Figure 7.10 – Diagram illustrating that the applied pressure during solidification could help stitch the bi-film defects allowing more metallic bonding.

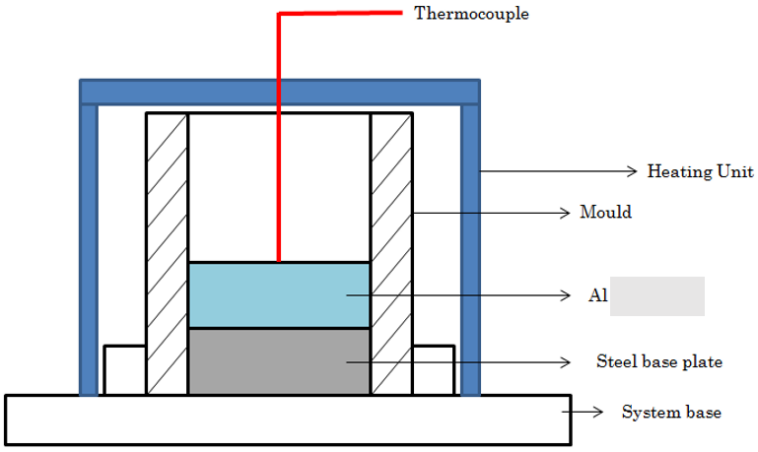

Figure 7.11 (a) – Diagram showing the set-up of the squeeze casting mould during the pre-heating stage

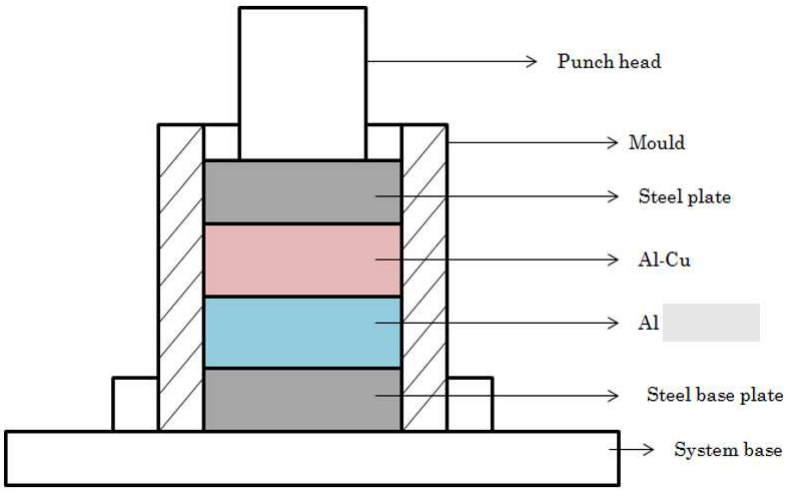

Figure 7.11 (b) – Diagram showing the set-up of the squeeze casting mould during the solidification stage

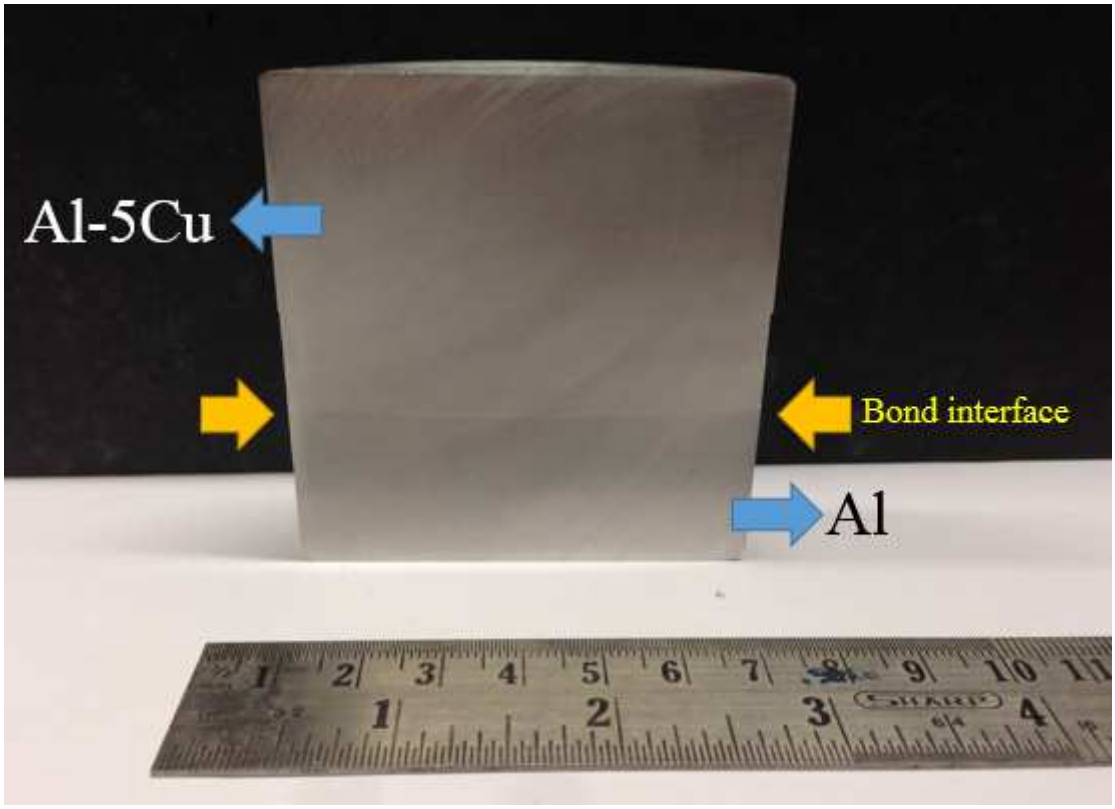

Figure 7.12 – Macrograph showing the cross section of a squeeze casted Al-5Cu/Al bi-metallic composite.

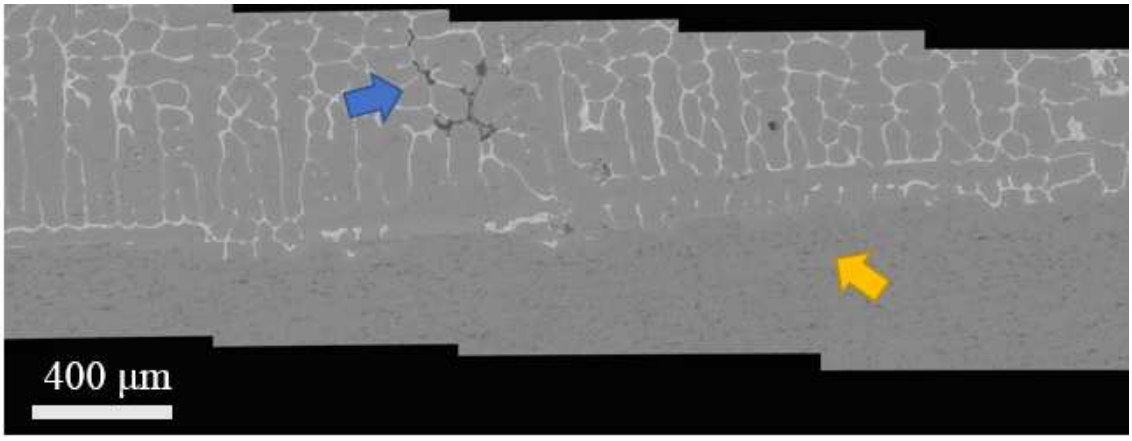

Figure 7.13 – Stitched BE image showing the bond interface morphology of a squeeze cast Al-5Cu/Al at the centre of the sample.

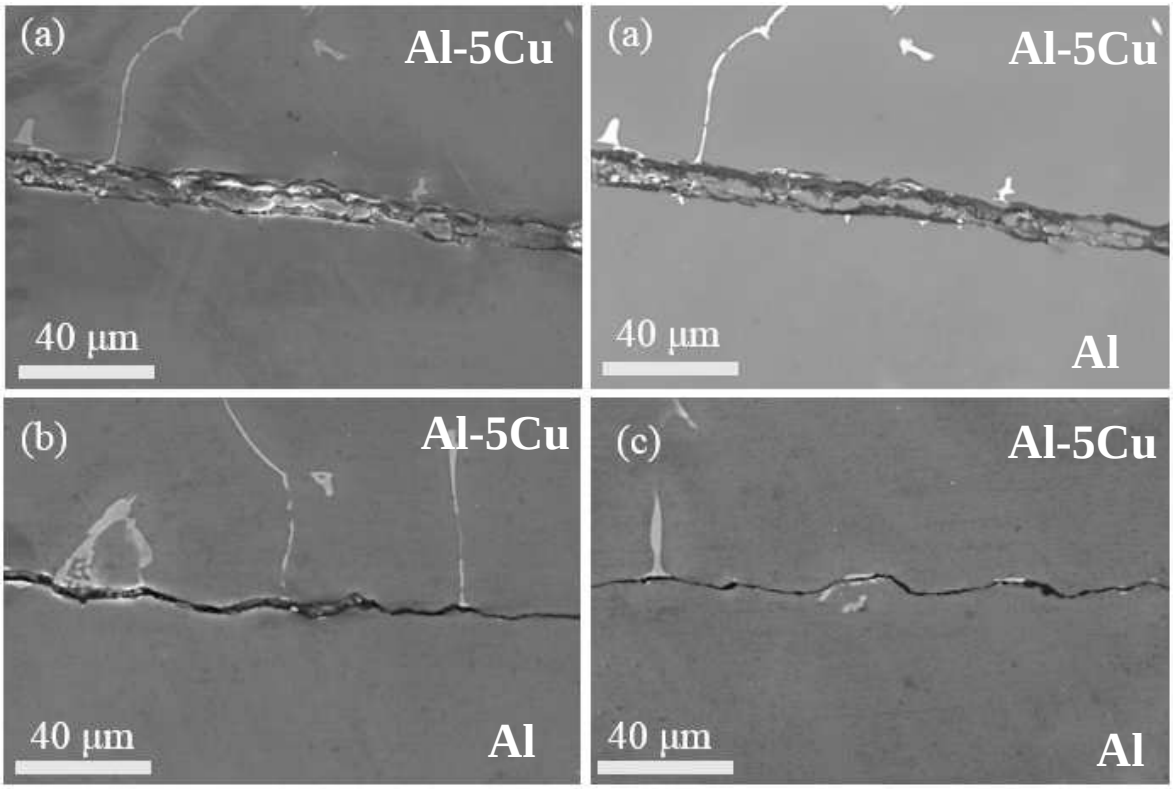

Figure 7.14 – SE and BE images showing the bond interface morphology of a squeeze casted Al-5Cu/Al at positions close to the mould (edges).

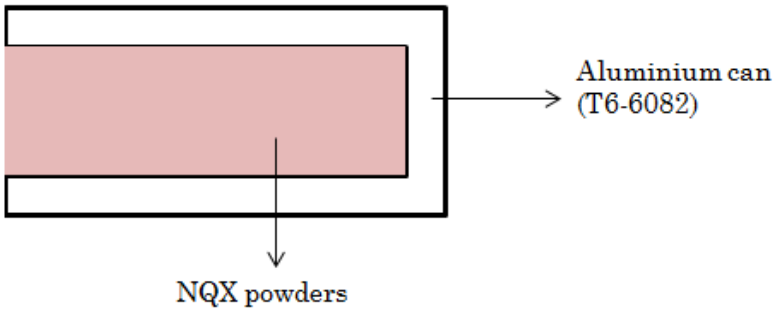

(a) Before extrusion

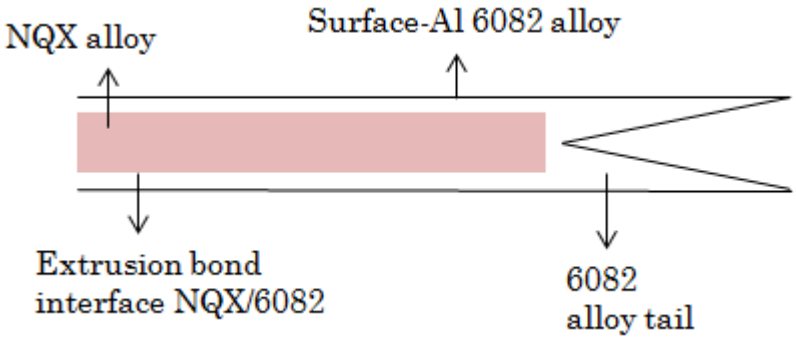

(b) After extrusion

Figure 7.15 – Diagram showing the production of an Al-Fe-Ti-Nb nanoquasicrystalline alloy extruded bar.

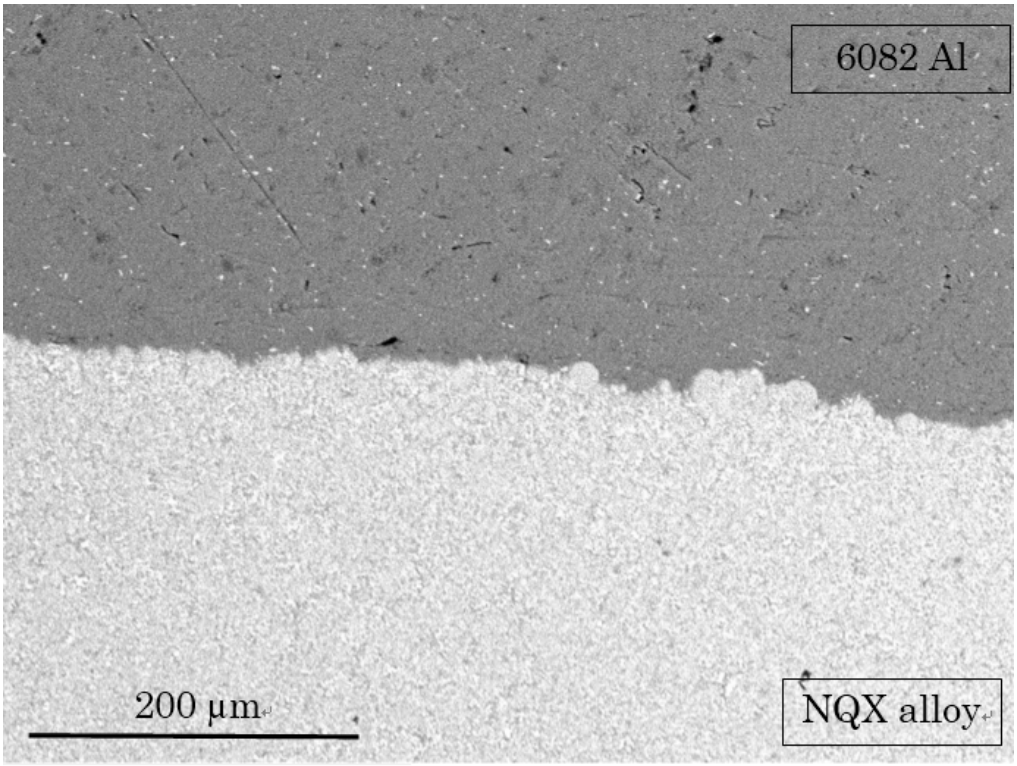

Figure 7.16 – BEI image showing the interface structure of an extrusion bonded 6082/NQX bi-metal.

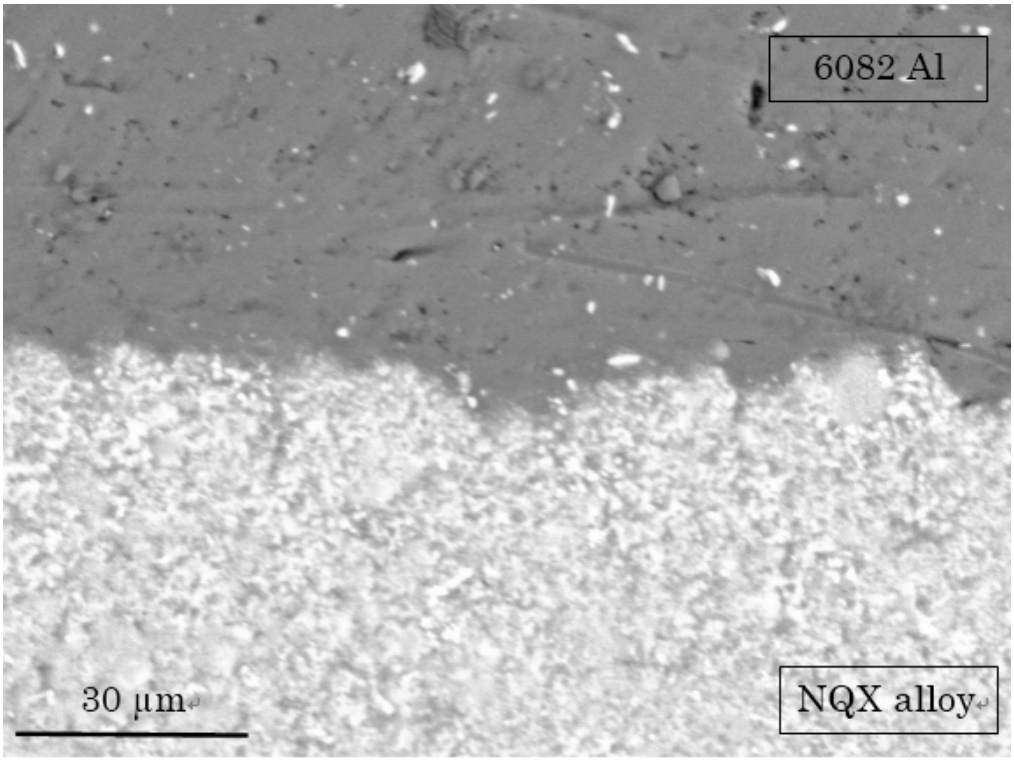

Figure 7.17 – High mag BEI image showing the diffuse interface morphology of an extrusion bonded 6082/NQX bi-metal.

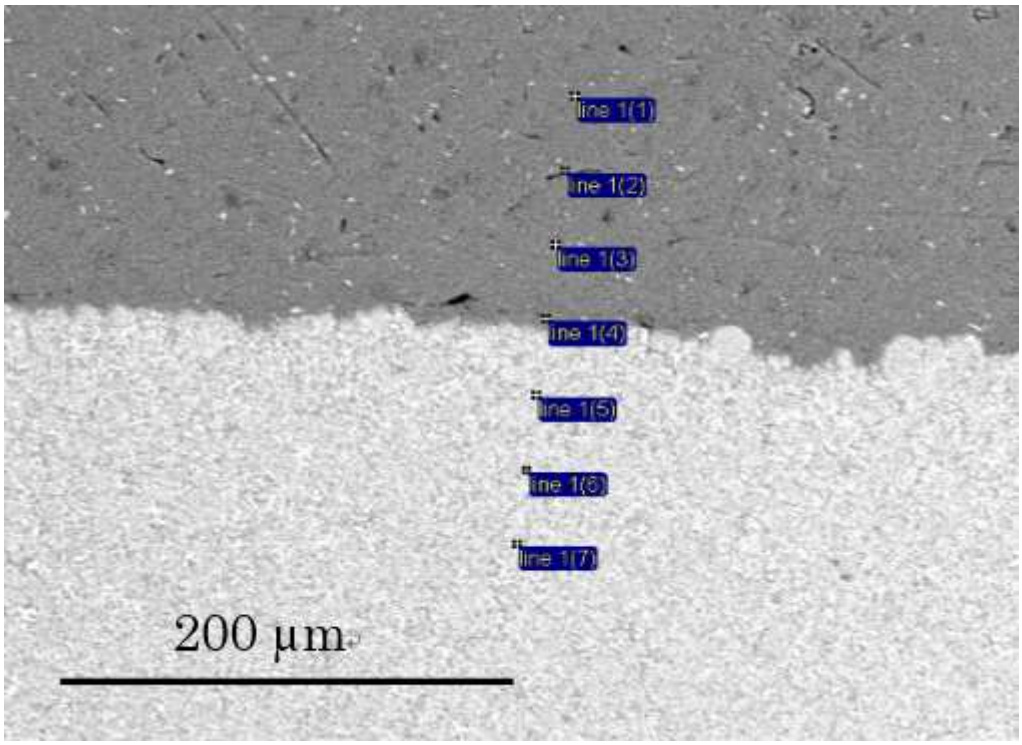

Figure 7.18 (a) – EDX line scan was used to profiling the chemistry across the bond interface.

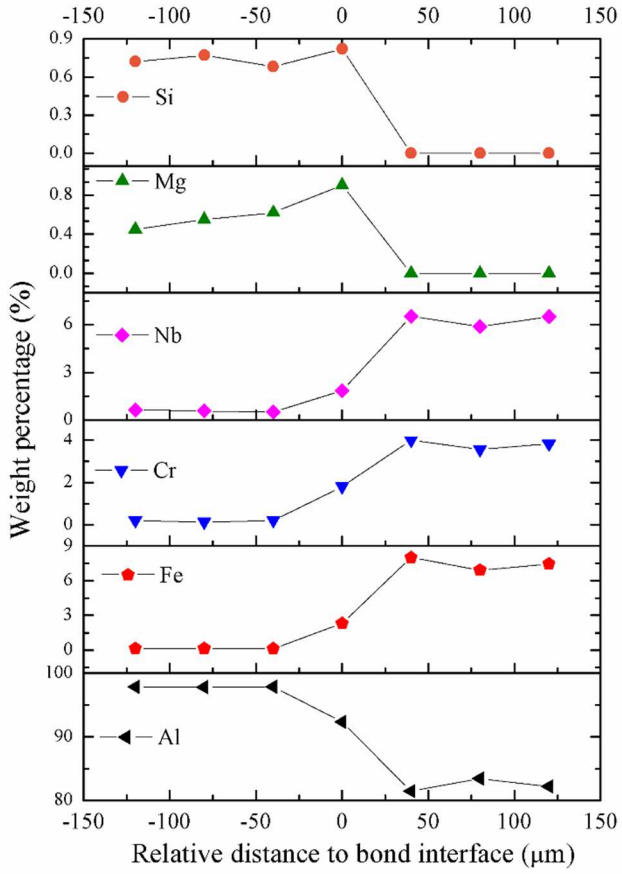

Figure 7.18 (b) – EDX quantified results showing the composition profile across the bond interface for different elements.

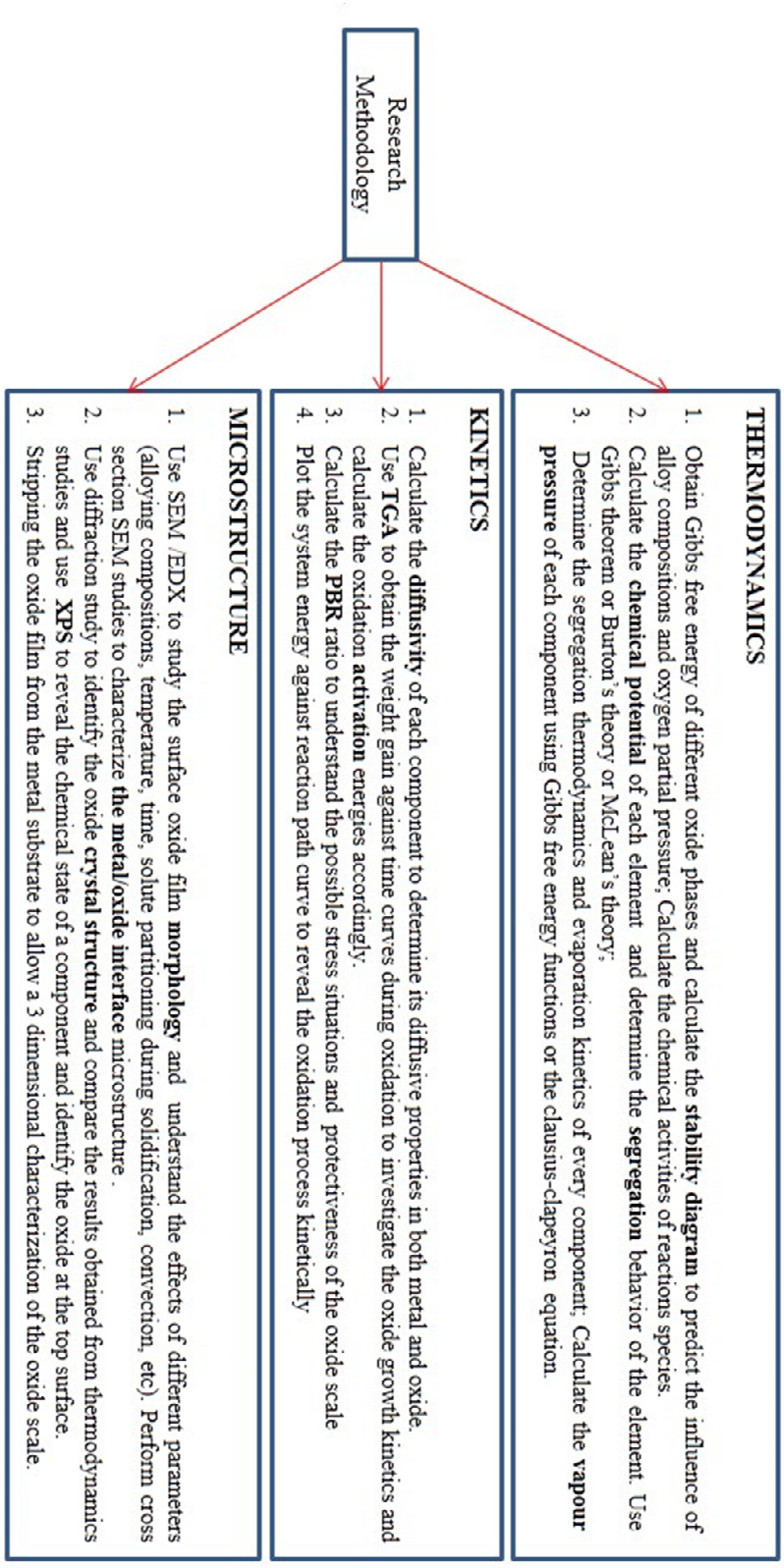

Figure 8.1 – Recommended methodology for oxidation studies of a system.